

NASA Conference Publication 3333

Flight Mechanics/ Estimation Theory Symposium 1996

*Proceedings of a symposium held at
NASA Goddard Space Flight Center
Greenbelt, Maryland
May 14 - 16, 1996*



NASA Conference Publication 3333

Flight Mechanics/ Estimation Theory Symposium 1996

Scott A. Greatorex, Editor
*Goddard Space Flight Center
Greenbelt, Maryland*

*Proceedings of a symposium sponsored by
NASA Goddard Space Flight Center
at Goddard Space Flight Center
Greenbelt, Maryland
May 14 - 16, 1996*



National Aeronautics and
Space Administration

**Scientific and Technical
Information Branch**

1996

This publication is available from the NASA Center for Aerospace Information,
800 Elkridge Landing Road, Linthicum Heights, MD 21090-2934, (301) 621-0390.

FOREWORD

The papers presented here have been derived primarily from speakers' summaries of talks presented at the Flight Mechanics/Estimation Theory Symposium held May 14-16, 1996, at the Goddard Space Flight Center. For completeness, abstracts are included for those papers which were presented but unavailable at the time of printing. Papers included in this document are presented as received from the authors, with little or no editing.

CONTENTS

	Page
SESSION 1	
A Simplified Pattern Match Algorithm For Star Identification	3
M. Lee (NASA/ GSFC)	
REQUEST- A Recursive QUEST Algorithm for Sequential Attitude Determination	15
I. Bar-Itzhack (NASA/ GSFC)	
Optimized TRIAD Algorithm for Attitude Determination	31
I. Bar-Itzhack, R. Harman (NASA/ GSFC)	
Variations on the Davenport Gyroscope Calibration Algorithm	41
G. Welter, J. Boia (CSC)	
M. Gakenheimer, E. Kimmer, D. Channell (ATSC)	
L. Hallock (NASA/ GSFC)	
Satellite Angular Rate Estimation from Vector Measurements	55
R. Azor, I. Bar-Itzhack, R. Harman (NASA/ GSFC)	
Attitude Estimation Using Modified Rodrigues Parameters	71
J. Crassidis (Catholic Univ. of America)	
F. Markley (NASA/ GSFC)	
SESSION 2	
Toward the Complete Regulator	87
D. Sonnabend (Analytical Engineering)	
Investigation of Models and Estimation Techniques for GPS Attitude Determination	89
J. Garrick (NASA/ GSFC)	

Attitude Drift Analysis for the WIND and POLAR Missions	99
P. Crouse (NASA/ GSFC)	
Solar and Heliospheric Observatory (SOHO) Flight Dynamics Simulations Using MATLAB	111
R. Headrick, J. Rowe (CSC)	
Attitude Accuracy Study for the Earth Observing System (EOS) AM-1 Spacecraft	125
J. Lesikar (CSC)	
J. Garrick (NASA/ GSFC)	
Attitude and Trajectory Estimation Using Earth Magnetic Field Data	135
J. Deutschmann, I. Bar-Itzhack (NASA/ GSFC)	
Attitude Determination Improvements for GOES	151
J. Crassidis	
F. Markley, A. Kyle (NASA/ GSFC)	
K. Kull (OSC)	

SESSION 3

An Evaluation of Attitude-Independent Magnetometer-Bias Determination Methods	169
J. Hashmall (CSC)	
J. Deutschmann (NASA/GSFC)	
Accuracy Studies of a Magnetometer-Only Attitude-and-Rate-Determination System	179
M. Challa, C. Wheeler (CSC)	
Geostationary Operational Environmental Satellite (GOES) Gyro Temperature Model	191
J. Rowe, C. Noonan (CSC)	
J. Garrick (NASA/ GSFC)	

ATTDES - An Expert System for Satellite Attitude Determination and Control, II	201
D. Mackison, K. Gifford (Univ. of Colorado)	
Balancing Science Objectives and Operations Constraints: A Mission Planner's Challenge	215
M. Weldy (ANSER)	
Modular Software for Spacecraft Navigation Using the Global Positioning System (GPS)	217
S. Truong, K. Hartman, D. Weidow, D. Berry (NASA/ GSFC)	
D. Oza, A. Long, E. Joyce, W. Steger (CSC)	
An Automated Real-Time Spacecraft Navigation System	229
P. Burkhart, V. Pollmeier (NASA/ JPL)	

SESSION 4

Experience Gained From Launch and Early Orbit Support of the Rossi X-Ray Timing Explorer (RXTE)	233
D. Fink, K. Chapman, W. Davis, J. Hashmall (CSC)	
R. Harman (NASA/ GSFC)	
South Atlantic Anomaly Entry and Exit As Measured by the X-Ray Timing Explorer	249
E. Smith, S. Antunes (Hughes STX)	
M. Stark (Univ. of Maryland)	
B. Giles (NASA/ GSFC)	
B. Gawne (ATSC)	
The Solar and Heliospheric Observatory Mission: An Overview of Flight Dynamics Support of the Early Mission Phase	257
R. Short, J. Behuncik (NASA/ GSFC)	

Flight Dynamics Mission Support And Quality Assurance Process	271
I. Oh (CSC)	
Experiences in Interagency and International Interfaces for Mission Support	283
G. Dell, W. Mitchell, T. Thompson, J. Cappellari (CSC)	
F. Flores-Amaya (NASA/ GSFC)	
Pulsed Plasma Thrusters for Small Spacecraft Attitude Control	295
M. McGuire (Analex Corp.)	
R. Myers (NYMA Inc.)	
Homotopy Solutions of Kepler's Equations	307
N. Fitz-Coy, J. Jang (Univ. of Florida)	

SESSION 5

Conversion Of Osculating Orbital Elements To Mean Orbital Elements	317
G. Der, R. Danchick (TRW)	
Downlink Probability Density Functions for EOS-McMurdo Sound	333
P. Christopher (Stanford Telecom)	
A. Jackson (NASA/ GSFC)	
Heuristic Modeling for TRMM Lifetime Predictions.	349
P. Jordan, P. Sharer (CSC)	
R. DeFazio (NASA/ GSFC)	
Autonomous Navigation with Ground Station One-Way Forward-Link Doppler Data	361
G. Horstkamp, D. Niklewski (CSC)	
C. Gramling (NASA/ GSFC)	
Reducing On-Board Computer Propagation Errors Due to Omitted Geopotential Terms By Judicious Selection of Uploaded State Vector	375
M. Beckman (NASA/ GSFC)	

Application of Tracking and Data Relay Satellite (TDRS) Difference

**One-Way Doppler (DOWD) Tracking Data for Orbit Determination
and Station Acquisition Support of User Spacecraft Without TDRS
Compatible Transponders 387**
 A. Olsezewski, T. Wilcox (CSC)
 M. Beckman (NASA/ GSFC)

FLIGHT MECHANICS/ESTIMATION THEORY SYMPOSIUM

MAY 14-16, 1996

SESSION 1

A Simplified Pattern Match Algorithm for Star Identification

Michael H. Lee

Goddard Space Flight Center (GSFC)

Greenbelt, Maryland, USA

Abstract

A true pattern matching star algorithm similar in concept to the Van Bezooijen¹ algorithm is implemented using an iterative approach. This approach allows for a more compact and simple implementation which can be easily adapted to be either an all-sky, no a priori algorithm or a follow on to a direct match algorithm to distinguish between ambiguous matches. Some simple analysis is shown to indicate the likelihood of mis-identifications. The performance of the algorithm for the all-sky, no a priori situation is detailed assuming the SKYMAP star catalog describes the true sky. The impact of errors and omissions in the SKYMAP catalog on performance are investigated. In addition, differing levels of noise in the star observations are assumed and results shown. The implications for possible implementation on-board spacecraft are discussed.

I. Introduction

The simplest approach to star identification is the "direct match" method. In this method, a star is considered to be identified if only one reference star is within a given angle of the observed star (transformed to an inertial frame by use of the estimated spacecraft attitude) and within a pre-determined tolerance of the observed light intensity.

With the advent of multi-observation star sensors, the possibility now exists to replace the direct match method of identifying stars onboard spacecraft with a pattern recognition system. However, existing pattern matching algorithms are not designed in a way which would allow maximum use of data from any onboard coarse attitude sensors. The concept of the algorithm described in this paper is to use a pattern match approach to distinguish the true match from a set of potential matches for each observed star. This allows a direct match approach to be

used to create the initial set of potential matches for each observation. In this way, the attitude determined from the coarse sensors, along with an estimate of the coarse attitude accuracy, can be used to determine a small set of potential matches for input to the pattern match algorithm. The algorithm is then more efficient than a traditional pattern match for ground systems and can be considered for onboard systems as the memory requirements are greatly reduced. For ease of reference, this algorithm will be known as the "hybrid" star identification method.

Other analysis presented here attempts to provide some practical guidelines in the use of pattern match algorithms. Various parameters such as observation noise and the number of stars identified have an influence on the likelihood of mis-identification of observed stars. Analysis is presented to determine the probability of incorrect identification for the simplest pattern, the 3 star case, and to show the influence due to pattern geometry.

Finally, the hybrid star identification algorithm will be applied to the "all-sky" case, where no attitude information is available. This is not a realistic case for most spacecraft which should have at least a knowledge of the Sun direction, and is especially not a reasonable approach if both the Sun and the magnetic field vector for the Earth are available (as for any low-earth orbiting spacecraft). However, although the hybrid algorithm does not give any efficiencies over other pattern matching algorithms in the all-sky case, the results for several situations (3, 4, and 5 stars observed with differing noise levels) illustrate the likelihood of mis-identification.

II. The Algorithm

The hybrid algorithm first uses a direct match algorithm which matches the stars in the reference catalog to the observations, choosing all stars within the (user input) angular and intensity tolerances as potential candidates for identification. These candidates are then input to the pattern matching portion of the algorithm. An estimate of the current attitude is needed for transforming the observations to the reference frame of the star catalog. This estimate can be derived from coarse sensors or based on previous star measurements propagated using gyro measurements.

The pattern matching part of the hybrid algorithm uses a pairwise matching approach similar to the Bezooijen approach. For each potential match for a given observation, the number of reference pairs which meet the matching tolerance are totaled, but with the restriction that only credit for one i - j pair will be counted for the i th star observation even if several potential candidates for the j th star meet the matching criteria. Clearly, counting several matches from a given i - j pair would be an error and, in this way, the maximum number of matches for a candidate for the i th star will be limited to $N-1$, where N is the total number of star observations.

After passing through all the pair combinations for the N observations, all candidates with fewer than a preset number of matches are removed from consideration and another pass through the remaining candidates is performed. The minimum number of matches for reliable star identification depends on the number of reference stars observed and the noise in the observations. This issue will be addressed in Section III.

The result is an iterative method, which was chosen for several reasons. The algorithm is simplified in comparison to methods which keep track of more information and can operate in one iteration (References 2 and 3). Less code is required for the iterative algorithm and, given reasonable initial attitude knowledge (within several degrees), should not require excessive processing. For some current missions (e. g. SWAS), memory capability onboard is more of a driver than availability of processing power, leading to the desirability of simplicity.

The iteration ceases when no more candidates are being removed, at which point the candidate with the greatest number of matches is chosen as the identified reference star. If there is a tie for a given star observation, several courses of action can be taken. For this paper, the star was determined to not be identified. Ties are generally due to close neighboring stars, and can be eliminated by implementing "nearest neighbor" restrictions on the reference star catalog.

If the algorithm is being used for single frame identification (all the star observations are taken at the same time), the number of matches should be equal to the number of identified stars minus 1. In the all-sky simulation discussed in Section IV, this is assumed to be the case. A match is considered to have been accomplished only if the final set of identified stars

meet this criteria. Onboard star identification processes are usually single frame.

Note that a "mirror image test" can be used to eliminate possible mismatches where the reference stars generate a reflection or mirror-image of the observed stars. This reduces the probability of mis-identifying stars by half. If the expected noise of the star sensor observations is low (on the order of 10 arcsecs) and a reasonable number of reference stars is observed in the field of view of the sensor, this probability is so low that the mirror test is not necessary. For the all-sky results included in this paper, extreme cases were investigated where the probability of mis-identification was significant and the mirror image test was implemented.

III. Probability of Mis-identification

The 2 and 3 star pattern cases will be considered. The positions of the reference stars are not randomly distributed, but in order to develop an estimate of pattern match mis-identifications, it will be assumed that the reference stars are evenly and randomly distributed in the sky.

Let the angular separation between two observed stars be R (radians) and let the maximum angular error given by the sensor noise be E (per axis of the star sensor, radians). The needed tolerance on pairwise matching to include all errors due to sensor noise is given by $T = 2\sqrt{2} \cdot E$. With the assumption that the reference stars are randomly and evenly distributed over the celestial sphere, the expected number of random matches to two observations separated by an angle R is given by

$$\frac{2 \cdot \pi \cdot \sin(R) \cdot [2 \cdot T] \cdot NSTARS}{4 \cdot \pi} \cdot NSTARS \quad (1)$$

where NSTARS is the number of reference stars visible to the sensor. The SKYMAP stars brighter than the predicted instrumental magnitude of 5.5 (for the Ball CT-601 CCD) were used as a test case, giving a total of 7306 stars in the test catalog. The estimated number of matches for a pairwise matching tolerance of 4 arcsecs versus the actual number seen in the catalog are tabulated below:

R (degrees)	Predicted # Matches	Observed # Matches
1	18.1	22
4	72.3	102
8	144.5	144
11.31	204.4	216

Table 1: Predicted Vs. Observed Matches for Star Pairs

Reasonable agreement between the theoretical and actual results is seen given the simplifying assumptions. The goal is to reach an order of magnitude estimate of the reliability of a pattern match algorithm. Note that the above table gives the number of stars matching the given separation R over the entire sky. If there is some a priori attitude information, the number of matches is reduced by a factor equal to the actual fraction of the sky which is searched for potential reference star matches.

Emboldened by the success of this simplistic approach, now consider a 3 star pattern. Let the 2 stars with the larger separation provide the base for the 3 star pattern (which will be a triangle unless the stars are co-linear). Assume that we have two stars which meet the pairwise matching tolerance for the base stars (with an angular separation of approximately R). Then the conditional probability of a mis-identification (given that the base stars have already been mis-identified) is the probability of a reference star existing near the expected location of the 3rd observed star given the error tolerance T on the pair matching algorithm. This area is depicted below (using plane geometry as an approximation to the spherical case). The shaded area in Figures 1 and 2 is intended to represent the intersection of two error bands, where the center of each error band is one of the two base stars.

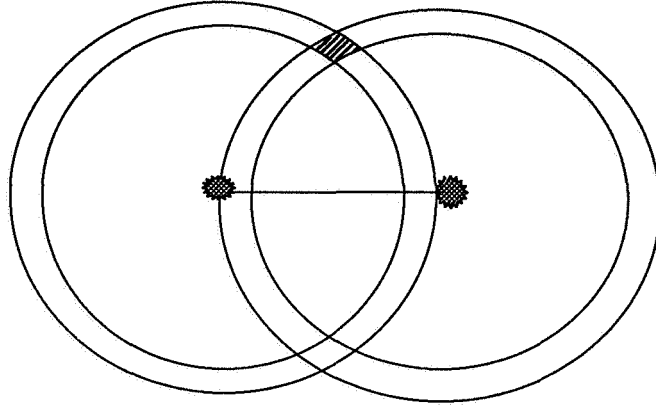


**Figure 1. Third Star Area to Pass Pairwise Tolerance Test:
Good Geometry Case**

The probability of mis-identification of the 3rd star depends on the geometry of the 3 observed stars. If the 3 stars are non-linear, the expected number of reference stars which will meet the pairwise match constraints approaches (for the best geometry cases)

$$\frac{[2 \cdot T]^2}{4 \cdot \pi} \cdot NSTARS \quad (2)$$

However, if the stars are co-linear, the area where stars will pass the pairwise matching test increases dramatically. This is illustrated in the figure below:

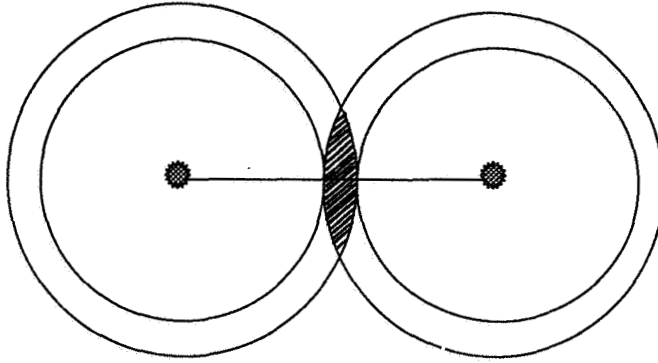


Figure 2. Third Star Area to Pass Pairwise Tolerance Test:
Bad Geometry Case

This results in a significant increase in the number of mis-identified stars. For the worst case geometry (the third star co-linear and equidistant from the 2 base stars), the expected number of reference stars which will meet the pairwise match constraints is approximated by the following expression,

$$2 \cdot T \cdot \frac{\sqrt{R \cdot T}}{4 \cdot \pi} \cdot NSTARS \quad (3)$$

where, as before, R is the separation of the 2 base stars. to ensure that the probability of 3 star pattern mis-identification is kept small, the worst case geometry must be considered when computing the expected number of mis-identified stars.

It is important to note that each additional star which is matched to a reference star via the hybrid match algorithm will decrease the probability of mis-identification by a factor dependent on the pairwise matching tolerance T (to a 3/2 power, for the worst case geometry). The less noise in the star

observations, the smaller the pairwise matching tolerance T . For the 5.5 magnitude test catalog used for Table 1, let the pairwise matching tolerance be 4 arcsec and assume 4 degrees for the 2 base star separation. The expected number of mis-identified stars, over the entire sky, is .003 using equations (1) and (3). This is a worst case number, showing that the identification of 3 reference stars from our test star catalog for a low noise sensor will be over 99.7% successful. Our result assumed a poor geometry situation and no a priori attitude information - thus grossly overestimating the probability of mis-identification. However, if a 4th star were matched, using equation (3) for a conservative estimate of the expected number of stars matching the 4th observation gives about 10^{-7} - about a 99.99999% success rate. As will be seen in the all-sky results, high levels of noise in the sensor observations can be countered if more stars are available for identification.

IV. All-sky Results

In order to test the hybrid match algorithm under extreme conditions, no a priori attitude information is assumed. In this case the hybrid algorithm is no different in concept from a standard pattern match technique. All stars in the reference catalog are taken as candidate matches for each observation.

The reference star catalog for this simulation is determined by choosing all stars with instrumental magnitudes of 5.0 or less from Version 3 of the SKYMAP catalog - a total of 4322 stars. Note that the tracker sensitivity can be selected, making this choice of catalog reasonable. The impact of observing non-catalog stars is discussed later. No other magnitude criteria is used to help identify stars, thus providing a greater challenge to the hybrid identification algorithm. Data from XTE has shown observed magnitude differences greater than 1.0 relative to the predicted magnitudes, so relying on magnitude criteria for all-sky matching can be ill-advised. Test cases are generated by evenly distributing tracker pointing attitudes about the celestial sphere and using those cases which contained the required number of reference stars.

As discussed in the previous section, given a star sensor's characteristics (observation noise and field of view size), rough estimates of the pattern match reliability in star identification can be made. The tolerance T for pairwise matching must be at least $2\sqrt{2}$ times the sensor noise (per axis) in order to accept all valid pairs. For the simulation, reference vectors from the SKYMAP catalog have random noise added to each component of the

pointing direction, with the noise limit given by the "noise" value in column 1 of Table 2.

Using equations (1) and (3) with $R = 4$ degrees, leads to the following estimates for the expected number of mis-identified star patterns for the shown values of T .

Noise/T (degrees)	3-Star Patterns	4-Star Patterns	5-Star Patterns
0.00/0.001	0.0003	4×10^{-9}	5×10^{-14}
0.005/0.015	0.26	.0002	2×10^{-7}
0.05/0.15	83	2	.05

Table 2: Expected Number of Mis-identified Patterns

Using the pattern match algorithm with no a priori attitude information, the following results were obtained. There were 114 3-star cases, 104 4-star cases, and 86 5-star cases. The frequency of mis-identified patterns in the simulation is reported as a fraction in the table below. Cases with expected number of mis-identifications greater than 1 are not simulated as each case would likely be mis-identified. If the expected number of mis-identified patterns is small, the probability of mis-identification is approximately equal to the expected number of mis-identified patterns. Thus, the expected number of mis-identified patterns should be a rough estimate of the fraction of mis-identified patterns seen (up to values on the order of a few tenths).

Noise/T (degrees)	3-Star Patterns	4-Star Patterns	5-Star Patterns
0.00/0.001	0.00	0.00	0.00
0.005/0.015	0.09	0.00	0.00
0.05/0.15	-	-	0.02

Table 3: Fraction of Mis-identified Patterns

In the statistics compiles above, cases where star patterns were correctly identified but a reference star was ambiguous due to the existence of multiple reference stars within the tolerance T of the correct reference star were deemed successful - enough stars were identified to allow computation of an accurate attitude. The algorithm is not required to distinguish between multiple reference stars closer than the assumed sensor noise. Reasonable correspondence of the simulated results with the

estimates of reliability is seen. The simulated results show better reliability (lower frequencies of mis-identification) than the estimates and this is expected as the estimated reliability assumed a worst case geometry for the star pattern.

The algorithm should behave well even if the sensor provides spurious observations or tracks non-catalog stars. As a test of this, the medium noise level (0.05 degrees) 5-star case was rerun using a catalog which was missing one of the reference stars for each 5-star pattern. In all cases, the remaining stars were identified correctly, duplicating the expected performance of the 4-star, medium noise case. As for all pattern match algorithms, the algorithm successfully eliminates observations which lack catalog stars and will still identify the reference stars which are available.

V. Implementation for Ground Systems

The implementation of star identification processing in a ground attitude determination system can lead to some additional problems. In ground systems, data over a long time might be accumulated using gyro data. The gyro data is used to form "clumps" of observations (which are assumed to represent observations from a single star) and to propagate these groups to a common time before transforming all the observation groups to the reference inertial frame. Then, the quality of the gyro data becomes the biggest factor in determining the parameters of the star identification procedure. The hybrid algorithm has been implemented in a test version of a ground system and spacecraft data from XTE has been processed. During a large angle slew, the number of distinct stars seen by XTE's 2 star trackers can number in the hundreds. To avoid the computing loads of testing all the pair combinations which increases geometrically with the number of stars observed, it was useful to feed the star observations in to the pattern match portion of the hybrid algorithm in smaller chunks (about 10 stars at a time). This has provided quick and accurate response. As a practical consideration, if the gyro propagation introduces a significant degree of error, it is important to increase the minimum number of star matches needed for star identification as the pairwise noise tolerance factor is increased.

For XTE, the matching tolerance T can be set to about 10 arcsecs while the spacecraft is inertial (and a minimum of 3 stars should be tracked for high reliability). When spacecraft maneuvers occur, the clumping errors force the tolerance T to be increased. As an example, using uncalibrated gyros on XTE to propagate observations (with approximately an 1 degree per hour

uncompensated bias), the matching tolerance T needed to be increased to 125 arcsec to allow identification of all reference stars. The minimum allowable number of matches was concurrently increased to 5, thus boosting the reliability of the star identification algorithm back to a high level. A feature of the hybrid algorithm is to provide adaptability to both high and low noise observations.

VI. Conclusions

The hybrid algorithm is robust with regard to inaccuracy in the a priori attitude and provides adaptability to extremes in gyro propagation errors and tracker noise. These features make it attractive for implementation in ground systems.

For onboard systems, current star sensors have the capability to track multiple stars simultaneously. Three or more stars are available over most of the sky (97% of the random attitudes used in the all-sky simulation had at least 3 stars brighter than instrumental magnitude 5.0 within 4 degrees of the sensor boresight). Missions such as XTE and SWAS are still using the direct match method. This method was implemented for spacecraft using trackers which could only track one star at a time and does not fully take advantage of the multi-star tracking.

The direct match technique leads to tight restrictions on spacecraft attitude determination accuracy over maneuvers, where the spacecraft typically is using gyro rate information only. An example of this is XTE, which must be within 200 arcsec of the target attitude after a maneuver in order for the onboard star identification to perform. Also, the spacecraft operators must ensure that the observed stars in the field of view after the maneuver have no other stars close enough to cause confusion - a "nearest neighbor" restriction. Depending on the expected accuracy of the spacecraft gyros, the nearest neighbor restriction can impose complex requirements on the spacecraft operators (SWAS is a good example of this, Reference 4). If a more sophisticated star identification algorithm were to be used onboard the spacecraft, these restrictions would be greatly eased. The hybrid algorithm is put forward as an example of an "add-on" to current onboard attitude determination software which would provide the robustness of pattern matching with only a modest increase in resource usage.

References

1. van Bezooijen, R. W. H., "Automated Star Pattern Recognition", PhD thesis, Stanford University, 1989
2. Murtagh, F., "A New Approach to Point-Pattern Matching", *Journal of the Astronomical Society of the Pacific*, Vol 104, April 1992
3. van Bezooijen, R. W. H., "True-sky Demonstration of an Autonomous Star Tracker", *Space Guidance, Control and Tracking*, Vol 2221, SPIE, Bellingham, WA, 1994
4. Daniel, W., et. al., "Development of a Direct Match Technique for Star Identification on the SWAS Mission", *Flight Mechanics Estimation Theory Symposium*, NASA Goddard Space Flight Center, Greenbelt, MD, May 1995

REQUEST - A RECURSIVE QUEST ALGORITHM FOR SEQUENTIAL ATTITUDE DETERMINATION

Itzhack Y. Bar-Itzhack*
Flight Dynamics Support Branch, Code 553
NASA Goddard Space Flight Center
Greenbelt, MD 20771

Abstract

In order to find the attitude of a spacecraft with respect to a reference coordinate system, vector measurements are taken. The vectors are pairs of measurements of the same generalized vector, taken in the spacecraft body coordinates, as well as in the reference coordinate system. We are interested in finding the best estimate of the transformation between these coordinate systems. The algorithm called QUEST yields that estimate where attitude is expressed by a quaternion. QUEST is an efficient algorithm which provides a least squares fit of the quaternion of rotation to the vector measurements. QUEST, however, is a single time point (single frame) batch algorithm, thus measurements that were taken at previous time points are discarded.

The algorithm presented in this work provides a recursive routine which considers all past measurements. The algorithm is based on the fact that the, so called, K matrix, one of whose eigenvectors is the sought quaternion, is linearly related to the measured pairs, and on the ability to propagate K. The extraction of the appropriate eigenvector is done according to the classical QUEST algorithm. This stage, however, can be eliminated, and the computation simplified, if a standard eigenvalue-eigenvector solver algorithm is used. The development of the recursive algorithm is presented and illustrated via a numerical example.

I. INTRODUCTION

The problem of finding attitude from vector observations is stated as follows. A sequence, b_i , $i=1,2, \dots, k$ of unit vectors is given. These unit vectors are the result of measurements performed in vehicle cartesian coordinates, of the directions to known objects. The sequence, r_i , $i=1,2, \dots, k$ of unit vectors, is the sequence of the corresponding unit vectors, resolved in a reference cartesian coordinate system. We wish to find the attitude matrix, A, which transforms vectors from the reference to the body coordinates. Obviously, A has to be an orthogonal matrix. In 1965, Wahba¹ posed this problem as a least squares problem as follows. Let

$$L(A) = \frac{1}{2} \sum_{i=1}^k |b_i - Ar_i|^2 \quad (1)$$

find that orthogonal 3x3 matrix, A, that minimizes L. We can weigh each measurement separately according to the accuracy of the particular vector measurement. In addition, we may want to find the quaternion, rather than the matrix, representation of attitude. In such case (1) is replaced by

*Sophie and William Shamban Professor of Aerospace Engineering. On sabbatical leave from the Faculty of Aerospace Engineering, Technion-Israel Institute of Technology, Haifa 32000, Israel. Member Technion Space Research Institute. IEEE Fellow. AIAA Associate Fellow.

This work was performed on a National Research Council NASA Research Associateship.

$$J(\mathbf{q}) = \frac{1}{2} \sum_{i=1}^k a_i | \mathbf{b}_i - A(\mathbf{q})\mathbf{r}_i |^2 \quad (2)$$

where $a_i, i=1,2, \dots, k$ are the positive weights assigned to each measurement. In (2) we are looking for that quaternion, \mathbf{q} , which minimizes J . Note that instead of minimizing J , we can maximize g defined as

$$g(\mathbf{q}) = 1 - J(\mathbf{q}) \quad (3)$$

It can be shown^{2,3} that $g(\mathbf{q})$ can be written as

$$g(\mathbf{q}) = \mathbf{q}^T \mathbf{K} \mathbf{q} \quad (4)$$

where \mathbf{K} is constructed as follows. Define

$$m_k = \sum_{i=1}^k a_i \quad (5.a)$$

$$\sigma = \frac{1}{m_k} \sum_{i=1}^k a_i \mathbf{b}_i^T \mathbf{r}_i \quad (5.b)$$

$$\mathbf{B} = \frac{1}{m_k} \sum_{i=1}^k a_i \mathbf{b}_i \mathbf{r}_i^T \quad (5.c)$$

$$\mathbf{S} = \mathbf{B} + \mathbf{B}^T \quad (5.d)$$

$$\mathbf{z} = \frac{1}{m_k} \sum_{i=1}^k a_i (\mathbf{b}_i \times \mathbf{r}_i) \quad (5.e)$$

Then

$$\mathbf{K} = \left[\begin{array}{c|c} \mathbf{S} - \sigma \mathbf{I} & \mathbf{z} \\ \hline \mathbf{z}^T & \sigma \end{array} \right] \quad (6)$$

where \mathbf{I} is the third order identity matrix. It was shown^{2,3} that \mathbf{q}^* , of unity length, which maximizes $g(\mathbf{q})$ in (4), satisfies the equation

$$\mathbf{K} \mathbf{q}^* = \lambda \mathbf{q}^* \quad (7)$$

where λ is a, yet undetermined, Lagrange multiplier. We realize that λ is an eigenvalue of \mathbf{K} and \mathbf{q}^* is the eigenvector which corresponds to λ . Substitution of this solution into (4) yields

$$g(\mathbf{q}^*) = \lambda \quad (8)$$

and since we wish to maximize g , we choose λ_{\max} , the largest eigenvalue of \mathbf{K} , as the desired eigenvalue, and then, \mathbf{q}^* is the eigenvector which corresponds to this λ_{\max} . Davenport² showed that once λ_{\max} is found, there is no need to solve for the eigenvector of \mathbf{K} , since \mathbf{y}^* , the optimal vector of Rodrigues parameters⁴, (also known as Gibbs vector⁵) can be computed as follows

$$y^* = [(\lambda_{\max} + \sigma)I - S]^{-1}z \quad (9)$$

and the optimal quaternion can be found using the known relation

$$q^* = \frac{1}{\sqrt{1 + |y^*|^2}} \begin{bmatrix} y^* \\ 1 \end{bmatrix} \quad (10)$$

Shuster^{6,7} showed how to, easily, compute λ_{\max} to arbitrary accuracy, and how to deal with a singular matrix in (9). It was also shown there that λ_{\max} is close to 1 and is exactly 1 when the measurements are error-free. (This property is due to the fact that all a_i 's in (2) add up to 1, or, equivalently, the introduction of the normalizing factor m_k in to (5.b, c, and e)). The algorithm for obtaining λ_{\max} and q^* from vector observations discussed above is known as the QUEST algorithm.

QUEST is a single point attitude determination algorithm; that is, it utilizes the vector measurements obtained at a single time point and uses them, and them only, to determine the attitude at that time point. This way, the information contained in past measurements, is lost. This fact has been recognized and in 1989, Shuster⁸ presented an algorithm which he named Filter QUEST that processes vector measurements recursively. The Attitude Profile Matrix, B, defined in (5.c), which plays a central role in the algorithm, is updated recursively for use in the QUEST algorithm. Much attention is given, in that paper, to covariance calculations.

In the present work, the matrix, which is updated recursively, is the K matrix defined in (5) and (6). Indeed, as can be seen in the algorithm described above, K is the most important element in QUEST. In the following section, we start our presentation of REQUEST by considering, first, the recursive time-invariant algorithm. Then, in Section III, we develop the recursive algorithm for the time-varying case and present an example. In Section IV we list the algorithm in a unified form. Finally, in Section V, we present our conclusions and recommendation for further work.

II. THE RECURSIVE TIME-INVARIANT ALGORITHM

Assume that the body axes are non-rotating with respect to the reference axes. Also assume that k vectors have been processed using the QUEST algorithm.

Let

$$m_k = \sum_{i=1}^k a_i \quad (11.a)$$

where m_k is not necessarily equal to 1. Also define

$$\sigma_k = \frac{1}{m_k} \sum_{i=1}^k a_i b_i^T r_i \quad (11.b)$$

$$B_k = \frac{1}{m_k} \sum_{i=1}^k a_i b_i r_i^T \quad (11.c)$$

$$S_k = B_k + B_k^T \quad (11.d)$$

$$z_k = \frac{1}{m_k} \sum_{i=1}^k a_i (b_i \times r_i) \quad (11.e)$$

The parameters σ_k , S_k and z_k , are then used to compute K , which for the case of k measurements, is denoted by K_k . The latter is used to find the optimal quaternion, based on k pairs of measured vectors. (Note that QUEST doesn't require the computation of K_k itself). As mentioned earlier, the coefficient m_k is used in (11.b, c, and e) to normalize the weights, a_i , such that λ_{\max} is closed to 1. (See Ref. 5 for the solution of λ_{\max}). Now suppose that an additional measurement has been acquired; that is, the $k+1$ st pair has to be processed. The question is then, do we have to re-compute the K_{k+1} matrix anew or can we, perhaps, update K_k to included the added pair. As will be shown next, the latter is possible. In fact, it forms the basis for the REQUEST algorithm. We formulate this quality of K in the following proposition.

Proposition 1: Let

$$\delta\sigma_{k+1} = a_{k+1} b_{k+1}^T r_{k+1} \quad (12.a)$$

$$\delta B_{k+1} = a_{k+1} b_{k+1} r_{k+1}^T \quad (12.b)$$

$$\delta S_{k+1} = \delta B_{k+1} + \delta B_{k+1}^T \quad (12.c)$$

$$\delta z_{k+1} = a_{k+1} (b_{k+1} \times r_{k+1}) \quad (12.d)$$

$$\delta K_{k+1} = \left[\begin{array}{c|c} \delta S_{k+1} - \delta\sigma_{k+1} I & \delta z_{k+1} \\ \hline \delta z_{k+1}^T & \delta\sigma_{k+1} \end{array} \right] \quad (12.e)$$

then

$$K_{k+1} = \frac{m_k}{m_{k+1}} K_k + \frac{1}{m_{k+1}} \delta K_{k+1} \quad (13)$$

Proof: By definition

$$m_{k+1} = \sum_{i=1}^{k+1} a_i \quad (14.a)$$

Now, it can be easily verifies that

$$\sigma_{k+1} \triangleq \frac{1}{m_{k+1}} \sum_{i=1}^{k+1} a_i b_i^T r_i = \frac{1}{m_{k+1}} \sum_{i=1}^k a_i b_i^T r_i + \frac{1}{m_{k+1}} a_{k+1} b_{k+1}^T r_{k+1} \quad (14.b)$$

$$B_{k+1} \triangleq \frac{1}{m_{k+1}} \sum_{i=1}^{k+1} a_i b_i r_i^T = \frac{1}{m_{k+1}} \sum_{i=1}^k a_i b_i r_i^T + \frac{1}{m_{k+1}} a_{k+1} b_{k+1} r_{k+1}^T \quad (14.c)$$

$$S_{k+1} \triangleq B_{k+1} + B_{k+1}^T = B_k + B_k^T + \delta B_{k+1} + \delta B_{k+1}^T \quad (14.d)$$

$$z_{k+1} \triangleq \frac{1}{m_{k+1}} \sum_{i=1}^{k+1} a_i (b_i \times r_i) = \frac{1}{m_{k+1}} \sum_{i=1}^k a_i (b_i \times r_i) + \frac{1}{m_{k+1}} a_{k+1} (b_{k+1} \times r_{k+1}) \quad (14.e)$$

Using the definitions in (11) and (12), (14.b) to (14.e) can be written as follows

$$\sigma_{k+1} = \frac{m_k}{m_{k+1}} \sigma_k + \frac{1}{m_{k+1}} \delta \sigma_{k+1} \quad (15.a)$$

$$S_{k+1} = \frac{m_k}{m_{k+1}} S_k + \frac{1}{m_{k+1}} \delta S_{k+1} \quad (15.b)$$

$$z_{k+1} = \frac{m_k}{m_{k+1}} z_k + \frac{1}{m_{k+1}} \delta z_{k+1} \quad (15.c)$$

When σ_{k+1} , S_{k+1} , and z_{k+1} defined in (15) are used to form K_{k+1} , using the format of (6), (13) results. This ends the proof.

We have assumed here that we add only one new measurement to the k measurements that were already processed. This can be extended to the case where two or more measurements are added as a group of measurements. Suppose that K was computed n times where at each time, one or more measurements were used to compute (initially) or to update K . Let this K be denoted by K_n , $n=1,2, \dots$, where K_1 is computed using (5) and (6), and where the index k is the number of measurements used to compute K_1 . Suppose that j new pairs of vectors are measured and we want to use them in the updating of K . We can, of course, update K_n j times, using the algorithm presented in Proposition I, and obtain the updated K , or we can lump the new j measurements together, and update K only once. The latter is performed according to the algorithm listed in the following proposition.

Proposition 2: Let

$$\delta m_{n+1} = \sum_{i=k+1}^{k+j} a_i \quad (16.a)$$

where k is the number of, already processed, pairs of vector measurements,

$$\delta \sigma_{n+1} = \sum_{i=k+1}^{k+j} a_i b_i^T r_i \quad (16.b)$$

$$\delta B_{n+1} = \sum_{i=k+1}^{k+j} a_i b_i r_i^T \quad (16.c)$$

$$\delta S_{n+1} = \delta B_{n+1} + \delta B_{n+1}^T \quad (16.d)$$

$$\delta z_{n+1} = \sum_{i=k+1}^{k+j} a_i (b_i \times r_i) \quad (16.e)$$

$$\delta K_{n+1} = \left[\begin{array}{c|c} \delta S_{n+1} - \delta \sigma_{n+1} I & \delta z_{n+1} \\ \hline \delta z_{n+1}^T & \delta \sigma_{n+1} \end{array} \right] \quad (16.f)$$

then

$$m_{n+1} = m_n + \delta m_{n+1} \quad (17.a)$$

and

$$K_{n+1} = \frac{m_n}{m_{n+1}} K_n + \frac{1}{m_{n+1}} \delta K_{n+1} \quad (17.b)$$

This proposition can be easily proven along the lines of the proof of the first proposition. The case described in the first proposition is a special case of the latter. we chose to split the introduction of the updating of K into two cases merely for methodical reasons.

III. THE RECURSIVE TIME-VARYING ALGORITHM

The updating algorithm of the static case can now be extended to the case where the body rotates between measurements. In the ensuing development we distinguish between two cases; namely, the error-free propagation case, and the propagation which is based on angular rate measurement, and as such, is contaminated by rate-measurement errors.

III.1 Error-Free Propagation

Assume that at time t_n , k pairs were processed, then the body rotated to a new orientation and there, at time t_{n+1} , j new vector measurements were performed. We wish to find the least squares fit of the quaternion to the first k measurements, at this new time point, and then do the same when the new j measurements are considered too. So first we are interested in finding $q_{n+1/n}^*$ which is the quaternion that expresses best the attitude at time t_{n+1} , based on the first k measurements which were performed previously, at time t_n . Let us re-write the cost function of (4) for q at time t_n based on the first k measurements which, as mentioned, were performed at time t_n

$$g(q_{n/n}) = q_{n/n}^T K_{n/n} q_{n/n} \quad (18)$$

It is well known⁹ that during the rotation, q changes according to the differential equation

$$\dot{q} = \frac{1}{2} \Omega q \quad (19)$$

where Ω is a 4x4 skew symmetric matrix whose elements are the body components of the vector of the angular velocity of the body with respect to the reference frame. The solution of (19) yields

$$q(t_{n+1}) = \Phi(t_{n+1}, t_n) q(t_n) \quad (20)$$

Ideally, when Ω is known perfectly, the matrix $\Phi(t_{n+1}, t_n)$, known as Transition Matrix, transforms the quaternion which represent the attitude at time t_n , to that which represents attitude at time t_{n+1} . For simplicity of notations, we denote it, simply, by Φ . The quaternion which we wish to transform from time t_n to time t_{n+1} is $q_{n/n}$, thus we set $q(t_n) = q_{n/n}$. Finally, we denote the quaternion, to which $q_{n/n}$ is transformed, by $q_{n+1/n}$, thus we set $q(t_{n+1}) = q_{n+1/n}$. Consequently (18) becomes

$$q_{n+1/n} = \Phi q_{n/n} \quad (21)$$

Since Ω is skew symmetric, Φ is orthogonal, thus we can write

$$\mathbf{q}_{n/n} = \Phi^{-1} \mathbf{q}_{n+1/n} = \Phi^T \mathbf{q}_{n+1/n} \quad (22)$$

Substitution of $\mathbf{q}_{n/n}$ of (22) into (18) yields

$$g(\mathbf{q}_{n/n}) = g'(\mathbf{q}_{n+1/n}) = \mathbf{q}_{n+1/n}^T \Phi K_{n/n} \Phi^T \mathbf{q}_{n+1/n} \quad (23)$$

We realize that the problem of finding $\mathbf{q}_{n/n}$ that maximizes g has been transformed into the problem of finding $\mathbf{q}_{n+1/n}$ which maximizes g' . Let

$$K_{n+1/n} = \Phi K_{n/n} \Phi^T \quad (24)$$

then (23) becomes

$$g'(\mathbf{q}_{n+1/n}) = \mathbf{q}_{n+1/n}^T K_{n+1/n} \mathbf{q}_{n+1/n} \quad (25)$$

One may ask oneself whether the problem of finding $\mathbf{q}_{n+1/n}$, which maximizes g' , is still related to Wahba's problem; that is, will the maximization of g' yield a quaternion which is a least squares fit to the k vector measurements. The answer is, of course, positive, since the maximizing $\mathbf{q}_{n+1/n}$ is directly related, through (22), to $\mathbf{q}_{n/n}$ which maximizes (18), and the latter is the solution of Wahba's problem, given the k measurements. It can be shown (see the Appendix) that, like before, $\mathbf{q}_{n+1/n}^*$, which is the $\mathbf{q}_{n+1/n}$ that maximizes g' , given in (25), satisfies the equation

$$K_{n+1/n} \mathbf{q}_{n+1/n}^* = \lambda_{n+1/n} \mathbf{q}_{n+1/n}^* \quad (26)$$

and that $\lambda_{n+1/n}^*$ is the eigenvalue of $K_{n+1/n}$ which corresponds to the largest eigenvalue of $K_{n+1/n}$. It is interesting to note that this solution to the constrained optimization problem is not specific to attitude determination. It stems from the fact that the cost function is defined as a quadratic form of a square matrix and that \mathbf{q} is required to be of unity length. (See the Appendix). Also note that although we assume error-free propagation, the measured vectors contain measurement errors. Finally, note that $K_{n+1/n}$, being a result of a similarity transformation on $K_{n/n}$, has the eigenvalues of the latter even though its eigenvectors are different.

Now that we have established the fact that $K_{n+1/n}$ is the proper K matrix for finding the least squares fit of the quaternion at time t_{n+1} based on all past k measurements, we can include j more measurements performed at t_{n+1} . For this we use (17.b) of Proposition II. Consequently from (24) and (17.b) we obtain

$$K_{n+1/n} = \Phi K_{n/n} \Phi^T \quad (27.a)$$

$$K_{n+1/n+1} = \frac{m_n}{m_{n+1}} K_{n+1/n} + \frac{1}{m_{n+1}} \delta K_{n+1} \quad (27.b)$$

We demonstrate the algorithm by way of the following example.

Example:

Data base:

Given are 4 error free vectors in the reference coordinate frame:

$$r1 = \begin{bmatrix} 0.267 \\ 0.535 \\ 0.802 \end{bmatrix} \quad r2 = \begin{bmatrix} -0.667 \\ -0.667 \\ -0.333 \end{bmatrix} \quad r3 = \begin{bmatrix} 0.267 \\ -0.802 \\ 0.535 \end{bmatrix} \quad r4 = \begin{bmatrix} -0.447 \\ 0.894 \\ 0.000 \end{bmatrix}$$

and a rotation from the reference to body axes described by the following Euler vector:

$$\phi^T = [0.9, 0.2, 0.8]$$

The corresponding quaternion is:

$$q(1)^T = [0.423, 0.094, 0.376, 0.819]$$

The four r vectors are transformed to the body frame and noise is added to the transformed vectors. The noise elements added to each component of the transformed vectors is drawn from a random number generator. The standard deviation of the noises are:

$$\sigma_1 = 0.01 \quad \sigma_2 = 0.05 \quad \sigma_3 = 0.03 \quad \sigma_4 = 0.02$$

The noise element added to each component of r_i is drawn from the random number generator whose standard deviation is σ_i , $i = 1, 2, 3, 4$. The vectors are then normalized. The resulting simulated measured vectors in body frame are then:

$$b1 = \begin{bmatrix} 0.688 \\ 0.662 \\ 0.297 \end{bmatrix} \quad b2 = \begin{bmatrix} -0.985 \\ -0.120 \\ -0.123 \end{bmatrix} \quad b3 = \begin{bmatrix} -0.280 \\ -0.030 \\ 0.959 \end{bmatrix} \quad b4 = \begin{bmatrix} 0.303 \\ 0.575 \\ -0.760 \end{bmatrix}$$

and the weights are chosen to be:

$$a_i = \sigma_i^{-2} \quad i = 1, 2, 3, 4$$

Application of QUEST to the first two pairs:

Using, initially, at time t_1 , the first two pairs of vectors, $r1$ and $b1$, and $r2$ and $b2$, we obtain $K_{1/1}$. Its largest eigenvalue and the corresponding eigenvector, which, according to our notations, is $q_{1/1}$, are:

$$\lambda_{1/1} = 1.0003551 \quad q_{1/1}^T = [0.427, 0.105, 0.383, 0.813]$$

The corresponding transformation matrix, $A_{1/1}$, the correct matrix, $A(1)$, and the difference (error) matrix, are:

$$A_{1/1} = \begin{bmatrix} 0.685 & 0.712 & 0.156 \\ -0.532 & 0.343 & 0.774 \\ 0.497 & -0.613 & 0.614 \end{bmatrix} \quad A(1) = \begin{bmatrix} 0.700 & 0.695 & 0.164 \\ -0.536 & 0.361 & 0.763 \\ 0.471 & -0.622 & 0.625 \end{bmatrix}$$

$$A_{1/1} - A(1) = \begin{bmatrix} -0.015 & 0.017 & -0.007 \\ 0.004 & -0.018 & 0.011 \\ 0.026 & 0.009 & -0.012 \end{bmatrix}$$

The Euclidean norm of the error matrix is:

$$|A_{1/1} - A(1)| = 0.044 \quad (28)$$

This error stems, of course, from the measurement error contained in the \mathbf{b} vectors.

Rotation of the body coordinate system:

We assume that after processing the first two pairs, which yielded $A_{1/1}$, the body rotates for 1 sec at the following angular rate:

$$\omega^T = [0.1, 0.2, -0.3] \text{ rad/sec}$$

The matrix Φ which propagates the quaternion of this rotation (see (21)), and, ΔA , the attitude matrix which expresses the change in the body coordinates are:

$$\Phi = \begin{bmatrix} 0.983 & -0.149 & -0.099 & 0.050 \\ 0.149 & 0.983 & 0.050 & 0.099 \\ 0.099 & -0.050 & 0.983 & -0.149 \\ -0.050 & -0.099 & 0.149 & 0.983 \end{bmatrix} \quad \Delta A = \begin{bmatrix} 0.936 & -0.283 & -0.210 \\ 0.303 & 0.951 & 0.068 \\ 0.181 & -0.127 & 0.975 \end{bmatrix}$$

Measurement update of K:

We use ΔA to transform \mathbf{b}_3 and \mathbf{b}_4 to the new time point, t_2 . Using these \mathbf{b} 's as the simulated measurements at t_2 , we compute δK_2 according to (16), and update K , using (27), as follows:

$$K_{2/1} = \Phi K_{1/1} \Phi^T$$

$$K_{2/2} = \frac{m_1}{m_2} K_{2/1} + \frac{1}{m_2} \delta K_2$$

The largest eigenvalue and the corresponding eigenvector (which is $\mathbf{q}_{2/2}$) of $K_{2/2}$ are:

$$\lambda_{2/2} = 1.0001957 \quad \mathbf{q}_{2/2}^T = [0.402, 0.253, 0.282, 0.834]$$

The corresponding attitude matrix is:

$$A_{2/2} = \begin{bmatrix} 0.713 & 0.673 & -0.195 \\ -0.267 & 0.518 & 0.813 \\ 0.648 & -0.528 & 0.549 \end{bmatrix}$$

Check:

We wish, now, to check this result. This is done as follows. We use ΔA to transform b_1 and b_2 to the new time point, t_2 . (Recall that b_3 and b_4 were already transformed in order to compute δK_2). Now we apply the QUEST algorithm to all four pairs of r and b . The resulting quaternion should be equal to the quaternion updated by the REQUEST algorithm. Indeed the two quaternions agree to at least 10^{-12} .

Remark:

When we compare, $A(2) = \Delta A \cdot A(1)$, which is the correct matrix which transforms from the reference to body axes at t_2 , to the attitude matrix $A_{2/2}$, obtained by REQUEST (and, as we just checked, by QUEST as well), we obtain:

$$A_{2/2} - A(2) = \begin{bmatrix} 0.005 & -0.006 & 0.000 \\ -0.001 & 0.007 & -0.005 \\ -0.006 & -0.001 & 0.007 \end{bmatrix}$$

The Euclidean norm of this error matrix is:

$$|A_{2/2} - A(2)| = 0.015$$

This error stems from the measurement noise in the b vectors and not from the algorithm. We note that the latter error is smaller than $|A_{1/1} - A(1)|$ shown in (28). This is expected, since $A_{2/2}$ is computed using four pairs of vectors whereas $A_{1/1}$ is computed using only two.

III.2 Noisy Propagation

In the preceding developments we considered the presence of noise only in the measurements and assumed that the angular rate vector, ω , was known to us perfectly. We wish to consider now errors also in our knowledge of ω . Let us denote the measured, or computed, ω by ω_m . We also assume that the error is additive, thus we can write

$$\omega_m = \omega + \varepsilon \tag{29}$$

where ε is the error component in the measured angular rate vector. We distinguish between two cases; namely, short time application, and long time application of REQUEST. The two are treated next.

III.2.1 Short Mission Duration

Since a typical update rate is once per second, typical gyro noise does not cause a considerable attitude error during such a short period. In fact, even with an update rate of once per 10 seconds, the attitude error amounts to a very small attitude error. To illustrate this point, we turn to the example. Suppose that we use a triad of single axis gyros, each having a constant drift rate of $1^\circ/h$,

which is about 100 times larger than that of inertial grade gyros. We use the first three measurements to compute $K_{1/1}$ and from it, $A_{1/1}$. We then propagate $K_{1/1}$ using Φ_m , the gyro-error ridden transition matrix, and obtain $K_{2/1,m}$ and then compute the corresponding attitude matrix, $A_{2/1,m}$. In parallel we do the same using Φ , the correct transition matrix, and obtain $A_{2/1}$, the corresponding attitude matrix. Doing so, we discover that the largest difference between the magnitude of the elements of the two attitude matrices, $A_{2/1,m}$ and $A_{2/1}$, is less than $5.23 \cdot 10^{-6}$. Next, following the REQUEST algorithm, we use the fourth measurement at time t_2 to compute δK_2 , update both, $K_{2/1,m}$ and $K_{2/1}$, and compute the corresponding attitude matrix for the correct and erroneous propagations. The largest error between the elements of the, updated, two attitude matrices is less than $2.55 \cdot 10^{-6}$. We see two interesting facts. First, indeed, the gyro error has little effect on the propagated K and, consequently, on the, propagated and the updated, attitude matrices. Second, the incorporation of a new measurement reduces the little error, caused by gyro drift, even further. As a consequence of this discussion, we conclude that for a short mission duration the build up of attitude errors as a result of gyro drift is negligible and the algorithm given in (27) is adequate.

III.2.2 Long Mission Duration

Space missions where QUEST is traditionally being used, are of long duration, therefore the initial measurements are propagated through the repeated use of (27.a) to the current time. This in turn reduces the accuracy of those measurements, and as time goes by they may corrupt the attitude rather than improve it. Consequently, we wish to gradually reduce the influence of old measurements, and eventually eliminate them altogether. This is usually done using the Fading Memory¹⁰ concept. Accordingly, instead of using (27.b) for updating K, we may want to use the following algorithm

$$K_{n+1/n+1} = \rho_n \frac{m_n}{m_{n+1}} K_{n+1/n} + \frac{1}{m_{n+1}} \delta K_{n+1} \quad (30.a)$$

where $0 < \rho_n \leq 1$. Note that ρ_n has to be larger than 0 for (28.a) to yield a meaningful K when only one measurement is performed at t_{n+1} . Also note that when no process noise is present, we set $\rho_n = 1$ which keeps the same relative weighting of past and present measurements as in (27.b). The value of ρ_n can be determined experimentally where a larger propagation noise is compensated by a smaller ρ_n value. Note that ρ_n can vary from step to step allowing the consideration of changing gyro noise. It should be noted that the introduction of m_n in the REQUEST algorithm stems from our wish to maintain $\lambda_{\max} \cong 1$. This is important if we use the classical QUEST method for solving for λ_{\max} [see ref. 7]. (If we use a given eigenvalue-eigenvector solver routine, this is irrelevant). When (28.a) is used and we are still interested in having λ_{\max} close to 1, we have to replace (28.a) by

$$K_{n+1/n+1} = \frac{\rho_n m_n}{\rho_n m_n + \delta m_{n+1}} K_{n+1/n} + \frac{1}{\rho_n m_n + \delta m_{n+1}} \delta K_{n+1} \quad (30.b)$$

Note that, as before, this K update algorithm still assures proper weighing of the measurements; that is, the measurement noise is properly considered.

IV. ALGORITHM SUMMARY

The REQUEST algorithm is summarized as follows.

1. Use the k measurements performed at the starting point, t_1 , to compute $K_{1/1}$. First compute:

$$m_k = \sum_{i=1}^k a_i \quad (31.a)$$

$$\sigma = \frac{1}{m_k} \sum_{i=1}^k a_i b_i^T r_i \quad (31.b)$$

$$B = \frac{1}{m_k} \sum_{i=1}^k a_i b_i r_i^T \quad (31.c)$$

$$S = B + B^T \quad (31.d)$$

$$z = \frac{1}{m_k} \sum_{i=1}^k a_i (b_i \times r_i) \quad (31.e)$$

Then compute:

$$K_{1/1} = \begin{bmatrix} S - \sigma I & z \\ z^T & \sigma \end{bmatrix} \quad (31.f)$$

2. Form the angular rate matrix:

$$\frac{1}{2} \Omega = \frac{1}{2} \begin{bmatrix} 0 & \omega_z & -\omega_y & \omega_x \\ -\omega_z & 0 & \omega_x & \omega_y \\ \omega_y & -\omega_x & 0 & \omega_z \\ -\omega_x & -\omega_y & -\omega_z & 0 \end{bmatrix} \quad (32)$$

where, $\omega_i, i=1,2,3$ are the components of the body axes, angular rate vector.

3. Compute Φ , the transition matrix from time t_1 to time t_2 , corresponding to this, generally time-varying, angular rate matrix. (Algorithms for computing Φ can be found in standard Control Theory or State Estimation texts. See e.g. Gelb¹¹.)

4. Propagate $K_{1/1}$ according to:

$$K_{2/1} = \Phi K_{1/1} \Phi^T \quad (33)$$

5. Compute δK_2 as follows:

$$\delta m_2 = \sum_{i=k+1}^{k+j} a_i \quad (34.a)$$

(where k is the number of, already processed, pairs of vector measurements, and j is the number of new measurement pairs performed at time t_2).

$$\delta \sigma_2 = \sum_{i=k+1}^{k+j} a_i b_i^T r_i \quad (34.b)$$

$$\delta B_2 = \sum_{i=k+1}^{k+j} a_i b_i r_i^T \quad (34.c)$$

$$\delta S_2 = \delta B_2 + \delta B_2^T \quad (34.d)$$

$$\delta z_2 = \sum_{i=k+1}^{k+j} a_i (b_i \times r_i) \quad (34.e)$$

$$\delta K_2 = \left[\begin{array}{c|c} \delta S_2 - \delta \sigma_2 I & \delta z_2 \\ \hline \delta z_2^T & \delta \sigma_2 \end{array} \right] \quad (34.f)$$

then set ρ_n in the range

$$0 < \rho_n \leq 1 \quad (34.g)$$

and compute

$$K_{2/2} = \frac{\rho_1 m_1}{\rho_1 m_1 + \delta m_2} K_{2/1} + \frac{1}{\rho_1 m_1 + \delta m_2} \delta K_2 \quad (34.h)$$

In preparation for the next time update, compute

$$m_2 = m_1 + \delta m_2 \quad (34.i)$$

6. Only if there is an interest in extracting the attitude from $K_{2/2}$, compute the attitude at this time point (t_2), otherwise go to step 7. The extraction of attitude from $K_{2/2}$ can be done using the algorithm given in QUEST, or any standard software package that can compute eigenvalues and eigenvectors of a symmetric matrix (e.g. MatlabTM or MathcadTM). If the latter approach is chosen, then, first, select the largest eigenvalue of $K_{2/2}$, and, then, compute the corresponding eigenvector.

7. Go to step 2 and increase the appropriate indices by 1, or stop if so desired.

V. CONCLUSIONS AND RECOMMENDATIONS

In this work we presented a recursive algorithm for attitude determination, from vector observations, that was derived from QUEST. The new recursive algorithm, which we call REQUEST, is based on the propagation and update of the K matrix, one of whose eigenvectors is the sought attitude quaternion. Using REQUEST, we do not lose information gathered by measurements performed at previous time points, and since we use prior information, even one measurement at a particular time point, to which K is propagated, is sufficient for updating the attitude. We showed how to apply the algorithm to cases where more than one measurement is taken at the new time point. We demonstrated that under normal conditions, and for short mission durations, there is no need to treat propagation noise (also known as process noise). For long mission durations we do have to consider the process noise. This is done using the Fading-Memory notion whereby the weight of the contribution of old measurements to K is reduced with time. We presented an example to illustrate the algorithm.

As mentioned, the new algorithm shows how the propagate and update K, but once K is computed, its largest eigenvalue and the corresponding eigenvector, which is the sought quaternion, are found using the method of QUEST. If, however, a standard eigenvalue-eigenvector solver algorithm, is used, then the eigenvalue and eigenvector can be found directly without solving for Rodrigues parameters, and without the need to be concerned about matrix singularity problems (see (9)).

As a follow up to this work, it is recommended that REQUEST be tested using real spacecraft data, and be tested against other recursive algorithms, such as the extended Kalman filter.

Acknowledgement

We wish to thank F. Landis Markley for his helpful comments, particularly on the damping of past measurements in long duration missions.

Appendix

In this appendix we prove that a cost function formulated as a quadratic form of a real symmetric matrix, with a unity constraint on the vector part of this form, has the following two qualities:

- I. Its maximum is equal to the value of the matrix largest eigenvalue.
- II. The vector which maximizes the cost function is the matrix eigenvector which corresponds to this eigenvalue

We present the proof in a form of a question and an answer as follows.

Problem: *Given*

$$\mu = \mathbf{x}^T \mathbf{M} \mathbf{x} \quad (\text{A.1}) \quad \text{where} \quad |\mathbf{x}| = 1 \quad (\text{A.2})$$

and \mathbf{M} is an $n \times n$ symmetric matrix, find \mathbf{x} which maximizes μ .

Solution: We use the method of Lagrange multipliers to incorporate the constraint of (A.2) in the cost function expressed in (A.1). Accordingly, we wish to maximize $\phi(\mathbf{x})$ given by

$$\phi(\mathbf{x}) = \mathbf{x}^T \mathbf{M} \mathbf{x} + \lambda(1 - \mathbf{x}^T \mathbf{x}) \quad (\text{A.3})$$

We denote the maximizing \mathbf{x} by \mathbf{x}^* , then we can express \mathbf{x} as follows

$$\mathbf{x} = \mathbf{x}^* + \varepsilon \mathbf{h} \quad (\text{A.4})$$

where ε is a scalar. Substitution of the latter into (A.3) yields

$$\phi(\varepsilon) = (\mathbf{x}^* + \varepsilon \mathbf{h})^T \mathbf{M} (\mathbf{x}^* + \varepsilon \mathbf{h}) + \lambda[1 - (\mathbf{x}^* + \varepsilon \mathbf{h})^T (\mathbf{x}^* + \varepsilon \mathbf{h})] \quad (\text{A.5})$$

An extremal point of $\phi(\varepsilon)$ satisfies the following

$$\left. \frac{d\phi(\varepsilon)}{d\varepsilon} \right|_{\varepsilon=0} = 0 \quad \text{for all } \mathbf{h} \quad (\text{A.6})$$

Now it can be easily verified that since \mathbf{M} is symmetric,

$$\left. \frac{d\phi(\varepsilon)}{d\varepsilon} \right|_{\varepsilon=0} = 2\mathbf{h}^T (\mathbf{M}\mathbf{x}^* - \lambda\mathbf{x}^*) \quad (\text{A.7})$$

Application of the condition for a stationary point of (A.6) to (A.7), yields

$$\mathbf{h}^T (\mathbf{M}\mathbf{x}^* - \lambda\mathbf{x}^*) = 0 \quad \text{for all } \mathbf{h} \quad (\text{A.8})$$

The latter condition can be met if and only if

$$\mathbf{M}\mathbf{x}^* = \lambda\mathbf{x}^* \quad (\text{A.9})$$

Substitution of $\mathbf{M}\mathbf{x}^*$ given by the last equation into (A.1) yields

$$\mu_{\max} = \lambda\mathbf{x}^{*T} \mathbf{x}^* \quad (\text{A.10})$$

and since \mathbf{x}^* is of unit length, $\mathbf{x}^{*T} \mathbf{x}^* = 1$, therefore (A.10) becomes

$$\mu_{\max} = \lambda \quad (\text{A.11})$$

and μ_{\max} takes its maximal value when λ is λ_{\max} , which is the largest eigenvalue of \mathbf{M} . (Note that since \mathbf{M} is symmetric, its eigenvalues are always real). Then

$$\mu_{\max} = \lambda_{\max} \quad (\text{A.12})$$

and \mathbf{x}^* is the eigenvector of \mathbf{M} which corresponds to λ_{\max} .

References

1. Wahba, G., "A Least Squares Estimate of Spacecraft Attitude," *SIAM Review*, Vol. 7, No. 3, July 1965, p.409.
2. Davenport, P., Private Communication, 1968.
3. Keat, J., *Analysis of Least-Squares Attitude Determination Routine DOAOP*, Computer Sciences corporation, CSC/TM-77/6034, Feb. 1977.
4. Rodrigues, M.O., "Des Lois Géométriques Qui Régissent les Déplacement d'un Système Solide dans L'espace, et de la Variation des Coordonnées Provenant de ces Déplacements Considérés Independamment des Causes qui Peuvent les Produire," *Journal de Mathematiques Pures et Appliquees, (Liouville)*, Vol. 5, 1840, pp. 380-440.
5. Wertz, J.R., (ed), *Spacecraft Attitude Determination and Control*, D. Reidel Publishing Co., Dordrecht, Holland, 1984, p. 512, 513.
6. Shuster, M.D., *Algorithms for Determining Optimal Attitude solutions*, Computer Sciences Corporation, CSC/TM-78/6056, April 1978.
7. Shuster, M.D., and Oh, S.D., "Three-Axis Attitude Determination from Vector Observations," *Journal of Guidance and Control*, Vol. 4, No. 1, Jan.-Feb, 1981, pp. 70-77.
8. Shuster, M.D., "A Simple Kalman Filter and Smoother for Spacecraft Attitude," *Journal of the Astronautical Sciences*, Vol. 37, No. 1, 1989, pp. 89-106.
9. Wertz, J.R., (ed), *Spacecraft Attitude Determination and Control*, D. Reidel Publishing Co., Dordrecht, Holland, 1984, p. 512.
10. Gelb, A., (ed), *Applied Optimal Estimation*, The M.I.T. Press, Cambridge, MA, 1988, pp. 285-287.
11. Ibid., 57-63, 296-298.

OPTIMIZED TRIAD ALGORITHM FOR ATTITUDE DETERMINATION

Itzhack Y. Bar-Itzhack[#] Richard R. Harman^{*}
Flight Dynamics Support Branch, Code 553
NASA Goddard Space Flight Center
Greenbelt, MD 20771

Abstract

TRIAD is a well known simple algorithm that generates the attitude matrix between two coordinate systems when the components of two abstract vectors are given in the two systems. TRIAD, however, is sensitive to the order at which the algorithm handles the vectors, such that the resulting attitude matrix is influenced more by the vector processed first.

In this work we present a new algorithm, which we call Optimized TRIAD, that blends, in a specified manner, the two matrices generated by TRIAD when processing one vector first, and then when processing the other vector first. On the average, Optimized TRIAD yields a matrix which is better than either one of the two matrices in that it is the closest to the correct matrix. This result is demonstrated through simulation.

I. BACKGROUND

When the components of two abstract vectors are given in two different coordinate systems, it is possible to find the orientation difference between the two systems. In particular, we can easily find the transformation matrix from one coordinate system to the other. TRIAD^{1,2} is an algorithm that does just that. The process of finding the matrix using TRIAD is as follows. Let w_1 and w_2 denote the column matrices whose elements are, respectively, the components of the two abstract vectors when resolved in body coordinates, and let v_1 and v_2 denote, respectively, the two column matrices whose elements are the components of the abstract vectors when resolved in the other, usually reference, system. The algorithm calls for the computation of the following column matrices in body coordinates:

$$r_1 = w_1 / |w_1| \quad (1.a)$$

$$r_2 = (r_1 \times w_2) / |r_1 \times w_2| \quad (1.b)$$

$$r_3 = r_1 \times r_2 \quad (1.c)$$

[#] Sophie and William Shamban Professor of Aerospace Engineering. On sabbatical leave from the Faculty of Aerospace Engineering, Technion-Israel Institute of Technology, Haifa 32000, Israel. Member Technion Space Research Institute. IEEE Fellow.

^{*} Aerospace Engineer.

This work was performed on a National Research Council
NASA Research Associateship.

and the following corresponding column matrices in the reference system:

$$s_1 = v_1 / |v_1| \quad (2.a)$$

$$s_2 = (s_1 \times v_2) / |s_1 \times v_2| \quad (2.b)$$

$$s_3 = s_1 \times s_2 \quad (2.c)$$

Then the attitude matrix that transforms from body to the reference coordinate system is computed as follows:

$$A = r_1 \cdot s_1^T + r_2 \cdot s_2^T + r_3 \cdot s_3^T \quad (3)$$

where T denotes the transpose.

Following the process indicated in (1) and (2), we realize that the vector which is designated as first, is normalized, but other than that, remains intact, whereas the other vector serves as a means to define the second vector in the triad pair which determines the attitude. There is, therefore, an uneven consideration of the two vectors where the first is given a preference in the determination of A. We say that the first vector serves as an anchor in the computation of the transformation matrix. It is, indeed, a good engineering practice to use the vector measured by the most accurate device as the anchor vector. For example, it is very logical to use the vector measured by a star tracker as anchor when the other vector is measured by magnetometers. One may wonder though whether this is the best one can do. We maintain that we can do better, and propose a TRIAD-based algorithm which yields better results. This algorithm, which we name Optimized TRIAD, is introduced next.

II. THE OPTIMIZED TRIAD

The accuracy of each vector-measuring device is quantified by the standard deviation of its error. Accordingly, the vector measured by a star tracker is assigned a standard deviation smaller than that assigned to a magnetometer, for example. Borrowing this notion, we assign a standard deviation to the TRIAD-computed attitude matrix that corresponds to the standard deviation of the anchor vector used in computing the matrix. Therefore, the attitude matrix A_1 , in whose computation vector no. 1 is used as anchor, is assigned the standard deviation σ_1 , which is the standard deviation of vector no. 1. Similarly, if vector no. 2 serves as anchor, we denote the computed attitude matrix by A_2 and assign to it the standard deviation σ_2 which is the standard deviation of vector no. 2. Actually, since the computation which yields the matrix is nonlinear and is based on both vectors, there is no simple linear relation between the standard deviation of the anchor vector and that of the resulting matrix, but since we are concerned only with the relative accuracy of A_1 and A_2 , the expression of their accuracy by σ_1 and σ_2 respectively, fits well our final purpose.

It is well known (see the appendix) that when y_1 and y_2 are independent unbiased scalar measurement of an unknown scalar, x , and their measurement errors have standard deviations σ_1 and σ_2 , respectively, then \hat{x} , the linear unbiased minimum variance estimate of x , is given by:

$$\hat{x} = \frac{\sigma_2^2}{\sigma_1^2 + \sigma_2^2} y_1 + \frac{\sigma_1^2}{\sigma_1^2 + \sigma_2^2} y_2 \quad (4)$$

Following (4), we postulate that given A_1 with its assigned standard deviation σ_1 and A_2 with its assigned standard deviation σ_2 , we can find \hat{A}' , an estimate of A which is better than either A_1 or A_2 , when using the estimator of (4); that is,

$$\hat{A}' = \frac{\sigma_2^2}{\sigma_1^2 + \sigma_2^2} A_1 + \frac{\sigma_1^2}{\sigma_1^2 + \sigma_2^2} A_2 \quad (5)$$

An interesting aspect of this estimator (as well as that of (4)) is the conclusion that adding some of the worse result to the better, may yield an estimate whose accuracy is greater than that of the better. Since \hat{A}' is a result of the addition of fractions of two orthogonal matrices, \hat{A}' is not necessarily orthogonal, and thus is not a legitimate attitude matrix, unless it is orthogonalized. Since \hat{A}' is close to being orthogonal, one orthogonalization cycle, as follows⁴, suffices:

$$\hat{A} = 0.5[\hat{A}' + (\hat{A}')^T] \quad (6)$$

It should be noted that the inversion of \hat{A}' is an easy task since the inverse of a 3×3 matrix can be computed analytically. It is cumbersome, if not impossible, to prove analytically that \hat{A} is better than either A_1 or A_2 ; however, we can try to show it empirically. This is done in the next section.

III. ALGORITHM TESTING

III.1 Static Testing

In the static testing we chose some fixed attitude matrix, A_{true} , and the components of the unit vectors v_1 and v_2 (two abstract vectors resolved in the reference system). Then A_{true} was used to transform v_1 and v_2 to the body system. To each component of the latter we added white measurement noise drawn from a random number generator. The added noise was unbiased and had a standard deviation $\sigma_1 = 0.1$ for the noise added to the components of the transform of v_1 and $\sigma_2 = 0.2$ for the noise added to the components of the transform of v_2 . The noisy column matrices were designated as w_1 and w_2 . TRIAD was then applied to the four column matrices as described in the preceding section, once when vector no. 1 was used as anchor and once when the other was used as anchor. This generated the attitude matrices A_1 and A_2 respectively, which then were used in (5) to generate \hat{A}' that was used in (6) to yield the optimized orthogonal matrix \hat{A} . The quaternions corresponding to A_{true} , A_1 , A_2 , and \hat{A} were computed and denoted by q_{true} , q_1 , q_2 , and \hat{q} respectively. The error quaternion of each transformation was computed as follows:

$$\delta q = q^{-1} \otimes q_{\text{true}} \quad (7)$$

When q was q_1 we obtained δq_1 , when q was q_2 we obtained δq_2 , and when it was \hat{q} , we obtained $\delta \hat{q}$. (Note that with the choice of (7) for computing the erroneous quaternion, we assume that δq is the transformation quaternion from the erroneous to the true coordinate system). Finally, we extracted from each δq the corresponding rotation angle $\delta \phi$. We thus have expressed the error in the computation of the attitude by a single angular error. That error was the angle by which the computed coordinate system had to be rotated about the appropriate Euler axis in order to coincide with the true body coordinates.

Since $\delta \phi$ is a random variable, we ran 100 runs (realizations), each for 60 sec and each starting with a

different seed. Along the time axis the computation was performed every second. We then averaged the 100 realizations at each time point and obtained the ensemble average of each error; that is, we obtained:

$$\delta\bar{\varphi}_1(t_k) = \frac{1}{100} \sum_{j=1}^{100} \delta\varphi_{1,j}(t_k) \quad (8.a)$$

$$\delta\bar{\varphi}_2(t_k) = \frac{1}{100} \sum_{j=1}^{100} \delta\varphi_{2,j}(t_k) \quad (8.b)$$

$$\delta\bar{\varphi}(t_k) = \frac{1}{100} \sum_{j=1}^{100} \delta\hat{\varphi}_j(t_k) \quad (8.c)$$

where j denotes the number of the realization, and t_k denotes the point in time where TRIAD and Optimal TRIAD were performed. The value of $\delta\bar{\varphi}_1(t_k)$, $\delta\bar{\varphi}_2(t_k)$ and $\delta\bar{\varphi}(t_k)$ as function of t_k is presented in Fig. (1). We see that $\delta\bar{\varphi}$ was always the smallest. We also computed the running time average of each

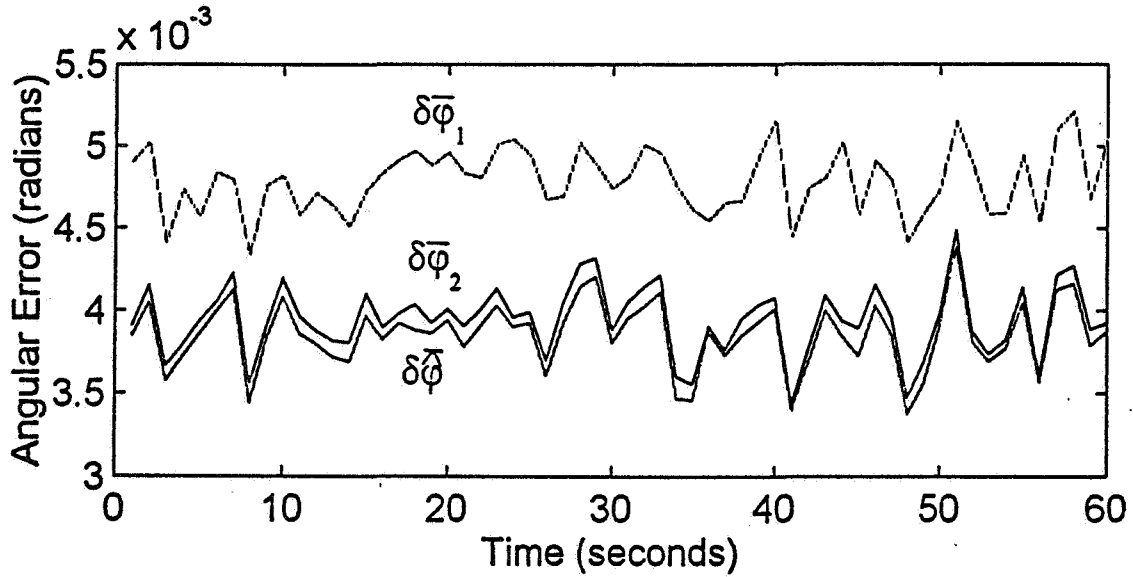


Fig. 1: Ensemble Average of the Error Associated with A_1 , A_2 , and \hat{A} .

ensemble average from the beginning of the run to time t_k . In other words, we computed:

$$\delta\bar{\varphi}_{1,av}(t_k) = \frac{1}{k} \sum_{i=1}^k \delta\bar{\varphi}_1(t_i) \quad (9.a)$$

$$\delta\bar{\varphi}_{2,av}(t_k) = \frac{1}{k} \sum_{i=1}^k \delta\bar{\varphi}_2(t_i) \quad (9.b)$$

$$\delta\bar{\varphi}_{av}^k(t_k) = \frac{1}{k} \sum_{i=1}^k \delta\bar{\varphi}(t_i) \quad (9.c)$$

The value of $\delta\bar{\varphi}_{1,av}^k(t_k)$, $\delta\bar{\varphi}_{2,av}^k(t_k)$ and $\delta\bar{\varphi}_{av}^k(t_k)$ as function of t_k is presented in Fig. 2. It is

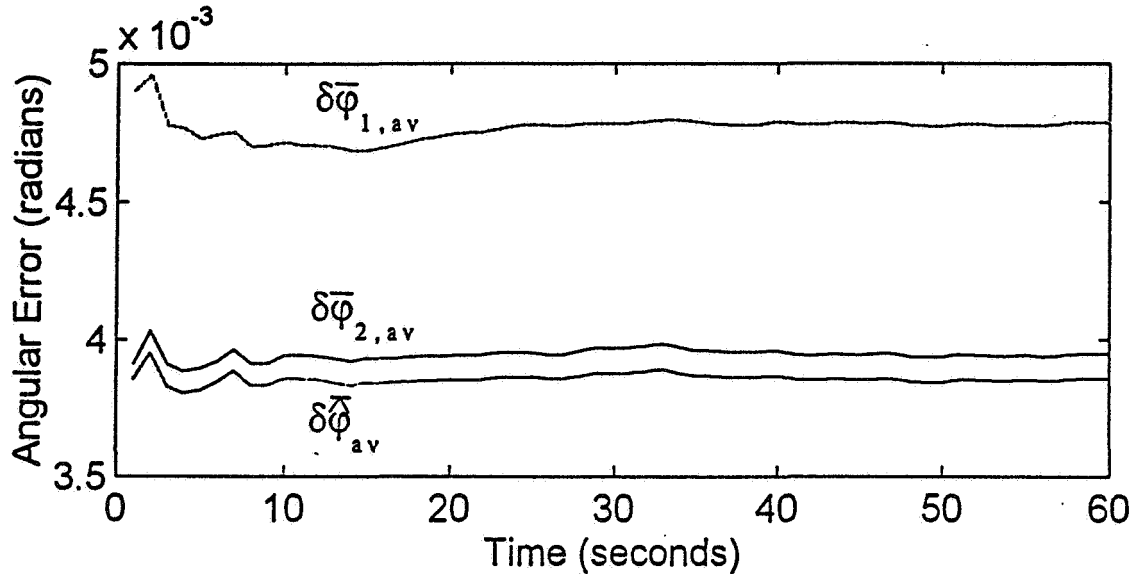


Fig. 2: Running Time Average of the Ensemble Average of the Error Associated with A_1 , A_2 , and \hat{A} .

obvious from Fig. 2 that \hat{A} is superior to either A_1 or A_2 . In other words, on the average, the Optimized TRIAD yields better results for the case tested.

III.1 Dynamic Testing

To check the influence of changing attitude, we repeated the same runs and computations as described before, for a changing A . The change in A was due to a the body rotation about an axis $\bar{\rho}$ defined as follows:

$$\bar{\rho} = \frac{1}{\sqrt{3}}[\bar{i}_b, \bar{j}_b, \bar{k}_b] \quad (10)$$

The rotation rate about this axis was 1 rpm. The graphs of the results of this case, which correspond to those presented in Figs. 1 and 2, are presented in Figs. 3 and 4 respectively. Since the idea behind this algorithm is borrowed from linear estimation theory of independent unbiased measurement errors, one would expect the ensemble average of the angular error to be zero; however, as can be seen in Figs. 1 and 3, this is not the case. This discrepancy stems from the fact that the displayed error is not linearly related to the averaged matrices. Also, the errors in the computed matrices, A_1 and A_2 , are not really independent.

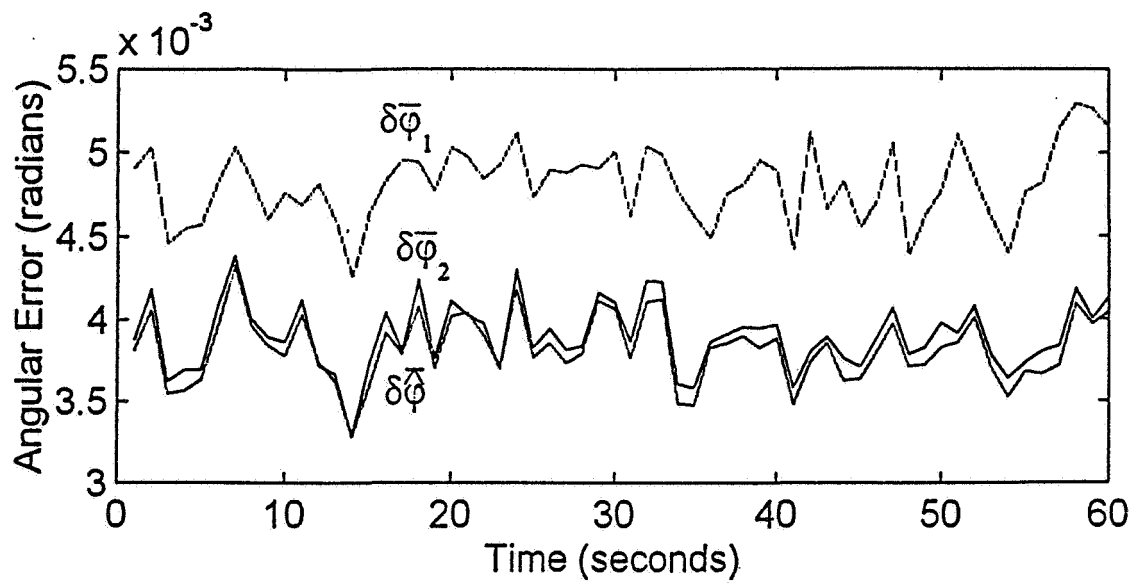


Fig. 3: Ensemble Average of the Error Associated with A_1 , A_2 , and \hat{A} when A_{true} was changing.

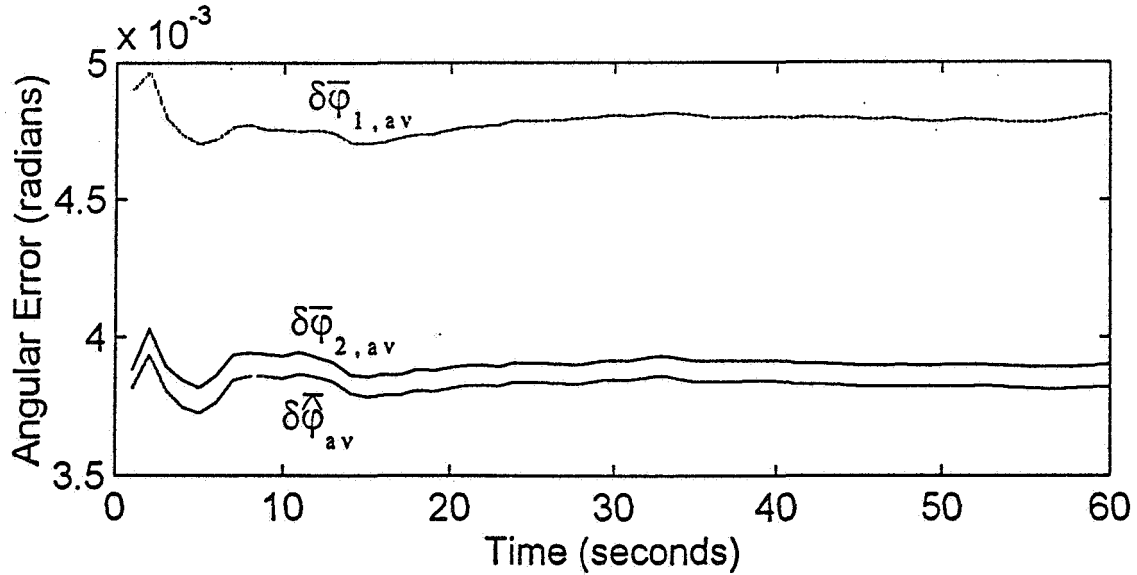


Fig. 4: Running Time Average of the Ensemble Average of the Error Associated with A_1 , A_2 , and \hat{A} when A_{true} was changing.

Finally, the vectors v_1 and v_2 , which are the components of the two abstract vector resolved in the reference coordinates, were constant through all runs. The angle between the two vectors was close to 90° . To investigate the behavior of the algorithm for a different separation angle, we chose two new v_1 and v_2 vectors the angle between which was close to 45° and ran the last test case. The results were similar to those presented in Figs. 3 and 4, only that, as expected, the errors of all three algorithms were nearly 25% higher.

V. CONCLUSIONS

In this work we have presented a simple TRIAD-based algorithm, which we call Optimized TRIAD, that performs better than TRIAD itself. The algorithm consists of running TRIAD twice, once with one vector as anchor and once with the other vector as anchor, and weight averaging of the two resultant matrices followed by one orthogonalization cycle. The weights are determined by the accuracy of the measuring devices that produced the vector measurements. The idea behind this algorithm is borrowed from linear estimation theory of independent unbiased measurement errors. However, although the blending of the two TRIAD-generated matrices is based on an unbiased minimum variance formula, the ensemble average of the angular error is not zero, as can be seen in Figs. 1 and 3. This, however, is no surprise, because the displayed error is not linearly related to the averaged matrices. Also, the errors in the computed matrices, A_1 and A_2 , are not really independent.

We have shown empirically that, indeed, the accuracy of the Optimized TRIAD is better than that of TRIAD even when the latter uses the vector measured most accurately as anchor. It should be noted though that in this statement we refer to the average performance. That is to say that occasionally TRIAD may yield results which are better than those obtained using Optimized TRIAD, but on the average, Optimized TRIAD performs better. It is interesting to note that like in Kalman filtering, the correct blending of the better TRIAD-generated attitude matrix with the worse, yields, on the average, a result which is more accurate than the better.

Appendix

Theorem: Given y_1 and y_2 where:

$$y_1 = x + v_1 \quad (1.a)$$

$$y_2 = x + v_2 \quad (1.b)$$

and

$$E\{v_1\} = 0 \quad (2.a)$$

$$E\{v_2\} = 0 \quad (2.c)$$

$$E\{v_1^2\} = \sigma_1^2 \quad (2.b)$$

$$E\{v_2^2\} = \sigma_2^2 \quad (2.d)$$

$$E\{v_1 v_2\} = 0 \quad (2.e)$$

Then, the following linear estimator:

$$\hat{x} = \frac{\sigma_2^2}{\sigma_1^2 + \sigma_2^2} y_1 + \frac{\sigma_1^2}{\sigma_1^2 + \sigma_2^2} y_2 \quad (3)$$

yields an unbiased minimum variance estimate of x .

Proof:

A linear estimator of x has the form:

$$\hat{x} = k_1 y_1 + k_2 y_2 \quad (4)$$

Substitution of (1) into (4) yields:

$$\hat{x} = (k_1 + k_2)x + k_1 v_1 + k_2 v_2 \quad (5)$$

Using (5) we can write the estimation error as follows:

$$e \triangleq x - \hat{x} = (1 - k_1 - k_2)x - k_1 v_1 - k_2 v_2 \quad (6)$$

Due to the unbiasedness of v_1 and v_2 expressed in (2.a,c), we obtain from (6):

$$E\{e\} = (1 - k_1 - k_2)x \quad (7)$$

For the estimate to be unbiased, $E\{e\}$ has to vanish, which yields the necessary condition for unbiasedness:

$$k_1 = 1 - k_2 \quad (8)$$

Using (8), (4) becomes:

$$\hat{x} = (1 - k_2)y_1 + k_2 y_2 \quad (9)$$

and (6) becomes:

$$e = -k_1 v_1 - k_2 v_2 \quad (10)$$

Now

$$\text{Var}\{e\} = \sigma_e^2 \triangleq E\{e^2 - E\{e\}^2\} \quad (11)$$

which in view of the unbiasedness of e becomes:

$$\sigma_e^2 = E\{e^2\} \quad (12)$$

Substitution of (10) into (12) yields:

$$\sigma_e^2 = E\{k_1^2 v_1^2 + k_2^2 v_2^2 + 2k_1 k_2 v_1 v_2\} \quad (13)$$

Using (2.b,d,e) and (8), (13) becomes:

$$\sigma_e^2 = (1 - k_2)^2 \sigma_1^2 + k_2^2 \sigma_2^2 \quad (14)$$

We want the estimator to be of minimum variance. From (14) we see that we still have one more design parameter to choose; namely k_2 . Consequently, we choose k_2 so as to minimize σ_e^2 . Searching for the minimum we differentiate (14) with respect to k_2 and equate the result to zero. This yields:

$$\frac{d}{dk_2}(\sigma_e^2) = -2(1 - k_2)\sigma_1^2 + 2k_2\sigma_2^2 = 0 \quad (15)$$

Consequently:

$$k_2 = \frac{\sigma_1^2}{\sigma_1^2 + \sigma_2^2} \quad (16.a)$$

It can be easily verified that the stationary point which σ_e^2 has at this k_2 , is a minimum point. Using (16.a) in (8), we obtain:

$$k_1 = \frac{\sigma_2^2}{\sigma_1^2 + \sigma_2^2} \quad (16.b)$$

Substitution of (16) into (4) yields:

$$\hat{x} = \frac{\sigma_2^2}{\sigma_1^2 + \sigma_2^2} y_1 + \frac{\sigma_1^2}{\sigma_1^2 + \sigma_2^2} y_2 \quad (17)$$

Q.E.D.

References

1. Black, H.D., "A Passive System for Determining the Attitude of a Satellite," *AIAA Journal*, Vol. 2, No. 7, July 1964, pp. 1350, 1351.
2. Shuster, M.D., and Oh, S.D., "Three-Axis Attitude Determination from Vector Observations," *Journal of Guidance and Control*, Vol. 4, No. 1, Jan.-Feb, 1981, pp. 70-77.
3. Bar-Itzhack, I. Y., and Meyer, J., "On the Convergence of Iterative Orthogonalization Processes," *IEEE Transactions on Aerospace Electronic systems*, Vol. AES-12, No. 2, March 1976, pp. 146-151.

Variations on the Davenport Gyroscope Calibration Algorithm

G. Welter and J. Boia
Computer Sciences Corporation

M. Gakenheimer, E. Kimmer, and D. Channell
AlliedSignal Technical Services Corporation

L. Hallock
National Aeronautics and Space Administration /
Goddard Space Flight Center

ABSTRACT

This paper presents a number of variations on the Davenport algorithm for in-flight gyroscope recalibration, or first-order initial calibration, specifically tailored for use with a minimum amount of satellite telemetry data. Central to one of the techniques described is the use of onboard integration of gyroscope data together with a detailed model of scheduled satellite slew profiles. Methods are presented for determining adjustments to either parameters for the standard linear model (i.e., a drift rate bias vector and/or a scale factor/alignment transformation matrix) or individual gyroscope scale parameters, both linear and nonlinear, in cases where the alignments are well known. The results of applying the methods in an analysis of the temporal evolution and nonlinear response of the gyroscopes installed on the Hubble Space Telescope following its first servicing mission are discussed. The two effects, when working coherently, have been found to result in slew errors of almost 1 arcsecond per degree. Procedures for selecting optimal operational gyroscope parameters subject to the constraint of using a linear model are discussed.

Introduction

Reference 1 presents a derivation of the Davenport gyroscope calibration algorithm, which has been used for the in-flight calibration of gyroscopes for a number of spacecraft missions, including those of the High Energy Astrophysics Observatories and the Hubble Space Telescope (HST). As usually implemented, and, in particular, as implemented for the HST mission (Reference 2), the algorithm assumes that the user has available for use in the calibration process a continuous and complete set of gyroscope data extending from an initial to a final spacecraft attitude (as determined by independent reference sensors) for an adequately large number of maneuvers. Empirically, we find that this constraint causes gyroscope scale factor and alignment calibration to be one of the more labor- and data-intensive activities needed in support of mission operations. Fortunately, we also have found that the scale factor and alignment parameters for the gyroscopes used for the HST mission are fairly stable; calibration is usually required only following initial deployment of gyroscopes (i.e., following HST's initial deployment in April 1990, activation of reserve gyroscopes in response to gyroscope failures, and installation of new gyroscopes during the first HST servicing mission in December 1993).

Although the HST gyroscopes are "fairly stable," a performance analysis conducted in September 1995 (Reference 3) has indicated that in the 18 months following the first HST servicing mission, the gyroscope response has changed systematically, the errors being most manifest in negative yaw maneuvers wherein systematic errors of roughly 0.8 arcsecond per degree occur.

Given this recent experience with the HST gyroscopes, we have found it desirable to develop an algorithm that permits recalibration of the gyroscopes, at least to first order in the change parameters, using a data set that is both much reduced in volume and readily available during normal mission operations. We also have found it useful to extend the algorithm to allow study of both isolated and nonlinear scale corrections. The algorithm that we present here requires as input from telemetry only the attitude error measurements determined by the onboard computer (OBC) pointing control subsystem following large vehicle maneuvers. All other required input can be obtained from the schedule of commanded maneuvers and the spacecraft parameters characterizing those maneuvers.

The body of this paper is divided into six sections, excluding this introduction. These include (1) background on the basics of the Davenport algorithm, (2) a reformulation taking advantage of OBC integration of gyroscope data and modeling of planned maneuver profiles, (3) some comments on the calibration of gyro bias, (4) an extension to both isolated and nonlinear scale factor corrections, (5) a discussion of selection of measurement weights to be used in the algorithms, and (6) an application of the algorithm to data accumulated for the gyroscopes used for the HST mission.

The Davenport gyroscope calibration algorithm, as well as the variations of it discussed in this paper, are envisioned as applied in a batch mode least-squares algorithm. Batch mode processing is strictly appropriate only if the time scale for collection of the calibration data is short compared with the time scale for any variation that may apply to the state vector parameters. Empirically, in the case of the gyroscopes used on HST, we have found the scale factor and alignment parameters sufficiently stable that a batch mode approach for their calibration is operationally viable. In cases where this fails to be true, reformulating the calibration equations presented here in terms of a Kalman filter (e.g., Reference 4) should be considered.

Section 1 - Background on the Basics of the Davenport Algorithm

Reference 1 presents the gyroscope calibration algorithm that is used in the HST mission for the calibration of scale factors, alignments, and biases of the gyroscopes when one or more gyroscopes are first activated for operational use. The basic equations are as follows. Consider a satellite gyro system consisting of N_g single-axis gyroscopes. In response to some angular motion of the satellite, the output response column matrix of gyro counts, C , consists of the N_g individual gyro readings. The response vector is translated into a measured angular velocity, Ω_m , in the spacecraft frame via

$$\Omega_m = G_o C - D_o \quad (1)$$

where G_o is the $3 \times N_g$ scale factor / alignment matrix, and D_o is the gyro system drift rate bias expressed in the spacecraft frame. The goal of the algorithm is to determine correction matrices m and d that may be applied to G_o and D_o so that a modified equation (1) will yield the true angular rate, Ω , as indicated in equations (2a) - (2c).

$$G = (I_3 + m) G_o \quad (2a)$$

$$D = (I_3 + m) D_o + d \quad (2b)$$

$$\Omega = G C - D = (I_3 + m) \Omega_m - d \quad (2c)$$

where I_3 is the 3x3 identity matrix. Gyroscope miscalibration information is sampled through any given maneuver via the error quaternion

$$\delta Q \equiv Q_r Q_o^{-1} \quad (3)$$

where Q_r represents the true vehicle rotation as determined from reference star measurements, and Q_o represents the vehicle rotation inferred from the gyroscope measurements. As discussed in Reference 1, δQ represents a rotation from the gyro-inferred to the true postmaneuver attitude, expressed in the premaneuver reference frame. The information content of δQ is related to m and d via the sensitivity equation

$$Z = 1/2 \int T (\Omega - \Omega_m) dt \quad (4a)$$

$$= 1/2 \int T (m \Omega_m - d) dt \quad (4b)$$

where Z is the vector component of δQ , T is the matrix that transforms vectors to premaneuver spacecraft coordinates, and the time integral is over the whole maneuver. Because equation (4b) is linear in m and d , it can be used as the basis for a linear least-squares algorithm to provide estimates for m and d . If a solution for all 12 correction terms is needed, at least 4 independent "maneuvers" are required to perform the calibration. The maneuvers must provide a reasonable sample of pitch, roll, and yaw variation, as well as an independent sample for bias determination; the latter is permitted to be a period of essentially constant attitude.

Although the information content is unchanged, it is often more convenient to reexpress Z in terms of an error vector, ζ , representing the rotation from the true postmaneuver attitude to the intended (and gyro-inferred, assuming closed-loop control) postmaneuver attitude, i.e., the rotation that the spacecraft must perform after it determines its postmaneuver error. The vector ζ is related to Z and $\{m, d\}$ via

$$\begin{aligned} \zeta &= -T_\tau^{-1} Z \\ &= -1/2 T_\tau^{-1} \int T (m \Omega_m - d) dt \end{aligned} \quad (5)$$

where τ represents the maneuver duration time, and its use as a subscript on T_τ means that T is to be evaluated at the maneuver end-time. The matrix T_τ^{-1} (which equals T_τ^T) is thus the premaneuver to postmaneuver reference frame transformation matrix.

Section 2 - Use of OBC Gyro Data Integration and Model Maneuver Profiles

As discussed in Reference 1, equation (5) is accurate only to first order in m and d , implying that the associated least-squares algorithm is intrinsically iterative. The matrix terms ζ , T , and Ω_M must be reevaluated on each iteration. Multiple iterations can only be applied if a complete set of gyroscope data from throughout each of the calibration maneuvers is available. In this section we discuss a procedure that excludes the possibility of multiple iterations, the gain being a drastic reduction in the total volume of data required to perform the calibration. This can be significant if either (1) the sheer volume of data for frequent, normal calibrations becomes unwieldy or (2) the standard telemetry format used does not contain an adequately dense sampling of gyro data for accurate integration.

If calibration needs are adequately met via a first order correction, it is possible to implement an algorithm with drastically lower data requirements. Integration of the full set of gyroscope data is required at two points in the use of equation (5): first in the determination of Q_G for the construction of ζ , and then in the time integral over $(Tm\Omega_M)$. Ground processing of gyro data to determine Q_G can be eliminated if the spacecraft OBC maintains and transmits an estimate of the spacecraft attitude based solely on gyroscope data, at least through the time period between the accumulation of star sensor data for pre- and postmaneuver definitive attitude estimation. Sampling the OBC's pre- and postmaneuver attitude estimates then allows construction of Q_G as the connecting eigenvector rotation between the two. Ground processing of the gyro data for use in the integral over $(Tm\Omega_M)$ can be eliminated if a sufficiently precise model of the maneuver profile is available. This follows because, to first order in the correction terms, equation (5) is unchanged if $m\Omega_M$ is replaced with $m\Omega_p$, Ω_p being the planned angular velocity as a function of time based on spacecraft design parameters. We make the latter substitution in what follows.

The simplifications noted in the preceding paragraph allow the elimination of all ground processing of the raw gyro data. The elimination of ground

processing of the reference star data may also be possible, although this results in a smaller gain. For many satellites, the OBC generates an attitude error estimate based upon postmaneuver reference star measurements and uses this estimate to generate an error nulling maneuver. If the vehicle attitude is maintained accurately by the onboard pointing control system during the periods between maneuvers, the postmaneuver error nulling maneuver will correspond to the error vector ζ required for our analysis. If this error vector is included in telemetry, no other spacecraft data are required.

We assume finally that each maneuver is a pure eigenaxis maneuver. This allows the analysis to be done in a coordinate system, designated here with a prime ($'$), in which the x' -axis is aligned along the maneuver axis. Expressed in the primed frame, equation (5) becomes

$$R(2\zeta) = -T_\tau^T \int T'(m'\Omega_p' - d') dt \quad (6a)$$

$$T' = \begin{bmatrix} 1 & 0 & 0 \\ 0 & \cos[\theta(t)] & -\sin[\theta(t)] \\ 0 & \sin[\theta(t)] & \cos[\theta(t)] \end{bmatrix}$$

$$= RTR^T = RTR^T \quad (6b)$$

$$m' = RmR^T = RmR^T \quad (6c)$$

$$d' = Rd \quad (6d)$$

$$\Omega_p' = [\omega(t), 0, 0]^T = R\Omega_p \quad (6e)$$

where R is the transformation matrix that converts premaneuver spacecraft coordinates to the premaneuver primed frame, $\theta(t)$ is the maneuver angle as a function of time, and $\omega = d\theta/dt$. The form of $\theta(t)$ will depend upon the total maneuver angle, Θ , and design parameters governing the execution of maneuvers. To first order, R may be based on the planned maneuver quaternion, Q_p . The eigenvector and rotation angle set, $\{r, \varphi\}$, defining the quaternion representation of R is constructed from the spacecraft frame Q_p eigenvector, η , and the spacecraft frame standard unit vectors, $\{x, y, z\}$, using

$$r = (x \times \eta) / |x \times \eta|$$

$$= (-y\eta_3 + z\eta_2) / (\eta_2^2 + \eta_3^2)^{1/2} \quad (7a)$$

$$\varphi = \cos^{-1}(x \cdot \eta) = \cos^{-1}(\eta_1) \quad (7b)$$

The simple forms of equations (6b) and (6e) allow equation (6a) to be reexpressed as

$$R (2 \zeta) = -T_{\tau}^{\prime T} [K_1 [m']_1 - K_0 d'] \quad (8a)$$

$$K_k \equiv \begin{bmatrix} K_k & 0 & 0 \\ 0 & K_{\alpha k} & -K_{\beta k} \\ 0 & K_{\alpha k} & K_{\beta k} \end{bmatrix} \quad (8b)$$

$$K_k \equiv \int \omega^k dt \quad (8c)$$

$$K_{\alpha k} \equiv \int \cos(\theta) \omega^k dt \quad (8d)$$

$$K_{\beta k} \equiv \int \sin(\theta) \omega^k dt \quad (8e)$$

where $[m']_1$ indicates the column matrix formed from the first column of m' . Note that the elements of K_1 are analytic, i.e., $K_1 = \Theta$, $K_{\alpha 1} = \sin(\Theta)$, and $K_{\beta 1} = [1 - \cos(\Theta)]$, whereas K_0 is equal to the maneuver duration, τ . The functional form of $\theta(t)$ enters only via $K_{\alpha k}$ and $K_{\beta k}$.

The multiplication of $T_{\tau}^{\prime T}$ into K_1 and K_0 in equation (8a), together with an application of the sine and cosine laws for two angle sums, produces

$$R (2 \zeta) = -[K^*_1 [m']_1 - K^*_0 d'] \quad (9a)$$

$$K^*_k \equiv \begin{bmatrix} K_k & 0 & 0 \\ 0 & K^*_{\alpha k} & K^*_{\beta k} \\ 0 & -K^*_{\alpha k} & K^*_{\beta k} \end{bmatrix} \quad (9b)$$

$$K^*_{\alpha k} \equiv \int \cos(\Theta - \theta) \omega^k dt \quad (9c)$$

$$K^*_{\beta k} \equiv \int \sin(\Theta - \theta) \omega^k dt \quad (9d)$$

Because K_1 depends only on Θ and not the form of $\theta(t)$, it can be shown that $K^*_1 = K_1^T$. This relationship holds for K^*_0 as well (actually, for all k) if $\omega(t)$ is an even function of time about the maneuver midpoint. This constraint, which is fairly standard for spacecraft maneuver profiles, also yields the following convenient equations for $K_{\alpha 0}$ and $K_{\beta 0}$ (expressed for general k):

$$K_{\alpha k} = \cos(\Theta/2) F_k(\Theta) \quad (10a)$$

$$K_{\beta k} = \sin(\Theta/2) F_k(\Theta) \quad (10b)$$

$$F_k(\Theta) \equiv \int \cos[\theta(t) - \Theta/2] \omega^k dt \quad (10c)$$

We now need to transform equation (9a) back into the spacecraft frame so as to have ζ related to m and d rather than to m' and d' . Defining m as the 9-by-1 column matrix $[[m]_1^T, [m]_2^T, [m]_3^T]^T$ and using equations (6b) and (6c), we can rewrite equation (9a) as

$$2 \zeta = -R^T K^*_1 B m + R^T K^*_0 R d \quad (11a)$$

$$B_{i, j+3(n-1)} \equiv R_{ij} R_{1n} \quad (11b)$$

where equation (11b) defines the elements of the 3-by-9 matrix B . Equation (11a) is our new least-squares algorithm sensitivity equation. Its use removes the need for an integration of the gyro telemetry data. The only required time integrations are for $K^*_{\alpha 0}$ and $K^*_{\beta 0}$, or, more simply, $F_0(\Theta)$ if the symmetry constraint on $\omega(t)$ is applied. Appendix A presents a specific, fairly common maneuver profile usable in the latter evaluation.

Section 3 - Bias-Only Calibration Assuming Fixed Scale and Alignment

We consider now the application of the algorithm of Section 2 to a bias-only calibration. This begins with the constraining assumption $m = 0$. This constraint is reasonable for many operational scenarios; empirically, it has been found that spacecraft gyro biases can change significantly within as little as a single day, whereas time scales for scale factor and alignment are considerably longer. For this situation, equation (11a) reduces to

$$2 \zeta = R^T K^*_0 R d \quad (12)$$

Two data gathering scenarios are of possible interest for this calibration. For the first scenario, the spacecraft is held at constant, or nearly constant, attitude over the time period of interest. "Nearly constant" in this context means that the magnitude of any net maneuver angle must be smaller than the product $\delta d \Delta t$, where δd is the maximum permitted error in the estimate for d , and Δt is the time period between two reference attitude measurements. For this case, $[R^T K^*_0 R]$ reduces to $I_3 \Delta t$, and equation (12) becomes

$$d = 2 \zeta / \Delta t \quad (13)$$

We have used Δt rather than τ here because there is no scheduled or executed maneuver for which we can evaluate $\tau(\Theta)$. The vector ζ may be constructed from separate initial and final reference star measurements or from an OBC-determined attitude

error at the end of the time period if the spacecraft applied an attitude correction at the start of the period. In the latter case, care must be taken to ensure that the onboard attitude propagation across the time period involved the use of gyroscope data only, i.e., no control-law feedback based on reference star data.

The second data gathering scenario uses the procedures outlined in Section 2 applied to equation (12). The potential operational advantage of using this approach arises if a set of dual mode gyroscopes, i.e., sensors with high-rate and low-rate modes, is being used -- the high-rate mode being used during large maneuvers to allow greater dynamic range, and the low-rate mode during periods of near-constant attitude to allow greater precision. For such gyroscopes, equation (13) can be used to calibrate the high-rate mode bias only if the gyroscopes are commanded to remain in high-rate mode during the calibration period, implying that dedicated spacecraft time would be required for the calibration. In contrast, the use of equation (12) would allow relatively frequent high-rate mode bias calibrations based on serendipitous maneuvers.

A caveat pertains here -- one of relevance to the next section. An estimate of the bias based on equation (12) applied to a single maneuver may fail to be good if the estimate for the scale factor / alignment matrix G is insufficiently accurate, because of either poor initial calibration or an actual change in the gyroscope parameters since the time of calibration. The effect of errors in estimates for linear scale factors would tend to cancel each other in the estimate for d if the least-squares fit is performed using an ensemble of randomly directed maneuvers or paired sets of oppositely directed maneuvers. Taking advantage of this fact to reduce the influence of possible scale factor errors may be desirable.

Section 4 - Isolated and Nonlinear Scale Factor Calibration

The original Davenport algorithm combines the observable aspects of alignment and scale factor changes into the single change matrix m . It also assumes that gyroscope response is purely linear. We have found it useful to be able to study the individual gyroscope response curves, with respect to both nonlinear corrections as well as temporal variations of the dominant (i.e., linear) terms. In this section we discuss an extension of the algorithm presented in Section 2 designed for this purpose.

To keep the initial discussion simple, we will assume that the state vector for our problem is restricted to scale factor adjustments. Specifically, we assume that the gyro alignments are well known and fixed, and that the adjustment to the operational drift rate bias is restricted to that associated with scale factor corrections (i.e., the " mD_0 " term in equation (2b)), with no intrinsic bias changes permitted (i.e., no d term in the state vector). We will relax both of these simplifications eventually. We will, however, not attempt to model ongoing temporal changes in the drift rate bias that occur during the time period over which the calibration data are accumulated. Given that bias changes occur relatively rapidly and are likely to be significant over the data accumulation time period, this last simplification may at first glance seem inappropriate. If, however, a good estimate of the changing bias vector associated with the operational alignment and scale calibration is maintained throughout the period of data accumulation (using the methods of Section 3), the effect of the bias will have been removed on an ongoing basis. From this perspective, we see that we are not actually neglecting the changing bias; rather, the bias effects have been precorrected as part of ongoing operations.

To allow for nonlinear scale effects, we assume a model for gyroscope responsivity of the form

$$C_n = S_n [\Omega_{in,n} + \sum s_{nk} g_k(\Omega_{in,n})] \quad (14)$$

where subscript n indicates the n th gyroscope, C_n is the resultant gyro reading, S_n is the nominal (or current best estimated) gyro scale factor, $\Omega_{in,n}$ is the spacecraft angular rate projected onto the gyro input axis, and the summation over k represents a set of small corrections to the predominantly linear relationship between $\Omega_{in,n}$ and C_n . The parameters s_{nk} are correction coefficients applied to the functions $g_k(\Omega_{in,n})$. The latter can be any convenient set of functions, subject only to the constraint that the same set of functions be used for all of the gyroscopes. To minimize the eventual size of the least-squares state vector, the functions should be selected so that a good fit can be found with as few correction functions as possible. For our HST analysis, we have found it convenient to use two: $g_1(\Omega) = \Omega$ and $g_2(\Omega) = g_{11}(\Omega) \equiv |\Omega|$. In this model, s_{n1} represents an average linear correction, and s_{n2} represents the difference between scale factors for positive and negative maneuvers.

We assume next that an acceptably accurate inverse to equation (14) can be written in the form

$$\Omega_{m,n} = C_n/S_n + \sum \sigma_{nk} g_k(C_n/S_n) \quad (15)$$

In principle, each σ_{nk} is a function of the full set $\{s_{n1}, s_{n2}, \dots\}$. However, if the sum $\sum s_{nk} g_k(\Omega_{m,n})$ and all of its individual terms are small relative to $\Omega_{m,n}$, and if the correction functions g_k vary continuously, then $\sigma_{nk} = -s_{nk}$ to first order in the correction terms for all n and k values. We will be using this approximation in what follows.

For notational compactness, equation (14) can be rewritten as

$$C = S (A \Omega + \sum s_k [{}^{sk} \cdot (A\Omega)]) \quad (16)$$

where C is a N_G -by-1 column matrix (the C_n 's), S and s_k are N_G -by- N_G diagonal matrices (the S_n 's and s_{nk} 's), A is the N_G -by-3 matrix of gyro input axis unit direction vectors, and the symbol $[{}^{sk} \cdot]$ is defined such that

$$[{}^{sk} \cdot V] \equiv [g_k(V_1), g_k(V_2), \dots, g_k(V_N)]^T \quad (17)$$

for any N -by-1 column matrix V . We also need a matrix version of equation (15) that gives Ω_m as a function of C . If N_G exceeds 3, our equation must include a weighting scheme for how the gyro data are to be combined in forming Ω_m . We use the following equation:

$$\begin{aligned} \Omega_m &= [A^T A]^{-1} A^T \Omega_m \\ &= \aleph (S^{-1} C + \sum \sigma_k [{}^{sk} \cdot (S^{-1} C)]) \end{aligned} \quad (18)$$

where Ω_m is the N_G -by-1 matrix formed from the various $\Omega_{m,n}$ estimates, $\aleph \equiv [A^T A]^{-1} A^T$, and σ_k is an N_G -by- N_G diagonal matrix (the σ_{nk} 's). By using equation (18) as the mechanism for constructing Ω_m from C , we have selected a convention whereby equal weight is given to each of the components of Ω_m . This is a change from the more typical convention in constructing the matrix G_0 for equation (1) whereby equal weight is given to each component of C .

At this point we should clarify notation a bit in preparation for constructing the least-squares algorithm for a recalibration of the s_{nk} coefficients. Equation (16) should be viewed as applying the true s_{nk} values; it represents the actual response of

the sensors. In contrast, equation (18) represents the users interpretation of the counts; thus the σ_{nk} are functions of $\{s_{n1,0}, s_{n2,0}, \dots\}$, where the subscript 0 indicates current estimate. The "small correction terms" approximation thus leads to $\sigma_{nk} = -s_{nk,0}$. The least-squares state vector will be the set $\{\delta s_{nk}\}$ for all n and k , where $\delta s_{nk} \equiv s_{nk} - s_{nk,0}$.

To proceed with a formulation of an extended least-squares algorithm based on equation (4a), we require an expression for $(\Omega - \Omega_m)$ linear in the correction terms δs_k . Combining equations (16) and (18) yields

$$\begin{aligned} \Omega_m &= \aleph \{ A\Omega + \sum s_k [{}^{sk} \cdot A\Omega] \\ &\quad + \sum \sigma_k [{}^{sk} \cdot (A\Omega + \sum s_k [{}^{sk} \cdot A\Omega])] \} \end{aligned} \quad (19)$$

The assumptions that the g_k functions vary continuously and that all of the s_k and σ_k elements are small imply that terms of the form $\sigma_k [{}^{sk} \cdot (A\Omega + \sum s_k [{}^{sk} \cdot A\Omega])]$ are equal to $\sigma_k [{}^{sk} \cdot A\Omega]$ to first order. Using this simplification and setting $\sigma_k = -s_{k,0}$ yields

$$(\Omega - \Omega_m) = -\aleph \sum \{ \delta s_k [{}^{sk} \cdot A\Omega] \} \quad (20)$$

To be able to follow our analytic maneuver model approach as developed in Section 2, we insert equation (20) into equation (4a) and apply appropriate transformations to the "primed" reference frame. The resulting sensitivity equation is

$$\begin{aligned} 2 \zeta &= R^T T_{\tau}^{-T} \int T' (R \aleph \sum \{ \delta s_k [{}^{sk} \cdot [AR^T] \Omega] \}) dt \\ &= R^T \sum \{ T_{\tau}^{-T} \int T' (R \aleph [{}^{sk} \cdot [\omega AR^T]_{1,D}] dt) \} [\delta s_k]_C \end{aligned} \quad (21)$$

where $[{}^{sk} \cdot [\omega AR^T]_{1,D}]$ indicates a diagonal matrix formed from the elements of $[{}^{sk} \cdot [\omega AR^T]_{1,D}]$, and $[\delta s_k]_C$ indicates the column matrix formed from the diagonal elements of δs_k (recall that δs_k is a diagonal matrix). If we impose the additional constraint on each g_k that it satisfy the commutivity relation $g_k(ab) = g_k(a)g_k(b)$, equation (21) can be written in the convenient form

$$2 \zeta = R^T \sum K_{sk}^* (R \aleph [{}^{sk} \cdot [AR^T]_{1,D}] [\delta s_k]_C) \quad (22)$$

where the K_{sk}^* matrices are defined analogously to the K_{sk}^* matrices discussed in Section 2, with $g_k(\omega)$ replacing ω^k in defining the required components. For the case of $\{g_1(\Omega) \equiv \Omega; g_2(\Omega) \equiv g_{11}(\Omega) \equiv |\Omega|\}$, equation (22) becomes

$$2 \zeta = R^T K^* R \mathfrak{N} \left(\left[[AR^T]_{1D} [\delta s_k]_c \right. \right. \\ \left. \left. + [^{\prime} [AR^T]_{1D} [\delta s_k]_c \right] \right) \quad (23)$$

where the symbol [$^{\prime}$] in the last term implies that the absolute value operation is applied to all of the elements of $[AR^T]_1$. The K^* matrix applies to the last term with no adjustments because ω is by definition positive in the primed reference frame.

For each maneuver used in the calibration process, equation (22) provides three linear equations in the $N_g \cdot k_{max}$ unknowns $\{\delta s_{nk}\}$. To get proper visibility for accurately measuring all of the $\{\delta s_{nk}\}$ elements, a range of both positive and negative maneuvers in all of the pitch, roll, and yaw directions must be sampled. With an appropriately large number of maneuvers sampled, equation (22) can be used as the basis for a standard least-squares algorithm to determine estimates for the correction terms.

As with the original Davenport approach to the calibration problem, adjustments to the scale factor calibration imply an associated adjustment to the current estimate for the drift rate bias vector. In equation (2b) this adjustment is represented by the quantity mD_0 . The analogous correction for the derivation in this section, which we will here call d_s , is given by

$$d_s = -\mathfrak{N} \sum \{ \delta s_k [^{\prime} A D_0] \} \quad (24)$$

which follows from equation (20) by replacing $(\Omega - \Omega_m)$ with d_s on the left-hand-side and Ω with D_0 on the right-hand-side. The D_0 value to be inserted into the equations is the most recent value determined for operational use.

Equation (22) can be generalized to allow for alignment and/or bias adjustments within the calibration state vector. This is done by simply combining equations (11a) and (22), with the restriction that the summation over k exclude the linear scale factor corrections, i.e.,

$$2 \zeta = -R^T K^* B m + R^T K^* R d \\ + R^T \sum K^*_{\delta s_k} (R \mathfrak{N}_0 [^{\prime} [A_0 R^T]_{1D}]) [\delta s_k]_c \quad (25)$$

with the set $\{\delta s_k\}$ restricted to nonlinear terms. The 0 subscript on \mathfrak{N}_0 and A_0 indicates that the current estimate for the gyro alignments is used in constructing the nonlinear correction coefficients. After the calibration set $\{m, d, \{\delta s_k\}\}$ has been determined, equations (26a) - (26d) can be used to calculate Ω .

$$\Omega = (G C - D) \\ - \mathfrak{N}_0 \sum \{ (s_{k_0} + \delta s_k) [^{\prime} A_0 (G C - D)] \} \quad (26a)$$

$$G = (I_3 + m) G_0 \quad (26b)$$

$$D = (I_3 + m) D_0 + d \\ - \mathfrak{N}_0 \sum \{ \delta s_k [^{\prime} A_0 D_0] \} \quad (26c)$$

$$G_0 = \mathfrak{N}_0 S^{-1} \quad (26d)$$

Although straightforward to use as the basis for a least-squares algorithm (i.e., to solve for the state vector $\{m, d, \{\delta s_k\}\}$ given an error set $\{\zeta\}$), equation (25) is somewhat unaesthetic in that it mixes a set of parameters pertaining to the combined gyro system (i.e., $\{m, d\}$) with another set pertaining to the individual gyroscopes (i.e., $\{\delta s_k\}$). For elegance in presentation and to support engineering analysis of individual gyro behavior, having a state vector consisting solely of specific parameters of the individual gyros would be desirable. Equation (25) could be so recast if we were dealing only with sets of three gyros. However, for gyro sets containing more than three gyros, the parameter set $\{m, d\}$ captures all of the functionally observable information available in the maneuver measurements. (Of course, if the full set of gyro data is available, the data can be processed for each combination of three gyros and the individual gyro parameters extracted, but this defeats the processing simplifications discussed herein.)

This point concerning observability raises a question: for how many gyroscopes can unique scale factor information be obtained when equation (22) is applied together with the constraint of fixed gyro alignments? This question may be readily answered for the case where the state vector is restricted to linear scale corrections, i.e., δs_k . In this case, the δs_k matrix transforms to an equivalent m matrix via

$$m = -\mathfrak{N} \delta s_k A = -[A^T A]^{-1} [A^T \delta s_k A] \quad (27)$$

Both $[A^T A]$ and $[A^T \delta s_k A]$ can be shown to be 3-by-3 symmetric matrices, implying that the product $[A^T A]^{-1} [A^T \delta s_k A]$ is as well. The change matrix m therefore has only six independent elements, from which we conclude that the techniques of this section can provide independent scale parameter corrections for at most six gyroscopes. ("At most" applies because any coaligned gyroscopes will have degenerate corrections irrespective of the total number).

Section 5 - Least-Squares Solution and Weight Matrix Specification

For completeness, we present in this section a few points pertaining to the selection of weights to be applied to the input measurements. As discussed in many references on least-squares algorithms (e.g., Reference 4), the solution for the batch linear least-squares problem associated with a matrix equation $H X = Y$ can generally be written as

$$X = (H^T W H + W_A)^{-1} (H^T W Y + W_A X_A) \quad (28)$$

For our problem, X (the state vector) will be some combination of m , d , and/or $\{\delta s_k\}$, Y is $[\zeta_1^T, \dots, \zeta_N^T]^T$ for N maneuvers, H is a matrix of state vector multiplying elements constructed from appropriate pieces of equation (25), W is a $3N$ -by- $3N$ weight matrix for the error measurements (the elements of Y), and W_A is a weight matrix associated with the a priori state vector estimate, X_A . For our problem, because the state vector consists of differential changes from the previous best estimate, we set $X_A = 0$. Our only remaining concern, therefore, is to establish reasonable estimates for W and W_A .

Often it is both convenient and reasonable to simply set W to I_{3N} and W_A to 0 . (We used this approach in our analysis of the HST maneuver data and have found it operationally acceptable.) Implicit in the approach are the following five assumptions: (1) the state vector correction terms are fairly stable over the time period of data collection, (2) the degree of correlation between measurement error components is fairly small, (3) the expected error component magnitudes are all approximately the same, (4) the data set spans the domain of state vector sensitivity sufficiently well that observability is not a problem, and (5) a sufficiently extensive data set has been accumulated that neglect of a priori information does not undermine operations. The first three points relate to setting W to I_{3N} , whereas the last two relate to setting W_A to 0 .

If any of the conditions indicated in the previous paragraph are significantly violated, a more sophisticated weighting scheme is required. We present here a method for specifying W that retains assumption 1, eliminates assumption 3, and replaces assumption 2 with a less restrictive one (called 2a) that the measurement errors associated with each maneuver are uncorrelated with those of all others. We will not consider the possible advantages of a

nonzero W_A . Assumptions 1 and 2a allow W to be expressed as a block diagonal matrix, with each block being a 3-by-3 matrix, w , associated with a specific maneuver. Given the block diagonal form, each w can be written as $(p_R + p_G)^{-1}$, where p_R is the covariance associated with reference attitude errors, and p_G is the covariance associated with random gyro errors. The attitude covariance matrix is given by

$$p_R = T_\tau^T p_i T_\tau + p_f \quad (29)$$

where p_i and p_f are the initial and final attitude covariance matrices in the instantaneous spacecraft frame, and T_τ is as used in equation (5). Reference 5 specifies an equation for attitude covariance matrices such as p_i and p_f . This equation, which depends upon the reference star distribution and the measurement and catalog errors for each star, is

$$p_{if} = \sigma_i^2 [I_3 - \Sigma(\sigma_i^2/\sigma_j^2) V_j V_j^T]^{-1} \quad (30)$$

where $\sigma_i^2 \equiv [\Sigma \sigma_j^2]^{-1}$, σ_j is the root-mean-square combined measurement and catalog error for the j th star, V_j is the j th star vector expressed in the spacecraft frame, and the sums are over all observations. This expression can be simplified for processing purposes in the case of observations from a number of well-separated star sensors with fairly narrow fields-of-view (narrow relative to the field-of-view separations). In this case, each V_j can be replaced with the boresight direction vector for the j th sensor expressed in spacecraft coordinates, with σ_j then indicating typical error size for that sensor. This substitution eliminates ground processing of the reference star data.

A reasonable, albeit heuristic, model for the covariance associated with gyro errors is

$$p_G \approx I_3 [\sigma_{gd}^2 \tau^2 + \sigma_{gna}^2 \Theta^2] \quad (31)$$

where σ_{gd} is the typical single-axis standard deviation of the gyro drift rate bias, and σ_{gna} is the typical scale factor/alignment maneuver error. Equation (31) does not attempt to model the physical mechanism that produces gyro noise, but rather requires the user to provide parameters σ_{gd} and σ_{gna} based on typical spacecraft performance. Empirically, for the HST gyroscopes working as a set, we find $\sigma_{gd} \sim 0.01$ arcsecond per second and $\sigma_{gna} \sim 0.2$ arcsecond per degree.

Section 6 - HST Gyroscope Behavior

The HST gyroscope system comprises three rate gyro assemblies (RGAs) manufactured by AlliedSignal Government Electronic Systems. Each RGA consists of two single-degree-of-freedom, dual-mode, rate integrating, mechanical gyroscopes. The high-rate mode has a range of ± 1800 degrees per hour and a resolution of 7.5 milliarcseconds per 40-hertz sample; the low-rate mode has a range of ± 20 degrees per hour and a resolution of 0.125 milliarcsecond per 40-hertz sample. The gyro alignments are such that any three can be used to completely sample rotations of the spacecraft. The onboard system is configured to nominally use four gyroscopes simultaneously, keeping the remaining two as backups.

RGA units 2 and 3 (those housing gyros 3, 4, 5, and 6) were replaced in December 1993 during the first HST servicing mission. All six gyroscopes were activated for the servicing mission and early on-orbit verification and calibration phase. The iterative calibration procedure described in References 1 and 6 was followed until convergence was achieved. Thereafter, the two gyros in RGA unit 1 were deactivated, leaving HST operating with four new, freshly calibrated gyroscopes. The active gyros are mounted with input-axis unit vectors of approximately $(\pm 0.586, \pm 0.617, -0.525)$, with the sign sense for the first two components being $(-, +, -, +)$, for gyros 3, 4, 5, and 6, respectively. The symmetry of these vectors about the yaw axis is significant for understanding the specific manifestation of an observed growing scale error.

As is typical with spacecraft gyroscopes, the biases vary fairly rapidly. For the HST gyroscopes, the change in the drift rate bias for both high- and low-rate modes has been found to be about 7 arcseconds per hour per day. The temporal variation of the high-rate mode drift bias vector (i.e., as measured in vehicle space) has been found to track the low-rate mode vector variations quite closely. This allowed implementation of an operational procedure whereby only the low-rate mode bias is measured frequently, based on data accumulated during science pointing with the spacecraft pointing control system locked on fine guidance sensor guide stars. The high-rate mode bias is then determined from the low-rate mode bias via an additive offset, which is monitored for constancy once every 4 to 6 weeks. The algorithm used for monitoring the offset had been, until recently, essentially that discussed in Section 3 in association with equation (13). The

spacecraft pointing control system is commanded to place the gyroscopes in high-rate mode while maintaining a constant attitude for approximately one orbit (about 95 minutes). Fixed-head star tracker star measurements are obtained at the beginning and end of this constant attitude period and used to determine the true attitude change.

In HST operations, most large maneuvers are predominantly about the yaw axis. The predominant symptom of the scale factor problem discovered in August 1995 was a substantially larger postslew pointing error for negative yaw maneuvers than for positive yaw maneuvers. Upon examining the quantity $E \equiv (2\zeta \cdot \eta / \Theta)$ for maneuvers between the time of the first servicing mission and August 1995 with $|\eta_3| > 0.9$ and $\Theta > 90$ degrees, we found that although the average value of E for positive yaw maneuvers stayed near zero, its value for negative yaw maneuvers was fairly well fit by the curve

$$\bar{E} \approx 0.2 + 0.6 (1 - e^{-\tau t})$$

arcseconds per degree

(32a)

$$T \approx 6 \text{ months}$$
(32b)

The sense of the error for negative yaw maneuvers was such that the spacecraft fell short of its intended destination. The random scatter for E is about 0.3 arcsecond per degree (3σ).

The analysis techniques described in this paper were developed to study the temporal change that was seen to have occurred in the HST RGAs. As part of our study, we have come to realize that the effects of gyroscope nonlinearities are as important as the temporal changes that precipitated the study. We applied our analysis to a combined set of 83 maneuvers collected in August 1994 and August 1995. (Our data indicate that the scale factors had stopped changing by August 1994.) For some of our analysis runs, we also included a 1-hour period of constant attitude. We find that studying the fit residuals associated with the constant attitude period is important for constructing a high-fidelity model of gyroscope response. The results of our analysis are specified below.

(1) To study the change in average linear scale relative to the original post-servicing-mission calibration, we performed a fit using the high mode bias offset vector and gyro frame linear scale factors as our state vector. The best fit values for this case are given in equations (33a) and (33b).

$$\mathbf{d}_{\text{OFFSET}} = [-1.8 \times 10^2, 3.4 \times 10^2, -7.7 \times 10^2]^T \pm 1 \times 10^2 \text{ arcsecond per second} \quad (33a)$$

$$[\delta s_{1c}]_c = [5.7 \times 10^5, 4.2 \times 10^5, 8.4 \times 10^5, 1.74 \times 10^4]^T \pm 1 \times 10^5 \quad (33b)$$

As will be discussed shortly, the bias offset adjustment is that required to compensate for gyroscope nonlinearities, the "true" bias at constant attitude already having been eliminated by the standard operational procedures. The $[\delta s_{1c}]_c$ elements represent the average change in the high-rate mode scale factors. The sign sense indicates that the gyros have become more sensitive (more counts per degree of actual slew). The largest single change, that for gyro 6, corresponds to an error of 56 arcseconds for a 90-degree slew about the input axis.

(2) Because of the difference in response for positive and negative slews, together with the fact that the bias determination procedure had been tuned to work accurately at zero angular rate, it seemed likely that some scale nonlinearity was involved. Taking $\mathbf{d} = \mathbf{0}$ as a constraint effectively imposed by the operational procedures, we investigated potential nonlinearities by solving for a state vector consisting of $[\delta s_{1c}]_c$ and $[\delta s_{1d}]_c$. The best-fit results in this case are

$$[\delta s_{1c}]_c = [6.0 \times 10^5, 2.9 \times 10^5, 1.27 \times 10^4, 1.48 \times 10^4]^T \pm 1 \times 10^5 \quad (34a)$$

$$[\delta s_{1d}]_c = [0.8 \times 10^5, 6.1 \times 10^5, 1.95 \times 10^4, 7.8 \times 10^5]^T \pm 1 \times 10^5 \quad (34b)$$

Comparing the nonlinear correction values with the average change values indicated for the first case, we see that the error associated with not taking the nonlinear effect into account can be as large as the temporal change. We also determined fit parameters for two other cases, one including \mathbf{d} in the state vector and another using $g_2(\Omega) = \Omega^2$ rather than $|\Omega|$. The former showed a slight reduction in the fit residuals, whereas the latter showed a slight increase in the fit residuals; the changes in residuals in both cases were insignificant.

Given our findings regarding scale factor nonlinearities, the spacecraft pointing control logic should ideally include compensation for this effect when estimating spacecraft angular rates. Although the HST pointing control system does not model scale factor nonlinearities, we can compensate to a significant degree for the nonlinearities by allowing

the low-to-high bias offset to absorb the average effect of the gyroscope nonlinearities as weighted by the actual distribution of maneuvers scheduled for the HST mission. This is effectively what happens with the fit procedure associated with equation (33a). The large negative third component for the bias in equation (33a) is associated with the positive sign of the components of $[\delta s_{1c}]_c$ in equation (34b), together with the fact that gyros 3 - 6 are, on average, pointing along the negative yaw axis. This weighting for mission maneuver distribution will also affect the estimated average scale factors, as can be seen by comparing equations (33b) and (34a). Empirically, it appears that adequate HST mission performance is achieved with this approach during normal operations. We note, however, that this approach does not give optimized performance for high-rate mode, inertial hold conditions, the implied spurious drift being about 300 arcseconds per hour.

Using the bias vector to absorb the average effect of gyroscope nonlinearities weighted according to the profile of mission maneuvers could be problematic for spacecraft that use single-mode gyroscopes. For such spacecraft, science operations would likely require the bias vector to be selected so that pointing performance is optimized with respect to constant attitude periods. Adjusting the bias to improve maneuver performance is therefore not an option. Mission engineers designing the pointing control and sensor calibration algorithms for such missions should consider including compensation for gyroscope nonlinearities, particularly if slewing accuracies better than 1 arcsecond per degree are required.

(3) As part of our analysis of the HST gyroscope changes, we also considered the possibility that the changes were associated with the gyroscope alignment matrix. We therefore performed a fit for a scale factor/alignment correction matrix (m) together with a bias adjustment (\mathbf{d}) based on equation (11a). We found that including the alignment adjustments did not significantly improve the residuals relative to those associated with the fit restricted to state vector $\{\mathbf{d}, [\delta s_{1c}]_c\}$. We specifically found that the alignment terms did not allow us to simultaneously obtain improved residuals for the maneuver data while maintaining small residuals for the constant attitude data. Our results are consistent with there being no significant change in the gyroscope alignments during the 18 months following the first HST servicing mission.

Conclusions

This paper has presented a number of variations on the Davenport algorithm for gyroscope calibration specifically designed to (1) allow analysis with a drastically restricted quantity of telemetry data and (2) extend the state vector domain to allow study of both isolated and nonlinear scale factor corrections. We have applied the techniques to data obtained during normal operations of HST as part of a study of temporal variations of the HST gyroscope scale factors. We have found that the HST replacement gyroscopes experienced significant change over the first 6 to 8 months following the first HST servicing mission, the largest individual change corresponding to an error in estimated projected rate about the input axis of about 56 arcseconds per 90 degrees. We have found scale factor nonlinearities that, when characterized as differences between scale factors associated with positive and negative rotations, are as large as 2 parts in 10000, i.e., about 65 arcseconds per 90 degrees. For spacecraft, such as HST, that use dual-mode gyroscopes, the effects of the nonlinearities can be accommodated to a significant degree via adjustments to the high-rate mode drift rate bias vector. This approach may be inadequate for missions using single-mode gyroscopes. Finally, we find, to within the accuracy of our data set, that no significant changes have occurred to the gyroscope alignments during the first 18 months following the servicing mission.

The work reported in this article was supported in part by National Aeronautics and Space Administration (NASA) contracts NAS 5-31500 and NAS 5-31000, which enable Computer Sciences Corporation and AlliedSignal Technical Services Corporation to provide systems engineering, analysis, and operations support to NASA's Goddard Space Flight Center.

Appendix - Model Maneuver Profile

In this appendix we present the details of one fairly common maneuver model. In addition to the total maneuver angle, the model uses three input parameters characterizing the spacecraft's maneuver execution algorithm. These parameters can be selected as the maximum jerk magnitude (J_m), the jerk pulse duration (δ), and the maximum angular velocity magnitude (ω_m). The maneuver profile is symmetric about the midtime ($\tau/2$); it is therefore sufficient to construct the maneuver profile through that time. Throughout the maneuver, the angle (θ), rate (ω), and acceleration (a) are continuous, and the jerk (the third time derivative of θ) takes on one of

three values: J , 0 , or $-J$. The maneuver through its midpoint is composed of two, three, or four segments, depending upon the value of Θ . The construction for each solution type is presented below.

Operationally, three auxiliary parameters are first calculated from the three input parameters:

$$\epsilon_{\max} = \omega_m / J_m \delta - \delta \quad (\text{A.1a})$$

$$\Theta_a = 2 J_m \delta^3 \quad (\text{A.1b})$$

$$\Theta_b = \Theta_a \{[(\epsilon_{\max}^2 + 3\delta\epsilon_{\max}) / 2\delta^2] + 1\} \quad (\text{A.1c})$$

These three equations will be derived below. The determination of whether a two-, three-, or four-segment half-maneuver pertains depends upon where Θ falls relative to Θ_a and Θ_b ; a two-segment solution pertains for Θ in the range $[0, \Theta_a]$, a three-segment solution for the range $[\Theta_a, \Theta_b]$, and a four-segment solution for $[\Theta_b, \pi]$.

Two-segment solution

The two-segment solution assumes that the jerk is equal to some positive value J for a time period δ and equal to $-J$ for a subsequent equal period. The functions $a(t)$, $\omega(t)$, and $\theta(t)$ are each required to be continuous through the point of discontinuous jerk. The angular velocity reaches its maximum value at exactly the midpoint of the maneuver, i.e., at $\tau/2 = 2\delta$. The solution for the two segments is specified below.

Segment 1: $0 < t < \delta$

$$J(t) = J \quad (\text{J yet unknown}) \quad (\text{A.2a})$$

$$a(t) = J t \quad (\text{A.2b})$$

$$\omega(t) = 1/2 J t^2 \quad (\text{A.2c})$$

$$\theta(t) = 1/6 J t^3 \quad (\text{A.2d})$$

Segment 2: $\delta < t < 2\delta$

$$J(t) = -J \quad (\text{A.2e})$$

$$a(t) = J \delta - J (t - \delta) \quad (\text{A.2f})$$

$$\omega(t) = 1/2 J \delta^2 + J \delta (t - \delta) - 1/2 J (t - \delta)^2 \quad (\text{A.2g})$$

$$\theta(t) = 1/6 J \delta^3 + 1/2 J \delta^2 (t - \delta) + 1/2 J \delta (t - \delta)^2 - 1/6 J (t - \delta)^3 \quad (\text{A.2h})$$

The unknown J is determined by the requirement that $\theta(\tau/2) = \Theta/2$. Substituting $t = 2\delta$ in equation (A.2h) yields

$$J = \Theta / 2\delta^3 \quad (\text{A.2i})$$

The two-segment solution applies until equation (A.2i) produces a value of J greater than J_m . This gives the limiting angle Θ_s , indicated in equation (A.1b).

Three-segment solution

For maneuvers with angle Θ exceeding Θ_s , the two periods of constant jerk are separated by a period of zero jerk, of duration ϵ (to be determined). For convenience, let us define a time point $\Delta = \delta + \epsilon$. The solution for the three segments is specified below.

Segment 1: $0 < t < \delta$

$$J(t) = J_m \quad (\text{A.3a})$$

$$a(t) = J_m t \quad (\text{A.3b})$$

$$\omega(t) = 1/2 J_m t^2 \quad (\text{A.3c})$$

$$\theta(t) = 1/6 J_m t^3 \quad (\text{A.3d})$$

Segment 2: $\delta < t < \Delta$

$$J(t) = 0 \quad (\text{A.3e})$$

$$a(t) = J_m \delta \quad (\text{A.3f})$$

$$\omega(t) = 1/2 J_m \delta^2 + J_m \delta (t - \delta) \quad (\text{A.3g})$$

$$\theta(t) = 1/6 J_m \delta^3 + 1/2 J_m \delta^2 (t - \delta) + 1/2 J_m \delta (t - \delta)^2 \quad (\text{A.3h})$$

Segment 3: $\Delta < t < \Delta + \delta$

$$J(t) = -J_m \quad (\text{A.3i})$$

$$a(t) = J_m \delta - J_m (t - \Delta) \quad (\text{A.3j})$$

$$\omega(t) = 1/2 J_m \delta^2 + J_m \delta \epsilon + J_m \delta (t - \Delta) - 1/2 J_m (t - \Delta)^2 \quad (\text{A.3k})$$

$$\theta(t) = 1/6 J_m \delta^3 + 1/2 J_m \delta^2 \epsilon + 1/2 J_m \delta \epsilon^2 + 1/2 J_m \delta^2 (t - \Delta) + J_m \delta \epsilon (t - \Delta) + 1/2 J_m \delta (t - \Delta)^2 - 1/6 J_m (t - \Delta)^3 \quad (\text{A.3l})$$

The unknown ϵ is determined by the requirement that $\theta(\tau/2) = \Theta/2$. Substituting $t = \Delta + \delta$ in equation (A.3l) yields the quadratic equation

$$\epsilon^2 + 3 \delta \epsilon - 2 \delta^2 (\Theta/\Theta_s - 1) = 0 \quad (\text{A.3m})$$

the solution for which is

$$\begin{aligned} \epsilon &= 3/2 \delta \{ [1 + 8/9 (\Theta/\Theta_s - 1)]^{1/2} - 1 \} \\ &= 1/2 \delta \{ [1 + 8 \Theta/\Theta_s]^{1/2} - 3 \} \end{aligned} \quad (\text{A.3n})$$

The three-segment solution applies until equation (A.3k), combined with equation (A.3n), produces a value of ω greater than ω_m . The maximum

permitted value of ϵ can be found by setting $\omega(t)$ in equation (A.3k) to ω_m at $t = 2\delta + \epsilon$. This results in

$$\epsilon_{\max} = \omega_m / J_m \delta - \delta \quad (\text{A.3o})$$

Note that for the progression of solutions to be consistent, we require $\omega_m \geq J_m \delta^2$. The maximum maneuver angle permitted for the three-segment model can be found by substituting ϵ_{\max} for ϵ in equation (A.3m); the result is equation (A.1c).

Four-segment solution

For maneuvers with angle Θ exceeding Θ_s , the third segment is followed by a period of constant angular rate at the maximum permitted value. This fourth segment lasts until the maneuver reaches the half-way point, i.e., until $\theta(t) = \Theta/2$. The result is that the maneuver profile for the first three segments is the same as that appropriate for a three-segment solution with $\epsilon = \epsilon_{\max}$, and during the fourth segment it is given by

$$J(t) = 0 \quad (\text{A.4a})$$

$$a(t) = 0 \quad (\text{A.4b})$$

$$\omega(t) = \omega_m \quad (\text{A.4c})$$

$$\theta(t) = \Theta_s/2 + \omega_m [t - (2\delta + \epsilon_{\max})] \quad (\text{A.4d})$$

The total maneuver duration in this case is determined by the requirement that $\theta(\tau/2) = \Theta/2$. Thus, τ is given in this case by

$$\tau/2 = (\Theta - \Theta_s)/2\omega_m + (2\delta + \epsilon_{\max}) \quad (\text{A.4e})$$

References

1. *Algorithm for In-Flight Gyroscope Calibration*, P. B. Davenport and G. L. Welter, Proceedings of the Flight Mechanics / Estimation Theory Symposium, Goddard Space Flight Center, May 1988.
2. Space Telescope POCC Applications Software Support (PASS) Requirements Specification (Revision E), L. Hallock et al., August 1993, Computer Sciences Corporation document CSC/TM-82/6045.
3. *Update on Gyro Slew Misdistances*, memo by M. Gakenheimer, August 30, 1995.
4. Spacecraft Attitude Determination and Control, J. R. Wertz (ed.), D. Reidel Publishing Company, Dordrecht: Holland, 1978.

5. *Three-Axis Attitude Determination from Vector Observations*, M. Shuster, and S. Oh, Journal of Guidance and Control, January 1981, vol. 4, no. 1, p. 70.

6. *The In-Flight Calibration of the Hubble Space Telescope Attitude Sensors*, G. L. Welter, Proceedings of the Flight Mechanics / Estimation Theory Symposium, Goddard Space Flight Center, May 1991.

G. Welter & J. Boia, Computer Sciences Corporation, 1100 West Street, Laurel MD 20707

M. Gakenheimer, E. Kimmer, and D. Channell, AlliedSignal Technical Services Corporation, Code 519.1, NASA / Goddard Space Flight Center, Greenbelt MD 20771

L. Hallock, Code 512.0, NASA / Goddard Space Flight Center, Greenbelt MD 20771

SATELLITE ANGULAR RATE ESTIMATION FROM VECTOR MEASUREMENTS

Ruth Azor*

MBT Systems and Space Technology, Electronics Division, Israel Aircraft Industries Ltd.
Yahud, Industrial Zone 56000, Israel

Itzhack Y. Bar-Itzhack#

Richard R. Harman+

Flight Dynamics Support Branch, Code 553 NASA Goddard Space Flight Center Greenbelt, MD 20771

Abstract

This paper presents an algorithm for estimating the angular rate vector of a satellite which is based on the time derivatives of vector measurements expressed in a reference and body coordinate. The computed derivatives are fed into a special Kalman filter which yields an estimate of the spacecraft angular velocity. The filter, named Extended Interlaced Kalman Filter (EIKF), is an extension of the Interlaced Kalman Filter (IKF) presented in the literature. Like the IKF, the EIKF is a suboptimal Kalman filter which, although being linear, estimates the state of a nonlinear dynamic system. It consists of two or three parallel Kalman filters whose individual estimates are fed to one another and are considered as known inputs by the other parallel filter(s). The nonlinear dynamics stem from the nonlinear differential equation that describes the rotation of a three dimensional body. Initial results using simulated data, and real RXTE data indicate that the algorithm is efficient and robust.

I. INTRODUCTION

Small inexpensive satellites which do not carry gyroscopes on board still need to know their angular rate vector for attitude determination and for control loop damping. The same necessity exists also in gyro equipped satellites when performing high rate maneuvers whose angular rate is out of range of the on board gyros. While the attitude determination task requires high precision angular rate measurements, low precision angular rate measurements are adequate for control loop damping. Satellites usually utilize vector measurements for attitude determination. Such measurements are, for example, of the direction of the nadir, of the sun, of the magnetic field vector, etc. The vector measurements can be differentiated in time in order to obtain valuable information. This approach was used by Natanson¹ for estimating attitude from magnetometer measurements and by Challa, Natanson, Deutschmann and Galal² to obtain attitude as well as rate.

Angular rate can be extracted from vector measurements in the following way. Let \mathbf{b} represent a vector measured by an attitude sensor such as Sun Sensor, Horizon Sensor, etc. For the time being let us assume that \mathbf{b} is the earth magnetic field vector. From the laws of dynamics it is known that

$$\dot{\mathbf{b}}^i = \dot{\mathbf{b}}^b + \boldsymbol{\omega} \times \mathbf{b}^b \quad (1)$$

where $\dot{\mathbf{b}}^i$ is the time derivative of \mathbf{b} as seen by an observer in inertial coordinates (i), $\dot{\mathbf{b}}^b$ is the time derivative of \mathbf{b} as seen by an observer in body coordinates (b), and $\boldsymbol{\omega}$ is the angular rate vector of coordinate system b with respect to coordinate system i. (Note that the choice of the inertial coordinate system as the reference coordinates is arbitrary). We can write (1) as follows

* Senior Control Engineer, System Engineering Department.

Sophie and William Shamban Professor of Aerospace Engineering.
On sabbatical leave from the faculty of Aerospace Engineering,
Technion-Israel Institute of Technology, Haifa 32000, Israel.
Member Technion Space Research Institute. IEEE Fellow.

+ Aerospace Engineer.

A part of this work was performed on a National Research Council NASA Research Associateship.

$$[b \times] \omega = \dot{b} - D_b^i b \quad (2.a)$$

where $[b \times]$ is the cross product matrix of the measured vector b . Note that b is computable since b is usually known from Almanac or a model, and \dot{b} is computable from the measurements. Consequently, all elements of (2.a) other than ω are known. Let us resolve (2.a) in the body coordinates and let us also denote the transformation matrix from i to b by D_b^i , then (2.a) can be written as

$$[b \times] \omega = \dot{b} - D_b^i b \quad (2.b)$$

where the dot denotes a simple time derivative. Note that b is resolved in the i coordinates and D_b^i has to be known. We realize that ω cannot be determined from (2.b) since $[b \times]$ is not invertible. If we add though one more vector measurement, c , from an *additional sensor*, then ω can be determined as shown next. Similarly to (2.b), we can write for c

$$[c \times] \omega = \dot{c} - D_c^i c \quad (3)$$

When we augment (2.b) and (3) into one equation we obtain

$$\begin{bmatrix} \dot{b} - D_b^i b \\ \dots \\ \dot{c} - D_c^i c \end{bmatrix} = \begin{bmatrix} 0 & -b_z & b_y \\ b_z & 0 & -b_x \\ -b_y & b_x & 0 \\ 0 & -c_z & c_y \\ c_z & 0 & -c_x \\ -c_y & c_x & 0 \end{bmatrix} \begin{bmatrix} \omega_x \\ \omega_y \\ \omega_z \end{bmatrix} \quad (4)$$

Define

$$d = \begin{bmatrix} \dot{b} - D_b^i b \\ \dots \\ \dot{c} - D_c^i c \end{bmatrix} \quad (5.a)$$

$$G = \begin{bmatrix} 0 & -b_z & b_y \\ b_z & 0 & -b_x \\ -b_y & b_x & 0 \\ 0 & -c_z & c_y \\ c_z & 0 & -c_x \\ -c_y & c_x & 0 \end{bmatrix} \quad (5.b)$$

$$\omega = \begin{bmatrix} \omega_x \\ \omega_y \\ \omega_z \end{bmatrix} \quad (5.c)$$

then (4) can be written as

$$d = G\omega \quad (6)$$

Next, define $G^\#$, the pseudo-inverse of G , as follows

$$G^\# = (G^T G)^{-1} G^T \quad (7)$$

where T denotes the transpose, then $\hat{\omega}$, the best estimate of ω in the least squares sense, is given by³

$$\hat{\omega} = G^\# d \quad (8)$$

Note that this solution exists only if b and c are not co-linear. An estimate of ω , better than that given in (8), can be obtained when the problem is treated as a stochastic problem and some kind of filtering is applied to the measurements. Moreover, filtering in the sense of estimation is a must when at each time point we have only one vector measurement. (Such case exists, for example, when we use a Sun Sensor and some other vector measuring sensor, and the satellite happens to be in a shadowed zone). In such case we use the vehicle dynamics for propagating the estimate of ω . As will be shown in the ensuing, the dynamics model of a spacecraft (SC) is a non-linear model, therefore a linear Kalman

filter (KF) is not suitable, and some kind of non-linear estimator is needed for estimating ω . The extended Kalman filter (EKF) is, then, the natural choice. However, Algrain and Saniie⁴ introduced the Interlaced Kalman filter (IKF) which is a sub-optimal filter that is a combination of two linear Kalman filters that operate simultaneously and feed one another. While the IKF of Algrain and Saniie was an ingenious idea, they did not utilize its full power since they fed the filter with the angular rate vector itself as measured by gyros and not with vector derivative information. Therefore they practically used the IKF merely as a low pass filter and not as an estimator. This is equivalent to using the IKF for filtering $\hat{\omega}$ computed in (8). In contrast to Algrain and Saniie, we use their idea to estimate the angular rate vector directly from vector measurements and their time derivatives and are able to obtain estimates even when we have a single measurement at each time point. We also extend their dynamics model farther to include products of inertia. This leads to the use of two or three more sophisticated KFs that make use of three dynamics models. We call the extended filter: Extended Interlaced Kalman Filter (EIKF). Finally, our work differs considerably from that of Natanson¹, and Challa, Natanson, Deutschmann and Galal² mainly because most of our investigation is dedicated to the filtering stage. In the next section we develop the dynamics models which give rise to the use of the EIKF. This leads to the development of measurement equations that correspond to the states of the dynamic models. This is done in Section III. In Section IV we present the stochastic models which are used by the EIKF. They are based on the dynamics and measurement models derived in Sections II and III respectively. Then in Section V we introduce several options for implementing the EIKF followed by test results of the EIKF which we show in Section VI. Finally, in Section VII we present our conclusions from this work.

II. SPACECRAFT DYNAMICS

In order to apply a recursive estimator to estimate the angular rate vector of a gyro-less spacecraft (SC), one needs to utilize the dynamics model of the SC. The angular dynamics of an SC is given in the following equation⁵

$$I\dot{\omega} + \dot{h} + \omega \times (I\omega + h) = T \quad (9)$$

where I is the moment of inertia matrix, ω is the angular velocity of the satellite with respect to inertial space, h is the angular momentum of the momentum, or reaction, wheels and T is the external torque applied to the SC. All vectors in (9) are resolved in the b system. Since I is nonsingular, we may write (9) as

$$\dot{\omega} = -I^{-1}(\omega \times (I\omega + h)) + I^{-1}(T-h) \quad (10)$$

The inertia matrix, I , is given by⁶

$$I = \begin{bmatrix} I_{xx} & -I_{xy} & -I_{xz} \\ -I_{xy} & I_{yy} & -I_{yz} \\ -I_{xz} & -I_{yz} & I_{zz} \end{bmatrix} \quad (11)$$

where I_{xx} , I_{yy} , and I_{zz} are the moments of inertia about the body major axes x , y and z respectively, and I_{xy} , I_{xz} and I_{yz} are the product moment of inertia terms. Using these notations, (10) can be written as follows. Define

$$H = \begin{bmatrix} 0 & h_z & -h_y \\ -h_z & 0 & h_x \\ h_y & -h_x & 0 \end{bmatrix} \quad (12.a)$$

$$I_{\omega\omega} = \begin{bmatrix} (I_{zz} - I_{yy}) & I_{xy} & -I_{xz} \\ -I_{xy} & (I_{xx} - I_{zz}) & I_{yz} \\ I_{xz} & -I_{yz} & (I_{yy} - I_{xx}) \end{bmatrix} \quad (12.b)$$

$$I_{\omega\omega\omega} = \begin{bmatrix} 0 & -I_{yz} & I_{yz} \\ I_{xz} & 0 & -I_{xz} \\ -I_{xy} & I_{xy} & 0 \end{bmatrix} \quad (12.c)$$

$$\chi = \begin{bmatrix} \omega_y \omega_z \\ \omega_x \omega_z \\ \omega_x \omega_y \end{bmatrix} \quad (12.d) \quad \lambda = \begin{bmatrix} \omega_x^2 \\ \omega_y^2 \\ \omega_z^2 \end{bmatrix} \quad (12.e)$$

then (10) can be written as

$$\dot{\omega} = -I^{-1}H \omega - I^{-1}I_{\omega\omega}\chi - I^{-1}I_{\omega\omega\omega}\lambda + I^{-1}(T-h) \quad (13)$$

Let

$$F_{\omega} = -I^{-1}H \quad (14.a)$$

$$B_{\omega} = -I^{-1}I_{\omega\omega} \quad (14.b)$$

$$B_{\omega\omega} = -I^{-1}I_{\omega\omega\omega} \quad (14.c)$$

$$f = I^{-1}(T-h) \quad (14.d)$$

then (13) can be written as follows

$$\dot{\omega} = F_{\omega} \omega + B_{\omega} \chi + B_{\omega\omega} \lambda + f \quad (15)$$

The latter is the desired rotational dynamics equation which expresses the time derivative of ω , the angular velocity vector of the SC with respect to inertial space, in terms of the known forcing function, f , and ω itself. This equation is the central equation in the development of the filter. We realize that the solution of (15) hinges on our knowledge of χ and λ . As will be shown later, they will be estimated by their own estimator. Those estimators will each need a dynamics model for the the vector it is set to estimate. The derivation of the dynamics model is presented next. First we differentiate (12.d) to obtain the second dynamics equation

$$\dot{\chi} = \begin{bmatrix} \dot{\omega}_y \omega_z + \omega_y \dot{\omega}_z \\ \dot{\omega}_x \omega_z + \omega_x \dot{\omega}_z \\ \dot{\omega}_x \omega_y + \omega_x \dot{\omega}_y \end{bmatrix} \quad (16)$$

Let

$$F_{\chi} = 0 \quad (17.a)$$

and

$$B_{\chi} = \begin{bmatrix} 0 & \dot{\omega}_z & \dot{\omega}_y \\ \dot{\omega}_z & 0 & \dot{\omega}_x \\ \dot{\omega}_y & \dot{\omega}_x & 0 \end{bmatrix} \quad (17.b)$$

then (16) can be written as

$$\dot{\chi} = F_{\chi} \chi + B_{\chi} \omega \quad (18)$$

which is the desired equation. To obtain the dynamics equation for λ , we differentiate (12.e). This yields

$$\dot{\lambda} = \begin{bmatrix} 2\dot{\omega}_x & 0 & 0 \\ 0 & 2\dot{\omega}_y & 0 \\ 0 & 0 & 2\dot{\omega}_z \end{bmatrix} \begin{bmatrix} \omega_x \\ \omega_y \\ \omega_z \end{bmatrix} \quad (19)$$

Let

$$F_\lambda = 0 \quad (20.a) \quad \text{and} \quad B_\lambda = \begin{bmatrix} 2\dot{\omega}_x & 0 & 0 \\ 0 & 2\dot{\omega}_y & 0 \\ 0 & 0 & 2\dot{\omega}_z \end{bmatrix} \quad (20.b)$$

then (19) can be written as

$$\dot{\lambda} = F_\lambda \lambda + B_\lambda \omega \quad (21)$$

Equations (15), (18) and (21) are the deterministic dynamics equations which describe the behavior in time of ω and the products of its components. They form the foundation of the stochastic dynamics model of the EIKF. Next we develop the measurement equations which will serve as the basis of the stochastic measurement model used by the EIKF to update its estimates.

III. MEASUREMENT EQUATIONS

III.1 Raw Vector Measurements

We start by deriving the measurement equation for the primary KF whose dynamics is given in (15) and which estimates ω . Re-write (2.b)

$$[b \times] \omega = \dot{b} - D_b^i b \quad (2.b)$$

Let

$${}^3z_{\omega b} = \dot{b} - D_b^i b \quad (22.a) \quad \text{and} \quad {}^3C_b = [b \times] \quad (22.b)$$

then (2.b) can be written as

$${}^3z_{\omega b} = {}^3C_b \omega \quad (22.c)$$

The measurement vector ${}^3z_{\omega b}$ is a computable three dimensional vector which is data to be fed into the EIKF part that estimates ω . We note that 3C_b is a 3×3 singular matrix. It is obvious that one of the three equations of (23) is a linear combination of the other two and, thus, is superfluous. Although a white noise will be added to ${}^3z_{\omega b}$ at a later stage (see(37)) and, thus, will turn the three equations in (23) into independent equations, the singularity of 3C_b will be troublesome. Problems may arise in the KF, designed to estimate ω , when computing its gain according to $K_\omega = P_\omega {}^3C_b^T [{}^3C_b P_\omega {}^3C_b^T + {}^3R_\omega]^{-1}$. ${}^3C_b P_\omega {}^3C_b^T + {}^3R_\omega$. The matrix ${}^3C_b P_\omega {}^3C_b^T$ is singular, and since the elements of the noise covariance matrix, ${}^3R_\omega$, are rather small, the inverse yields a matrix whose elements are very large. This in turn yields a very inaccurate gain matrix. All that keeps the inverted matrix from being strictly singular is the noise covariance matrix. The physical meaning of this ill-conditioned case is that the noise is the added information which causes the dependent deterministic equations to be independent. This information is, of course, meaningless and should not be considered. As a remedy to this ill-conditioned case, we eliminate one of the rows of (22.c). The question is then which row to eliminate. It is clear that the answer to this question hinges on the value of the components of ${}^3z_{\omega b}$. Obviously, if the SC rotates fast about the body z axis and not at all about the other two, then it can be seen either from (2.b) or (22.a) that the third component of ${}^3z_{\omega b}$ is negligible and thus the third row of (22.c) should be eliminated. For the sake of the ensuing presentation we will assume that this is the case. This check, however, has to be performed before every measurement update of the filter. Having made the latter assumption, define

$$z_{\omega b} = \begin{bmatrix} {}^3z_{\omega b,1} \\ {}^3z_{\omega b,2} \end{bmatrix} \quad (23.a)$$

and

$$C_b = \begin{bmatrix} 0 & -b_z & b_y \\ b_z & 0 & -b_x \end{bmatrix} \quad (23.b)$$

then

$$z_{\omega b} = C_b \omega \quad (23.c)$$

Next we have to develop the measurement equation needed to estimate χ and λ . We can choose one of two options which are based on entirely different approaches. According to one approach we obtain the needed measurements from a second differentiation of a measured direction. It is well known, and indeed very easily shown, that, using the notation

$$w = b \quad (24.a)$$

and

$$u = b \quad (24.b)$$

the following holds

$$D_b^i w = \dot{u} + 2\omega \times u + \dot{\omega} \times b + \omega \times (\omega \times b) \quad (25)$$

where w is resolved in the i coordinates and, as before, the dot symbolizes time differentiation performed in the b coordinates. Let

$${}^3z_{\chi\lambda b} = D_b^i w - \dot{u} - 2\omega \times u - \dot{\omega} \times b \quad (26)$$

then (25) can be written as

$${}^3z_{\chi\lambda b} = \omega \times (\omega \times b) \quad (27.a)$$

Let

$${}^3M_b = \begin{bmatrix} 0 & b_z & b_y \\ b_z & 0 & b_x \\ b_y & b_x & 0 \end{bmatrix} \quad (27.b)$$

$${}^3N_b = \begin{bmatrix} 0 & -b_x & -b_x \\ -b_y & 0 & -b_y \\ -b_z & -b_z & 0 \end{bmatrix} \quad (27.c)$$

then it can be easily verified that (27.a) can be written as

$${}^3z_{\chi\lambda b} = {}^3M_b \chi + {}^3N_b \lambda \quad (28)$$

Note that like ${}^3z_{\omega}$ before, ${}^3z_{\chi\lambda b}$ too is a computable vector which is data to be fed into the EIKF part that estimates χ and λ . Now, the argument that led to the reduction of the expressions in (22) to the corresponding expression in (23), holds here too. Consequently, we eliminate one row in the expressions in (27). (As before, the row to be eliminated is determined by the relative size of the components of ${}^3z_{\chi\lambda b}$). Assume that here too, the third row is eliminated, then if we define

$$z_{\chi\lambda b} = \begin{bmatrix} {}^3z_{\chi\lambda b,1} \\ {}^3z_{\chi\lambda b,2} \end{bmatrix} \quad (29.a)$$

$$N_b = \begin{bmatrix} 0 & b_z & b_y \\ b_z & 0 & b_x \end{bmatrix} \quad (29.b)$$

$$N_b = \begin{bmatrix} 0 & -b_x & -b_x \\ -b_y & 0 & -b_y \end{bmatrix} \quad (29.c)$$

it can be easily verified that (28) can be written as

$$z_{\chi\lambda b} = M_b \chi + N_b \lambda \quad (29.d)$$

If we now have a second vector measurement, say c , then we get an identical set of equations when now b is replaced by c and the subscript b is replaced by the subscript c . Explicitly, we do the following. Define

$$z_{\omega c} = \dot{c} - D_b^i c \quad (30.a)$$

and

$$C_c = [c \times] \quad (30.b)$$

$$m = c \quad (30.c);$$

$$n = c \quad (30.d);$$

$$z_{\chi\lambda c} = D_b^i m - \dot{n} - 2\omega \times n - \dot{\omega} \times c \quad (30.e)$$

$$M_c = \begin{bmatrix} 0 & c_z & c_y \\ c_y & c_x & 0 \end{bmatrix} \quad (30.f)$$

$$N_c = \begin{bmatrix} 0 & -c_x & -c_x \\ -c_y & 0 & -c_y \end{bmatrix} \quad (30.g)$$

then the measurement equations are

$$z_{\omega_c} = C_c \omega \quad (31.a)$$

$$z_{\chi\lambda_c} = M_c \chi + N_c \lambda \quad (31.b)$$

From the above, the extension of the measurement equations in case that we have more than two vector measurements at one time point is obvious. The other option for obtaining measurement equations needed to estimate χ and λ is based on $\hat{\omega}$, the EIKF-generated estimate of ω . We will postpone the introduction of this option until we present the EIKF.

III.2 Pre-Processed Vector Measurements

When we measure two different vectors at the same time point, then, as shown in (8), we have enough equations to obtain an estimate of ω without resorting to a recursive estimator. Therefore we can, first, compute an estimate of ω using (8), and then filter the estimate using the EIKF. As mentioned before, this is what was basically done in [6], only that there, ω was obtained as an output of gyroscopes rather than an analytic solution based on vector measurements. Although this approach does not fully utilize the capabilities of a recursive estimator, for the sake of completeness, we show here how to formulate the measurement equation in order to apply the EIKF in this case too. Re-write (8)

$$\hat{\omega} = G^\# d \quad (8)$$

Let

$$z_{\omega_p} = G^\# d \quad (32)$$

and let U denote the 3×3 identity matrix, then we can write (30) as

$$z_{\omega_p} = U \omega \quad (33)$$

The last equation is the measurement equation which corresponds to the dynamics equation of (15). The measurement equation for estimating χ and λ can be either those presented in the preceding sub-section; namely (29) and/or (31.b), or they can be directly related to $\hat{\omega}$ computed in (8). The latter will be explained later when we introduce the suitable EIKF.

IV. THE EIKF MODELS

The dynamics and measurement equations presented in Section II and Section III respectively, are nominal equations. In preparing the equations for use in a filtering routine, we add to them white noise vectors to express model uncertainties. These uncertainties stem from two sources, first, there are modeling errors because the equations are not the exact dynamics and measurement models, and second, in the sub-optimal filter that we will use, we will assume that χ and λ are constant in the propagation time-interval that we will use to propagate the estimate of ω . This assumption is clearly wrong even though it enables us to obtain satisfactory results. The importance of the white noise added to the each dynamics equation is in its PSD matrix which we adjust by trial and error to obtain the best filter performance. Similarly, the white noise added to each of the measurement equations indicates the measurement accuracy expressed by the covariance matrix of the noise vectors. This covariance too, is adjusted in order to yield the best filter performance. Adding the white noise vector, n_{ω} , to the central dynamics equation in (15), yields the following main dynamics model

$$\dot{\omega} = F_{\omega} \omega + B_{\omega} \chi + B_{\omega 2} \lambda + f + n_{\omega} \quad (34)$$

Similarly we add white noise vectors to the right hand side of (18) and (21) which become

$$\dot{\chi} = F_{\chi} \chi + B_{\chi} \omega + n_{\chi} \quad (35)$$

$$\dot{\lambda} = F_{\lambda} \lambda + B_{\lambda} \omega + n_{\lambda} \quad (36)$$

Adding white noise to the measurement equations turns, respectively, (23.c), (29.d) and (33) into

$$z_{\omega b} = C_b \omega + v_{\omega b} \quad (37)$$

$$z_{\chi \lambda b} = M_b \chi + N_b \lambda + v_{\chi \lambda b} \quad (38)$$

$$z_{\omega p} = U \omega + v_{\omega} \quad (39)$$

The extension of (37) and (38) to the case where we have more than one vector measurements is obvious. As mentioned before, several measurement models which are based on the estimate of ω , will be introduced when we present the EIKF in the next section.

V. THE EXTENDED INTERLACED KALMAN FILTER

Given the models of the preceding sections, we have several options for designing an EIKF. Like the models, the EIKF itself can be divided into two basic categories. The first is one which handles raw vector measurements, and the second category is one which handles pre-processed vector measurements. In the ensuing we only present the models to be used in the interlaced linear KFs. The KF algorithm itself can be found, of course, in standard KF texts.

V.1 Raw Vector Measurements

We have several options for designing an EIKF when given raw vector measurements. The following are some options.

Option 1:

We run three parallel linear KFs. The equations of the filters are as follows.

Filter 1

The dynamics equation is derived from (34) and the measurement equation is given in (37)

$$\dot{\omega} = F_{\omega} \omega + B_{\omega} \hat{\chi} + B_{\omega 2} \hat{\lambda} + f + n_{\omega} \quad (40.a)$$

$$z_{\omega b} = C_b \omega + v_{\omega b} \quad (40.b)$$

Note that $\hat{\chi}$ and $\hat{\lambda}$ are inputs from the other two filters that run in parallel to Filter 1.

Filter 2

The dynamics equation of the second filter is derived from (35) and the measurement equation is derived from (38)

$$\dot{\chi} = F_{\chi} \chi + B_{\chi} \hat{\omega} + n_{\chi} \quad (41.a)$$

$$z_{\chi \lambda b} - N_b \hat{\lambda} = M_b \chi + v_{\chi \lambda b} \quad (41.b)$$

Here $\hat{\omega}$ and $\hat{\lambda}$ are inputs from the other two parallel filters.

Filter 3

The dynamics equation of the third filter is derived from (36) and the measurement equation from (38)

$$\dot{\lambda} = F_{\lambda} \lambda + B_{\lambda} \hat{\omega} + n_{\lambda} \quad (42.a)$$

$$z_{\chi \lambda b} - M_b \hat{\chi} = N_b \lambda + v_{\chi \lambda b} \quad (42.b)$$

Here $\hat{\omega}$ and $\hat{\chi}$ are inputs from the other two parallel filters. Note that the preceding measurement

equations are based on a single vector measurement; namely, b . If we obtain another vector measurement, say c , at a certain time point, then we use (30) and (31) to generate measurement models similar to (40.b), (41.b) and (42.b) and perform consecutive measurement updates of the three interlaced filters, or we can augment the two vector measurements in each filter and perform in each of them one combined measurement update at that time point. The extension of this case to more than two simultaneous measurements is immediate. The three filter model of Option 1 is summarized in Table I.

<i>Dynamics</i>	<i>Measurement</i>
$\dot{\omega} = F_{\omega} \omega + B_{\omega} \hat{\chi} + B_{\omega 2} \hat{\lambda} + f + n_{\omega}$ (40.a)	$z_{\omega b} = C_b \omega + v_{\omega b}$ (40.b)
$\dot{\chi} = F_{\chi} \chi + B_{\chi} \hat{\omega} + n_{\chi}$ (41.a)	$z_{\chi \lambda b} - N_b \hat{\lambda} = M_b \chi + v_{\chi \lambda b}$ (41.b)
$\dot{\lambda} = F_{\lambda} \lambda + B_{\lambda} \hat{\omega} + n_{\lambda}$ (42.a)	$z_{\chi \lambda b} - M_b \hat{\chi} = N_b \lambda + v_{\chi \lambda b}$ (42.b)

Table I: Filter Model of Option 1

A block diagram representation of the EIKF of Option 1 is depicted in Fig. 1.

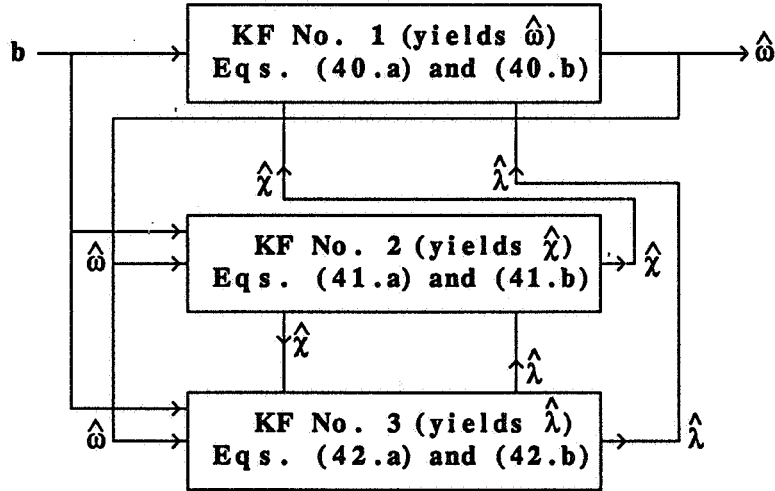


Fig.1: Block Diagram of the EIKF of Option 1.

Option 2:

Here we run only two parallel interlaced linear KF. They are as follows.

Filter 1

This filter is identical to Filter 1 of the preceding option.

Filter 2

In order to present Filter 2, we adopt the following definitions

$$X = \begin{bmatrix} \chi \\ \lambda \end{bmatrix} \quad (43.a)$$

$$F_x = \begin{bmatrix} F_{\chi} & 0 \\ 0 & F_{\lambda} \end{bmatrix} \quad (43.b)$$

$$B_x = \begin{bmatrix} B_\chi \\ B_\lambda \end{bmatrix} \quad (43.c) \quad n_x = \begin{bmatrix} n_\chi \\ n_\lambda \end{bmatrix} \quad (43.d)$$

$$z_{xb} = z_\chi \lambda_b \quad (44.a) \quad C_{xb} = \begin{bmatrix} M_b & N_b \end{bmatrix} \quad (44.b) \quad v_{xb} = v_\chi \lambda_b \quad (44.c)$$

then (41.a) and (42.a) can be augmented into the single dynamics equation

$$\dot{X} = F_x X + B_x \hat{\omega} + n_x \quad (45.a)$$

and (38) can be written to suit (45.a) as

$$z_{xb} = C_{xb} X + v_{xb} \quad (45.b)$$

The EIKF model of Option 2 is summarized in Table II. A block diagram representation of the EIKF is depicted in Fig. 2.

<i>Dynamics</i>	<i>Measurement</i>
$\dot{\omega} = F_\omega \omega + B_\omega \hat{\chi} + B_{\omega 2} \hat{\lambda} + f + n_\omega \quad (40.a)$	$z_{\omega b} = C_b \omega + v_{\omega b} \quad (40.b)$
$\dot{X} = F_x X + B_x \hat{\omega} + n_x \quad (45.a)$	$z_{xb} = C_{xb} X + v_{xb} \quad (45.b)$

Table II: Filter Model of Option 2

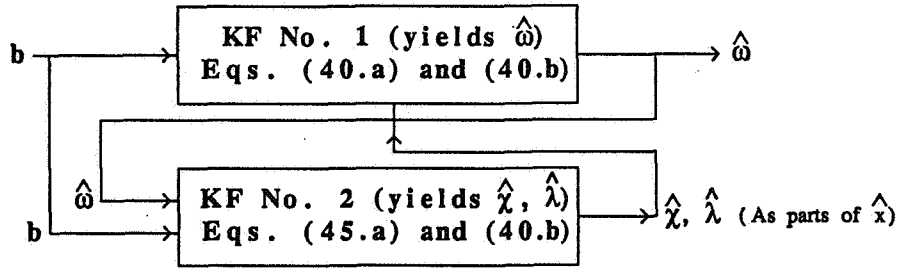


Fig.2: Block Diagram of the EIKF of Option 2.

Option 3:

Recall that in Option 1, as well as in Option 2, we had to use the second time derivative of the measured vectors in order to generate the data for the measurement models. We can use a different approach though that does not require a second differentiation. We simply use $\hat{\omega}$ which is estimated in Filter 1 and treat it in the other parallel filters as a "measurement" of χ and λ for they are functions of ω (see (12.d.e)). Doing so we obtain the following measurement equations

$$\begin{bmatrix} \hat{\omega}_y & \hat{\omega}_z \\ \hat{\omega}_x & \hat{\omega}_z \\ \hat{\omega}_x & \hat{\omega}_y \end{bmatrix} = \begin{bmatrix} 1 & 0 & 0 \\ 0 & 1 & 0 \\ 0 & 0 & 1 \end{bmatrix} \begin{bmatrix} \omega_y & \omega_z \\ \omega_x & \omega_z \\ \omega_x & \omega_y \end{bmatrix} + \begin{bmatrix} v_{\chi x} \\ v_{\chi y} \\ v_{\chi z} \end{bmatrix} \quad (46.a)$$

$$\begin{bmatrix} \hat{\omega}_x^2 \\ \hat{\omega}_y^2 \\ \hat{\omega}_z^2 \end{bmatrix} = \begin{bmatrix} 1 & 0 & 0 \\ 0 & 1 & 0 \\ 0 & 0 & 1 \end{bmatrix} \begin{bmatrix} \omega_x^2 \\ \omega_y^2 \\ \omega_z^2 \end{bmatrix} + \begin{bmatrix} v_{\lambda x} \\ v_{\lambda y} \\ v_{\lambda z} \end{bmatrix} \quad (46.b)$$

which we can write as

$$\boxed{z_\chi = U \chi + v_\chi} \quad (47.a)$$

and

$$\boxed{z_\lambda = U \lambda + v_\lambda} \quad (47.b)$$

where, as before, U is the identity matrix. We added the white noise vectors, v_χ and v_λ since on the left hand side of the above equations we do not have χ and λ , but rather their estimates. In this Option The three parallel filters are as follows.

Filter 1

This filter is identical to Filter 1 in Option 1.

Filter 2

The dynamics equation of this filter is exactly like the one given in (41.a), but the measurement equation is that given in (47.a); that is,

$$\dot{\chi} = F_\chi \chi + B_\chi \hat{\omega} + n_\chi \quad (48.a)$$

$$z_\chi = U \chi + v_\chi \quad (48.b)$$

Filter 3

The dynamics equation of this filter is exactly like the one given in (42.a), but the measurement equation is that given in (47.b); that is,

$$\dot{\lambda} = F_\lambda \lambda + B_\lambda \hat{\omega} + n_\lambda \quad (42.a)$$

$$z_\lambda = U \lambda + v_\lambda \quad (47.b)$$

The EIKF model of Option 3 is summarized in Table III.

<i>Dynamics</i>	<i>Measurement</i>
$\dot{\omega} = F_\omega \omega + B_\omega \hat{\chi} + B_{\omega 2} \hat{\lambda} + f + n_\omega \quad (40.a)$	$z_{\omega b} = C_b \omega + v_{\omega b} \quad (40.b)$
$\dot{\chi} = F_\chi \chi + B_\chi \hat{\omega} + n_\chi \quad (41.a)$	$z_\chi = U \chi + v_\chi \quad (47.a)$
$\dot{\lambda} = F_\lambda \lambda + B_\lambda \hat{\omega} + n_\lambda \quad (42.a)$	$z_\lambda = U \lambda + v_\lambda \quad (47.b)$

Table III: Filter Model of Option 3

A block diagram representation of the EIKF of Option 3 is depicted in Fig. 3.

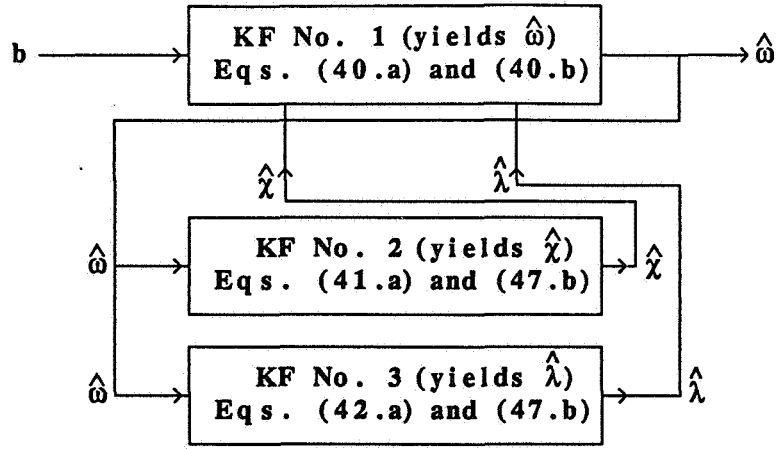


Fig.3: Block Diagram of the EIKF of Option 3.

V.2 Pre-Processed Vector Measurements

As we have already seen, pre-processed vector measurements yield an estimate of ω , and as mentioned earlier, the full advantage of a recursive estimator is not utilized when a measurement or an estimate of ω is available; however, for the sake of completeness, we present an EIKF scheme for this case too. The filter model of this case is similar to the model of Option 3. The dynamics equation of the present Filter 1 is identical to that of Option 3 but the measurement equation is different. Now the measurements that are fed into Filter 1 are not vector measurement, but rather a preliminary estimate of ω , which we denote by $\hat{\omega}_p$, thus following (8) and (32) we define

$$\hat{\omega}_p = G^{\#} d \quad (48.a)$$

and

$$z_{\omega p} = \hat{\omega}_p \quad (48.b)$$

and then, following (39), we write the measurement equation of Filter 1 as

$$z_{\omega p} = U \omega + v_{\omega} \quad (48.c)$$

As for Filters 2 and 3, while their dynamics equations are identical to those of Option 3, their measurement equations can be based on either the input $\hat{\omega}_p$ (which is also the input to the present Filter 1), or on $\hat{\omega}$ which is the input to Filters 2 and 3 of Option 3. The EIKF of this case is as follows.

The EIKF for the Pre-Processed Vector Measurements:

We run three linear filters in parallel.

Filter 1

The dynamics equation is identical to that of Option 3. The measurement equation is

$$z_{\omega p} = U \omega + v_{\omega} \quad (48.c)$$

Filter 2

The dynamics model is identical to that of Filter 2 of Option 3. As for the measurement model, define

$$z_{\chi P} = \begin{bmatrix} \hat{\omega}_{py} & \hat{\omega}_{pz} \\ \hat{\omega}_{px} & \hat{\omega}_{pz} \\ \hat{\omega}_{px} & \hat{\omega}_{py} \end{bmatrix} \quad (49.a)$$

then

$$z_{\chi P} = U \chi + v_{\chi P} \quad (49.b)$$

Filter 3

The dynamics model is identical to that of Filter 3 of Option 3. As for the measurement model, define

$$z_{\lambda P} = \begin{bmatrix} \hat{\omega}_{px} \\ \hat{\omega}_{py} \\ \hat{\omega}_{pz} \end{bmatrix} \quad (50.a)$$

then

$$z_{\lambda P} = U \lambda + v_{\lambda P} \quad (50.b)$$

The model of the EIKF for the pre-processed vector measurements is summarized in Table IV.

<i>Dynamics</i>	<i>Measurement</i>
$\dot{\omega} = F_{\omega} \omega + B_{\omega} \hat{\chi} + B_{\omega 2} \hat{\lambda} + f + n_{\omega} \quad (40.a)$	$z_{\omega P} = U \omega + v_{\omega} \quad (48.c)$
$\dot{\chi} = F_{\chi} \chi + B_{\chi} \hat{\omega} + n_{\chi} \quad (41.a)$	$z_{\chi P} = U \chi + v_{\chi P} \quad (49.b)$
$\dot{\lambda} = F_{\lambda} \lambda + B_{\lambda} \hat{\omega} + n_{\lambda} \quad (42.a)$	$z_{\lambda P} = U \lambda + v_{\lambda P} \quad (50.b)$

Table IV: Model of the EIKF for Pre-Processed Vector Measurements

A block diagram representation of the latter EIKF is depicted in Fig. 4. As mentioned earlier, here too we have several options. We can, for example, use $\hat{\omega}_p$ in the dynamics equation of Filters 2 and 3 in addition to using it as measurements in these two filters.

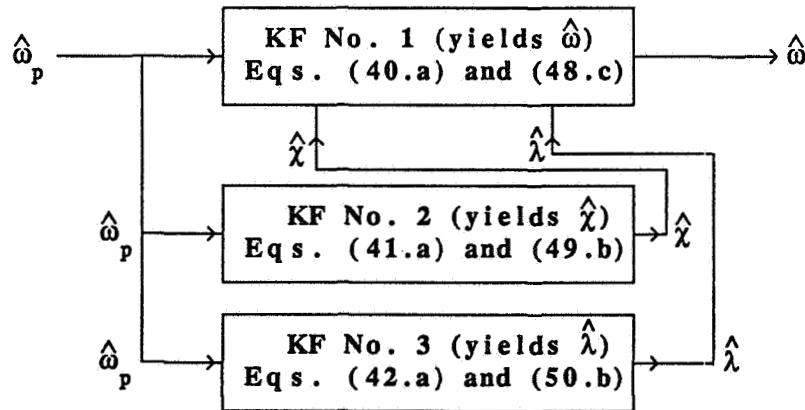


Fig.4: Block Diagram of the EIKF for Pre-Processed Vector Measurements

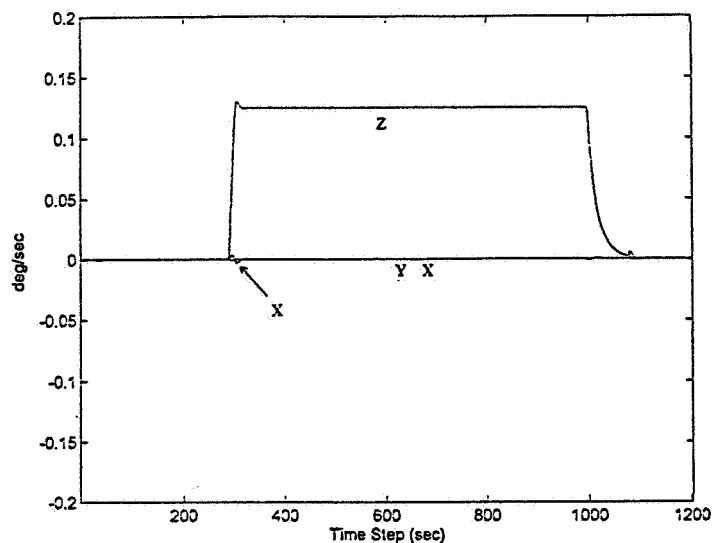


Fig. 5: True RXTE Angular Velocity Components

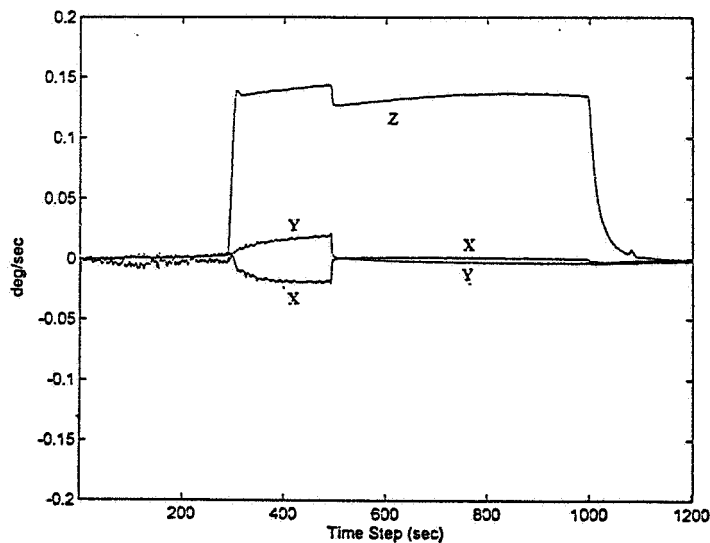


Fig. 6: Estimated RXTE Angular Velocity Components

V. FILTER TESTING

As a first step in the testing of the EIKF for estimating ω , we applied the filter presented as Option 1 (see Table I and Figure 1) to simulated data. After obtaining satisfactory results we applied the filter to real data obtained from the RXTE satellite which was launched on Dec. 30, 1995. We used the downlinked magnetometer data (b_i) and Sun sensor data (c_i) as well as the wheel momentum data. We applied the EIKF just before the beginning of a maneuver; namely, at 21h, 43min and 31.148sec on Jan. 4, 1996. The true rates, estimated rates, and the estimation errors are shown in Figs. 5, 6, and 7, respectively.

VI. CONCLUSIONS

In this paper we presented an algorithm for estimating the angular velocity of a rigid body like satellite. The algorithm is based on vector measurements and their derivatives. The algorithm is an

extension of an estimator named, Interlaced Kalman Filter (IKF), which was introduced in the past by Algrain and Saniie. The IKF enables the use of several linear filters running in parallel for estimating the state of a non-linear dynamic system. In this paper we developed an IKF for a more general dynamic model and named it Extended Interlaces Kalman Filter (EIKF). Unlike Algrain and Saniie, we make a full use of the estimator in that we use direction vectors, rather than measured angular velocity to obtain an estimate of the angular velocity. In this paper we presented several versions of the EIKF for angular velocity estimation.

Simulation results indicate that the EIKF is an efficient and stable estimator of the angular velocity vector.

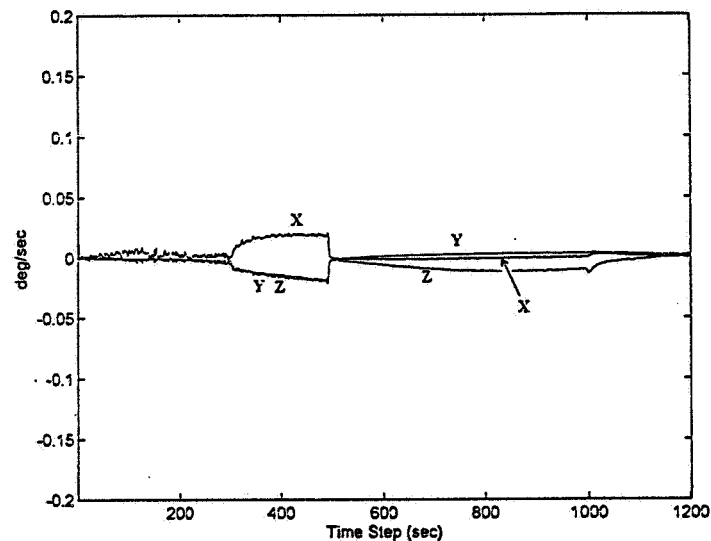


Fig. 7: Estimation Error of the RXTE Angular Velocity Components

REFERENCES

1. Natanson, G., "A Deterministic Method for Estimating Attitude from Magnetometer Data Only," Proceedings of the 43rd IFA Congress, Paper No. IFA-92-0036, Washington, DC, Aug. 28 - Sept. 5, 1992.
2. Challa, M., Natanson, G., Deutschmann, J., and Galal, K., "A PC-Based Magnetometer-Only Attitude and Rate Determination System for Gyroless Spacecraft," Proceedings of the Flight Mechanics/Estimation Theory Symposium, NASA-Goddard Space Flight Center, May 16-18, 1995. pp. 83-96.
3. Gelb, A., (ed.), *Applied Optimal Estimation*, MIT Press, Cambridge, MA, 1974, p. 19.
4. Algrain, M. C., and Saniie, J., "Interlaced Kalman Filtering of 3-D Angular Motion Based on Euler's Nonlinear Equations," *IEEE Trans. on Aerosp. and Electr. Sys.*, Vol. 30, No. 1, 1994, pp. 175-185.
5. Wertz, J. R., (Ed.), *Spacecraft attitude dynamics and Control*, Reidel Publishing Co., Dordrecht, Holland, 1999, p. 523.
6. Agrawal, B. N., *Design of Geosynchronous Spacecraft*, Prentice-Hall, Englewood, NJ, 1999, p. 109.
7. Meriam, J.L., and Kraige, L.G., *Engineering Mechanics Volume 2, Dynamics*, Wiley, New-York, NY, 1992, pp. 383-386.

Attitude Estimation Using Modified Rodrigues Parameters

John L. Crassidis

Assistant Professor

Catholic University of America

Department of Mechanical Engineering

Washington, D.C. 20064

F. Landis Markley

Staff Engineer

Goddard Space Flight Center

Guidance and Control Branch, Code 712

Greenbelt, MD 20771

Abstract

In this paper, a Kalman filter formulation for attitude estimation is derived using the Modified Rodrigues Parameters. The extended Kalman filter uses a gyro-based model for attitude propagation. Two solutions are developed for the sensitivity matrix in the Kalman filter. One is based upon an additive error approach, and the other is based upon a multiplicative error approach. It is shown that the two solutions are in fact equivalent. The Kalman filter is then used to estimate the attitude of a simulated spacecraft. Results indicate that the new algorithm produces accurate attitude estimates by determining actual gyro biases.

Introduction

A widely used parameterization for attitude estimation is the quaternion representation. Advantages of using quaternions include: 1) the kinematic equations are linear with respect to angular velocities, 2) singularities are not present for any eigenaxis rotation, and 3) the attitude matrix is algebraic in the quaternion components. However, since the quaternion parameterization involves the use of four components to represent the attitude motion, the quaternion components are non-minimal (dependent). This leads to a constraint that the quaternion must have unit norm.

The quaternion normalization constraint produces a singularity in the Kalman filter covariance matrix. Three solutions (two of which yield identical results) to this problem are summarized by Lefferts et al. [1]. The first approach uses the transition matrix of the state-error vector to obtain a reduced order representation of the error covariance. The second approach deletes one of the quaternion components in order to obtain a truncated error covariance expression. The third approach uses an incremental quaternion error which results in a representation that is identical to the first approach. This approach is most commonly used to maintain normalization for the estimated quaternion.

Three-dimensional parameterizations of attitude are still useful for many control applications (e.g., see [2-3]). Since spacecraft control algorithms require estimates of attitude and/or rate, it is therefore advantageous to develop a Kalman filter which utilizes a three-dimensional parameterization. A number

of three-dimensional parameterizations is shown in an excellent survey by Shuster [4]; including, the Euler angle representation, the Rodrigues parameters, and the modified Rodrigues parameters. It is widely known that all three-dimensional parameterizations have singularities (e.g., the Rodrigues parameters are singular for 180 degree rotations [4]). The choice of parameters depends on a number of factors; for example, the type of rotation maneuver for the spacecraft, computational requirements, physical representation insight, etc.

Most control applications require a parameterization that has the singularity as far from the origin as possible. Specifically, the modified Rodrigues parameters (MRP) [5] have recently been used for spacecraft control applications, since they allow for rotations up to 360 degrees. Tsiotras [6] utilized the MRP to derive a new class of globally asymptotically stabilizing feedback control laws. Schaub et. al. [7] utilized the MRP to estimate external torques by tracking a Lyapunov function. Crassidis and Markley [8] utilized the MRP to develop a sliding mode controller for spacecraft maneuvers. However, the aforementioned control schemes assume that the attitude (i.e., the MRP) is already known. For this reason, a Kalman filter using the modified Rodrigues parameters is developed in this paper.

The organization of this paper proceeds as follows. First, a brief review of the quaternion and MRP kinematic equations is shown. Then, a brief review of the Kalman filter is shown using the quaternion representation. Next, a Kalman filter for attitude estimation is derived using the MRP. Also, the sensitivity matrix is derived using both an additive and a multiplicative approach. Finally, the new algorithm is used to estimate the attitude of the Tropical Rainfall Measurement Mission (TRMM) spacecraft.

Attitude Kinematics

In this section, a brief review of the kinematic equations of motion using the modified Rodrigues parameters is shown. This parameterization is derived by employing a stereographic projection of the quaternions. The quaternion representation is given by

$$\underline{q} \equiv \begin{bmatrix} \underline{q}_{13} \\ q_4 \end{bmatrix} \quad (1)$$

with

$$\underline{q}_{13} \equiv \begin{bmatrix} q_1 \\ q_2 \\ q_3 \end{bmatrix} = \hat{n} \sin\left(\frac{\theta}{2}\right) \quad (2a)$$

$$q_4 = \cos\left(\frac{\theta}{2}\right) \quad (2b)$$

where \hat{n} is a unit vector corresponding to the axis of rotation and θ is the angle of rotation. The quaternion kinematic equations of motion are derived by using the spacecraft's angular velocity ($\underline{\omega}$), given by

$$\dot{\underline{q}} = \frac{1}{2} \Omega(\underline{\omega}) \underline{q} = \frac{1}{2} \Xi(\underline{q}) \underline{\omega} \quad (3)$$

where $\Omega(\underline{\omega})$ and $\Xi(\underline{q})$ are defined as

$$\Omega(\underline{\omega}) \equiv \begin{bmatrix} -[\underline{\omega} \times] & \vdots & \underline{\omega} \\ \dots & \vdots & \dots \\ -\underline{\omega}^T & \vdots & 0 \end{bmatrix} \quad (4a)$$

$$\Xi(\underline{q}) \equiv \begin{bmatrix} q_4 I_{3 \times 3} + [\underline{q}_{13} \times] \\ \dots \\ -\underline{q}_{13}^T \end{bmatrix} \quad (4b)$$

where $I_{3 \times 3}$ is a 3×3 identity matrix. The 3×3 dimensional matrices $[\underline{\omega} \times]$ and $[\underline{q}_{13} \times]$ are referred to as cross product matrices since $\underline{a} \times \underline{b} = [\underline{a} \times] \underline{b}$, with

$$[\underline{a} \times] \equiv \begin{bmatrix} 0 & -a_3 & a_2 \\ a_3 & 0 & -a_1 \\ -a_2 & a_1 & 0 \end{bmatrix} \quad (5)$$

Since a three degree-of-freedom attitude system is represented by a four-dimensional vector, the quaternions cannot be independent. This condition leads to the following normalization constraint

$$\underline{q}^T \underline{q} = \underline{q}_{13}^T \underline{q}_{13} + q_4^2 = 1 \quad (6)$$

The modified Rodrigues parameters are defined by [5]

$$\underline{p} = \frac{\underline{q}_{13}}{1 + q_4} = \hat{n} \tan\left(\frac{\theta}{4}\right) \quad (7)$$

where \underline{p} is a 3×1 vector. The kinematic equations of motion are derived by using the spacecraft's angular velocity ($\underline{\omega}$), given by [4]

$$\dot{\underline{p}} = \frac{1}{4} \left\{ \left(1 - |\underline{p}|^2 \right) \underline{\omega} - 2 \underline{\omega} \times \underline{p} + 2 (\underline{\omega} \bullet \underline{p}) \underline{p} \right\} \quad (8)$$

where $|\cdot|$ is the norm operator, and \bullet is the dot product. This equation may be re-written as

$$\dot{\underline{p}} = \frac{1}{2} \left\{ \frac{1}{2} (1 - \underline{p}^T \underline{p}) I_{3 \times 3} + [\underline{p} \times] + \underline{p} \underline{p}^T \right\} \underline{\omega} \quad (9)$$

The measurement model is assumed to be of the form given by [4]

$$\underline{B}_B = A(\underline{p}) \underline{B}_I \quad (10)$$

where \underline{B}_I is a 3×1 dimensional vector of some reference object (e.g., a vector to the sun or to a star, or the Earth's magnetic field vector) in a reference coordinate system, \underline{B}_B is a 3×1 dimensional vector defining the components of the corresponding reference vector measured in the spacecraft body frame, and $A(\underline{p})$ is given by

$$A(\underline{p}) = I_{3 \times 3} - \frac{4(1 - \underline{p}^T \underline{p})}{(1 + \underline{p}^T \underline{p})^2} [\underline{p} \times] + \frac{8}{(1 + \underline{p}^T \underline{p})^2} [\underline{p} \times]^2 \quad (11)$$

which is the 3×3 dimensional (orthogonal) attitude matrix.

Kalman Filter Development

In this section, a Kalman filter is derived for attitude estimation using the modified Rodrigues parameters. First a brief review of basic principles of the Kalman filter using quaternions is shown (see [1] for more details). The state error vector has seven components consisting of a four-component error quaternion ($\delta \underline{q}$) and a three-vector gyro bias error $\Delta \underline{b}$, given by

$$\Delta \underline{x}_f = \begin{bmatrix} \delta \underline{q} \\ \Delta \underline{b} \end{bmatrix} \quad (12)$$

The error quaternion is defined as

$$\delta \underline{q} = \underline{q} \otimes \hat{\underline{q}}^{-1} \quad (13)$$

where \underline{q} is the true quaternion and $\hat{\underline{q}}$ is the estimated quaternion. Also, the operator \otimes refers to quaternion multiplication (see [4] for details). Since the incremental quaternion corresponds to a small rotation, Equation (13) can be approximated by

$$\delta \underline{q} \approx \begin{bmatrix} \delta q_{13} \\ \dots \\ 1 \end{bmatrix} \quad (14)$$

which reduces the four-component error quaternion into a three-component (half-angle) representation. Equation (14) is then used to derive a quaternion based Kalman filter (see [1] for details).

The state equation for the new algorithm consists of the modified Rodrigues parameters (\underline{p}) and a gyro bias corrections (\underline{b}), given by

$$\underline{x} = \begin{bmatrix} \underline{p} \\ \underline{b} \end{bmatrix} \quad (15)$$

The true angular velocity is assumed to be modeled by

$$\underline{\omega} = \tilde{\underline{\omega}} - \underline{b} - \underline{\eta}_1 \quad (16)$$

where $\underline{\omega}$ is the true angular velocity, $\tilde{\underline{\omega}}$ is the gyro-measured angular velocity, and \underline{b} is the gyro drift vector, which is modeled by

$$\dot{\underline{b}} = \underline{\eta}_2 \quad (17)$$

The 3×1 vectors, $\underline{\eta}_1$ and $\underline{\eta}_2$, are assumed to be modeled by a Gaussian white-noise process with

$$\underline{w} \equiv \begin{bmatrix} \underline{\eta}_1 \\ \underline{\eta}_2 \end{bmatrix} \quad (18a)$$

$$E\{\underline{w}(t)\} = \underline{0} \quad (18b)$$

$$E\{\underline{w}(t)\underline{w}^T(t')\} = Q\delta(t-t') \quad (18c)$$

The true state-model equation can now be written as

$$\dot{\underline{p}} = \underline{f}(\underline{p}, \underline{b}, \underline{\tilde{w}}, t) + \underline{g}(\underline{p}, \underline{\eta}_1, t) \quad (19a)$$

$$\dot{\underline{b}} = \underline{\eta}_2 \quad (19b)$$

where

$$\underline{f}(\underline{p}, \underline{b}, \underline{\tilde{w}}, t) = \frac{1}{2} \left\{ \frac{1}{2} (1 - \underline{p}^T \underline{p}) I_{3 \times 3} + [\underline{p} \times] + \underline{p} \underline{p}^T \right\} (\underline{\tilde{w}} - \underline{b}) \quad (20a)$$

$$\underline{g}(\underline{p}, \underline{\eta}_1, t) = -\frac{1}{2} \left\{ \frac{1}{2} (1 - \underline{p}^T \underline{p}) I_{3 \times 3} + [\underline{p} \times] + \underline{p} \underline{p}^T \right\} \underline{\eta}_1 \quad (20b)$$

The extended Kalman filter utilizes a first-order Taylor series expansion for the state-error equation, given by

$$\Delta \dot{\underline{x}} = F \Delta \underline{x} + G \underline{w} \quad (21)$$

where

$$F = \begin{bmatrix} \frac{\partial \underline{f}}{\partial \underline{p}} & \vdots & \frac{\partial \underline{f}}{\partial \underline{b}} \\ \dots & \vdots & \dots \\ \mathbf{0}_{3 \times 3} & \vdots & \mathbf{0}_{3 \times 3} \end{bmatrix} \quad (22a)$$

$$G \equiv \begin{bmatrix} G_{11} & \vdots & G_{12} \\ \dots & \vdots & \dots \\ G_{21} & \vdots & G_{22} \end{bmatrix} \quad (22b)$$

and

$$G_{11} = \frac{\partial \underline{g}}{\partial \underline{\eta}_1} = -\frac{1}{2} \left\{ \frac{1}{2} (1 - \underline{p}^T \underline{p}) I_{3 \times 3} + [\underline{p} \times] + \underline{p} \underline{p}^T \right\} \quad (23a)$$

$$G_{12} = G_{21} = \mathbf{0}_{3 \times 3} \quad (23b)$$

$$G_{22} = I_{3 \times 3} \quad (23c)$$

The estimated state-error equation is given by

$$\Delta \dot{\hat{\underline{x}}} = F|_{\underline{x}=\hat{\underline{x}}} \Delta \hat{\underline{x}} \equiv \hat{F} \Delta \hat{\underline{x}} \quad (24a)$$

$$\Delta \hat{x} = \underline{x} - \hat{x} \quad (24b)$$

The partial derivatives in Equation (24a) for the state-error matrix are given by

$$\left. \frac{\partial f}{\partial \underline{p}} \right|_{\underline{x}=\hat{x}} = \frac{1}{2} \left\{ \hat{\underline{p}} \hat{\underline{\omega}}^T - \hat{\underline{\omega}} \hat{\underline{p}}^T - [\hat{\underline{\omega}} \times] + (\hat{\underline{\omega}}^T \hat{\underline{p}}) I_{3 \times 3} \right\} \quad (25a)$$

$$\left. \frac{\partial f}{\partial \underline{b}} \right|_{\underline{x}=\hat{x}} = -\frac{1}{2} \left\{ \frac{1}{2} (1 - \hat{\underline{p}}^T \hat{\underline{p}}) I_{3 \times 3} + [\hat{\underline{p}} \times] + \hat{\underline{p}} \hat{\underline{p}}^T \right\} \equiv \hat{G}_{11} \quad (25b)$$

where

$$\hat{\underline{\omega}} = \tilde{\underline{\omega}} - \hat{\underline{b}} \quad (26)$$

State-observable discrete measurements are assumed to be modeled by

$$\underline{z}_k = \underline{h}_k(\underline{x}_k) + \underline{v}_k \quad (27)$$

where

$$\underline{h}_k(\underline{x}_k) = A(\underline{p}_k) \underline{B}_{I_k} \quad (28)$$

and \underline{v}_k is assumed to be modeled by a zero-mean Gaussian process with

$$E\{\underline{v}_k\} = \underline{0} \quad (29a)$$

$$E\{\underline{v}_k \underline{v}_l^T\} = R \delta_{kl} \quad (29b)$$

The sensitivity matrix can be written as

$$H_k = [L \quad ; \quad 0_{3 \times 3}] \quad (30)$$

where L can be derived using an additive approach or a multiplicative approach. The additive approach expands $\underline{h}_k(\underline{x}_k)$ in a power series about \hat{x}_k , given by

$$\underline{h}_k(\underline{x}_k) = \underline{h}_k(\hat{x}_k) + \left. \frac{\partial \underline{h}_k}{\partial \underline{p}} \right|_{\underline{x}_k=\hat{x}_k} \Delta \underline{x}_k \quad (31)$$

The brute force differentiation in Equation (31) can be shown to be given by

$$\begin{aligned} \left. \frac{\partial \underline{h}_k}{\partial \underline{p}} \right|_{\underline{x}_k=\hat{x}_k} &= \frac{4}{(1 + \hat{\underline{p}}^T \hat{\underline{p}})^2} \left\{ [\underline{B}_I \times] \left((1 - \hat{\underline{p}}^T \hat{\underline{p}}) I_{3 \times 3} - 2 \hat{\underline{p}} \hat{\underline{p}}^T \right) + 2 \hat{\underline{p}} \underline{B}_I^T - 4 \underline{B}_I \hat{\underline{p}}^T + 2 (\hat{\underline{p}}^T \underline{B}_I) I_{3 \times 3} \right\} \Bigg|_{I_k} \\ &+ \frac{16}{(1 + \hat{\underline{p}}^T \hat{\underline{p}})^3} \left\{ 2 (\hat{\underline{p}}^T \hat{\underline{p}}) \underline{B}_I \hat{\underline{p}}^T - (1 - \hat{\underline{p}}^T \hat{\underline{p}}) [\underline{B}_I \times] \hat{\underline{p}} \hat{\underline{p}}^T - 2 \hat{\underline{p}} \hat{\underline{p}}^T \underline{B}_I \hat{\underline{p}}^T \right\} \Bigg|_{I_k} \end{aligned} \quad (32)$$

which is somewhat complicated. The multiplicative approach assumes that the true parameters are given by

$$\underline{p} = \delta \underline{p} \otimes \hat{\underline{p}} \quad (33)$$

where $\delta \underline{p}$ is the error MRP. The composition rule for the MRP leads to the following

$$\underline{p} = \frac{\left(1 - |\hat{\underline{p}}|^2\right) \delta \underline{p} + \left(1 - |\delta \underline{p}|^2\right) \hat{\underline{p}} - 2[\delta \underline{p} \times] \hat{\underline{p}}}{1 + |\delta \underline{p}|^2 |\hat{\underline{p}}|^2 - 2\delta \underline{p} \bullet \hat{\underline{p}}} \quad (34)$$

For small $\delta \underline{p}$, Equation (34) can be approximated using

$$\begin{aligned} \underline{p} &\approx (1 + 2\delta \underline{p} \bullet \hat{\underline{p}}) \left[\left(1 - |\hat{\underline{p}}|^2\right) \delta \underline{p} + \hat{\underline{p}} - 2[\delta \underline{p} \times] \hat{\underline{p}} \right] \\ &\approx \hat{\underline{p}} + \left[\left(1 - |\hat{\underline{p}}|^2\right) I_{3 \times 3} + 2[\hat{\underline{p}} \times] + 2\hat{\underline{p}} \hat{\underline{p}}^T \right] \delta \underline{p} \end{aligned} \quad (35)$$

From

$$A(\underline{p}) = A(\delta \underline{p}) A(\hat{\underline{p}}) \quad (36)$$

it follows that

$$L \equiv \frac{\partial h_k}{\partial \underline{p}} \Big|_{\underline{x}_k = \hat{\underline{x}}_k} = \frac{\partial}{\partial \underline{p}} A(\delta \underline{p}) A(\hat{\underline{p}}) \underline{B}_I \Big|_{\hat{\underline{p}}} \quad (37)$$

and using the fact that for small $\delta \underline{p}$

$$A(\delta \underline{p}) \approx I_{3 \times 3} - 4[\delta \underline{p} \times] \quad (38)$$

Equation (37) can now be evaluated using the chain rule to yield

$$\begin{aligned} L &= 4 \left[A(\hat{\underline{p}}) \underline{B}_I \times \left\{ \left(1 - \hat{\underline{p}}^T \hat{\underline{p}}\right) I_{3 \times 3} + 2[\hat{\underline{p}} \times] + 2\hat{\underline{p}} \hat{\underline{p}}^T \right\}^{-1} \right] \Big|_{t_k} \\ &= \frac{4}{\left(1 + \hat{\underline{p}}^T \hat{\underline{p}}\right)^2} \left[A(\hat{\underline{p}}) \underline{B}_I \times \left\{ \left(1 - \hat{\underline{p}}^T \hat{\underline{p}}\right) I_{3 \times 3} - 2[\hat{\underline{p}} \times] + 2\hat{\underline{p}} \hat{\underline{p}}^T \right\} \right] \Big|_{t_k} \end{aligned} \quad (39)$$

which is in a simpler form as compared with Equation (32). In fact, these equations are identical, thereby proving the equivalence between a multiplicative and an additive approach for the MRP in the Kalman filter. Also, the matrix in Equation (39) has at most rank two, which reflects the fact that the observation vector contains no information about rotations around an axis specified by that vector at each measurement point. The extended Kalman filter equations for attitude estimation are summarized by

$$\dot{\hat{x}} = \underline{f}(\hat{x}, t) \quad (40a)$$

$$\dot{P} = \hat{F}P + P^T \hat{F} + \hat{G}Q\hat{G}^T \quad (40b)$$

$$\hat{x}_k(+)=\hat{x}_k(-)+K_k[z_k-h_k(\hat{p}_k(-))] \quad (40c)$$

$$P_k(+)=\left[I_{6\times 6}-K_k H_k(\hat{x}_k(-))\right]P_k(-) \quad (40d)$$

$$K_k=P_k(-)H_k^T\left[H_k P_k(-)H_k^T+R\right]^{-1} \quad (40e)$$

where

$$\hat{G}=\begin{bmatrix} \hat{G}_{11} & \vdots & 0_{3\times 3} \\ \dots & \vdots & \dots \\ 0_{3\times 3} & \vdots & I_{3\times 3} \end{bmatrix} \quad (41)$$

Spacecraft Simulation and Results

A simulation study is performed using the Tropical Rainfall Measurement Mission (TRMM) spacecraft orbit parameters. The TRMM spacecraft (see Figure 1) is due to be launched in 1997 with a nominal mission life of 42 months. The main objectives of this mission include: (i) to obtain multi-year measurements of tropical and subtropical rainfall, (ii) to understand how interactions between the sea, air, and land masses produce changes in global rainfall and climate, and (iii) to help improve the modeling of tropical rainfall processes and their influence on global circulation. The simulated spacecraft has a near circular orbit at 350 km. The nominal mission mode requires a rotation once per orbit (i.e., 236 deg/hr) about the spacecraft's y-axis while holding the remaining axis rotations near zero. The attitude sensors used in the simulation include a three-axis magnetometer (TAM) and two digital sun sensors (DSSs).

The magnetic field reference is modeled using a 10th order International Geomagnetic Reference Field (IGRF) model. TAM sensor noise is modeled by a Gaussian white-noise process with a mean of zero and a standard deviation of 0.5 mG. The two DSSs each have a field of view of about $50^\circ\times 50^\circ$, and combine to provide sun measurements for about 2/3 of a complete orbit. Figure 2 shows the availability of the sun sensor as a function of time. The DSS sensor noise is also modeled by a Gaussian white-noise process with a mean of zero and a standard deviation of 0.05° . The gyro "measurements" are simulated using Equations (16) and (17), with a gyro noise standard deviation of 0.062 deg/hr, a ramp noise standard deviation of 0.235 deg/hr/hr, and an initial drift of 0.1 deg/hr on each axis.

A plot of the estimated MRP for a typical simulation run using the extended Kalman filter is shown in Figure 3. Since, the rotation does not exceed 360° a discrete jump to the origin is not required. A plot of the corresponding gyro-bias estimates is shown in Figure 4. Plots of the attitude covariance and gyro-bias covariances are shown in Figures 5 and 6, respectively. The increase in the attitude covariance (at approximately the second and fifth hour) is due to the fact that the rotation approaches 360° as shown in Figure 7 (i.e., the fourth quaternion component is close to 1). A plot of the roll, pitch, and yaw attitude errors is shown in Figure 8. From these figures, it is clear that the extended Kalman filter developed in this paper is able to accurately estimate the attitude and gyro-biases of the simulated spacecraft, and achieves the same degree of accuracy as the quaternion-based Kalman filter (see [9]).

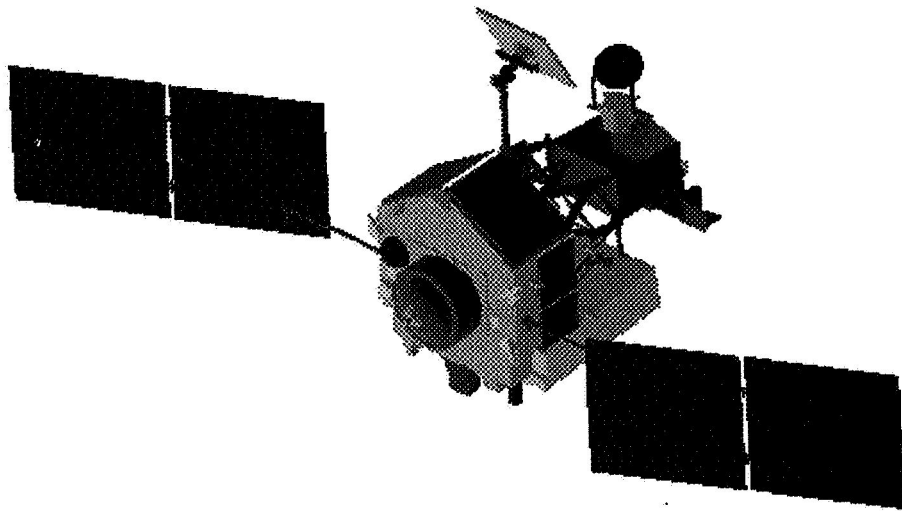


Figure 1 TRMM Spacecraft

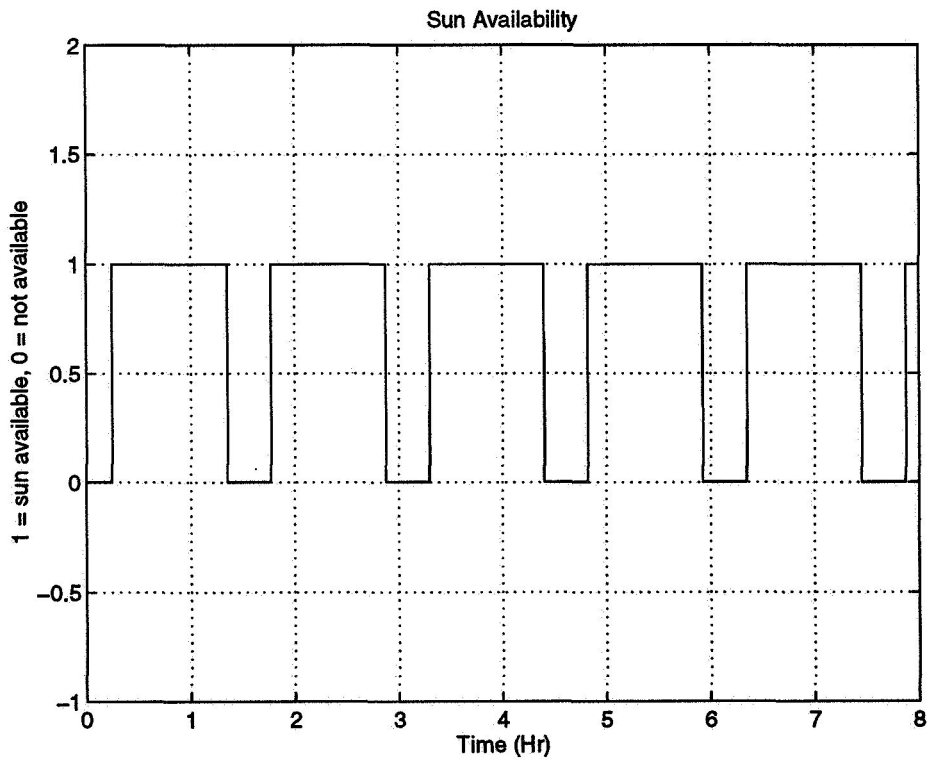


Figure 2 Plot of the Sun Availability

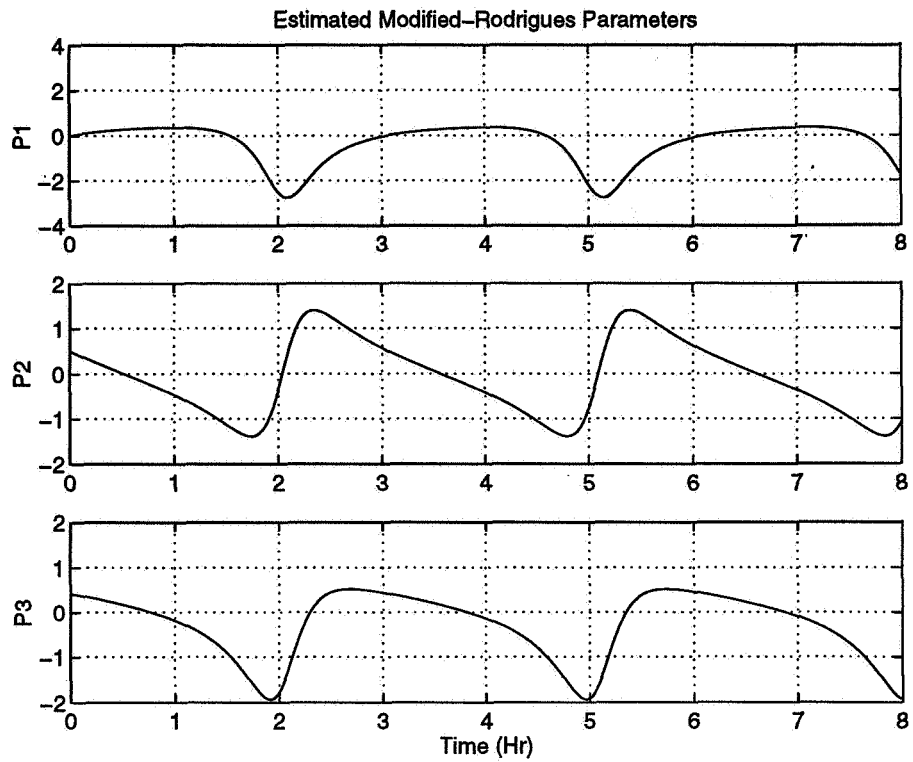


Figure 3 Plot of Kalman Filter MRP Estimates

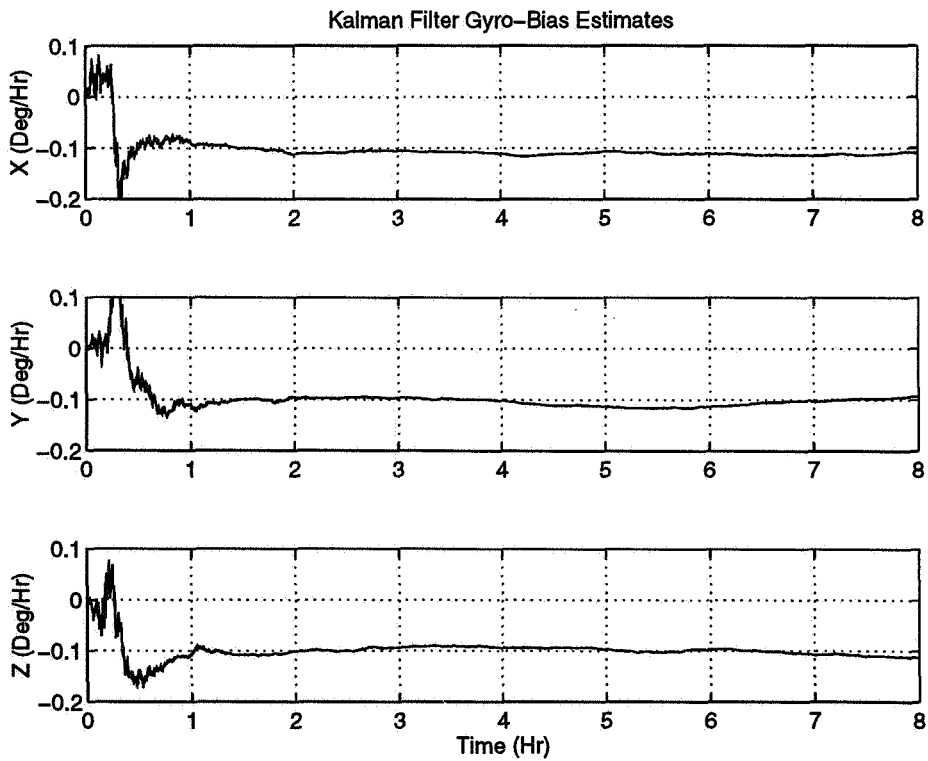


Figure 4 Plot of Kalman Filter Gyro-Bias Estimates

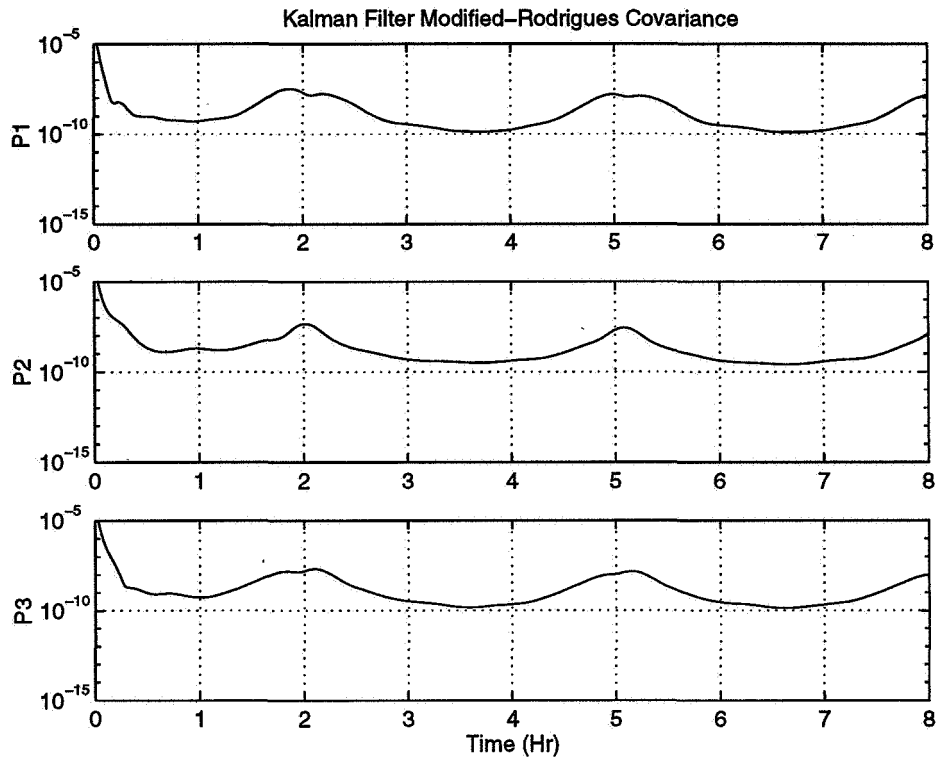


Figure 5 Plot of Attitude Covariances

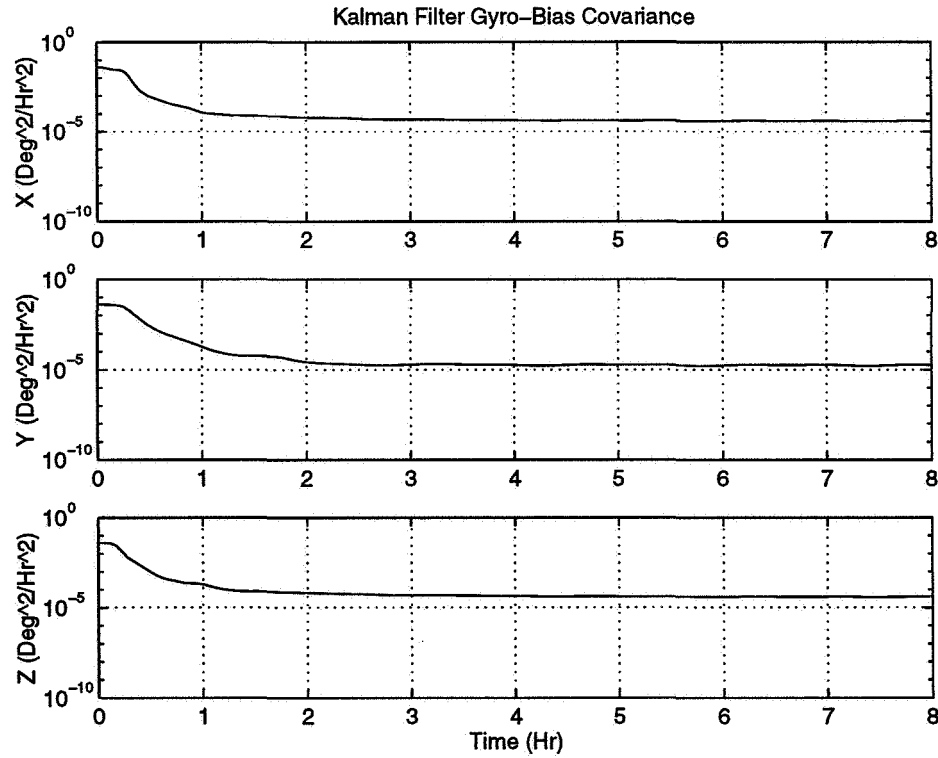


Figure 6 Plot of the Gyro-Bias Covariances

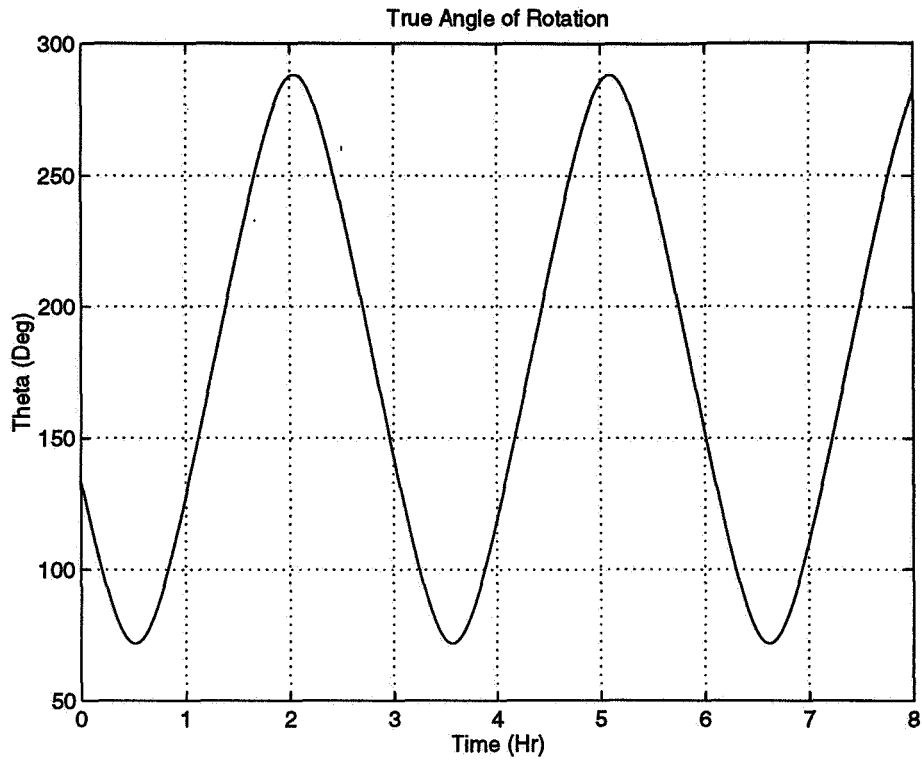


Figure 7 Plot of True Rotation Angle

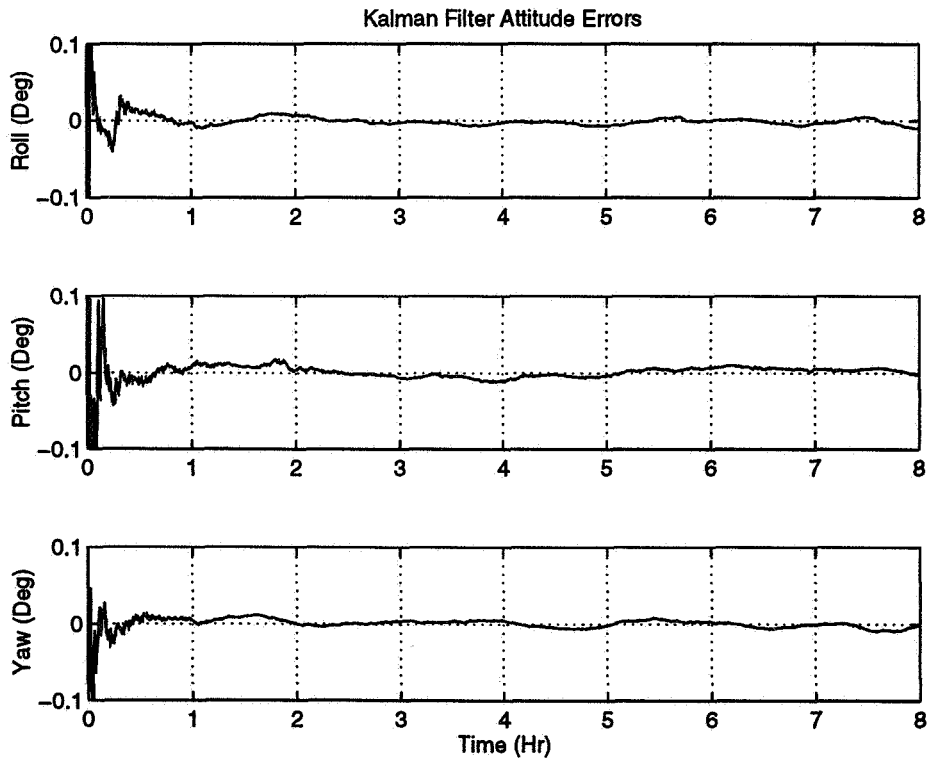


Figure 8 Plot of Attitude Error Trajectories

Conclusions

In this paper, a Kalman filter was developed for attitude estimation using the modified Rodrigues parameters. Conceptually, the computational requirements for the new algorithm are comparable to the quaternion-based Kalman filter. However, the formulation shown in this paper avoided the normalization constraint associated with the quaternion representation. Therefore, methods to maintain a singular covariance matrix using the quaternion representation in the Kalman filter have been eliminated. However, a singularity exists for 360 degree rotations. This may be avoided by allowing for a discrete jump to the origin when the rotation approaches the singularity. Simulation results indicate that the new algorithm was able to accurately estimate for the spacecraft attitude and the gyro-biases.

Acknowledgments

The first author's work is supported by a National Research Council Postdoctoral Fellowship tenured at NASA-Goddard Space Flight Center. The author greatly appreciates this support. Also, this author wishes to thank Malcolm D. Shuster for introducing him to the modified Rodrigues parameters.

References

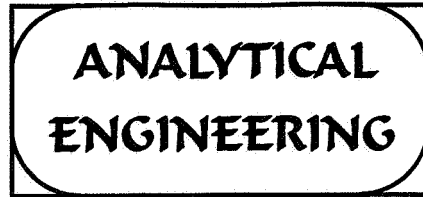
- [1] Lefferts, E.J., Markley, F.L., and Shuster, M.D., "Kalman Filtering for Spacecraft Attitude Estimation," *Journal of Guidance, Control and Dynamics*, Vol. 5, No. 5, Sept.-Oct. 1982, pp. 417-429.
- [2] Ramirez, H.S., and Dwyer, T.A.W., "Variable Structure Control of Spacecraft Reorientation Maneuvers," *Proceedings of AIAA Guidance, Navigation, and Control Conference*, Williamsburg, VA, Aug. 1986, AIAA Paper #86-1987, pp. 88-96.
- [3] Slotine, J.-J.E., and Di Benedetto, M.D., "Hamiltonian Adaptive Control of Spacecraft," *IEEE Transactions on Automatic Control*, Vol. 35, No. 7, July 1990, pp. 848-852.
- [4] Shuster, M.D., "A Survey of Attitude Representations," *The Journal of the Astronautical Sciences*, Vol. 41, No. 4, Oct.-Dec. 1993, pp. 439-517.
- [5] Marandi, S.R., and Modi, V.J., "A Preferred Coordinate System and Associated Orientation Representation in Attitude Dynamics," *Acta Astronautica*, Vol. 15, No. 11, Nov. 1987, pp. 833-843.
- [6] Tsiotras, P. "Recent Results on the Attitude Control Problem," *Journal of Guidance, Control and Dynamics*, in review.
- [7] Schaub, H., Junkins, J.L., and Robinett, R.D., "Adaptive External Torque Estimation by Means of Tracking a Lyapunov Function," *Proceedings of the AAS/AIAA Space Flight Mechanics Meeting*, Austin, TX, Feb. 1996, AAS Paper #96-172.
- [8] Crassidis, J.L., and Markley, F.L., "Sliding Mode Control Using Modified Rodrigues Parameters," *Journal of Guidance, Control and Dynamics*, in review.
- [9] Crassidis, J.L., Andrews, S.F., Markley, F.L., and Ha, K., "Contingency Designs for Attitude Determination of TRMM," *Proceedings of the Flight Mechanics/Estimation Theory Symposium*, NASA-Goddard Space Flight Center, Greenbelt, MD, 1995, pp. 419-433.

FLIGHT MECHANICS/ESTIMATION THEORY SYMPOSIUM

MAY 14-16, 1996

SESSION 2

Fixed
Price
Answers



5423 Glendale Gulch
Boulder, CO 80301
303-530-9641

Flight Mechanics/Estimation Theory Symposium
Goddard Space Flight Center, May 1996

Abstract

Toward the Complete Regulator

David Sonnabend, President

In the 1994 Symposium, I presented a new optimal observer, capable of performance well beyond that obtainable from Kalman theory. It used a much better performance index, and made use of all the available information on the power spectra of the process and measurement noises. In the 1995 Symposium, my paper "Post Kalman Progress" extended these ideas to optimal regulators; and LQG theory was completely replaced. However, it was assumed there that the controls were computed from an exact estimate of the current state. Here, in 1996, the loop will be closed, in that an observer provides a noisy estimate of the state, and both sets of gains must be chosen to deliver optimal regulator performance.

There have been casualties along the way – besides the abandonment of white noise, and performance indices lacking engineering relevance, the range of application of the "Separation Theorem" has been severely restricted to where the design of the observer and regulator can no longer be completely separated; and the "Certainty – Equivalence Principle" no longer has any validity in any practical problem. If possible in 20 minutes, I'll sketch out the new complete regulator theory, and indicate what still needs to be done. The paper will conclude with a fully worked out example, showing dramatic improvements over a corresponding design based on separated LQG and Kalman theory.

Investigation of Models and Estimation Techniques for GPS Attitude Determination

J. Garrick
 NATIONAL AERONAUTICS AND
 SPACE ADMINISTRATION
 GODDARD SPACE FLIGHT CENTER
 Greenbelt, Maryland, USA 20771

ABSTRACT

Much work has been done in the Flight Dynamics Analysis Branch (FDAB) in developing algorithms to meet the new and growing field of attitude determination using the Global Positioning System (GPS) constellation of satellites. Flight Dynamics has the responsibility to investigate any new technology and incorporate the innovations in the attitude ground support systems developed to support future missions. The work presented here is an investigative analysis that will produce the needed adaptation to allow the Flight Dynamics Support System (FDSS) to ingest GPS phase measurements and produce observation measurements compatible with the FDSS.

A simulator was developed to produce the necessary measurement data to test the models developed for the different estimation techniques used by Flight Dynamics. This paper will give an overview of the current modeling capabilities of the simulator, models and algorithms for the adaptation of GPS measurement data, and results from each of the estimation techniques. The paper will also outline future analysis efforts to evaluate the simulator and models against inflight GPS measurement data.

Background

Originally the GPS constellation was conceived to produce accurate position information for ground, air and space based systems. This information would be available to anyone who possessed a GPS receiver,

on a continuous basis. With the advance of technology that produced low cost and lightweight receivers, arose a new application of the GPS constellation; attitude determination. It was discovered that with a pair of GPS antenna a user can determine a phase difference between like signals of that antenna pair. This process is commonly known as the interferometric principle, and has been used in the Minitrack system in the early days of space flight orbit determination. This principle is illustrated by Figure 1 below, which shows the relationship between wavelength (a function of phase difference) and the wavefront angle.

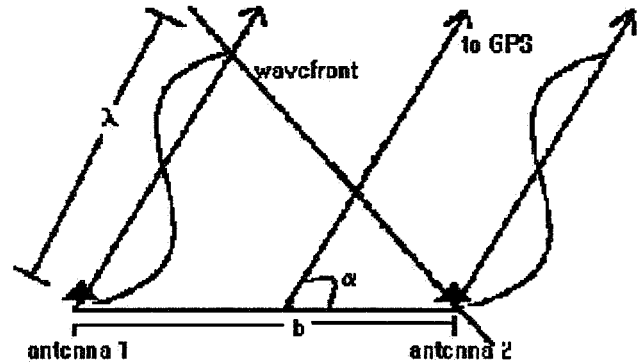


Figure 1. Baseline phase/angle relationship

As a center of expertise for attitude determination and calibration, the FDD began to investigate this new technology to determine it's capabilities. This investigation begins with a fundamental equation which governs the phase difference computation. The fundamental equation can be determined from Figure 1 and is given by:

$$\cos \alpha = (n + k\phi) (\lambda / b) \quad (\text{Equation 1})$$

where

α is the angle between the baseline and line of sight to the GPS spacecraft

n is the integer number of cycles in the phase difference between receivers

ϕ is the decimal part of the phase difference received from the GPS signal

k is a scale factor which depends on ϕ 's units

λ is the wavelength of the GPS signal (GPS has two frequencies,
 L1 at 1575.42 MHz., and
 L2 at 1227.6 MHz.

The wavelengths are
 0.19042541 meters and 0.24437928 meters,
 respectively)

b is the baseline length

If we were to rewrite equation 1 as

$$n + k\phi = (b/\lambda) \cos \alpha \quad (\text{Equation 2})$$

we can determine the integer limits for a given baseline length. To see this let the baseline length be 1 meter, which is what is used for all analysis presented here. Then let $\alpha = 0$ and use the L1 frequency, for which $\lambda = 0.1904$ meters. Solving this equation we get $n + k\phi = 5.25$. So we know as the GPS spacecraft enters the field of view and traverses from 0 to 180 degrees, then the integer component of the phase difference, in units of wavelengths, will range from +5 to -5.

If we again rewrite equation 1 as

$$\alpha = \text{acos}[(n + k\phi)(\lambda / b)] \quad (\text{Equation 3})$$

let $\phi = 0$, and let n range from +5 to -5, we can create a table of angle ranges for each integer, again based on a 1 meter baseline. Figure 2 gives the table of angle ranges for the 1 meter baseline.

Angular Range (deg)	Integer Part of Phase
180.00 - 162.20	-5
162.19 - 139.61	-4
139.60 - 124.84	-3
124.83 - 112.38	-2
112.37 - 100.98	-1
100.97 - 90.01	-0
90.00 - 79.02	+0
79.01 - 67.61	1
67.60 - 55.16	2
55.15 - 40.38	3
40.37 - 17.80	4
17.79 - 0.00	5

Figure 2. Angular Range for a 1 meter baseline

From this range table we can determine how the phase difference would look like as it ranges through the field of view of the baseline sensor. The measured phase difference is determined by comparing in the electronics the signals from both antennae of a baseline and shifting on until both signals are in phase. Thus the most that can be detected is just under one wavelength difference. This produces a plot that looks like Figure 3 for the 1 meter baseline.

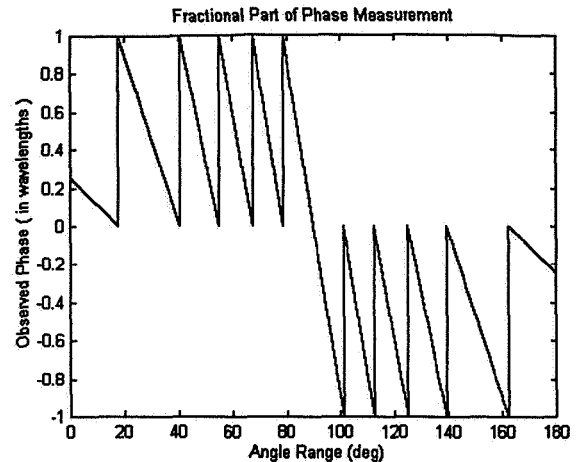


Figure 3. Phase measurement for 1 m. baseline

The lack of integer information is the well documented problem of integer ambiguity. There are several methods that can be used for the initial determination of the integer values. The most straightforward method involves a search method over the integer values using the table in Figure 2 to fit the visible GPS observations to the correct integer. This can be used on the ground for off-line processing because of the high power computers and the fact that the process is not a real-time process. After the initial integers are determined, then the phase difference measurement can be monitored to track when the integer value should change, as is illustrated by Figure 3. Other methods will be discussed when we talk about the extended Kalman Filter later.

Still this is only one bit of the information needed to compute the desired observation vector. FD ground attitude determination software makes use of time tagged observation vectors in BCS and reference vectors in GCI to determine the attitude solution. With the use of another baseline, preferably orthogonal to the first, the line of sight vector from the user spacecraft to a GPS space vehicle (SV) can be determined.

Knowing this cosine of the angle and that from another baseline, it is possible to determine the observation vector of the visible GPS SV. The angle determined by one of the baselines describes a cone around the baseline vector and likewise for the second baseline. Where the two cones intersect (see Figure 4) are the two possible solutions. Knowing the normal vector to the two baseline's plane can

reconcile which is the true solution. Paired with a known reference vector of the GPS SV at that time, the analyst can determine the attitude using several well known and established attitude estimation techniques employed within the FDOA.

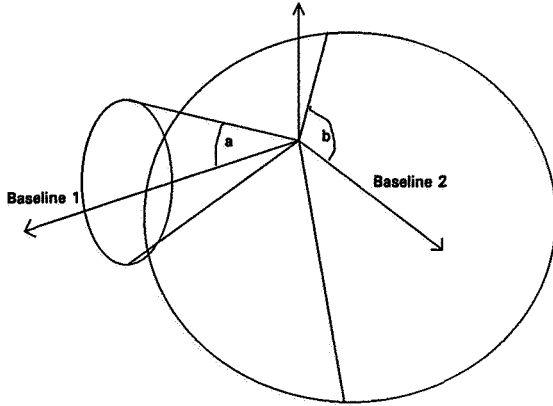


Figure 4. Observation vector resolution

Figure 4 shows the geometry of the two orthogonal baselines and the intersection of the two cones. Using Equation 1 we can relate the direction cosines to the phase differences as

$$\cos \alpha = (n_1 + k\phi_1) (\lambda/b) \quad (\text{Equation 1a})$$

$$\cos \beta = (n_2 + k\phi_2) (\lambda/b) \quad (\text{Equation 1b})$$

$$\cos \gamma = [1 - \cos^2 \alpha - \cos^2 \beta]^{1/2} \quad (\text{Equation 4})$$

These define a unit vector in the receiver coordinate system defined by the two orthogonal receiver baselines fixed in the spacecraft and, therefore, the body coordinate system frame. That is

$$x_B = [M] x_R$$

where $x_R = [x_T \ y_T \ z_T]$ transposed, the observation vector in receiver coordinates
 x_B is the observation vector in BCS
 $[M]$ is the transformation matrix from the receiver to BCS

and

$$x_T = \cos \alpha$$

$$y_T = \cos \beta$$

$$z_T = \cos \gamma$$

Error Sources

If the integer ambiguity in Equation 1 were the only parameter that needed to be computed, then the matter of attitude determination would be straightforward and no calibration would be necessary. However, as all engineers know there is some uncertainty in every measurement taken, and it's these uncertainties that need to be characterized and/or compensated for. Figure 5 shows a graphical representation of the difference between the observed GPS measurement and what is the truth.

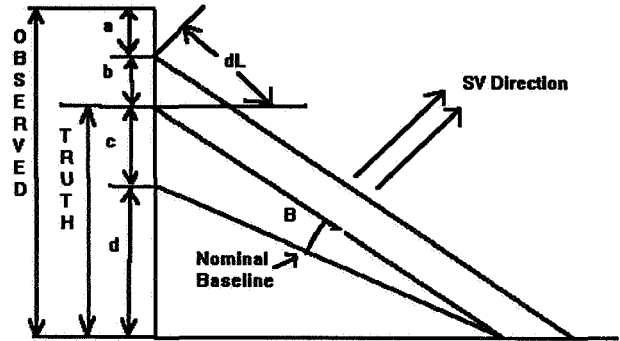


Figure 5. Components of Observed and Truth

It can be seen that the true measurement is the nominal quantity d , that is what you would expect if the system were perfect, added with a quantity associated with any misalignments. What is observed are the additional two components, a and b . The component a is a bias associated with the electronics and is different for every GPS antenna. It represents a time bias in the system. The component b is associated with the unknown length of the baseline. Although these two parameters can be measured quite accurately here on the ground (self survey mode), when in space the thermal and other environmental perturbations effects change the known values. Likewise the alignment of the sensors can be determined very accurately before launch, but the vibrations do to launch shock will result in some displacement. This may necessitate a postlaunch calibration to determine alignment and or placement of each antenna. These additional parameters change the fundamental equation to:

$$\cos \alpha = (n + k\phi + \text{noise} + \text{line bias})(\lambda / [M](b + db)) \quad (\text{Equation 5})$$

In this equation only the noise cannot be determined as a systematic error and taken out by determining the correct compensation.

Multipath

Both solutions also lack the modeling of multipath, which can be a large source of error. Multipath is essentially the reflection of a GPS SV signal off a surface on the spacecraft and received basically as an echo of the original signal. The echo obviously has the same identification as the original signal but has a different phase shift of the wavelength, giving erroneous measurements if it were not weeded out as the false signal. Spacecraft engineers can greatly reduce this source of error by mounting the antennas on booms away from the main body, or flush with spacecraft surfaces and strategically placed to reduce signal reflection.

Prediction Utility

In order to enhance the analysis process of GPS attitude determination algorithms and techniques for specific missions, it was necessary to produce a tool that would give accurate predictions for the GPS constellation as viewed by the user spacecraft. The utility was developed as an analysis tool on an IBM compatible PC using Microsoft FORTRAN and executing under the DOS operating system. The prediction tool allows the user to input parameters to fit the simulation. The setup used for all analysis and predictions is:

- Earth pointing mission (+Z BCS is nadir)
- Semi-major axis = 6728.83 km
- Altitude = 350.8 km
- Eccentricity = 0.001
- Inclination = 28.5 deg.
- RA of Asc. Node = 90.0 deg.
- Mean Anomaly = 0.0 deg.
- Arg. of Perigee = 0.0 deg.

The boresight of each antenna point in the anti-nadir direction, or in vector form

boresight vector = [0.0 0.0 -1.0] transpose, BCS

The predictions and analysis are all done at a step size of 10 seconds and a total simulation/prediction time of 1000 steps. This is about 1.6 orbits.

Internally the utility models the 24 GPS SV constellation by storing their Keplerian elements and

epoch time, and using a simple two-body propagator. The simulation produces two kinds of output data. The first is a time ordered history file of GPS spacecraft visible to the user's antenna baseline and the second produces a statistical analysis of the simulation. The statistics and parameters outputted are:

- report of simulation user supplied input parameters selected
- Acquisition and loss of signal for each GPS SV based on line of sight and beam width mask
- total time each GPS spacecraft is visible to the antenna baseline
- percentage of simulation time that each GPS spacecraft is visible to the antenna baseline
- the total number of GPS observations
- density distribution of GPS spacecraft (count of how many times n number of spacecraft are visible to the antenna baseline at any simulation step)
- maximum and minimum amount of continuous time for each event of the density distribution described above
- maximum and minimum continuous visibility time for each GPS spacecraft.

The two output datasets are written to DOS ASCII files (alphanumeric, readable format) and can be edited and printed. The data can easily be input to a plotting package for a more graphical representation. Figures 6 and 7 give two examples of the statistics for a half cone angle for each antenna of 90 degrees. This showed that the antenna baseline system would see a total of 9024 GPS observations.

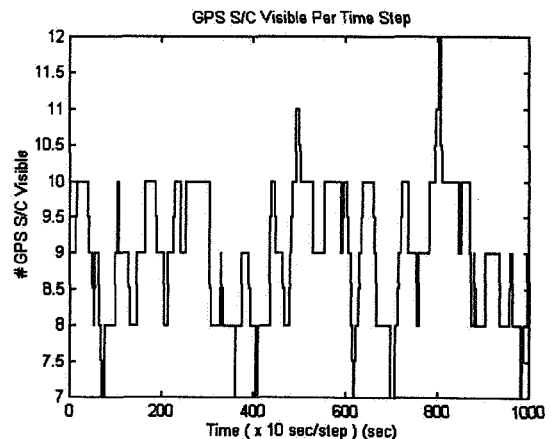


Figure 6. Distribution for half cone of 90 deg.

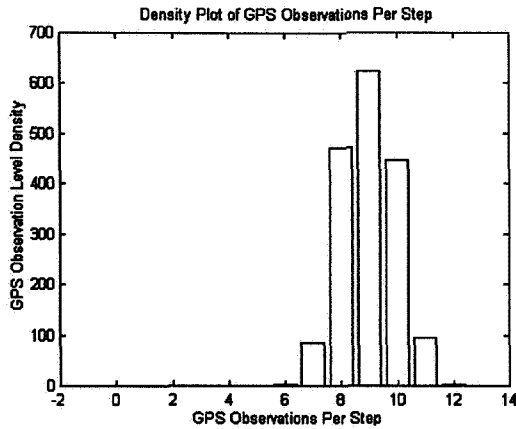


Figure 7. Density for half cone of 90 deg.

Repeating this same test case setup, except we will use only the main lobes of the antenna pattern, which changes the half cone angle for each antenna to be 32 degrees. Figures 8 and 9 show the same distribution and density plots for this setup. The total number of GPS observations in this case is considerably less, 920 observations.

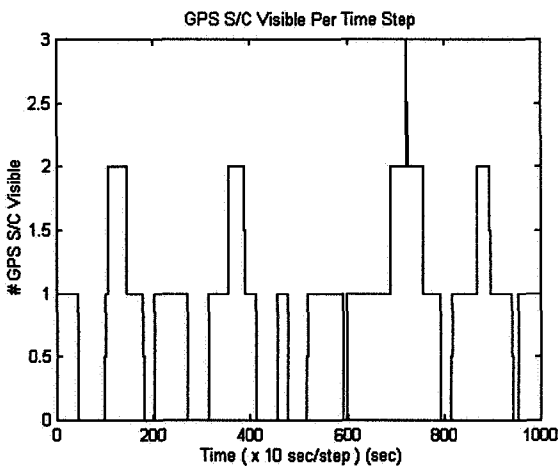


Figure 8. Distribution for half cone of 32 deg.

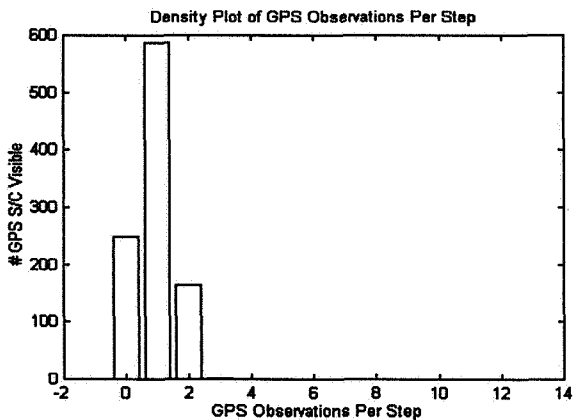


Figure 9. Density for half cone of 32 deg.

Estimation Simulator

The uncertainties in the phase measurements make it necessary to employ estimation techniques to determine attitude and/or each of the parameters listed in the error budget above. To this end an estimation simulator was developed to investigate new algorithms, and to test the GPS attitude determination capabilities. The simulator essentially models a given spacecraft's ephemeris and dynamics, and uses the above equations to produce the observed phase difference. The processing of the phase difference employs a selection algorithm and methods for resolving the integer ambiguity (several methods have been examined for this simulator).

A couple of methods were used successfully, but the method that was used for this analysis involves using the tables of integers and angle ranges generated earlier for a one meter baseline. The method is simply a search through all the possible integer values (for a one meter baseline there are only 11, values from -5 to +5) and matching the angular separation to within some tolerance using the angular separation of the reference vectors after they have been transformed to the nominal BCS coordinate frame. This can be done at every time point or once the initial integers are found they can be updated by monitoring the change in phase measurements. The first method is a good way to go for non real-time estimation. It simply is easier to implement. But for a real-time attitude estimation where computer time is at a premium, it is more efficient to initialize the integers and then monitor for changes. Once the integer phase has been determined it is simple to compute the observation vectors, as defined by equations listed earlier. The resulting observation vectors are paired with reference vectors and form the input data for an extended Kalman Filter and a single frame estimator. The simulator provides a means to vary modeling and algorithms to investigate the affect.

Figure 10 gives a plot of what the simulated true attitude is for the test case scenario. The scenario is an earth pointing 1 rotation per orbit (RPO) spacecraft. The dynamics also has a small noise characteristic which produces the small amount of jitter in the plot. This is probably a very smooth case as compared to actual spacecraft attitude behavior, but it serves as a basis for further analysis.

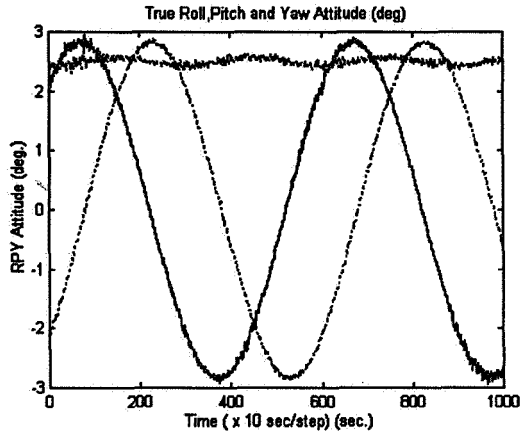


Figure 10. Plot of True RPY Attitude

Figure 11 illustrates what the simulator would output for a GPS SV that transverses the entire angle range from 0 to 180 degrees with the addition of attitude errors and noise. This plot has a measurement noise of 0.1 wavelengths or about 2 cm. It demonstrates some things that need to be considered for when monitoring of phase changes is used for updating the integers. First as can be seen the phase difference will change integer values without getting close to 1.0 or 0.0 because of the noise. This has to be considered, as the wrong choice of the integer can add an error as much as 18.0 degrees in the observation vector computation. What is not seen here but does happen is sometimes the integer oscillates between two integers for a brief time before moving on. This has to do with attitude motion as much as the noise.

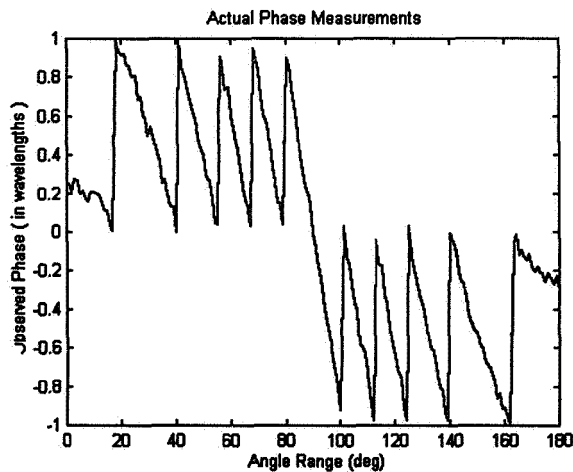


Figure 11. Plot of Actual Measured Phase

The estimation techniques that are used in this paper, an extended Kalman Filter and a single frame estimator (QUEST), will look at two cases which

represents the best and worse case scenarios as far as noise on the phase measurements. They are the 0.1 wavelength (2 cm) case and the 0.01 wavelength (0.2 cm) case. Estimates have been made that the measurement noise can be reduced to about 0.5 cm. (reference 2). Thus the use of 0.2 cm and 2.0 cm. certainly represents the best and worse case scenarios. For both cases it is assumed that the the location of the antennas and the time bias have been determined so as not to affect the solution. Both cases also use the a hemispherical antenna pattern, which is to say a half cone of 90 degrees for the antenna field of view. In actual use the half cone of 32 degrees may be used because of the higher noise characteristics for observations in the higher angle region, or the side lobes of the antenna pattern. The affect of signal to noise ratio on observation depending on their location in the main or side lobes will be investigated in subsequent analysis. The worse case scenario will use the higher noise characteristic, but will apply it to all observations. Thus the expected in-flight accuracy will be somewhere between the worse and best case scenarios.

Estimation Models

The first estimation technique is the extended Kalman Filter. Originally a basic Kalman Filter was used and produced good results. However after implementing an extended Kalman Filter the results were much improved. This simply has to do with adding some knowledge to the system about the expected trajectory. This additional knowledge simply evaluates the measurement matrix and the dynamics, or state transition, matrix based upon the last estimate of the state. In the case of the extended Kalman Filter the state consists of errors or deltas away from the a priori attitude at each step. Once an estimate of the error at a time step is made then the attitude error is updated based on the state deltas, the measurement and state dynamics matrices are recomputed using this new updated state and the filter is reset for the next time step. The math specifications for equations that are specific to the extended Kalman Filter are:

$$\Delta \dot{x}(t) = \left[\frac{\partial f}{\partial x} \right]_{x=x^*} \cdot \Delta x(t) + u(t)$$

$$[z - h(x^*, t)] = \left[\frac{\partial h}{\partial x} \right]_{x=x^*} \cdot \Delta x(t) + v(t)$$

Trajectories are evaluated along current estimate of the updated attitude error. This is found by taking the deltas at this time step and adding them to the previous error estimate, or

$$x_i = x_{i-1} + \Delta x_i$$

The reader is directed to reference 3 for a detailed discussion on the extended Kalman filter.

Figures 12, 13 and 14 show the attitude error (true minus the estimated attitude) and the statistics for the worse case scenario. It has a lot of structure to the plot, but a upper and lower bound is around 0.5 degrees.

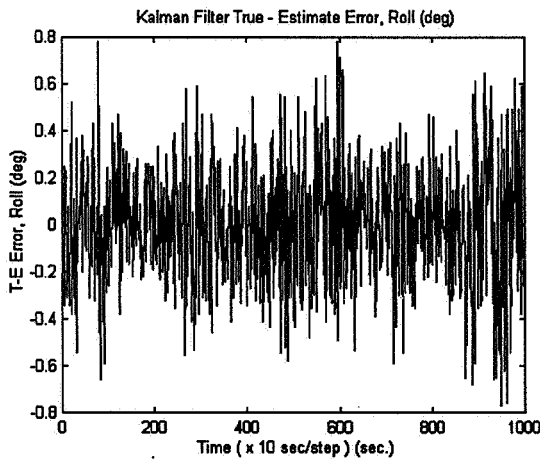


Figure 12. Roll Error for worse case

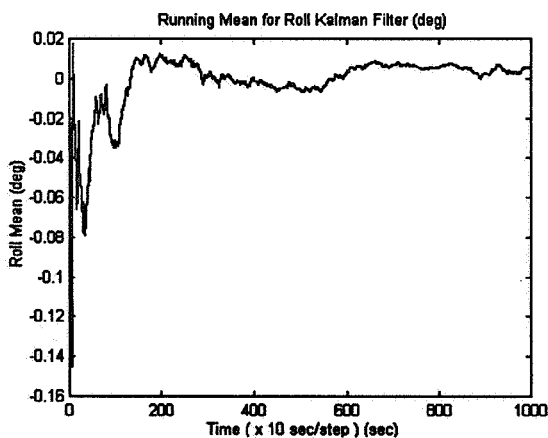


Figure 13. Roll running mean for worse case

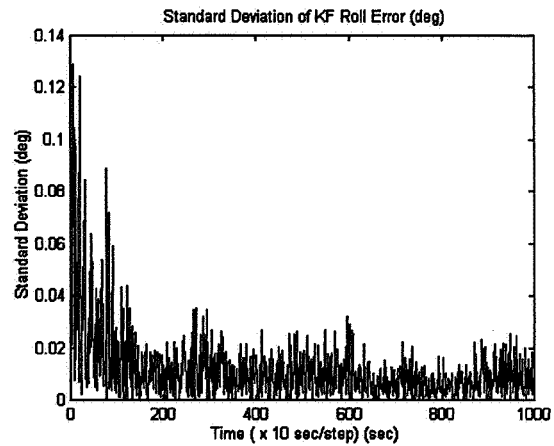


Figure 14. Roll running std. dev. for worse case

Figures 15, 16 and 17 show the results for the best case scenario. Figure 15 shows a bound around 0.1 degrees.

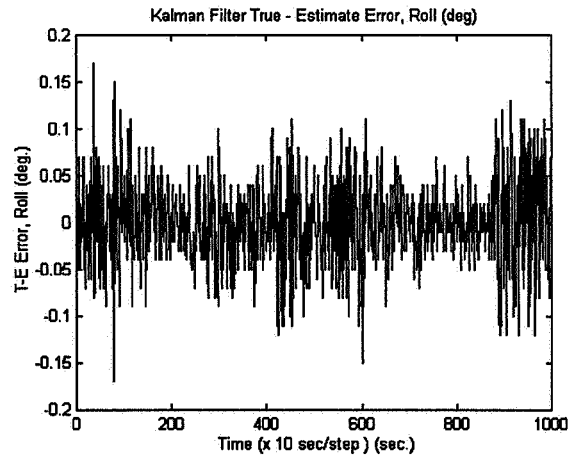


Figure 15. Roll Error for best case

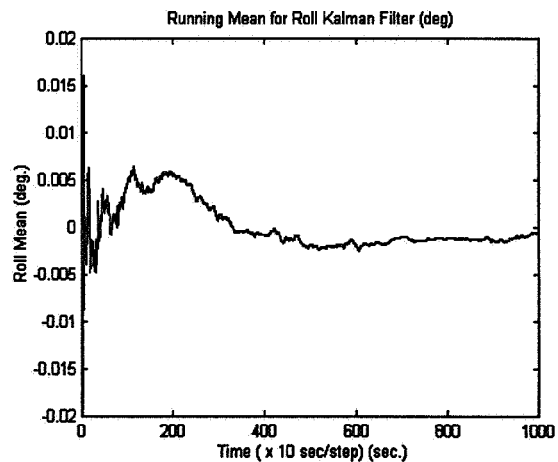


Figure 16. Roll running mean for best case

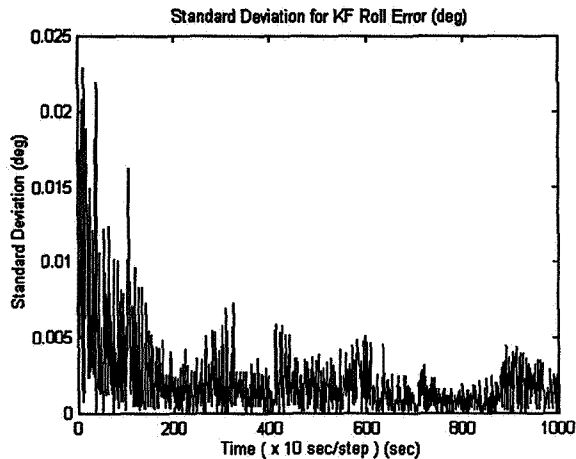


Figure 17. Roll running std. dev. for best case

It is obvious that both show convergence. The best interpretation for this case study is that one can expect to achieve somewhere between 0.2 degrees and 0.5 degrees accuracy depending on the measurement noise and how accurately the noise is compensated for in the filter. In both of these cases perfect knowledge of the measurement noise characteristics was known and compensated for in the filter's state measurement noise covariance matrix.

Single Frame Estimation (QUEST)

The QUEST modeling likewise has demonstrated that a less sophisticated method can still achieve accuracies of less than one degree using GPS measurement data. The reader is referred to another source (see reference 1) for a detailed description of the QUEST attitude determination algorithm. Here again the method for determining the integer ambiguity was the search method employed by extended Kalman Filter. The monitoring method was examined also and produced the same results, however it was more convenient to compute the integers again at each step and without a timing constraint it presented no problems.

A unique problem exists for the single frame solution that the filter does not have, simply because it processes one observation at a time. The single frame method, however, needs at least two observation vectors to determine an attitude and as a further constraint they must not be collinear. The best solution would be to find three observation vectors that are orthogonal to each other, or as close to this configuration as possible. This describes the

geometric selection problem for the single frame solution.

Three test cases were run to demonstrate the importance of employing a selection scheme. Figure 18 shows the results of the case where all observation vectors were used. Figure 19 shows the case where the first four observation vectors were used. And Figure 20 shows the results when the selection algorithm was employed. In all three cases the best case scenario was used, which translates to almost having perfect knowledge of the system.

The selection algorithm used is based on the statement made earlier of finding three observation vectors (actually using the reference vectors) that as close as possible form an orthogonal triad. This is simply done by looking at all combinations of three observation vectors and use the group that has the smallest sum of the dot products. Assuming that a maximum of 12 observations are visible at any one time, and choosing three at a time from this, there are 220 groupings to search. This isn't bad and in fact takes very little time because of the simplicity of the algorithm.

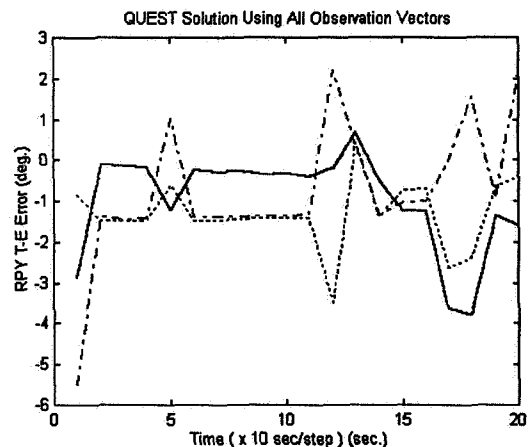


Figure 18. Single Frame Error; all observations

It's obvious that the selection algorithm produces the best solution, with using any four (in this case the first four) being the second best method. The reasoning behind this can be interpreted as being over observed. That is the other observations add more uncertainty to the estimation. The residual spikes, at this time, have no resolution, with the data and estimation algorithm having been verified for correctness.

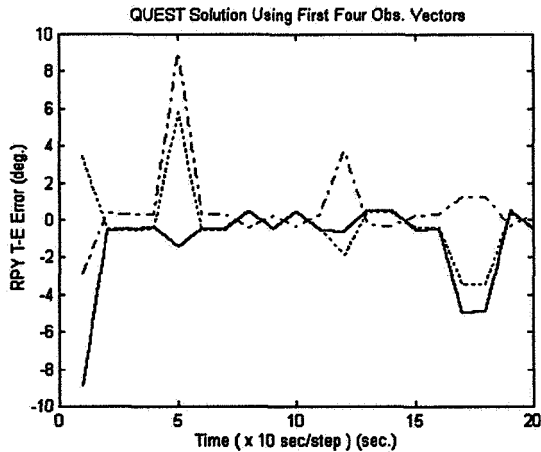


Figure 19. Single Frame Error, first 4 observe.

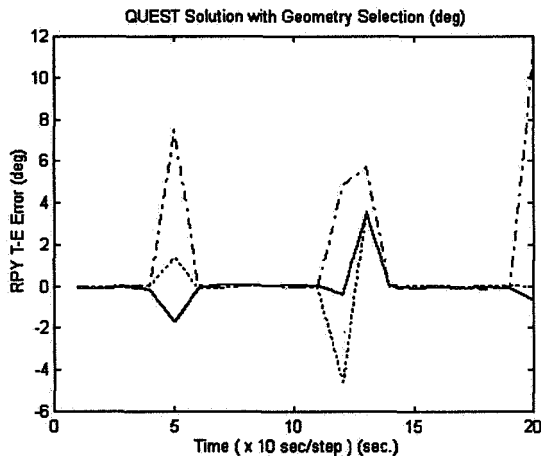


Figure 20. Single Frame Error; with selection

One more case was run for the single frame estimation method. This was using the geometry selection algorithm, but using the worse case scenario. Figure 21 illustrates the results.

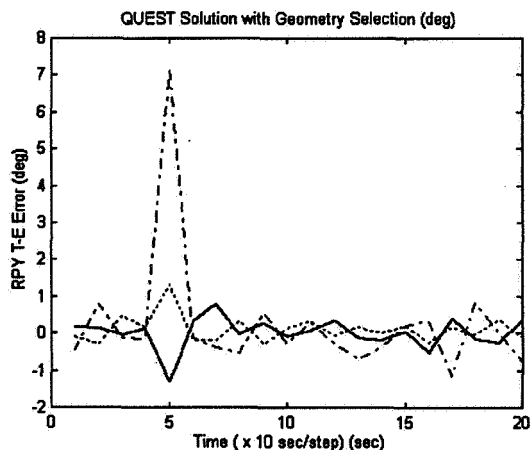


Figure 21. Single Frame Error, worse case

From this analysis of the worse case and best case, and using a selection algorithm, the QUEST method for attitude determination can produce an accuracy between 0.5 and 1.0 degrees.

Future Analysis

There are many future items to be implemented and considered connected with this analysis. They are listed below according to function or system.

Estimation Simulator Enhancements

- Expansion of user input parameters such as:
 - 1) allow varying of baseline length
 - 2) allow varying placement of antennas
 - 3) allow varying number of antennas
 - 4) model boom and uncertainties due to deflection of boom
 - 5) model main and side lobes in antenna pattern for differing noise characteristics
 - 6) implement P-code for investigation of a more accurate measurement

Extended KF

- extend state to include gyro and/or antenna biases
- add misalignments to state for calibration

Single frame solutions

- continue to look at geometric considerations and selection process
- look at REQUEST implementation

Processing of Actual Inflight GPS Data

- have acquired Crista-SPAS data
- looking to use Spartan/GADACS data

Conclusions

The Kalman Filter has demonstrated that it is possible to get better than 0.5 degrees per axis in determining attitude for a one meter baseline. And likewise it is possible to get better than one degree from a single frame attitude solution using a geometry selection algorithm. All of these analyses were done with a 90 degree half cone angle field of view for each antenna, that is both main and side lobes of the antenna pattern. Further analysis needs

to be done using only the main lobe and analysis which uses both lobes but implements a better noise characterization based on the angle from the antenna boresight. And of course the processing of GPS phase measurements from on-orbit spacecraft will be done to validate the algorithms used so far.

The main purpose of this paper is to demonstrate that the GPS phase measurements can be adapted to the existing ground attitude determination software. With the use of the cones method for resolving the line of sight vector to the observed GPS SV and also with new methods for the integer ambiguity resolution it is definitely possible to use the existing method of processing time tagged observation and reference vector pairs.

Although the field of attitude determination using GPS is still young, this study has shown that it is possible to adapt the GPS measurements to the existing design of FD ground attitude determination systems. Still, there is much yet to be done for future analysis in order for GPS to be routinely accepted as an alternative to more expensive sensor configurations.

References

1. J. Wertz, "Spacecraft Attitude Determination and Control"; Reidel Publishing Co., 1984.
2. C. Cohen, & B. Parkinson; "Expanding the Performance Envelope of GPS Based Attitude Determination"; Proc. Int. Tech. Mtg., ION GPS, Albuquerque, NM, Sept. 1991.
3. A. Gelb, (editor); "Applied Optimal Estimation"; M.I.T. Press; 1989

ATTITUDE DRIFT ANALYSIS FOR THE WIND AND POLAR MISSIONS

Patrick Crouse
Goddard Space Flight Center (GSFC)
Greenbelt, Maryland

Abstract

The spin axis attitude drift due to environmental torques acting on the Global Geospace Science (GGS) Interplanetary Physics Laboratory (WIND) and the Polar Plasma Laboratory (POLAR) and the subsequent impact on maneuver planning strategy for each mission is investigated. A brief overview of each mission is presented, including mission objectives, requirements, constraints, and spacecraft design. The environmental torques that act on the spacecraft and the relative importance of each is addressed. Analysis results are presented that provided the basis for recommendations made pre-launch to target the spin axis attitude to minimize attitude trim maneuvers for both spacecraft their respective mission lives. It is presented that attitude drift is not the dominate factor in maintaining the pointing requirement for each spacecraft. Further, it is presented that the WIND pointing cannot be met past 4 months due to the Sun angle constraint, while the POLAR initial attitude can be chosen such that attitude trim maneuvers are not required during each 6 month viewing period.

INTRODUCTION

This paper investigates the attitude drift due to environmental disturbance torques on the Global Geospace Science (GGS) Interplanetary Physics Laboratory (WIND) and the Polar Plasma Laboratory (POLAR) spacecraft during routine mission conditions. Spin axis attitude drift due to environmental disturbances will be predicted and compared against mission requirements to determine the attitude control strategy required. A portion of this work is the compilation of several analysis memoranda prepared from November, 1991 to January, 1996. These memoranda were prepared by Computer Sciences Corporation (CSC) under the direction of the National Aeronautics and Space Administration (NASA) Goddard Space Flight Center (GSFC) Flight Dynamics Division (FDD)(References 1-5).

MISSION OVERVIEW AND SPACECRAFT DESCRIPTION

The GGS program is part of the overall International Solar Terrestrial Physics (ISTP) program which will use multiple spacecraft in complementary orbits to assess processes in the Sun-Earth interaction chain. The two specific objectives to be accomplished by the GGS portion are investigations of the solar wind-magnetosphere coupling and the global magnetosphere energy transport. These include: solar wind source and 3-D features, global plasma storage flow and transformation, deposition of energy into the atmosphere, and basic plasma states and characteristics. Both spacecraft have a common design heritage and have been constructed by Lockheed Martin Corporation (formerly the Astrospace Division of General Electric) to be spin stabilized cylindrical spacecraft about 2.44 meters in diameter and 1.85 meters tall. The individual WIND and POLAR missions are presented below.

WIND

The nominal WIND spacecraft attitude is South Ecliptic Normal, with the spin axis aligned within 1 degree of the South Ecliptic Pole and the spin rate is 20 revolutions per minute (rpm). The Sun angle is constrained to be 89.65 to 91 degrees, measured from the +Z-axis, due to thermal considerations. The initial spacecraft orbit is a dayside double lunar swingby that will require about 2 years to traverse. This is followed by an insertion into a halo orbit about the Sun-Earth libration point (L_1). Orbit maneuvers will occur at regular intervals throughout the mission. Attitude maneuvers will consist of trim maneuvers as necessary. The WIND spacecraft, shown in Figure 1, was launched in November 1994.

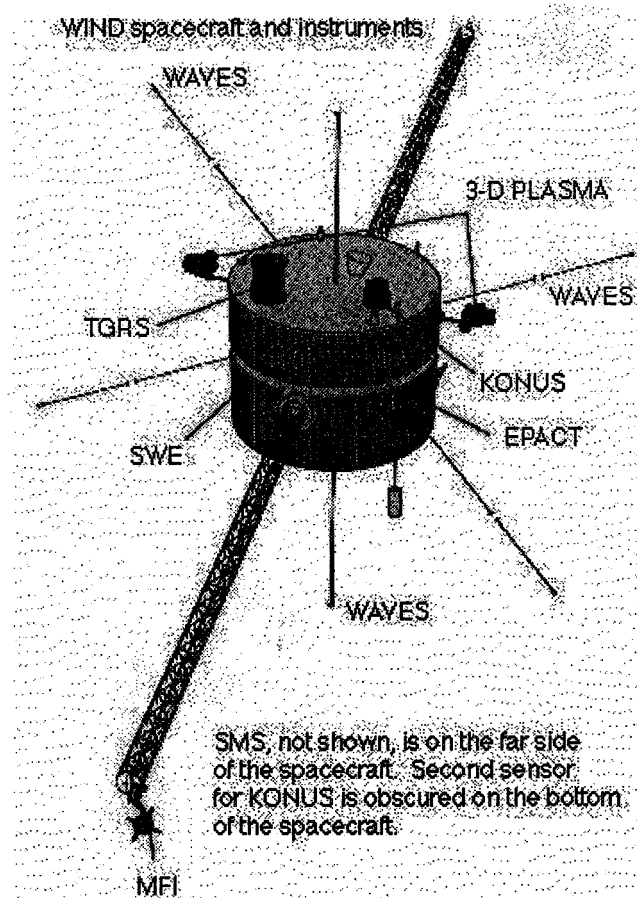


Figure 1: WIND Spacecraft

POLAR

In the normal mission mode, POLAR will point its spin axis within 1 degree of \pm orbit normal, and will maintain a spin rate of 10 rpm. The selection of \pm orbit normal is based on a Sun angle constraint of 90 to 160 degrees from the +Z-axis due to power and thermal needs. The nominal POLAR orbit is 1.8 X 9.0 Earth Radii (R_e) with an inclination of 86 degrees. Upon reaching the mission orbit, no other orbit maneuvers are required, however, 180 degree attitude maneuvers will be performed every 6 months in order to maintain the Sun angle constraint. The minimization of attitude trim maneuvers between reorientation maneuvers is desirable in order to save fuel to increase mission life. The POLAR spacecraft, shown in Figure 2, was launched in February 1996.

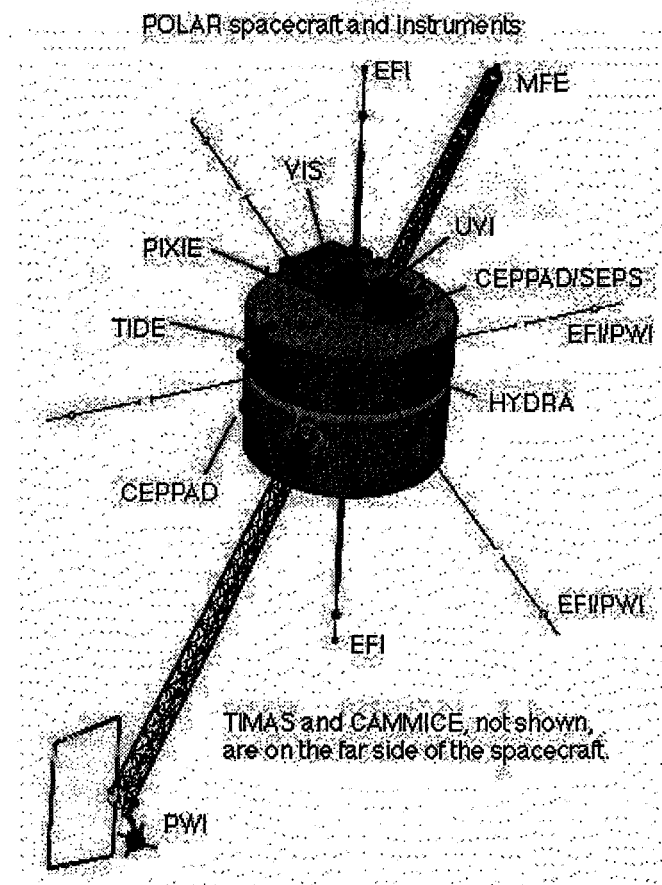


Figure 2: POLAR Spacecraft

ENVIRONMENTAL TORQUES

The WIND and POLAR spacecraft main bodies are modeled as simple right circular cylinders. The booms on WIND were also considered for their effect on the center of pressure (Reference 6). The spacecraft spin axis (+Z-axis) is assumed to lie along the principal axis, as does the location of the center of mass. Therefore, there is no nutation or coning. The environmental disturbance torques considered for the spacecraft are solar radiation pressure, Earth gravity gradient, and magnetic dipole moment.

Solar Pressure Torque

The center of pressure for a right circular cylinder is located at the volume centroid. The total force due to solar radiation can be assumed to act at the center of pressure, which lies along the principal axis. Therefore, the lever arm from the center of mass to the center of pressure also lies along the principal axis. Under the assumptions stated, the solar pressure torque is always perpendicular to the spin axis, and, thus, the spin rate is unchanged.

The force on a right circular cylinder is given in Reference 7 as:

$$\vec{F} = -P\left(\left[\sin \beta\left(1 + \frac{1}{3}C_s\right) + \frac{\pi}{6}C_d\right]A_1 + (1 - C_s)\cos \beta A_2\right)\hat{S}$$

$$+ \left[\left(-\frac{4}{3}C_s \sin \beta - \frac{\pi}{6}C_d\right)\cos \beta A_1 + 2\left(C_s \cos \beta + \frac{1}{3}C_d\right)\cos \beta A_2\right]\hat{A}$$

where:

$$A_1 = 2rh$$

$$A_2 = \pi r^2$$

$$P \approx 4.5 \times 10^{-6} \text{ N / m}^2 = \text{solar mean momentum flux}$$

r = radius of the cylinder (48 inches for each spacecraft)

h = height of the cylinder (73 inches for each spacecraft)

\hat{S} = unit vector from spacecraft to Sun

\hat{A} = spacecraft spin axis (+Z - axis for each spacecraft)

β = Sun angle

C_s = probability that radiation is reflected specularly (16.9%)

C_d = probability that radiation is reflected diffusely (8.5%)

C_a = probability that radiation is absorbed (74.6%)

$$\text{and } C_a + C_d + C_s = 1$$

The above equation is good for Sun angles less than or equal to 90 degrees, but only minor changes are required for Sun angles greater than 90 degrees. In addition, the relationship between the radiation reflection and absorption probabilities was used to eliminate the coefficient of absorption, C_a , from the equation. The torque on the spacecraft then is :

$$\vec{N}_{sp} = (\vec{R}_{cp} - \vec{R}_{cm}) \times \vec{F}$$

where:

$\vec{R}_{cp} - \vec{R}_{cm}$ = vector from the center of mass of the spacecraft to the center of pressure

Gravity Gradient Torque

The gravity gradient torque for a spacecraft, assuming that the center of mass is at the geometric center of the body, is given in Reference 7 as:

$$\vec{N}_{GG} = \frac{3\mu}{R_s^3} [\hat{R}_s \times (I \cdot \hat{R}_s)]$$

where:

R_s = geocentric position vector of the origin of the body reference system

I = moment of inertia tensor

For a spinning spacecraft, it is convenient to average the torque of one rotation period. Let the spin axis be the Z-axis and the spin rate ω . The body coordinate system at time t can be expressed at $t = 0$ as:

$$\begin{aligned}\hat{X} &= \cos \omega t \hat{X}_0 + \sin \omega t \hat{Y}_0 \\ \hat{Y} &= -\sin \omega t \hat{X}_0 + \cos \omega t \hat{Y}_0 \\ \hat{Z} &= \hat{Z}_0\end{aligned}$$

The unit vector \hat{R}_s can be written as:

$$\begin{aligned}\hat{R}_{s1} &= \hat{R}^0_{s1} \cos \omega t + \hat{R}^0_{s2} \sin \omega t \\ \hat{R}_{s2} &= -\hat{R}^0_{s1} \sin \omega t + \hat{R}^0_{s2} \cos \omega t \\ \hat{R}_{s3} &= \hat{R}^0_{s3}\end{aligned}$$

The instantaneous gravity gradient torque is averaged over one spin period to obtain

$$\bar{N}_{GG_s} = \frac{1}{2\pi} \int_0^{2\pi} \bar{N}_{GG} d\theta$$

substitution, then provides the spin-averaged gravity gradient torque as:

$$\bar{N}_{GG_s} = \frac{3\mu}{R_s^3} \left[I_{zz} - \left(\frac{I_{xx} + I_{yy}}{2} \right) \right] (\hat{R}_s \cdot \hat{Z})(\hat{R}_s \times \hat{Z})$$

Magnetic Disturbance Torque

Magnetic disturbance torques are a result of the interaction of the residual magnetic field surrounding the spacecraft with the geomagnetic field. As described in Reference 7, the primary sources of magnetic disturbance torques are the spacecraft magnetic moments, eddy currents, and hysteresis. The magnetic moment is the dominant source of magnetic disturbance torques, and it is the only one considered here. The instantaneous magnetic disturbance torque is:

$$\bar{N}_{mag} = \bar{m} \times \bar{B}$$

where:

\bar{m} = effective magnetic moment ($A \cdot m^2$)

\bar{B} = geocentric magnetic flux density (Wb / m^2)

EQUATIONS OF MOTION

The total disturbance torque then is the sum of the solar pressure, gravity-gradient, and magnetic moment torques discussed above. The attitude equations of motion are simply:

$$\frac{d\bar{L}}{dt} = \bar{N}_{total}$$

where \bar{L} is the spacecraft angular momentum vector in the inertial frame. There is assumed to be no nutation, so the spin axis, and the angular momentum vector will remain along the Z-axis.

RESULTS

WIND

Due to the nature of the WIND orbit, only solar pressure torques were considered. The analysis indicated that the attitude drift would not exceed 0.8 degrees over a 180 day period. In fact, the attitude drift caused by solar pressure only was such that the spacecraft spin axis would sweep out a path that almost closes upon itself at the end of one year, and the angular distance from the target attitude would not exceed 1 degree. Therefore, the 1 degree control box could be maintained without using attitude trim maneuvers by selecting the proper initial attitude. A closer examination of the Sun angle requirement to maintain the Sun angle between 89.65 and 91.0 degrees was then performed. A set of representative attitudes were examined for both attitude drift and change in Sun angle over time. The change in Sun angle was found to be such that the constraint was violated within at most 4 months, and subsequent flight data has confirmed this result.

Operationally, WIND is required to perform orbit maneuvers to maintain proper targeting to make the most efficient use of the double lunar swingby trajectory. For efficiency of operations planning, attitude maneuvers, if required, are designed to immediately follow the orbit maneuvers. Whenever possible, the spin axis attitude is trimmed such that a subsequent attitude trim burn is not required prior to another orbit maneuver. During the long phases of the outer loops of the double lunar swingby, the effect of the Sun angle change dictates the need for attitude trims without an accompanying orbit maneuver.

POLAR

The POLAR mission has an obvious interest in fuel conservation, since the mission lifetime is dictated by the ability to perform 180 degree attitude reorientation every 6 months. The less fuel used to maintain the 1 degree attitude pointing requirement, the longer the mission life. Since POLAR is in an Earth orbit, albeit a highly elliptical one, gravity gradient and magnetic moment disturbance torques were considered along with the solar pressure torque. A residual magnetic moment of $1 \text{ A} \cdot \text{m}^2$ was used based on manufacturer analysis (Reference 6).

The spacecraft manufacturer examined the effect of each of the disturbance torques individually, then combined the results to form a worst case. The result of that worst case indicated that there would be cases in which the spacecraft attitude constraint could not be maintained over the 6 month period between attitude maneuvers. The FDD then analyzed the effect of the three disturbance torques acting simultaneously. Since each torque is a function of the spacecraft attitude, any attitude changes will affect the magnitude and direction of subsequent torques acting on the spacecraft. Therefore, the approach was expected to produce different results than those provided by the manufacturer. The maximum attitude drift over a 6 month period was determined to be about 0.4 degrees for the disturbance torques considered. As was the case for WIND, the attitude control box could be maintained without attitude maneuvers when only the disturbance torques were considered.

The requirement for POLAR is to maintain the attitude within 1 degree of the orbit normal. What if the orbit normal is moving? The drift of the orbit normal due to orbit perturbations was examined. The Keplerian elements and force models used to create a representative ephemeris are presented in Table 1. The effect of orbit normal drift is illustrated in Figure 3. The orbit normal at the epoch points out of the page at the center of the plot. The subsequent orbit normal calculated for each day of the next 6 months is projected onto the initial orbit plane. The circle indicates a 1 degree separation from the original orbit normal. The result determined was that the orbit normal will move about 2.0 degrees over a 6 month period. In light of this result, the combination of orbit normal drift and attitude drift due to the application of external disturbance torques was next examined to determine if it is possible to maintain the 1 degree attitude constraint without performing attitude trim maneuvers between the reorientation maneuvers.

Table 1: POLAR Orbit Elements

Orbit Element	Value
Epoch	3/21/96 11:04:42
Semimajor axis	34483.62918 kilometers
Eccentricity	0.6577685
Inclination	86.248803 degrees
Right ascension of the ascending node	3.55071 degrees
Argument of Perigee	288.89277 degrees
Mean Anomaly	221.01808 degrees
Spacecraft area	4.8 square meters
Spacecraft mass	1112.0 kilograms
Solar radiation pressure	ON
Sun/Moon perturbations	ON
Earth geopotential model	JGM-2 4x4

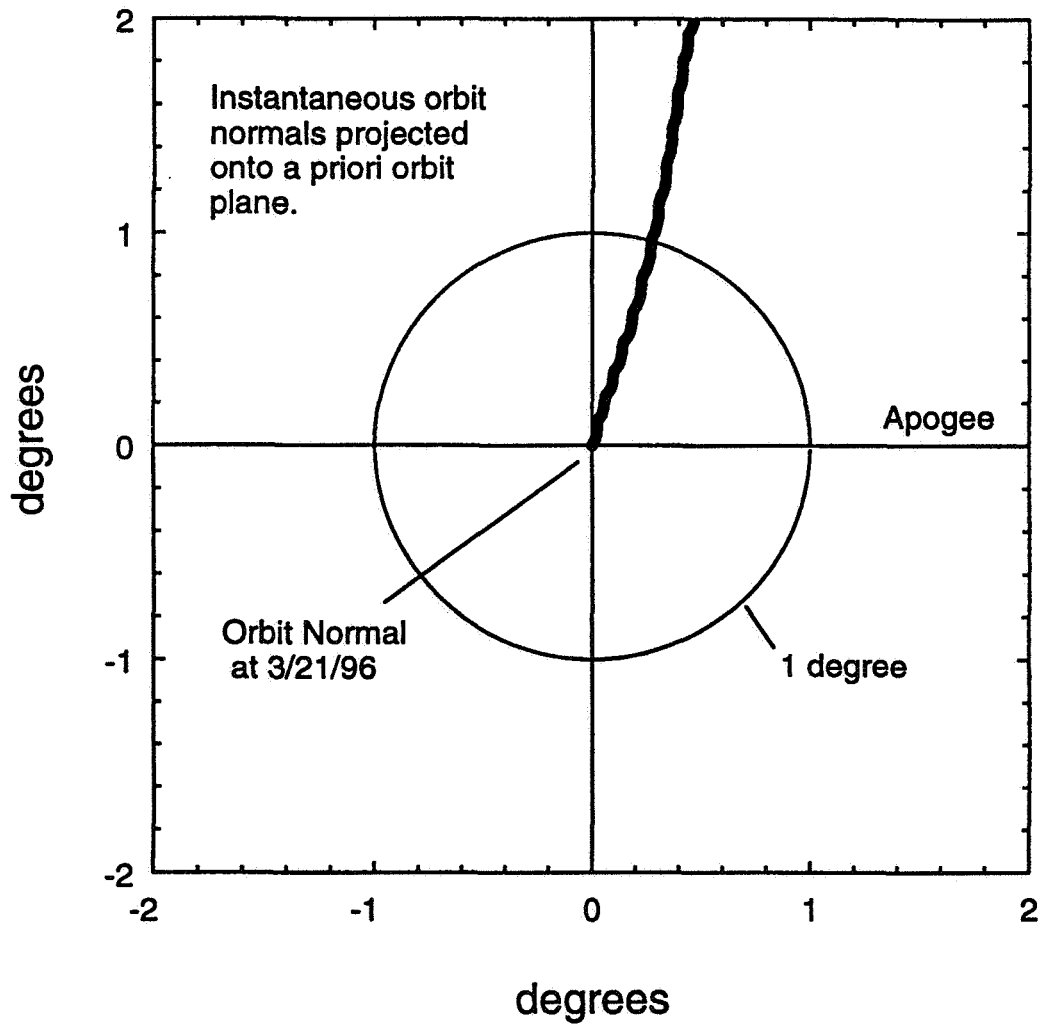
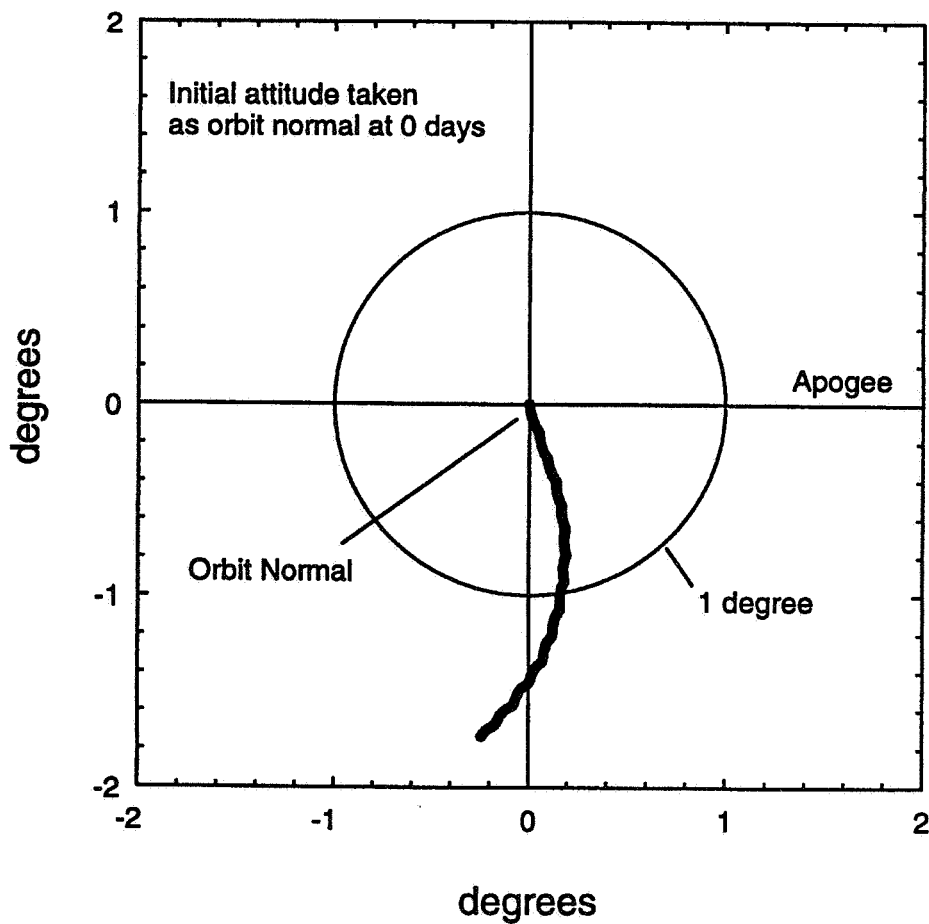


Figure 3: POLAR Orbit Drift from 3/21/96 through 9/21/96

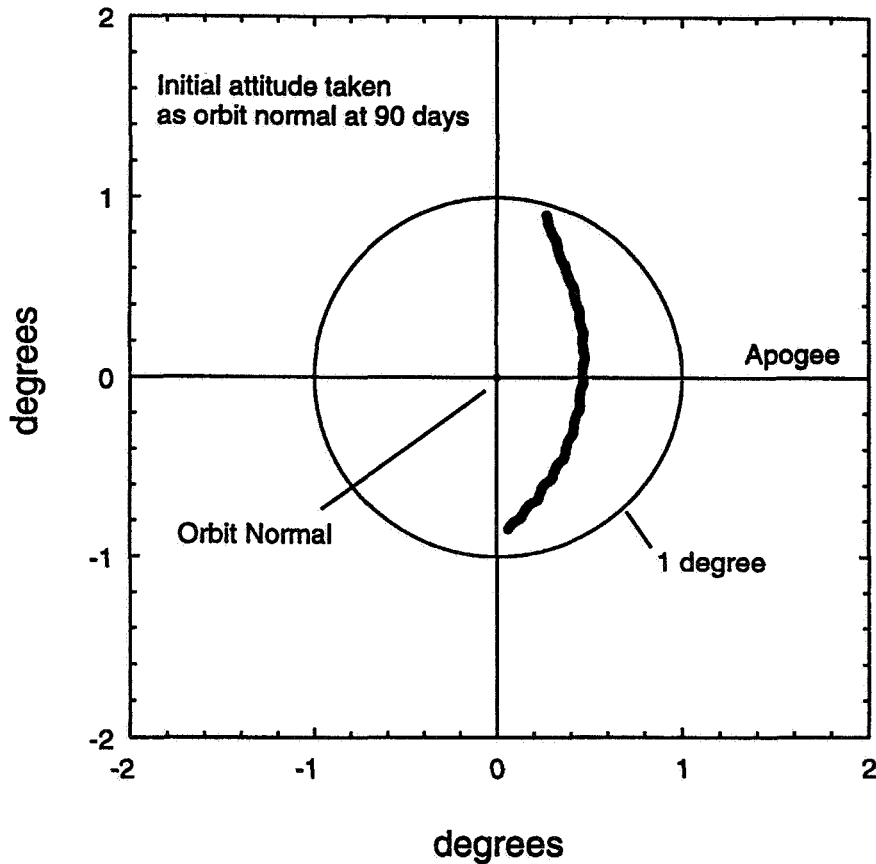
The equation of motion presented previously was integrated numerically, using the parameters presented in Table 2, and with the initial attitude that of the orbit normal vector at time 0, 60, 70, 80, 85, 90, 95, and 100 days since epoch. Figure 4 illustrates the effect of combining the orbit normal drift with the attitude drift due to the disturbance torques. In this case, the initial attitude is aligned with the orbit normal at the beginning of the investigation.

Table 2: Input Parameters for Attitude Propagation

Parameter	Value
Moments of inertia	$I_{xx} = 3290.988 \text{ kg-m}^2$ $I_{yy} = 3805.400 \text{ kg-m}^2$ $I_{zz} = 5974.542 \text{ kg-m}^2$
Spin rate	10 rpm
Spacecraft radius	1.2192 m
Spacecraft height	1.8542 m
Distance from center of mass to center of pressure	-0.3048 m
Coefficient of specular reflection	16.9%
Coefficient of diffuse reflection	8.5%
Spacecraft residual magnetic dipole moment	1.0 ATM ²



**Figure 4: Attitude Drift Projected onto Instantaneous Orbit Plane
Initial Attitude is the Orbit Normal at 0 days from Epoch**



**Figure 5: Attitude Drift Projected onto Instantaneous Orbit Plane
Initial Attitude is the Orbit Normal at 90 days from Epoch**

As illustrated in Figure 5, by selecting the initial attitude to be aligned with the orbit normal vector at 90 days into the investigation, it is possible to maintain the 1 degree pointing requirement. In Figure 4, the requirement was violated about midway through the investigation. Figure 6 presents the maximum separation angles between the instantaneous orbit normal and the attitude vector over the 6 month period for each of the cases examined. The figure indicates that for this particular period, the maximum separation angle between the attitude vector and the orbit normal vector would occur when the initial attitude is selected to align with the orbit normal at about 86 days from epoch.

The relative importance of the individual torques was also examined. In Figure 7, the attitude drift is plotted for the case of the initial attitude chosen to coincide with the orbit normal vector at 90 days. The attitude drift is calculated for the three following cases: no external torques applied, torque due to solar radiation pressure only, and torque due to solar radiation, magnetic moment, and gravity gradient. As expected, solar radiation pressure is the dominant environment disturbance torque, although the effect of the orbit normal drift is the most important aspect to consider when devising a strategy to maintain the attitude pointing constraint.

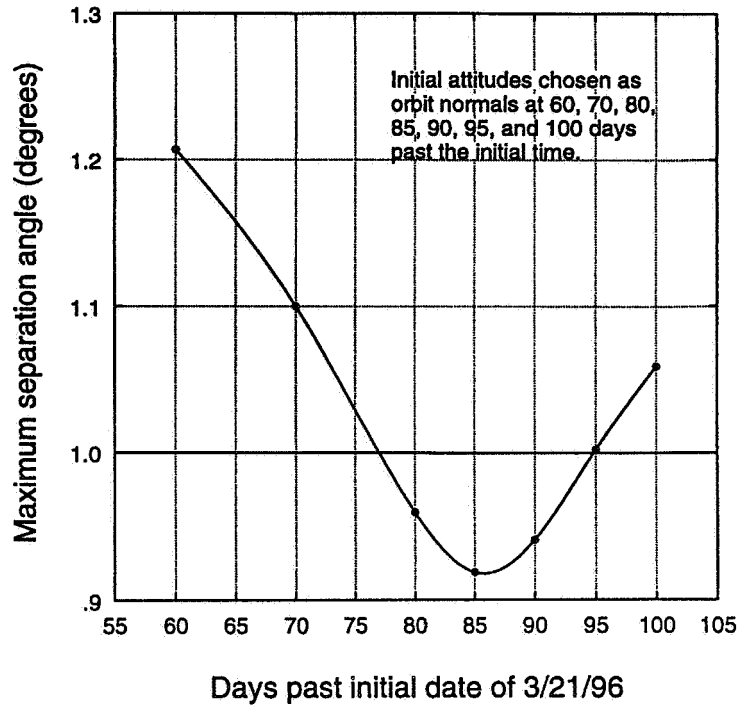


Figure 6: Maximum Separation Angle Between Attitude and Orbit Normal

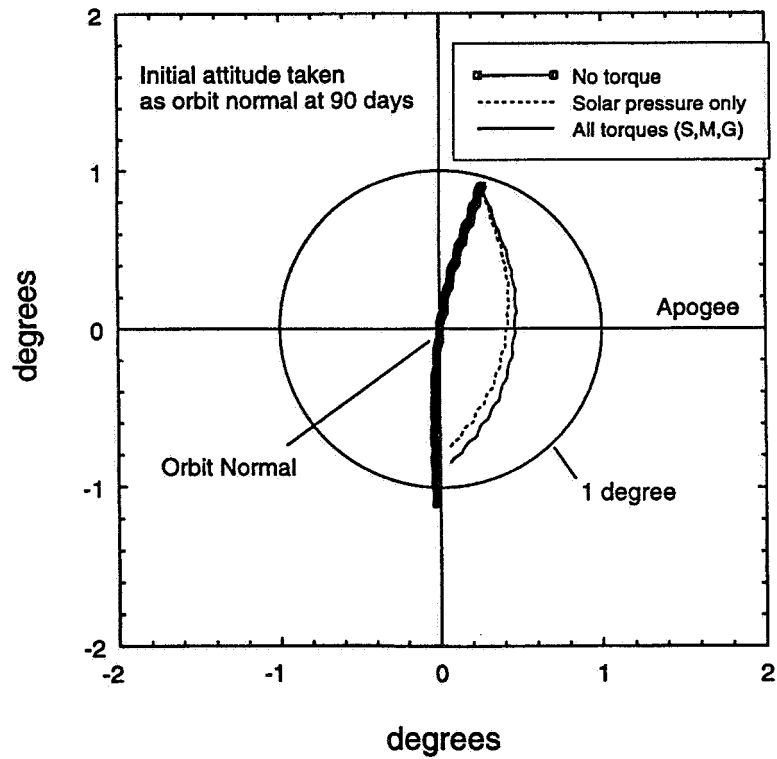


Figure 7: Relative Effect of the Disturbance Torques

CONCLUSIONS

The attitude drift for due to environmental disturbance torques was examined for both the WIND and POLAR spacecraft. It was determined that the drift due to environmental disturbance torques was sufficiently small that the pointing constraints for each mission could be met if attitude drift was the only factor. In the case of WIND, it was discovered that the additional Sun angle constraint makes it impossible to eliminate attitude trim maneuvers between orbit maneuvers. The maximum amount of time that can be expected between attitude trim maneuvers is about 4 months due to the Sun angle variation over time. In the case of POLAR, it was discovered that the drift of the location of the orbit normal itself was the major factor to be considered in determining how to eliminate trim burns between reorientation maneuvers. It was illustrated that the pointing constraint could be achieved, without additional trim burns required, by selecting the initial attitude to be the location of the orbit normal vector near the center of the 6 month period. Further, it was also illustrated that of the three disturbance torques considered, the solar radiation pressure torque dominates the others.

ACKNOWLEDGMENTS

The author wishes to thank the individuals, both civil servants and contractors, who have contributed to the success of the Flight Dynamics Division support for the WIND and POLAR missions. The author especially acknowledges the efforts of Jefferey Dibble, Dave Niklewski, and Neil Ottenstein for their efforts over the past 5 years on the attitude drift analysis for both WIND and POLAR.

REFERENCES

1. Goddard Space Flight Center, Flight Dynamics Division, 554-FDD-91/154, ISTP/GGS WIND and POLAR Missions Attitude Drift Rate Analysis, D. Niklewski (CSC) and N. Ottenstein (CSC), November 1991.
2. Computer Sciences Corporation, CSC 53708 17, "WIND Spin Axis Attitude Drift", (Memorandum), N. Ottenstein, July 14, 1993.
3. Computer Sciences Corporation, CSC 53708 15, "POLAR Attitude Drift Study", (Memorandum), R. Edmonds, July 14, 1993.
4. Computer Sciences Corporation, CSC 55708 09, "POLAR Attitude Drift Study", (Memorandum), D. Niklewski, August 29, 1995.
5. Computer Sciences Corporation, CSC 56708 07, "POLAR Attitude Drift Study", (Memorandum), D. Niklewski, January 19, 1996.
6. Martin Marietta, GGS-ACS-023 "GGS Spin Axis Disturbances and Control," (G.E. Memorandum), D. Swanson, March 1, 1993.
7. Wertz, James R., ed., Spacecraft Attitude Determination and Control, Boston: Kluwer Academic Publishers, 1978.

Solar and Heliospheric Observatory (SOHO) Flight Dynamics Simulations Using MATLAB[®]*

R. D. Headrick and J. N. Rowe
Computer Sciences Corporation (CSC)
Lanham-Seabrook, Maryland, USA 20706

Abstract

This paper describes a study to verify onboard attitude control laws in the coarse Sun-pointing (CSP) mode by simulation and to develop procedures for operational support for the Solar and Heliospheric Observatory (SOHO) mission. SOHO was launched on December 2, 1995, and the predictions of the simulation were verified with the flight data. This study used a commercial off-the-shelf (COTS) product (MATLAB[®]) to do the following:

- Develop procedures for computing the parasitic torques for orbit maneuvers
- Simulate onboard attitude control of roll, pitch, and yaw during orbit maneuvers
- Develop procedures for predicting firing times or both on- and off-modulated thrusters during orbit maneuvers
- Investigate the use of feed-forward or prebias torques to reduce the attitude hangoff during orbit maneuvers—in particular, determine how to use the flight data to improve the feed-forward torque estimates for use on future maneuvers.

The study verified the stability of the attitude control during orbit maneuvers and the proposed use of feed-forward torques to compensate for the attitude hangoff. Comparison of the simulations with flight data showed that

- Parasitic torques provided a good estimate of the on- and off-modulation for attitude control
- Feed-forward torque compensation scheme worked well to reduce attitude hangoff during the orbit maneuvers

The work has been extended to prototype calibration of thrusters from observed firing times and observed reaction wheel speed changes.

This study demonstrated the use of MATLAB[®] simulations to support flight dynamics analysis and development of operational procedures in the Goddard Space Flight Center (GSFC) Flight Dynamics Division (FDD).

1.0 Introduction

During orbit maneuvers, SOHO attitude control system (ACS) in the CSP mode is subject to disturbance torques from several sources: thruster alignment, hot/cold burning of thrusters, payload movement, fuel slosh, and solar array flexing. Analysis of the control laws by Smallwood (Reference 1) indicated an attitude hangoff because of these disturbance torques, which could be compensated in the control loops by uplinking a feed-forward torque to improve the pointing performance. To meet the Flight Dynamics requirement to provide inflight estimation of the disturbance torques, prelaunch analysis (Reference 2) recommended using the average pointing errors (the difference between the commanded and ground-computed attitude angles) during an orbit maneuver to estimate the feed-forward torque for the next maneuver.

This paper reports work in modeling the propulsion and attitude control systems to verify this procedure through simulation and SOHO flight experience in using it. Thruster and center of mass (CM) alignment effects were also predicted and evaluated from a computer-assisted plant identification technique.

* This work was supported by the National Aeronautics and Space Administration (NASA)/Goddard Space Flight Center (GSFC), Greenbelt, Maryland, under Contract NAS 5-31500.

2.0 Simulation

A description of the simulation models in this study and the results are given below.

2.1 Simulation Models

A key feature of the SOHO propulsion system is the coupling of the roll, pitch, and yaw control loops through “parasitic” torques. Parasitic torques, \vec{T}_{po} , are unwanted torques generated during thrusting (e.g., a delta-V in the z direction, applying torque about the x-axis), which also affect the other two axes. They occur because the thrusters are not mounted along orthogonal axes. These torques cause attitude-pointing errors to grow in the control loop until they exceed a deadband limit and a thruster fires to compensate.

The simulation was implemented using MATLAB[®], a commercial software tool designed for matrix manipulation and control law simulation. The simulation was designed with the following features and limitations:

- The thruster model of $\vec{R} \times \vec{F}$ torques is based on the manufacturer's values of location, direction, nominal CM, and average beginning of life (BOL) thrust magnitude. Provision is made for easily modifying the CM to study the sensitivity to changes that are expected with fuel usage. In addition, the user can modify the direction and efficiency of the thrusters to adjust the model. Orbit thrusters (see Figure 1 on the next page) are fired in couples about the primary axis. The thruster configuration is shown in Table 1.

Table 1. Definition of Cases for Orbit Thrust Simulations

Case No.*	Delta-V Direction	Thruster Pair	Torque Axis
1	-X	1 / 2	Y (pitch)
2	+X	3 / 4	Z (yaw)
3	-Z	5 / 6	X (roll)
4	+Z	7 / 8	X (roll)

* The case number refers to British Aerospace (BAe) simulation cases (Reference 3).

- Pulse-width modulation (PWM) is simulated with the onboard computer (OBC) values for minimum on time and saturation (References 2–5). The on-modulation axis control model is shown in Figure 2 (from Reference 3). The control loop converts torque demand to thruster on time and induces a reactive thrust torque when the on time is above the minimum or deadband. While delta-V thrusting is active, the primary torque axis is off modulated; that is, the thruster firing is nearly continuous during the burn while maintaining the attitude-pointing errors within deadband limits. Off modulation rebalances the thruster torques based on the attitude reaction by reducing the on time of one of the paired thrusters and increasing the on time of the other. On modulation and off modulation can occur simultaneously on different axes.
- To model steady-state behavior, thrust level is approximated as the average during the 2-second actuation period, ignoring details of thruster ramp up and time delays.
- The spacecraft rigid body dynamics model is given by

$$I\dot{\vec{\omega}} = \vec{N}_{th} - \vec{\omega} \times \vec{L}$$

where I = moment of inertia tensor

$\vec{\omega}$ = body rate vector

N = thruster torque vector

L = total angular momentum vector given by

$$\vec{L} = I\vec{\omega} + \vec{h}_{wh}$$

where \vec{h}_{wh} is the wheel angular momentum vector.

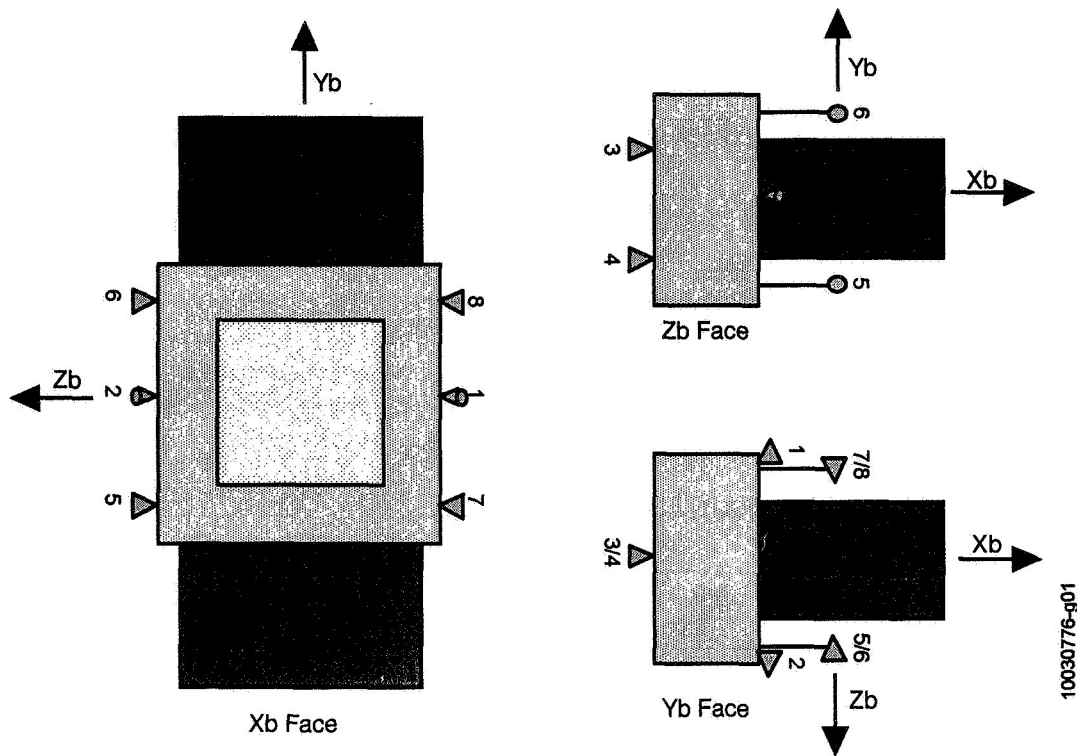


Figure 1. SOHO Spacecraft Thruster Orientations

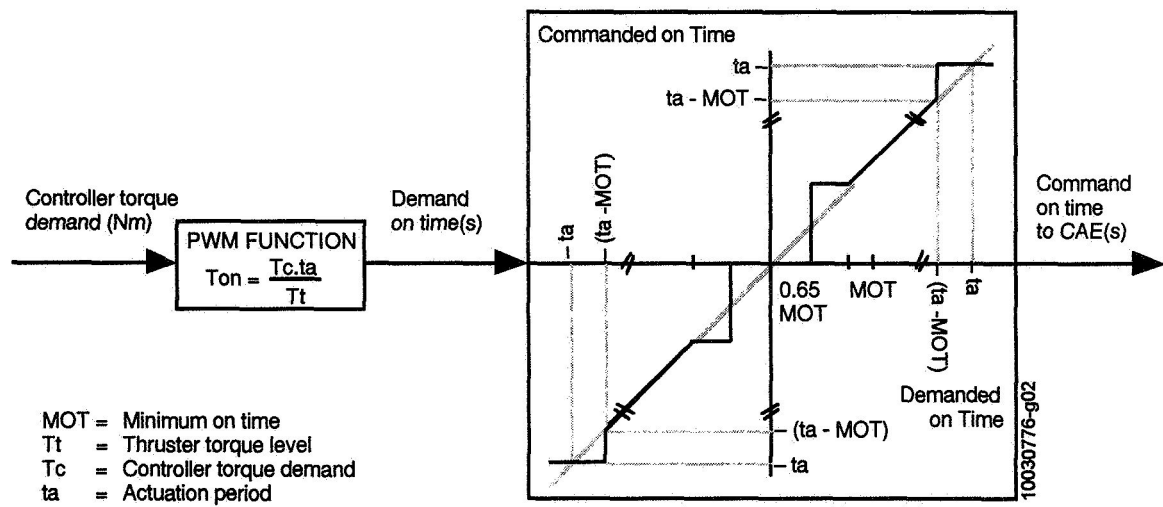


Figure 2. PWM Function of On Modulation

Torque from solar radiation pressure ($\sim 10^{-7}$ Nm) is negligible compared to thrust torques. The simulation ignores contributions from fuel sloshing, solar panel flexure, and antenna motion, because they have transient effects. Plume impingement is not modeled.

Figure 3 is a block diagram of the model. The left half of the diagram shows the control section, with provision for input for delta-V and feed-forward torques. The PWM block indicates deadband and saturation for thrust on each axis. Cross-coupling is shown explicitly, where the cross-terms include the parasitic torques and the $\vec{\omega} \times \vec{L}$ term.

The right-hand side of the block diagram shows the second order model that is symmetric for the three loops. They are represented by the discrete time equations

$$\begin{aligned}\dot{\vec{x}}_{i+1} &= \dot{\vec{x}}_i + \dot{\vec{\omega}}_i dt \\ \vec{x}_{i+1} &= \vec{x}_i + \dot{\vec{x}}_i dt\end{aligned}$$

where the state vector \vec{x} consists of the attitude angles $\vec{x} = (\phi \ \theta \ \psi)^T$, where ϕ = roll, θ = pitch, ψ = yaw, and $\dot{\vec{x}}$ = the rates. The control vector $\dot{\vec{\omega}}$ is updated at the 2-second actuation period and includes the cross-coupling effects. The time equations are integrated over the OBC cycle of 0.05 second.

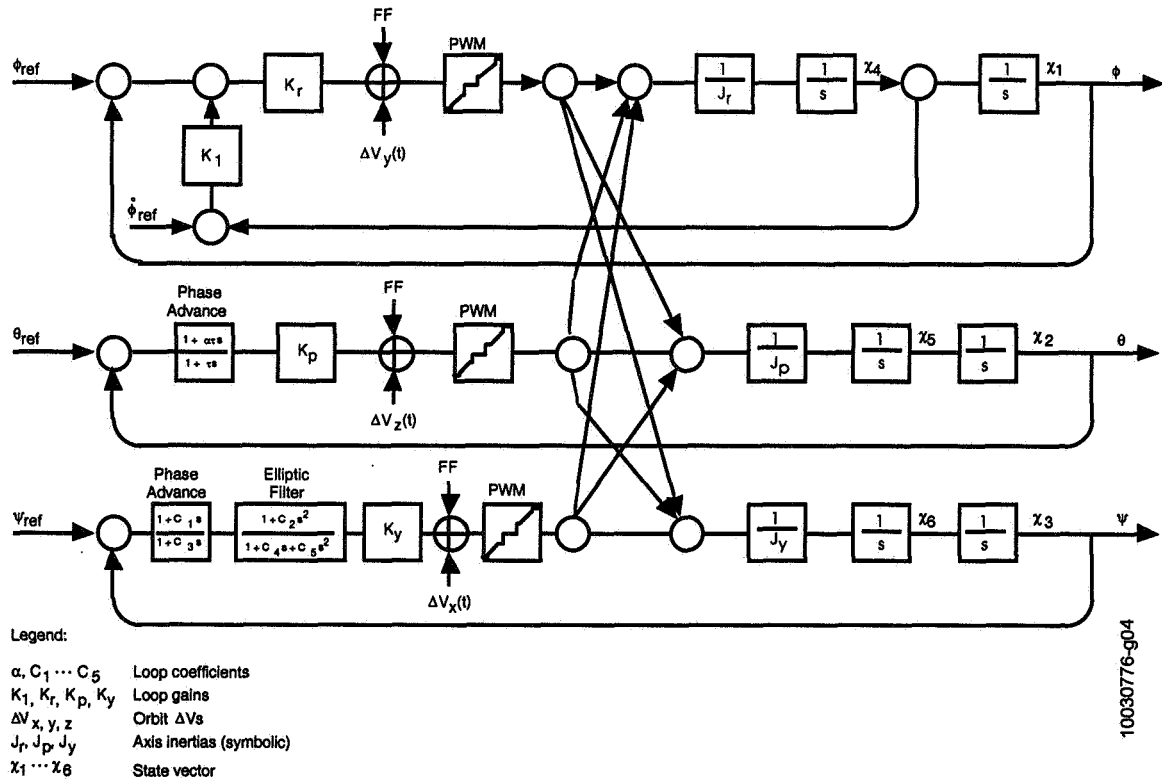


Figure 3. Schematic of Coupled Attitude Control Loops

2.2 Simulation Results

Figures 4 through 6 illustrate the occurrence of pointing errors during delta-V $-X$ thrusting (case 1). The pointing errors arise from two sources: the effects from the parasitic torques and the offsets from a position-only controller. The secondary axes react to parasitic torques with their on-modulated control torques when they exceed the minimum. The simulator reproduced the general patterns of the BAe simulations (Reference 3) cases 1 through 4 for delta-V in $\pm X$ and $\pm Z$ directions. (BAe's performance analysis demonstrated the stability of the SOHO ACS under worst-case conditions, while our purpose was to define ground support procedures for SOHO Flight Dynamics.) Figure 7(a) shows a single-sided deadband pattern in pitch, and Figure 7(b) shows the pitch pointing error reduction after including a feed-forward torque from the measured pointing error.

The initial estimate of the feed-forward torque, \vec{F}_0 , was calculated from

$$\vec{F}_0 = -\mu \vec{T}_{po}$$

where μ is the percent on time for the off-modulated axis (nominally 75 percent), and \vec{T}_{po} is the nominal parasitic torque calculated from

$$\vec{T}_{po} = \vec{N}_+ + \vec{N}_-$$

where \vec{N}_+ and \vec{N}_- are the torque vectors (based on location, direction, CM, thrust, and efficiency) applied in the positive or negative sense about the control axis. For subsequent maneuvers, the attitude hangoff is evaluated and a new value is calculated for the feed-forward torque, \vec{F}_{new} , for uplink on the next maneuver

$$\vec{F}_{new} = \vec{F}_0 - \vec{T}_D$$

where, for each axis,

$$T_{D_i} = K_i \times \Gamma_{meas_i}$$

In these equations, $\vec{\Gamma}$ is the attitude hangoff, \vec{K} is the loop gain, and \vec{F}_0 is the value of feed-forward torque at which $\vec{\Gamma}$ was measured.

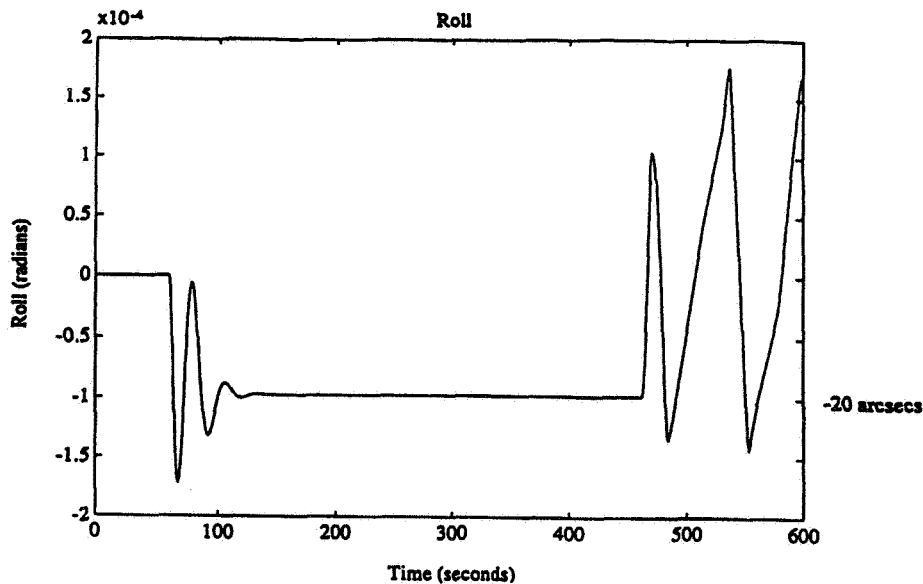


Figure 4. Spacecraft Roll Angle for $-X$ Delta-V (Case 1)

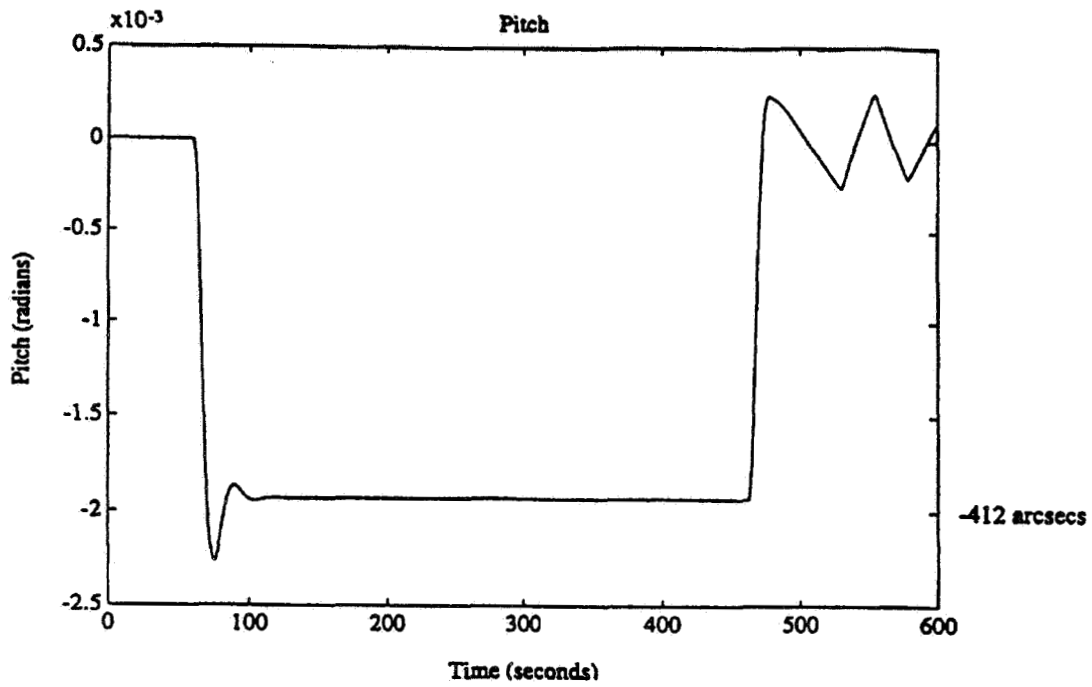


Figure 5. Spacecraft Pitch Angle for -X Delta-V (Case 1)

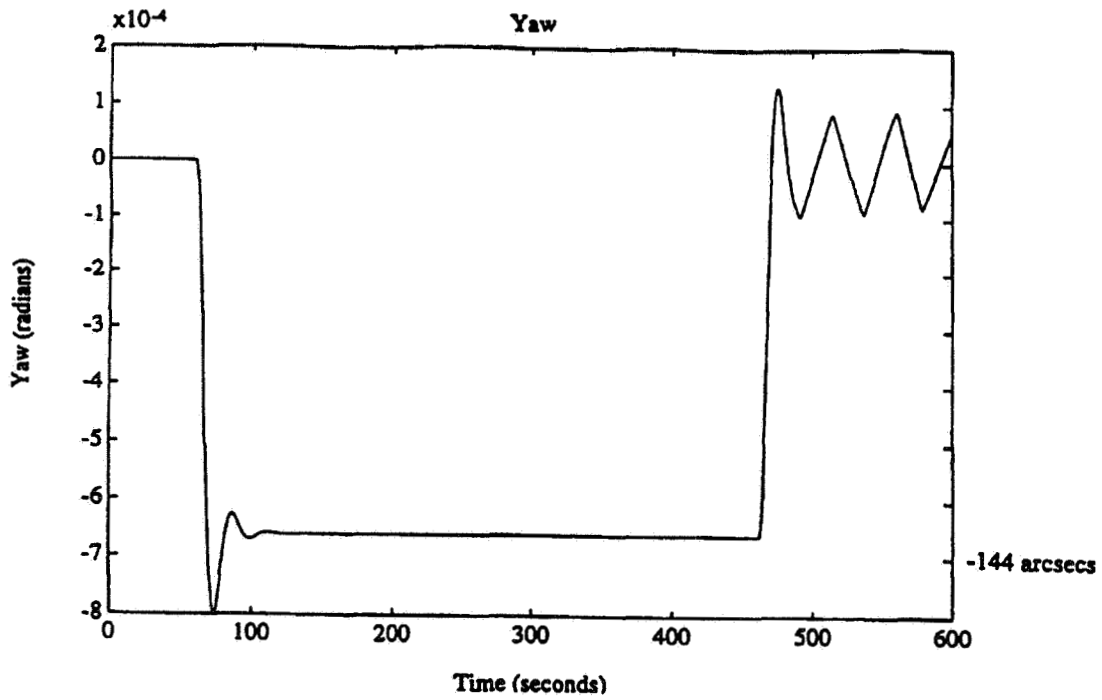
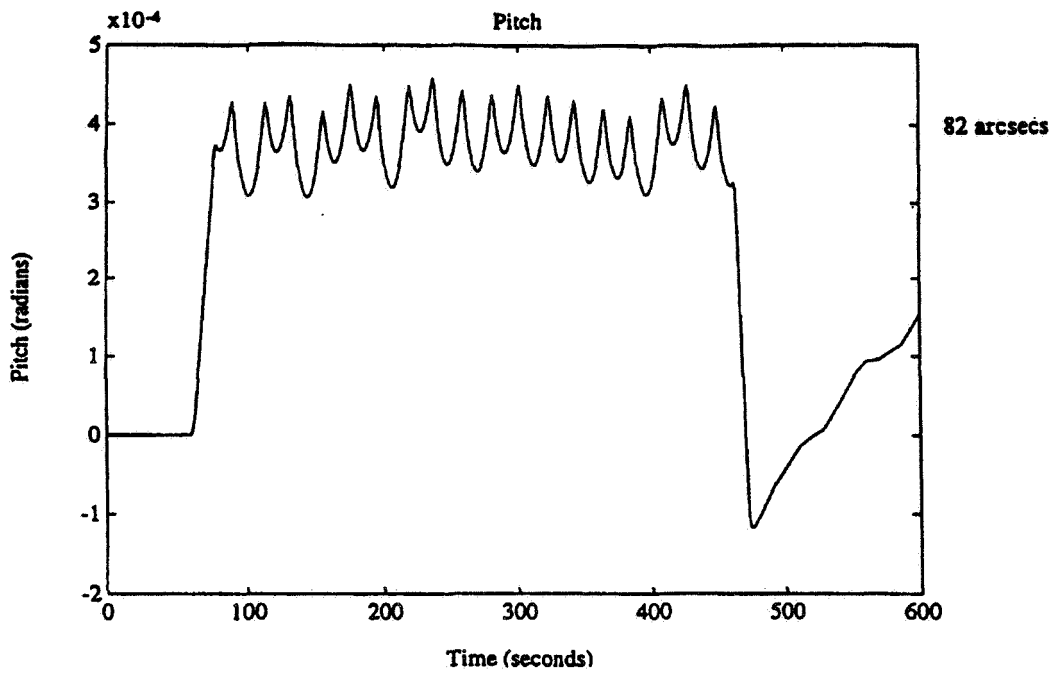
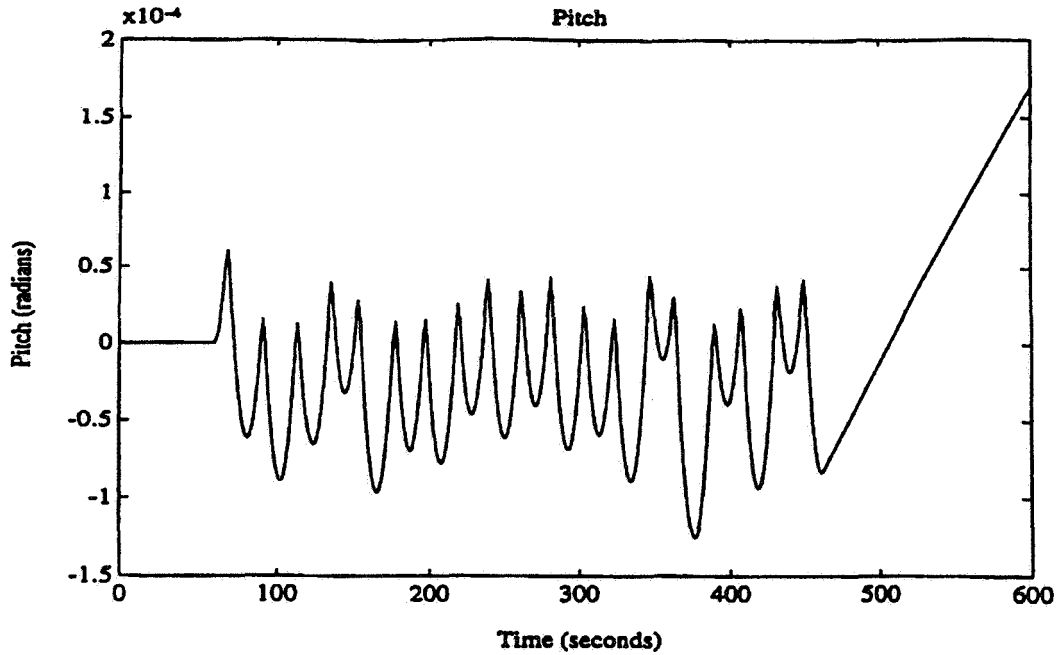


Figure 6. Spacecraft Yaw Angle for -X Delta-V (Case 1)



(a) Initial Feed-Forward



(b) Feed-Forward

Figure 7. Spacecraft Pitch Angle for +X Delta-V (Case 2)

3.0 Flight Experience

SOHO flight experience involving feed-forward torques and thruster alignment are described in the following sections.

3.1 Feed-Forward Torques

This section discusses the results of the first three orbit maneuvers on SOHO in terms of attitude hangoff and the use of feed-forward torques to compensate.

Table 2 shows a summary of the values observed on SOHO for the roll axis. The hangoffs in pitch and yaw were ≤ 0.03 deg, and no attempt was made to compensate for those. The “thrusters” column in this table indicates which thrusters were used to provide the delta-V.

Table 2. Summary of Roll Axis Feed-Forward Torques

Maneuver	Segment	Thrusters	F_0 (Nm)	Attitude Error Γ (deg)	F_{new} (Nm)
MCC1	X-1	1A, 2A	0	+0.07	-0.096 (a)
	X-2	1A, 2A	0	— (b)	—
MCC2	Z-1	7A, 8A	-0.096	-0.08	+0.10
	Z-2	7A, 8A	+0.10	+0.03	+0.042 (c)
	X-1	1A, 2A	+0.10	+0.13	-0.15
HOI	X-1	1A, 2A	-0.15	+0.04	

Notes: (a) Calculated based on a hangoff of 0.05 to be conservative
 (b) Not obtained because of telemetry gap at start of maneuver
 (c) Not used because the next maneuver was in the X-direction

These results are based on visual analysis of plots of the roll attitude. As the difference between the commanded and achieved attitudes, hangoff is visible as a jump in angle at the start of a maneuver. The hangoff at the end of the maneuver was more difficult to estimate because of control system settling (and its deadband). Figures 8 and 9 show as examples the transitions at the start and end of the midcourse correction (MCC)2 X-1 maneuver. This may be compared with Figure 10, which shows the start of the halo orbit insertion (HOI) X-1 burn where the hangoff is significantly smaller. The ramp in Figure 10 before the maneuver start is caused by a small residual inertial reference unit (IRU) bias.

Comparing the MCC2 Z-1 and Z-2 burns and the MCC2 X-1 with HOI X-1 shows that the technique of uplinking feed-forward torques does reduce the attitude errors, although because they are already small, it is not necessary for successful execution of the maneuvers.

3.2 Thruster Alignment

Prelaunch and postlaunch thruster analysis and the thruster results are discussed in the following subsections.

3.2.1 Prelaunch Thruster Analysis

The predicted burn times of the secondary thrusters are a byproduct of the ACS simulations. As a result, this study was extended to support prelaunch thruster analysis. In CSP mode, the momentum wheels are free running and the attitude angles are controlled to their commanded values (usually zero). Thus, any torque applied by the primary thruster pair (off modulated) must be compensated by firings of secondary (on-modulated) thrusters. This analysis showed that the secondary burn times can be predicted with good accuracy from the thrust torque vectors alone. This is an important result, because it removes reliance on the accuracy of any simulation. While these firings are a small fraction of the main thrusts, their effects were predictable in advance and were included in delta-V targeting for the highly successful major orbit maneuvers.

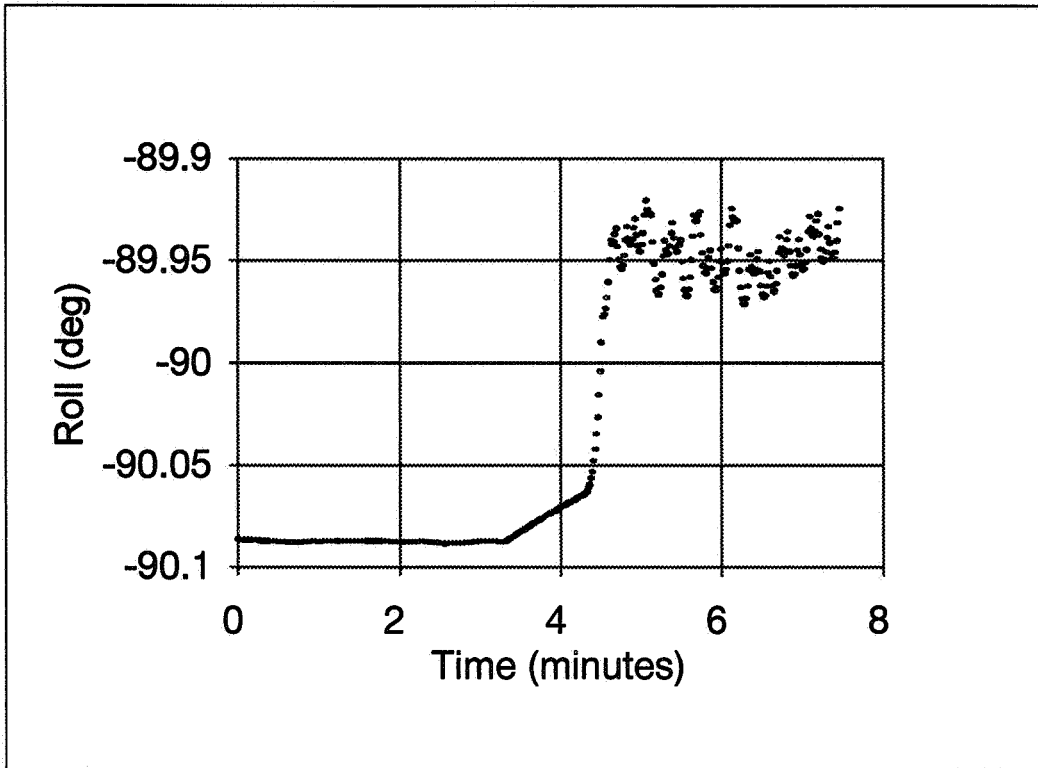


Figure 8. Roll Angle at Start of MCC2

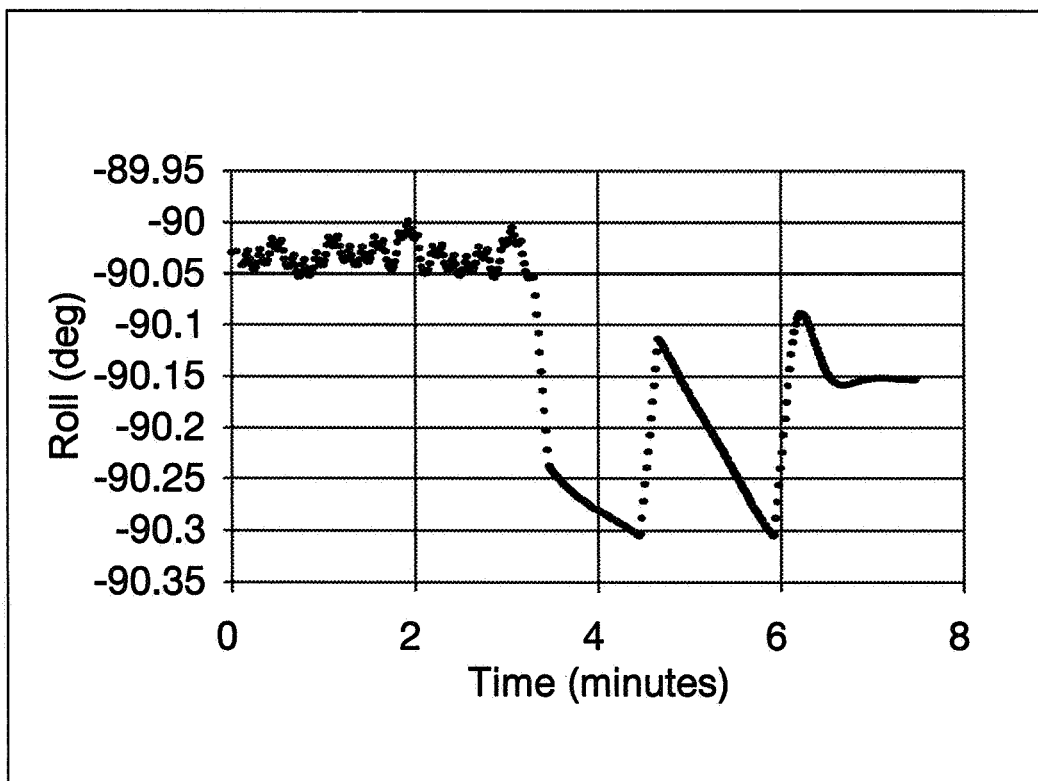


Figure 9. Roll Angle at End of MCC2

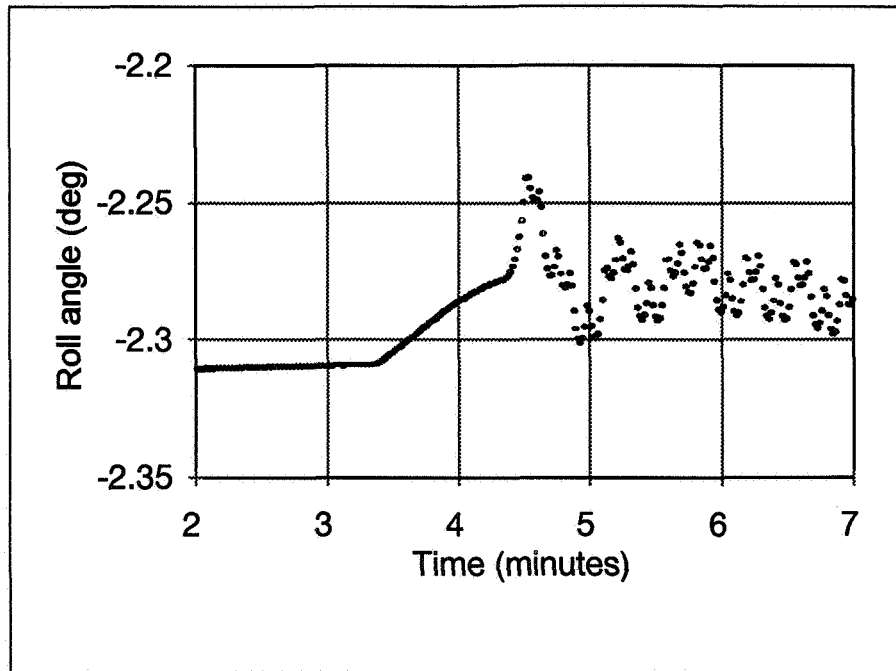


Figure 10. Roll Angle at Start of HOI

The thruster model was evaluated from $\vec{T} = \vec{R} \times \vec{F}$ with CM at the beginning of transfer (BOT) value with solar panels deployed, yielding the following nominal torque matrix, Tmat, for thrusters 1A–8A (in Nm):

	1A	2A	3A	4A	5A	6A	7A	8A
Tx	0.0471	0.0848	0.0119	-0.0067	3.2634	-3.1015	-3.1512	3.1126
Ty	5.7332	-5.7727	0.3441	-0.2174	0.2971	0.3044	-0.3083	-0.2874
Tz	0.0616	-0.1494	-2.8434	2.8063	-0.0091	0.0001	0.0055	0.0119

For example, the -X orbit delta-V (case 1) uses thruster pair 1/2, with the Y (pitch) axis off modulated, yielding a nominal parasitic torque, T_{po} , computed from summing the torque vectors for the firing pair

$$\vec{T}_{po} = (0.1319 \quad -0.0395 \quad -0.0878)^T$$

The T_{po} components on the roll and yaw axes are compensated to conserve angular momentum. When the X (roll) axis control loop accumulates a pointing error in excess of the deadband, it induces a reactive torque from its on-modulated thruster pair (6/7 for +/- senses). Because $T_{po}(1)$ is positive, it must be compensated by the negative roll torque of magnitude 3.1015, leading to an expected value of 0.1319/3.1015 (or 4.2%) of the planned 900-second orbit delta-V burn, or 38-second split evenly between #6 and #7. Similarly, on the Z (yaw) axis, thruster pair 4/3 has an expected value of 0.0878/2.8063 (or 3.1%) of the main burn or 27.9 second with only thruster #4 activated. These values were verified by simulation. Because the on times grow linearly with the length of the orbit burn, they can be scaled for different burn times.

These predicted secondary firings were compared with telemetry during MCC1, and the results are shown in Table 3. When the burn times agreed to within a fraction of a percent, it confirmed that the maneuvers were proceeding nominally.

The initial thruster alignment was so accurate that no recalibration was needed; however, we had prepared a technique to assist in thruster realignment if necessary. While the nominal T_{po} is a predictor of off-axis firings, the observed firing times from telemetry can be used to infer actual thrust torque values and alignment. A sensitivity study was performed in advance to prepare for possible nonnominal conditions and to establish a baseline for their resolution, using prelaunch values for the nominal thruster model. Nominal and perturbed thruster parameters, efficiency, and CM were used to create the sensitivity matrix. These results were available to aid in matching observed thruster firing times. Because the problem is underdetermined, the most sensitive parameters were considered first.

Table 3. Predicted and Observed Thruster Firing Times From X-1 Maneuver

Thruster Number	Predicted On Time	Observed On Time
1A	900 sec (nominal)	903.9111
2A	900 sec	896.0319
3A	0	0.0
4A	28	27.2743
5A	0	0.0
6A	19	20.5540
7A	19	20.5540
8A	0	0.0

3.2.2 Postmaneuver Thruster Analysis

After several maneuvers, the secondary firings began to be predicted less well, and we adjusted the SOHO thruster model using the principle of conservation of angular momentum. As discussed above, in CSP mode the momentum wheels are free running and the attitude axes are controlled to zero; thus, each maneuver segment must conserve total angular momentum. The burn times of the primary and secondary thrusters were evaluated for MCC1 and MCC2 maneuver segments based on the change in angular momentum, $d\vec{L}$ ($= \vec{T} * dt$), calculated from the thrust torque model and the actual burn times. Any residual dL above the noise level indicates inaccuracy in the thruster model.

The technique of plant identification was used to improve the salient parameters in the model and minimize the error vector dL , and the validity of the resultant model was tested by application to the next maneuver (HOI). In control theory, plant identification is the term applied to the systematic process of estimating the parameters that control the dynamics of the system under study, in our case the SOHO ACS under thrusting. The process diagram is presented in Figure 11. Although it could be completely automated when necessary, in the present case it was implemented as a computer-assisted procedure with the analyst in the loop. The process was facilitated by use of models already available for the thruster torque, sensitivity partials, and a CM model as a linear function of fuel use between the BOT and BOL phases.

The procedure for computing the nominal angular momentum change for each maneuver segment is as follows:

- Compute the maneuver dL error vector using nominal values for the thruster/CM model, with the root-sum-squared (RSS) dL error vector as a figure of merit.
- Balance the efficiency of the primary thrusters to minimize their error along the primary axis.
- Adjust other torque model parameters in the order of their sensitivity to minimize the sum of all maneuver error vectors.

Torque is modeled from $\vec{T} = \vec{R} \times \vec{F}$ with current values of CM and efficiency, and the change in angular momentum $d\vec{L}$ ($= \vec{T} * dt$) is calculated from

$$d\vec{L} = T_{mat} * \vec{t}_{on_i}$$

where T_{mat} is the 3x8 matrix of torques for the eight thrusters, adjusted for CM motion, and \vec{t}_{on_i} is the 8x1 vector of thruster on times for the i^{th} maneuver. The RSS is given by

$$RSS_i = \sqrt{(dL_1)^2 + (dL_2)^2 + (dL_3)^2}$$

and the overall figure of merit to be minimized is given by

$$RSS_{tot} = \sum_i RSS_i$$

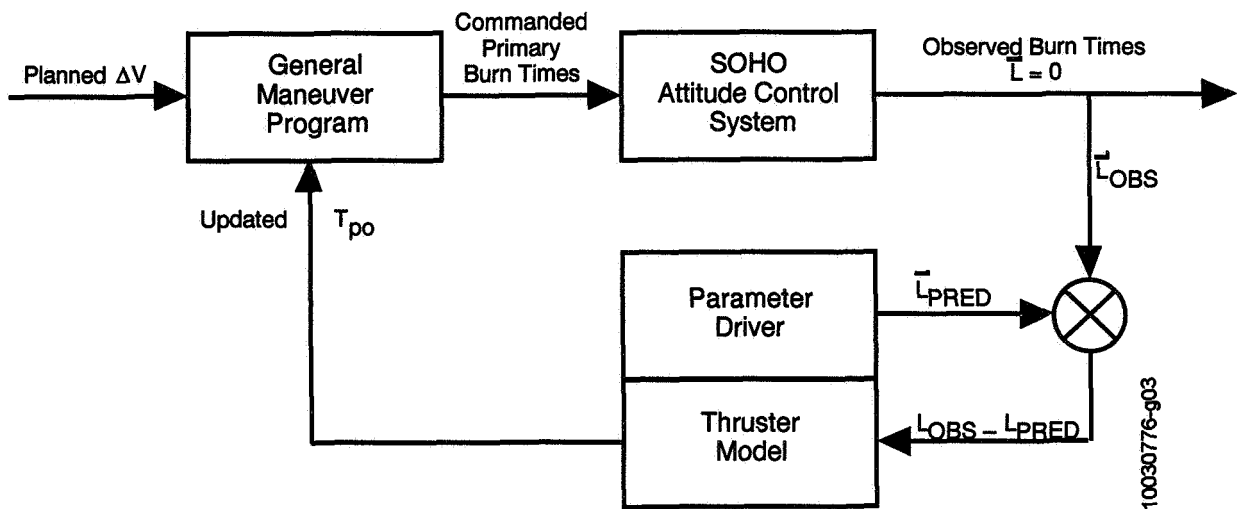


Figure 11. Schematic Diagram of Plant Identification

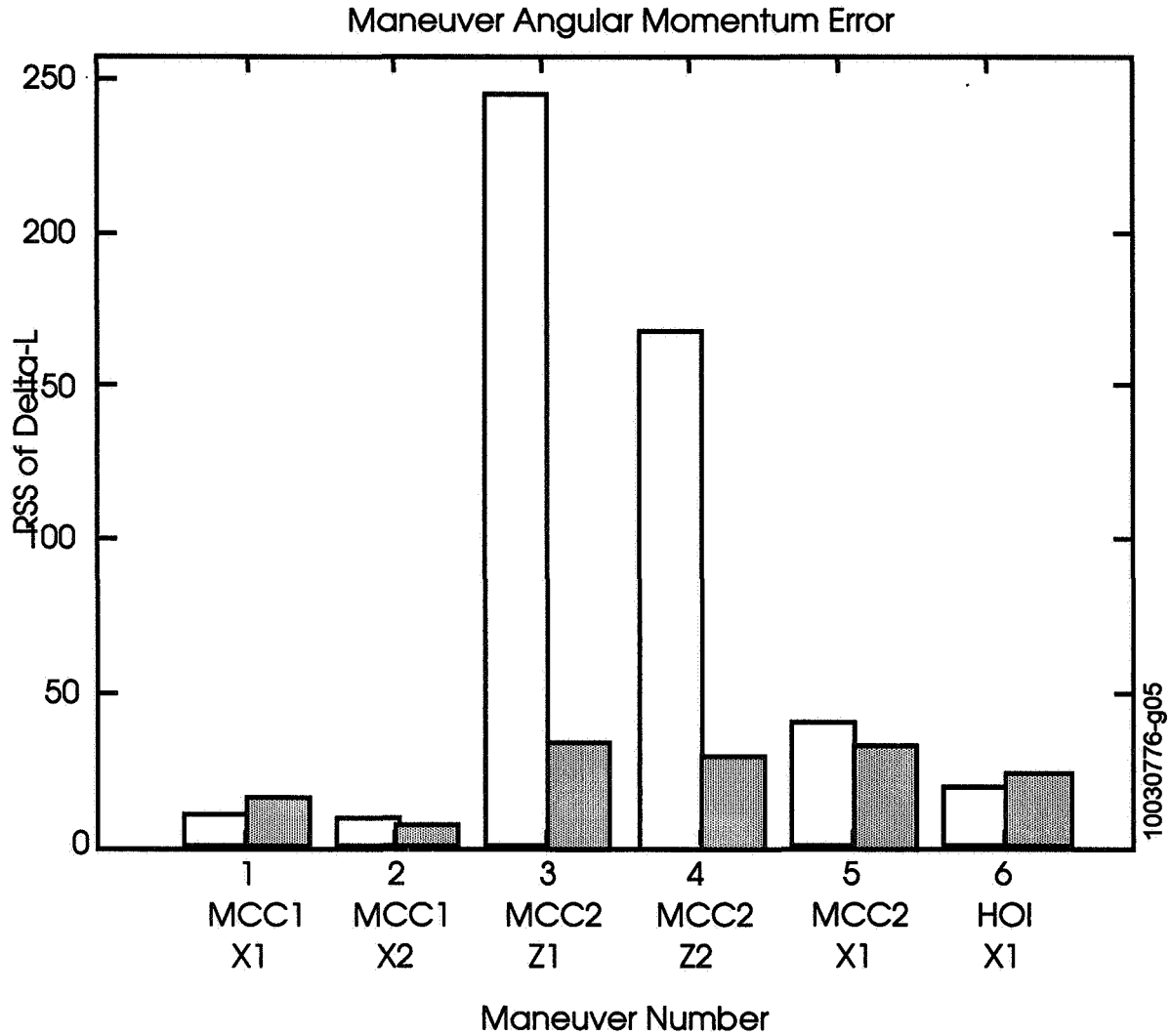
3.2.3 Thruster Results

The results of thruster model tuning for MCC1 and MCC2 are shown in Figure 12. The initial model (unshaded) fit the -X delta-V maneuvers well, but the Z delta-V maneuvers fit poorly; sensitivity analysis showed that these were strongly affected by the exact model of CM, both the initial value (bias) and the motion (slope) with fuel usage.

The results of the plant identification are as follows:

- Efficiency correction to thruster 8: $dEff(8) = -0.0148$
- Variation in the initial CM: $dcm = (0.0047, 0.0, 0.001)$
- Variation in slope of CM function: $dcm0 = 0.99$

The shaded bars show a reduction in maneuver errors of about a factor of 5 with the new values in the thruster model.



KEY: Unshaded = Nominal Thruster Model Shaded = Adjusted Thruster Model

Figure 12. Maneuver Angular Momentum Error

4.0 Conclusions

The conclusions from this study are as follows:

- The use of feed-forward torques is effective in reducing attitude hangoff in flight.
- Simulation is a valuable tool for understanding the operation of onboard attitude control systems and preparing operational procedures.
- Attitude effects can provide valuable diagnostic information on the thrusters in addition to that available from telemetry and postmaneuver orbit determination.
- COTS tools such as MATLAB® provide means for rapid implementation of computer-assisted analysis.

Acknowledgments

The authors would like to thank Paula Jordan (CSC) for sharing data on orbit maneuver planning, Tom Becher (CSC) for several helpful discussions, and John Behuncik (GSFC Flight Dynamics) for support and encouragement. We would also like to thank the following European members of the SOHO team for profitable discussions related to the spacecraft operation: Guido Coupe, Michel Janvier, Maryse Hervieux, Philippe Temporelli, and Ton Von Overbeek.

References

1. British Aerospace Ltd., SH-BAe-RP-1321, Issue 3, Performance Review Document, Volume V: *Coarse Sun Pointing Mode*, J. Smallwood, September 1993
2. Goddard Space Flight Center, Flight Dynamics Division, 533-FDD-93/088R0UD0, *Disturbance Torque Estimates for the SOHO Mission*, T. Becher (CSC) and J. Rowe (CSC), prepared by Computer Sciences Corporation, September 1993
3. British Aerospace Ltd., SH-BAe-RP-1317, Issue 2, Performance Review Document, Volume I: *Mathematical Models*, P. Singh, July 1993
4. ---, SH-BAe-RP-1324, Issue 2, Performance Review Document, Volume VIII: *Additional Analyses*, D. F. Lebrun, J. Smallwood, T. D. Wood, February 1994
5. ---, SH-BAe-RS-632, Issue 8, *SOHO ACS Software User Requirements*, T. J. Biglin, March 1994

Attitude Accuracy Study for the Earth Observing System (EOS) AM-1 Spacecraft*

James D. Lesikar II
COMPUTER SCIENCES
CORPORATION
Lanham-Seabrook, Maryland, USA 20706

Joseph C. Garrick
NATIONAL AERONAUTICS AND
SPACE ADMINISTRATION
GODDARD SPACE FLIGHT CENTER
Greenbelt, Maryland, USA 20771

ABSTRACT

Earth Observing System (EOS) spacecraft will make measurements of the earth's clouds, oceans, atmosphere, land and radiation balance. These EOS spacecraft are part of the National Aeronautics and Space Administration (NASA) Mission to Planet Earth, and consists of several series of satellites, with each series specializing in a particular class of observations. This paper focuses on the EOS AM-1 spacecraft, which is the first of three satellites constituting the EOS AM series (morning equatorial crossing) and the initial spacecraft of the EOS program. EOS AM-1 has a stringent onboard attitude knowledge requirement, of 36/41/44 arc seconds (3σ) in yaw/roll/pitch, respectively.

During normal mission operations, attitude is determined onboard using an extended Kalman sequential filter via measurements from two charge-coupled device (CCD) star trackers, one Fine Sun Sensor, and an Inertial Rate Unit. The Attitude Determination Error Analysis System (ADEAS) was used to model the spacecraft and mission profile, and in a worst-case scenario with only one star tracker in operation, the attitude uncertainty was 9.7/11.5/12.2 arc seconds (3σ) in yaw/roll/pitch. The quoted result assumed the spacecraft was in nominal attitude, using only the 1-rotation per orbit (rpo) motion of the spacecraft about the pitch axis for calibration of the gyro biases. Deviations from the nominal attitude would show greater attitude uncertainties, unless

calibration maneuvers which roll and/or yaw the spacecraft have been performed; this permits computation of the gyro misalignments, and the attitude knowledge requirement would remain satisfied.

INTRODUCTION

Purpose and Methodology

Attitude error analysis studies are needed to determine whether the EOS-AM1 satellite can meet its attitude accuracy requirements using its onboard computer and sensor complement.

The present study determines:

1. The accuracy to which attitude sensor and gyro calibrations can be performed.
2. The expected attitude determination error for various sensor combinations.

The Attitude Determination Error Analysis System (ADEAS) is an analysis software tool that provides a general-purpose linear error analysis capability for various spacecraft attitude geometries, sensor complements, and determination processes. An appropriate NAMELIST setup permits ADEAS to model the salient features of the EOS AM-1 spacecraft and mission profile.

* This work was supported by the National Aeronautics and Space Administration (NASA)/Goddard Space Flight Center (GSFC), Greenbelt, Maryland, under Contract NAS 5-31500.

Background

EOS-AM1 is the first of three satellites constituting the EOS-AM (morning equatorial crossing) series in support of NASA's "Mission to Planet Earth" and is the initial spacecraft of the EOS program.

EOS-AM1 will be launched from the Western Test Range, Vandenberg Air Force Base, California, with the General Dynamics Atlas IIAS launch vehicle in June 1998. EOS-AM1 has a planned mission lifetime of 5 years.

The initial parking orbit has an altitude of 525 by 705 km with an inclination of 98.2 deg. After a series of orbit-raising maneuvers, the mission orbit will be described as follows:

- Sun-synchronous polar
- Inclination = 98.2 deg
- 10:30 a.m. \pm 15 min descending node, local mean solar time
- 705 km altitude, circular
- Groundtrack repeats in 233 orbits/16 days, with \pm 20 km cross-track error at node crossings

Spacecraft Attitude Control System

The EOS-AM1 spacecraft is being manufactured by Lockheed-Martin, Valley Forge, Pennsylvania. The spacecraft will have the following complement of attitude sensor and actuator hardware:

- CCD star tracker (CCDST) (2)
- Earth scanner assembly (ESA) (2)
- Fine sun sensor (FSS) (1)
- Three axis magnetometer (TAM) (2)
- Coarse Sun sensor (CSS) (9 pairs)
- Inertial rate unit (IRU) (6 axes)
- Reaction wheels (4)
- Magnetic torquer rods (3)

Immediately after launch, the onboard computer, via the attitude thrusters, uses ESA data to roll and pitch the spacecraft to acquire the Earth and to orient the spacecraft body Z axis to nadir-pointing, then performs orbital gyrocompassing to align the body X axis roughly parallel to the velocity vector. When in normal mission mode, attitude is determined via sequential filter using the two CCDSTs (the FSS can substitute for one CCDST if one fails) and the IRU and is controlled by the reaction wheels.

The onboard computer uses an extended Kalman sequential filter to determine attitude during normal mission mode operations. The state vector is composed of an attitude quaternion and the IRU rate biases. Star observations are taken from alternate star trackers, and a particular star is used as a valid observation only if (1) it is in the onboard star catalog, and (2) it is visible in two consecutive observations by the same star tracker (16.384 sec later). The attitude propagation cycle time is 0.512 sec, based on using filtered gyro rates (the measured gyro data are available every 0.128 sec).

Attitude Requirements

The spacecraft attitude is described by a 3-1-2 (yaw-roll-pitch) Euler rotation sequence, which relates the body coordinate system (BCS) to the orbital coordinate system (OCS). The spacecraft null attitude has the BCS coincide with the OCS. The OCS is a rotating coordinate system. The OCS coordinate axes originate in the spacecraft's center of mass. The +Z axis points to the geocenter, the +Y axis points to the negative orbit normal, and the +X axis completes the orthogonal triad. The null attitude, in which the three Euler angles are zero, has the OCS and BCS coincide. Null attitude is the desired attitude during normal mission mode.

The attitude knowledge requirements (the accuracy of the attitude determination) during normal mission mode are specified to be:

- 41 arc seconds in roll (3σ)
- 36 arc sec in yaw (3σ)
- 44 arc sec in pitch (3σ)

Sources of Attitude Error

When EOS-AM1 is in normal mission mode, the following quantities influence the sequential filter attitude error:

- IRU (a.k.a. gyros)
 - Rate bias errors (deg/sec)
 - Scale factor errors (dimensionless)
 - Alignment errors (deg)
 - Gyro noise such as
 - a) Inverse gyro bias noise time (1/sec)
 - b) Attitude error vector noise (deg/sec^{1/2})
 - c) Gyro bias noise (deg/sec^{3/2})

- CCDSTs
 - Alignment errors (deg)
 - Measurement noise (deg)
 - Field of view errors
- FSS
 - Alignment errors (deg)
 - Measurement noise (deg)
 - Field of view errors
- Kalman filter tuning parameters. Same units as:
 - Attitude error vector noise (deg/sec^{1/2})
 - Gyro bias noise (deg/sec^{3/2})

THE ADEAS MODEL

What ADEAS Can Do

ADEAS is capable of modeling, on option, either the batch weighted least-squares filter or the sequential filter with Kalman gain. The latter mode is chosen for the analyses presented here. The various gyro noise parameters, CCDST and FSS measurement noises, and Kalman filter tuning parameters are user-input and are held constant for each run of ADEAS. The attitude determination uncertainty is always solved for; an initial (a priori) attitude uncertainty is specified at the beginning of the run and is usually chosen to be large to permit the filter to properly converge by avoiding numerical instabilities.

The IRU rate bias, scale factor and alignment errors, CCDST alignment and field-of-view (FOV) errors, and FSS alignment and FOV errors, can either be held at constant value (i.e., not solved for) or solved for, given a set of a priori starting values. Quantities referred to as "consider" parameters are held at constant value; the term "perfect" is sometimes used in this paper to denote a consider parameter with a value of zero (no error). Conversely, "solve-for" parameters evolve with time (as more measurements are made) and use the a priori values as initial estimates for the parameters.

This report is primarily concerned with evaluating the influence of IRU biases and scale factors and IRU, CCDST and FSS misalignments on the attitude uncertainty. The CCDST and FSS FOV errors are "perfect." (FOV errors are errors resulting from component alignments within the sensor, optical distortions, and manufacturing aberrations.)

Orbit Model Used

For purposes of internal propagation, the model orbit has the following Keplerian orbital elements, which satisfy a 10:30 a.m. mean local time descending node (Reference 1):

Epoch	980630.040000
Semimajor axis	7083.14 km
Eccentricity	0.0001
Inclination	98.2 deg
Right ascension of ascending node	255.356 deg
Argument of perigee	90.0 deg
Mean anomaly	270.0 deg

All orbit perturbative forces that can be modeled by ADEAS are enabled. These forces include the Earth oblateness J2 effect, solar and lunar point mass perturbations, and atmospheric drag with a spacecraft ballistic coefficient of 2.2.

Star Catalog Used

A prototype spectral response curve (color index) for the Ball CT-601 solid state star tracker was obtained from the Submillimeter Wave Astronomy Satellite (SWAS) project. This curve is necessary to convert star catalog visual (V) magnitudes into instrumental (I) magnitudes.

The prototype SWAS spectral response curve is

$$V - I_{\text{SWAS}} = 0.0043S^3 - 0.0015S^2 + 0.0214S - 0.1733$$

where S is the spectral index. For the Sun, a spectral class G2 star, S is equal to 4.2.

The source catalog for creating the prototype EOS run catalog is the SKYMAP Master Catalog version 3.7, a sequential file that contains approximately 248,000 stars. The SKYMAP library routine CAT then uses the prototype SWAS spectral response curve to convert V-magnitudes into I-magnitudes. It then assembles an EOS specific intermediate run catalog in a direct-access format containing stars brighter than I-magnitude 9. Intermediate catalogs are created taking into account the following criteria for each star:

- Limited to I magnitudes ranging from 2 to 6
- Excludes stars with V-magnitude uncertainties greater than 0.1

- Excludes variable stars with V-magnitude amplitudes greater than 0.1
- Excludes multiple star systems with the two brightest components having V-magnitude differences less than 5.0
- Excludes stars with proper motions greater than 0.7 arc sec per year
- Excludes stars with position uncertainties greater than 3.0 arc sec
- Uses near neighbor checks such that no star is within 0.25 degree and is within 3 I-magnitudes of the candidate star

The final sequential catalog contains 2197 stars in an ASCII-readable format. Another catalog was then produced in direct-access MMS star record format by using the SKYMAP Library routine CAT with the ASCII catalog as input. This direct access catalog is the file that is actually used by ADEAS for EOS-AM1 attitude error analysis studies. Further details on the creation of this catalog, and its comparison to the EOS star catalog created in 1990 by General Electric, can be found in Reference 2.

Alignment Angles

Reference 3 is the primary source of sensor parameters presented here. Reference 4 only slightly modifies the FSS performance requirements into a form that is identical to those for the Upper Atmosphere Research Satellite (UARS) (Reference 5).

All sensor boresights point in the +Z direction for each respective sensor coordinate system. Euler rotations in the 3-1-3 sequence transform from the BCS coordinates into each sensor coordinate system. Table 1 shows the rotation angles and Table 2 shows boresight unit vectors expressed in BCS coordinates.

Table 1. Sensor Euler Rotation Angles

Sensor	1st Rotation Z _B axis	2nd Rotation X _{B'} axis	3rd Rotation Z _{B''} axis
CCDST 1	-44.0	-112.5	0.0
CCDST 2	44.0	-112.5	0.0
FSS	134.299	-149.3	0.0

Table 2. Sensor Boresight Vectors (BCS)

Sensor	X	Y	Z
CCDST 1	0.6418	0.6646	-0.3827
CCDST 2	-0.6418	0.6646	-0.3827
FSS	-0.3651	-0.3563	-0.8601

Charge-Coupled Device Star Trackers

The two Ball CT-601 CCDSTs are mounted symmetrically about the BCS Y-Z plane, such that a star that appears in the FOV of CCDST1 will, in the normal mode of the attitude control system, appear in the FOV of CCDST2 after about one-third of an orbit.

Each of the CCDSTs has an 8-deg by 8-deg FOV, is sensitive to stars with I-magnitudes from +2.0 to +5.7, and can track five stars simultaneously. The major constraint to tracking to specification for these CCDSTs is that all stars within a 0.25 deg radius of a catalog star need to be at least 3 magnitudes dimmer. The CCDSTs are unreliable for the Sun within 45 deg of the CCDST boresight, or for the Moon within 17 deg of the boresight.

Current understanding of the CCDST has it raster scan from "top" to "bottom" until the first five guide stars are encountered. This approach differs from the two ADEAS CCD options: (1) choosing the five brightest stars in the FOV and (2) performing a spiral scan about the boresight until five stars are encountered. Since 4-pi steradians equals 41252.9 deg., the sky is covered by 645 CCD FOVs, for an average of 3.4 stars if the prototype EOS catalog with 2197 stars is used; so on average the chosen ADEAS option is unimportant, and option 1 is used arbitrarily. Table 3 has the required CCDST performance.

Table 3. CCDST Performance Values

	Magnitude +2.0 to +4.0	Magnitude +4.0 to +5.7
Position Accuracy 3σ, w.r.t. mounting	10 arc sec	16 arc sec
Magnitude Accuracy 3σ	0.25	0.5
Noise Equivalent Angle (NEA) 1σ	3.0 arc sec	5.0 arc sec

Here it is assumed that the position accuracy and NEA are on a per axis basis. The star catalog position uncertainty (Reference 6, per axis, 3σ) is taken to be 3 arc sec.

One ADEAS input is the standard deviation of measurement noise, which is computed for dim and bright stars, depending on whether a star is less than or

greater than I-magnitude 4 in brightness. The standard deviation of measurement noise is calculated by taking the star tracker position accuracy, noise equivalent angle, and star catalog position accuracy in quadrature.

Standard deviation of measurement noise (bright stars, 3σ)

$$= [10^2 + (3 \times 3)^2 + 3^2]^{1/2} = 13.78 \text{ arc sec} \\ = 6.683 \times 10^{-5} \text{ rad}$$

Standard deviation of measurement noise (dim stars, 3σ)

$$= [16^2 + (3 \times 5)^2 + 3^2]^{1/2} = 22.14 \text{ arc sec} \\ = 1.073 \times 10^{-4} \text{ rad}$$

The 3σ alignment uncertainty, per axis, is 0.05 deg.

Fine Sun Sensor

The Adcole FSS (Model 42050 sensor and Model 42070 electronics) is composed of two orthogonally mounted single-axis Sun sensors. Each single-axis Sun sensor consists of two reticles: a fine reticle and a coarse reticle. The coarse reticle pattern is gray-coded and encodes the coarse angle over the entire FOV. The fine reticle patterns and the resultant photocell currents are used to generate fine-angle data. The overall FOV is 64 deg square. The output resolution is 14 arc sec per least significant bit. The overall accuracy for a 32-deg half-cone is 60 arc sec, and the accuracy between the half-cone of 32 deg and the FOV of ± 32 deg is 120 arc sec.

As the above description also applies to the UARS FSS, we may extract the standard deviation of measurement noise from Reference 5, which gives the value 75 arc sec or 0.02083 deg for 3σ uncertainty. The 3σ alignment uncertainty, per axis, is 0.05 deg.

Inertial Rate Unit

The Kearfott IRU is composed of three independent channels, each channel having one two-axis gyro and associated electronics. Under command, the IRU is sensitive to either of two rate ranges:

- Low Rate: ± 0.11 deg/sec maximum rate, with a scale factor of 0.05 arc sec/pulse for incremental output
- High Rate: ± 2.0 deg/sec maximum rate, with a scale factor of 0.8 arc sec/pulse for incremental output

The analog rate output range is ± 2.0 deg/sec.

ADEAS does not model low or high IRU rates, or the analog output, since ADEAS uses engineering units internally, rather than counts or pulses.

The following 3σ uncertainties are allocated per axis:

- Noise (white)	0.0001 deg/sec ^{1/2}
- Noise (drift)	0.00138 deg/hr ^{3/2} = 6.3889 $\times 10^{-9}$ deg/ sec ^{3/2}
- Alignment	0.1 deg
- Bias	2.0 deg/hr = 5.5555 $\times 10^{-4}$ deg/sec

From Reference 5, the 3σ uncertainty in the standard deviation of the scale factor, per axis, is 1.4×10^{-5} (UARS value). The inverse gyro bias noise time constant is assumed to be 0.0, an appropriate value for white noise.

Kalman Filter Parameters

The Kalman filter parameters were chosen to have the same values as the attitude error vector noise (white noise) and gyro bias noise (drift noise) tabulated for the IRU above. No attempt was made in this analysis to tune these parameters for optimum convergence.

ESTIMATED SENSOR UNCERTAINTIES

Methodology

Numerous runs of duration 6000 sec (slightly longer than one orbital period) were performed, with CCDST and FSS sensor data simulated at 10-sec intervals. Various combinations of solve-for and consider sensor parameters were used, with a priori and consider values taken from the prelaunch errors of Table 4 below. CCDST1 was assumed to be "perfect" and was therefore the reference coordinate system for the calibrations. The initial attitude uncertainty was set to 999.0 deg to ensure that the starting attitude knowledge was unknown.

Throughout this section and the next, two systems of units are used, the ADEAS inputs/outputs (in degrees and degrees per second) and units more suitable for interpretation and comparison with mission requirements (arc seconds and arc seconds per hour).

Table 4. Prelaunch Uncertainties (3 σ)

Sensor	Quantity	Value	Equivalent Value
Inertial Reference Unit (IRU)	Rate Biases	5.555E-4 deg/sec	7200 arc sec/hr
	Scale Factor	1.4E-5	n/a
	Misalignment	0.1 deg	360 arc sec
CCD Star Trackers (CCDST)	Misalignment	0.05 deg	180 arc sec
Fine Sun Sensor (FSS)	Misalignment	0.05 deg	180 arc sec

Calibration results for CCDST2 and the FSS did not improve (results were much larger than the prelaunch values, by up to a factor of 3), and the attitude uncertainties would not shrink below about 0.3 deg, unless IRU rate biases were solved-for simultaneously. This empirical observation makes sense. During periods when no sensor data are available, the attitude is propagated using the IRU bias, the fixed bias uncertainty, and noise. When the CCDST2 and FSS do have data, their observation vectors conflict with that expected from the dynamically modeled attitude, and the CCDST2/FSS alignment errors grow to compensate. The necessity to continually solve for IRU biases was independent of the size of the bias uncertainties when specified as consider parameters, as the computed CCDST2/FSS alignment errors remained large, as did the attitude uncertainties.

Attempting to solve for all parameters at once took an inordinate amount of time, and the IRU scale factor uncertainties did not change at all. Thus, calibration runs solved for IRU rate bias errors and IRU, CCDST2, and FSS alignment errors.

Calibration runs were performed for 14 different attitude maneuver scenarios. Table 5 below lists the details of three schemes. Maneuver 1 is the nadir-pointing 1 rpo case, which is the nominal attitude profile. Maneuver 2 is a ± 5 deg roll offset from nominal, not unlike what UARS used for its on-orbit calibration. Maneuver 3 is a ± 20 deg roll offset version of Maneuver 2. The table indicates the attitude angles and rates at the beginning and end of the run, along with times at which new attitude rates are commanded and the attitude offsets at those times.

Table 5. Attitude Maneuver Profiles

Maneuver # and Description	Time t into run (sec)	Roll (deg)	Roll rate (deg/sec)
Maneuver 1 (1 rpo)	0	0.0	0.0
	6000	0.0	0.0
Maneuver 2 (± 5 deg roll)	0	0.0	0.0
	1800	0.0	8.33E-3
	2400	5.0	-8.33E-3
	3600	-5.0	8.33E-3
	4200	0.0	0.0
Maneuver 3 (± 20 deg roll)	0	0.0	0.0
	1800	0.0	3.33E-2
	2400	20.0	-3.33E-2
	3600	-20.0	3.33E-2
	4200	0.0	0.0
6000	0.0	0.0	

CCDST and FSS Alignment Uncertainties

The computed results for CCDST2 uncertainties were independent of the maneuver scheme used, as one would expect. FSS uncertainties did vary between maneuver schemes, but this variation can be attributed to differing periods of Sun visibility (23 minutes for Maneuvers 1 and 2 and 20 minutes for Maneuver 3), so differing amounts of data were available for calibration. For example, the FSS uncertainties from Maneuver 3 were 20 percent larger than for Case 1 of Table 6.

The results presented in Table 6 were all derived from Maneuver 1, a nominal pointing scenario. Case 2 is identical to Case 1, except that it is a 12,000-sec run. Case 3 used the results of Case 1 as a priori uncertainties, which illustrates that repeated sensor alignment calibrations will result in smaller alignment uncertainties. Thus, longer spans of data, and accurate estimates of alignments after a calibration run, will result in subsequent calibration runs having smaller uncertainties. In principle, with sufficiently long runs, these misalignment errors can be made arbitrarily small. However, the overall sensor uncertainty will not necessarily behave similarly, since the sensor measurement noises become the dominant effect. The prelaunch alignment uncertainties are shown in Table 6 for comparison.

The X, Y, and Z components of CCDST2 and FSS alignment uncertainties need to be interpreted carefully, as they represent uncertainties in rotation angles about the nominally aligned sensor coordinate system for each sensor, with Z being the boresight vector.

Table 6. Alignment Uncertainties (arc sec, 3σ)

Case and Description	CCDST2 (arc sec, 3σ)			FSS (arc sec, 3σ)		
	X	Y	Z	X	Y	Z
Prelaunch	180	180	180	180	180	180
Case 1: 1 orbit	10.4	4.0	11.5	6.1	12.6	14.8
Case 2: 2 orbits	7.2	2.8	7.9	4.3	9.0	10.4
Case 3: use case 1 as a priori	5.4	2.1	7.9	4.3	7.2	10.4

IRU Alignment and Rate Bias Uncertainties

Table 7 is a comparison of the prelaunch IRU rate bias uncertainties and the IRU misalignment uncertainties with the uncertainties computed for the three attitude maneuver calibration schemes of Table 5.

Table 7. IRU Rate Bias and Alignment Uncertainties

Maneuver Scheme and Description	IRU Rate Bias Uncertainty (arc sec/hr, 3σ)			IRU Alignment Uncertainty (arc sec, 3σ)		
	X	Y	Z	X	Y	Z
Prelaunch	7200	7200	7200	360	360	360
No. 1 (1 rpo)	1296	21	1296	353	360	353
No. 2 ±5 deg roll	233	21	518	137	54	61
No. 3 ±20 deg roll	58	21	143	36	15	15

From Table 7 we can draw the following conclusions:

1. The IRU misalignment errors cannot be improved unless maneuvers that deviate from nominal attitude (scheme No. 1) are performed.
 2. Larger calibration maneuvers result in smaller IRU alignment uncertainties.
 3. Larger calibration maneuvers result in smaller IRU X- and Z-axis rate bias uncertainties.
- . The IRU Y-axis rate bias uncertainty is unaffected by the magnitude of the calibration maneuver.

The latter conclusion is explained by maneuvers decreasing the magnitude of the Y-axis angular rate, whereas an increase in the rate would be required to reduce the rate bias uncertainty.

ESTIMATED ATTITUDE UNCERTAINTIES

Results Using Prelaunch Alignment Uncertainties

Attitude was solved-for using various combinations of prelaunch consider values and "perfect" values for the attitude sensors and IRU parameters. This was done to gain some appreciation of which consider parameters had the most impact upon the computed attitude uncertainty. Table 8 indicates that prelaunch consider values for the IRU biases are the greatest single contributor, followed by the CCDSTs and FSS, the IRU misalignments, and, finally, the IRU scale factors, which had an 8 arc sec level of uncertainty.

Table 8. Attitude Errors With Prelaunch Uncertainties (IRU Bias not Solved For)

Solve-for Parameters	Prelaunch Consider Values	"Perfect" (Consider=0)	Attitude Uncertainty (arc sec, 3σ)
Attitude only	IRU RBs IRU SFs IRU M/As CCD1 M/As CCD2 M/As FSS M/As		673
	IRU RBs IRU SFs IRU M/As CCD2 M/As FSS M/As	CCD1 M/As	644
	IRU RBs IRU SFs IRU M/As	CCD1 M/As CCD2 M/As FSS M/As	605
	CCD1 M/As CCD2 M/As FSS M/As	IRU RBs IRU SFs IRU M/As	292
	IRU RBs	IRU M/As IRU SFs CCD1 M/As CCD2 M/As FSS M/As	601
	IRU M/As	IRU RBs IRU SFs CCD1 M/As CCD2 M/As FSS M/As	86
	IRU SFs	IRU RBs IRU M/As CCD1 M/As CCD2 M/As FSS M/As	8
LEGEND: RBs: Rate Biases SFs: Scale Factors M/As: Misalignments CCD: CCDST			

Attitude and IRU biases were also solved-for, mimicking the onboard computer and its sequential filter and using prelaunch consider values for all other sensors, with differing combinations of the CCDSTs and FSS functioning. These combinations are shown in Table 9. The first case is for all three sensors "on" as a baseline, even though this is not a flight mode. The other three combinations shown are flight modes, namely CCDST1 and 2, CCDST1 and FSS, and CCDST1 by itself. As one would expect, the last case shows the largest uncertainty.

Table 9. Attitude Errors With Prelaunch Uncertainties (IRU Bias Solved For)

Solve-for Parameters	Prelaunch Consider Values Used	Sensor Combination Used	Attitude Uncertainty (arc sec, 3 σ)
Attitude and IRU RBs	IRU SFs IRU M/As CCD1 M/As CCD2 M/As FSS M/As	CCD1 CCD2 FSS	292
	IRU SFs IRU M/As CCD1 M/As CCD2 M/As	CCD1 CCD2	292
	IRU SFs IRU M/As CCD1 M/As FSS M/As	CCD1 FSS	288
	IRU SFs IRU M/As CCD1 M/As	CCD1	317
LEGEND: RBs: Rate Biases SFs: Scale Factors M/As: Misalignments CCD: CCDST			

The root sum square (RSS) uncertainties shown in Tables 8 and 9 were for the attitude uncertainties at the end of each respective ADEAS run.

Results Using Solved-For Alignment Uncertainties

All of the results in this section were based on a sequential filter, solving for the attitude and IRU rate bias uncertainties, as does the actual EOS-AM1 onboard computer. The computed attitude uncertainties are with respect to the BCS. The attitude uncertainties based on the prelaunch uncertainties utilize the uncertainties for all sensors (CCDST1, CCDST2, FSS, and IRU misalignment errors), whereas the attitude uncertainties computed using the calibration profile based on Maneuver 1, also known as "on-orbit" nominal, assume that the CCDST1 alignment is perfectly known. The prelaunch consider values for the IRU scale factor errors were used in all cases.

The calibration profiles based on Maneuvers 2 and 3 were also applied against Maneuver 1, with no change in results, and are therefore not shown in Tables 10 through 12.

Use is also made of ADEAS' capability to display the error budget for each computed uncertainty. This shows the contribution of each consider parameter, measurement noise, and dynamic noise to the overall error.

Two CCDSTs and One FSS

This is not a flight mode for the onboard computer, but these solutions are provided as a baseline. The attitude uncertainties based on the prelaunch sensor alignment uncertainties are dominated by the CCDST1 and CCDST2 uncertainties (large), whereas the attitude uncertainties based on the 1-rpo calibration are dominated by CCDST2 misalignment uncertainties (small), closely followed by measurement noise. Use of the 1-rpo calibration profile easily satisfies mission requirements for EOS-AM1 in the nominal attitude.

Table 10. Attitude Error for CCDST1 & 2, FSS

Calibration Profile	Maneuver Profile	Attitude Uncertainty (arc sec, 3 σ)		
		X	Y	Z
Mission Requirement	N/A	41.0	44.0	36.0
Prelaunch Values	Maneuver 1 (1 - RPO)	166.0	184.0	155.0
On-Orbit (1-RPO)	Maneuver 1 (1-RPO)	8.3	9.0	5.4

Two CCDSTs

The nominal sensor complement for onboard attitude determination is two CCDSTs. These numbers do not differ at all from those of Table 10, and the error budgets are identical. Thus the conclusions for two CCDSTs are identical to those presented for two CCDSTs and the FSS, except that the FSS would not improve the attitude solution. This is as one would expect intuitively.

One CCDST and One FSS

This is the first contingency mode for the onboard computer, in case one CCDST fails. The attitude uncertainties based on the prelaunch sensor alignment uncertainties are dominated by the CCDST1

uncertainties (large), closely followed by the FSS uncertainties. The attitude uncertainties based on the 1-rpo calibration are dominated by measurement noise. Use of the 1-rpo calibration profile easily satisfies mission requirements for EOS-AM1 in the nominal attitude, and the error is only slightly worse than the cases with two CCDSTs.

Table 11. Attitude Error for CCDST1 & FSS

Calibration Profile	Maneuver Profile	Attitude Uncertainty (arc sec, 3σ)		
		X	Y	Z
Mission Requirement	N/A	41.0	44.0	36.0
Prelaunch Values	Maneuver 1 (1 - RPO)	176.0	155.0	166.0
On-Orbit (1-RPO)	Maneuver 1 (1-RPO)	11.5	12.2	9.7

One CCDST

This is the second and last contingency mode for the onboard computer, in case one CCDST and the FSS both fail. The error budgets for the various cases parallel those listed in the previous section, ignoring all references to the FSS. Again, use of the 1-rpo calibration profile easily satisfies mission requirements for EOS AM-1 in the nominal attitude. Notice that the lack of FSS measurements did not change the level of uncertainty from the CCDST/FSS scenario.

Table 12. Attitude Error for CCDST1 Only

Calibration Profile	Maneuver Profile	Attitude Uncertainty (arc sec, 3σ)		
		X	Y	Z
Mission Requirement	N/A	41.0	44.0	36.0
Prelaunch Values	Maneuver 1 (1 - RPO)	180.0	180.0	180.0
On-Orbit (1-RPO)	Maneuver 1 (1-RPO)	11.5	12.2	9.7

CONCLUSIONS

Relative to one star tracker, the alignment uncertainties of the other star tracker and the fine Sun sensor become smaller asymptotically with the use of longer spans of sensor data. These results are independent of the

attitude maneuver scenario, except for the maneuver's influence upon the length of time that the Sun is visible to the FSS.

Attitude maneuvers that deviate from nominal pointing are necessary for improving the IRU alignment uncertainties. The larger the attitude maneuvers, the smaller the IRU alignment uncertainties, which in turn reduces the IRU rate bias uncertainties. The smaller the IRU rate bias uncertainties, the more accurate will be the propagated attitude solution in the onboard Kalman sequential filter during those times when sensor observations are unavailable. The statements of this and the preceding paragraph, although derived from the particulars of the EOS-AM1 mission, are true independent of the details of a particular satellite.

Since performing a ±20 deg roll maneuver reduces the IRU alignment uncertainties by a factor of 10 or more, and reduces the IRU rate bias uncertainties by a factor of 50 or more (in both cases relative to the prelaunch uncertainties), it is recommended that attitude calibration maneuvers have at least a 20 deg excursion from the nominal 1-rpo attitude profile and, if possible, that they include both roll and yaw maneuvers.

If no calibrations are performed, and the EOS-AM1 sequential filter is used to solve for the attitude and IRU rate biases, then the RSS absolute attitude uncertainty is of the order of 300 arc sec, which is far in excess of the mission requirements. Therefore, some attempt at calibration must be made. A calibration profile solely based upon the nominal 1-rpo motion will suffice for all sensor combinations.

As suggested by data presented in this report, calibration maneuvers should have a minimum of 20 deg in roll and yaw, which would provide robustness to the accuracy of attitude solutions for large deviations from nominal 1-rpo pointing. Previous analyses for other missions have indicated that 30-deg maneuvers about each axis are needed to achieve the best results. As the EOS orbits will have plenty of star observations for attitude determination, the choice of one CCDST as backup to the two-CCDST configuration is adequate. The FSS would not improve the attitude solution unless star observations were unavailable due to Sun/moon interference in the CCDST, during times when the Sun is visible to the FSS.

The results of this analysis show that the onboard attitude determination function will be more than able to meet the uncertainty requirements.

REFERENCES

1. Computer Sciences Corporation, SEAS Quick Note QN-52473-06, "Propagation of Earth Observing System (EOS) Epoch State and Force Model Errors," A. Schanzle (CSC) and J. Rovnak (CSC), August 7, 1992
2. Goddard Space Flight Center, Flight Dynamics Division 553-FDD-94/003R0UD0, Earth Observing System (EOS) Flight Dynamics Analysis Task Prototype Star Catalog, J. Lesikar (CSC) and S. Barriga (CSC), prepared by Computer Sciences Corporation, February 1994
3. General Electric Astro-Space Division, EOS-AM 1 Spacecraft Guidance, Navigation and Control Subsystem Preliminary Design Review, September 23-24, 1992.
4. Martin-Marietta Astro-Space Division, DR SP-601, "Performance Specification, Guidance, Navigation & Control (GN&C) Subsystem for EOS-AM," July 22, 1993
5. Goddard Space Flight Center, Flight Dynamics Division, FDD/554-90/057, Upper Atmosphere Research Satellite (UARS) 1990 Flight Dynamics Analysis Report 7: UARS Ground Definitive Attitude Determination Analysis, J. Golder (CSC) and M. Nicholson (CSC), prepared by Computer Sciences Corporation, January 1991
6. Goddard Space Flight Center, Flight Dynamics Division, 553-FDD-93/013R0UD0, 1993 Star Catalog Analysis Report 1: SKYMAP Master Catalog Data Analysis, M. Slater (CSC), A. Miller (CSC), prepared by Computer Sciences Corporation, February 1993

ATTITUDE AND TRAJECTORY ESTIMATION USING EARTH MAGNETIC FIELD DATA

Julie Deutschmann and Itzhack Bar-Itzhack¹
National Aeronautics and Space Administration
Goddard Space Flight Center
Greenbelt, Maryland 20771

Abstract

The magnetometer has long been a reliable, inexpensive sensor used in spacecraft momentum management and attitude estimation. Recent studies have shown an increased accuracy potential for magnetometer-only attitude estimation systems. Since the earth's magnetic field is a function of time and position, and since time is known quite precisely, the differences between the computed and measured magnetic field components, as measured by the magnetometers throughout the entire spacecraft orbit, are a function of both the spacecraft trajectory and attitude errors. Therefore, these errors can be used to estimate both trajectory and attitude. Traditionally, satellite attitude and trajectory have been estimated with *completely separate systems*, using different measurement data. Recently, trajectory estimation for low earth orbit satellites was successfully demonstrated in ground software using only magnetometer data. This work proposes a *single augmented Extended Kalman Filter* (EKF) to simultaneously and autonomously estimate both spacecraft trajectory and attitude with data from a magnetometer and either dynamically determined rates or gyro-measured body rates.

I. Introduction

The magnetometer, due to its reliability and low cost, has been the focus of many studies in the recent past. Emphasis has been placed on using the magnetometer alone, without any additional input, to estimate the spacecraft trajectory (References 1, 2, and 3) and attitude (References 4 and 5). Studies have also been performed to determine the ultimate accuracy of the magnetometer in estimating attitude when accurate rate information is available (Reference 6).

In using the magnetometer to estimate attitude, the spacecraft position is required to compute the reference magnetic field. In using the magnetometer to estimate position, including the spacecraft attitude improves the results. The data used to estimate either the position or the attitude is a function of the difference between the observed magnetometer measurements and the reference magnetic field. In this work we use this difference to estimate *both* the spacecraft attitude and position. This is an extension of the work performed by Shorshi and Bar-Itzhack (Reference 1) to add the attitude to the trajectory state vector.

Many of the future missions, such as the Small and Mid-size Explorer Series and university class explorers, are looking for low cost and autonomous approaches to navigation and attitude estimation. This work could prove valuable to these missions as a prime navigation system, with coarse accuracy requirements, or a backup to a prime system where more stringent accuracy is required.

In this work we present the method of expanding the Extended Kalman Filter of Reference 1 to include the estimation of the spacecraft attitude, and the results of tests on the combined filter using simulated data. Incorporating the attitude into the filter requires an estimate of the rates. In this work we assume that the

¹ Sophie and William Shamban Professor of Aerospace Engineering, Faculty of Aerospace Engineering, Technion-Israel Institute of Technology, Haifa 32000 Israel, Currently at NASA GSFC as an NRC NASA Research Associate.

rates would be provided by gyroscopes. A method similar to that of Challa (Reference 4) or Azor, Baritzhack, and Harman (Reference 7) could be applied, though, in the absence of gyroscope data.

II. Extended Kalman Filter Algorithm

The EKF algorithm is based on the following assumed models:

$$\text{System Model:} \quad \dot{\underline{X}} = \underline{f}(\underline{X}(t), t) + \underline{w}(t) \quad (1)$$

$$\text{Measurement Model:} \quad z_k = \underline{h}_k(\underline{X}(t_k)) + v_k \quad (2)$$

where $\underline{w}(t)$ is a zero mean white process, v_k is a zero mean white sequence, and $\underline{X}(t)$ is the state vector defined as

$$\underline{X}^T = [a, e, i, \Omega, \omega, \theta, C_d, \underline{q}]$$

The first six elements of $\underline{X}(t)$ are the classical Keplerian elements which determine the spacecraft position and velocity, namely the semi-major axis (a), eccentricity (e), inclination (i), right ascension of the ascending node (Ω), argument of perigee (ω), and true anomaly (θ). C_d is the drag coefficient and \underline{q} represents the attitude quaternion.

Measurement Update Stage:

The linearization of equation (2) results in

$$z_k = H_k \underline{X}_k + v_k \quad \text{where } H_k = [H_o \mid H_a] \quad (3)$$

H_o is the measurement matrix for the orbital states and is derived in Reference 1, and H_a is the measurement matrix for the attitude states. The derivation of H_a is given in Appendix A. The effective measurement used by the filter is given as

$$z_k = \underline{B}_{m,k} - \hat{\underline{B}}(\hat{\underline{X}}_k, t_k) \quad (4)$$

where $\underline{B}_{m,k}$ is the magnetic field vector measured by the magnetometer and $\hat{\underline{B}}(\hat{\underline{X}}_k, t_k)$ is the estimated magnetic field vector as a function of the estimated state $\hat{\underline{X}}_k$ at time t_k . The dependence of $\hat{\underline{B}}(\hat{\underline{X}}_k, t_k)$ on the position and the attitude is seen in the derivation of equation (3) in Appendix A.

The state update equation is

$$\hat{\underline{X}}_k(+) = \hat{\underline{X}}_k(-) + K_k z_k \quad (5)$$

where K_k is the Kalman gain computed according to

$$K_k = P_k(-) H_k^T [H_k P_k(-) H_k^T + R_k]^{-1} \quad (6)$$

R_k is the measurement noise matrix and the covariance matrix is updated as usual with

$$P_k(+) = [I - K_k H_k] P_k(-) [I - K_k H_k]^T + K_k R_k K_k^T \quad (7)$$

Equation (5) is used to update the orbital states, but not the attitude states. The update of the attitude states is done as follows. As shown above, the state vector contains the attitude represented by a quaternion. The

EKF estimates an error in the quaternion, expressed as a vector of three small angles, $\underline{\alpha}$, defined in Appendix A and derived in Reference 8. This error is combined with the current estimate of the quaternion to give an updated estimate of the quaternion, which is then propagated to the next time point.

Propagation Stage:

The *filter* dynamics model is given as

$$\underline{X}'_{k+1} = A_k(\underline{X}'_k) \underline{X}'_k + \begin{bmatrix} w_o \\ w_a \end{bmatrix} \quad \text{where} \quad A_k(\underline{X}'_k) = \begin{bmatrix} A_o & 0 \\ 0 & A_a \end{bmatrix} \quad (8)$$

where $\underline{X}'^T = [a, e, i, \Omega, \omega, \theta, C_d, \underline{\alpha}]$

A_o is the linearized transition matrix for the orbital states and is a function of the *estimated* orbital states, which are elements of \underline{X}' . A_o is defined in Reference 9. A_a is the transition matrix for the attitude error, $\underline{\alpha}$, which are also included in \underline{X}' . A_a is based on the development from Reference 8. The transition matrices A_o and A_a are first order approximations computed from the Jacobian $F_k(\underline{X}'_k)$ derived from the linearization of equation (1).

The covariance matrix is propagated from time t_k to time t_{k+1} using:

$$P_{k+1}(-) = A_k(\hat{\underline{X}}'(+)_{k+1}) P_k(+) A_k(\hat{\underline{X}}'(+)_{k+1})^T + Q_k \quad (10)$$

Q_k is the process noise covariance matrix for both the orbit and attitude states. The orbit states are propagated by solving equation (1) numerically without the noise component, as in Reference 8. The dynamics of the attitude states is linear. Assuming a constant angular velocity between gyro measurements, the attitude states are propagated using

$$\hat{\underline{q}}_{k+1}(-) = \Phi_k \hat{\underline{q}}_k(+) \quad (11)$$

where

$$\Phi_k = I + \Psi_k T + \frac{1}{2!} (\Psi_k T)^2 + \frac{1}{3!} (\Psi_k T)^3 + \frac{1}{4!} (\Psi_k T)^4 + \frac{1}{5!} (\Psi_k T)^5 + \dots \quad (12)$$

and $\Psi_k = 0.5 \begin{bmatrix} 0 & w(3) & -w(2) & w(1) \\ -w(3) & 0 & w(1) & w(2) \\ w(2) & -w(1) & 0 & w(3) \\ -w(1) & -w(2) & -w(3) & 0 \end{bmatrix}$ and $\underline{w} = \underline{w}_k$

T is the time between gyro measurements, \underline{w} is the angular velocity vector, and the arguments 1, 2, 3 refer to the 3 components of \underline{w} . Equations (10) through (12) are particularly suitable when testing with simulated data, because the rates are almost constant, with added noise. When the filter is applied to real data, equation (1) will be solved numerically without the noise component, as in Reference 8.

III. Simulation

A basic simulation was developed to test the EKF outlined above. The scenario consisted of simulating a spacecraft in low-earth-orbit with an earth-pointing attitude, i.e. maintaining a one revolution-per-orbit (RPO) attitude. The spacecraft axes, or body axes, are aligned with the orbital axes as defined in Figure 1.

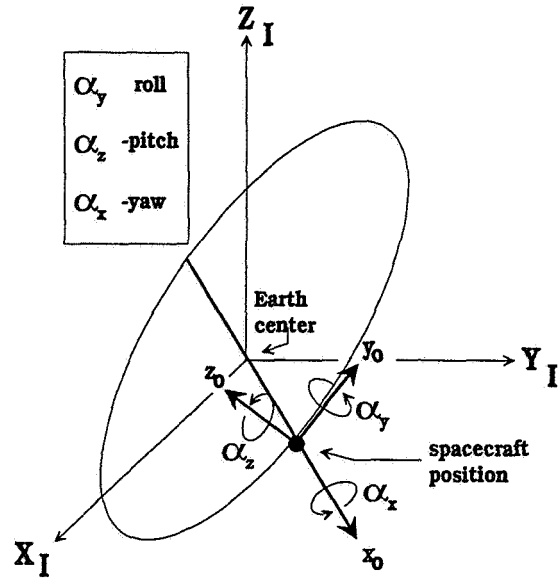


Figure 1. Definition of Orbital Axes

The rotation rate, $\underline{\omega}$, used in equation (11), has a component only about the z_o axis. The derivation of the instantaneous rate experienced by the spacecraft is given in Appendix B. The axes labeled with 'I' refer to the inertial coordinate system. Those marked with 'o' refer to the orbital coordinates. The quaternion represents the rotation from inertial coordinates to body coordinates. The attitude error, $\underline{\alpha}$, represents three small Euler angles around the body coordinates, which rotate the estimated quaternion to the true quaternion. The attitude displayed in the table below and in the results section is given in terms of Euler angles also. These Euler angles describe the attitude with respect to the orbital coordinates. Euler angles were chosen for the display since the true Euler angles are all zero.

The parameters which define the baseline simulated orbit and attitude are given below.

<u>Parameter</u>	<u>Truth</u>	<u>A-priori estimate</u>
a (km)	7000	8000
e	0.05	0.06
i (deg)	50	54
Ω (deg)	90	85
ω (deg)	0	5
θ (deg)	45	50
C_d	0.02	1
roll (deg)	0	10
pitch (deg)	0	10
yaw (deg)	0	10

IV. Results

The simulation described above was run for 300,000 seconds. Noise was added to the simulated magnetometer data and to the simulated rate data. The magnetometer measurement noise was 2 milliGauss and the noise in the measured rate was $0.017 \text{ deg/sec}^{1/2}$.

Figures 2 through 4 show the root-sum-square (RSS) error in the position estimate. The a-priori position error is 1453 km (computed from the orbital parameters given above). Figure 2 shows the error for the entire 300,000 seconds, approximately 51 revolutions (the orbital period is 97 minutes). Figure 3 shows the first 20,000 seconds. The error converges to less than 100 km within 10,000 seconds, which is roughly 1.7 orbits. Figure 4 shows the final 50,000 seconds. The average converged position error is about 4 km.

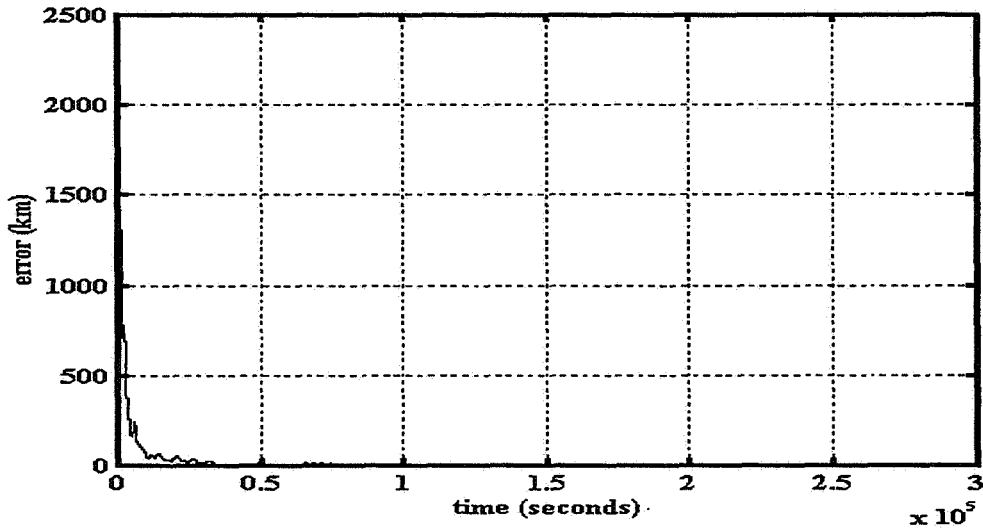


Figure 2. RSS Position Error

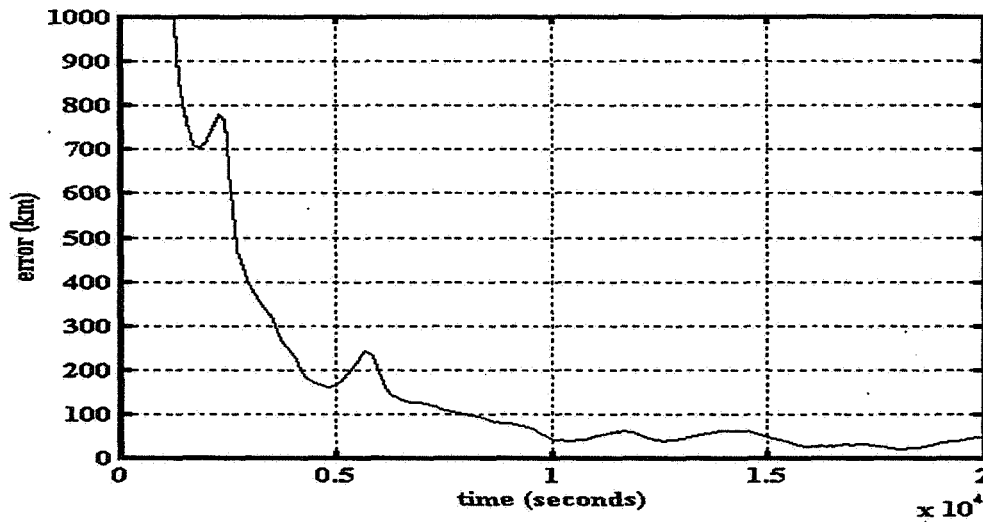


Figure 3. RSS Position Error - First 20,000 Seconds

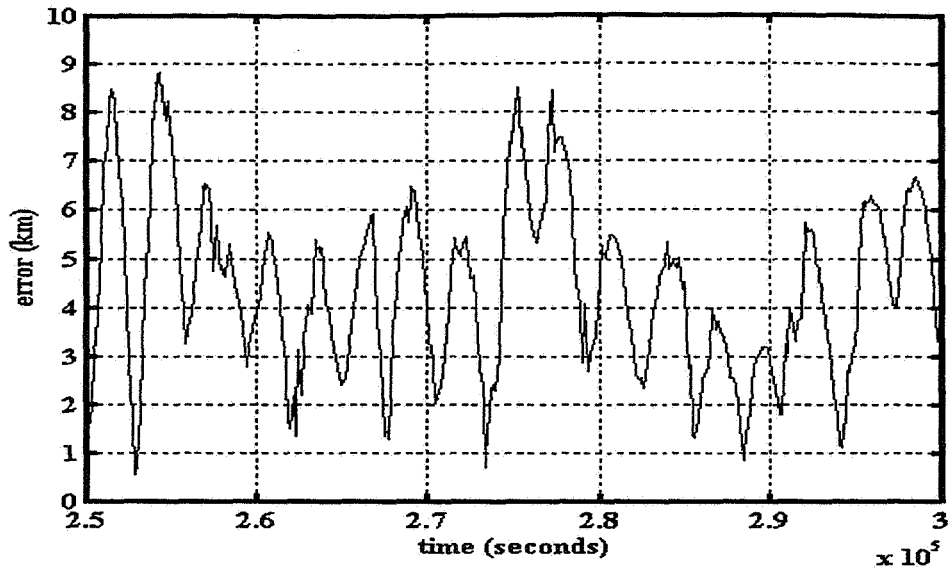


Figure 4. RSS Position Error - Last 50,000 Seconds

Figures 5 through 7 show the RSS attitude error. The attitude converges quickly, to less than 5 degrees, within 3,000 seconds as shown in Figures 5 and 6. Figure 7 shows that the average steady state error is less than 1 degree.

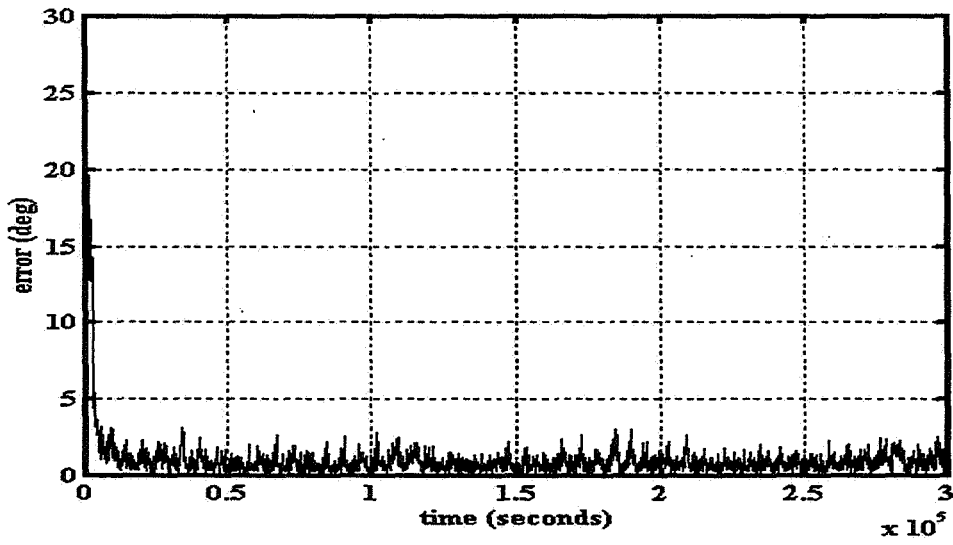


Figure 5. RSS Attitude Error

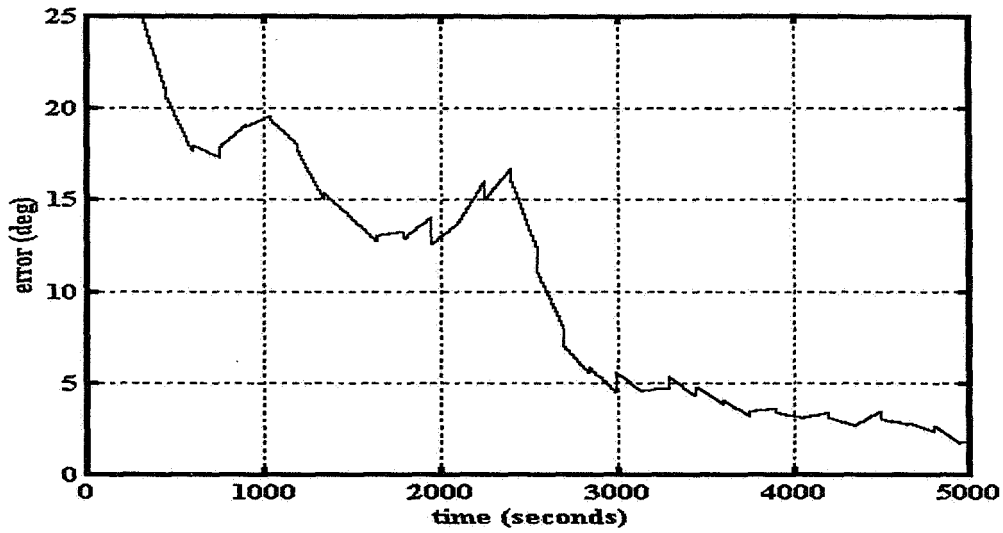


Figure 6. RSS Attitude Error - First 5,000 seconds

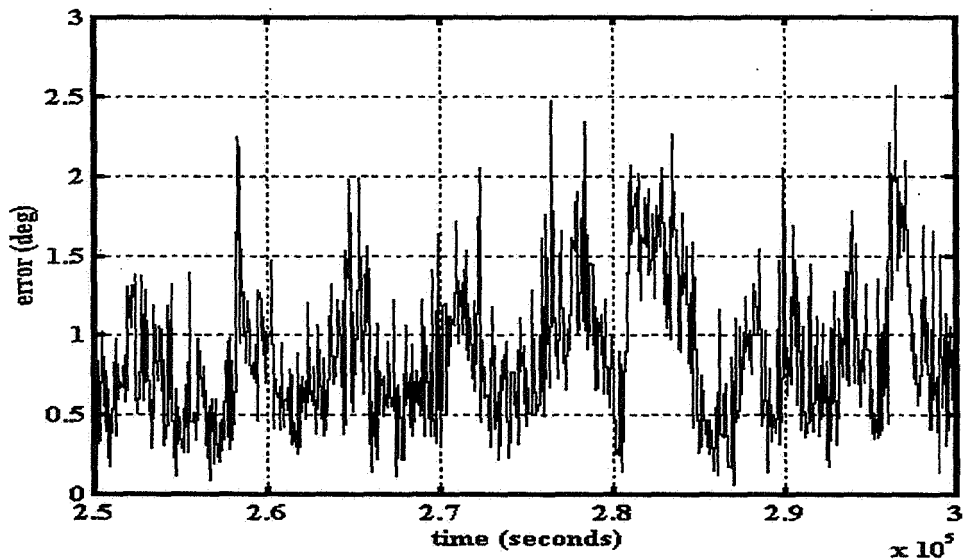


Figure 7. RSS Attitude Error - Last 50,000 Seconds

Figures 8 through 10 show the RSS velocity error. The a-priori velocity error is 0.96 km/sec. Like the position, the velocity error converges within 10,000 seconds, as shown in Figure 8. Figure 9 shows that the error is less than 0.25 km/sec at the end of the first 5,000 seconds. Figure 10 shows that the steady state velocity error is approximately 0.004 km/sec.

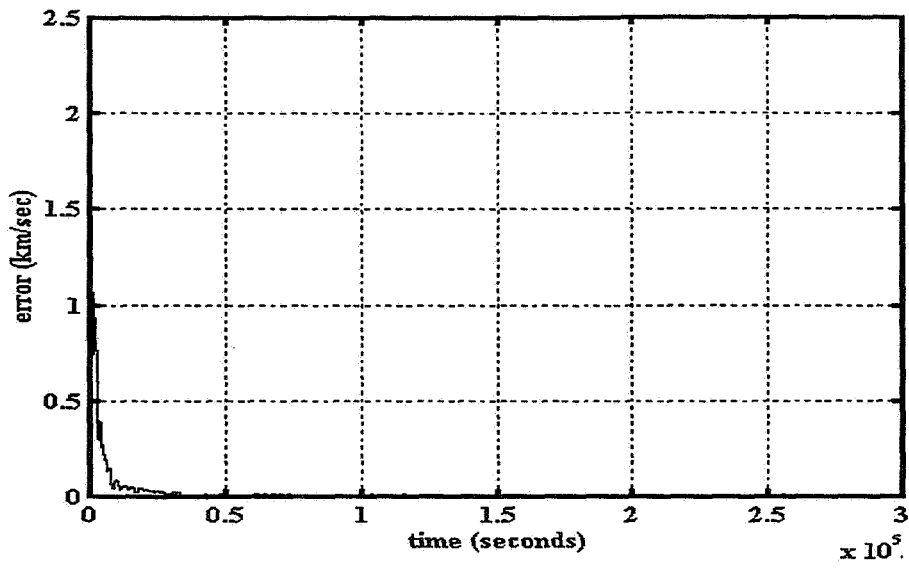


Figure 8. RSS Velocity Error

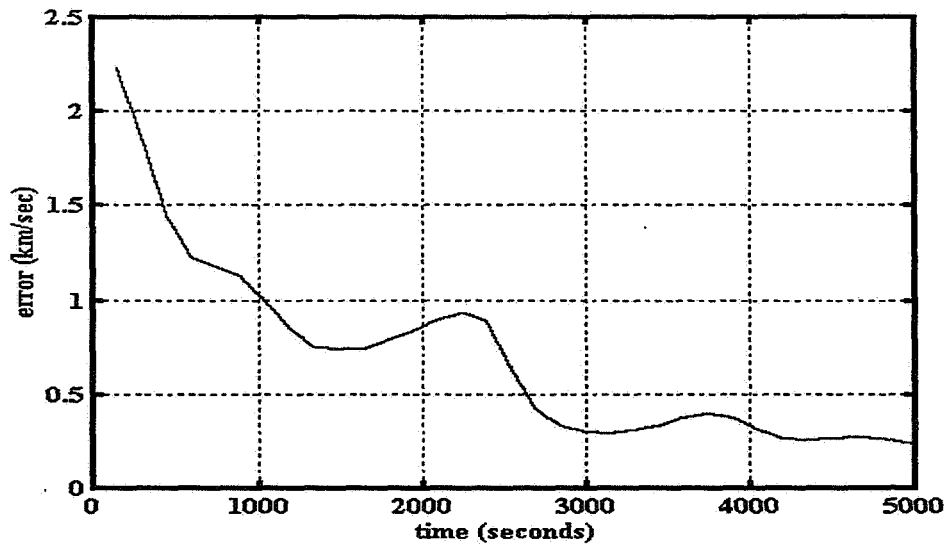


Figure 9. RSS Velocity Error - First 5000 Seconds

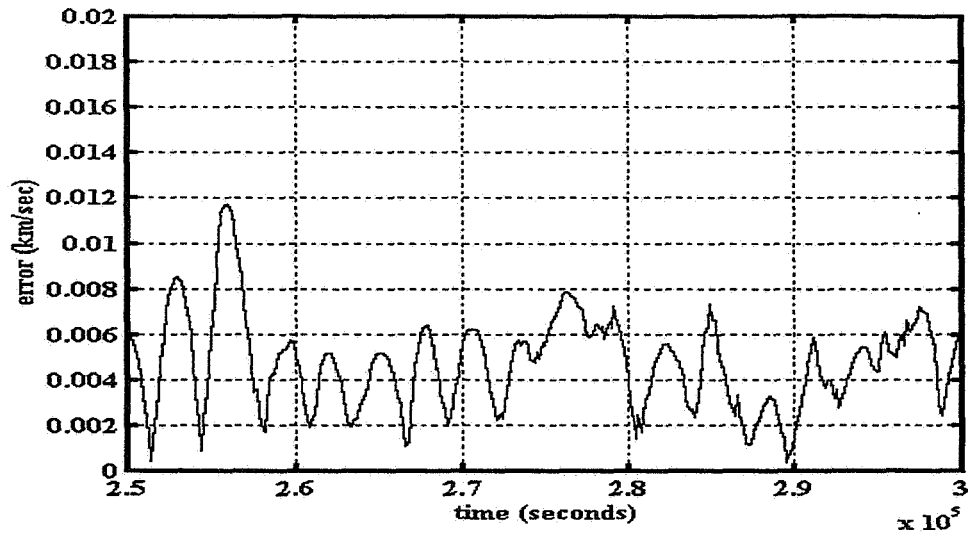


Figure 10. RSS Velocity Error - Last 50,000 Seconds

Figure 11 shows the RSS measurement residuals for the first 70,000 seconds (the residuals are computed using equation (4)). The average value is approximately 4 milliGauss. The residuals also converge quickly from an initial value of 186 milliGauss (RSS).

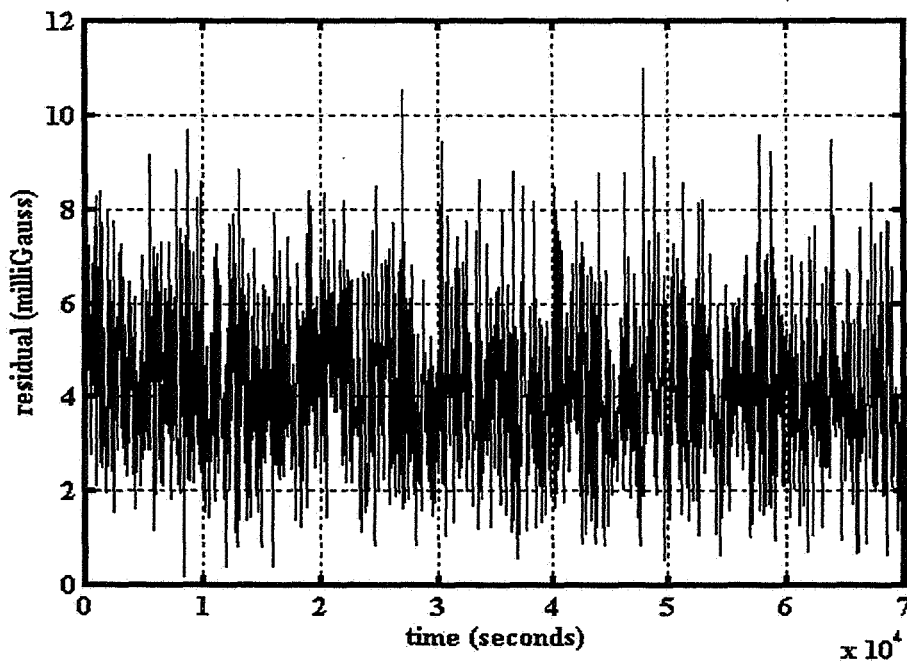


Figure 11. RSS Residual

V. Conclusions and Future Work

This work presents a *single augmented Extended Kalman Filter* that simultaneously estimates both spacecraft trajectory and attitude using data from magnetometers and gyroscopes. The results from the first test of this filter using simulated data, indicate that the filter can indeed estimate both the trajectory and attitude. Starting with errors (RSS) of over 1400 km in position and 10 degrees in attitude, the filter converged to less than 5 degrees in attitude within 3,000 seconds and to less than 100 km in position in 10,000 seconds (1.7 orbits). The average steady state values are less than 1 degree for attitude and 4 km for position. The steady state velocity errors (RSS) are approximately 4 m/sec and the average magnetometer residual is about 4 milliGauss (RSS).

Further testing will be conducted both with simulated and real spacecraft data. The magnetic field varies more at higher inclinations. Therefore, the effect of the orbit inclination angle will be studied. Tests will be conducted as to the filter's ability to estimate attitude and trajectory at low inclinations. The sensitivity to errors in Ω will be examined. Shorshi and Bar-Itzhack (References 1 and 9) found that the estimation of Ω was critical to the convergence of the position error. Additional errors will be introduced into the simulated data, e.g. magnetometer and gyro biases. The state vector will be expanded to include these biases and the ability of the filter to estimate these added states will be tested. Finally, tests with real spacecraft data from satellites such as the Gamma Ray Observatory, the Upper Atmospheric Research Satellite, and the Extreme Ultraviolet Explorer will be conducted.

References

1. Shorshi, G. , and Bar-Itzhack, I., "Satellite Autonomous Navigation Based on Magnetic Field Measurements", *Journal of Guidance, Control, and Dynamics*, Vol. 18, No. 4, July-August, 1995, pp. 843-850.
2. Ketchum, E., "Autonomous Spacecraft Orbit Determination Using the Magnetic Field and Attitude Information", Paper No. AAS 96-005, presented at the 19th Annual AAS Guidance and Control Conference, Breckenridge, Colorado, February 1996.
3. Psiaki, M., "Autonomous Orbit and Magnetic Field Determination Using Magnetometer and Star Sensor Data", *Journal of Guidance, Control, and Dynamics*, Vol. 18, No. 3, May-June 1995, pp. 584-592.
4. Challa, M., Natanson, G., Deutschmann, J., and Galal, K., "A PC-Based Magnetometer-Only Attitude and Rate Determination System for Gyroless Spacecraft", Paper No. 07, presented at the GSFC FDD Flight Mechanics/Estimation Theory Symposium 1995, NASA Goddard Space Flight Center, Greenbelt, Maryland, May 16-18, 1995.
5. Martel, F., Pal, P., and Psiaki, M., "Three-Axis Attitude Determination via Kalman Filtering of Magnetometer Data", presented at the GSFC FDD Flight Mechanics/Estimation Theory Symposium 1988, NASA Goddard Space Flight Center, Greenbelt, Maryland, May 10-11, 1988.
6. Hashmall, J., Liu, K., and Rokni, M., "Accurate Spacecraft Attitudes from Magnetometer Data", Paper No. MS95/007, presented at the CNES International Symposium on Space Dynamics, Toulouse, France, June 19-23, 1995.
7. Azor, R., Bar-Itzhack, I., and Harman, R., "Satellite Angular Rate Estimation from Vector Measurements", presented at the GSFC FDD Flight Mechanics/Estimation Theory Symposium 1996, NASA Goddard Space Flight Center, Greenbelt, Maryland, May 14-16, 1996.

8. Deutschmann, J., Bar-Itzhack, I., and Rokni, M., "Comparison and Testing of Extended Kalman Filters for Attitude Estimation of the Earth Radiation Budget Satellite", presented at the GSFC FDD Flight Mechanics/Estimation Theory Symposium 1990, NASA Goddard Space Flight Center, Greenbelt, Maryland, May 22-24, 1990.
9. Shorshi, G. and Bar-Itzhack, I., "Satellite Autonomous Navigation Based on Magnetic Field Measurements", TAE No. 714, Technion-Israel Institute of Technology, Haifa, Israel, April 1994
10. Kaplan, M., *Modern Spacecraft Dynamics & Control*, John Wiley & Sons, New York, 1976.

APPENDIX A - Derivation of the Measurement Model

The magnetic field vector can be resolved in the magnetic spherical coordinates, as shown in Figure A.1, as $\underline{B}_F^T = [B_r, B_{\theta B}, B_{\phi B}]$.

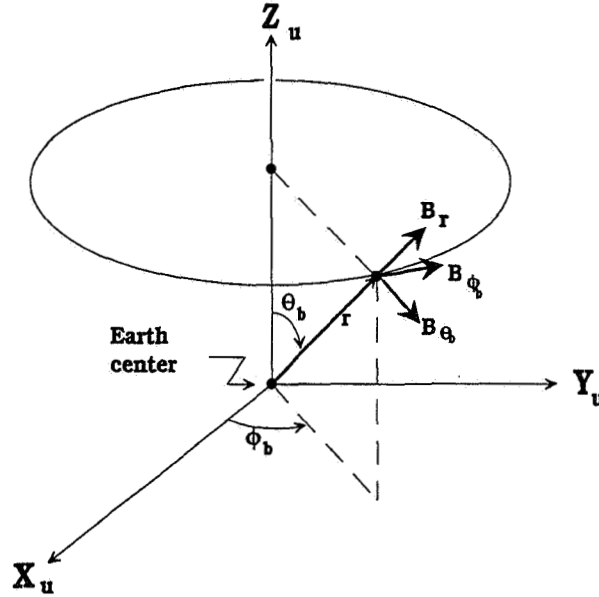


Figure A.1. Definition of the Magnetic Spherical Coordinates

The magnetic field at the spacecraft location, computed using the IGRF magnetic field model and the estimated position, can be written as

$$\hat{\underline{Y}} = \hat{D}_b^I \hat{D}_I^F \hat{\underline{B}}_F + \underline{n}' \quad (\text{A.1})$$

and the measured magnetic field vector, as measured by the magnetometer can be written as

$$\underline{Y}_m = D_b^I D_I^F \underline{B}_F + \underline{n}_m \quad (\text{A.2})$$

where

D_b^I = the transformation from inertial to body coordinates

D_I^F = the transformation from magnetic spherical to inertial coordinates

\underline{n}' = the magnetic field model error

\underline{n}_m = the magnetometer measurement error

The effective measurement, \underline{z} , is defined as follows

$$\underline{z} = \underline{Y}_m - \hat{\underline{Y}} = D_b^I D_I^F \underline{B}_F + \underline{n}_m - \hat{D}_b^I \hat{D}_I^F \hat{\underline{B}}_F - \underline{n}' \quad (\text{A.3})$$

Rewriting the transformation of $\hat{\underline{B}}_F$ as

$$\hat{D}_b^I \hat{D}_I^F \hat{\underline{B}}_F = D_b^I D_I^F \underline{B}_F + \Delta(D_b^I D_I^F \underline{B}_F) \quad (\text{A.4})$$

and

$$\underline{n} = \underline{n}_m - \underline{n}' \quad (\text{A.5})$$

This leads to

$$\underline{z} = \Delta(D_b^I D_I^F \underline{B}_F) + \underline{n} \quad (\text{A.6})$$

where

$$\Delta(D_b^I D_I^F \underline{B}_F) = \Delta D_b^I (D_I^F \underline{B}_F) + D_b^I \Delta(D_I^F \underline{B}_F) \quad (\text{A.7})$$

The second term on the right hand side of equation (A.7) is the derivation of the measurement matrix for the orbital states given in Reference 9. The expansion of the first term leads to the measurement matrix for the attitude states. Rewriting that term as

$$\Delta D_b^I (D_I^F \underline{B}_F) = \Delta D_b^I \underline{B}_I \quad (\text{A.8})$$

where

\underline{B}_I = the computed magnetic field vector in inertial coordinates

The error in the transformation can be defined as the difference between the true body coordinates and an intermediate coordinate system, referred to as the computed body coordinate system. The matrix that is computed is \hat{D}_b^I , which is equivalent to a transformation to the computed body coordinate system, which can be written as

$$\hat{D}_b^I = D_c^I = D_c^b D_b^I \quad (\text{A.9})$$

so

$$\Delta D_b^I = D_c^b D_b^I - D_b^I \quad (\text{A.10})$$

where D_b^I is the true transformation from inertial to body coordinates. For small attitude error we can assume that the matrix D_c^b is composed of small angles, thus

$$D_c^b = I - \begin{bmatrix} 0 & -\psi & \phi \\ \psi & 0 & -\phi \\ -\phi & \phi & 0 \end{bmatrix} = I - [\underline{\alpha} \ x] \quad (\text{A.11})$$

therefore from equation (A.11)

$$\Delta D_b^I = I - [\underline{\alpha} \ x] D_b^I - D_b^I = -[\underline{\alpha} \ x] D_b^I \quad (\text{A.12})$$

Substituting equation (A.13) into the first term on the right-hand side of equation (A.7) yields

$$\Delta D_b^I (D_I^R \underline{B}_F) = -[\underline{\alpha} \ x] D_b^I \cdot \underline{B}_I = -[\underline{\alpha} \ x] \underline{B}_b = [\underline{B}_b \ x] \underline{\alpha} \quad (A.13)$$

Substituting equation (A.13) into equation (A.6) along with the measurement matrix for the orbital states, gives

$$\underline{z} = [\underline{B}_b \ x] \underline{\alpha} + H_o \underline{x}_o + \underline{n} = [H_o \ [\underline{B}_b \ x]] \underline{x} + \underline{n} \quad (A.14)$$

where H_o is the measurement matrix for the orbital states, \underline{x}_o , and \underline{x} is composed of both the orbital states and the small angular errors in the attitude, $\underline{\alpha}$. Since \underline{B}_b is not known, the magnetic field vector measured by the magnetometer is used instead. The combined measurement matrix is then given as

$$H = [H_o \ [\underline{B}_b \ x]] = [H_o \ H_a] \quad (A.15)$$

APPENDIX B - Derivation of Spacecraft Rotation Rate

The instantaneous rotation rate about the spacecraft z_o is derived here from the orbital parameters which

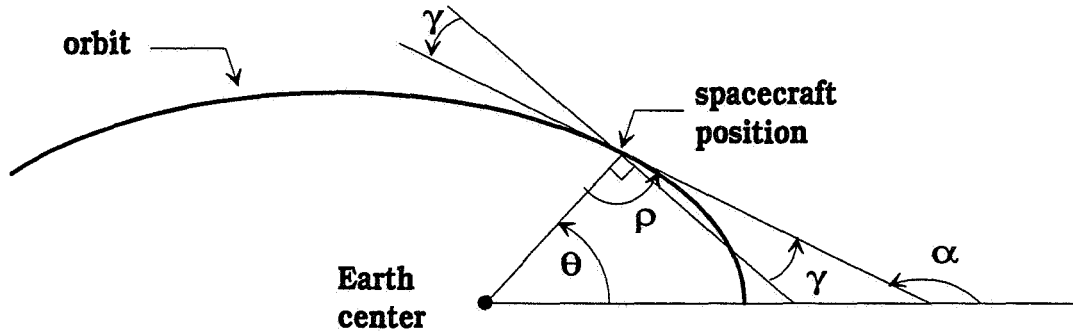


Figure B.1. Relationship Between Orbital Angles

describe an elliptical orbit (the average rate is 1 RPO). Figure B.1 defines the angles α , ρ , z , and γ . The rotation rate, w_z , is defined as

$$w_z = \dot{\alpha} \quad (B.1)$$

The angle, α , can be written as

$$\alpha = \theta + \rho \quad (B.2)$$

but

$$\rho = \pi / 2 + \gamma \quad (\text{B.3})$$

therefore

$$\alpha = \theta + \pi / 2 + \gamma \quad (\text{B.4})$$

Equation (B.1) then becomes

$$w_z = \dot{\alpha} = \dot{\theta} + \dot{\gamma} \quad (\text{B.5})$$

The relationship between the Keplerian elements, e , θ , and γ is given as (Reference 10)

$$\tan(\gamma) = \frac{e \cdot \sin(\theta)}{1 + e \cdot \cos(\theta)} \quad (\text{B.6})$$

then

$$\frac{d}{dt} \tan(\gamma) = \frac{d}{dt} \left[\frac{e \cdot \sin(\theta)}{1 + e \cdot \cos(\theta)} \right] \quad (\text{B.7})$$

Performing the differentiation in equation (B.7) leads to the following equation

$$w_z = \dot{\theta} - \frac{\cos^2(\gamma)}{1 + e \cdot \cos(\theta)} \left[\frac{e^2 \cdot \sin^2(\theta) \dot{\theta}}{1 + e \cdot \cos(\theta)} + e \cdot \cos(\theta) \dot{\theta} \right] \quad (\text{B.8})$$

ATTITUDE DETERMINATION IMPROVEMENTS FOR GOES

John L. Crassidis
Catholic University of America
Dept. of Mech. Eng.
Washington, D.C. 20064

F. Landis Markley, Arthur M. Kyle
Goddard Space Flight Center
Guidance and Control Branch, Code 712
Greenbelt, MD 20771

Kathie Kull
Orbital Sciences Corporation
Greenbelt, MD 20770

Abstract

In this paper, a summary of the basic simulation parameters and results of a new study for the Geostationary Operational Environmental Satellite (GOES) is shown. The study for GOES involves the simulation of minor modifications to the current spacecraft, so that the relative performance of these modifications can be analyzed. The first modification studied requires the placement of a baseline inertial reference unit, such as the Dry Rotor Inertia Reference Unit (DRIRU-II) or the Hemispherical Resonator Gyro (HRG), onto the spacecraft. The imager/sounder assembly is currently used to obtain landmark and/or star observations in order to compensate for spacecraft motions and external disturbances through ground processing. The study utilizes the imager/sounder assembly as another attitude sensor for on-board attitude determination. Also, the addition of star trackers is used to provide precise attitude knowledge.

Introduction

The current (GOES I-M) spacecraft specification for the knowledge requirement is $112 \mu\text{rad}$. This requirement is met through ground processing 99% of the time in the east/west direction and 95% of the time in the north/south direction. The spacecraft specification for the within-frame registration is $42 \mu\text{rad}$. The current spacecraft uses an Earth Sensor Assembly (ESA) to provide roll and pitch information. Yaw knowledge is not sensed. However, yaw control is achieved through roll/yaw coupling. A set of gyros based on the Digital Integration Rate Assembly (DIRA) also is on the current spacecraft. However, the DIRA has an operational lifetime of 2000 hours. Therefore, the on-board gyros are not used for mission mode attitude determination and control.

An outline of the remainder of this paper proceeds as follows. First, the simulation model for the gyro, the ESA, and the imager/sounder assembly are shown. This includes the simulation parameters used for Earth clouds and Earth radiance/gradients effects in the ESA, and non-repeatable errors in the imager/sounder assembly. Then, the simulated attitude sensor and gyro measurements are used in a Kalman filter for attitude determination. Results are presented for two

cases: 1) using the ESA, and 2) using both the ESA and imager/sounder assembly. Next, results using a star tracker are shown. This includes simulation results with and without the addition of gyros. Finally, conclusions are stated based on the simulation results.

Earth Sensor, Imager/Sounder

In this section, a brief overview of the simulation parameters for the gyro model, the ESA model, and the imager/sounder model is shown. The true angular velocity is assumed to be modeled by [1]

$$\underline{\omega} = \underline{\tilde{\omega}}_g - \underline{b} - \underline{\eta}_1 \quad (1)$$

where $\underline{\omega}$ is the true angular velocity, $\underline{\tilde{\omega}}_g$ is the gyro-determined angular velocity, and \underline{b} is the gyro drift vector,

$$\underline{\dot{b}} = \underline{\eta}_2 \quad (2)$$

The 3×1 vectors, $\underline{\eta}_1$ and $\underline{\eta}_2$, are assumed to be modeled by a Gaussian white-noise process with

$$E\{\underline{\eta}_i(t)\} = \underline{0} \quad i = 1, 2 \quad (3)$$

$$E\{\underline{\eta}_i(t)\underline{\eta}_j^T(t')\} = Q_i \delta_{ij} \delta(t-t') \quad i, j = 1, 2 \quad (4)$$

where

$$Q = \begin{bmatrix} \sigma_v^2 I_{3 \times 3} & 0_{3 \times 3} \\ 0_{3 \times 3} & \sigma_u^2 I_{3 \times 3} \end{bmatrix} \quad (5)$$

The DRIRU-II drift-rate noise and measurement noise characteristics are given by $\sigma_u = 2.15 \times 10^{-4} \mu\text{rad}/\text{sec}^{3/2}$ and $\sigma_v = 0.206 \mu\text{rad}/\text{sec}^{1/2}$. The nominal motion of the spacecraft involves a rotation once per orbit about the spacecraft's y-axis. Therefore, the nominal angular velocity is given by

$$\underline{\omega} = \begin{bmatrix} 0 \\ \omega_n \\ 0 \end{bmatrix} \quad (6)$$

where ω_n is the orbit rotation (7.27×10^{-5} rad/sec).

The ESA measures the spacecraft's roll and pitch angles. These angles are measured with respect to a moving Earth frame. The gyros provide attitudes with respect to an inertially fixed frame (e.g., GCI). Since the body rotation axis is about the spacecraft's y-axis, the body measurement vector is given by [2]

$$\underline{B}_e = \begin{bmatrix} -\sin(p)\cos(r) \\ \sin(r) \\ \cos(p)\cos(r) \end{bmatrix} \quad (7)$$

where r and p are the scanner roll and pitch angles, respectively. The inertial reference vector is given by

$$\underline{I}_e = A^T(q)\underline{B}_e \quad (8)$$

where q is the true quaternion (obtained by kinematic propagation using the true angular velocity). The ESA "measurements" are obtained by using the following model

$$\tilde{p} = p + v_p + w_p \quad (9)$$

where v_p is a zero-mean Gaussian process with a 3σ value of 0.02 degrees, and w_p represents the non-repeatable errors due to Earth cloud and Earth radiance/gradients effects. The non-repeatable error is assumed to be modeled by the following discrete process

$$w_p(i+1) = A w_p(i) + L(1 - A^2)^{1/2} g(i) \quad (10a)$$

$$A = \exp(-4 \Delta t B) \quad (10b)$$

where Δt is the sampling interval (0.25 seconds for the ESA), B is the bandwidth (for weather purposes, this set to about 1/6 days), L is the 1σ amplitude (experience has shown that this is about 200 μ rad), and g is a zero-mean normal Gaussian process. This same error model is applied to the Earth roll "measurement." Since the roll and pitch measurements from the Earth sensor are small, the body measurements can be approximated by

$$\tilde{\underline{B}}_B^e \approx \begin{bmatrix} -\tilde{p} \\ \tilde{r} \\ 1 \end{bmatrix} \quad (11)$$

The imager/sounder assembly can measure stars in a 23° E/W \times 21° N/S field of view, outside of the Earth limb. The orbit-attitude tracking system contains a catalog of bright stars visible by the imager/sounder which can sense three stars at 45 second intervals. For simulation purposes these stars are assumed to be found in different quadrants in the field of view. The imager/sounder star windows are staggered so that the data is acquired every 15 minutes. The imager/sounder measures the tangent of two angles, β_1 and β_2 , resulting in a body vector given by [2]

$$\underline{B}_{i/s} = \frac{1}{\sqrt{1 + \tan^2 \beta_1 + \tan^2 \beta_2}} \begin{bmatrix} \tan \beta_1 \\ \tan \beta_2 \\ 1 \end{bmatrix} \quad (12)$$

The imager/sounder "measurements" are obtained by using the following model

$$\tan \tilde{\beta}_i = \tan \beta_i + v_{b_i} + w_{b_i}, \quad i = 1, 2 \quad (13)$$

where v_b is a zero-mean Gaussian process with a 3σ value of 28 μ rad. The non-repeatable error in the imager/sounder is assumed to be modeled by the following process

$$\dot{\underline{x}} = \begin{bmatrix} 0 & 1 \\ -\omega_n^2 & 0 \end{bmatrix} \underline{x} + \begin{bmatrix} 0 \\ 1 \end{bmatrix} \eta \quad (14a)$$

$$w_b = [1 \ 0] \underline{x} \quad (14b)$$

where η is a zero-mean Gaussian process. The standard deviation of η is selected such that the output of w_b has a 3σ value of about 200 μ rad.

Simulation Results

For this part of the study, an investigation of the relative performance between using on-board gyros and without the use of gyros was examined. For the on-board gyro case, a standard Kalman filter with a gyro propagated model was used for attitude determination. The simulations were run for six cases, which include: 1) ESA only with no non-repeatable (NR) errors, 2) ESA only with NR errors, 3) ESA and imager/sounder (I/S) with no NR ESA errors and no NR I/S errors, 4) ESA and I/S with no NR ESA errors and with NR I/S errors, 5) ESA and I/S with NR ESA errors and no NR I/S errors, and 6) ESA and I/S with both NR ESA errors and NR I/S errors.

The first two cases involve using the ESA only. A plot of a typical non-repeatable (radiance/gradients) error effect is shown in Figure 1. From this plot, the magnitude of the error is seen to be about 200 μ rad. A Monte Carlo type analysis shows that 200-250 μ rad is about the 3σ range for this error. Error angle plots for the first two cases are shown in Figures

2 and 3. With no NR errors in the ESA, the attitude accuracy is within 60 μrad . With the NR errors in the ESA, this accuracy is degraded to about 200 μrad . The large errors in the yaw angle estimates are due to filter un-observability. The observability of using an ESA combined with gyro measurements in a Kalman filter can be shown by using the simplifying assumption of a constant coefficient system. The state vector in the Kalman filter is given by [1]

$$\Delta \underline{x} = \begin{bmatrix} \Delta \underline{\alpha} \\ \Delta \underline{b} \end{bmatrix} \quad (15)$$

where $\Delta \underline{\alpha}$ is a 3×1 angle error vector (roll, pitch, yaw), and $\Delta \underline{b}$ is a 3×1 gyro-bias error vector. The system error equations, state matrix and sensitivity matrix are given by

$$\begin{aligned} \Delta \dot{\underline{x}} &= F \Delta \underline{x} + G \Delta \eta \\ \Delta \underline{z} &= H \Delta \underline{x} + \Delta \underline{y} \end{aligned} \quad (16a)$$

$$F = \begin{bmatrix} -[\underline{\omega} \times] & -I_{3 \times 3} \\ 0_{3 \times 3} & 0_{3 \times 3} \end{bmatrix} \quad (16b)$$

$$H = \left[\left[A(\underline{q}) \underline{B}_I^e \times \right] \ ; \ 0_{3 \times 3} \right] \quad (16c)$$

where the angular velocity vector ($\underline{\omega}$) is given by Equation (6), and $[\underline{\omega} \times]$ is the cross product matrix. Therefore, the state error angle equations are given by

$$\Delta \dot{\alpha}_1 = -\omega_n \Delta \alpha_3 - \Delta b_1 \quad (17a)$$

$$\Delta \dot{\alpha}_2 = -\Delta b_2 \quad (17b)$$

$$\Delta \dot{\alpha}_3 = \omega_n \Delta \alpha_1 - \Delta b_3 \quad (17c)$$

The first and third equations show the coupling effects between roll and yaw. The nominal body measurements for the ESA are given by

$$V = \begin{bmatrix} 0 & -1 & -2.64 \times 10^{-5} & 0 & 0 & 0 \\ 0 & -2.64 \times 10^{-5} & 1 & 0 & 0 & 0 \\ 7.27 \times 10^{-5} & 0 & 0 & 0 & 0 & 1 \\ 1 & 0 & 0 & 0 & 0 & -7.27 \times 10^{-5} \\ 0 & 0 & 0 & 1 & 0 & 0 \\ 0 & 0 & 0 & 0 & -1 & 0 \end{bmatrix} \quad (22)$$

$$\underline{B}_B^e = A(\underline{q}) \underline{B}_I^e = \begin{bmatrix} 0 \\ 0 \\ 1 \end{bmatrix} \quad (18)$$

which reflects the fact that the spacecraft is Earth-pointing. From Equations (16)-(18), the state matrix (F) and sensitivity matrix (H) are now constant.

The observability matrix is given by

$$O = \begin{bmatrix} H \\ H F \\ H F^2 \\ \vdots \\ H F^5 \end{bmatrix} \quad (19)$$

which is an 18×6 dimensional matrix. This matrix must be rank 6 for the system to be fully observable. However, using the system matrices in Equation (16) yields a rank 5 observability matrix. A singular value decomposition (SVD) of the observability matrix can provide an insight to which states are observable, as well as the degree of observability. The SVD of Equation (19) is given by

$$U S V^T = O \quad (20)$$

where S is an 18×6 diagonal matrix, and U and V are unitary matrices with dimensions 18×18 and 6×6 , respectively. The diagonal elements of the first 6 rows of S yield the singular values of the system. These singular values yield the degree of observability, which is determined to be

$$S = \begin{bmatrix} 1 \\ 1 \\ 1 \\ 1 \\ 7.27 \times 10^{-5} \\ 0 \end{bmatrix} \quad (21)$$

The columns of V shows which states are observable, and also show the degree of cross correlated observability in the states. This matrix is determined to be

The first four columns of V correspond to completely observable states. The second and third columns of V indicate that the roll and pitch angle states are completely observable. Also, there is some correlation between these states, shown by the -2.64×10^{-5} term. The sixth column of V is associated with a singular value of zero. This shows that the yaw angle state is not observable. This reflects a higher covariance in the yaw angle estimate, as compared to the roll and pitch angle covariances (see Figure 4). The fourth column of V corresponds to the pitch drift-rate state, which is completely observable, since its associated singular value is one. The fifth column of V corresponds to the yaw drift-rate state, which is weakly observable, since its associated singular value is small (i.e., 7.27×10^{-5}). However, this state is completely decoupled from any other

state. The first column of V , as well as the sixth column, shows the coupling between the yaw angle state and the roll drift-rate state (due to quarter-orbit coupling). This indicates that the error in this state is attributed to both actual roll rate errors and yaw angle errors. Since the yaw angle state is not observable, the roll drift-rate errors and yaw angle errors cannot be separated. A plot of the gyro drift-rate covariances is shown in Figure 5. The error covariance of the roll drift-rate state is larger than the yaw drift-rate error covariance. This is most likely due to the fact the yaw angle errors cannot be separated from the roll drift-rate error.

Plots of the four remaining cases, which include the imager/sounder as an attitude sensor, are shown in Figure 6-9. A summary of the results for all cases is shown in Table 1.

Table 1 Attitude Errors for Various Sensor Configurations and Error Sources

Case	Error Sources	Roll Errors	Pitch Errors	Yaw Errors
1	no NR ESA	60 μ rad	60 μ rad	1×10^5 μ rad
2	NR ESA	200 μ rad	200 μ rad	1×10^5 μ rad
3	no NR ESA, no NR I/S	60 μ rad	60 μ rad	200 μ rad
4	no NR ESA, NR I/S	100 μ rad	100 μ rad	200 μ rad
5	NR ESA, no NR I/S	100 μ rad	100 μ rad	200 μ rad
6	NR ESA, NR I/S	200 μ rad	200 μ rad	300 μ rad

Since the imager/sounder can measure stars which are off nadir, yaw angle information is possible. From Table 1, using the imager/sounder as another sensor significantly improves the yaw angle estimate. Also, since the magnitude of the non-repeatable errors is assumed to be approximately the same in the ESA and in the imager/sounder assembly, the attitude errors are also approximately equal when adding these errors to each sensor individually (i.e., case four and five). The sixth case involves using both the ESA and imager/sounder assembly with non-repeatable errors added to each sensor. A purely deterministically found attitude using the QUEST method yields errors which are approximately the same magnitude as case six (see Figure 10). Therefore, the addition of gyros does not seem to significantly improve the attitude accuracy.

In order to possibly estimate the non-repeatable effects in the imager/sounder, a colored noise Kalman filter was developed. An analysis can be performed by expanding upon Farrenkopf's model. The assumed model for the colored-noise Farrenkopf analysis is given by [3]

$$\dot{\theta} = \tilde{\omega}_g - \eta_v - b \quad (23a)$$

$$\dot{b} = \eta_u \quad (23b)$$

$$\dot{\underline{l}} = A_l \underline{l} + B_l \underline{\eta}_l \quad (23c)$$

where θ is the scalar (single-axis) attitude angle, $\tilde{\omega}_g$ is the gyro output, b is the gyro-drift rate, \underline{l} is the colored-noise output, η_v , η_u , and $\underline{\eta}_l$ are zero-mean Gaussian processes with standard deviations of σ_v , σ_u , and σ_l , respectively, and A_l and B_l are the colored-noise system matrices, given by

$$A_l = \begin{bmatrix} 0 & 1 \\ -\omega_n^2 & 0 \end{bmatrix} \quad (24a)$$

$$B_l = \begin{bmatrix} 0 \\ 1 \end{bmatrix} \quad (24b)$$

where ω_n is set to orbit rate. Therefore, the full continuous system matrix from Equations (23) and (24) is given by

$$F = \begin{bmatrix} 0 & -1 & 0 & 0 \\ 0 & 0 & 0 & 0 \\ 0 & 0 & 0 & 1 \\ 0 & 0 & -\omega_n^2 & 0 \end{bmatrix} \quad (25)$$

with the state-transition matrix of F denoted by Φ . The measurement model is given by

$$\tilde{y} = H \begin{bmatrix} \theta \\ b \\ l \end{bmatrix} + v \quad (26)$$

where v is a zero-mean Gaussian process with covariance r , and H is given by

$$H = [1 \ 0 \ 1 \ 0] \quad (27)$$

Equations (26) and (27) show that the colored-noise is added to the measurement. The state-noise covariance matrix can be computed as

$$Q = \begin{bmatrix} \sigma_v^2 \Delta t + 1/3 \sigma_u^2 \Delta t^3 & -1/2 \sigma_u^2 \Delta t^2 & 0 & 0 \\ -1/2 \sigma_u^2 \Delta t^2 & \sigma_u^2 \Delta t & 0 & 0 \\ 0 & 0 & 0 & 0 \\ 0 & 0 & 0 & \sigma_l^2 \Delta t \end{bmatrix} \quad (28)$$

where Δt is the sampling interval. The steady-state error covariance just subsequent to an update is given by

$$P = \Phi P \Phi^T - P H^T [H P H^T + r]^{-1} H P + Q \quad (29)$$

which can be solved using an eigenvector decomposition of the Hamiltonian matrix, where Φ is the state transition matrix of Equation (25).

The standard deviation of the colored-noise input varies from $\sigma_l = 1 \times 10^{-7} \mu\text{rad}$ to $\sigma_l = 1 \times 10^{-5} \mu\text{rad}$, which corresponds to a colored-noise magnitude ranging from $15 \mu\text{rad}$ to $1800 \mu\text{rad}$ (these are 3σ values). This colored-noise output simulates the non-repeatable effect in the imager/sounder assembly. A plot of the steady-state colored-noise attitude accuracy is shown in Figure 11. Note that the standard Farrenkopf analysis with no colored-noise gives an attitude accuracy of $56 \mu\text{rad}$ (3σ value), which is similar to the results shown in Figure 6. This colored-noise analysis shows that using an *accurate* model for the non-repeatable errors can reduce the attitude errors when using a Kalman

filter. However, an analysis using actual data should be performed to investigate the validity of this approach.

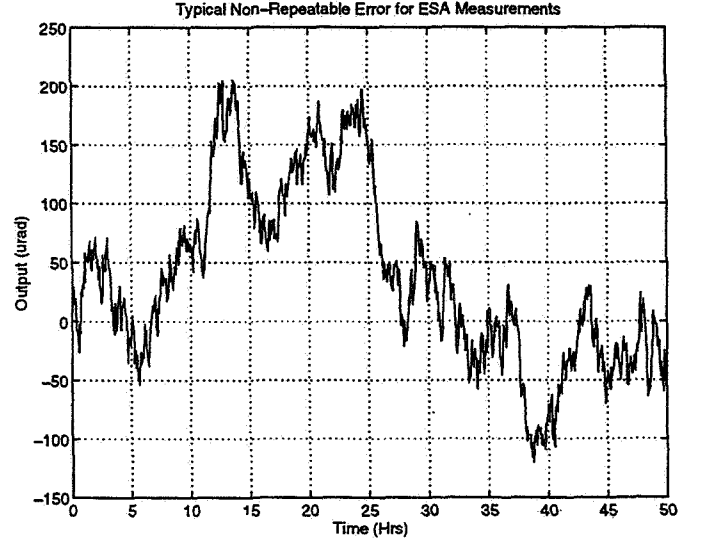


Figure 1 Non-Repeatable Errors for the ESA in Both Roll and Pitch

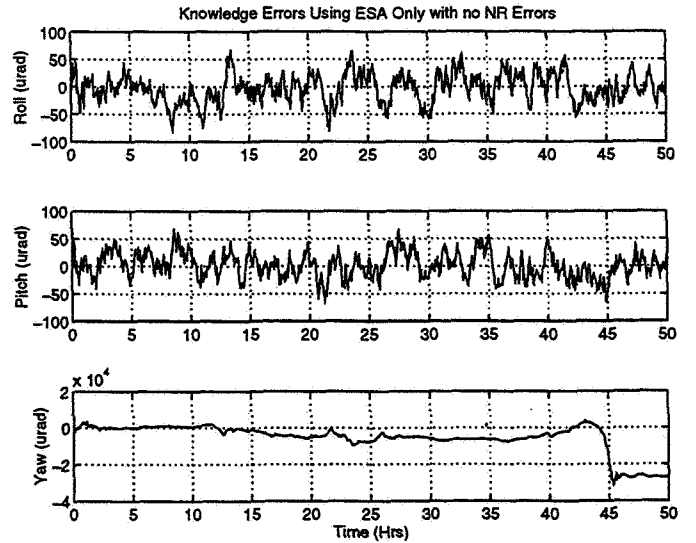


Figure 2 Attitude Errors Using ESA with No Non-Repeatable Errors

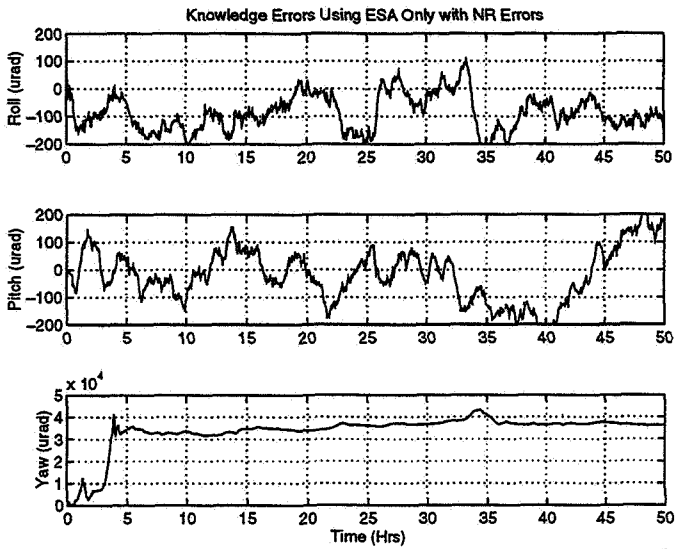


Figure 3 Attitude Errors Using ESA with Non-Repeatable Errors

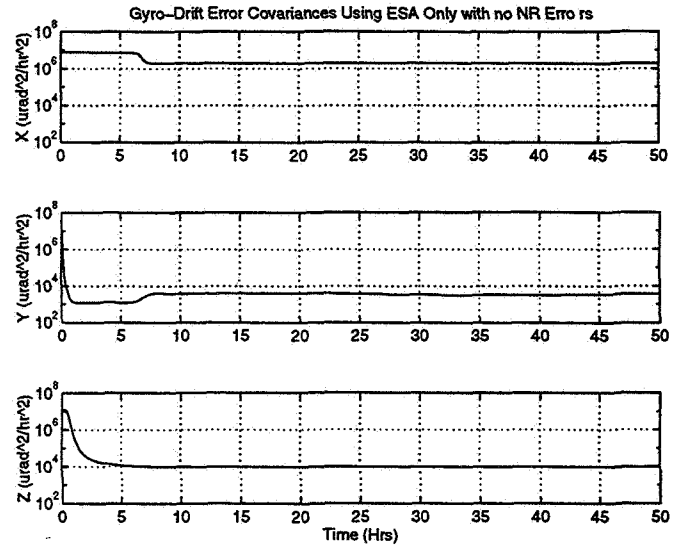


Figure 5 Gyro Drift Covariance

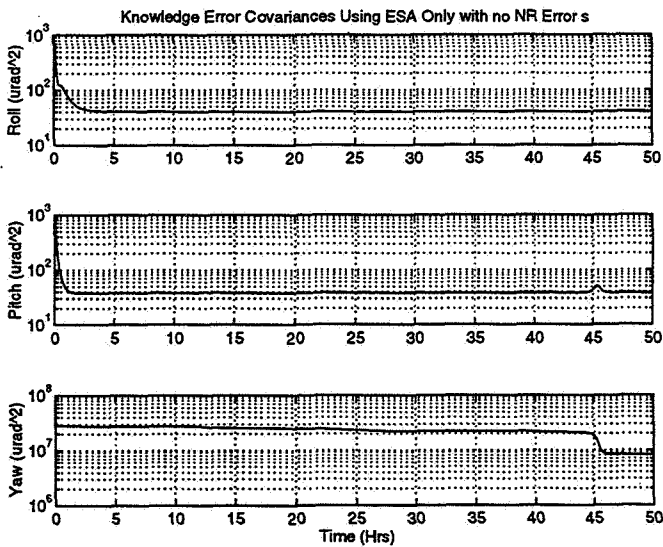


Figure 4 Attitude Error Covariance

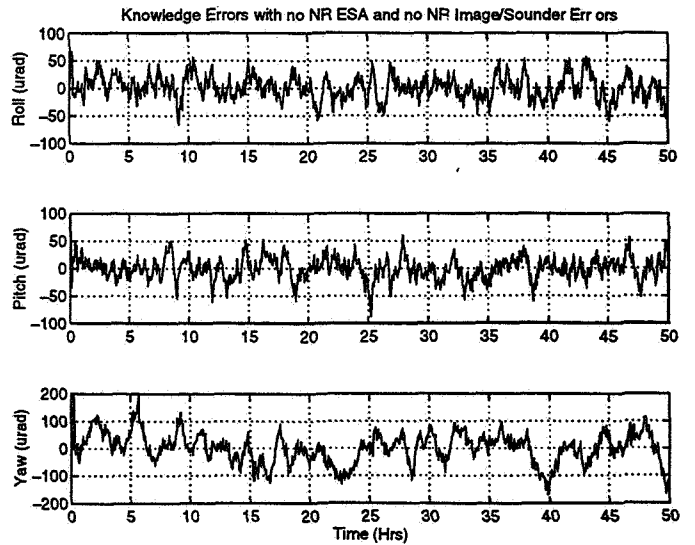


Figure 6 Attitude Errors with No Non-Repeatable ESA Errors and No Non-Repeatable I/S Errors

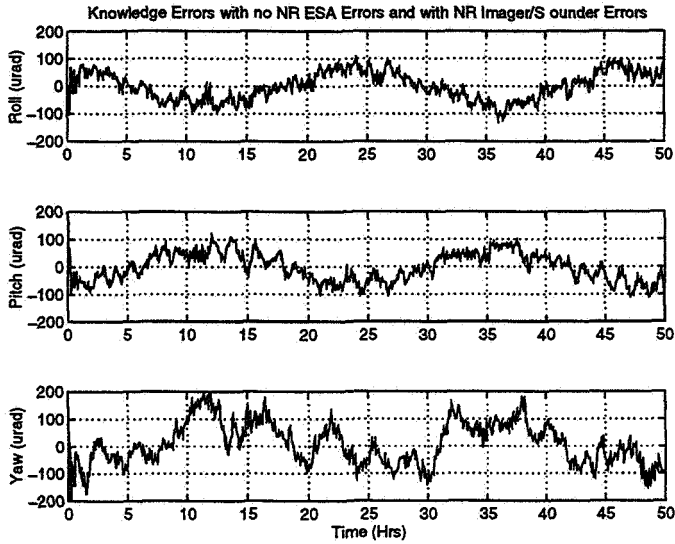


Figure 7 Attitude Errors with No Non-Repeatable ESA Errors and with Non-Repeatable I/S Errors

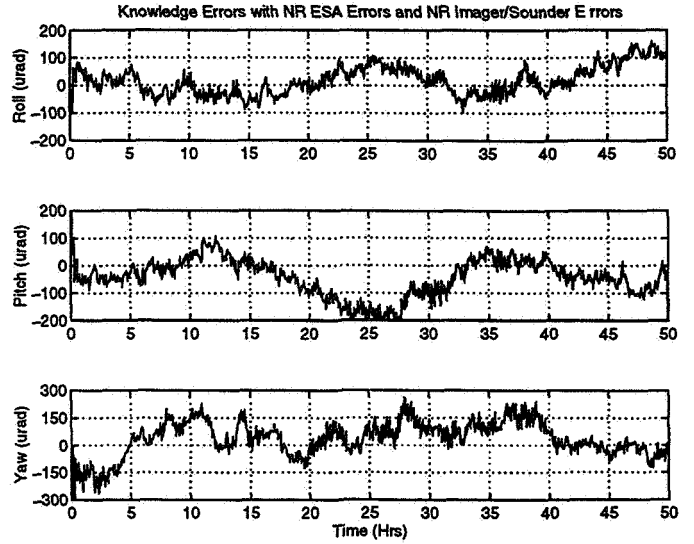


Figure 9 Attitude Errors with Non-Repeatable ESA Errors and with Non-Repeatable I/S Errors

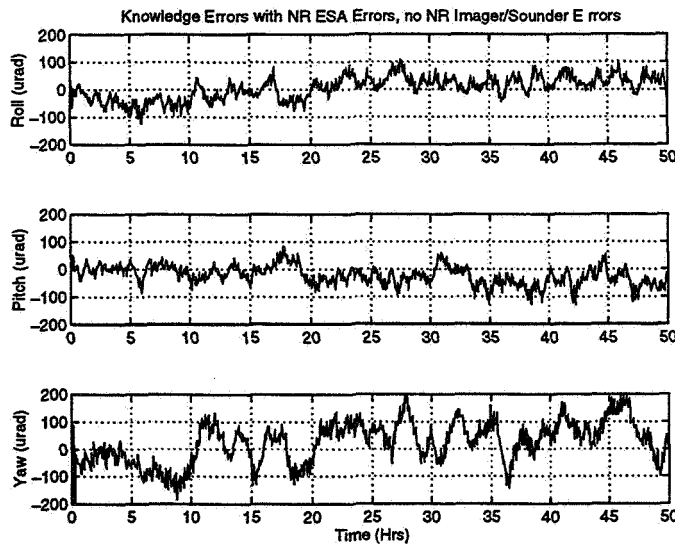


Figure 8 Attitude Errors with Non-Repeatable ESA Errors and No Non-Repeatable I/S Errors

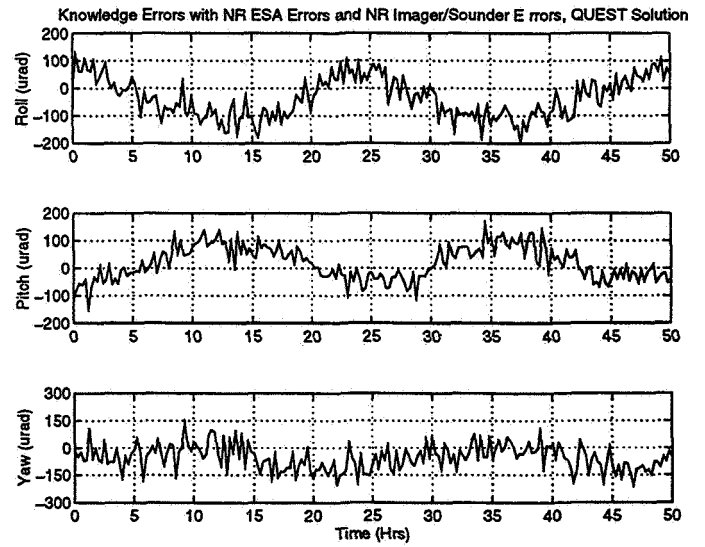


Figure 10 Determined Attitude Errors Using QUEST

Star Tracker

In this section, the simulation results using a star tracker with and without gyros are presented. First, the star tracker model and parameters are shown. Then, a covariance analysis is presented in order to determine the optimal orientation of the star trackers. Next, the availability of actual stars for the GOES orbit is shown. Results are then presented using QUEST [4] to determine the spacecraft attitude. An Enhanced QUEST algorithm is also derived which filters sensor noise. Finally, simulation results are presented using gyros and a Kalman filter.

All results shown in this section include the dynamics and external disturbance in the spacecraft. The GOES Flight Software Dynamics Model implements the GOES AOCE firmware emulation FORTRAN code from the SS/L into a six degree of freedom dynamics model. The initial model was developed to examine the replacement of the ESA with gyros, and the current capability was developed to compare with actual GOES performance using the ESA. A star tracker and star tracker/gyro were also added into the simulation. The simulation includes rotating solar array inertia effects with fully coupled inertia tensor dynamics, magnetic torquers with ideal torque response, and gravity gradient and solar pressure disturbances.

The star tracker can sense up to six stars in an $8^\circ \times 8^\circ$ field of view with a sampling interval of 0.1 seconds. The catalog contains stars which can be sensed up to a 6.0 magnitude. The star tracker measures the tangent of two angles, β_1 and β_2 , resulting in a body vector given by

$$B_s = \frac{1}{\sqrt{1 + \tan^2 \beta_1 + \tan^2 \beta_2}} \begin{bmatrix} \tan \beta_1 \\ \tan \beta_2 \\ 1 \end{bmatrix} \quad (30)$$

where the z-axis of the star tracker is along the boresight. The star tracker "measurements" are obtained by using

$$\tan \tilde{\beta}_i = \tan \beta_i + v_{s_i}, \quad i = 1, 2 \quad (31)$$

where v_s is a zero-mean Gaussian process with a 3σ value of $87.2665 \mu\text{rad}$ (18 arc-sec).

Each star tracker must be positioned so that sun obtrusions can be avoided at all times. For the GOES orbit, and available sun shade for the star tracker, the minimum exclusion area (allowing for a 3° safety margin) is from 55° North to 55° South of the Nadir vector. For the single star tracker case, the 55° orientation produces the following order for knowledge accuracy: (1) roll angle (i.e., about the spacecraft's x-axis) is known most accurately, then (2) yaw angle (i.e., about the spacecraft's y-axis), and (3) pitch angle (i.e., about the spacecraft's z-axis) being the least accurate.

The roll is determined to be most accurate since the star tracker is perpendicular to this spacecraft's x-axis. Pitch accuracy cannot be improved since the 55° star tracker position leads to the y-axis being the least "orthogonal" axis with respect to the tracker boresight.

For the two tracker case, a covariance analysis was performed in order to determine the optimal orientation. Assuming that each star tracker measures one star for simplicity, the error covariance matrix is given by [5]

$$P = \frac{\sigma^2}{|b_1 \times b_2|^2} \left[b_1 b_1^T + b_2 b_2^T + \frac{1}{2} (b_1 \times b_2)(b_1 \times b_2)^T \right] \quad (32)$$

where σ is the measurement error standard deviation, and b_1 and b_2 are measurement vectors of each star. For a North-South configuration, these measurement vectors are given by

$$b_1 = \begin{bmatrix} 0 \\ \sin 55^\circ \\ \cos 55^\circ \end{bmatrix} \equiv \begin{bmatrix} 0 \\ s \\ c \end{bmatrix} \quad (33a)$$

$$b_2 = \begin{bmatrix} 0 \\ -\sin 55^\circ \\ \cos 55^\circ \end{bmatrix} \equiv \begin{bmatrix} 0 \\ -s \\ c \end{bmatrix} \quad (33b)$$

Using Equation (33), the covariance in Equation (32) becomes

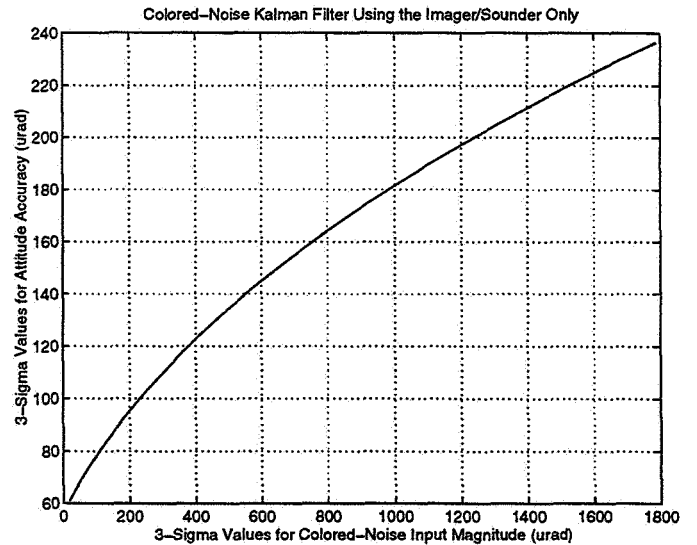


Figure 11 Steady-State Colored-Noise Kalman Filter

$$P = \frac{\sigma^2}{2} \begin{bmatrix} 1 & 0 & 0 \\ 0 & \frac{1}{c^2} & 0 \\ 0 & 0 & \frac{1}{s^2} \end{bmatrix} \quad (34)$$

The next configuration studied was to place the both star trackers 55° North (or South) from Nadir and separated by an angle ϑ , The measurement vectors for this case are given by

$$b_1 = \begin{bmatrix} c\tilde{s} \\ s \\ c\tilde{c} \end{bmatrix}, \quad b_2 = \begin{bmatrix} -c\tilde{s} \\ s \\ c\tilde{c} \end{bmatrix} \quad (35)$$

where $\tilde{s} \equiv \sin\vartheta$, and $\tilde{c} \equiv \cos\vartheta$. The covariance matrix in Equation (32) for this case is given

$$P = \frac{\sigma^2}{2(c^4\tilde{s}^2\tilde{c}^2 + c^2\tilde{s}^2s^2)} \times \begin{bmatrix} c^2\tilde{s}^2 & 0 & 0 \\ 0 & s^2 + c^4\tilde{s}^2\tilde{c}^2 & cs\tilde{c} - c^3\tilde{s}^2\tilde{c}s \\ 0 & cs\tilde{c} - c^3\tilde{s}^2\tilde{c}s & c^2\tilde{c}^2 + c^2\tilde{s}^2s^2 \end{bmatrix} \quad (36)$$

In order to determine the optimal separation angle, a cost function involving roll and pitch errors (i.e., allowing for relaxed yaw error conditions) is defined, given by

$$J(\vartheta) = \frac{\sigma^2}{2(c^4\tilde{s}^2\tilde{c}^2 + c^2\tilde{s}^2s^2)} (c^2\tilde{s}^2 + s^2 + c^4\tilde{s}^2\tilde{c}^2) \quad (37)$$

Minimizing this cost function with respect to ϑ leads to the optimal separation given by $\vartheta = 90^\circ$. Therefore, the covariance matrix in Equation (36) becomes

$$P = \frac{\sigma^2}{2} \begin{bmatrix} \frac{1}{s^2} & 0 & 0 \\ 0 & \frac{1}{c^2} & 0 \\ 0 & 0 & 1 \end{bmatrix} \quad (38)$$

Equation (38) shows that the yaw angle contains the smallest error, even though yaw was relaxed for the optimal separation angle. Therefore, comparing Equation (34) and Equation (38) leads to the conclusion that the optimal location for the two tracker case is given by one tracker 55° North and one tracker 55° South from Nadir.

Simulation Results

Figure 12 shows the actual number of stars within the North pointing tracker field of view. There is always a minimum of 2 stars, except for the interval from 2.15 to 2.283 hours. A star with quality 1, but with a magnitude of 6.256, was added in this interval for the QUEST solution. Figure 13 shows the number of stars within the South pointing tracker field of view. A quality 2 star (5.137 magnitude) from the interval 15.45 to 15.483 hours, and another quality 1 star (6.138 magnitude) can be added to insure a minimum of two stars. This was not done to the South tracker catalog, since the North tracker was used for simulations involving one tracker. Figure 14 shows the combined number of stars for both trackers (without the addition of any stars). This shows that a minimum of 4 stars is available for the two tracker case. Also, the percentages of time in the orbit with the number of stars in the field of view are shown by Tables 2 and 3.

Table 2 North Pointing Star Catalog

Number of Stars	Percentage in FOV
0	0.0
1	0.625
2	10.972
3	15.625
4	27.709
5	23.958
6	21.111

Table 3 South Pointing Star Catalog

Number of Stars	Percentage in FOV
0	0.0
1	1.458
2	8.056
3	20.972
4	28.889
5	23.272
6	17.153

In this section simulation results using the QUEST and Enhanced QUEST algorithms without gyros are presented. The QUEST algorithm minimizes the following cost function

$$J(A) = \frac{1}{2} \sum_{k=1}^n \frac{1}{\sigma^2} |B_{s_k} - A I_{s_k}|^2 \quad (39)$$

where A is the attitude matrix, and n is the number of stars available. QUEST is a deterministic approach which utilizes a point-by-point solution. Therefore, previous measurements are not utilized in the attitude solution. This algorithm requires at least two star measurements to determine the attitude. Therefore, a star is added (as previously described) to the single star tracker case.

In general, the attitude knowledge is determined more accurately as the number of star measurements at one time increases and/or the separation distance between stars increases. This can be seen by the deterministic error covariance, given by [4]

$$P_{\tilde{q}\tilde{q}_k} = \sigma^2 \sum_{k=1}^n \left[I_{3 \times 3} - B_{s_k} B_{s_k}^T \right]^{-1} \quad (40)$$

Figure 15 shows the attitude errors from QUEST determined attitude using a single (North) star tracker. Note the large errors about 2 hours into the simulation, which corresponds to the point where the star availability is mostly only 2 stars. Figure 15 also shows the attitude errors along with the 3σ bounds from Equation (40). This shows excellent agreement between theory and simulation. Figure 16 shows the attitude errors using both star trackers. Figure 17 also shows the 3σ bounds for the two star tracker case. This shows the significant improvement in attitude knowledge by using two trackers.

In order to further improve the attitude accuracy, an Enhanced QUEST algorithm (EQA) was developed. This is a simple first-order Kalman filter which combines a propagated model with the QUEST determined attitudes. Since gyros are not used for this case, the angular velocity is assumed to be perfect (i.e., given by Equation (6)). This assumption is not true, since external disturbances, and control and sensor errors are present in the actual system. Typical control errors using the ESA are shown in Figure 17. This shows the large errors and dynamic coupling in the roll/yaw axis. The EQA is given by

$$\hat{q}_{k+1}(-) = \exp\left\{\frac{1}{2}\Omega(\underline{\omega})\Delta t\right\}\hat{q}_k(+) \quad (41a)$$

$$\hat{q}_k(+) = (1-\alpha)\hat{q}_k(-) + \alpha\tilde{q}_k \quad (41b)$$

where $\Delta t = 0.1$ seconds, \tilde{q}_k is the QUEST determined attitude at time t_k , and α is a scalar gain. This gain was determined by minimizing the attitude errors from the simulated runs. A value which is too small adds too much model corrections, and tends to neglect measurements. A

value which is too large adds too much measurement noise, and tends to neglect model corrections. A value of $\alpha = 0.05$ was determined to be optimal. The EQA covariance is derived by re-writing Equation (41) as

$$\hat{q}_{k+1} = \Phi_4 \hat{q}_k \otimes \left[I + \alpha \left\{ \Phi_4 \hat{q}_k \right\}^{-1} \otimes \tilde{q}_{k+1} - I \right] \quad (42a)$$

$$\Phi_4 \equiv \exp\left\{\frac{1}{2}\Omega(\underline{\omega})\Delta t\right\} \quad (42b)$$

where \otimes denotes quaternion multiplication (see [1]). The QUEST determined quaternion is written as

$$\tilde{q}_{k+1} = \begin{bmatrix} \delta\tilde{q}_{k+1} \\ 1 \end{bmatrix} \otimes q_{k+1} \quad (43)$$

where q_{k+1} is the true quaternion, and $\delta\tilde{q}_{k+1}$ is a three component error vector. Substituting Equation (43) into Equation (42a), and post-multiplying both sides of the resulting equation by q_{k+1}^{-1} yields

$$\hat{q}_{k+1} \otimes q_{k+1}^{-1} \approx \begin{bmatrix} \delta q_{k+1} \\ 1 \end{bmatrix} = \Phi_4 \hat{q}_k \otimes q_{k+1}^{-1} (1-\alpha) + \alpha \begin{bmatrix} \delta\tilde{q}_{k+1} \\ 1 \end{bmatrix} \quad (44)$$

Using a first-order approximation yields the following covariance covariance for the EQA

$$P_{\hat{q}\hat{q}_{k+1}} = (1-\alpha)^2 \Phi_3 P_{\hat{q}\hat{q}_k} \Phi_3^T + \alpha^2 P_{\tilde{q}\tilde{q}_k} \quad (45)$$

where Φ_3 is the state transition matrix of $[\underline{\omega} \times]$. Since this matrix is constant and nearly the identity matrix, the diagonal elements of Equation (45) approach the following steady-state

$$P_{\hat{q}\hat{q}_k} \approx \frac{\alpha}{2-\alpha} P_{\tilde{q}\tilde{q}_k} \quad (46)$$

Figure 18 shows the attitude errors and bounds from Equation (46) using one star tracker and the EQA. Comparing Figure 18 with Figure 15 shows a significant improvement using the EQA. Figure 19 shows the attitude errors using two trackers and the EQA. Comparing Figure 19 with Figure 16 again shows a significant improvement using the EQA.

In this section, the results using gyros and a Kalman filter are presented. Two gyro cases are simulated. The first case involves the utilization of the DRIRU-II. The second case involves the utilization of the of the HRG. The parameters for both gyros are summarized in Table 4.

Table 4 Gyro Parameters

Parameters	DRIRU-II	HRG
σ_u (white noise)	$2.15 \times 10^{-4} \mu\text{rad}/\text{sec}^{3/2}$	$1.55 \times 10^{-4} \mu\text{rad}/\text{sec}^{3/2}$
σ_v (random walk)	$0.206 \mu\text{rad}/\text{sec}^{1/2}$	$1.6 \mu\text{rad}/\text{sec}^{1/2}$

The gyro model is shown by Equations (1) and (2). The relative performance of the attitude estimation can be found by numerically iterating the Kalman filter equations to steady state, but Farrenkopf [3] obtained analytic solutions for the case when the three attitude error angles are assumed decoupled. Farrenkopf's results for the preupdate and postupdate attitude error standard deviations, denoted by $\sigma(-)$ and $\sigma(+)$, respectively, can be written as

$$\sigma(-) = \sigma \left(\xi^2 - 1 \right)^{\frac{1}{2}} \quad (47a)$$

$$\sigma(+) = \sigma(-) / \xi \quad (47b)$$

where

$$\xi = \frac{1}{2} \left[\gamma + \frac{1}{2} S_u + \left(\gamma S_u + S_v^2 + \frac{1}{3} S_u^2 \right)^{\frac{1}{2}} \right] \quad (48a)$$

$$\gamma = \left[4 + S_v^2 + (1/12) S_u^2 \right]^{\frac{1}{2}} \quad (48b)$$

$$S_u = \sigma_u \Delta t^{\frac{3}{2}} / \sigma \quad (48c)$$

$$S_v = \sigma_v \Delta t^{\frac{1}{2}} / \sigma \quad (48d)$$

In the limiting case of very frequent updates, the preupdate and the postupdate attitude error standard deviations both approach the continuous-update limit, given by

$$\sigma_{\infty} = \Delta t^{\frac{1}{4}} \sigma^{\frac{1}{2}} \left(\sigma_v^2 + 2\sigma_u \sigma_v \Delta t^{\frac{1}{2}} \right)^{\frac{1}{4}} \quad (49)$$

Using the parameters in Table 4 in Equation (49), it was determined that the DRIRU-II steady-state error is approximately 2.8 times better (i.e., more accurate) than the HRG. This is also shown in the simulations. Figures 20 and 21 show the attitude errors using the HRG for the one tracker and two tracker cases, respectively. Figures 22 and 23 show the attitude errors using the DRIRU-II for the one tracker and two tracker cases, respectively. Comparing Figure 20 to Figure 22, and Figure 21 to Figure 23, it is seen that the DRIRU-II is approximately 2 to 3 more accurate for the attitude knowledge than using the HRG. Results for the cases without gyros and cases with gyros are shown in Table 5 and Table 6, respectively.

Table 5 Attitude Error Results Without Gyros

Cases Simulated	Roll Error (μrad) 3σ	Pitch Error (μrad) 3σ	Yaw Error (μrad) 3σ
QUEST (1 Tracker)	60	1250	900
QUEST (2 Trackers)	35	70	50
EQA (1 Tracker)	12	225	175
EQA (2 Trackers)	6	10	8

Table 6 Attitude Error Results With Gyros

Cases Simulated	Roll Error (μrad) 3σ	Pitch Error (μrad) 3σ	Yaw Error (μrad) 3σ
KF, DRIRU-II (1 Tracker)	3	15	10
KF, DRIRU-II (2 Trackers)	2	3	2.5
KF, HRG (1 Tracker)	7	30	12
KF, HRG (2 Trackers)	5	9	7

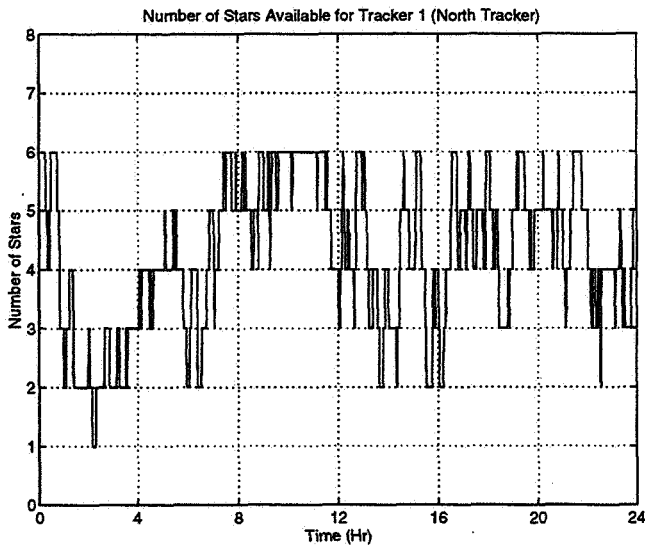


Figure 12 Availability of Stars for the North Tracker

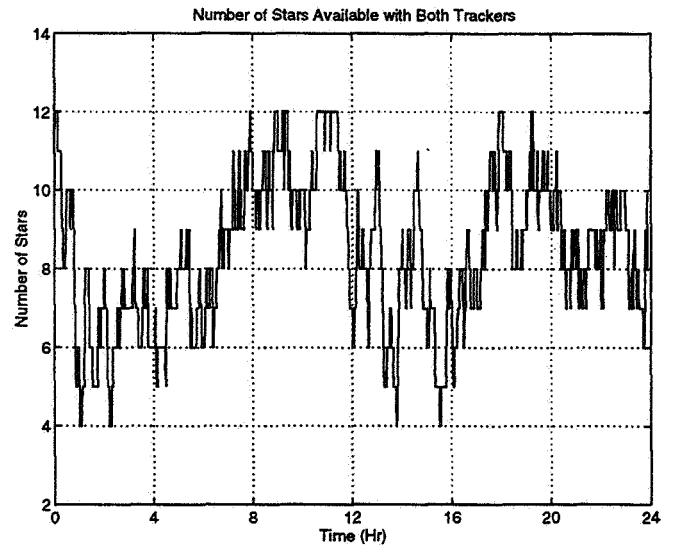


Figure 14 Availability of Stars for Both Trackers

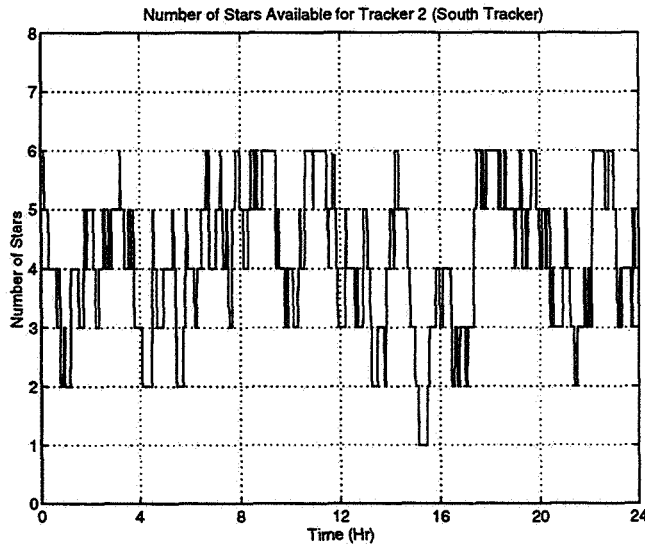


Figure 13 Availability of Stars for the South Tracker

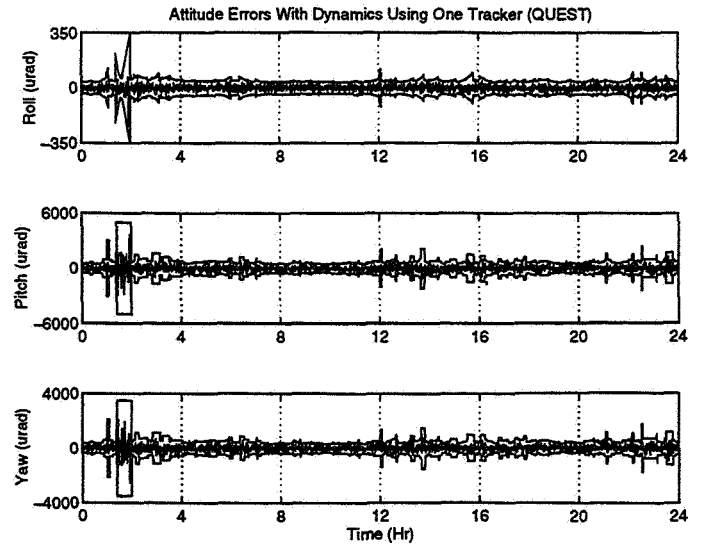


Figure 15 Attitude Errors and Bounds Using One Tracker (QUEST)

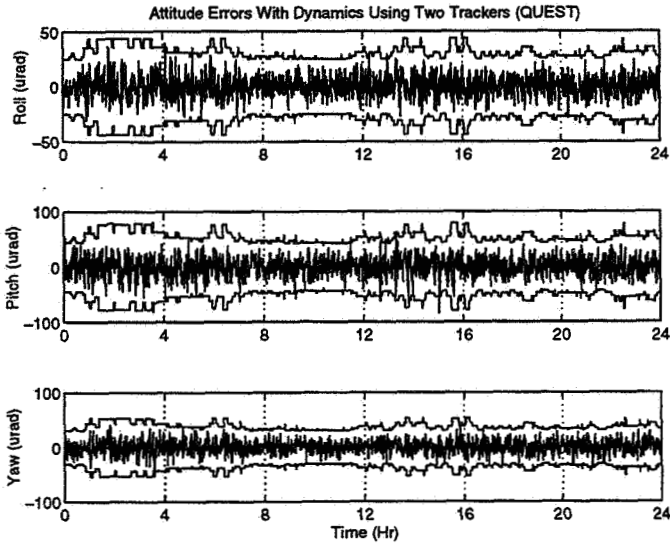


Figure 16 Attitude Errors and Bounds Using Two Trackers (QUEST)

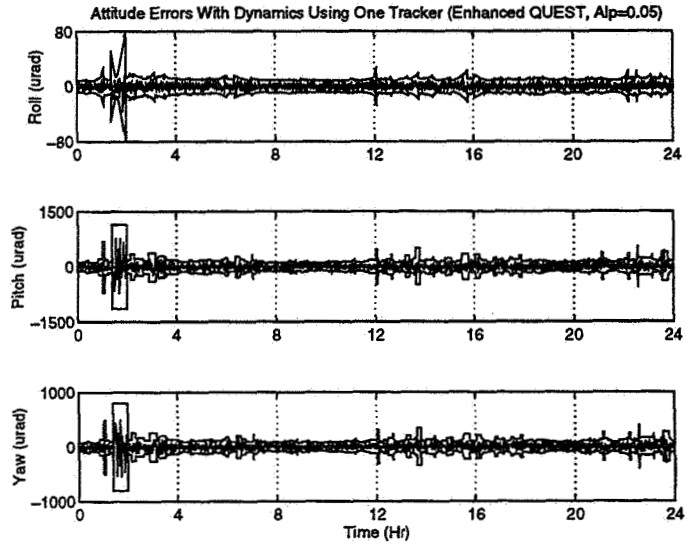


Figure 18 Attitude Errors and Bounds Using One Tracker (Enhanced QUEST)

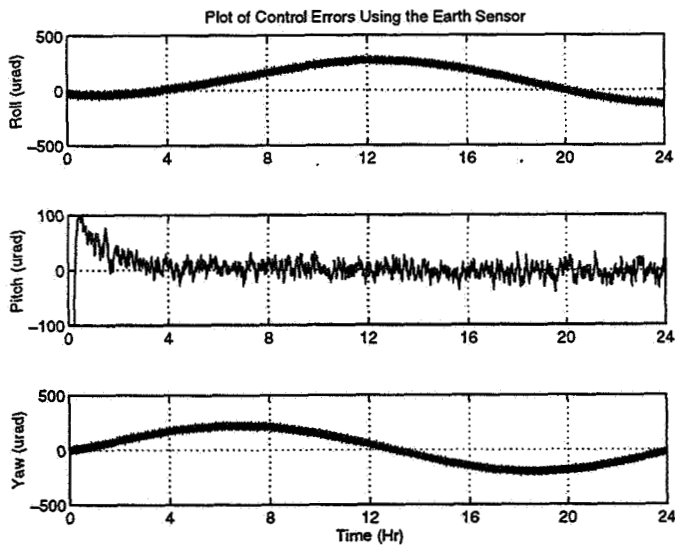


Figure 17 Control Errors

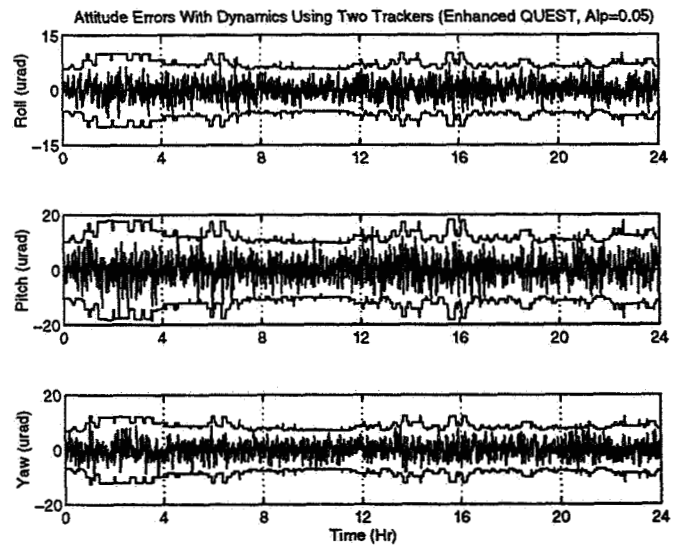


Figure 19 Attitude Errors Using Two Trackers (Enhanced QUEST)

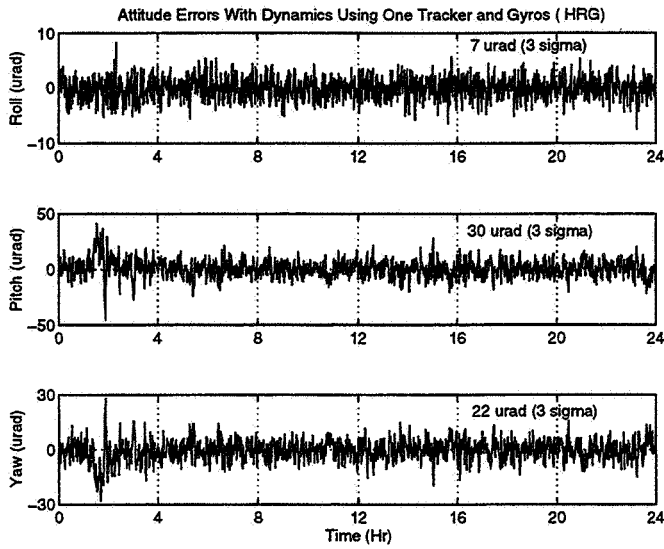


Figure 20 Attitude Errors Using One Tracker (Kalman Filter, HRG)

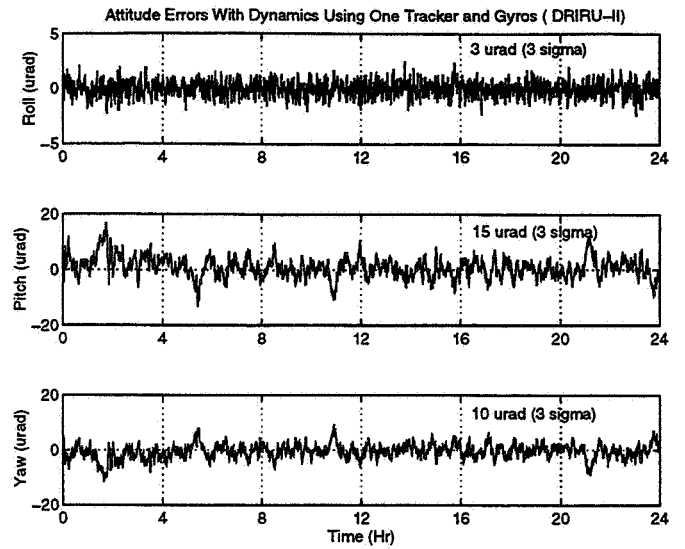


Figure 22 Attitude Errors Using One Tracker (Kalman Filter, DRIRU-II)

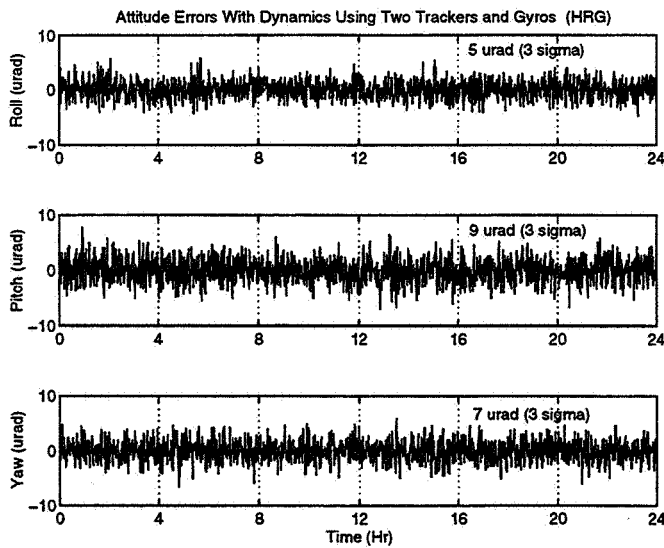


Figure 21 Attitude Errors Using Two Trackers (Kalman Filter, HRG)

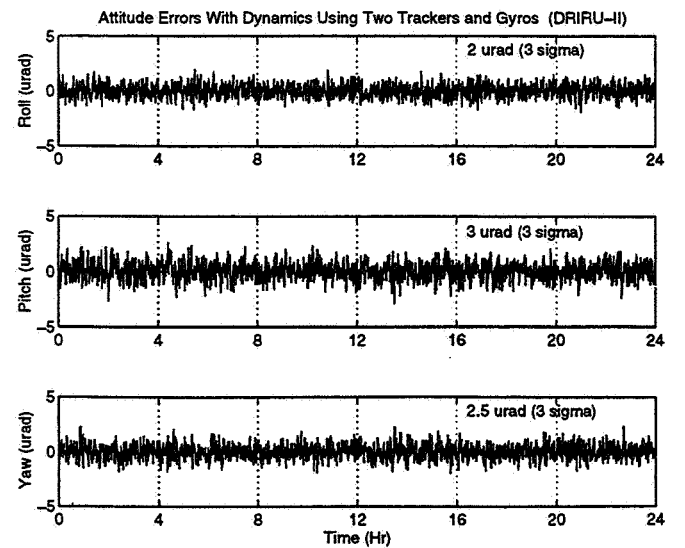


Figure 23 Attitude Errors Using Two Trackers (Kalman Filter, DRIRU-II)

Conclusions

This study provided some insightful information for using gyros on the GOES spacecraft. It was determined that the gyros do not significantly reduce the non-repeatable errors in the ESA. This was shown by comparing Figure 9 with Figure 10. Since the relative error is approximately equal in these two plots, we conclude that the utilization of on-board gyros does not significantly improve performance. Also, using gyros does not provide any observability in the yaw angle estimate, when using the ESA.

The star tracker simulation results show a significant improvement over the ESA attitude knowledge errors. The greatest improvements were showing using either: (1) two trackers with the EQA, or (2) one tracker and a DRIRU-II type gyro, and (3) two trackers and either an HRG type gyro or a higher quality gyro such as the DRIRU-II. Adding gyros to the spacecraft is the most ideal case since the filter bandwidth is larger than the EQA filter bandwidth (i.e., the Kalman filter with gyros can sense higher frequency spacecraft motions than an EQA). The utilization of on-board gyros may also improve the pointing accuracy, since the controller bandwidth may be increased.

Acknowledgments

The first author's work was supported by a National Research Council Postdoctoral Fellowship tenured at NASA-Goddard Space Flight Center. The author greatly appreciates this support. Also, the authors wish to thank Jim Kaidy for provided the dynamic simulation for the GOES spacecraft.

References

- [1] Lefferts, E.J., Markley, F.L., and Shuster, M.D., "Kalman Filtering for Spacecraft Attitude Estimation," *Journal of Guidance, Control and Dynamics*, Vol. 5, No. 5, Sept.-Oct. 1982, pp. 417-429.
- [2] Wertz, J.R., (editor) *Spacecraft Attitude Determination and Control*, Kluwer Academic Publishers, Dordrecht, 1978.
- [3] Farrenkopf, R.L., "Analytic Steady-State Accuracy Solutions for Two Common Spacecraft Attitude Estimators," *Journal of Guidance and Control*, Vol. 1, July-Aug. 1978, pp. 292-284.
- [4] Shuster, M.D., and Oh, S.D., "Three-Axis Attitude Determination from Vector Observations," *Journal of Guidance and Control*, Vol. 4, No. 1, Jan.-Feb. 1981, pp. 70-77.
- [5] Markley, F.L., "Attitude Determination Using Vector Observations: A Fast Optimal Matrix Algorithm," *Journal of the Astronautical Sciences*, Vol. 41, No. 2, April-June 1993, pp. 261-280.
- [6] Markley, F.L., Bauer, F.H., Deily, J.J., and Femiano, M.D., "Attitude Control System Conceptual Design for the Geostationary Operational Environmental Satellite Spacecraft Series," *Journal of Guidance, Control, and Dynamics*, Vol. 18, No. 2, March-April 1995, pp. 247-255.

FLIGHT MECHANICS/ESTIMATION THEORY SYMPOSIUM

MAY 14-16, 1996

SESSION 3

An Evaluation of Attitude-Independent Magnetometer-Bias Determination Methods*

J. Hashmall
Computer Sciences Corporation
Lanham-Seabrook, Maryland, USA 20706

J. Deutschmann
National Aeronautics and Space Administration
Goddard Space Flight Center
Greenbelt, Maryland, USA 20771

Abstract

Although several algorithms now exist for determining three-axis magnetometer (TAM) biases without the use of attitude data, there are few studies of the effectiveness of these methods, especially in comparison to attitude-dependent methods. This paper presents results of a comparison of three attitude-independent methods and an attitude-dependent method for computing TAM biases.

The comparisons are based on in-flight data from the Extreme Ultraviolet Explorer (EUVE), the Upper Atmosphere Research Satellite (UARS), and the Compton Gamma-Ray Observatory (GRO). The effectiveness of an algorithm is measured by the accuracy of attitudes computed using biases determined with that algorithm. The attitude accuracies are determined by comparison with known, extremely accurate, star-tracker-based attitudes.

In addition, the effect of knowledge of calibration parameters other than the biases on the effectiveness of all bias determination methods is examined.

1. Introduction

The recent emphasis on cost reduction in space missions has led to renewed interest in the use of magnetometers as attitude sensors. Because of their role in momentum management systems, three-axis magnetometers (TAMs) are nearly ubiquitous on near Earth-orbiting, three-axis-stabilized spacecraft. The cost of using TAMs for attitude determination is minimal, not only because of their use in momentum control, but also because they are inexpensive, reliable sensors. For these reasons, methods have been proposed to not only compute spacecraft attitudes, but also rates and even ephemerides (References 1–3).

Magnetometers contribute to attitude knowledge because the observed magnetic field best approximates a reference magnetic field when they are expressed in the same coordinate system and the transformation between the local spacecraft coordinate system and an Earth-reference system defines the spacecraft attitude. To best use TAMs for attitude determination, calibration parameters that are used to adjust observed magnetic fields must be determined. Chief among the calibration parameters that can be determined are magnetometer biases.

Magnetometer biases can be determined using a number of different algorithms (References 4–6). Although magnetometer bias determination methods all must use the observed magnetic field and the reference magnetic field (computed using the spacecraft ephemeris), some methods make use of additional information such as attitude rates (which can be obtained from gyroscope measurements) or spacecraft attitudes (obtained using more accurate sensors). Prior to bias determination, the magnetometer observations may be corrected for other calibration parameters, including magnetometer misalignments, nonunity scale factors, and the time-dependent effects of other instruments onboard the spacecraft that produce magnetic fields.

* This work was supported by the National Aeronautics and Space Administration (NASA)/Goddard Space Flight Center (GSFC), Greenbelt, Maryland, under Contract NAS 5-31500.

The purpose of this paper is to compare the utility of magnetometer biases computed using different attitude-independent methods for computing magnetometer-based spacecraft attitudes. Their utility is determined by comparing the accuracy of attitudes computed using identical magnetic field observations adjusted using the various computed biases. The data for computing the biases and attitude accuracies are obtained from flight data on three missions supported by the National Aeronautics and Space Administration (NASA) Goddard Space Flight Center (GSFC). These comparisons are made using magnetometer data adjusted with various combinations of other calibration parameters applied. Biases determined using an accurate attitude-dependent method are included for comparison.

2. Background

The three methods that were compared include two that require no rate data and one that does. They consist of the TWOSTEP, TAMCAL, and CFADS algorithms. In addition to these three attitude-independent methods, an attitude-dependent method was used to compute biases for comparison. This attitude-dependent method is referred to as the CFADS attitude-dependent algorithm.

TWOSTEP Algorithm—Attitude Independent (Reference 6)

The TWOSTEP method determines the bias by first computing a centered bias estimate based on a cost function derived from centering the measurements (about weighted averages of the measurements), where the centered measurements depend only linearly on the magnetometer bias. The centered bias estimate is then used as an initial estimate to compute a corrected bias, where the correction is due to the center term. This method was developed to correct the incorrect treatment of correlations in the Gambhir algorithm and to include information from data that that algorithm discards. The TWOSTEP method is attitude independent. Although it has been extended to compute calibration parameters other than the bias, only bias estimates are considered in this work.

TAMCAL Algorithm—Attitude Independent (Reference 5, 7)

The TAMCAL algorithm minimizes a loss function, L , defined by

$$L = \sum_t w_t \left[\left| \bar{B}_R(t) \right|^2 - \left| \bar{B}_O(t) - \bar{b} \right|^2 \right] \quad (1)$$

where w_t is a weight and $\bar{B}_R(t)$ and $\bar{B}_O(t)$ are the reference and observed magnetic field vectors at time t and \bar{b} is the bias vector. The bias is solved by an iterative refinement of an initial bias estimate. This method is truly attitude independent, because the magnitudes of the reference and estimated observed (observed-minus-estimated bias) magnetic field vectors are used, and these magnitudes are attitude independent. This algorithm is embodied in the Multimission Three-Axis Stabilized Attitude Spacecraft (MTASS) Flight Dynamics Support System (FDSS) magnetometer calibration utility used by the Flight Dynamics Division (FDD) at GSFC.

CFADS Algorithm—Attitude Independent (Reference 7)

The CFADS algorithm for bias determination consists of a particular use of the MTASS FDSS Coarse/Fine Attitude Determination System (CFADS). In this use of CFADS, a batch least-squares method is used to solve for a state vector containing an epoch attitude, rate biases, and TAM biases. The solution uses only TAM observations and attitude rate data (usually obtained from gyroscopes). Because neither attitude information nor data from more accurate attitude sensors are used in it, this method is also considered attitude independent.

CFADS Attitude-Dependent Algorithm (Reference 7)

The CFADS attitude-dependent algorithm uses MTASS FDSS CFADS and solves for the same state vector as does the CFADS attitude-independent algorithm. The difference arises from the additional use of pseudo-observations at times throughout the batch and from the choice of observation weights. Pseudo-observations consist of estimates of the spacecraft attitude previously obtained using more accurate sensors (in this case, star trackers). The CFADS loss function includes differences between a representation of each attitude (from a pseudo-observation), propagated to the epoch time using rate data, and the attitude portion of the state vector. The

pseudo-observation weights are set to values, sufficiently high compared with the magnetic field observations, so that the attitude solution is negligibly affected by the magnetic field observations. This procedure is equivalent to including highly weighted, more accurate sensor observations directly as input to CFADS.

The three spacecraft included in this study were the Extreme Ultraviolet Explorer (EUVE) (Reference 8), the Compton Gamma-Ray Observatory (GRO) (Reference 9), and the Upper Atmosphere Research Satellite (UARS) (Reference 10). Each of the missions contain unique features that must be considered in order to understand the results. The three spacecraft all use fixed-head star trackers (FHSTs) and accurate gyroscopes as primary sensors. Their onboard computer (OBC) attitude accuracies have stringent requirements (1σ attitude accuracy requirements: EUVE = 6 arcseconds, UARS = 20 arcseconds, and GRO = 27 arcseconds); therefore, compared with the TAM-based attitudes described later, the OBC attitudes can be considered truth.

The three spacecraft contain similar magnetometers, and all are in nearly circular orbits. While EUVE and GRO have 28.5-degree (deg) orbital inclinations, the UARS orbit has an inclination of about 57 deg. During the periods when data for this study were obtained, the spacecraft mean altitudes were about 513 kilometers (km) for EUVE, 582 km for UARS, and 379 km for GRO.

EUVE and GRO have magnetic torquer bars (MTBs) situated relatively near the TAMs, while the UARS MTBs were designed to be at a sufficient distance from the TAMs to have only a small effect on the measured magnetic field. As a result, MTB data were not available to FDD in the UARS telemetry. None the less, FDD personnel have seen data that indicate the possibility of an uncalibrated MTB effect of 1 to 3 milligauss (mG) on UARS. For EUVE and GRO, the time-dependent effects of the MTBs can be minimized through application of a coupling matrix.

Magnetometer measurements on UARS and EUVE are received with a precision of about 7.8 mG, while on GRO the least significant telemetry bit represents about 0.3 mG.

During the periods when the data for this study were obtained, EUVE and GRO were inertially pointing while UARS rotated at 1 revolution per orbit (RPO) to maintain an Earth-pointing attitude. Continuous telemetry was not available for GRO, and the data gaps of up to 10 minutes were filled with gyro data, created assuming constant attitude rates between the attitudes at either end of each gap. While EUVE and UARS TAM data were received in an unaltered state, the GRO TAM data used had been previously adjusted using prelaunch calibration parameters.

3. Method and Results

Prior to bias determination, the magnetometers on each spacecraft were calibrated using a complete, attitude-dependent calibration method applied to a long span (8 to 14 orbits) of data. This method is different from the attitude-dependent bias determination method. The calibrations performed on EUVE, UARS, and GRO have been verified by computing TAM/gyro attitudes using all of the calibration parameters and achieving attitude accuracies (compared with star-tracker-based attitudes) of about 0.06 deg for UARS and EUVE (Reference 11) and 0.02 deg for GRO.

These calibrations determined parameters in the magnetometer adjustment equation:

$$\bar{B}_o(t) = A_{bs} \left\{ \bar{B}_s(t) + C_{st} \bar{D}_t(t) \right\} - \bar{b}_b \quad (2)$$

where

\bar{b}_b = bias vector in the body frame

$\bar{D}_{t,b}$ = commanded torquer dipole at time t

C_{st} = torquer coupling matrix that converts from the torquer dipole in the torquer frame to the magnetic field in the magnetometer frame

\vec{B}_s = measured magnetic field in the sensor frame

A_{bs} = alignment/scale factor matrix that both converts magnetic field estimates in the sensor frame to the body frame and corrects them for scale factor deviations in the magnetometer

The bias vector compensates for any time-independent magnetic fields in the spacecraft, the torquer dipole vector and coupling matrix compensate for the major source in the time-varying spacecraft magnetic field, and the alignment/scale factor matrix puts the results into the body frame while compensating for linear errors in the magnetometer response. This matrix, which will be henceforth referred to as the A-matrix, is not constrained to be either orthogonal or normal and can be viewed as being composed of columns representing the alignment of the three independent one-axis magnetometers, each multiplied by its separate scale factor.

For each spacecraft, a 193-minute (approximately 2 orbits) span of data was selected for bias determination. This span was selected so that magnetometer, magnetic torquer (except for UARS), gyroscope, and OBC reference attitudes were available. The data were independent of those used for the full calibration of the magnetometers. To simulate conditions in which some of the calibration parameters might be unknown or inaccurate, the magnetometer data for EUVE and GRO were adjusted in four ways to produce four separate sets of corrected magnetometer data. UARS data, because magnetic torquer data were not available, were adjusted in only the two ways that do not require torquer data.

The four types of adjustments made were the following:

1. No adjustment

2. Coupling only: $\vec{B}_o(t) = \vec{B}_s(t) + C_{st} \vec{D}_t(t)$

3. A-matrix only: $\vec{B}_o(t) = A_{bs} \vec{B}_s(t)$

4. Both: $\vec{B}_o(t) = A_{bs} [\vec{B}_s(t) + C_{st} \vec{D}_t(t)]$

Note that no bias adjustments were performed.

For each of the sets of adjusted data, separate bases were determined using each of the three attitude-independent bias determination methods and, for comparison, using the CFADS attitude-dependent method. The computed biases are shown in Table 1.

Separate sets of data spanning 193 minutes for each spacecraft were selected and adjusted in the four ways detailed above. In addition, the corresponding biases were subtracted from the data (biases determined using the no-adjustment case of the first set of data, subtracted from the no-adjustment case of the second set of data, etc.). Each of these sets of adjusted data with bias correction were used with gyroscope data to determine spacecraft attitudes at 5-second intervals over the 193 minutes. The attitude solutions were computed using a batch least-squares method with gyroscope biases and attitude as the only elements of the state vector. Similar attitude solutions were obtained with each set of adjusted data from which no magnetometer biases had been subtracted. In all attitude computations, the reference fields were obtained using the International Geomagnetic Reference Field (IGRF) model, evaluated to 10th order, and using the 1990 definitive coefficients including the secular terms.

A total of 20 sets of attitudes each were computed for EUVE and GRO and an additional 10 for UARS. The attitude rotations between the computed attitude and the reference (OBC—star-tracker-based) attitude were expressed as an Euler sequence at 5-second intervals, and the root-mean-square (RMS) of these error rotations was determined. Table 2 contains these RMS errors over all axes* throughout the period. These values represent the accuracy of the attitudes obtained with the different biases and are labeled as attitude errors.

* Except for UARS where a timing error introduced a systematic offset in the pitch component. In the case of UARS, the mean of the other two axes is given.

Table 1. Comparison of Magnetometer Bias Computed Using Different Methods

Spacecraft	Adjustment	Axis	Bias Determination Method			
			TWOSTEP	TAMCAL	CFADS	Attitude Dependent
EUVE	None	X	5.53	7.06	3.41	6.00
		Y	1.43	2.57	0.32	-3.26
		Z	-10.74	-11.65	-10.59	-10.08
	Coupling Matrix	X	-3.27	-1.70	-2.94	-1.94
		Y	3.76	2.60	3.02	0.64
		Z	-2.19	-3.15	-1.74	-0.54
	A-Matrix	X	9.81	15.38	7.78	8.57
		Y	-5.41	-13.51	-5.69	-5.83
		Z	-6.80	-4.04	-7.21	-8.04
	Both	X	0.89	6.33	1.19	0.40
		Y	-2.99	-11.00	-2.76	-1.70
		Z	1.81	4.67	1.62	1.51
GRO	None	X	0.41	2.31	0.47	1.39
		Y	-0.96	-1.94	-1.13	-1.99
		Z	-6.10	-6.65	-2.86	-2.82
	Coupling Matrix	X	0.46	2.35	0.35	1.24
		Y	-1.11	-2.09	-1.38	-2.13
		Z	-6.12	-6.67	-2.82	-2.74
	A-Matrix	X	-2.42	-3.36	-2.43	-2.39
		Y	-2.50	-4.96	-2.54	-2.38
		Z	-2.24	1.20	-2.07	-2.06
	Both	X	-2.37	-3.32	-2.55	-2.51
		Y	-2.63	-5.10	-2.75	-2.51
		Z	-2.26	1.18	-2.00	-1.99
UARS	None	X	-4.82	-4.77	-3.54	-3.07
		Y	-7.58	-7.36	-7.14	-8.34
		Z	-4.96	-4.91	-4.71	-4.49
	A-Matrix	X	-2.81	-0.70	-1.58	-2.25
		Y	-6.58	-5.21	-6.37	-6.27
		Z	-2.60	-0.07	-2.05	-2.16

For each spacecraft and each bias source, the mean values of the attitude errors were computed and are presented as rows labeled "mean" under each spacecraft in Table 2. Similarly, for each bias source, the mean of the attitude errors for all spacecraft and each adjustment method, as well as the overall mean for all spacecraft and all adjustments, are presented as rows labeled by the adjustment method under the category "mean" in this table. These data are also presented for the three spacecraft as Figures 1, 2 and 3. Note that in these figures, the order of the series has been changed to improve visibility.

To more clearly show the relative accuracies, the attitude accuracy results were converted to ratios. Table 3 presents the ratios of the attitude accuracies given in Table 2. For each row of attitude errors in Table 2, the value in each column (representing a bias determination method) was divided by the attitude error from biases obtained using the attitude-dependent method (representing the "best" biases with this adjustment). The resulting ratios show how close to the "best" adjustment a given set of biases comes. An additional column shows the attitude errors for each adjustment divided by the attitude errors obtained using all available adjustments. The biases used to obtain both the numerator and denominator of these ratios were found using the attitude-dependent method. This column shows how important each type of adjustment is for each spacecraft.

Table 2. Comparison of Magnetometer Based Attitude Accuracies Computed Using Different TAM Biases

Spacecraft	Adjustment	Attitude Error (Degrees)				
		With Bias Determination Method:				
		No Bias	TWOSTEP	TAMCAL	CFADS	Attitude Dependent
EUVE	None	2.795	1.258	1.276	1.388	0.916
	Coupling Matrix	0.364	0.864	0.734	0.704	0.323
	A-Matrix	2.895	0.873	1.021	0.985	0.847
	Both	0.408	0.407	0.553	0.388	0.230
	Mean	1.616	0.851	0.896	0.866	0.579
GRO	None	0.665	0.639	0.478	0.534	0.347
	Coupling Matrix	0.658	0.626	0.544	0.518	0.337
	A-Matrix	0.573	0.050	0.470	0.057	0.049
	Both	0.519	0.048	0.429	0.058	0.034
	Mean	0.604	0.341	0.479	0.292	0.192
UARS	None	1.694	0.823	0.837	0.790	0.693
	A-Matrix	0.753	0.143	0.407	0.131	0.049
	Mean	1.224	0.483	0.622	0.461	0.371
Mean	None	1.718	0.907	0.864	0.904	0.652
	Coupling Matrix	0.511	0.745	0.639	0.611	0.330
	A-Matrix	1.530	0.469	1.162	0.501	0.422
	Both	0.464	0.227	0.489	0.223	0.132
	Mean	1.148	0.558	0.666	0.540	0.381

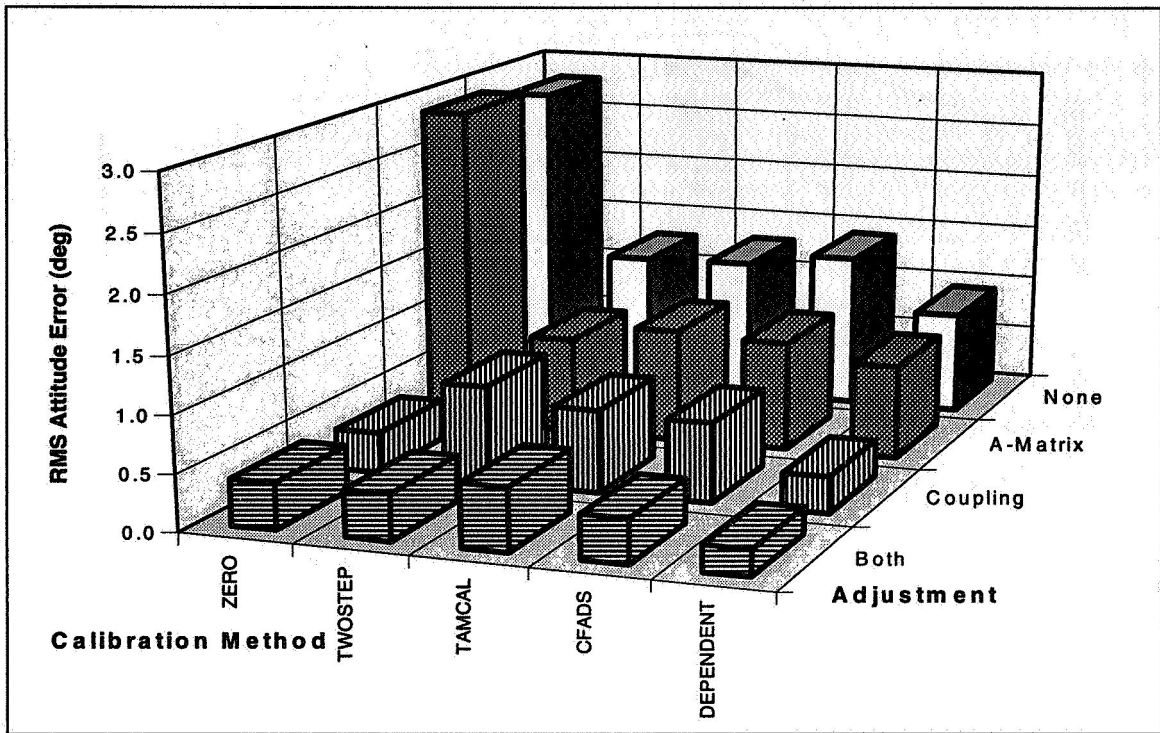


Figure 1. EUVE Attitude Errors

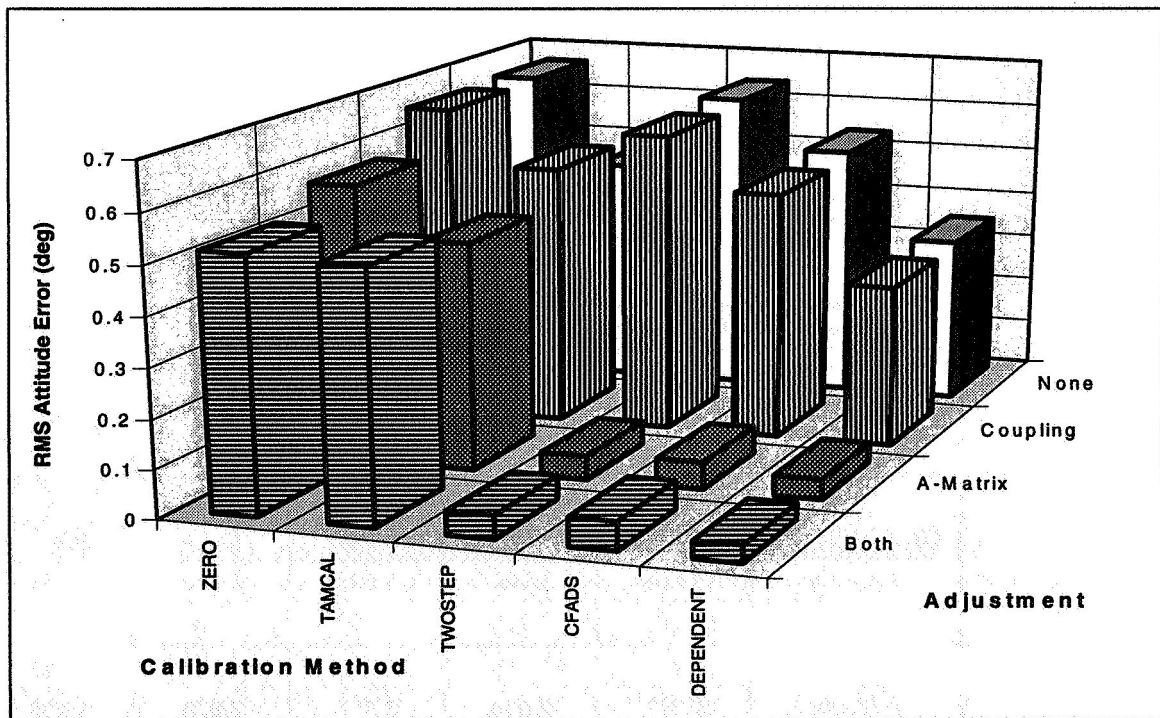


Figure 2. GRO Attitude Errors

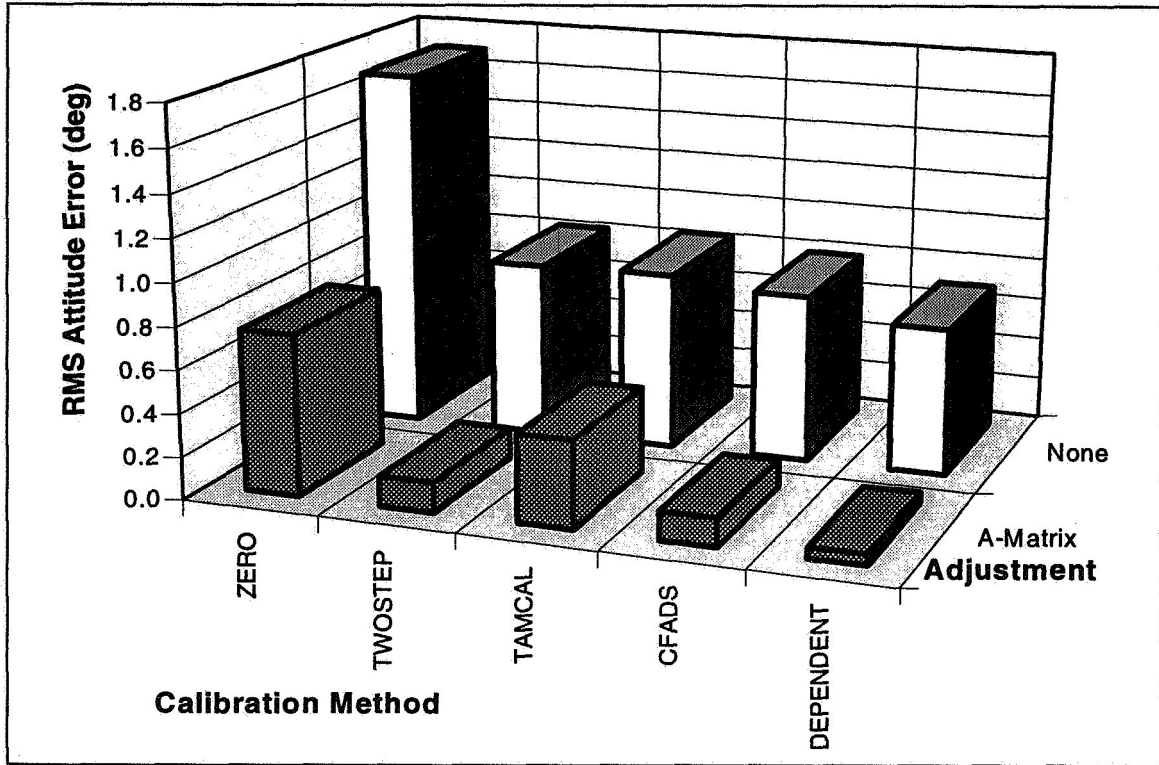


Figure 3. UARS Attitude Errors

Table 3. Relative Attitude Accuracies Computed Using Different TAM Biases

Spacecraft	Adjustment	Attitude Error Ratio				
		With Bias Determination Method				
		No Bias	TWOSTEP	TAMCAL	CFADS	Overall Ratio
EUVE	None	3.051	1.373	1.393	1.515	3.983
	Coupling Matrix	1.127	2.675	2.272	2.180	1.404
	A-Matrix	3.418	1.031	1.205	1.163	3.683
	Both	1.774	1.770	2.404	1.687	1.000
GRO	None	1.916	1.841	1.378	1.539	10.206
	Coupling Matrix	1.843	1.858	1.524	1.451	9.912
	A-Matrix	11.694	1.020	9.592	1.163	1.441
	Both	15.265	1.770	12.500	1.706	1.000
UARS	None	2.444	1.188	1.208	1.140	14.143
	A-Matrix	15.367	2.918	8.306	2.673	1.000

5. Discussion and Conclusions

For interpretation of the results, EUVE and UARS represent cases where there is a large error in unadjusted calibration parameters (e.g., A-matrix and coupling matrix) as well as larger data noise. The dominant term in the EUVE and UARS magnetometer noise is telemetry digitization, which has a uniform distribution and a range of 7.8 mG; for GRO, the dominant errors arise from systematic errors in the magnetic field model.

Although UARS is in a higher inclination orbit than either GRO or EUVE, resulting in a larger variation in the magnetic field throughout the orbit and a slight decrease in the accuracy of the reference magnetic field model at extreme latitudes, insufficient examples are available to reach reliable conclusions about the effect of orbit inclination.

Two elementary conclusions are clear and not surprising:

- Attitude-dependent biases yield consistently more accurate attitudes than do any of the attitude-independent biases.
- Attitude-independent biases obtained using rate data generally yield more accurate attitudes than do the other attitude-independent biases.

Comparing the results using biases computed with the TWOSTEP method with those computed using TAMCAL shows the following:

- TWOSTEP yields slightly better attitude accuracies than does TAMCAL. This conclusion is most easily seen from the somewhat lower mean values for TWOSTEP than for TAMCAL in Table 2. The GRO TAMCAL values are obviously seriously flawed.
- TWOSTEP is more robust than TAMCAL. TAMCAL sometimes yields biases that produce attitude errors that are out of the range of the attitude errors produced with the other methods. The attitude accuracies may even be worse than if no biases had been applied. These flawed biases were computed for GRO data where most of the significant adjustment had been applied before any of these computations were performed. Even without any further adjustment, the GRO attitudes are quite accurate. It seems possible that the minimization algorithm used in TAMCAL is unstable when it starts very near a minimum; in this case, an initial large jump may lead to poor results.

Comparing the results using different adjustments to the magnetometer data yields an extremely important conclusion:

The algorithm used to compute magnetometer biases affects attitude accuracies significantly less than does knowledge of the additional parameters (A-matrix and torquer coupling) that can be used to adjust the data. This conclusion is most evident in Table 3 where the attitude error ratios vary far less among the calibration methods than does the overall attitude error ratio among the adjustment types.

Comparing the results from the three spacecraft studied indicates the following:

- Comparing the results for EUVE and GRO show that for EUVE the major contributing factor to attitude error is uncertainty in the coupling matrix; whereas for GRO, the uncertainty in the A-matrix dominates. The relative importance of the calibration parameters varies from spacecraft to spacecraft.
- Comparing the attitude errors with all adjustments made and with attitude-dependent biases shows that the better sensor digitization on GRO yields significantly improved magnetometer-based attitude accuracies than the coarse sensor digitization on UARS and EUVE.

These results have shown that to maximize the performance of magnetometers for attitude determination, complete on-orbit calibration should be performed. If this is impossible, accurate prelaunch calibration is desirable. Magnetometer data should be adjusted to compensate for misalignment, scale factor, and torquer coupling, as well as for biases.

Where possible, attitude-dependent bias calibration is preferred. If accurate attitudes are unavailable, inclusion of attitude rate data in the bias calibration improves results. If neither accurate attitude data nor rate data are available, the TWOSTEP method yields more reliable results than does TAMCAL. In addition, the TWOSTEP algorithm is very easy to apply; produces results quickly; and, even in the absence of other calibration, does significantly improve attitudes.

Further work on this subject is needed to evaluate the usefulness of various algorithms (including TWOSTEP) for determining the full set of magnetometer calibration parameters. Extension of this work to spacecraft in polar orbits could also provide further insight into the relative merits of calibration algorithms in different conditions.

References

1. Challa, M., G. Natanson, J. Deutschmann, and K. Galal, *A PC-Based Magnetometer-Only Attitude and Rate Determination System for Gyroless Spacecraft*, Paper No. 07, presented at the GSFC FDD Flight Mechanics/Estimation Theory Symposium 1995, NASA/Goddard Space Flight Center, Greenbelt, Maryland, May 16–18, 1995
2. Shorsi, G., and Bar-Itzhack, "Satellite Autonomous Navigation Based on Magnetic Field Measurements," *Journal of Guidance, Control, and Dynamics*, Vol. 18, No. 4, July–August 1995, pp. 843-850
3. Ketchum, E., *Autonomous Spacecraft Orbit Determination Using the Magnetic Field and Attitude Information*, Paper No. AAS 96-005, presented at the 19th Annual AAS Guidance and Control Conference, Breckenridge, Colorado, February 1996
4. Computer Sciences Corporation, CSC/TM-75/6248, *Determination of Magnetometer Biases Using Module RESIDG*, B. Gambhir, March 1975
5. Davenport, P., W. Ruml, and G. Welter, *In-Flight Determination of Spacecraft Magnetic Bias Independent of Attitude*, presented at the GSFC FDD Flight Mechanics/Estimation Theory Symposium 1988, NASA/Goddard Space Flight Center, Greenbelt, Maryland, May 1988
6. Shuster, M., and R. Alonso, *Magnetometer Calibration for the First Argentine Spacecraft*, Paper No. AAS 95-302, presented at the AAS/AIAA Astrodynamics Specialist Conference, Halifax, Nova Scotia, Canada, August 1995
7. Goddard Space Flight Center, Flight Dynamics Division, 553-FDD-93/032R1UD0, *Multimission Three-Axis Stabilized Spacecraft (MTASS) Flight Dynamics Support System (FDSS) Mathematical Background, Revision 1*, M. Lambertson, J. Keat, and E. Scheidker (CSC), prepared by Computer Sciences Corporation, June 1994
8. Goddard Space Flight Center, Flight Dynamics Division, 554-FDD-93/006R0UD0, *Extreme Ultraviolet Explorer (EUVE) Postlaunch Report*, J. Bez (CSC), prepared by Computer Sciences Corporation, March 1993
9. Goddard Space Flight Center, Flight Dynamics Division, 554-FDD-91/114R0UD0, *Gamma Ray Observatory (GRO), Flight Dynamic Analysis Team Postlaunch Report*, L. Kulp and W. Davis (CSC), prepared by Computer Sciences Corporation, February 1992
10. Goddard Space Flight Center, Flight Dynamics Division, 554-FDD-92/029R0UD0, *Upper Atmosphere Research Satellite (UARS) Postlaunch Report*, J. Bez (CSC), prepared by Computer Sciences Corporation, March 1992
11. Hashmall, J., K. Liu, and M. Rokni, *Accurate Spacecraft Attitudes From Magnetometer Data*, Paper No. MS95/007, presented at the CNES International Symposium on Space Dynamics, Toulouse, France, June 19–23, 1995

Accuracy Studies of a Magnetometer-Only Attitude-and-Rate-Determination System*

M. Challa and C. Wheeler
Computer Sciences Corporation (CSC)
Lanham-Seabrook, Maryland, USA 20706

Abstract

A personal computer-based system was recently prototyped that uses measurements from a three-axis magnetometer (TAM) to estimate the attitude and rates of a spacecraft using no *a priori* knowledge of the spacecraft's state. Past studies using in-flight data from the Solar, Anomalous, and Magnetospheric Particles Explorer focused on the robustness of the system and demonstrated that attitude and rate estimates could be obtained accurately to 1.5 degrees (deg) and 0.01 deg per second (deg/sec), respectively, despite limitations in the data and in the accuracies of the truth models. This paper studies the accuracy of the Kalman filter in the system using several orbits of in-flight Earth Radiation Budget Satellite (ERBS) data and attitude and rate truth models obtained from high-precision sensors to demonstrate the practical capabilities.

This paper shows the following:

- Using telemetered TAM data, attitude accuracies of 0.2 to 0.4 deg and rate accuracies of 0.002 to 0.005 deg/sec (within ERBS attitude control requirements of 1 deg and 0.005 deg/sec) can be obtained with minimal tuning of the filter.
- Replacing the TAM data in the telemetry with simulated TAM data yields corresponding accuracies of 0.1 to 0.2 deg and 0.002 to 0.005 deg/sec, thus demonstrating that the filter's accuracy can be significantly enhanced by further calibrating the TAM.

Factors affecting the filter's accuracy and techniques for tuning the system's Kalman filter are also presented in this paper.

1. Introduction

Contingency algorithms for determining the attitude and rates of a spacecraft using only a three-axis magnetometer (TAM) and using no *a priori* knowledge of the spacecraft's state have been of interest recently in view of situations such as the control anomaly on the Earth Radiation Budget Satellite (ERBS) in 1987 (Reference 1) and the control system failure on the Relay Mirror Experiment (RME) satellite (Reference 2). It has recently been shown (Reference 3) using in-flight data from the Solar, Anomalous, and Magnetospheric Particles Explorer (SAMPEX) mission that an optimal combination of two different algorithms—the Deterministic Attitude Determination From Magnetometer-Only Data (DADMOD) (Reference 2) and the Real-Time Sequential Filter (RTSF) (References 4 and 5)—solves the problem by maintaining both accuracy and robustness. The concept was subsequently automated by prototyping a personal computer (PC)-based system (Reference 6) referred to here as TAMONLY for the Flight Dynamics Division (FDD) at the National Aeronautics and Space Administration (NASA) Goddard Space Flight Center (GSFC).

The working principle of TAMONLY involves using DADMOD to obtain coarse estimates of the epoch state of the spacecraft and then using this state as the initial state for the RTSF's finer estimates. The previous study of TAMONLY (Reference 6) involved extensive tests using a variety of SAMPEX in-flight data and demonstrated that accuracies of 1.5 degrees (deg) in attitude and 0.01 deg per second (deg/sec) in spacecraft rates could be obtained.

* This work was supported by the National Aeronautics and Space Administration (NASA)/Goddard Space Flight Center (GSFC), Greenbelt, Maryland, under Contract NAS 5-31500.

Note that these accuracies are within the attitude requirements for SAMPEX (2 deg). These accuracy estimates, however, are only coarse because of the following factors:

- The most accurate sensor onboard SAMPEX is the Sun sensor, which is accurate to 0.5 deg.
- SAMPEX does not have gyros so that the truth model for the rates was obtained by differentiating the attitude truth model data.
- Short spans of data (< 3000 sec) were used.
- The TAM was not calibrated.
- The TAM is used to determine the pitch angle of the attitude truth model.

TAMONLY was also used to study the above-mentioned ERBS control anomaly, and similar accuracies were obtained (Reference 7). Here again, accurate truth models were absent and only coarse accuracy estimates could be obtained during periods when gyro data were unsaturated in the B-Dot control mode of the spacecraft.

This paper attempts to remedy the situation by focusing on accuracy evaluation of the RTSF in TAMONLY using ERBS in-flight data. The data are from a period when the spacecraft was in its nominal mission mode soon after its launch in 1984; during this period, accurate truth models are available for the attitude via Earth-sensor and fine-Sun-sensor measurements, and accurate gyro data provide the truth model for the rates.

Section 2 of this paper describes the Kalman filter, and Section 3 describes ERBS and the characteristics of the data used in this study. A discussion of the criteria used to evaluate the RTSF is given in Section 4. The results obtained using telemetered TAM data and the results obtained using simulated TAM data are given in Sections 5 and 6, respectively. Section 7 presents a summary of the conclusions of the study.

2. Description of the Kalman Filter

In view of space considerations, only details relevant to the tuning of the RTSF are presented here. A full mathematical description of the RTSF has been provided elsewhere (References 4 and 5).

The RTSF's state vector $\bar{\mathbf{X}}$ comprises of the four components of the attitude quaternion, $\bar{\mathbf{q}}$, and the corrections, $\bar{\mathbf{b}}$, to the spacecraft's rates, $\bar{\boldsymbol{\omega}}$:

$$\bar{\mathbf{X}} = \begin{bmatrix} \bar{\mathbf{q}}^T & \bar{\mathbf{b}}^T \end{bmatrix}^T \quad (1)$$

(Note that the components of $\bar{\mathbf{b}}$ and $\bar{\boldsymbol{\omega}}$ are resolved along the spacecraft's x, y, z axes.)

The RTSF uses sensor data to estimate $\bar{\mathbf{q}}$ as well as $\bar{\mathbf{b}}$, with $\bar{\mathbf{b}}$ being estimated kinematically in the same manner as gyro biases for a gyro-based spacecraft; i.e., by attributing differences between the measured and propagated attitudes to errors in $\bar{\boldsymbol{\omega}}$. The $\bar{\mathbf{b}}$ estimates are then used to correct $\bar{\boldsymbol{\omega}}$, and these corrected rates are used as initial conditions to propagate Euler's equation to the next measurement time. The propagation of $\bar{\mathbf{b}}$ is modeled via a first-order Markov model:

$$\frac{d\bar{\mathbf{b}}}{dt} = -\frac{\bar{\mathbf{b}}}{\tau} + \bar{\boldsymbol{\eta}}_b \quad (2)$$

where $\bar{\boldsymbol{\eta}}_b$ is a white noise term, and τ is a finite time constant. A suitable value for τ is the time between measurements –5 seconds for the SAMPEX data and 16 seconds for the ERBS data used here. (In contrast, the same model, when used for gyro bias estimation, requires a τ of several hours.)

The rates are assumed to contain a white noise component, $\bar{\boldsymbol{\eta}}_a$, and are propagated using Euler's equation after accounting for the angular momentum contributed by the wheels, and the total external torques acting on the spacecraft. TAMONLY currently models the gravity-gradient torque and the magnetic control torque acting on the spacecraft. (The aerodynamic drag torque and the radiation pressure torque have been intentionally omitted to reduce the amount of spacecraft modeling required. The RTSF relies on the rate-corrections, $\bar{\mathbf{b}}$, to compensate for the small effects of these torques.)

The covariance matrix, P , is propagated by numerically integrating the following equation:

$$\frac{dP}{dt} = F(\bar{\omega})P + P F^T(\bar{\omega}) + Q \quad (3)$$

Here $F(\bar{\omega})$ is described in Reference 5; the quantity of interest is the 6×6 matrix Q that quantifies the propagation noise and is of the following diagonal form:

$$Q = \text{diag} [Q_{ax}, Q_{ay}, Q_{az}, Q_{bx}, Q_{by}, Q_{bz}] \quad (4)$$

Here Q_{ax} , Q_{ay} , and Q_{az} represent the strength of the noise term $\bar{\eta}_a$ and contribute to the growth of the attitude error covariances about the body X-, Y-, and Z-axes during propagation. Similarly, Q_{bx} , Q_{by} , and Q_{bz} represent the strength of the noise term η_b , and contribute to the growth of the error covariances of the rate corrections during propagation. These six elements of Q are collectively referred to here as the Q -parameters and rough estimates of their numerical values for ERBS are given in the next section. Another quantity that we must consider during tuning is σ_{TAM} , the strength of the white noise in the TAM measurements.

3. Description of ERBS and Data Characteristics

ERBS is an Earth (geodetic)-pointing three-axis stabilized spacecraft with nominal inclination 57 deg and a nominal altitude of 610 kilometers (References 8 and 9). The onboard attitude requirement of 1.0 deg is met by using a fine Sun sensor of accuracy 0.05 deg and a scan wheel-type Earth sensor of accuracy 0.02 deg. These high-precision sensors are complemented by a TAM onboard the spacecraft. Rate information is obtained from gyros that are accurate to 0.001 deg/sec. Attitude control is achieved through magnetic torquer bars (MTBs) and a momentum wheel that provides momentum bias along the pitch axis (negative orbit normal). A small angular momentum contribution also arises from the scan wheels in the Earth sensor assembly. ERBS also uses thrusters for its monthly 180-deg yaw maneuvers, but these were not activated during the data period discussed here.

The data used in this study are a 13-hour span of processed (adjusted) engineering data generated on the mainframe computers using the ERBS Attitude Ground Support System (AGSS) and covering the period 841225.221932 to 841226.105348. The adjustments comprised mainly bias determinations for the Sun and Earth sensors, the gyros, and the TAM. It is important to note here that the TAM was not calibrated for misalignments and MTB coupling. As shown in Reference 10, these calibrations can significantly alter the performance. The attitude history generated by the AGSS using the adjusted Earth and Sun sensor data is taken as the attitude truth model, and the adjusted gyro data are taken as the truth model for the rates. For the remainder of this paper, the times of events are described relative to the epoch of 841225.221932.

These data were then downloaded to a PC where a dataset having the TAMONLY input format was generated. The processed telemetry was input to TAMONLY at a period of 16 sec (equal to the availability of control torque data) and consisted of the following:

- Time
- Reference magnetic field
- Measured magnetic field
- Dipole moments of the MTBs
- Wheel speeds
- Position and velocity of the spacecraft

The profile of the truth models is presented in Figures 1a through 1c, where Figure 1a shows the true attitude, Figure 1b shows the true rates (where the rate components in the figure are denoted by “wx” “wy” “wz”), and Figure 1c shows the TAM residuals generated by the true attitude. Note the statistics of the data presented in Figures 1a through 1c. For example, it can be seen that the mean residuals are different from zero; in fact, these mean values had to be subtracted off from the TAM measurements input to TAMONLY to improve its performance slightly.

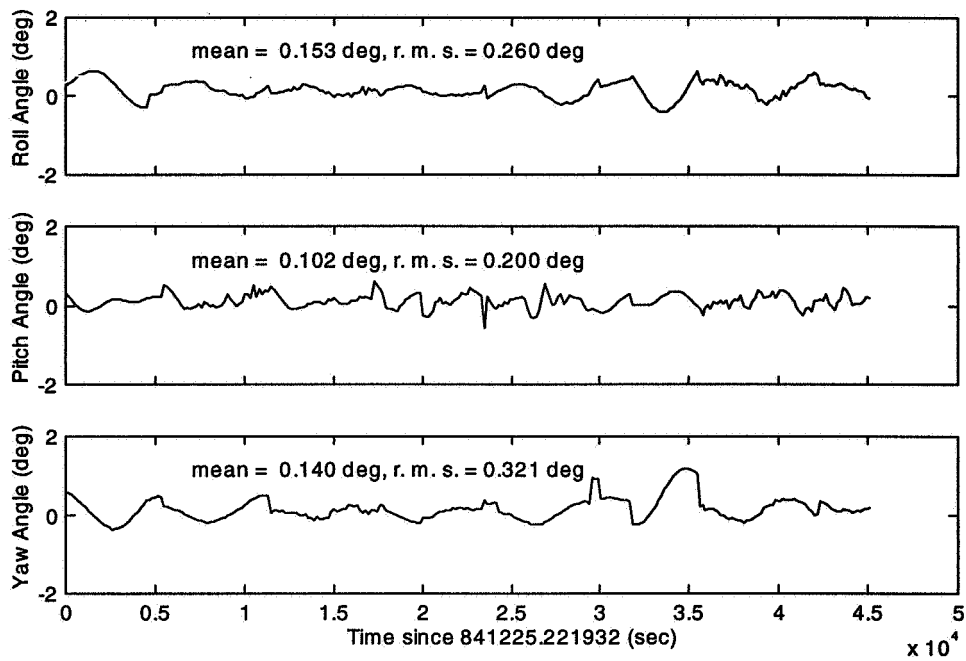


Figure 1a. Profile of the Attitude Truth Model Obtained Using Earth and Sun Sensors

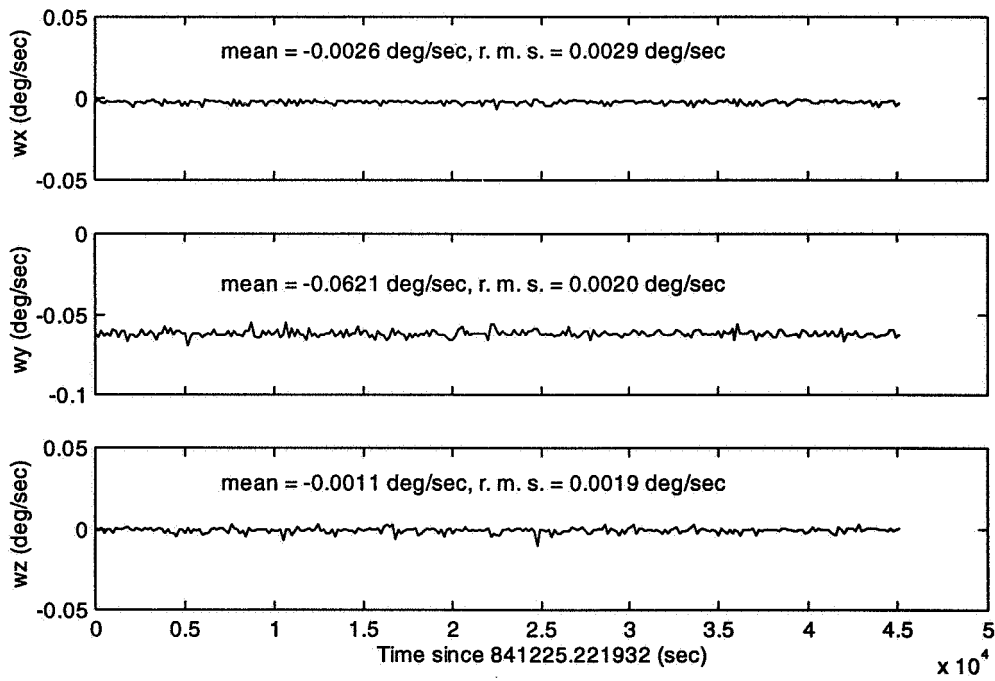


Figure 1b. Profile of the Rate Truth Model Obtained Using Gyros

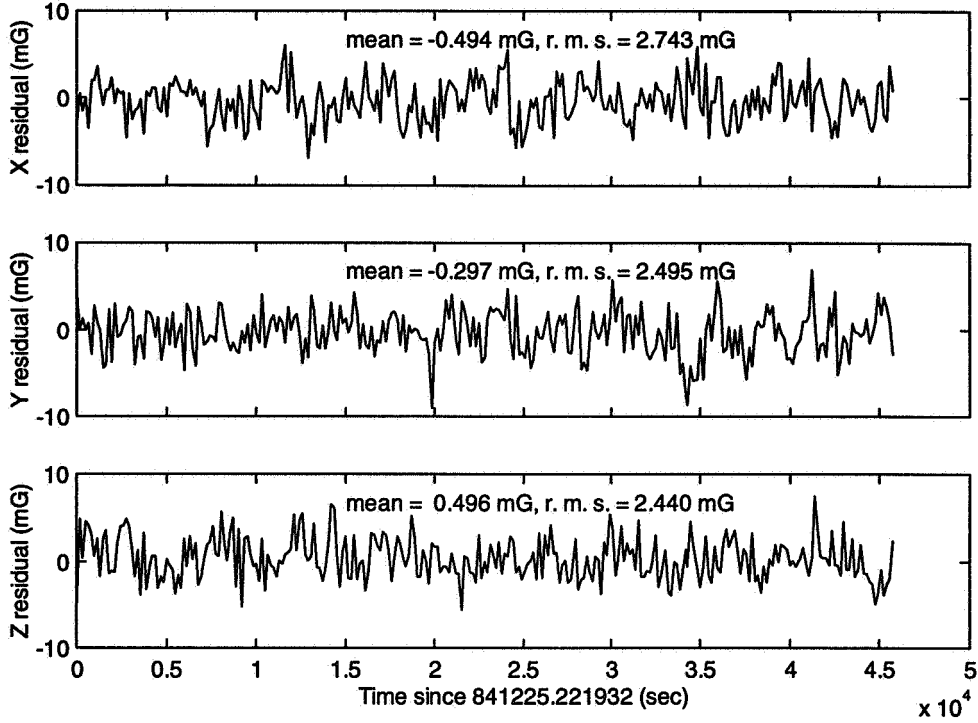


Figure 1c. TAM Residuals Obtained Using the Attitude Truth Model

During the course of this investigation, the optimal tuning parameters for the telemetered data (Section 5) indicated that calibration of the TAM might be in order. To see what effects a perfect TAM might have, simulated TAM data with no noise were generated using the true attitude and the reference magnetic field. These simulated TAM data were then used in place of the actual TAM measurements thus providing a much-needed degree of control over the study, and the results are described in Section 6. Note that only the TAM data were replaced; other quantities, such as the MTB and wheel data, were left untouched in this process.

The noise parameters were determined as follows by considering the noise in the data. The nominal value of σ_{TAM} was determined as 6.4 milligauss (mG), which is the discretization of the TAM data in the telemetry. Regarding the Q-parameters, it was found that the principal source of noise during propagation was the digitization in the telemetered wheel momenta, which was about 0.7 Newton-meter-second (N-m-s) along the Y-axis and 0.01 N-m-s along the Z-axis. In view of the telemetry period of 16 sec, this generated torques of the order of 0.04 N-m and 0.0006 N-m, respectively. It was assumed that the noise torque along the X-axis was of the same magnitude as that about the Z-axis. The squares of the corresponding uncertainties in the spacecraft rates are then

$$(\Delta\omega_x)^2 = 2.3 \times 10^{-8} \text{ radians}^2/\text{second}^2 \text{ (rad}^2/\text{sec}^2) \quad (5)$$

$$(\Delta\omega_y)^2 = (\Delta\omega_z)^2 = 10^{-11} \text{ rad}^2/\text{sec}^2 \quad (6)$$

During the telemetry period, Δt , the attitude error covariances corresponding to the i^{th} axis grow by $(\Delta\omega_i)^2 (\Delta t)^2 \text{ rad}^2$. Because, from Equation (3), Q is the rate of change of P , this yields:

$$Q_{ai} = (\Delta\omega_i)^2 \Delta t \text{ rad}^2/\text{sec}, \text{ (} i = x, y, z) \quad (7)$$

where $\Delta t = 16 \text{ sec}$ and Equations (5) and (6) are to be used for $(\Delta\omega_i)^2$.

The bottom three elements of Q are assigned numerical values by invoking the following relationship (Reference 11) between the steady-state covariance, p_∞ , of an exponentially correlated random variable (such as \bar{b}) and its spectral density, q :

$$q = \frac{2p_\infty}{\tau} \quad (8)$$

It is assumed that the noise in \bar{b} is of the same order of magnitude as that in the rates themselves, so that p_∞ was chosen equal to the squares of the rate uncertainties to yield

$$Q_{bi} = 2 (\Delta\omega_i)^2 / \tau \text{ rad}^2/\text{sec}^3 \quad (i = x, y, z) \quad (9)$$

where $\tau = 16$ sec and the numerical values of $(\Delta\omega_i)^2$ are to be used from Equations (5) and (6).

From Equations (7) and (9), it can be seen that the Q-parameters can be parametrized by the rate uncertainties according to this scheme, and these uncertainties will be used in describing the results of tuning the RTSF. It should be noted that this study is limited to tuning the RTSF noise parameters to improve its performance, and that the errors contributed by imperfect models of the spacecraft's dynamics are ignored here. The latter contributions may, in fact, be sizable because a great number of error sources exist, such as spacecraft mass properties (inertia tensor), flexible modes of the spacecraft, misalignments of the wheel axes, scale factors for the wheel speeds, misalignments of the MTBs, and limitations of the numerical integration algorithms.

4. Accuracy Criteria

The following criteria were adopted to determine the accuracy of the RTSF as well as the optimality of the tuning parameters:

- *Attitude differences*, which are the differences between the true attitude and RTSF estimates
- *Rate differences*, which are the differences between the true rates and RTSF estimates
- *TAM residuals*, which depend upon the accuracy of the propagation, the accuracy of the reference magnetic field, and the accuracy of the TAM. Accurate RTSF estimates are typified by TAM residuals of less than 10 mG.
- *The RTSF's rate corrections*, \bar{b} , which are not to be confused with the rate differences noted above. Accurate RTSF estimates are typified by rate-correction estimates of less than 2 deg/hour. In this study, the rate-correction estimates are used only qualitatively, i.e., they are used to confirm the convergence of the RTSF to the truth model.

DADMODO usually initializes the RTSF to within 5 deg of the true attitude and 0.05 deg/sec of the true rates. The results from the first 5000 sec of a run were omitted from the statistics to allow for filter convergence. Typical results of a TAMONLY run are presented in Figure 2a and 2b where results for the Y- and Z-axes are shown. In these figures, the rate components are denoted by "wy" and "wz," and the components of the RTSF's rate corrections are denoted by "by" and "bz."

5. Results Using In-Flight ERBS Data

About 25 runs were made using a wide range of the noise parameters. A notable (and welcome) feature was that a wide range of numerical values did not alter the accuracies substantially. A sample of the results is shown in Table 1. The first column of Table 1 denotes the numerical values of the noise parameters [σ_{TAM} , $(\Delta\omega_x)^2$, and $(\Delta\omega_z)^2$], together with a mnemonical description of the set. Against each set of tuning parameters, the mean and root-mean-square (r.m.s.) of the attitude differences, rate differences, and TAM residuals for each body axis are displayed. *Note that accuracies of the RTSF are taken to be the r.m.s. values of the differences from the truth model.*

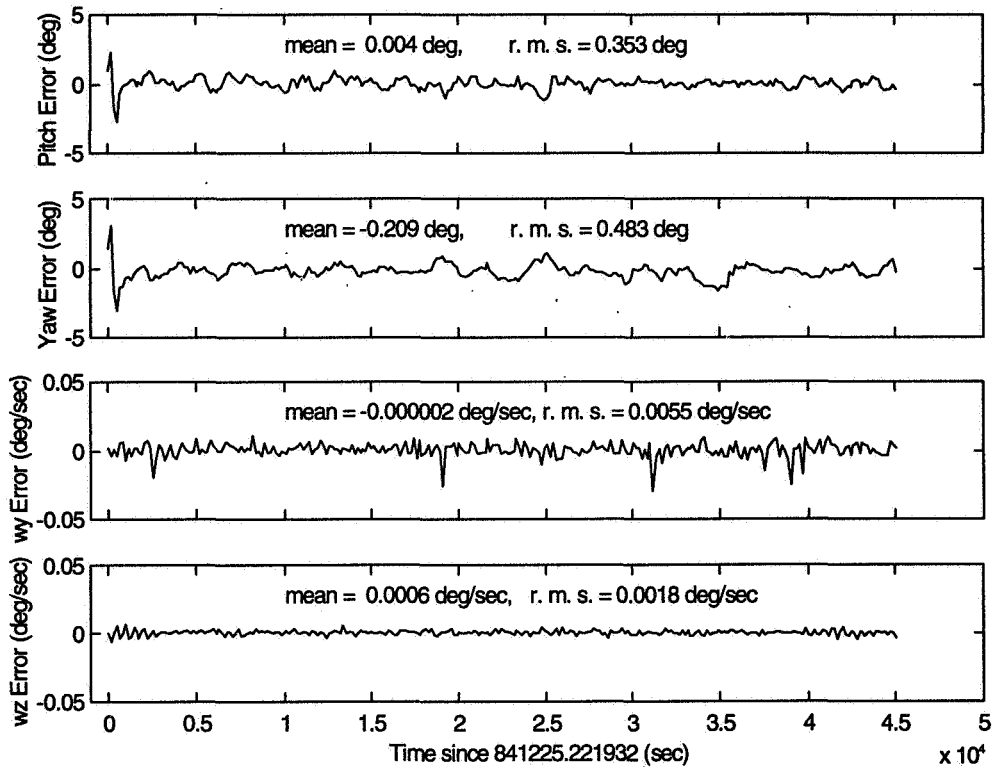


Figure 2a. Typical Attitude Results (Top Two Plots) and Rate Results (Bottom Two Plots) Obtained Using TAMONLY

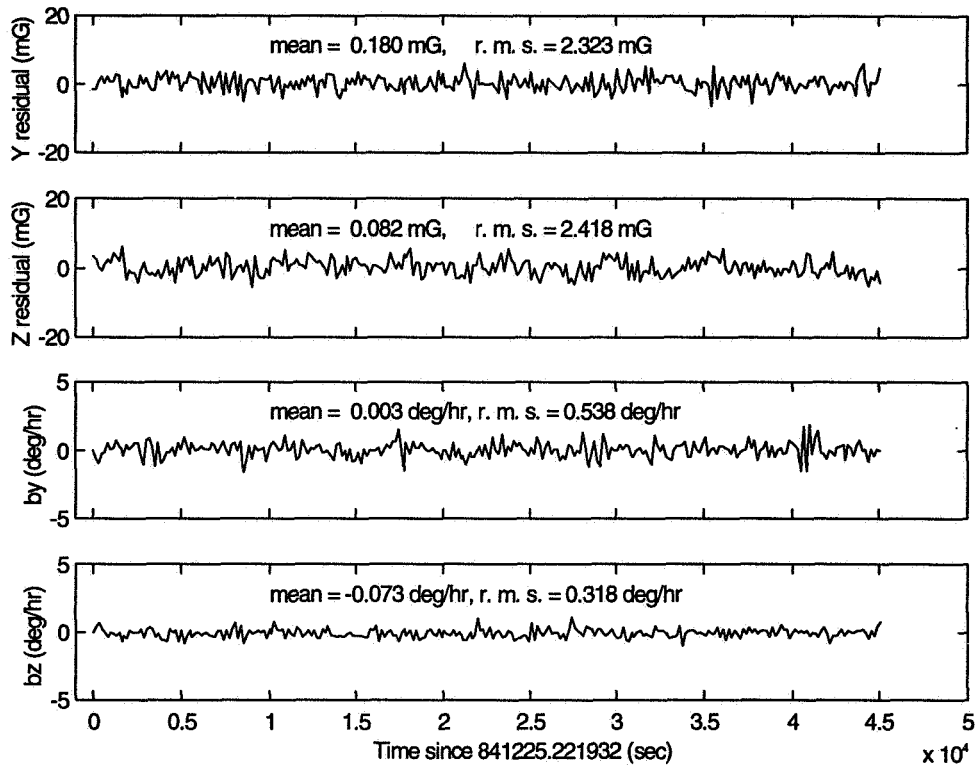


Figure 2b. TAM Residuals (Top Two Plots) and Rate-Correction Estimates (Bottom Two Plots) Obtained During the Run of Figure 2a

Table 1. Error Statistics and Tuning Using 40,200 Sec of Telemetered TAM Data

Description [σ_{TAM} , $(\Delta\omega_x)^2$, $(\Delta\omega_z)^2$]	Attitude Differences With Truth (deg) Mean / r.m.s.			Rate Differences With Truth (deg/sec) Mean / r.m.s.			TAM Residuals (mG) Mean / r.m.s.		
	x	y	z	x	y	z	x	y	z
Optimal [40, 3×10^{-8} , 3×10^{-8}]	-0.071 / 0.214	0.085 / 0.406	-0.080 / 0.434	0.0025 / 0.0030	0.00029 / 0.0054	0.00076 / 0.0020	-0.570 / 2.615	0.229 / 2.327	0.005 / 2.425
SAMPEX defaults (10.4, 3×10^{-8} , 3×10^{-8})	-0.063 / 0.287	0.031 / 0.395	-0.105 / 0.588	0.0026 / 0.0048	0.000033 / 0.0062	0.00076 / 0.0036	-0.140 / 2.756	0.355 / 2.642	0.089 / 2.554
Modeled Q for ERBS (6.4, 2.3×10^{-8} , 10^{-11})	-0.428 / 0.508	0.032 / 0.451	-0.560 / 0.663	0.0026 / 0.0040	0.000083 / 0.0062	0.0005 / 0.0031	-0.457 / 2.784	-0.240 / 3.493	0.756 / 2.681
Large Q (40, 10^{-8} , 10^{-6})	-0.081 / 0.298	0.022 / 0.392	-0.147 / 0.529	0.0026 / 0.0043	0.000030 / 0.0067	0.00077 / 0.0030	-0.137 / 2.812	0.351 / 2.587	0.092 / 2.564
Small Q (3, 10^{-11} , 10^{-11})	-0.275 / 0.383	0.063 / 0.851	-0.453 / 0.610	0.0026 / 0.0038	0.000088 / 0.0057	0.00050 / 0.0029	-0.617 / 2.952	-0.451 / 3.206	0.949 / 2.802

A number of useful deductions can be made by examining Table 1:

- The optimal (i.e., best) parameters yield higher accuracies (0.2 to 0.4 deg in attitude and 0.002 to 0.005 deg/sec in rates) than was concluded from past studies.
- The rate accuracies are relatively insensitive to tuning, indicating that they are dominated by the accuracy of the dynamical modeling (mass properties and torque models) rather than noise modeling.
- The optimal parameters yield TAM residuals comparable in quality with those of Figure 1c, which were obtained from the truth model.
- The large value of σ_{TAM} in the optimal parameters indicates a need for calibrating the TAM for misalignments and for the effects of the MTBs. This, in turn, may be necessitating the different numerical values for the Q parameters than what was roughly estimated in Section 3.

Another issue studied was whether taking averages over an integral number of orbits made a difference in the statistics. Two sets of averages were determined by dividing the timespan into sections spanning: (1) one orbit each (5864 sec) and (2) spanning 4000 sec each. Sample results are presented in Tables 2a and 2b; no significant orbital period effects were detected in the statistics.

6. Results Using Simulated TAM Data

As noted in Section 3, the TAM measurements in the telemetry were replaced with simulated TAM data and the results are shown in Table 3. A number of additional useful deductions can be made by comparing the optimal parameter results of Table 1 with those of Table 3:

- The optimal parameters of Table 1 understandably yield poorer results now, because the σ_{TAM} value of 40 mG is significantly different from the simulated value of 0 mG.
- The TAM residuals are significantly smaller than in Table 1, correctly reflecting the perfect sensor situation.
- The best results (third row of Table 3) are obtained when the modeled noise parameters for ERBS are used and result in accuracies of 0.1 to 0.2 deg in attitude. Note that, although $\sigma_{TAM} = 0$ ideally, a small nonzero value for σ_{TAM} is necessary in practice to avoid divergences. No further improvements in performance were detected for smaller values of σ_{TAM} .
- As in Table 1, the rate accuracies are relatively insensitive to the noise parameters, indicating that further improvements in accuracy must originate from dynamical models.

**Table 2a. Error Statistics Over Orbital Period
(Using Optimal Parameters of Table 1)**

Time Span (seconds)	Attitude Accuracies (deg)		
	Roll (mean, r.m.s)	Pitch (mean, r.m.s)	Yaw (mean, r.m.s)
5008–10880	–0.047, 0.150	0.098, 0.470	–0.092, 0.350
16752–22640	–0.025, 0.207	–0.070, 0.345	–0.106, 0.424
34384–40256	–0.130, 0.223	–0.004, 0.233	–0.357, 0.631

**Table 2b. Error Statistics Over 4000-Second Spans
(Using Optimal Parameters of Table 1)**

Time Span (seconds)	Attitude Accuracies (deg)		
	Roll (mean, r.m.s)	Pitch (mean, r.m.s)	Yaw (mean, r.m.s)
9008–13008	–0.044, 0.169	–0.025, 0.391	–0.165, 0.338
21008–25008	–0.043, 0.200	–0.171, 0.187	–0.329, 0.480
37008–41008	–0.213, 0.296	–0.008, 0.274	–0.282, 0.373

Table 3. Error Statistics and Tuning Using Simulated TAM Data

Description [σ_{TAM} , $(\Delta\omega_x)^2$, $(\Delta\omega_z)^2$]	Attitude Differences With Truth (deg) Mean / r.m.s.			Rate Differences With Truth (deg/sec) Mean / r.m.s.			TAM Residuals (mG) Mean / r.m.s.		
	x	y	z	x	y	z	x	y	z
	Optimal Parameters of Table 1 [40, 3×10^{-8} , 3×10^{-8}]	–0.134 / 0.207	0.042 / 0.313	–0.260 / 0.373	0.0026 / 0.0029	0.00015 / 0.0055	0.00060 / 0.0016	–0.312 / 1.055	0.053 / 0.574
Small σ_{TAM} (10^{-2} , 3×10^{-8} , 3×10^{-8})	–0.117 / 0.230	0.003 / 0.100	–0.190 / 0.282	0.0026 / 0.0031	0.00010 / 0.0054	0.00089 / 0.0019	0.129 / 0.500	0.062 / 0.269	–0.306 / 0.423
Modeled Parameters (10^{-2} , 2.3×10^{-8} , 10^{-11})	–0.093 / 0.179	0.0004 / 0.088	–0.137 / 0.219	0.0026 / 0.0030	0.00008 / 0.0053	0.001 / 0.0019	0.117 / 0.495	0.046 / 0.255	–0.291 / 0.414

7. Conclusions

The principal conclusions derived from this study are as follows:

- Using telemetered TAM data, the accuracies (r.m.s. differences from the truth models) of TAMONLY were found to be

0.2 to 0.4 deg for attitude

0.002 to 0.005 deg/sec for rates

Note that part of the uncertainties here could be due to the errors in the truth models (0.02 deg in roll and pitch angle estimates, 0.05 deg in yaw angle estimates, and 0.001 deg/sec in the gyro rate estimates). Note that these accuracies are within the ERBS control requirements of 1.0 deg for attitude and 0.005 deg/sec for rates.

- The results are *not* severely degraded if the default (SAMPEX) parameters are used. This is a very useful result, since tuning a Kalman filter is a manpower-intensive exercise.
- No significant orbital-period effects were seen in the error statistics.
- The simulated ERBS TAM data were useful by demonstrating the following:
 - Additional calibration of the TAM for misalignments and MTB coupling effects will extract better performance from the RTSF.
 - The modeled noise parameters indeed give better results when the TAM data are of high quality.
 - Very little improvement resulted in the r.m.s. values for rate differences, thus indicating that further improvements in accuracy must be generated by more accurate dynamics, i.e., through improved propagation algorithms and more accurate spacecraft and torque models.

References

1. J. Kronenwetter, M. Phenneger, and W. Weaver, "Attitude Analysis of the Earth Radiation Budget Satellite (ERBS) Yaw Turn Anomaly," *Proceedings of the Flight Mechanics and Estimation Theory Symposium*, NASA Conference Publication 3011, NASA GSFC, Greenbelt, MD, May 1988
2. G. Natanson, "A Deterministic Method for Estimating Attitude From Magnetometer Data Only," Paper No. IAF-92-0036, *Proceedings of the World Space Congress*, Washington, DC, September 1992
3. G. Natanson, M. Challa, J. Deutschmann, and D. Baker, "Magnetometer-Only Attitude and Rate Determination for a Gyroless Spacecraft," *Proceedings of the Third International Symposium on Space Mission Operations and Ground Data Systems*, Greenbelt, MD, November 1994, pp 791–798
4. Goddard Space Flight Center, Flight Dynamics Division, 553-FDD-93/024/R0UD0, *Solar, Anomalous, and Magnetospheric Particles Explorer (SAMPEX) Real-Time Sequential Filter (RTSF) Evaluation Report*, M. Challa (CSC), prepared by Computer Sciences Corporation, April 1993
5. M. Challa, G. Natanson, D. Baker and J. Deutschmann, "Advantages of Estimating Rate Corrections During Dynamic Propagation of Spacecraft Rates—Application to Real-Time Attitude Determination of SAMPEX," *Proceedings of the Flight Mechanics and Estimation Theory Symposium*, NASA Conference Publication 3265, NASAGSFC, Greenbelt, MD, May 1994
6. M. Challa, G. Natanson, J. Deutschmann, and K. Galal, "A PC-Based Magnetometer-Only Attitude and Rate Determination System for Gyroless Spacecraft," *Proceedings of the Flight Mechanics and Estimation Theory Symposium*, NASA Conference Publication 3299, NASA GSFC, Greenbelt, MD, May 1995
7. Computer Sciences Corporation, Memo No. 55701-05, "Attitude Dynamics Studies," M. Challa (CSC) to GSFC Flight Dynamics Division, August 1995
8. ———, CSC/SD-82/6013, *Earth Radiation Budget Satellite (ERBS) Attitude Ground Support System (AGSS) Functional Specifications and Requirements*, G. Nair et al., September 1982
9. ———, CSC/TM-84/6071, *Earth Radiation Budget Satellite (ERBS) Attitude Analysis and Support Plan*, M. Phenneger et al., August 1984
10. J. Hashmall (CSC) and J. Deutschmann (GSFC), "An Evaluation of Attitude-Independent Magnetometer-Bias Determination Methods," *Proceedings of the Flight Mechanics/Estimation Theory Symposium*, Greenbelt, MD, May 1996
11. A. Gelb (ed.), *Applied Optimal Estimation*. The MIT Press: Cambridge, Massachusetts, 1974

Geostationary Operational Environmental Satellite (GOES) Gyro Temperature Model*

J. N. Rowe and C. H. Noonan
Computer Sciences Corporation
Lanham-Seabrook, Maryland, USA 20706

J. Garrick
National Aeronautics and Space Administration
Goddard Space Flight Center
Greenbelt, Maryland, USA 20771

Abstract

The Geostationary Operational Environmental Satellite I/M (GOES I/M) series of spacecraft are geostationary weather satellites that use the latest in weather imaging technology. The inertial reference unit package onboard consists of three gyroscopes measuring angular velocity along each of the spacecraft's body axes. This digital integrating rate assembly (DIRA) is calibrated and used to maintain spacecraft attitude during orbit delta-V maneuvers.

During the early orbit support of GOES-8 (April 1994), the gyro drift rate biases exhibited a large dependency on gyro temperature. This complicated the calibration and introduced errors into the attitude during delta-V maneuvers. Following GOES-8, a model of the DIRA temperature and drift rate bias variation was developed for GOES-9 (May 1995). This model was used to project a value of the DIRA bias to use during the orbit delta-V maneuvers based on the bias change observed as the DIRA warmed up during the calibration. The model also optimizes the yaw reorientation necessary to achieve the correct delta-V pointing attitude. As a result, a higher attitude accuracy was achieved on GOES-9 leading to more efficient delta-V maneuvers and a propellant savings.

This paper will summarize the

- Data observed on GOES-8 and the complications it caused in calibration
- DIRA temperature/drift rate model
- Application and results of the model on GOES-9 support

Introduction

The GOES I/M series of spacecraft are the new generation of geostationary weather satellites. The first two spacecraft of this series have been launched (GOES-8 on April 13, 1994 and GOES-9 on May 23, 1995) and are operational. The third, GOES-K, is currently planned for launch in March 1997. A summary of the characteristics of the GOES spacecraft, mission profile, and flight dynamics experience during the orbit-raising support of GOES-8 is given in References 1 and 2. The present paper expands on the topic of DIRA calibration that was introduced in Reference 1, and discusses calibration results from GOES-9.

Figure 1 shows the GOES spacecraft in its configuration during the orbit-raising phase of the mission with the solar array partially deployed. The roll, pitch, and yaw axes are indicated, along with the locations of the main satellite thruster (MST) on the $-X$ face and the DIRA on the $-Y$ face.

* This work was supported by the National Aeronautics and Space Administration (NASA)/Goddard Space Flight Center (GSFC), Greenbelt, Maryland, under Contract NAS 5-31500.

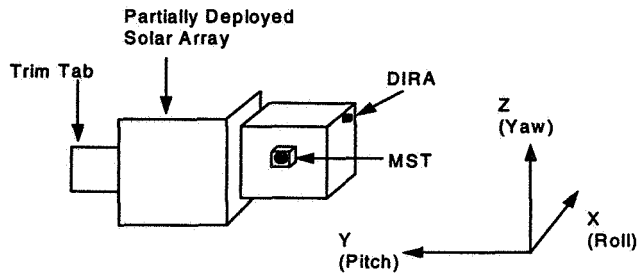


Figure 1. GOES Transfer Orbit Configuration

For some of the GOES mission attitude control modes, the spacecraft is dependent on the DIRA to maintain accurate pointing. In particular, during orbit maneuvers the yaw axis DIRA is used for position control to maintain the spacecraft yaw attitude. Maintaining the delta-V pointing attitude as close as possible to the target allows for an efficient orbit transfer. This requires, however, that the rate bias of the DIRA be determined and then compensated in the onboard control system by uplinking the bias to the spacecraft. Because of the length of the burns, which can approach 100 minutes, any DIRA rate bias residual can accumulate over the length of the burn to produce a significant pointing error, resulting in excess expenditure of fuel.

It is because of this potential for a large error that the Flight Dynamics Facility (FDF) produces a calibration scheme for the DIRA. Under ideal conditions, the DIRA would be calibrated under attitude pointing conditions that would exist for the burn. Unfortunately, the mission does not allow for the ideal. A series of perigee-raising maneuvers are performed during the orbit-raising phase. During the half orbit before each of these maneuvers a sequence of events is executed that includes a yaw reorientation (reor) to cool the MST, DIRA calibration, uplink of the DIRA bias, switch of the control mode to put the yaw DIRA in the control loop, update of the DIRA bias uplink, and finally yaw and pitch reors to the maneuver attitude. During a practice of this sequence in the half orbit before the first apogee all of these steps are performed, except no actual maneuver takes place. The first maneuver is done on fourth apogee.

The experience on GOES-8 showed variations in the determined DIRA rate biases from the time of calibration and uplink to the time of the maneuver. The major cause of this was found to be variable DIRA temperatures combined with a strong, but not consistent, dependence of the rate bias on the temperature. The temperature variations were caused by the changing spacecraft-Sun geometry throughout the premaneuver period. Thus it became desirable to create a model to account for these variations and predict an accurate DIRA rate bias for a future time.

DIRA Temperature and Bias Characteristics

The temperature of the DIRA varies during the course of calibration and the orbit maneuver because of the changing Sun angle. Figure 2 shows as an example the history of the DIRA temperature during the GOES-9 apogee maneuver firing (AMF)-1 activities. This behavior may be understood by considering Figures 3 and 4, which illustrate the orbit and attitude geometry, respectively, during this period.

Figure 3 illustrates the geometry looking into the orbit plane. The -X axis points generally toward the Sun, and the Z-axis toward the Earth. Figure 4 is an edge-on view of the orbit plane looking from the direction of apogee back toward the Earth to illustrate the yaw attitude geometry. The quiescent attitude [Figure 4(a)] has the Sun on the -X axis, and is intended to maximize power on the solar array during orbits without maneuvers. At the start of the DIRA calibration (time = 0 in Figure 2), the Earth is captured with the Earth sensor, followed by a yaw reor to

move the Sun as far as possible off the $-X$ axis. This yaw reor was not in the initial GOES mission design, but was added during the GOES-8 support when a thermal problem in the MST caused the first maneuver to be aborted. Yaw is controlled with the digital Sun sensor (DSS) at this time, and the mounting of the DSS forces the yaw reor to be in the direction shown in Figure 4(b). While keeping the MST cool, this reor has the effect of allowing the Sun to hit the DIRA mounted on the $-Y$ face, so its temperature increases. This increase continues until the yaw reor to the AMF attitude [Figure 4(c)], where the DIRA is in shadow again and begins to cool down. This yaw reor occurs at time = 3 hr in Figure 2.

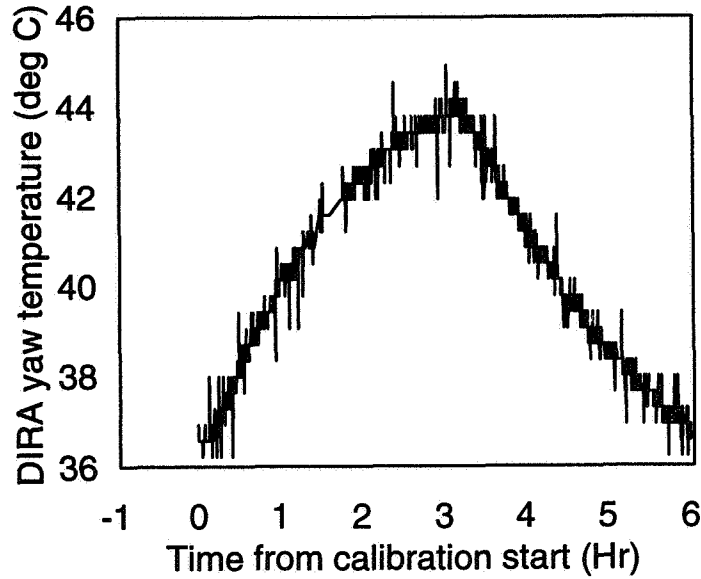


Figure 2. DIRA Temperature During GOES-9 AMF-1

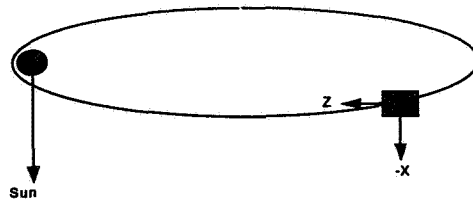
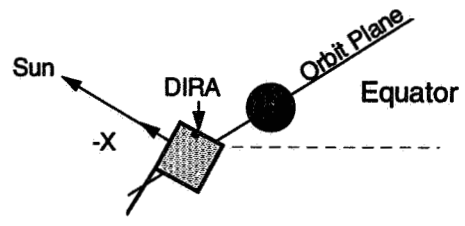
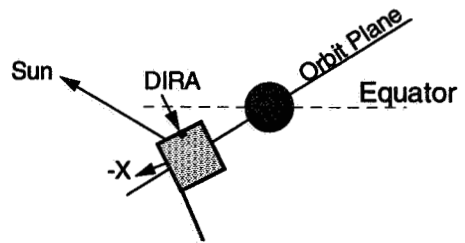


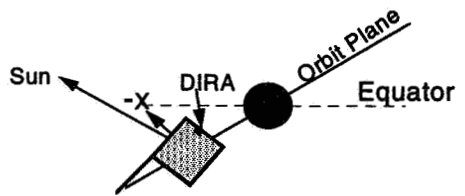
Figure 3. GOES Orbital Geometry



(a)



(b)



(c)

Figure 4. GOES Attitude Geometry

This temperature variation by itself would not be a problem, except that during the DIRA calibration activities for the GOES-8 mission, a temperature dependence of the DIRA rate bias was detected. A linear variation of the rate bias with temperature was measured, as shown in Figure 5. To further complicate the problem, the slope and intercept were not consistent from one maneuver to the next. On GOES-8, the rate of change of rate bias ranged from 0.12 to 0.24 deg/hr/deg C and the bias at constant temperature up to 2 deg/hr. The requirement for attitude control during the AMFs is 1.57 deg, so the variations noted in Figure 5 have a significant effect. As a result of this, and in spite of attempts to project the best value of bias to use, attitude errors during the orbit maneuvers on GOES-8 were as large as 0.6 deg.

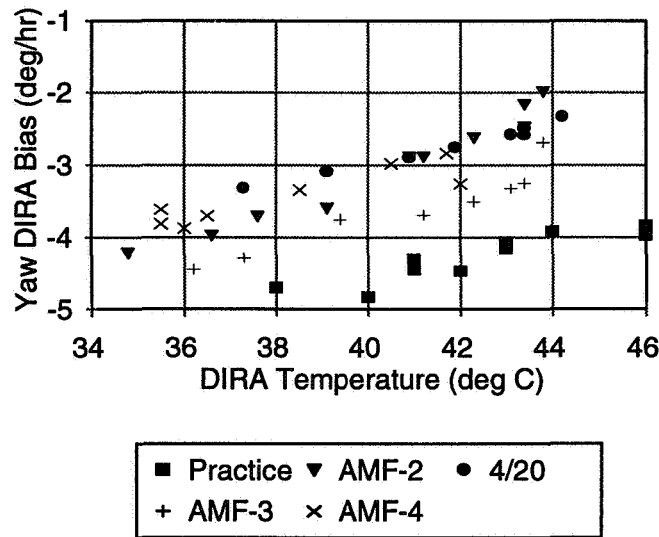


Figure 5. DIRA Biases for GOES-8

The ideal situation is to have the attitude constant at the target value during the entire AMF, because this is the way the maneuver software models the burn. However, the continuously varying DIRA temperature produces a continuously varying bias, and hence a continuously varying yaw attitude when the DIRA is used to control the attitude. Only a constant value of the bias can be uplinked, and so the attitude rate can be made zero only at one point. Thus, selection of an uplink rate bias value is at best a compromise. The compromise chosen was to make the attitude rate zero at the midpoint of the burn, and then a target for the reor was chosen such that the attitude is correct at the midpoint of the burn.

Two models were actually developed: one to describe the DIRA rate bias variations and one to describe the resulting yaw attitude variations. These are discussed in the next section.

Model Development

From the data collected during the early mission support of GOES-8, a model for the temperature profile and the rate bias behavior was developed to serve as the basis for the GOES-9 calibration procedure. Review of the GOES-8 DIRA temperature histories indicated a consistent pattern of temperature increasing at an average rate of 2.8 deg/hr until the AMF yaw reor, and then decreasing at an average rate of 4.0 deg/hr afterward, as illustrated schematically in Figure 6. In particular, the ratio, K , of the slopes was found to be nearly constant from maneuver to maneuver at an average value of -1.43 . The small exponential variation evident in Figure 2 was neglected.

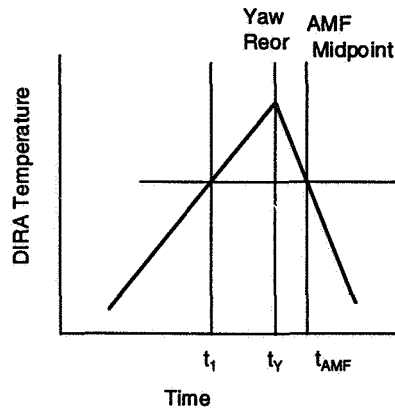


Figure 6. Typical DIRA Temperature Profile

Although the temperature dependence of the DIRA bias changed from maneuver to maneuver on GOES-8, the dependence was always linear. Thus, we expect the DIRA bias at t_1 , the time where the DIRA temperature is the same as it is at t_{AMF} (the midpoint of the AMF), to be the same as the DIRA bias at t_{AMF} , and this along with K being constant forms the basis of the model. The time t_1 can be found given K , the AMF midpoint time, t_{AMF} , and the yaw reorientation time t_Y .

$$t_1 = t_Y + K(t_{AMF} - t_Y)$$

Note that the validity of this model depends on K being constant from maneuver to maneuver (which was in fact observed on GOES-8) and on the reor and burn occurring on the times in the script. The actual bias and time rate of change of the bias are determined for each maneuver and thus need not be constant from maneuver to maneuver.

During the DIRA calibration period, 20-minute sliding batch-least squares solutions are obtained and a linear function of time fit to these measurements. Typically, the first DIRA bias uplink is required before t_1 is reached, so the fit is actually extrapolated to this time. The fit also has the effect of smoothing the scatter in the 20-minute solutions.

At a time t_p (after the first bias uplink), the spacecraft is put into a mode where the yaw attitude is controlled by the yaw DIRA. At a later time t_u , an updated bias of value B_u is uplinked. This value is obtained from the fit as before, but it now covers a longer period of time such that t_1 is within the period of the fit. Also, any effects from orbit rate coupling are included in this uplink. The orbit rate coupling effect occurs because of nonzero yaw and pitch attitude during the time the spacecraft rotates about the yaw axis at the orbit rate. This uplink is followed by the reor to the maneuver attitude at time t_Y , and finally by the maneuver itself, with time of midpoint t_{AMF} .

Because the temperature is a linear function of time and the bias is a linear function of temperature, the bias, B , will be a linear function of time

$$B(t) = B_0 + \dot{B}(t - t_0) \quad \text{for } t < t_Y$$

where B_0 and \dot{B} are obtained from the linear fit of bias versus time as described above. Because the bias is a linear function of the temperature, the ratio of the rates of change of the bias before and after the yaw reor will also be equal to K , so

$$B(t) = B_0 + \dot{B}(t_Y - t_0) + K\dot{B}(t - t_Y) \quad \text{for } t \geq t_Y$$

K is found from the slopes of temperature versus time before and after the yaw reorientation. After the event is over, K is found and used on the next event. In general, the yaw attitude rate is given by the following:

$$\dot{Y} = B_C - B(t)$$

where B_C is the commanded DIRA drift rate bias, and the yaw attitude by

$$Y = Y_0 + \int_{t_0}^t \dot{Y} dt$$

The above equations may be evaluated to predict Y , keeping in mind that B_C has one value at t_P and another at t_U . The value of the orbit rate coupling is added to B at the time of the pitch reor. The initial yaw attitude is Y_0 at t_P as determined from attitude solutions; the value at t_Y is incremented by a step of the amount of the yaw reorientation. In actual use, the size of the yaw reorientation is adjusted, and the model is run in an iterative fashion until the best approximation to the target maneuver attitude is obtained.

Application of the Model to GOES-9

Following is a summary of the results obtained on GOES-9 for the three cases (practice, AMF-1, and AMF-2) when the DIRA temperature variation occurred. Detailed results are shown for AMF-1, and the other events are summarized.

The DIRA temperature profile during the practice DIRA calibration showed a ratio of the rise and fall slopes to be approximately -1.0 rather than the -1.43 observed on GOES-8. Because of this, the predicted bias after the yaw reorientation did not match well with the actual bias. This was not a problem because no maneuver took place, and the goal of the practice calibration was in fact to refine the parameters of the model for use on AMF-1 and on AMF-2.

The DIRA yaw temperature variation for AMF-1 was shown in Figure 2. Note that the shape is not strictly linear (as assumed in the model) but has an apparent exponential component, as might be expected from thermodynamics. Modeling this may be a way to refine the model for the future. In any event, the fit of the DIRA drift rates as a function of time is shown in Figure 7. The peak-to-peak residual from the linear fit is about 0.2 deg/hr, which includes the effect of nonlinearity in the bias as well as scatter in the bias solutions. This is an indication of the size of the DIRA bias uncertainty.

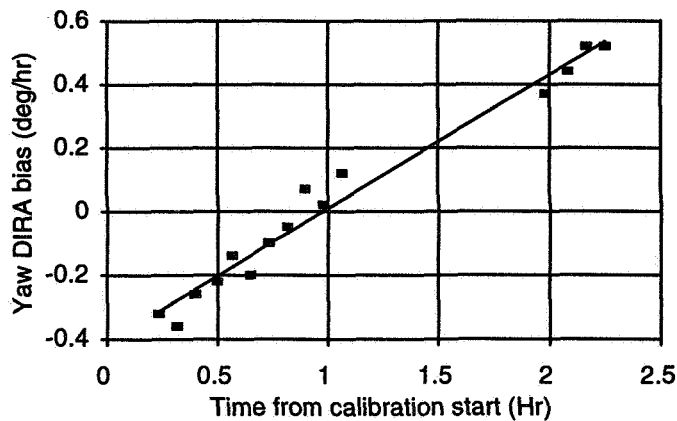


Figure 7. Yaw DIRA Bias Versus Time for GOES-9 AMF-1

A 4-minute telemetry dropout occurred during the calibration period for AMF-1. This gap was too large to interpolate across accurately and hence affected the quality of the solutions. Therefore, biases were not computed for a period of 20 minutes on either side of the gap. Based on the fit before the gap, a DIRA yaw bias of 0.7 deg/hr was selected. The value was then updated to 0.5 deg/hr after the gap (the additional data reduced the slope slightly). This value inadvertently did not include the predicted orbit rate coupling of -0.16 deg/hr. The yaw reo was then planned, taking into account the fact that the orbit rate coupling had not been included in the bias uplink. Figure 8 shows predicted and observed yaw attitudes starting shortly after the yaw reor. The prediction was done at the time using the actual uplinks and modeling the effect of the orbit rate coupling given these uplinks. The horizontal line in this figure indicates the target attitude; the midpoint of the AMF occurs at the 4-hour mark.

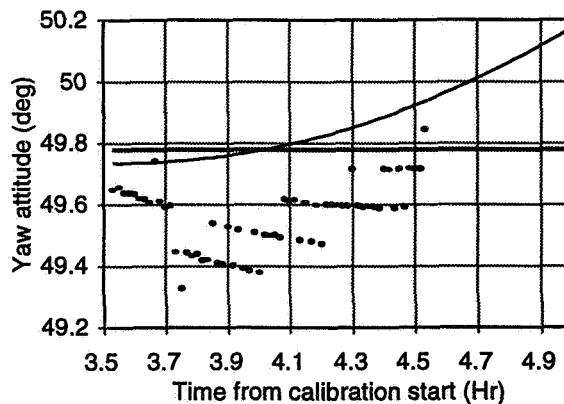


Figure 8. Predicted and Observed Yaw Attitude for AMF-1

Figure 8 indicates that the attitude should have been correct at the midpoint of the burn with a positive rate because the orbit rate coupling in the DIRA bias was not included. However, because of a negative yaw hangoff during AMF-1, the actual attitude was 49.6 deg on average, slightly less than the target of 49.78 deg. The actual attitude

rate was positive as expected. The yaw hangoff was neglected by prelaunch agreement with the flight operations team (FOT), because the value was uncertain before launch but expected to be well within the allowable yaw attitude error. In fact, AMF-1 turned out to be a very successful maneuver with the final inclination within 0.13 deg of the target.

In the case of AMF-2, the DIRA temperature and DIRA drift rate bias as a function of time were similar to AMF-1. A yaw hangoff of -0.2 deg was included in the yaw reor command, based on the value at the end of AMF-1. The orbit rate coupling was negligible. The final attitude during AMF-2 was very close to the target (31.36 deg versus 31.29 deg), and predicted rates agreed well.

Temperature Dependence of DIRA Bias for GOES-9

On GOES-8 the temperature dependence of the DIRA biases varied in a nonsystematic way from event to event. The behavior on GOES-9 up through AMF-2 was much more consistent, as shown in Figure 9. The slope of the linear fit in Figure 9 is 0.18 deg/hr.

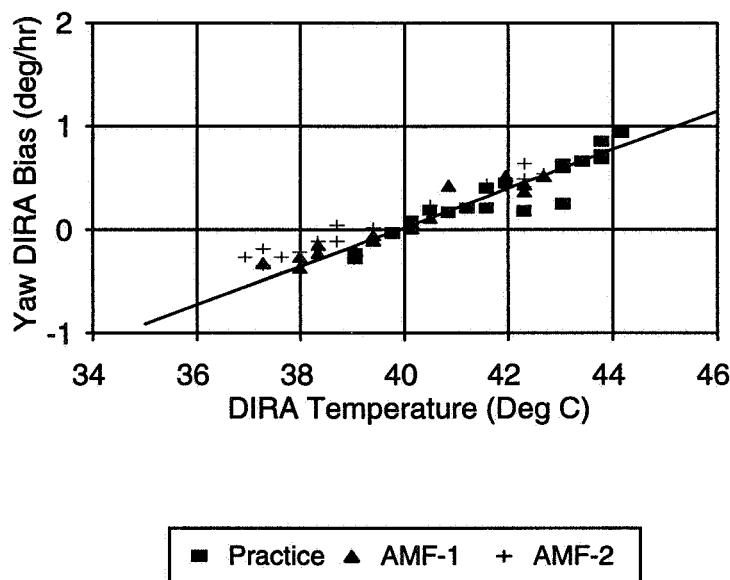


Figure 9. DIRA Biases for GOES-9

Conclusions

The experiences on GOES-8 and GOES-9 described in this paper provide an interesting case study of how real life in mission support is often different from what is expected before launch. The technique described here for estimating the DIRA drift rate biases and the yaw reorientation resulted in actual average yaw attitudes within 0.3 deg of the target attitude in the presence of changing DIRA temperatures and drift rates. This is a factor of two improvement over GOES-8. More importantly, mechanizing the procedure reduces greatly the chances of a much larger error occurring because of human error in trying to estimate a value of bias to use. Major sources of error in this technique include nonlinearity in the time dependence of the bias, uncertainty in the bias solutions, and variations in the actual times of reorientations and bias uplinks from those planned in the script. Modeling the nonlinearity might be a way to improve the results, but, considering that 0.3 deg is already much less than the requirement of 1.57 deg and that the other sources of error will still exist, the point of diminishing returns has probably been reached. However, a study of the actual and predicted yaw hangoffs for AMF-1 on GOES-8 and

GOES-9 might be useful to determine if a predicted yaw hangoff could reasonably be included in the AMF-1 planning for future GOES missions.

Acknowledgment

The authors wish to express their appreciation to S. Kirschner of Computer Sciences Corporation for his helpful review and assistance in the preparation of this paper.

References

1. C. H. Noonan, et al., "Geostationary Operational Environmental Satellite (GOES)-8 Mission Flight Experience," presented at the Flight Mechanics/Estimation Theory Symposium, GSFC, May 16–18, 1995.
2. W. Forcey, et al., "Evaluation and Modeling of Autonomous Attitude Thrust Control for the Geostationary Operational Environmental Satellite (GOES)-8 Orbit Determination," presented at the Flight Mechanics/Estimation Theory Symposium, GSFC, May 16–18, 1995.

ATTDES- An Expert System for Satellite Attitude Determination and Control, II

Donald. L. Mackison
Kevin Gifford

University of Colorado
Aerospace Engineering Sciences
Campus Box 429
Boulder, CO 80309-0429

(303) 492-6417
(303) 492-5514 (FAX)
mackison@spot.colorado.edu (e-mail)

Abstract

The design, analysis, and flight operations of satellite attitude determination and attitude control system (ADACS) require extensive mathematical formulations, optimization studies, and computer simulations. This is best done by an analyst with extensive education and experience. The development of programs such as ATTDES permit the use of advanced techniques by those with less experience. Typical tasks include the mission analysis to select stabilization and damping schemes, attitude determination sensors and algorithms, and control system designs to meet program requirements. ATTDES is a system that includes all of these activities, including high fidelity orbit environment models that can be used for preliminary analysis, parameter selection, stabilization schemes, the development of estimators and covariance analyses, and optimization, and can support ongoing orbit activities. The modification of existing simulations to model new configurations for these purposes can be an expensive, time consuming activity that becomes a pacing item in the development and operation of such new systems. The use of an integrated analysis tool such as ATTDES significantly reduces the effort and time required for these tasks.

Introduction

ATTDES consists of an extensive library of programs that covers much of these areas, and which is linked through a user driven system to model a wide range of configurations and to perform analyses. So that the

system may easily model a wide variety of satellites, the equations of motion are developed with generalized models. Whereas the formulation of dynamical equations of motion for simple spacecraft can be accomplished with essentially equal ease by means of any one of a number of methods, the task of formulating such equations for complex spacecraft can become prohibitively laborious unless a particularly effective method is employed. Kane, Roberson, Wittenburg and others have developed such methods. Through the use symbolic mathematics capability of MAPLE and the MATLAB Symbolic Math Toolbox, general equations of motion for very complex dynamic system can be developed by specifying symbolically the elements to be included in the equations of motion, including their alignment, location, and mass properties.

The software platform on which ATTDES is developed is the extremely popular MATLAB that is the present and foreseeable state-of-the-art in numerical computation as well as control design and simulation. With over 100,000 installed systems world-wide, MATLAB has become the standard high performance computing platform in control engineering and science. Because of the integrated nature of MATLAB, the evolution of ATTDES will include image processing and signal processing capabilities. Not only can such systems be modeled, but flight code can be generated quickly in standardized ANSI C. The use of MATLAB enables the system to run on all major computer platforms, including mainframes, workstations, and personal computers. Further, the complete MATLAB collection of toolboxes for Control Design, Robust Control Design, Optimization, Neural Networks is available for application to the satellite dynamic model in the workspace. By having the system cover a broad range of satellite configurations, the development of control laws for complex spacecraft will cease to be a pacing item in the development of new and unique attitude control systems. Rather, such analysis may be performed accurately and efficiently in a minimum amount of time. This system has been used to support design ADACS's for AXAF (Advanced X-Ray Astrophysical Facility), and for the STILLSAT (Staring, Imaging, Long-Look Satellite) and CUPS (Celestial Ultraviolet Photometric Survey) proposals to NASA/USRA.

Generalized architectures for equations of motion, together with the automatic generation of dynamic equations using the MAPLE symbolic manipulation capabilities through the MATLAB Symbolic Math Toolbox allow the inclusion of arbitrary structures such as flexible elements (i.e., the solar panels on the Hubble Space Telescope), angular momentum devices such as control moment gyros and momentum wheels, along with N₂, hydrazine, and electric thrusters. Conventional attitude sensors such a Sun, Earth, and star sensors, as well as new technologies including Gravity Gradiometer and GPS sensors are easily included in the generalized attitude determination package. Advanced capabilities of ATTDES include extensive use of the image processing capabilities of MATLAB for visualization of stability and robustness information generated through the design process.

A common problem in the preliminary design of satellite attitude control systems and attitude determination systems is the generation of design data. One approach is to take the detailed simulation of the latest spacecraft design and modify it to match the new configuration. This can be an excruciating process, and often as not, does not lead to the desired result- a successful preliminary design analysis. Our objective here was to use Matlab in such a fashion that an inexperienced analyst could generate equations of motions for a variety of satellite configurations, specify a desired orbit, choose a stabilization scheme, linearize the equations of motion in a desired coordinate frame, design control gains, apply the control scheme to the linearized system, and finally, to generate a detailed nonlinear simulation including aerodynamic, gravity gradient, and radiation pressure effect.

Functions

It is intended that the programs in ATTDES will easily perform control system design, attitude determination, closed loop attitude determination/attitude control, and attitude covariance analysis. To this end, the principal function of ATTDES is the construction of the equations of motion for the chosen satellite configuration, and the generation of an appropriate linearization of the equation for control systems design, the development of attitude estimators, and covariance analysis studies.

Program Structure

The Matlab program consists of 50 programs run under a menu tree structure, selected by a menu utility (DOS version) or by push buttons and radio knobs (windows version). Data is entered into .dat files to create a model, or read from .dat files, modified, and stored in data files to modify the model. All data is passed through argument lists to each of the functions, and there is no common or global data throughout the system.

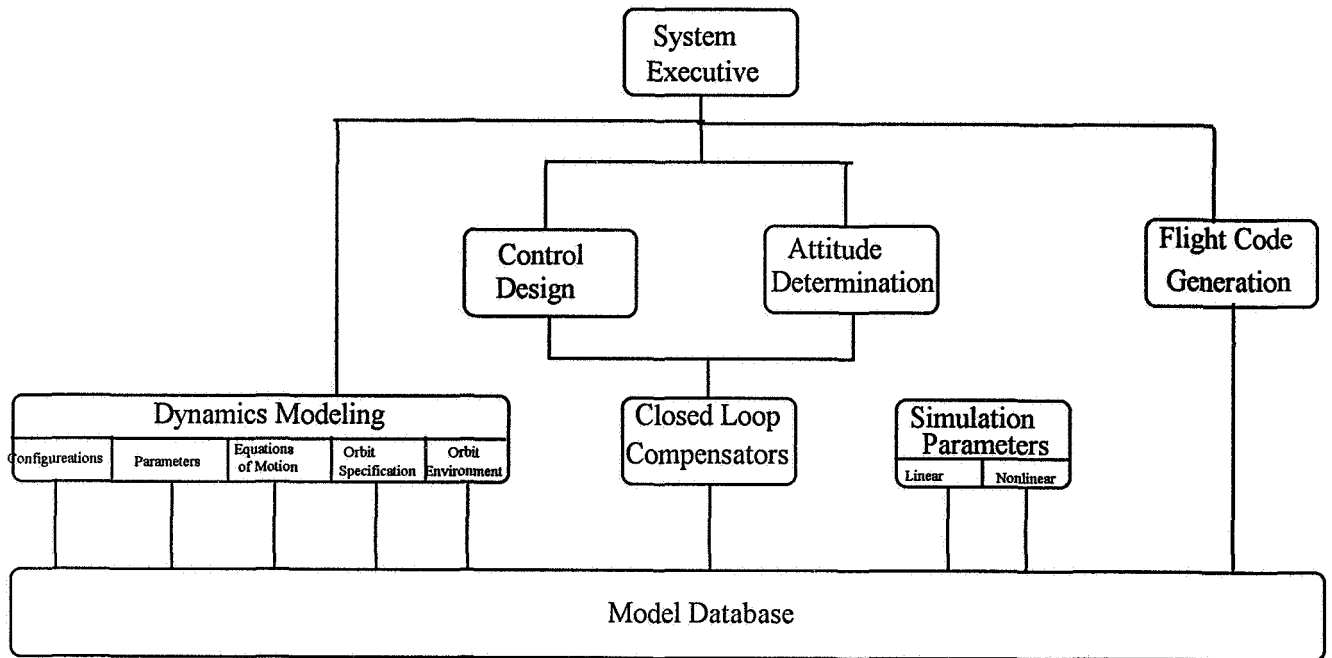


Figure 1: High Level Software Flow Diagram for the ATTDES System

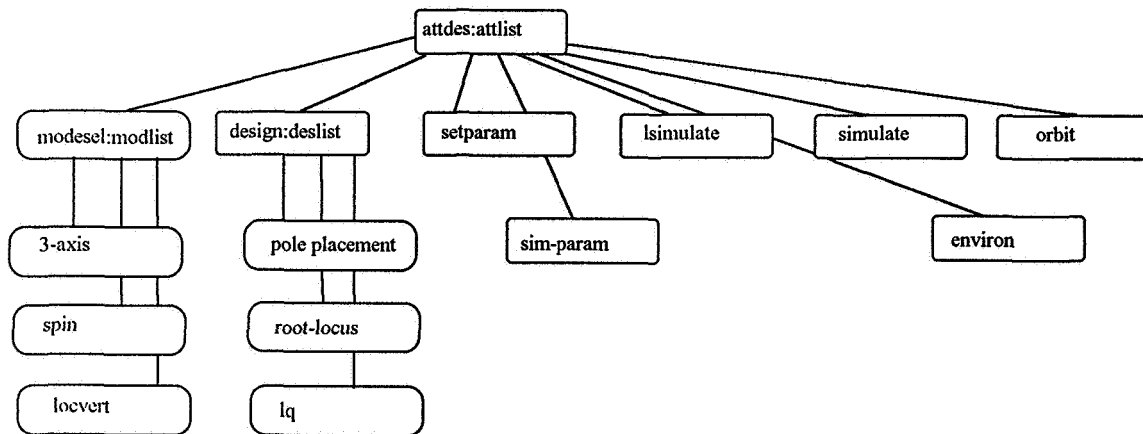
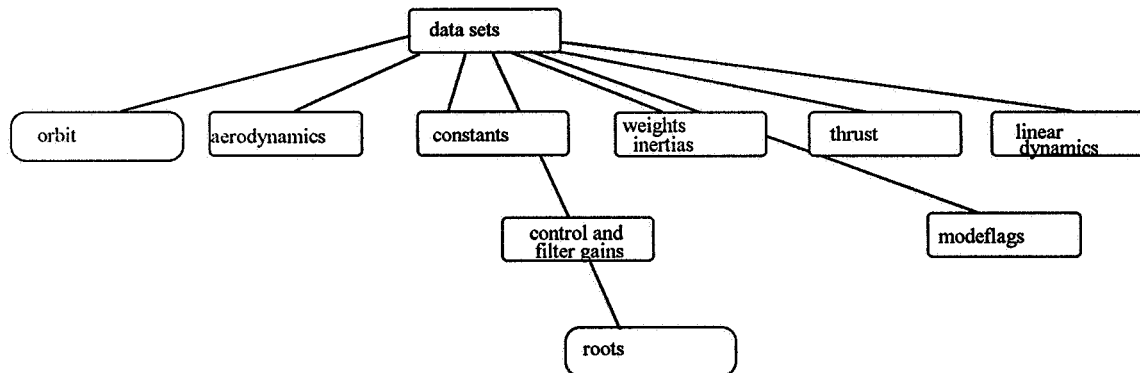


Figure 2: Detailed Flow for ATTDES System

- ATTDES: Program executive
- Modsel: Select mode of dynamics (3-axis, spin, dual spin, gravity gradient, momentum bias local vertical, etc.)
- Generate full nonlinear dynamic equations of motion for the configuration (Euler's equations for coupled bodies) and kinematic equations (quaternions)

	Generate linearized equations of motion
Design:	Compute control gain- pole placement, root locus, lq, etc. Compute filter gains
Setparam	Set satellite physical parameters including mass and inertia, cross section for atmospheric and radiation pressure effects
Sim-param	Set simulation parameters- initial state vector, limits on integration
Lsimulate	Propagate the state vector using the state transition matrix.
Simulate	Integrate the full non-linear equation using a Runge-Kutta Felberg algorithm (rkf45)
Orbit	Select the satellite orbit, generate transformation from ECI to LV to Body frame.
Environ	Examine the magnetic, solar, and atmospheric environment over the orbit.

As each function of the program is exercised data is read from these data sets, new parameters computed, and saved into the appropriate data set.

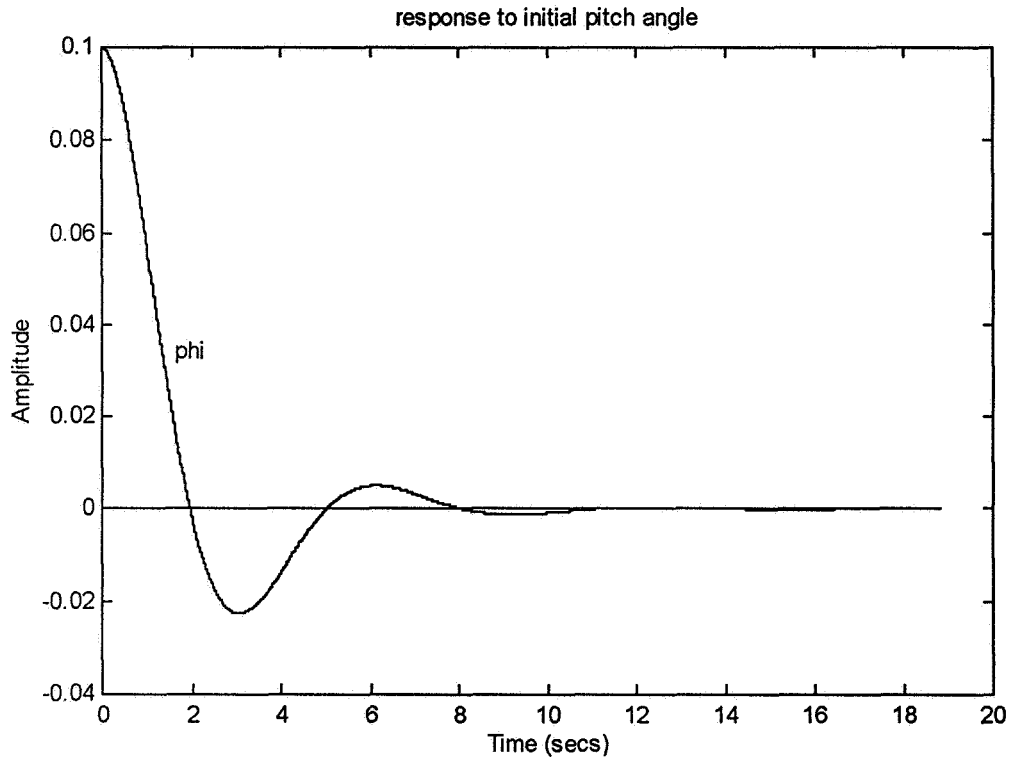


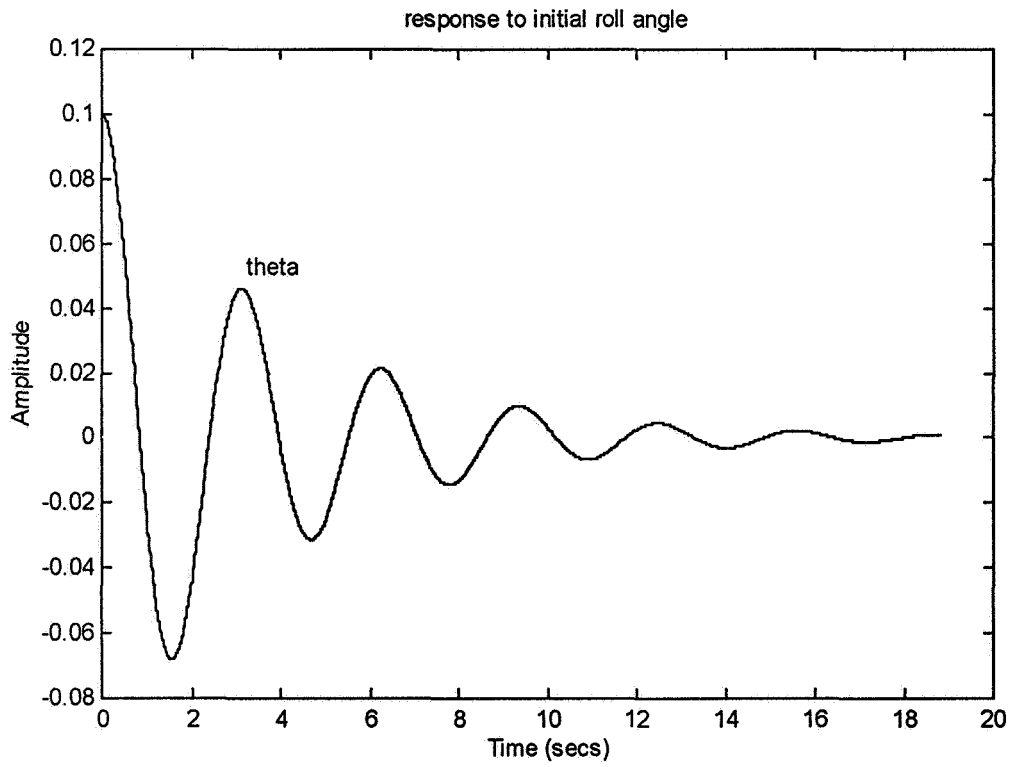
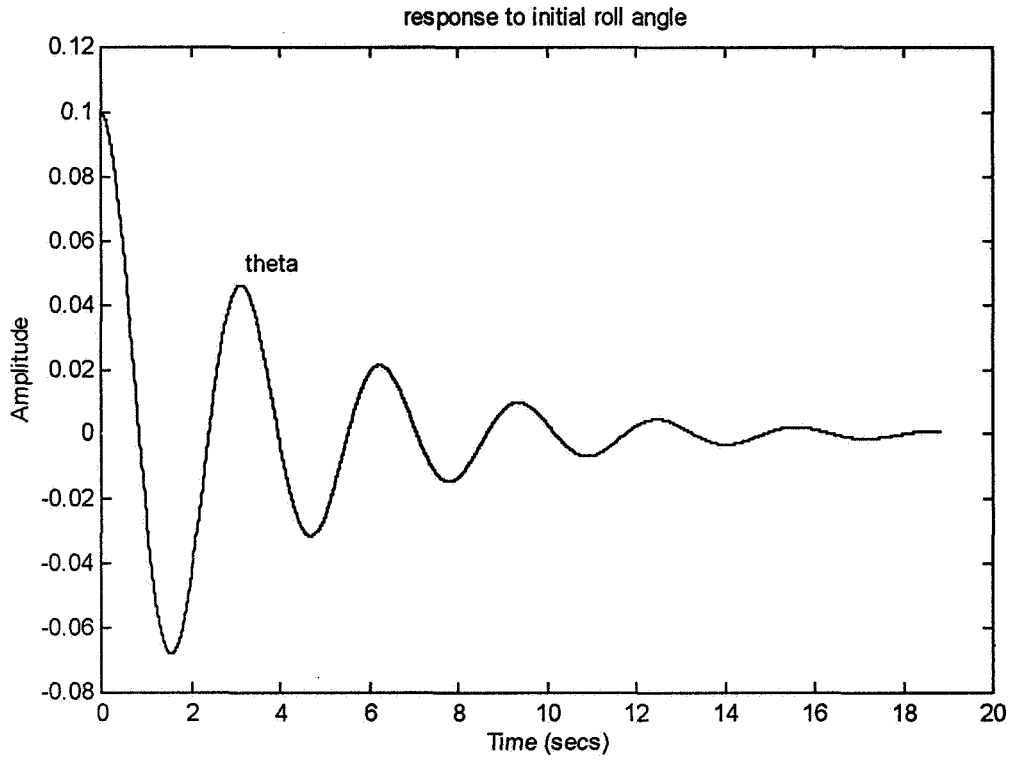
Because all of the dynamics and transformations between reference coordinate frames (ECI, LV, SC, Sensor, etc.) are available at all times in the system, ATTDES is equally applicable to satellite attitude determination problems. In order to accomplish this, sensor model files are available which include not only sensor geometry transformations (transformations from each sensor frame to the appropriate body reference frame) but also covariance matrices appropriate for each sensor. Therefore, within the basic ATTDES structure, one can perform attitude control studies, attitude determination and covariance analysis studies.

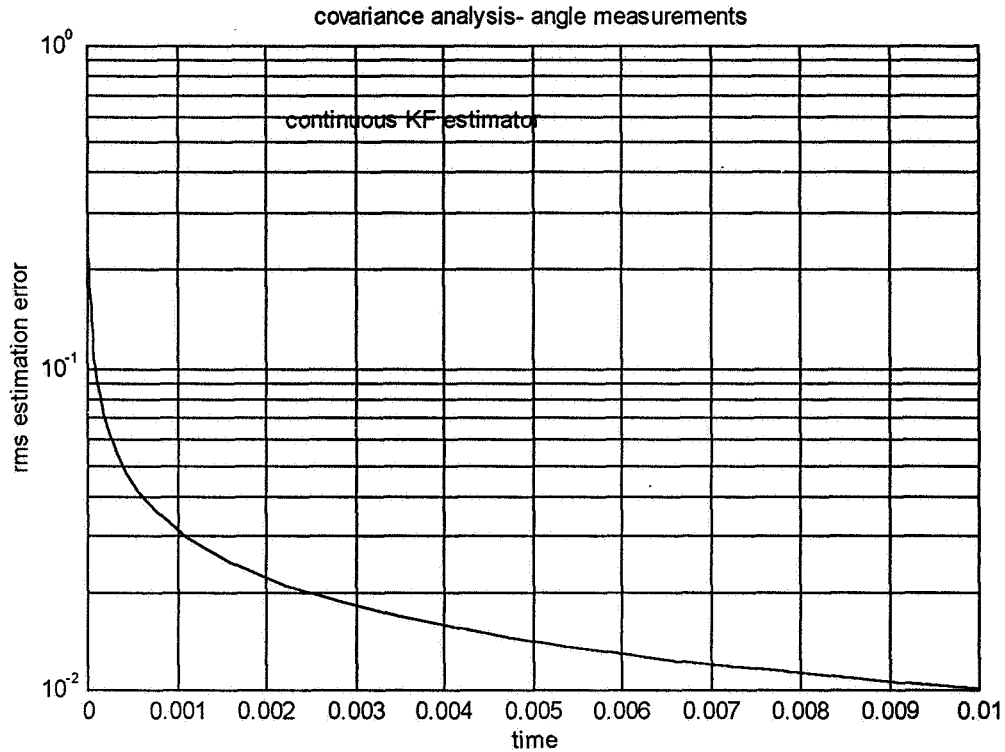
Example

For a simple example, we chose a gravity gradient stabilized satellite, with the control torques generated by small momentum wheels. The equations of motions are built into the system. We specify the control gains by using the linearized equations of motion and appropriate state and control weighting matrices to

solve the Riccati equation, and then generate the simulation using the state transition matrix. Further, using sensor models, we can generate an appropriate estimator for the attitude- either for attitude determination, or to include as part of a closed loop attitude control system. We can also use the loop transmission recovery utilities to generate the closed loop controller.







Covariance vs. time

Ongoing Development

MATLAB has an extensive data visualization capability. Forthcoming features to be added to ATTDES using this capability include

- Attitude dynamics movies, based on the analysis data set, which shows a lighted, shaded figure rotating in the appropriate coordinate frame.
- Color graphics visualization of robustness information, which permits an intuitive understanding of the effects of parameter uncertainties, and singular vector surfaces which may indicate problems in parameter scaling and sensitivity for both control and estimation problems.

Conclusions

The use of Matlab for satellite attitude control system and satellite attitude design systems permits the analyst the use of high level numerical analysis software for performing design studies. Further, the use of the database capabilities of the system permits one to quickly modify a previous example, and to demonstrate the dynamic behavior of the closed loop system. The inclusion of orbit models, very general attitude dynamics models, and sensor models will allow the support of a wide variety of satellite configuration.

References

- Thomas R. Kane, Peter W. Likins, and David A. Levinson, Spacecraft Dynamics, McGraw -Hill Book Company, New York, 1983.
- Donald L. Mackison, "ATTDES- An Expert System Tool for Satellite Attitude Control Problems," University of Colorado, Aerospace Engineering Sciences, September 1990.
- Donald L. Mackison, "Guaranteed Cost Control of Flexible Space Structures," University of Colorado, *Electrical and Computer Engineering*, 1988.
- Donald L. Mackison, Computer Aided Control Systems Design- A Course in CACSD Using MATLAB, University of Colorado, July 1991.
- MATLAB- High Performance Numeric Computation and Visualization Software, The Mathworks, Natick, Mass., Ver. 4.2.1.c, August 1992.
- Denise Chen and Cleve Moler, Symbolic Math Toolbox For Use With MATLAB, The Mathworks, Natick, Mass., August 1993.
- Andrew Grace, Alan J. Laub, John N. Little, Clay M. Thompson, Control System Toolbox for Use with MATLAB. User's Guide, The Mathworks, Natick, Mass., August 1992.
- Andrew Grace, Optimization Toolbox For Use with MATLAB, The Mathworks, Natick, Mass., December 1992.
- Donald L., Mackison, "GAMS Attitude Determination Covariance Analysis". Mackison Associates Technical Report, 7 June 1994.
- Sonnabend, David, "Measuring Attitude with a Gradiometer", Analytical Engineering Co. Report AE-1, May 3, 1994.
- Donald L Mackison, "Modal Weighting of Linear Quadratic Regulators," AIAA Guidance, Navigation, and Control Conference, Proceedings, Monterey, CA, August 1993.
- Donald L. Mackison, "Autonomous Rendezvous and Docking of Satellites- A Covariance Analysis", AIAA Guidance, Navigation, and Control Conference, Hilton Head, South Carolina, August 10-12, 1992.
- F.L. Markley, "New Dynamic Variables for Rotating Spacecraft", *Spacecraft Dynamics*, 1993, Proceedings of the AAS/NASA International Symposium, Greenbelt, MD, Apr. 26-30, 1993.
- John E. Cochran, T.S. No, and Norman G. Fitz-Coy, "Simulation of Spacecraft Attitude Dynamics using TREETOPS and Model-Specific Computer Codes", NASA, Goddard Space Flight Center, Flight Mechanics/Estimation Theory Symposium, 1989
- John W. Hunt, Jr., "Modeling Spacecraft Attitude Dynamics on a Personal Computer", 1988 Annual Summer Computer Simulation Conference, 20th, Seattle, WA, July 25-28, 1988, Proceedings.
- P.C. Hughes, Spacecraft Attitude Dynamics, John Wiley and Sons, 1986.
- D.L. Mackison and K. Gifford, ATTDES- An Expert System for Satellite Attitude Determination and Control, 6th AAS/AIAA Space Flight Mechanics Meeting, Austin, TX, February 11-15, 1996.

Anon, Matlab Compiler- User's Guide, The Math Works, Natick, Mass., September, 1995.

Arthur Gelb, Ed., Applied Optimal Estimation, M.I.T. Press, Cambridge, Mass., 1974.

Appendix

Examples of Graphical Output for a Momentum Bias Satellite With Momentum Wheel Control

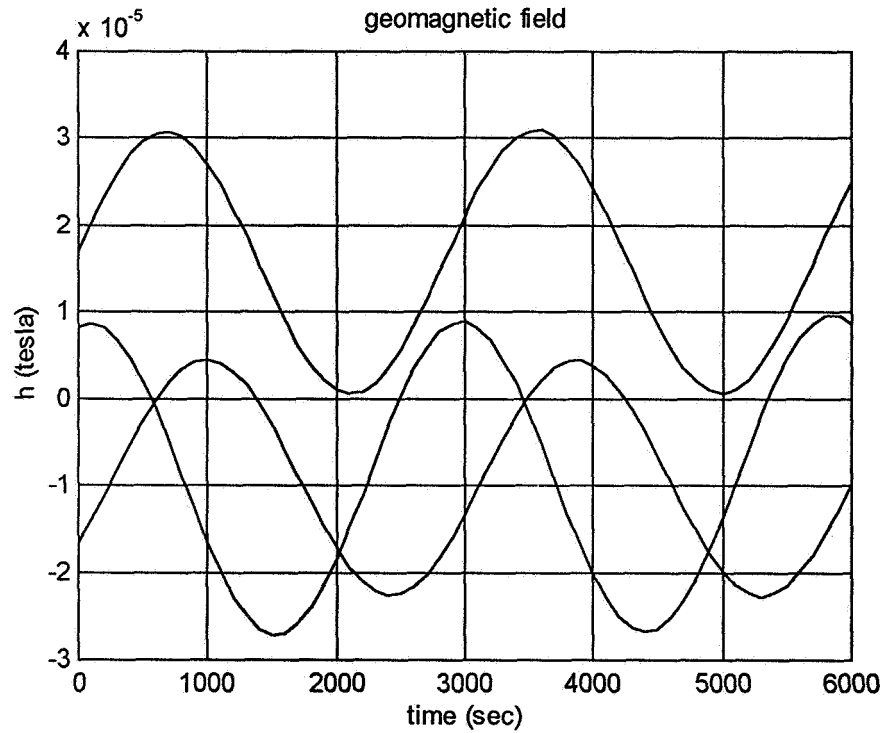


Figure 1. Geomagnetic Field Components Over An Orbit
Earth Centered Inertial Coordinates

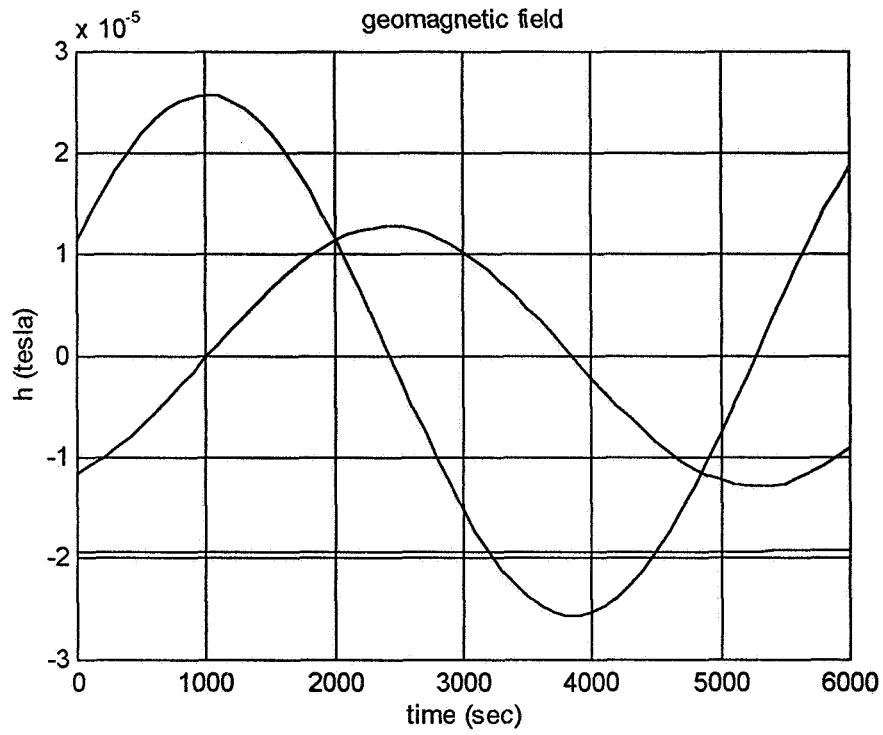


Figure 2. Geomagnetic Field Components Over An Orbit-Local Vertical Coordinates

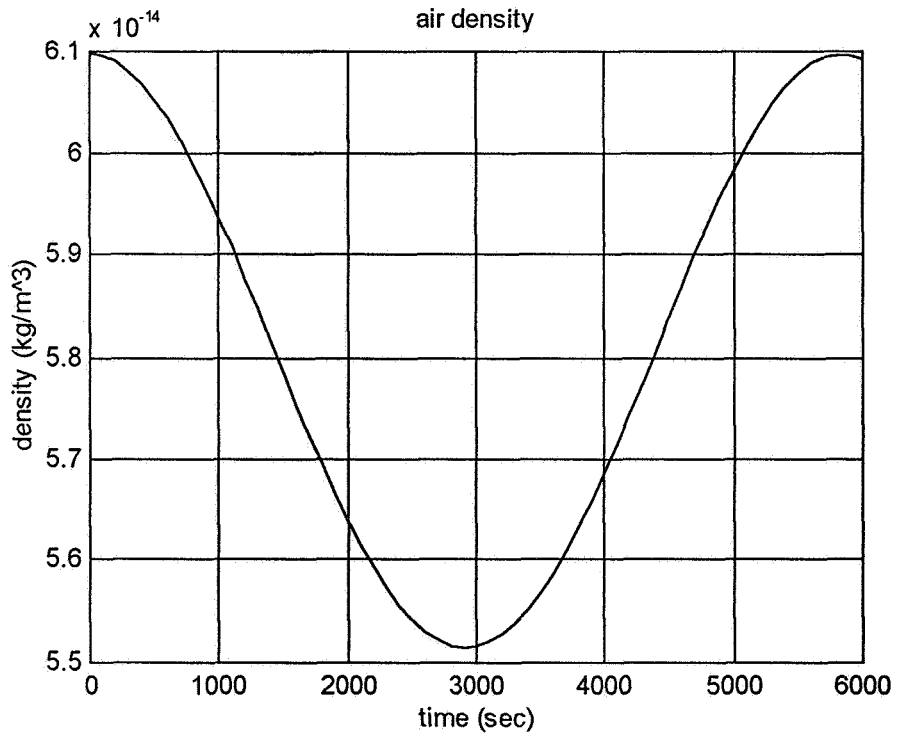


Figure 3. Air Density Over an Orbit

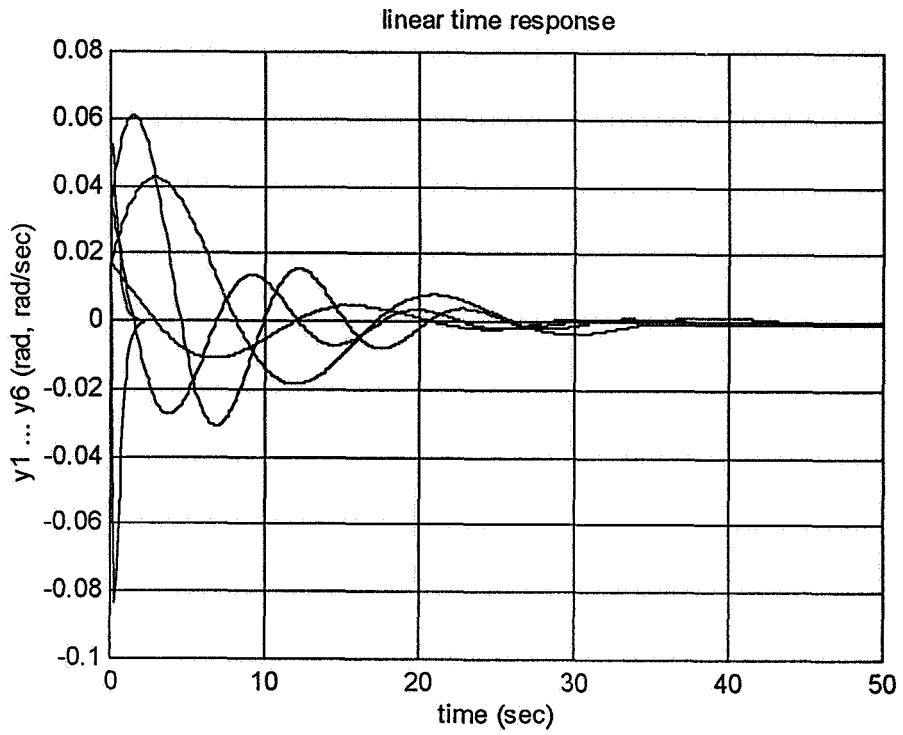


Figure 4. Response From Non-Zero Initial Conditions

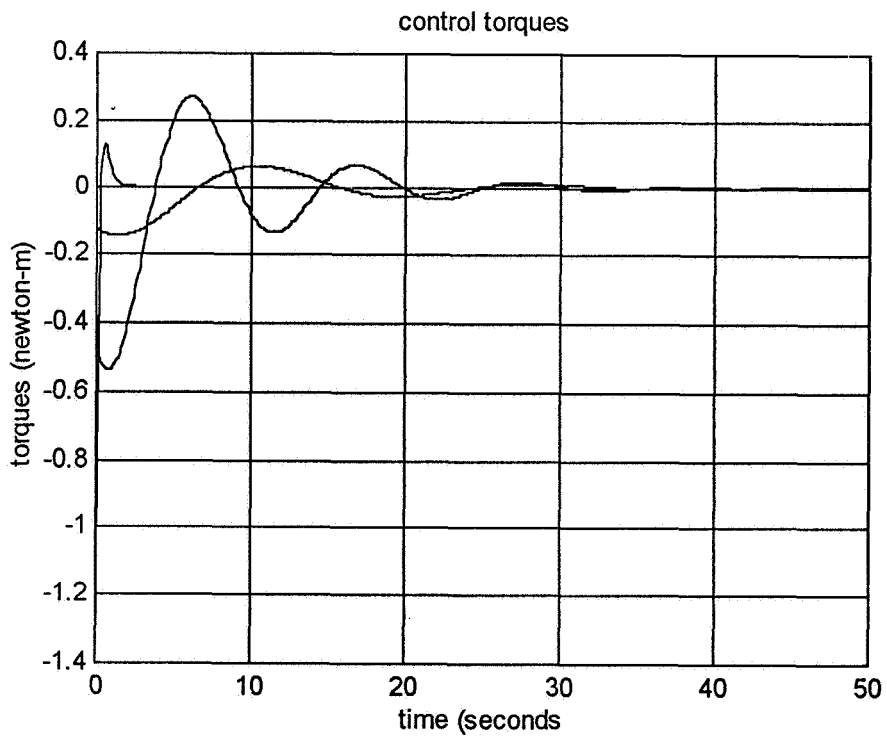
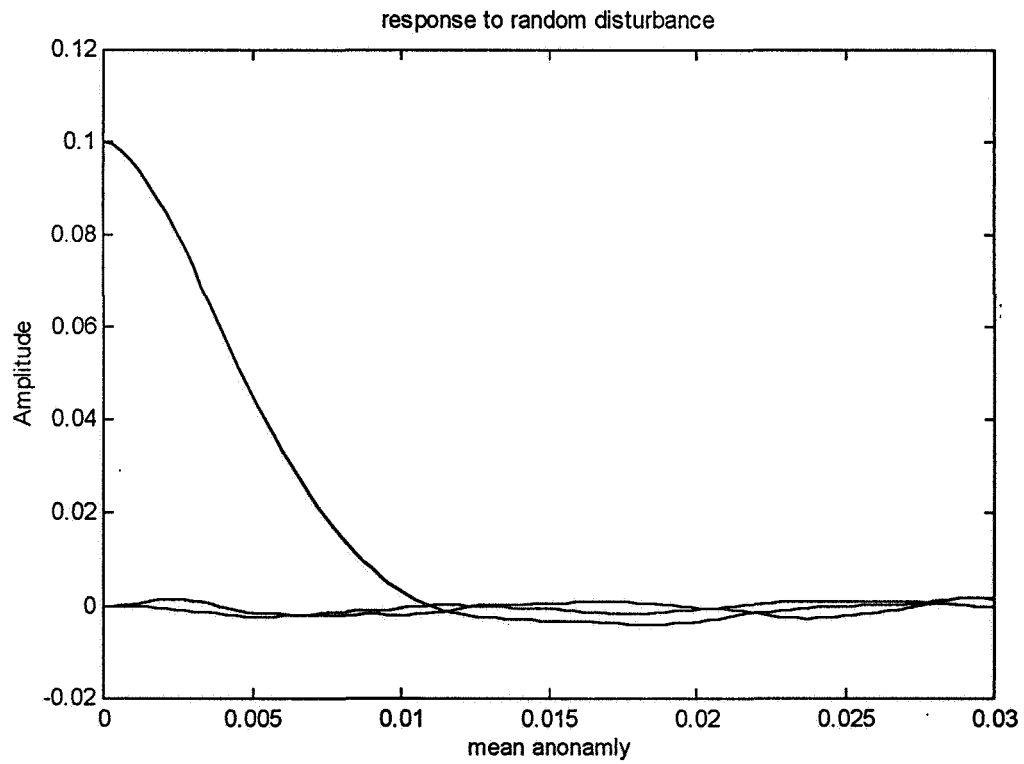
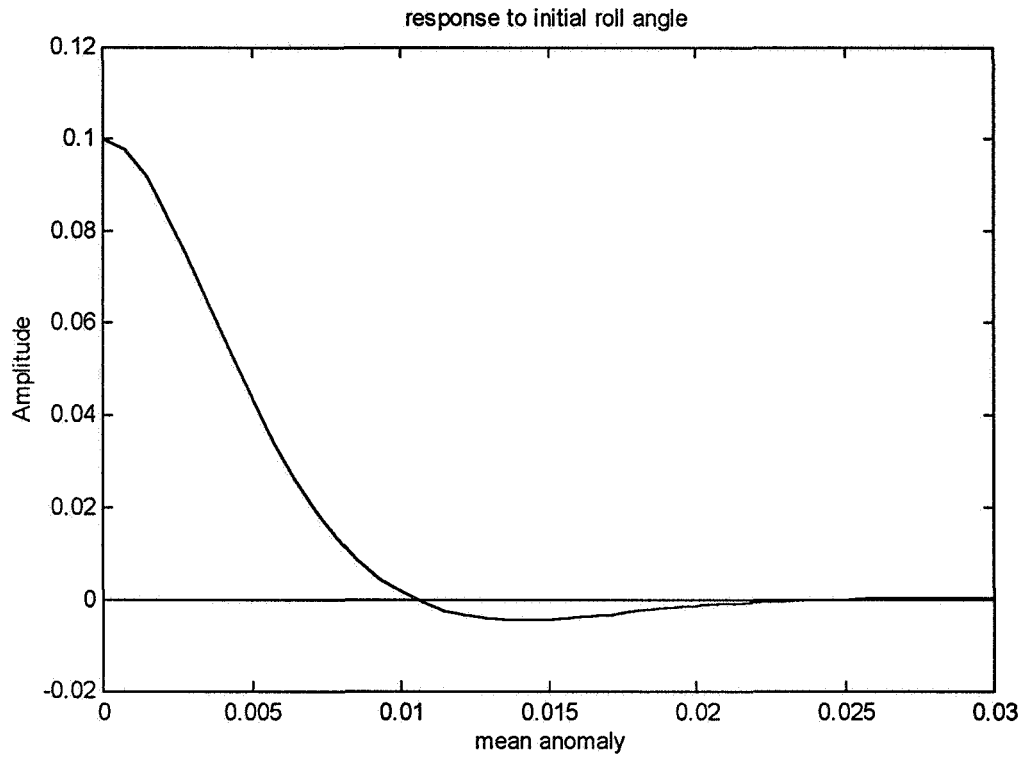


Figure 5. Control Torques



**BALANCING SCIENCE OBJECTIVES AND OPERATIONAL CONSTRAINTS:
A MISSION PLANNER'S CHALLENGE**

**Michelle Weldy
ANSER
Suite 800
1215 Jefferson Davis Highway
Arlington, VA 22202-3251**

Abstract

The Air Force Miniature Sensor Technology Integration (MSTI-3) satellite's primary mission is to characterize Earth's atmospheric background clutter. MSTI-3 will use three cameras for data collection: a mid-wave infrared imager (MWIR), a short-wave infrared imager (SWIR), and a visible imaging spectrometer (VIS).

Mission science objectives call for the collection of over 2 million images within the one year mission life. In addition, operational constraints limit camera usage to four operations of twenty minutes per day, with no more than 10,000 data and calibration images collected per day. To balance the operational constraints and science objectives, the Mission Planning Team has designed a planning process to create event schedules and sensor operations timelines. Each set of constraints, including spacecraft performance capabilities, the camera filters, the geographical regions and the spacecraft-Sun-Earth geometries of interest, and remote tracking station deconflictions has been accounted for in this methodology.

To aid in this process, the Mission Planning Team is building a series of tools from Commercial Off-the-Shelf software. These include the Mission Manifest which builds a daily schedule of events, and the MSTI Scene Simulator which helps build geometrically correct scans. These tools provide an efficient, responsive, and highly flexible architecture that maximizes data collection while minimizing mission planning time.

Modular Software for Spacecraft Navigation Using the Global Positioning System (GPS)*

S. H. Truong, K. R. Hartman, D. A. Weidow, and D. L. Berry
National Aeronautics and Space Administration
Goddard Space Flight Center (GSFC)
Greenbelt, Maryland, USA 20771

D. H. Oza, A. C. Long, E. Joyce, and W. L. Steger
Computer Sciences Corporation (CSC)
Lanham-Seabrook, Maryland, USA 20706

Abstract

The Goddard Space Flight Center (GSFC) Flight Dynamics and Mission Operations Divisions have jointly investigated the feasibility of engineering modular Global Positioning System (GPS) navigation software to support both real-time flight and ground postprocessing configurations. The goals of this effort are to define standard GPS data interfaces and to engineer standard, reusable navigation software components that can be used to build a broad range of GPS navigation support applications. The paper discusses the GPS Modular Software (GMOD) system and operations concepts, major requirements, candidate software architecture, feasibility assessment, and recommended software interface standards. In addition, ongoing efforts to broaden the scope of the initial study and to develop modular software to support autonomous navigation using GPS are addressed.

1.0 Introduction

The Department of Defense (DOD) Global Positioning System (GPS) is becoming a more attractive navigation option for National Aeronautics and Space Administration (NASA) spacecraft due to the recent declaration that the GPS is fully operational. The NASA Mission Operations and Control Architecture (MOCA) Program (Reference 1) has shown that GPS has the potential to provide significant economies for NASA spacecraft navigation.

The GPS civilian Standard Positioning Service (SPS) can deliver spacecraft navigation accuracies in the 20- to 100-meter (1σ) range in a real-time flight environment, improving to the submeter level in a postprocessing ground environment (References 2 and 3). The DOD intentionally limits the real-time navigation accuracy achievable using GPS SPS by applying Selective Availability (SA) corruption to the GPS signals. The GPS military Precise Positioning Service (PPS) can deliver spacecraft navigation accuracies in the 5- to 15-meter (1σ) range in a flight environment, but PPS access and use are restricted and subject to security classification requirements (Reference 2).

Currently, major drawbacks to the use of GPS on NASA spacecraft include the lack of standardization in the products available from commercial GPS receivers and the lack of reusable navigation flight software and ground support software. To promote rapid, cost-effective deployment of GPS technology, NASA's Goddard Space Flight Center (GSFC) Flight Dynamics Division (FDD) and Mission Operations Division (MOD) were jointly funded by NASA Headquarters/Code OI to perform a quick-reaction study to define the standard GPS data interfaces and to investigate the feasibility of engineering modular software components to support both flight and ground GPS navigation applications.

* This work was supported by the National Aeronautics and Space Administration (NASA)/Goddard Space Flight Center (GSFC), Greenbelt, Maryland, under Contract NAS 5-31500.

The core GPS Modular Software (GMOD) team consisted of representatives from the GSFC MOD flight software development, FDD ground software development, and FDD operations and analysis disciplines. Draft materials were distributed to NASA Headquarters/Code OI, Johnson Space Center (JSC), and Jet Propulsion Laboratory (JPL) representatives for review.

Due to the short timeframe of the initial study (i.e., 3 months), the scope of the study was limited to single-spacecraft navigation using a commercial GPS SPS receiver. All major study objectives were accomplished:

- A complete end-to-end candidate system was defined to provide single spacecraft autonomous navigation using a single frequency GPS SPS receiver.
- GPS data interface standards were recommended.
- Operational configurations were recommended that logically partition GPS navigation functions between flight and ground segments to support several levels of spacecraft autonomy.
- An open system architecture design was developed that provides the flexibility to host standard navigation software components onboard or on the ground to provide a range of mission-selectable flight/ground functional partitions.

Based on this investigation, the GMOD team did not identify any inherent obstacles to the development of an open system architecture that partitions the GPS navigation software between flight and ground. Follow-on activities are underway to extend the scope of this initial study to address use of the GPS PPS, multiple spacecraft navigation applications, and high-accuracy postprocessing applications and to demonstrate the feasibility of the GMOD concepts.

Reference 4 provides a detailed discussion of the results from the initial GMOD feasibility study. This paper summarizes these accomplishments. Section 2.0 discusses the system and operations concepts, Section 3.0 addresses the software architecture design accomplishments, and Section 4.0 lists follow-on activities resulting from this study.

2.0 System and Operations Concepts

The following GMOD system goals were defined for this initial study:

- The GPS Modular software will support the following navigation functions: geometric position computation, state (i.e., spacecraft position and velocity and GPS receiver time bias) estimation, state prediction, orbit maintenance, and navigation performance monitoring and calibration for a single user spacecraft.
- The modular software will support real-time and near-real-time autonomous navigation operations to provide spacecraft navigation accuracies in the 20-meter (1σ) range using a single-frequency commercial GPS SPS receiver, with SA at typical levels.
- The modular software will support several levels of autonomy ranging from ground processing of downlinked GPS receiver measurements to autonomous onboard state estimation and orbit adjustment.
- GPS modular software will require standardization of its external interfaces, such as GPS measurement interface, command interface, and telemetry interface. GPS data interface standards will be defined, and custom interface software will be needed to convert the output of the selected GPS receiver to the standard data interface format.

This section discusses the system and operations concepts for modular software that satisfies these goals.

2.1 Major Functional and Operational Capabilities

The following major GPS navigation support capabilities were identified based on the GSFC FDD's Tracking and Data Relay Satellite System (TDRSS) Onboard Navigation System (TONS) (References 5 and 6), GPS Enhanced Orbit Determination Experiment (GEODE) (References 7 and 8), TONS Ground Support System (TGSS) (Reference 9), and the institutional navigation and orbit maintenance software in use in GSFC's Flight Dynamics Facility (FDF):

- **Geometric Positioning**—Computing the spacecraft position and receiver's time bias by iteratively solving four simultaneous pseudorange measurement equations and computing the spacecraft velocity and receiver's time bias rate by solving four simultaneous pseudorange rate (derived from the frequency shift of the carrier signal) measurement equations. This purely geometric approach provides instantaneous "point" solutions at the measurement times. This capability is available within most commercial GPS receivers.
- **Spacecraft State Estimation**—Computing corrected estimates for the spacecraft position, velocity, receiver time bias, receiver time bias rate, and atmospheric drag coefficient by filtering pseudorange and/or Doppler measurements or, alternatively, geometric positioning states. This approach models the spacecraft dynamics and therefore does not require continuous tracking of four or more GPS space vehicles (SVs) simultaneously.
- **Spacecraft State Propagation**—Predicting the spacecraft position, velocity, and time bias ahead in time using a high-accuracy model of the spacecraft dynamics.
- **Orbit Adjustment**—Identifying when an orbit maneuver is required to maintain the orbit within mission-specific constraints (typically arising from frozen orbit, Sun-synchronous orbit, or ground-track repeatability requirements for low Earth orbit (LEO) missions); determining the time, location, magnitude, and direction of the maneuver; and computing the associated thruster on/off times.
- **Navigation Performance Monitoring and Calibration**—Verifying the quality of the GPS measurements and the accuracy of the spacecraft state estimation and orbit adjustment computations and calibrating models to improve navigation performance.

2.2 Navigation Configurations

Table 1 lists a set of GPS navigation configurations, developed based on Reference 1, that provide increasing levels of autonomous onboard functions and require decreasing levels of ground support functions. The total set of navigation support functions remains essentially the same, regardless of the flight or ground computing environment. The GMOD team developed detailed descriptions for the first four navigation configurations, addressing the major functions and associated external and internal data interfaces. This information is presented in detail in Section 2.2 of Reference 4. The last three configurations, which involve the use of differential GPS measurements from multiple spacecraft or possibly multiple ground stations, are beyond the scope of the initial GMOD study but are being addressed in a follow-on study.

Figure 1 illustrates the functional partitioning developed for the autonomous navigation configuration, which provides accurate real-time position and velocity computation onboard using a real-time extended Kalman filter estimation approach with a high-fidelity spacecraft dynamic model. This autonomous navigation configuration reduces the need for definitive ground state estimation to a backup function except for periodic validation and calibration of onboard performance. A major advantage of this configuration is that accurate position, velocity, and time estimates are available for autonomous precision attitude control and direct downlink with the science data, eliminating the need to uplink predicted ephemeris information to the spacecraft and to perform postfacto state estimation on the ground. In addition, real-time position and velocity estimates are available on the spacecraft to support reinitialization of the GPS receiver if required.

Table 1. Summary of GPS Navigation Configurations

Navigation Configuration	Onboard Functions	Ground Functions
Repeater Configuration	GPS signal digitization, storage, and forwarding*	GPS measurement/broadcast message extraction State estimation and prediction Navigation performance monitoring and calibration Orbit adjustment
Geometric Positioning Configuration	GPS measurement/broadcast message extraction* Geometric position computation**	State estimation and prediction Navigation performance monitoring and calibration Orbit adjustment
Autonomous Navigation	GPS measurement/broadcast message extraction* Geometric position computation** State estimation and prediction Navigation performance monitoring	Navigation performance calibration Orbit adjustment
Autonomous Orbit Maintenance	GPS measurement/broadcast message extraction* Geometric position computation** State estimation and prediction Navigation performance monitoring Orbit adjustment	Navigation performance calibration
Postprocessed Differential Navigation	GPS measurement/broadcast message extraction* Geometric position computation (optional)**	State estimation using differential pseudorange and phase measurements Navigation performance monitoring and calibration Orbit adjustment
Real-Time User Spacecraft Constellation Navigation	GPS measurement/broadcast message extraction* State estimation using differential ranges from neighboring spacecraft Navigation performance monitoring	Navigation performance calibration Orbit adjustment
Formation Flying/Rendezvous	GPS measurement/broadcast message extraction* Compute relative positions between two spacecraft using differential ranges Navigation performance monitoring Orbit adjustment to maintain range/close distance	Navigation performance calibration

Notes: * Standard receiver function
**Provided by most commercial receivers

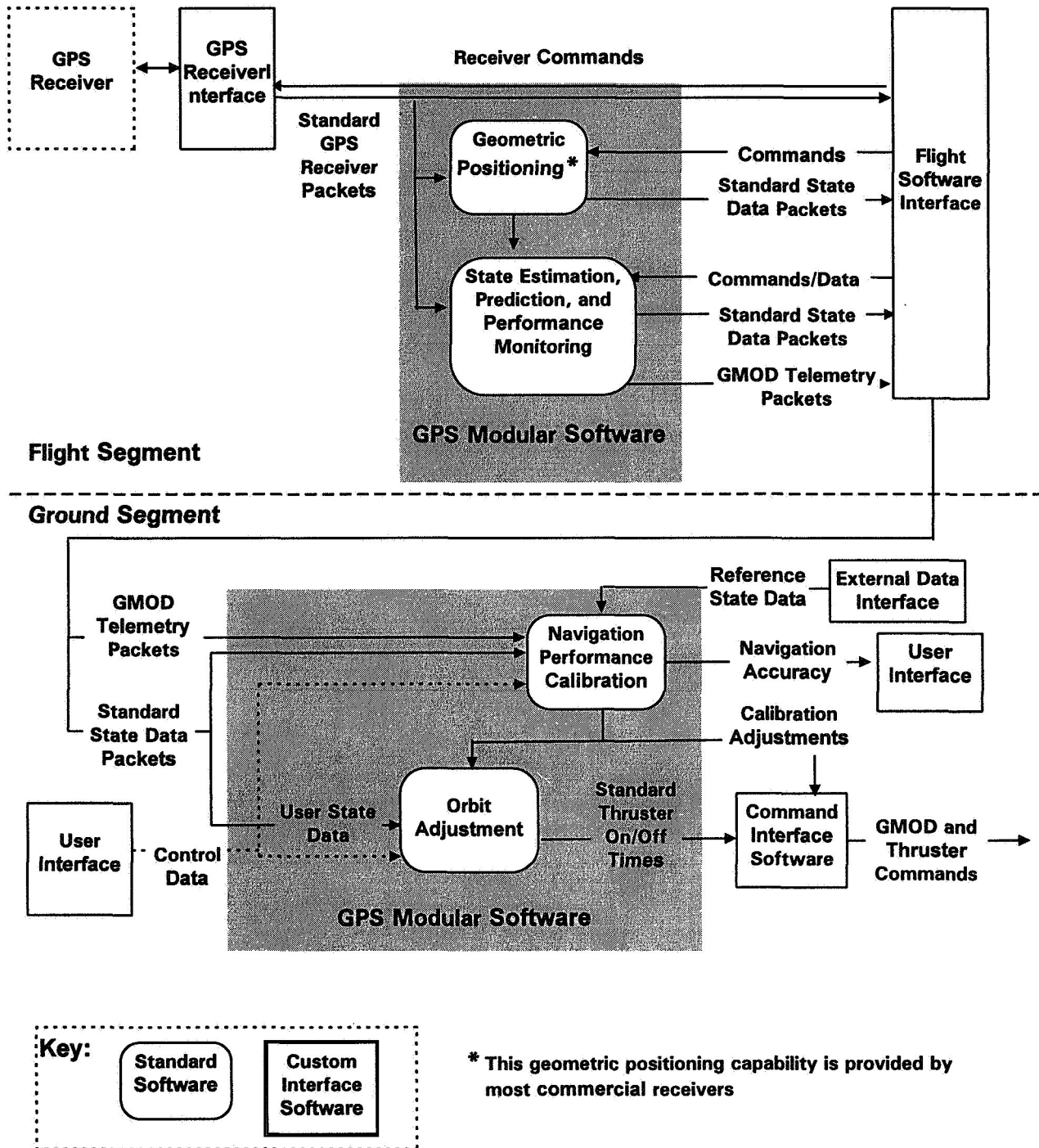


Figure 1. GPS Navigation Processing Components for Autonomous Navigation Configuration

GPS receiver interface software is hosted onboard to convert the output of the commercial GPS receiver (e.g., measurements, GPS broadcast messages, and geometric state estimates) to standard GPS receiver packet formats for downlink and/or use by GMOD and other spacecraft processes. The onboard navigation software functions can be hosted on a processor within the GPS receiver unit, on the spacecraft's onboard computer (OBC), or on a separate processor, whichever processor has sufficient available resources. The geometric positioning solution can optionally be used to provide an initial state vector for the filter processing, as well as to provide a real-time onboard performance check. Monitoring of the real-time performance of the state estimation process is also performed onboard, consistent with the MOCA goal of reducing the need for ground contacts to one per day. GMOD telemetry packets are provided at a commandable rate; these packets contain data needed for in-depth performance calibration and problem diagnosis.

The downlinked state estimates are propagated in ground software for use in the orbit adjustment computations and in the generation of predicted orbit product data. The ground-based GPS navigation calibration functions consist of reporting any available GPS health and receiver status information; verifying the accuracy of the spacecraft state estimation and orbit adjustment ground computations; and, optionally, verifying the quality of the GPS measurements and computing modeling adjustments to improve navigation performance. Calibration of the accuracy of the estimated spacecraft state can include comparison with a reference solution, such as one generated using another tracking system.

2.3 System Requirements

The GMOD context diagram, shown in Figure 2, illustrates the interfaces between GMOD and the other flight and ground software components. The GPS receiver interface software, which converts the output of the selected GPS receiver to standard GPS data interface formats, is specific to each receiver vendor/product. The flight system executive and spacecraft command, telemetry, and product data interfaces are specific to the flight environment in which GMOD is embedded. Similarly, the ground system executive, user control and display, product data, and external data interfaces are specific to the ground environment in which GMOD is embedded.

Functional requirements were defined for the following major GMOD functions:

- Determine geometric position
- Estimate user state
- Predict user state
- Monitor/calibrate GPS navigation performance

In addition, high-level operational and performance requirements were defined to support the four GPS operational configurations. These requirements are provided in Sections 3.2 through 3.4 of Reference 4, respectively.

3.0 GMOD Architecture and Design

This section discusses the definition of a candidate GMOD software architecture and a standard set of software applications that provide the recommended software partitioning between the flight and ground segments. Also given is a preliminary assessment of the feasibility of using a C++ based implementation for the GMOD software.

3.1 GMOD Software Architecture

The major design goals for the GMOD software architecture are the following:

- **Modularity and Configurability**—The software components that comprise the GMOD software must be able to be combined in a flexible manner to meet the required software configurations as defined in the GMOD operations concepts.
- **Reuse**—The design of the GMOD software must facilitate use of the same software components in both the flight and ground segments, to the extent possible.

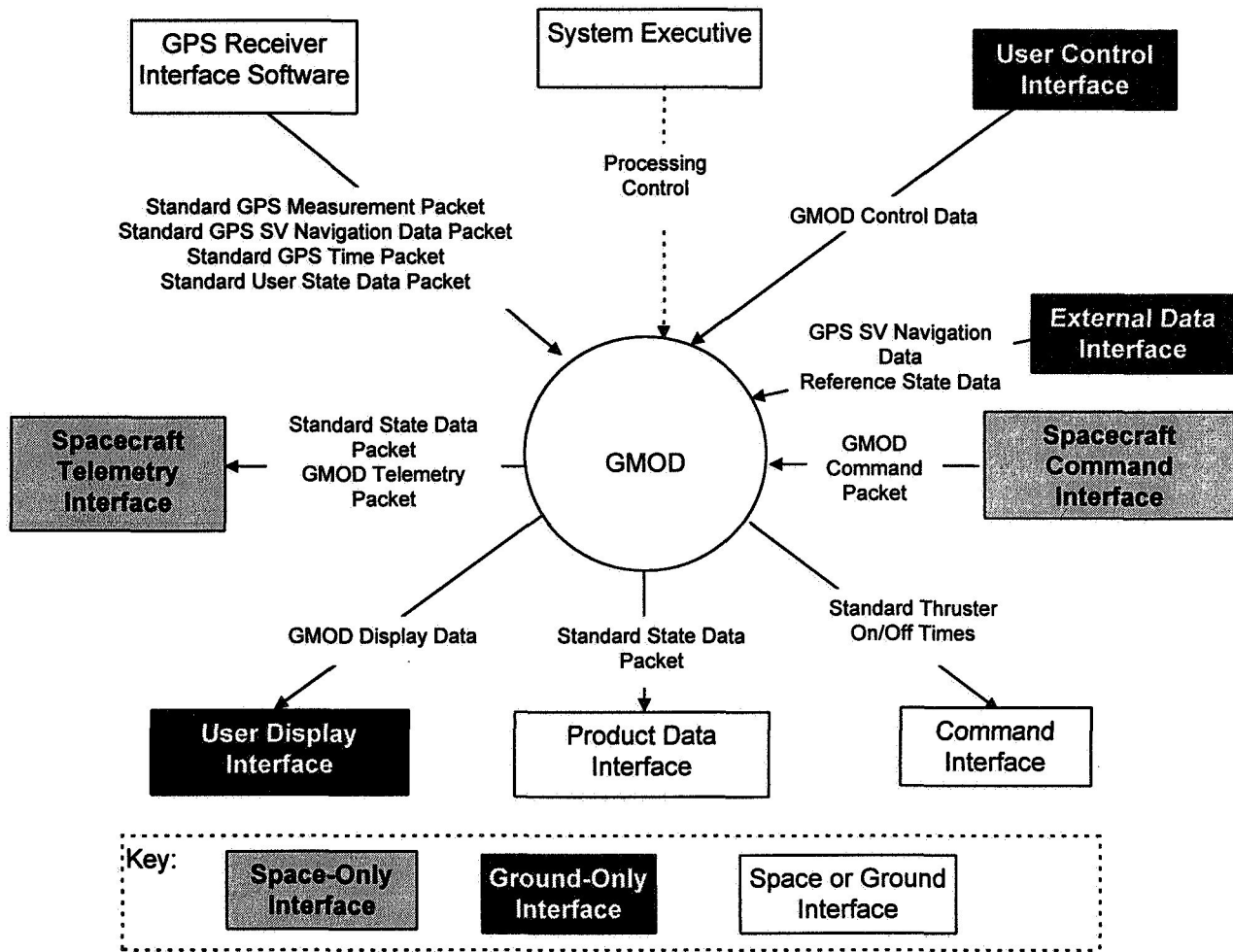


Figure 2. GMOD Interface Diagram

- Encapsulation of Interfaces**—The GMOD software design should support isolation of the external interfaces (data and control) to the GMOD software to minimize the customization needed to interface the GMOD software with various commercial GPS receivers and spacecraft computer environments.

The selected GMOD software architecture depicted in Figure 3 meets each of these goals. The GMOD software architecture is based on the concepts developed for the GSFC FDD's Flight Dynamics Distributed System (FDDS) Generalized Support Software (GSS) for configuring application programs from a set of object-oriented, modular reusable components (classes) resident in a class library (Reference 10). The GSFC FDD has developed a set of software implementation standards and a generic software architecture for building reusable components for ground-based systems. The software implementation standards are referred to as the GSS implementation concepts. The GMOD architecture for the ground segment is based directly on FDDS/GSS, and the GMOD flight segment architecture extends the FDDS/GSS concepts to support the flight environment.

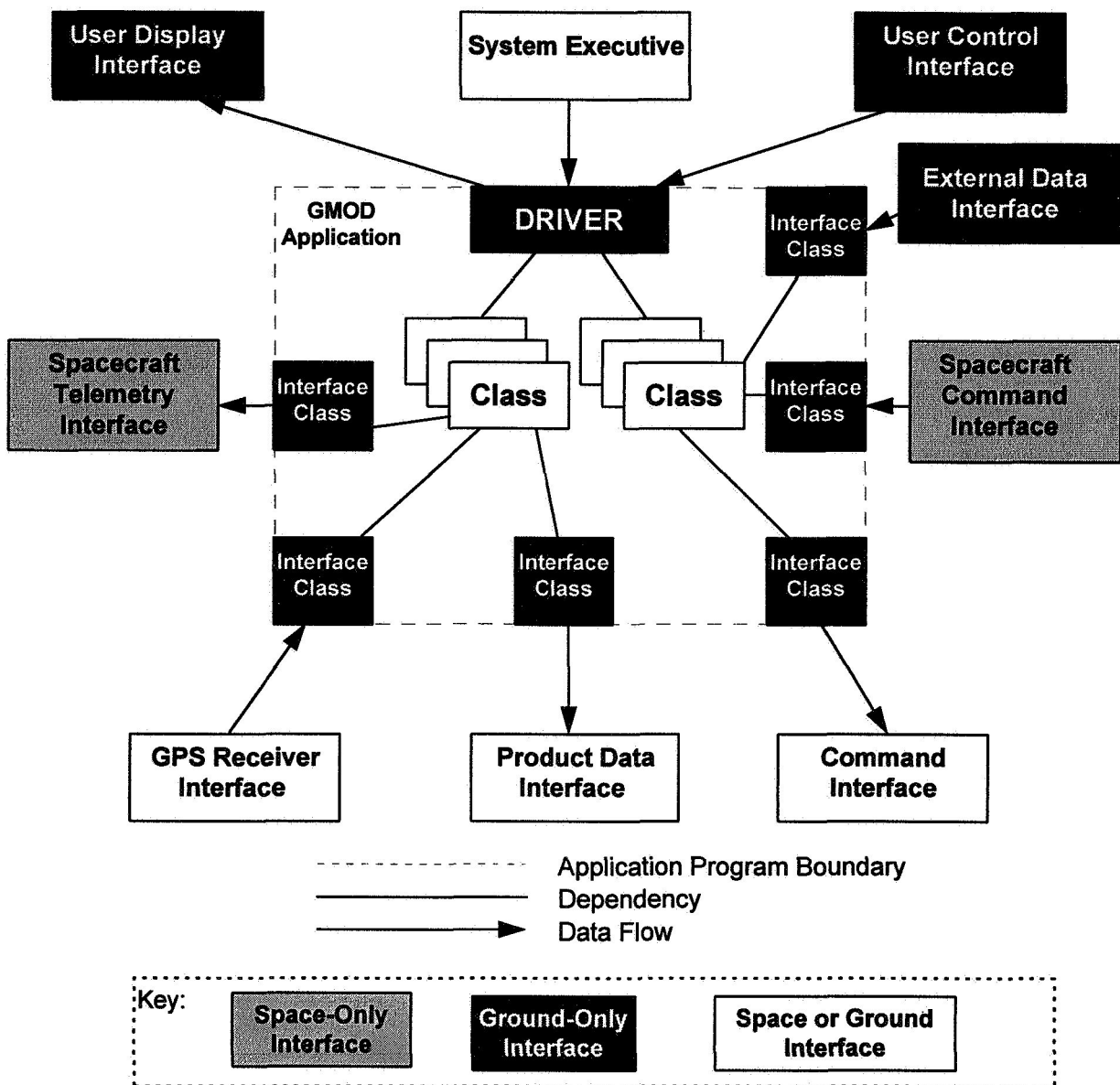


Figure 3. GMOD Software Architecture

As shown in Figure 3, the basic building blocks for a GMOD application are classes and drivers. A class is a software representation (abstraction) of an object in the GMOD problem domain of autonomous spacecraft navigation. Examples of objects in the GMOD problem domain are “physical” objects, such as the spacecraft, Earth, Sun, and Moon, and more abstract or “algorithmic” objects, such as integrators and measurement models. The shading of the boxes that represent the external interfaces to the GMOD application indicates whether the interface is ground only, space only, or both. The dark shaded boxes inside the dashed box that represents the GMOD application (labeled “Driver” and “Interface Class”) are those elements of the GMOD software architecture that may require some degree of customization for each mission-specific ground and space segment hardware/software configuration. The unshaded boxes (labeled “Class”) indicate those elements of the GMOD software that are reusable between specific mission ground and flight hardware configurations.

Classes are also used to encapsulate external data interfaces and associated access methods. As depicted in Figure 3, an interface class can be defined for the GPS receiver that contains the member functions that perform the data conversion needed to transform the receiver-specific data formats into the standard GMOD data format.

The driver element of the GMOD software architecture is the "glue" that binds the classes and data objects into an executable application (module). The driver element consists of an overall executive routine that manages the flow of execution in the configured application and a set of routines that manages the data exchange between the GMOD application and the user interface/executive (ground segment) or the flight software executive (flight segment).

3.2 Standard Software Components

The GMOD team also defined a set of standard applications that could be used to provide the functionality defined for each of the GMOD navigation configurations. Based on an analysis of the GMOD requirements and designs of existing FDD software systems that have similar requirements, the following six applications were defined:

- **Geometric Positioning**—Determines spacecraft position using the geometric positioning method; this function is typically resident in the software included in the GPS receiver unit by the GPS receiver manufacturer
- **Message Extraction**—Extracts the data from the GPS receiver custom data formats (onboard) or from the downlink telemetry stream (ground) and converts it to the GMOD standard data formats
- **Navigation**—Provides the autonomous navigation functions, including processing the GPS measurements and performing user spacecraft state estimation and prediction
- **Navigation Performance Evaluation**—Provides data analysis and calibration functions for the navigation application program
- **Orbit Adjustment**—Provides the autonomous orbit maintenance functions of planning, executing, and calibrating spacecraft orbit adjust maneuvers

Each of the applications listed above has the same software architecture as that depicted in Figure 3.

Section 4.2 of Reference 4 provides a preliminary list of software classes that comprise each of these applications.

3.3 Preliminary Feasibility Assessment

One of the ground rules given to the GMOD team at the start of the project was that the desired implementation language for GMOD was C++, because of its increasing use by the GSFC FDD in developing FDD's reusable software. To evaluate the use of C++ and also to evaluate the feasibility of using the FDDS/GSS software implementation standards (concepts), the GMOD team produced a small scale prototype of the Earth gravity model in C++. Based on the evaluation of the memory usage and central processing unit (CPU) usage, the GMOD team determined that there were no inherent problems with using C++ and the FDDS/GSS implementation standards for both the ground and space segments of GMOD. Prototyping of a larger application is currently in progress and will be evaluated prior to the start of full-scale implementation of the GMOD software. Section 4.3 of Reference 4 provides a detailed discussion of the associated feasibility issues.

3.4 Interface Standards

Data interface formats were defined for each of the GMOD software interfaces shown in Figure 3. These packet formats are defined so as to conform with the Consultative Committee on Space Data Standards (CCSDS) recommended packet structure defined in Reference 11. The CCSDS packet definition was adopted based on the recommendations of the MOCA program and because of its increasing use among NASA missions. Although the packet structures were designed to support the flight system interfaces, they should also be usable for the ground system user control and display data interfaces. A detailed description of each command and telemetry packet is provided in Section 5 of Reference 4.

4.0 Follow-On Activities

The initial GMOD study established the feasibility of developing modular software to support GPS navigation using commercial GPS SPS receivers. Beginning in July of 1996, the GSFC FDD will use the autonomous navigation configuration associated with the GEODE experiment hosted on the Small Satellite Technology Initiative (SSTI)/Lewis spacecraft (Reference 12) as an opportunity to assess the performance of the autonomous navigation configuration and the overall completeness of the GMOD capabilities to support this configuration.

Currently, the FDD is pursuing activities to broaden the scope of the initial study and demonstrate that modular software applications can be built that are suitable for both flight and ground environments. These activities include extending the domain of the GMOD concepts, requirements, interfaces, and software architecture to address impacts arising from the following items:

- Performance improvements to be gained through the use of Wide-Area Augmentation System (WAAS)-compatible GPS SPS receivers and GPS PPS receivers
- Expected performance for spacecraft with limited or intermittent GPS visibility, e.g., geosynchronous spacecraft, Space Shuttle, Space Station
- Improving the reliability of GPS autonomous navigation by using the GMOD autonomous navigation filter solution to reinitialize the GPS receiver
- Multiple spacecraft applications (e.g., formation flying and rendezvous)
- Very-high-accuracy differential GPS applications
- Detailed system requirements for autonomous orbit adjustment

In addition, the FDD is currently developing a prototype GMOD application to demonstrate the GMOD application development concept. The prototyping effort is divided into two phases. In the first phase, an autonomous navigation application is being developed to operate as a ground-based application. This phase will demonstrate that an autonomous navigation application can be built using a set of generalized C++ routines. This phase will also provide a benchmark against which the second phase prototype may be evaluated. The second phase will be to port the core classes of the first phase prototype into a typical flight software environment. The flight software environment will be provided by one of the GSFC MOD flight software test beds. This phase is intended to demonstrate that the software being developed to support GMOD ground applications can be reused in a flight environment with a minimal amount of modification.

Acknowledgments

The GMOD work was supported by NASA Headquarters (HQ)/Code OI and was a cooperative effort between personnel from the GSFC FDD and MOD, JSC, and JPL. The authors wish to thank the staff from GSFC, JSC, and JPL who contributed to this effort. Special acknowledgment is given to John Rush (NASA HQ/Code OI), Russell Carpenter (JSC), and Lawrence Young (JPL) for their support of this work. The authors acknowledge the contributions from D. Bolvin, J. Chang, C. Ewald, and J. Lorah of CSC and J. Pepper of GSFC.

References

1. Goddard Space Flight Center, *Final Report of the MOCA's GPS (MOCA/GPS) Splinter Team*, March 20, 1995
2. National Research Council, *The Global Positioning System A Shared National Asset*. Washington, DC: National Academy Press, 1995
3. M. Lichten et al., "An Automated Low-Earth Orbit Determination System with High-Accuracy Real-Time Capability," presented at the 1995 National Technical Meeting of the Institute of Navigation, Anaheim, California, January 18–20, 1995

4. Goddard Space Flight Center, Flight Dynamics Division, 553-FDD-95/014R0UD0, *Global Positioning System (GPS) Modular Software (GMOD), Feasibility Analysis Report*, D. Berry et al., prepared by Computer Sciences Corporation, September 1995
5. Goddard Space Flight Center, Flight Dynamics Division, 553-FDD-93/030R1UD0, *Tracking and Data Relay Satellite System (TDRSS) Onboard Navigation System (TONS) Flight Software Recommended Algorithms, Revision 1*, A. C. Long (CSC) et al., prepared by Computer Sciences Corporation, December 1993
6. Martin Marietta Corporation Astro-Space, Document No. 20045510, *Software Requirements Specification Flight Software—Navigation CSCI for EOS-AM Spacecraft (SD-110a)*, J. R. Herberg, November 7, 1994
7. Goddard Space Flight Center, Flight Dynamics Division, 553-FDD-95/011R0UD0, *Global Positioning System (GPS) Enhanced Orbit Determination Experiment (GEODE) Requirements and Functional Specifications*, Draft, A. C. Long (CSC) et al., prepared by Computer Sciences Corporation, May 1995
8. ---, Flight Dynamics Division, 553-FDD-95/013R0UD0, *Global Positioning System (GPS) Enhanced Orbit Determination Experiment (GEODE) Mathematical Specifications*, Draft, T. Lee and A. C. Long (CSC), prepared by Computer Sciences Corporation, February 1995
9. ---, Flight Dynamics Division, 553-FDD-94/007R1UD0, *Tracking and Data Relay Satellite System (TDRSS) Onboard Navigation System (TONS) Ground Support System (TGSS) Requirements and Functional Specifications, Revision 1*, G. Horstkamp (CSC) et al., prepared by Computer Sciences Corporation, July 1995
10. Goddard Space Flight Center, Flight Dynamics Division, 552-FDD-95/010R0UD0, *Flight Dynamics Distributed System (FDDS) Software Architecture, Volume 1*, Draft, D. Boland (CSC) et al., prepared by Computer Sciences Corporation, June 1995
11. Consultative Committee on Space Data Standards, CCSDS 102.0-B-3 Blue Book, Recommendation for Space Data System Standards, *Packet Telemetry*, November 1992
12. Frank H. Bauer et al., "The GPS Attitude Determination Flyer (GADFLY): A Space-Qualified GPS Attitude Receiver on the SSTI-Lewis Spacecraft," *ION GPS-95 Proceedings*, ION GPS-95 Conference, Palm Springs, California, September 1995

Title: ARTSN: An Automated Real-Time Spacecraft Navigation System

Authors: Dr. P. Daniel Burkhart and Vincent M. Pollmeier

An effort is underway at the Jet Propulsion Laboratory (JPL) to design a filter to automate the deep space navigation process. This project, the Automated Real-Time Spacecraft Navigation (ARTSN) filter task, is part of the Deep Space Network (DSN) Advanced Technology Program.

The prototype is currently a FORTRAN77 package operating on an HP-9000/700 series workstation running HP-UX 9.05. This will be converted to C, which will be the maintained operational version. The processing tasks required can be divided into four groups; read a measurement, integrate the spacecraft state to the current measurement time, compute the observable based on the integrated state, and incorporate the measurement information into the state using an EKF. This filter processes radiometric data (currently only two-way differenced-range Doppler) collected using the DSN. The dynamical (force) models currently include point mass gravitational terms for all planets, Sun and Moon, solar radiation pressure, finite maneuvers, and attitude maintenance activity modeled quadratically. In addition, observable errors due to the troposphere are included. Further data types, force models and observable models will be included to enhance the accuracy of the models and capability of the package. The heart of ARTSN is a current-state continuous-discrete extended Kalman filter. This is a departure from the epoch state/pseudo-epoch state formulation used currently for deep space navigation, but is necessary to mesh with the data driven nature of real time processing. The filter is implemented in the standard form, except for the use of the general covariance update formula for an arbitrary gain matrix to enhance the numerical properties of the process. Further numerical enhancement using UD and/or SRIF forms of the Kalman filter will be implemented.

Results will be presented for the simulated data used to test the implementation at various stages of development, along with results from processing actual mission data.

--

FLIGHT MECHANICS/ESTIMATION THEORY SYMPOSIUM

MAY 14-16, 1996

SESSION 4

Experience Gained From Launch and Early Orbit Support of the Rossi X-Ray Timing Explorer (RXTE)*

D. R. Fink, K. B. Chapman, W. S. Davis, J. A. Hashmall,
S. E. Shulman, S. C. Underwood, and J. M. Zsoldos[†]
Computer Sciences Corporation
Lanham-Seabrook, Maryland, USA 20706

R. R. Harman
National Aeronautics and Space Administration
Goddard Space Flight Center
Greenbelt, Maryland, USA 20771

Abstract

This paper reports the results to date of early mission support provided by the personnel of the Goddard Space Flight Center (GSFC) Flight Dynamics Division (FDD) for the Rossi X-Ray Timing Explorer (RXTE) spacecraft. For this mission, the FDD supports onboard attitude determination and ephemeris propagation by supplying ground-based orbit and attitude solutions and calibration results. The first phase of that support was to provide launch window analyses. As the launch window was determined, acquisition attitudes were calculated and calibration slews were planned. Postlaunch, these slews provided the basis for ground-determined calibration. Ground-determined calibration results are used to improve the accuracy of onboard solutions. The FDD is applying new calibration tools designed to facilitate use of the simultaneous, high-accuracy star observations from the two RXTE star trackers for ground attitude determination and calibration. An evaluation of the performance of these new tools is presented in the paper. The FDD provides updates to the onboard star catalog based on preflight analysis and analysis of flight data. The in-flight results of the mission support in each area are summarized and compared with premission expectations.

1. Introduction

A background discussion of the Rossi X-Ray Timing Explorer (RXTE) and a description of the spacecraft attitude sensors are given in this section.

1.1 Background

RXTE is a three-axis stabilized inertially pointing spacecraft (mean of J2000.0 reference) with the goal of studying the time characteristics of astrophysical sources of x-rays. The mission is designed to study up to 20 science targets per day and to have a minimum lifetime of 2 years with a goal of 5 years. RXTE has no propulsion system and was built by GSFC Code 700.

RXTE was launched on December 30, 1995, by a Delta II launch vehicle into a 580-kilometer (km) circular orbit with a 23-degree (deg) inclination. The in-orbit checkout (IOC) phase began at separation from the Delta second stage and continued for approximately the first 30 days of the mission. During this phase, all the instruments were activated and tested. Also, various attitude maneuvers were performed to test the attitude control, power, and communications systems and to calibrate the science and attitude instruments.

* This work was supported by the National Aeronautics and Space Administration (NASA)/Goddard Space Flight Center (GSFC), Greenbelt, Maryland, under Contract NAS 5-31500.

[†] Currently at Orbital Sciences Corporation, Germantown, Maryland, USA, 20874

RXTE has the following power and thermal constraints during its mission (different constraints apply at Delta separation):

- The Sun must be in the +Z-hemisphere of the spacecraft (see Figure 1).
- The Sun must be within 5 degrees (deg) of the spacecraft XZ-plane to maximize power to the solar array and to prevent illumination of the spacecraft sides.
- The Sun must be further than 30 deg from the spacecraft +X-axis to prevent illumination of the star trackers and the science instruments.

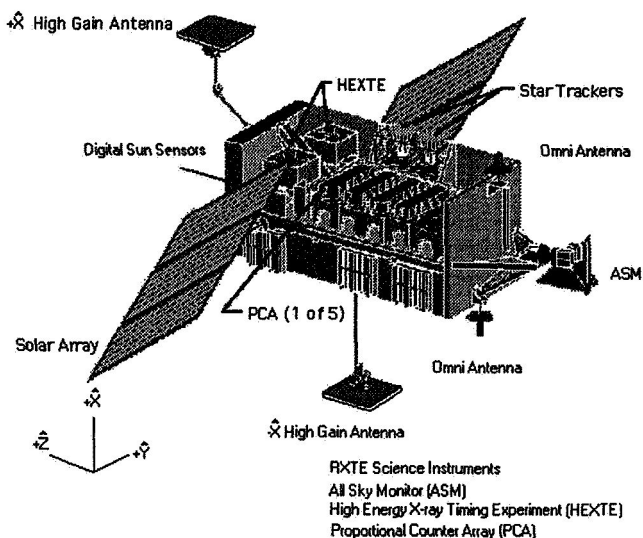


Figure 1. RXTE Spacecraft Diagram

The three-sigma attitude determination requirement on the RXTE onboard attitude system is 60 arc seconds (arc sec) around the X-axis and 42 arc sec each around the Y- and Z-axes. RXTE's attitude sensors and actuators are as follows:

- Two charge-coupled device (CCD) star trackers (STs)
- Eight coarse Sun sensors (CSSs)
- Two digital Sun sensors (DSSs)
- Two three-axis magnetometers (TAMs)
- One inertial reference unit (IRU) (three two-axis mechanical gyroscopes)
- Magnetic torquer bars (MTBs)
- One interferometric fiber optic gyroscope (IFOG), as an experiment
- Reaction wheel assembly (RWA)

1.2 Spacecraft Attitude Sensors

The RXTE STs are Ball Aerospace CT-601 CCD star trackers. They have an instrumental magnitude limit of 5.9, a field of view (FOV) of nominal dimension 8x8 deg, a noise equivalent angle of less than 3 arc sec (1σ), systematic position errors less than 3 arc sec, a magnitude uncertainty of 0.25, and a resolution of 0.5 arc sec. Each tracker can simultaneously track up to five stars. For specified performance, the Sun must be at least 30 deg from the boresight, the Moon must be at least 8 deg from the boresight, and the lit Earth must be at least 17.9 deg from the boresight. For RXTE, the boresight of ST1 nominally coincides with the spacecraft X-axis. The ST2 boresight is 9.9 deg from the spacecraft X-axis toward the Z-axis. The STs are rotated by 45 deg around each boresight, and their FOVs overlap by about 1 square deg. The onboard star catalog (OSC) used by the onboard computer (OBC) has 2844 stars in the range of 1.0 to 6.5 instrumental magnitude (instrumental magnitude corresponds to visual magnitude for a star of the same color as the Sun—for red stars it can be as much as two magnitudes brighter) and covers the sky with no “holes.” This means that an ST will see at least one star in the catalog for any pointing direction. A new catalog is being prepared to eliminate those stars between magnitude 5.9 (the actual CCD detection limit) and 6.5 (the old catalog limit). This catalog does have small holes but these constitute no more than about 0.1 percent of the possible attitudes.

The RXTE digital Sun sensors are Adcole devices, which are functionally similar to sensors on other missions such as Gamma Ray Observatory (GRO), Upper Atmosphere Research Satellite (UARS), and Extreme Ultraviolet Explorer (EUVE). They have a FOV dimension of 64x64 deg, an approximate digital resolution of 15 arc sec, a noise of $\pm 1/2$ the digital resolution, and an accuracy of 60 arc sec within a 32-deg radius. The DSS1 boresight is

18 deg from the spacecraft Z-axis toward the X-axis, and the DSS2 boresight is 42 deg from the spacecraft Z-axis toward the -X-axis.

The RXTE inertial reference unit is the Kearfott SKIRU-DII and is functionally similar to the Teledyne DRIRU (Dry Rotor IRU)-IIs used on spacecraft such as GRO, UARS, and EUVE. It consists of three 2-axis gyroscopes, which provide six channels of rate information, two for each spacecraft body axis. The IRU axes are nominally aligned with spacecraft body axes. The IRU has a low-rate resolution of 0.1 arc sec/count and high-rate resolution of 1.6 arc sec/count. The prelaunch measured noise parameters for the IRUs are rate noise of 6.7×10^{-3} arc sec/sec^{1/2} and bias noise of 3.4×10^{-5} arc sec/sec^{3/2}.

The three-axis magnetometers were built by GSFC Code 700 and are nominally aligned with the spacecraft axes. They have a digital resolution of 0.293 mG/count and are used both in the spacecraft momentum control logic and as backup sensors.

The interferometric fiber optic gyroscope is an experimental device built by Honeywell, which provides three channels (X, Y, and Z) of rate information. Each channel consists of a coil of fiber optic cable with counter-propagating beams of light. The measured phase shift of these beams is proportional to the angular rate around the axis of the coil. On each channel, the incremental angle is measured at 0.250second (sec) time intervals. With a digital resolution of 2^{-36} radians per count, the data then has a scale factor of 3.34×10^{-9} deg/sec per count.

2. Prelaunch Activities

A discussion of the RXTE prelaunch activities, including launch windows, launch slips, and attitude planning, is given below.

2.1 Launch Windows

The RXTE launch window was determined by three constraints: the spacecraft +Z-axis had to be within 9 deg of the spacecraft-to-Sun vector at separation, the spacecraft had to separate during spacecraft day, and separation needed to occur before 0900 local time at the release longitude. These constraints led to an 88-minute (min) window starting at 1438 coordinated universal time (UTC) for the first RXTE launch attempt on December 10, 1995.

2.2 Launch Slips

The first four launch attempts were scrubbed due to high-level wind constraint violations. As a result, investigations began on opening up the launch window by 1 hour on each side. Both Code 700 Attitude Control System (ACS) engineers and FDD agreed that there were no major problems with opening up the launch window; but to verify the assumptions, a spacecraft independent validation and verification facility (SIVVF) simulation should be done. If launch occurred at the opening of the extended window, RXTE would be in darkness for more than 4 minutes and over 23 deg off the Sun line at separation. The simulation later showed the window could be widened safely. The fifth launch attempt was scheduled for the following day, December 18, too soon to open up the window, as the simulation results were not yet in hand. Therefore, launch was scheduled using the nominal launch window constraints. Approximately 15 minutes into the window, high level winds had lowered to within launch constraints, but at T-minus 2.5 seconds, there was a main engine cut off (MECO) due to a faulty liquid oxygen valve.

The sixth launch attempt was scheduled for 1347 UTC on December 29, 1995, using the extended launch window. Even with a launch window more than 3 hours wide, high-level winds also scrubbed this launch attempt. RXTE was finally launched on the seventh attempt at 1348 UTC on December 30, 1995.

2.3 Attitude Planning

For each launch opportunity, attitude planning consisted of two activities: (1) predicting separation and acquisition attitudes and (2) planning maneuvers for calibration of the attitude sensors. Because launch dates commonly slip many times, automating these activities as much as possible is desirable.

For each mission, the Delta project provides a document called *Detailed Test Objectives* (DTO), which gives the attitude of the second stage at the time it releases the spacecraft. This attitude is independent of the launch time because it is referenced to an inertial frame defined by the Earth and launch site at the time of launch. Thus, given

the alignment of the spacecraft with respect to the second stage, the location of the launch site, and the time of launch, the attitude of the spacecraft with respect to a mean of J2000.0 inertial coordinate system can be computed. After separation from the second stage, the spacecraft nulls any tip-off rates, deploys its solar arrays, and maneuvers its Z-axis to point toward the Sun. To obtain an approximate prediction of the attitude achieved by this process (the acquisition attitude), it was assumed that the Z-axis rotates from its direction at separation toward the Sun by the smallest rotation; i.e., around the direction perpendicular to both the Z-axis and the Sun. A MATLAB® (Reference 1) program was written to compute the separation and acquisition attitudes as a function of launch time and date. It also computes the angle between the Sun and the Z-axis at the separation attitude. The program computes these quantities at 1-minute intervals. Separation Z-axis-to-Sun angles of 9 deg or less define the original launch window, which typically lasted 80 to 85 minutes. This tool was also used to predict attitudes and Sun angles for the extended (200 minutes) launch windows.

A total of 28 attitude maneuvers on four days was planned to obtain calibration data for the attitude sensors (see Section 7, Attitude Sensor Calibration). These maneuvers were required to have continuous star coverage by the star trackers, a few minutes before, during, and a few minutes after each maneuver. The maneuvers were also required to exercise all axes of the gyroscope and move the Sun around in the FOV of the Sun sensors. The maneuvers were restricted by Sun angle limits for thermal and power constraints and by Earth and Moon interference of the star trackers. On previous missions, manually planning such maneuvers for each launch opportunity consumed much analyst time. With the goal of automating some of these processes, the RXTE planning was initially done in a coordinate frame defined by the Sun and the orbit normal with origin at the center of the Earth. The start and end of each maneuver were defined by attitudes in this frame and the orbit angles relative to the Sun. Maneuver scenarios could then be designed for continuous tracker coverage (avoiding Earth interference) while also satisfying Sun requirements and restrictions. For each launch opportunity, a program was run to convert the reference frame of each start and end attitude from the Sun/orbit-normal frame to an inertial mean-of-J2000.0 frame and to convert the start and end orbit angles relative to the Sun to date and time. Unfortunately, a single maneuver scenario was not sufficient to accommodate the Sun both above and below the orbit plane and to avoid Moon interference in all maneuvers for all dates. Thus, several scenarios were developed to accommodate various Sun and Moon configurations.

The RXTE launch had to be planned for 13 dates. The automated tools previously described significantly reduced the analyst workload and response time. The main lesson learned from these experiences was that an extra margin for lit Earth interference of the trackers should be applied to allow for attitude settling, delays in starting maneuvers, and larger-than-expected Earth interference limits.

3. Launch and Separation

The attitude acquisition and orbit for RXTE during launch and separation are described below.

3.1 Attitude Acquisition

The solar arrays were deployed within 1 minute after separation from the Delta. The original timeline called for the spacecraft then to maneuver its Z-axis to the Sun using the CSSs (CSS Sun acquisition mode). However, as a result of the extended launch window, the spacecraft was still in shadow after solar array deployment. When the spacecraft entered sunlight, the maneuver to the Sun line was nominal. The early mission Sun angle history is given in Figure 2. Key attitude events during the first 10 minutes after separation are summarized in Table 1. FDD was able to solve for attitude soon after sunlight entry. The ground Real-Time Attitude Determination System (RTADS) was able to provide an accurate attitude and IRU bias within 5 minutes after the initial star acquisition. At about 49 minutes from separation, the OBC started to use the DSS to maintain the spacecraft Z-axis pointing toward the Sun (DSS Sun acquisition mode). The RTADS attitude was used to initialize the OBC ACS by 2 hours, 20 minutes, after separation. At separation plus 3.4 hours, the OBC entered initial tracker hold mode where it used star tracker data to hold an inertial attitude. Unfortunately, after about 20 minutes (min), problems with the star trackers forced a return to the DSS acquisition mode (see Section 4, In-Flight Anomalies).

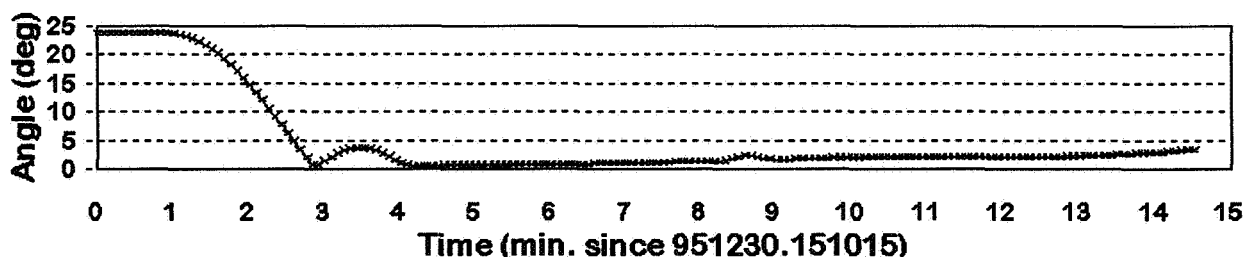


Figure 2. RXTE Z-Axis to Sun Angle Post Separation

Table 1. Key Separation Attitude Events

UTC (yymmdd.hhmmss)*	Separation + ΔT (min:sec)	Event
951230.150620	00:00	RXTE Separation from Delta-II: spacecraft +Z-Axis to Sun Angle = 23.970° Attitude (3-2-1): Yaw =169.369° Pitch = -14.999° Roll = -106.399°
951230.150723	01:03	First valid CCD observation
951230.150800	01:40	Solar array deployment
951230.151105	04:45	Spacecraft enters daylight and starts maneuver to sunline
951230.151111	04:51	First valid DSS-2 observation
951230.151223	06:03	First valid DSS-1 observation
951230.151435	08:15	Maneuver to sunline complete: spacecraft +Z-Axis to Sun Angle = 0.610° Attitude (3-2-1): Yaw = -167.929° Pitch = -6.094° Roll = -113.916°

* yymmdd.hhmmss = year, month, day.hour, minute, seconds

3.2 Orbit

The RXTE orbit injection was close to nominal. Table 2 lists the nominal best estimated trajectory (BET), supplied prelaunch by McDonnell Douglas, and gives the differences from that nominal state from the redundant inertial flight control avionics (RIFCA) telemetry for second engine cut off II (SECO-II) at SECO-II epoch, which was 145850 Zulu (Z) (Zulu time is equivalent to UTC) on December 30, 1995. It also compares the BET at two epochs with the first operational FDD orbit solution computed using TDRS tracking data, E4.

Table 2. RXTE Orbit Injection State, Nominal Versus Actual

Parameter	Units	BET Orbit State	Δ BET to SECO-II	Δ BET to E4 at 1500Z	Δ BET to E4 at 1930Z
X	km	-4191.8098	-24.5395	-28.4313	-57.4932
Y	km	5553.1506	-18.2510	-27.3535	29.1369
Z	km	63.0661	12.2428	16.2096	13.1289
XDOT	km/sec	-5.54439	0.0215	0.0289	-0.0296
YDOT	km/sec	-4.21984	-0.0288	-0.0349	-0.606
ZDOT	km/sec	2.95639	-0.00047	-0.0015	0.0245
Semimajor Axis	km	6957.966	0.5091	-0.9563	-0.9304
Eccentricity		0.0001129	0.00001	-0.00014	0.000016
Inclination	deg	22.99837	-0.0016	-0.0018	-0.0015
Argument of Perigee	deg	88.3213	-20.4621	-13.0053	8.3147
R. A. Asc. Node*	deg	125.823	0.0142	0.0068	0.0054
True Anomaly	deg	273.0080	20.7202	13.3500	-7.7780
Period	min	6.2683	0.0106	-0.0199	-0.0193

* R. A. Asc. Node = right ascension of the ascending node

4. In-Flight Anomalies

In-flight anomalies for the RXTE mission included encounters with debris, star tracking problems, onboard computer/extended-precision vector (OBC/EPV) problems, and solar array power degradation. These anomalies are discussed in the following subsections.

4.1 Debris

Shortly after launch, it became apparent that there was some debris in the proximity of RXTE. This debris was of interest due to potential interference with the operation of RXTE sensors, as well as the possibility of collision. Later, when the prospect of collision seemed unlikely, this interest turned to the possibility of determining the origin and nature of the debris.

FDD requested and received unclassified North American Air Defense Command (NORAD) vectors and two-line elements for the debris. These types of elements are guaranteed by NORAD to be accurate within 5 km at their epoch. The elements were propagated into ephemerides. Ephemeris data were also generated to represent RXTE and Delta trajectories resulting from the SECO events (SECO-1, -2, -3, and -4) from the RIFCA data. The NORAD ephemerides were then compared with the SECO ephemerides to determine whether origin and collision points might be established.

These comparisons support the premise that these objects may have originated from the Delta/RXTE flight paths. The comparison results from Object 23758 to the SECO-3 and SECO-4 trajectories are interesting in that the distance is small at a time close to Delta maneuvers. Similarly, Object 23759's close trajectory to the SECO-2/RXTE state suggests a common original trajectory. However, these data are not sufficient to determine the exact origin and nature of the debris.

4.2 Star Tracking Problems

Each ST can track up to five stars in one of two modes. It can track a star at a directed position in the FOV or it can map the FOV, following each star detected for a programmed time. Each of the potential stars in the FOV occupy a logical "slot" in the star tracker. After launch, all five slots were programmed to map mode. Once a satisfactory inertial attitude had been achieved, three or four of the slots (during different periods) were programmed to track stars and the other one or two were directed to map. It was noticed that the STs frequently stopped tracking stars that they had been directed to track. The ST manufacturer claims that the only circumstance in which this could occur was if an object, brighter than the star being tracked, passed through the ST FOV and passed close to the star position. The occurrence of these tracking terminations (or break tracks) seemed to be explained by debris passing through the ST FOV.

This hypothesis was supported by the observation that in some cases when break tracks occurred, one could see a sudden increase in star brightness coupled with motion of the tracked object that soon moved out of the FOV. Additional support came from the star tracks observed in the ground star identification process. During this process, the spacecraft attitude is used to convert ST observations into vectors in inertial space. Occasionally, these vectors changed systematically along an apparent trajectory. Similar behavior had previously been observed only when an ST was pointed toward the unlit portion of the Earth (tracking city lights). For RXTE in the early mission, these trajectories appeared even when the STs were pointed away from the Earth.

By day 21, when the calibration validation maneuvers occurred, some break track events were still occurring. It seems likely that debris caused some of the break track events in the initial days after launch, but that other unexplained break tracks persisted after the debris dispersed.

As a consequence of the unexpected break track events, the DSS acquisition period was extended while ACS engineers and FDD analysts investigated the problem. For that mode, DSS1 maintains pitch (Y-axis) and roll (X-axis) control, while the IRU controls around the yaw (Z-axis). Over several hours, a small gyro bias caused the spacecraft to drift significantly around the Z-axis. Later, when engineers were more confident about the ST operation, the OBC was again allowed to use the star trackers to control the attitude. However, the original OBC program would command the STs to search for and acquire star only after maneuvers or after the end of periods of Earth occultation. Consequently, during inertial periods when the trackers were not occulted by the Earth, stars acquired at the start of the period would be lost one by one. By the end of the unocculted period, few or no stars

remained to be tracked. The OBC was reprogrammed at FDD request to command an ST to reacquire dropped stars even during nonoccultation periods.

GSFC Code 700 personnel have analyzed 31 hours of ST data provided by the FDD. They found 40 loss of tracking (LOT) events. Of these events, they attribute 24 to interference with unknown moving objects (e.g. debris or other satellites). The other 16 LOT events remain unexplained.

4.3 OBC-EPV Related Problems

After the first tracking data solution and extended precision vectors (EPVs) were delivered, the RXTE EPV from the first tracking data solution was not uplinked. The Tracking and Data Relay Satellite (TDRS) -7 EPV had also not been refreshed as advised. These two events, combined with the Network Control Center (NCC) not updating with the proper current RXTE vectors for TDRS, led to a TDRS-7 pass that suffered poor lock. Updates to the vectors at NCC cured the problem mid-pass. At that point, the RXTE propagations of the old EPV differed from the correct ephemeris by approximately 97 km; the TDRS-7 compares were approximately 16 km. These EPVs were then refreshed.

4.4 Solar Array Power Degradation

The power output of the solar arrays is 17 percent lower than expected. GSFC Code 700 engineers attribute the loss to a manufacturer defect which cracks individual solar cells. The defect affects five of the six panels. Such cracking is aggravated by stresses in the arrays. Therefore, ACS engineers have taken the following steps to reduce thermal and dynamic stress:

- Reprogram the on-board software to accelerate the arrays slowly whenever they are repositioned
- During periods of inertial pointing, position the normal of the panels 45 deg from the Sun (instead of the nominal 0 deg) to reduce the maximum temperatures of the array components
- Limit the maximum rate of attitude slews to 6 deg/min (instead of the nominal 12 deg/min)

The 45-deg tilt does result in an even lower power output. However, if no further degradation occurs, the spacecraft will still be able to carry out its mission. The CSS eyes are mounted both on the spacecraft body and on the arrays. The onboard CSS algorithm assumes that the arrays directly face the Sun. The use of a 45-deg solar array tilt invalidates this algorithm.

5. Performance of Star Trackers

Star tracker magnitude calibration and noise and distortion for RXTE are described below.

5.1 Magnitude Calibration

The flight software (FSW) gets 10 data samples per second for each star. The RXTE Kalman filter only processes a star once per second. The FSW star data processing averages the magnitude counts of the ten samples to obtain C_{ave} for each star, and then applies the following counts-to-magnitude conversion: $m = k_S * \ln(C_{ave}) + k_B$, where k_S is a constant that is the same for both trackers. Its value is -1.085736 , which equals $-2.5/\ln(10)$. The parameter k_B was determined preflight by measuring a class A0V reference star in each tracker. The preflight observed magnitude counts, C_0 , yield the following bias values:

$$\text{Tracker 1: } k_B = 11.851 = 2.5 * \log_{10}(C_0) \quad C_0 = 54988 \text{ (Reference 2)}$$

$$\text{Tracker 2: } k_B = 11.887 = 2.5 * \log_{10}(C_0) \quad C_0 = 56835 \text{ (Reference 2)}$$

The on-orbit magnitude calibration solution for ST1 combined data from the day of launch, and from the DSS calibration, IRU calibration, and calibration validation maneuvers. There were 736 total stars in all batches, of which 275 were OSC stars. Of those 275 stars, 250 were accepted for magnitude calibration. The solution ST2 used the same data spans as for ST1. For ST2, there were 619 total stars in all batches, of which 259 were OSC stars. Of

those 259 stars, 244 were accepted for magnitude calibration. Table 3 shows the results. Note that k_s and k_B are known in the FSW as the variables MagColScale and MagColBias, respectively.

In conclusion, both star trackers' premission magnitude calibration constants were within 0.06 magnitude of the values determined on-orbit. The constants can continue to be refined as more flight data are accumulated.

Table 3. On-Orbit Magnitude Calibration Results

Tracker	Prelaunch k_B	On-Orbit k_B	Δk_B (On-Orbit-Prelaunch)
1	11.851	11.9097 \pm 0.0481 (3 σ)	0.0587
2	11.887	11.9148 \pm 0.0418 (3 σ)	0.0278

5.2 Noise and Distortion

To obtain a quantitative estimate of the effects of noise and distortion on the star tracker observations, consider the combined residuals for both axes of both trackers obtained from single-frame attitude determination. For each star observation, the residual is the absolute magnitude of the difference between the observed and catalog vectors, both in spacecraft body coordinates. Star observations during maneuvers were used to obtain information throughout the FOV. For each time frame of the residual computation process, an attitude is computed using the single-frame quaternion estimation (QUEST) method (Reference 3) with star observations at or near that time. Propagation over short time intervals is used to group the observations at a common time. Then, the root-mean-square (RMS) of the residuals from all the frames is computed. These residuals are consistently about 3.0 arc sec RMS. The following error sources affect the residuals computed in that manner: sensor noise, sensor FOV calibration errors, attitude error, sensor bias and alignment errors, star catalog position errors, and center of brightness position shifts due to nearby stars. Stars used for this process were restricted to have a catalog position uncertainty of less than 1 arc sec and a predicted center of brightness shift less than 1 arc sec. In reality, most of the catalog stars have an uncertainty much less than 1 arc sec. These residuals are normally computed at the end of the alignment calibration process (see the section on Calibration Methods). Because attitude and alignments are solved-for with the same data used to compute the residuals, the RMS residuals are statistically reduced relative to the sensor residuals due to other error sources. Using the number of measurements and the number of quantities solved-for with these measurements, the RMS residuals are adjusted to compensate for this reduction (Reference 4). Table 4 shows these results for calibration maneuvers done on four separate days.

Table 4. Star Tracker Residuals From Alignment Calibrations

Day of Mission / Type of Data	RMS Residuals (arc sec)	Number of Attitudes Solved-for	Number of Star Observations	Adjusted RMS Residuals (arc sec)
1 / inertial	2.91	162	756	3.54
5 / maneuver	3.01	4169	18266	3.71
6 / maneuver	3.12	4343	17916	3.91
21 / maneuver	3.13	2152	9359	3.87

The RMS systematic errors across the FOV of the star tracker are specified to be no greater than 3 arc sec per axis, and the RMS noise is specified to be no more than 3 arc sec per axis. Combining these two sources of errors for both axes yields 6 arc sec. The adjusted RMS residuals are well within the specified 6 arc sec limit for all three sets of maneuvers (see Table 4), even though the adjusted residuals still contain catalog errors and nearby star errors up to 1 arc sec each. Future analyses are planned to obtain separate noise and distortions for each axis of each star tracker.

6. OBC Performance

RXTE OBC performance results in the areas of attitude and orbit accuracy are described below.

6.1 Attitude Accuracy

The RXTE spacecraft attitude determination requirement during the mission phase is for accuracy better than 0.02 deg. Requirements for attitude knowledge are 60 arc sec for the spacecraft X-axis and 42 arc sec for the Y- and Z-axes (all values are 3σ) (Reference 5). Results were obtained using the Coarse/Fine Attitude Determination System (CFADS) batch least-squares attitude determination algorithm. Table 5 illustrates ground-versus-OBC computed attitudes and their residuals from the most recent data at the time of this printing.

Table 5. OBC-Versus-Ground Solutions From CFADS

Epoch	OBC Attitude (degrees)			Ground Attitude (degrees)			Residuals* (arcsec)		
960303.0147	79.229	-45.999	91.060	79.231	-45.997	91.061	5.130	0.083	-1.979
960304.0232	79.229	-45.996	91.438	79.228	-46.000	91.438	-1.285	0.110	7.228
960308.0124	40.199	-61.254	126.890	40.201	-61.255	126.886	5.533	0.219	0.465
960315.0127	14.202	-60.756	158.853	14.203	-60.755	158.850	-3.591	0.504	0.364
960319.0231	-129.893	57.143	-124.258	-129.888	57.139	-124.254	0.857	-0.244	-6.055

* Average values based on the entire span of data using MTASS Attitude Validation Utility.

6.2 Orbit Accuracy

The RXTE OBC propagates the position for itself and up to three TDRS. This propagation is based on EPVs that are uplinked to the spacecraft. Fresh EPVs for RXTE are uplinked daily; the TDRS vectors are uplinked once per week. At launch, three TDRSs were in use for RXTE: TDRS-4, TDRS-5, and TDRS-7. These were designated TDRS-East, TDRS-West, and TDRS-Spare, respectively. TDRS-7 was later dropped from the lineup.

As a result of the stationkeeping being performed on TDRS-4 and -5, it is possible to use center of box (COB) EPVs for uplink to RXTE. The position uncertainty for TDRS-4 and -5 COB is approximately 130 km, corresponding to about 0.25 deg antenna-pointing error at RXTE. This approach was agreed to by the Project and has eliminated the need to support maneuvers for those TDRS. For COB propagation to be used onboard, the propagation modeling for the OBC was modified to use a table of geopotential values, enabling the proper modeling to be used for each spacecraft. For COB TDRS, the geopotential modeling is zeroed out in the table for those TDRS. For the other propagations, a truncated JGM-2 model is kept in the table.

During a simulation prior to launch, FDD discovered that the COB modeling had mistakenly been put in the RXTE OBC for TDRS-7. Analysis predicted that the OBC-versus-ground ephemeris error would be approximately 180 km, which fell within acceptable antenna-pointing error limits. This was brought to the attention of the Project, and the decision was made to fly with the error.

Initial analysis simulating the onboard propagator with a more complete environmental model than the OBC indicated the RXTE orbit state propagation error was <4 km over 1 day at the beginning of mission, and under 30 km per day throughout the solar cycle. However, prelaunch tests with the actual OBC propagator in the SIVVF and RXTE itself showed RXTE state propagation errors within 12 km per day typically, and the COB TDRS propagation errors within 26 meters at all times. The non-COB TDRS propagations were expected to perform similarly to the RXTE propagation.

At about 2 hours after separation, the OBC-versus-ground ephemeris comparisons computed by RTADS were as displayed in Table 6. Note that the comparison for TDRS-7 is high. The TDRS-7 orbit had changed as the result of a momentum control maneuver, and the Mission Operations Center (MOC) was advised that a new TDRS-7 EPV needed to be uplinked. Shortly after this comparison, it was uplinked. Since then, the observed propagation comparison results have RXTE staying within 12 km over a day and the COB TDRS maintaining < 26 meters.

Table 6. OBC Propagated Positions Versus Ground Ephemeris on 95/12/30 at ~1645Z

Spacecraft	RXTE	TDRS-4	TDRS-5	TDRS-7
Comparison (meters)	605	23	24	6493

7. Attitude Sensor Calibration

The calibration requirements, strategy and maneuvers, methods, and results for the RXTE mission are described below.

7.1 Calibration Requirements

The FDD was required to produce the following attitude sensor calibration products for the early RXTE mission:

- ST alignments
- DSS alignments and FOV calibration
- IRU alignment, scale factor, and bias calibration
- TAM alignment, scale factor, and bias calibration

The alignments of all sensors were to be referenced to ST1, which means that the alignment of ST1 should be unchanged as a result of the calibration process.

For the OBC to identify stars properly, the relative alignment error between the star trackers must be less than 200 arc sec. Although experiences with previous missions (Reference 6) have shown alignment launch shifts for star trackers to be less than this limit, the ACS engineers wanted to be prepared for larger launch shifts. Thus, the FDD needed to be able to calibrate the star tracker alignments on mission day 1.

The RXTE OBC does not use star data to update the attitude during maneuvers. The attitude during maneuvers is determined by propagating the last star tracker-based attitude solution with IRU data. Thus, it is important to have an accurate calibration of the IRU alignment and scale factor.

7.2 Calibration Strategy and Maneuvers

All attitude sensors were running soon after separation (mission day 1) from the Delta second stage. During the first 3 hours after separation, the FDD used ST and IRU data during an inertial period to solve for attitude and IRU bias. These were uplinked to the OBC to initialize the ACS Kalman filter. Next, analysts obtained preliminary star tracker alignments with a method that is insensitive to IRU calibration errors. These alignments are constrained so that the ST1 alignment does not change and the ST2 alignment absorbs all of the alignment correction. These alignments were uplinked to the OBC and used in the FDD ground system.

On mission day 3, the spacecraft carried out a sequence of moderate-sized maneuvers (about 25 deg) to obtain ST and IRU data for a preliminary IRU alignment/scale factor calibration, also to be uplinked to the OBC and used in the FDD ground system. These maneuvers were designed to obtain rotation information about all three IRU axes. In this calibration, the IRU alignment is referenced to the STs.

On mission day 5, a sequence of large (48- to 175-deg) maneuvers was executed to obtain data for comprehensive ST alignment calibration and IRU alignment/scale factor calibration. These maneuvers give rotation information about all three IRU axes, and star observations before, during, and after each maneuver. Analysts used the ST data to obtain comprehensive star tracker alignments. Again, these alignments are constrained so that the ST1 alignment does not change. Then, these data were used to obtain a comprehensive alignment/scale factor calibration of the IRU. Again, these were uplinked to the spacecraft and used by the ground system.

On mission day 6, a sequence of large (49- to 122-deg) maneuvers was executed to obtain data for comprehensive alignment and FOV calibration of the DSSs. These maneuvers were designed to sweep the Sun through the entire FOV of both DSSs, consistent with Sun constraints. Using ST and DSS data, the DSSs were first aligned relative to the STs. Then, adjustments to the Sun's image within the FOV were made. These results were uplinked to the OBC and used by the ground system.

On mission day 21, another sequence of large (49- to 180-deg) maneuvers was executed to obtain independent data for validating the IRU and ST calibrations.

Any convenient interval of continuous data may be used for the magnetometer calibration. Day 5 data are being used for calibration of the IFOG.

7.3 Calibration Methods

The alignment calibration method for the star trackers and Sun sensors must be able to handle multiple star observations at one time from the star trackers and single object observations from the Sun sensors, and must also be able to digest such data coming at different times and rates. It is also necessary to have a method that produces results on mission day 1. Past experiences with in-flight calibration have shown gyroscope calibration to be lengthy with many complications. Thus, it is desirable to separate the alignment calibration of star trackers and Sun sensors from that of gyroscopes. Specifically, the ST/DSS alignment algorithm should be insensitive to gyroscope alignment/scale factor errors.

The chosen alignment algorithm computes attitude and alignment at the times of the observations of one of the star trackers, the *primary* sensor. Observations from the other star tracker and from the Sun sensors are made at different times. Using IRU data, the other sensor data are rotated to the attitudes at which the primary sensor observations are made. Because the time intervals over which these rotations are made are small, less than 1 sec, the error introduced by IRU alignment/scale factor error is negligible (less than 0.045 arc sec). At each such time, a new attitude is computed, while alignment adjustments are accumulated over all the times (Reference 7).

To model systematic errors in the gyroscopes, both in-flight and ground attitude systems compute the average angular rate $\bar{\omega}$ from IRU incremental angle counts $\Delta\bar{N}$ during time interval Δt with the following equation:

$$\bar{\omega} = G \begin{bmatrix} k_x \Delta N_x \\ k_y \Delta N_y \\ k_z \Delta N_z \end{bmatrix} \frac{1}{\Delta t} - \bar{b}$$

where G is the 3×3 alignment/scale factor matrix; k_x , k_y , and k_z are scale factors for each channel; and \bar{b} is the bias vector. FDD IRU calibration systems solve for a matrix M and a vector $\delta\bar{b}$, which are used to adjust the calibration parameters as follows: $G' = (I + M)G$ and $\bar{b}' = \bar{b} + \delta\bar{b}$. The elements of the matrix M are small and provide for adjustments to the scale factors as well as the alignment of each axis of the IRU. However, at inertial attitudes, alignment/scale factor errors are not observable; maneuvers are needed to distinguish them from the bias. Kalman filters onboard the spacecraft and in the ground system can accurately solve for attitude and IRU bias with ST and IRU data, but errors in the IRU alignment/scale factor matrix manifest themselves during attitude maneuvers. Several methods are available for calibration of the gyroscope. The Davenport gyroscope calibration algorithm (Reference 8) is used to solve for these errors. This algorithm compares attitudes before and after maneuvers to the rotation obtained by integrating IRU data for the same maneuvers. Initial and final attitudes are computed with inertial data to free them from alignment/scale factor errors. Maneuver data from RXTE mission days 3, 5, or 21 may be used for this calibration.

As an extension to the Davenport method with inertial attitudes, note that during the constant rate portion of maneuvers, an attitude determination algorithm that also solves for IRU bias can get an accurate attitude, independent of gyro alignment/scale factor error. Even though the IRU bias is corrupted by the IRU alignment/scale factor error, the attitude is accurately determined. Thus, the Davenport method may also be used with attitudes derived from constant rate data during maneuvers.

A successful method for calibrating the DSS FOV distortions in flight is documented by Hashmall (References 9 and 10). This method incorporates adjustments to the coefficients of the manufacturer-supplied calibration function with additional adjustments that account for a relative misalignment between the two heads of the DSS. The method requires an accurate attitude history obtained from ST and IRU data. This history is obtained from the DSS calibration maneuvers (mission day 6), where the Sun is swept across the FOVs of the DSSs. Using this history and the calibrated DSS alignments, the reference Sun vector, obtained from precision Sun ephemeris and corrected for

velocity aberration and parallax, is transformed into the Sun sensor coordinate frames and then used to compute angles within the FOV. The difference between these references and the observed Sun angles in the FOV is used to compute the corrections to the calibration coefficients using batch least squares methods.

As with the DSS FOV calibration, the magnetometer calibration relies on an accurate attitude history obtained from ST and IRU data. With this history, a model of the Earth magnetic field, and the spacecraft ephemeris, the reference Earth field is transformed to body coordinates and compared with the magnetic field computed from magnetometer measurements and adjusted for bias and magnetic torquer effects. Using a batch least squares method, the differences between the two fields are used to compute adjustments to the magnetometer bias, alignment, scale factors, and torquer-to-magnetometer coupling matrix.

7.4 Calibration Results

Because ST1 is used as a reference sensor (its alignment is kept fixed), the change in the ST2 alignment is equal to the change in the relative alignment between the two sensors. Table 7 summarizes the results of four alignment calibrations. The table shows the change in relative alignments with respect to the prelaunch alignments.

Table 7. ST-Calibrated Relative Alignment Adjustments

Type of Data	X-Axis (arc sec)	Y-Axis (arc sec)	Z-Axis (arc sec)
Day 1 Inertial	-27.66	-15.18	2.37
Day 5 Maneuver	-24.24	-18.05	1.36
Day 6 Maneuver	-28.40	-17.69	3.13
Day 21 Maneuver	-24.44	-17.05	2.10

These relative alignment change results are also plotted in Figure 3. Table 5, in Section 5, shows the amount of data that was used for each of these solutions.

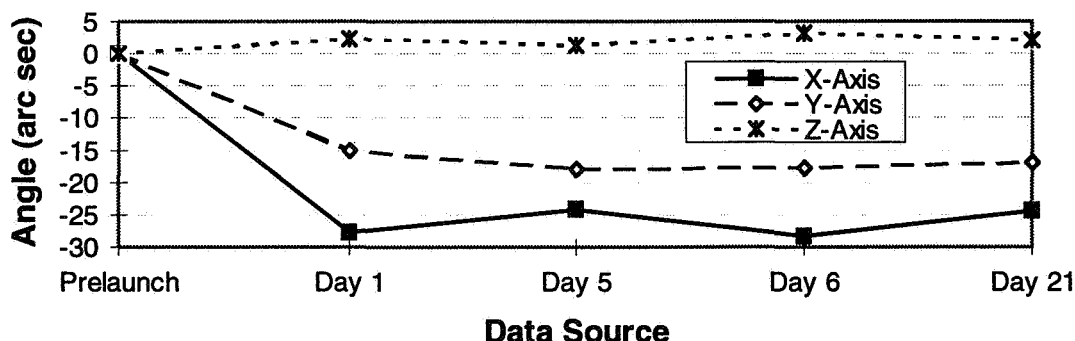


Figure 3. RXTE ST1/ST2 Relative Alignment Results

To obtain an idea of the uncertainty of the ST alignment calibration results, a separate ST alignment calibration was done for each of the nine maneuvers on mission day 6. The alignment calibration of that day is a weighted sum of the results of each individual maneuver. The dispersion of these individual solutions indicates the uncertainty of the weighted sum. The empirical 1σ uncertainties for the day 6 solution are 5.1, 0.4, and 1.3 arc sec for the X-, Y-, and Z-axes, respectively.

The relative ST alignment calibration data show some interesting results. The relative alignment fluctuations around the X-axis are greater than the other two axes. This behavior is expected, because the relatively small FOV of the trackers (± 4 deg) results in higher rotational errors around their boresights, and because the ST1 boresight is aligned

along the body X-axis, and the ST2 boresight is less than 10-deg from the body X-axis. An important result is that the relative alignment between ST1 and ST2 is stable from day to day. In particular, the fluctuations of calibrations of mission days 5, 6, and 21, which use relatively large amounts of data, are consistent with the day 6 empirical uncertainty. Another interesting point is that the calibration of mission day 1, which used much smaller amounts of data (see Table 4), is very close to the other calibrations.

Table 8. Bias Solutions for Low-Rate Primary IRU Channels

Data and Processing	X-Axis (deg/hr)	Y-Axis (deg/hr)	Z-Axis (deg/hr)
Prelaunch	-0.1916	-1.0165	0.7144
Day 1 CFADS	-0.2319	-1.1042	0.8121
Day 3 IRUCAL for Preliminary Calibration	-0.2282	-1.0984	0.8101
Day 5 CFADS	-0.2224	-1.1023	0.8072
Day 6 CFADS	-0.2341	-1.1022	0.8068
Day 21 IRUCAL for Calibration Validation	-0.2292	-1.0989	0.8059

Table 8 summarizes a few of the many IRU bias solutions obtained using two different software packages. The CFADS is a batch least squares processor, used to solve for attitude and IRU bias using ST and IRU data. The IRU calibration system (IRUCAL) implements the Davenport gyroscope calibration algorithm and was used to solve for both IRU bias and the alignment/scale factor matrix. As seen in Table 8, both methods give consistent results that were stable over the early mission. Figure 4 presents the bias changes graphically. In this figure, the bias is expressed relative to the prelaunch value. On some other missions, IRU biases drifted over the first few days after launch (Reference 6)]. On RXTE, this effect was not seen.

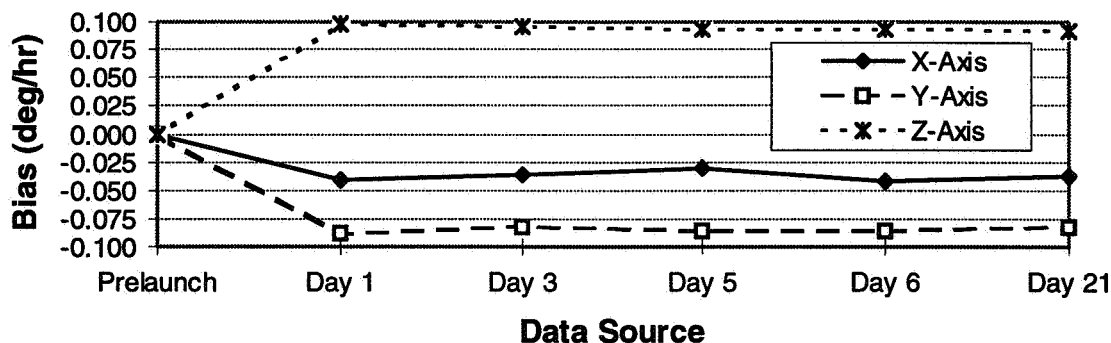


Figure 4. RXTE IRU Bias Relative to Prelaunch

In addition to CFADS and IRUCAL, the FDD ground system also computed an IRU bias using two Kalman filters, one running in real time (RTADS) and another running off-line (FILTER). The IRU bias for all four systems was consistent with each other and with the bias from the OBC Kalman filter.

Adjustments to the IRU alignment/scale factor matrix are given by the matrix M (see Section 7.3, Calibration Methods). The components of this matrix correct for the propagation error in each direction per angle rotated for each axis of rotation. These components are dimensionless, but can be interpreted to have the units “radians of propagation error per radian of rotation.” The diagonal components of the matrix M provide adjustments to the scale factor of each axis, because they give propagation errors along the direction of rotation. Whereas, the off-diagonal components provide propagation errors in the directions perpendicular to the rotation axes. The off-diagonal components also give alignment errors of the IRU axes. This dual interpretation occurs because a misalignment will cause a body axis rate to project a small amount onto the incorrect IRU axis, leading to the propagation error. It is

convenient to express this matrix in the units “arc sec of propagation error per radian of rotation,” which also gives alignment errors in arc sec.

Some of the results of the IRU calibration effort are given in Table 9. Alignment/scale factor adjustments are given relative to the prelaunch calibration. IRU alignments and scale factors obtained from the adjustments of the first and last solutions in Table 9 were delivered for use in the OBC and in the ground system. Analysts experienced difficulty in processing the IRU data for calibration, especially the day 5 data. Data gaps, particularly during the acceleration segments of maneuvers, complicated the analysis. Improved methods for handling such gaps and algorithms that do not require rate data at evenly spaced intervals will be used in future missions.

Table 9. Results of IRU Alignment/Scale Factor Calibration

Method	Davenport Algorithm With Inertial Attitudes			Davenport Algorithm With Rotating Attitudes			Davenport Algorithm With Inertial Attitudes		
Data	Day 3 Preliminary Calibration Maneuvers			Day 5 IRU Calibration Maneuvers			Day 21 Calibration Validation Maneuvers		
<i>M</i> (arc sec/rad)	-19.20	30.20	-7.75	-0.03	6.40	-19.57	-1.01	18.39	-24.54
	-24.10	-8.33	-39.36	6.97	-14.42	-54.33	-0.23	-18.22	-57.54
	28.88	44.83	-16.13	27.00	44.72	-10.46	28.59	46.31	-4.39

FDD analysts used data from the mission day 6 maneuvers to calibrate the DSS alignments with respect to the star trackers. The alignment adjustment around each axis of each sensor is given in Table 10. These adjustments are relative to the prelaunch alignments and are expressed in body coordinates.

Table 10. DSS Alignment Adjustments

Sensor	X-Axis (arc sec)	Y-Axis (arc sec)	Z-Axis (arc sec)
DSS1	-54.27	166.99	-25.86
DSS2	17.12	26.14	-49.30

The DSS FOVs were also calibrated with data from mission day 6 maneuvers, improving the residuals as indicated in Table 11. Separate residuals are given for each of the two angles, α and β , in the FOV. Because the Sun is constrained to be within 5 deg of the RXTE XZ-plane, the total variation in β is ± 5 deg at the center of each FOV, and ± 5.890 deg at the edge of the FOV. The α angle is allowed to vary over its full ± 32 -deg range. For this reason, the DSS FOV calibration must fit the data over a smaller portion of the β range than the α range. The initial FOV calibration residuals are smaller

Table 11. DSS FOV Calibration Residuals

Residuals	Initial (arc sec)	Final (arc sec)
DSS1 α	20.67	18.42
DSS1 β	18.14	9.70
DSS2 α	24.21	22.97
DSS2 β	14.41	8.51

than the initial residuals of the Sun sensors of other missions. This behavior is attributed to the restricted DSS FOV for RXTE. The final residuals after calibration are smaller for β than for α , because the smaller range of β contains less systematic variations than the full ± 32 -deg range. Were it not for the constraint on β , a more accurate fit could be obtained. However, as long as β remains small, any deficiency in the fit cannot be observed.

At the time this paper was written, the magnetometer calibration was still preliminary. FDD analysts have succeeded in obtaining improved calibration parameters, which reduce the error of attitude solutions using only TAM and IRU data from 0.5 deg to 0.2 deg per axis (1σ). However, systematic errors are still evident in the residuals. For previous similar missions, such errors have been reduced to less than 0.07 deg per axis (1σ). Analysts are investigating inconsistencies in the processing.

8. Conclusions

RXTE launch and in-orbit checkout support by the FDD was successful despite the anomalies encountered. The FDD was able to provide the orbit and attitude state vectors and the calibration information to the RXTE Project that were needed to transition the RXTE spacecraft into its operational phase. The most serious anomalies occurred with the CCD star trackers. Although they are superb attitude instruments, the debris and dropped star problems show they, nonetheless, are capable of strange behavior. Future flight software and FDD support procedures must be designed with these experiences in mind.

Acknowledgments

A few of the many other people who contributed significantly to the FDD's RXTE effort since its inception in 1992 are listed alphabetically below:

David Bolvin	James Cappellari	David Green	Leeann Lindrose	Joseph Sedlak
Robert Boyer	Lynn Carlson	Tom Gwynn	Chad Mendelsohn	David Shoup
Dan Brasoveanu	Murty Challa	James Heimerl	Douglas Moore	Mark Summerfield
Len Brockman	Donald Chu	Vilas Johnson	Neil Ottenstein	Susan Ray Valett
Evette Brown-Conwell	Orville Filla	Jon Landis	Anthony Paola	Scott Wallace
Alexander Calder	Jonathan Glickman	Michael Lee	Robert Rashkin	

The authors also acknowledge valuable conversations with Joseph Whitacre, Michael Femiano, Kong Ha, and Lou Hallock, and express their gratitude to the entire Flight Operations Team for the excellent teamwork.

References

1. The MathWorks, Incorporated, *MATLAB High-Performance Numeric Computation and Visualization Software, Reference Guide*. Natick, Massachusetts: The MathWorks, October 1992 (and reprints July 1993, September 1994, April 1995)
2. P. Newman, Swales & Associates, Inc., electronic memorandum, *GOV_IP.MCD*, September 15, 1994
3. M. Shuster and S. Oh, "Three-Axis Attitude Determination from Vector Observations," Paper No. AIAA 81-4003, *J. Guidance and Control*, Vol. 4, No. 1, January-February 1981, p. 70
4. W. Press, B. Flannery, S. Teukolsky, and W. Vetterling, *Numerical Recipes in C, The Art of Scientific Computing*, 2nd ed. Cambridge: Cambridge University Press, 1995, p. 662
5. Goddard Space Flight Center, *Detailed Mission Requirements-Issue 2 (DMR-2) Final Draft for the X-ray Timing Explorer (XTE)*, S. Coyle and J. Joyce, April 1993
6. W. Davis, J. Hashmall, J. Garrick, and R. Harman, "Postlaunch Calibration of Spacecraft Attitude Instruments," Paper No. AAS 93-325, *Spaceflight Dynamics 1993, Volume 84 of Advances in the Astronautical Sciences*, American Astronautical Society, April 1993
7. Goddard Space Flight Center, Flight Dynamics Division, 554-FDD-91/070R1UD0, *Multimission Three-Axis Stabilized Spacecraft (MTASS) Flight Dynamics Support System (FDSS) Functional Specifications Revision 1*, Jon Landis (CSC), prepared by Computer Sciences Corporation, September 1995
8. Computer Sciences Corporation (CSC), CSC/TM-77/6082, *Gyro Calibration Analysis for the High Energy Astronomy Observatory-A (HEAO-A)*, J. Keat, June 1977
9. J. Hashmall and D. Baker, "An Improved Transfer Function for the Fine Sun Sensor," presented at the International Symposium on Spaceflight Dynamics, sponsored by the Russian Space Academy, May 1994
10. W. Davis, J. Hashmall, A. Garber, H. Kang, and J. Zsoldos, "In-Flight Calibration of Alignment and Field of View Distortion for Spacecraft Attitude Sensors," Paper No. AAS 95-303, presented at the American Astronautical Society (AAS)/American Institute of Astronautics and Aeronautics (AIAA) Astrodynamics Specialists Conference, Halifax, Nova Scotia, August 1995

South Atlantic Anomaly Entry and Exit As Measured by the X-Ray Timing Explorer

Evan Smith (Hughes STX), Michael Stark (U Md), Barry Giles (GSFC/USRA),
Sandy Antunes (Hughes STX) and Bill Gawne (Allied Signal)

Abstract

The Rossi X-Ray Timing Explorer (RXTE) carries instruments that must switch off high voltages (HV) when passing through the South Atlantic Anomaly (SAA). The High Energy X-Ray Timing Experiment (HEXTE) contains a particle monitor that detects the increased particle flux associated with the SAA and autonomously reduces its voltage. The Proportional Counter Array (PCA) relies on uplinked predictions of SAA entry/exit times based on ephemeris data provided by the Flight Dynamics Facility (FDF). A third instrument, the All-Sky Monitor (ASM) also uses a predicted SAA model to reduce voltage when passing through the SAA. Data collected from the HEXTE particle monitor, as well as other instrument readings near the times of SAA entry/exit offer the potential for refining models of the boundaries of the SAA.

The SAA has an increased particle flux which causes high rates of detection in the RXTE instruments designed to observe X-rays. The high counting rates could degrade the PCA if HV is not reduced during SAA passages. On the other hand, PCA downtime can be minimized and the science return can be optimized by having the best possible model of the SAA boundary. Thus, the PCA team planned an extensive effort during in-orbit checkout (IOC) to utilize both HEXTE particle monitor data and instrument counting rates to refine the model of the SAA boundary.

The times of SAA entry and exit are compared with the definitive ephemeris to determine the precise location (latitude and longitude) of the SAA boundary. Over time, the SAA and its perimeter were mapped. The RXTE Science Operations Center (SOC) is continuously working to feed back the results of this effort into the science scheduling process, improving the SAA model as it affects the RXTE instruments, thus obtaining more accurate estimates of the SAA entry/exit times.

1. Introduction

The X-Ray Timing Explorer (XTE) was launched from the Eastern Test Range (ETR) on December 30, 1995, aboard a Delta II rocket. XTE was designed and built at the Goddard Space Flight Center (GSFC) and both the Mission Operations Center (MOC) and Science Operation Center (SOC) are located at GSFC. The XTE mission is intended to study the X-ray universe with unprecedented time-resolution (References 1 and 2). On February 28, 1996, NASA renamed XTE the Rossi X-ray Timing Explorer (RXTE) in honor of Bruno B. Rossi, the early pioneer in the field of X-ray astronomy.

The RXTE orbit is a 580-km altitude, near-circular orbit with a 23-degree inclination. The mission design altitude was the result of a trade-off between conflicting requirements. Arguing for a higher altitude was the goal of maximizing the longer achievable orbital lifetime. However, a lower altitude avoids to a greater degree the South Atlantic Anomaly (SAA), which has a larger spatial extent at higher altitudes. There is also an increased overall particle flux at higher altitudes. The reduced inclination, which required a plane-change maneuver at the first ascending node, also helps to reduce time spent in the SAA. Achieving an even lower inclination, though desirable, was not possible since the RXTE mass (2840 kg) was near the maximum for the launch vehicle. Without a plane-change maneuver, it is not possible to achieve an orbit with an inclination less than the latitude of the launch site, in this case, 28.5 degrees.

The SAA is a region of increased particle flux where the Van Allen radiation belts extend to lower altitudes than normal. X-ray detectors are sensitive to particle events in addition to X-rays. The SAA interferes with RXTE science

operations since the energetic particles trigger high counting rates in the RXTE detectors, degrading them over time. The RXTE instruments must safe themselves during passages through the SAA to avoid damage to the detectors. Though this damage is cumulative, even short exposure to high SAA particle rates with the high voltage (HV) turned on was considered unacceptable for the PCA.

This paper discusses the efforts of the RXTE SOC to optimize an SAA model for use in science planning. The following section provides additional background about the RXTE detectors and SAA models for past X-ray astronomy missions. Section 3 describes the development of the initial SAA model. Section 4 describes the post-launch efforts to collect, analyze and interpret the data that led to the optimized SAA model. Section 5 presents the new SAA contour. Section 6 gives the conclusions of this study.

2. Background

RXTE carries three instruments for studying the X-ray universe. Each of these must reduce HV when passing through the SAA. The High Energy X-Ray Timing Experiment (HEXTE) (Reference 3), designed and built at the University of California - San Diego (UCSD), consists of two clusters of four phoswich crystal scintillators that are sensitive in the range from 15 to 250 KeV. HEXTE contains two particle monitors that detect the increased particle flux associated with the SAA and autonomously reduce the HV. The Proportional Counter Array (PCA) (Reference 4), designed and built at GSFC by the Laboratory for High Energy Astrophysics (LHEA), consists of five gas proportional counter units (PCUs) co-aligned with HEXTE. For reducing HV, the PCA relies on uplinked predictions of SAA entry/exit times calculated using the SAA model discussed in this paper with ephemeris data provided by the Flight Dynamics Facility (FDF). A third instrument, the All-Sky Monitor (ASM) (Reference 5), designed and built at the Massachusetts Institute of Technology (MIT) consists of three Scanning Shadow Cameras (SSCs) for monitoring the X-ray sky for transient behavior. The three detectors, one-dimensional imaging gas proportional counters, also must reduce HV when passing through the SAA. The ASM considers other factors besides just the SAA contour in its algorithm for calculating when to reduce HV.

All astronomical satellites in low Earth orbit are adversely affected by the SAA. Before launch, an initial estimate was made of the contour of satellite longitude and latitude for which the particle fluxes would be potentially harmful to the PCA detectors. Once in orbit, the size of the SAA model was increased more than once during the first 2 weeks, before a safe contour was obtained. Later, based on the analysis presented here, the size and shape were changed to a more optimal contour.

High counting rates associated with the SAA degrade the PCA if HV is not reduced during SAA passages. The PCA contains a High Rate Monitor (HRM) that switches off the HV when excessive counting rates are detected. The HRM works on signals from within the active PCUs and does not use a separate particle monitor device as HEXTE does. Each of the five PCUs has its own independent HRM protection system. The HRM could be used to lower the HV upon SAA entry, but it cannot provide information about when to increase the HV back up to operational levels. The PCA proposal included a Geiger counter that would monitor the particle rate and provide a signal when the HV should be turned back up. This was the method of detector protection used on the Cosmic X-ray Spectroscopy Experiment on the Orbiting Solar Observatory (OSO-8). This part of the instrument was eliminated by the program managers in a cost-cutting measure based on the belief that the expense of building hardware to do the job of HV management would exceed the expense of commanding HV on the basis of calculations and commands stored on-board.

For the first 2 months of the mission, PCA HV was simply reduced by stored command to a minimal level during SAA passages. However, the HRM was a safety feature that was utilized several times during the in-orbit checkout (IOC) phase of the RXTE mission before an SAA model of sufficient size was implemented. These switch-offs avoided the most intense fluxes of the SAA, and thus damage to the detectors, but were inconvenient since ground commanding was required to restore the PCA to operating condition. So the first step in the optimization process was to find an SAA model that was bigger on all borders than the actual SAA contour. Even after several attempts, the SOC would still occasionally find a new extension of the SAA that was not included in the latest model.

Although having an oversized SAA model avoids damage to the PCA, or at least the inconvenience of having to turn it back on by ground command, PCA downtime can be minimized and the science return can be optimized by having

the best possible model of the SAA boundary. Thus, the PCA team, in conjunction with the SOC, conducted an extensive effort during in-orbit checkout (IOC) to utilize both HEXTE particle monitor data and instrument counting rates to refine the model of the SAA boundary.

3. Initial SAA Model

Prior to launch, the RXTE SOC arrived at an initial starting definition for the SAA based on three independent sources of information. The World Maps of B, L and Flux Contours (Reference 6) provided information about proton and electron predicted flux levels. However, there are difficulties relating these flux levels directly to estimated PCA count rates, prompting the more practical approach of relying on past mission history.

The HEAO-A mission of 1977 carried many large detectors. The A-2 experiment, comprised of proportional counters, was the basis for the RXTE PCA design. That experiment also did not fly a Geiger counter for budgetary reasons, and the detectors were turned on and off by command. The detector data for the period when the detectors were on provided evidence about the contours of the SAA that applied at that time. Furthermore, the HEAO-A4 experiment carried a particle monitor (for protons) and, as the orbit decayed from 453 km to 333 km, the science team built up a data cube of the integrated history of all scans through the SAA region. This data set (Reference 7) showed an SAA profile with a pronounced funnel shape, rapidly increasing in size at higher altitudes. Unfortunately, the top layer of the cube was still well below the planned RXTE orbital height, leaving the problem of trying to extrapolate to the higher altitude, as well as the question of whether the boundaries applicable in 1977-1978 were applicable to 1996. The extent of the SAA appears to show a variation correlated with the 11-year solar cycle.

The current Japanese ASCA mission has a higher inclination than RXTE and therefore scans all the geographic locations that RXTE can overfly. The ASCA orbital altitude of 566 km is similar to the 580-km RXTE orbital altitude. However, the ASCA imaging detectors are much smaller than the PCA and thus likely to be able to operate nearer the mean SAA center. The SAA perimeter in use for ASCA was compared with the HEAO-A perimeter. Except for an eastward extension at low latitude, the ASCA SAA profile fell inside of the HEAO-A profile. After examining these sources for determining the geographical extent of the SAA, a contour was chosen with the intent of adjusting it after launch. The contour described an approximately "half moon" shape centered on the South Atlantic. The Science Operations Facility (SOF) scheduling tools, SPIKE and Needle, require a string of longitude, latitude pairs. This format became the standard for the initial and subsequent deliveries to the SOF.

It was realized that the HRM might turn off the PCA detectors during the entrance to the SAA if the SAA model was too small, and that then ground commands would be required to turn them on again. Since the detector HVs were turned down and not off, the PCA detectors still provided information, at a reduced count rate, of the particle flux. This data, PCA counting rates at reduced HV, supplemented the HEXTE particle monitor data as a source of information for determining the appropriate SAA contour for RXTE science operations.

4. Post-Launch Analysis

The SAA model is incorporated into the SOF scheduling software, SPIKE and its derivative, Needle. Needle is used for fine-tuning the schedule, allowing the user to visualize the various constraints on an observation. The primary constraints are: (1) the target is not Earth-occulted; (2) RXTE is not within the SAA; (3) the target is not within 30 degrees of the Sun. The times of SAA entry and exit are determined by Needle using the RXTE ephemeris provided by the FDF, and the current SAA model, which has already been iterated several times since launch. The SAA entry and exit times trigger PCA HV up or down commands that are incorporated into the Daily Activity Plan (DAP), which is the primary means of conveying science commands to the spacecraft. The RXTE MOC processes the DAP, and uploads the commands to the spacecraft. By monitoring the instrument data in the SOF, it is possible to quickly assess whether any given SAA model is adequate for HV management.

Following launch, there was a 30-day IOC period. The first week was devoted primarily to overall spacecraft checkout, but the RXTE instruments were also activated and checked out. The balance of the IOC period was used for astronomical calibrations and pointings. The regular program of peer-reviewed science targets by Guest Observers (GOs) started as scheduled around day 30 of the mission.

For the first week, the MOC conducted general spacecraft testing primarily during the daytime shift, while the SOC was able to proceed with instrument checkout much of the nighttime hours. Fortunately, almost all SAA passes occurred in the spacecraft priority daytime shift, meaning that nighttime checkouts were essentially un-hindered by SAA passages. Before the PCA high voltages could be left on at the end of the night shifts' testing, it was essential to check that the PCA HV up and down commands were happening at the specified time. By the end of the third night after launch, all five of the Proportional Counter Units (PCUs) had been run at their full HV settings.

At the start of the third night, the PCA was tripped off unexpectedly by the HRM. This was the first indication that an SAA pass had occurred at a time other than that predicted by the SAA model. The HRM safety trip had been fully tested on the previous night. As all other aspects of the chain of events relating to PCA SAA HV commanding had been checked and were working, the failure to predict this extra SAA pass was clearly due to the SAA perimeter definition being optimistically small. By monitoring the PCA HRM trip-offs over the following few days, a process of trial and error was begun leading to a gradually increasing SAA perimeter size.

Due to the relative orbit geometry, RXTE traverses the SAA during consecutive orbits for a portion of each day. With the pre-launch model, this portion amounted to about half a day. With the eventual model that resulted after several increases in size that were required to prevent HRM trip-offs of the PCA, the SAA passages occurred on about three quarters of the orbits each day. Additionally, each SAA passage was extended in time by a few minutes. As a result, there was a significant increase in the amount of time that the PCA had to be operated with HV off due to predicted SAA passages. The desire to reclaim some of this time for doing actual science observations prompted the more systematic approach to optimizing the SAA definition that is the primary focus of this paper. It is worth pointing out, however, that science data collected near the SAA boundary may still have high background counting rates, or rapidly changing rates, making the data unsuitable for some science programs. On the other hand, the PCA design includes a propane layer that acts to veto out false detections caused by particles events.

5. Optimization of the SAA Contour

Data collected from the HEXTE particle monitor, as well as PCA data collected in, or just outside, the SAA offer the potential for refining models of the boundaries of the SAA. The times of SAA entry and exit are evident from the HEXTE particle monitor data. These times are compared with the RXTE ephemeris to determine the precise location (latitude and longitude) of the SAA boundary. In addition, the PCA HRM trip-offs, though inadvertent, provided a good measurement of the SAA border since any point where the PCA tripped off represented a practical limit for commanding the HV reduction. For the most efficient science operations, RXTE should get as close to the SAA as possible before turning down the PCA HV since science data are then lost until SAA exit. However, a safe margin must be maintained to account for SAA time-variability and spatial shifting. Over time, the entire SAA region was mapped and thus an outer perimeter of the SAA was determined.

Each refinement of the SAA model was fed back into the science scheduling process. The RXTE ephemeris and the latest SAA model are used to predict future SAA entry and exit times, and then commands to reduce high voltage are inserted into the daily activity plan (DAP). Figure 1 shows a contour map of the SAA at the RXTE altitude based on HEXTE HRM data. Figure 2 shows a similar contour based on data from the PCA. The PCA was able to map the central region of the SAA because the HV was only lowered, not turned completely off. (The 0 setting, or lowest high voltage, setting is about 1000 V, while typical operational settings are around 2200 V.) However, on March 20, 1996, the PCA mode of operation was changed such that the PCA HV is now turned off for passages through the SAA. The PCA HRM trip-offs show up as small diamonds. This occurs because identical particle rates generate much higher counting rates when the HV is at the operational setting.

It is interesting to look at the concept of weather in the SAA. Figures 3a and 3b show the maximum and minimum contours, respectively, from the HEXTE particle monitor count rates. Similarly, figures 4a and 4b show the maximum and minimum contours, respectively, from the PCA count rates at low voltage settings. This weather, or day to day variability in the SAA, complicates efforts to optimize the contour. For operational reasons, the boundary should be larger than the maximum extent of the SAA.

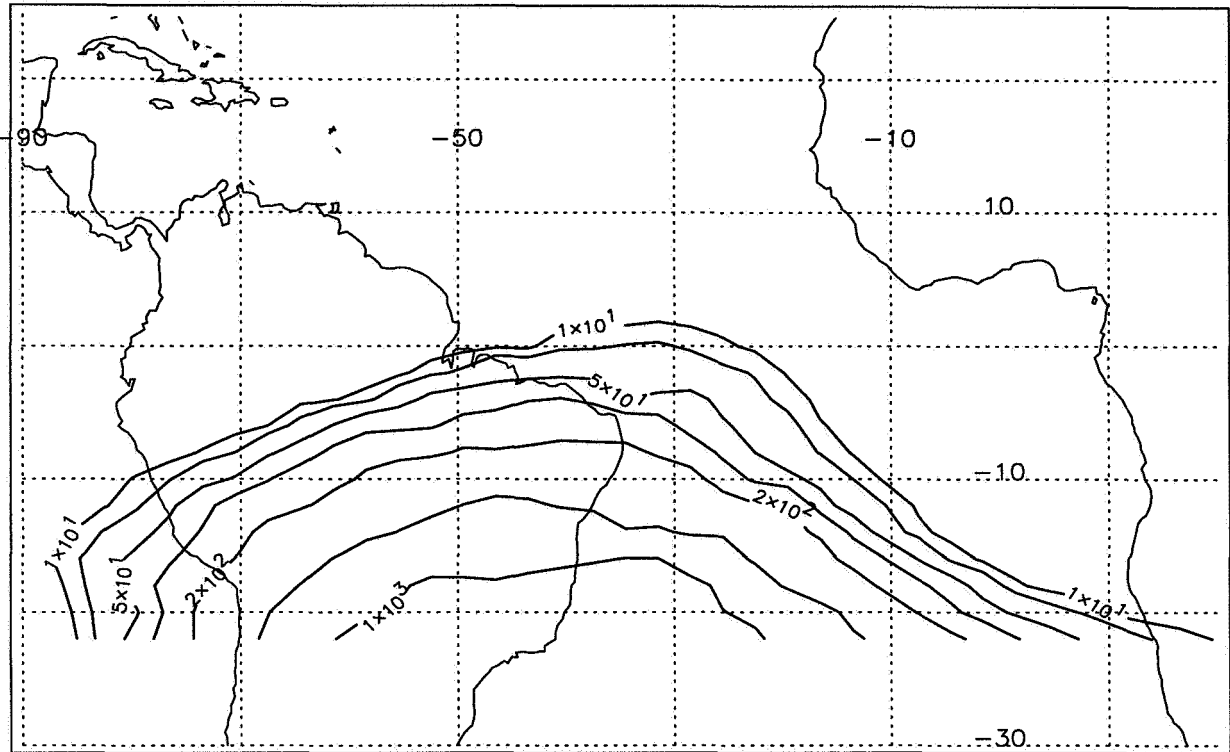


Figure 1. SAA Contour from Average HEXTE Particle Monitor Count Rates

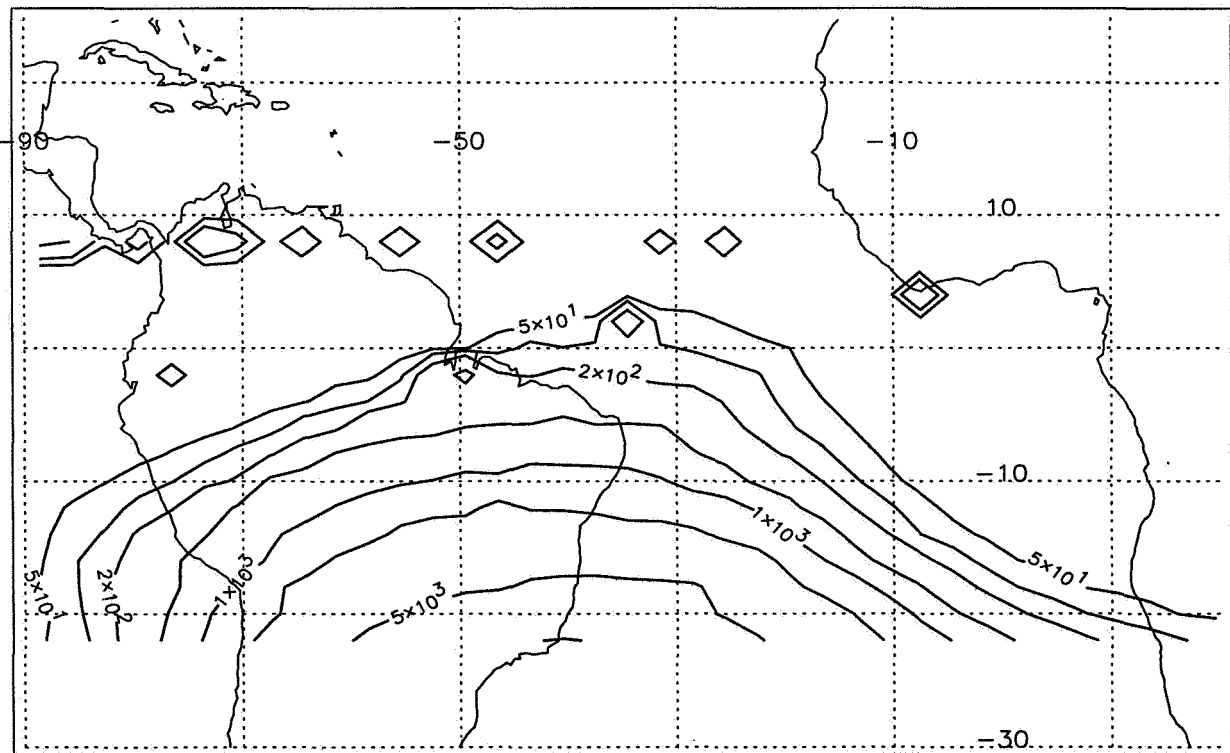


Figure 2. SAA Contour from Average PCA Count Rates at Reduced HV

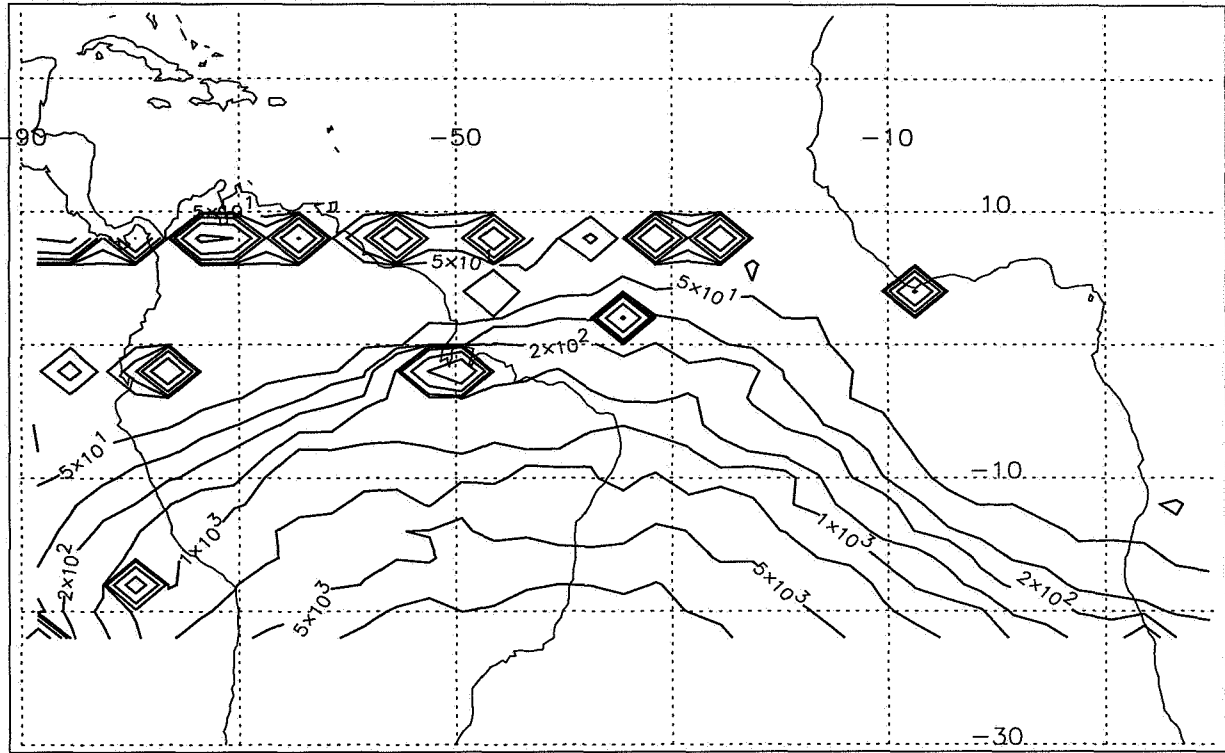


Figure 4a. SAA Contour from Maximum PCA Count Rates at Reduced HV

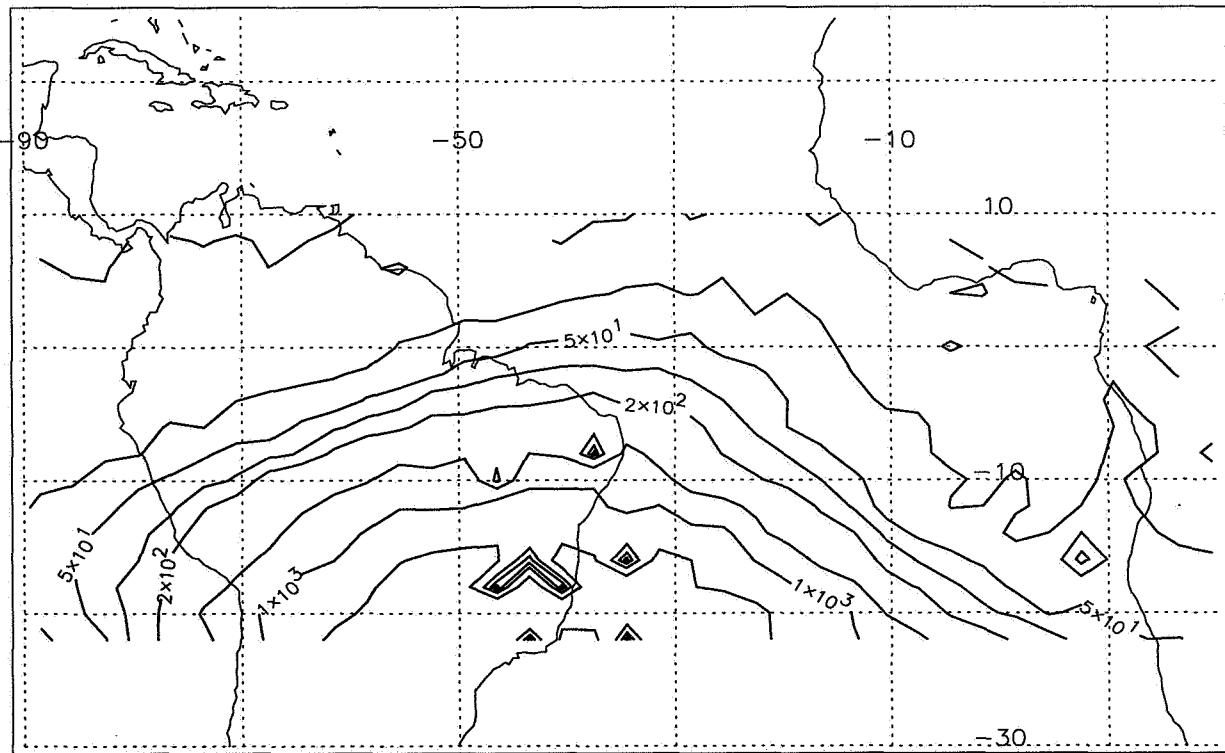


Figure 4b. SAA Contour from Minimum PCA Count Rates at Reduced HV

6. Conclusions

This effort to optimize the SAA model demonstrates a practical application of flight dynamics products and concepts in a science operations arena. Based on the precise ephemeris data available from the FDF, the time-tags for instrument readings could be accurately converted into a longitude and latitude of the sub-Earth point. The instrument counting rates are thus converted into contour maps of the SAA at the RXTE orbital altitude. By trial and error, the SAA contours are fed back into the science planning process to increase the efficiency of RXTE science operations.

Additionally, the contour maps of instrument counting rates can be used by scientists studying the near-Earth environment. At the very least, these data will be useful to planners of future X-ray astronomy missions, just as the RXTE science team relied on similar data from previous X-ray missions.

Although a savings in on-source science time was achieved by optimizing the SAA perimeter, the variability of the SAA on both short and long timescales limits the gain in efficiency. The SAA model must be larger than the maximal extent of the SAA or unplanned HV switch-offs will nullify the increased on-source time. In fact, the difficulties encountered in ground commanding of SAA management argue the case for using hardware to accomplish this task for future X-ray astronomy missions. Having a feedback control loop for turning down HV gets around the problem of imprecise knowledge of the SAA boundary, and has worked very well for HEXTE.

The authors acknowledge useful feedback from Jean Swank and Keith Jahoda of the PCA team.

References

1. Giles, A.B., Jahoda, K., Swank, J.H., and Zhang, W., 1995, *Publ. Astron. Soc. Aust.*, 12, 219.
2. Swank, J.H., Jahoda, K., Zhang, W., Giles, A.B., Marshall, F.M., Bradt, H.V., Levine, E.H., Morgan, E.H., Remillard, R.A., Rothschild, R.E., Gruber, D.E., Hink, P.L., and Pelling, M.R., 1994, in *Lives Of Neutron Stars*, NATO ASI Series, Kluwer Academic Publishers, p 525.
3. Pelling, M.R., et al, 1991, in *EUVE, X-Ray and Gamma Ray Instrumentation for Astronomy II*, Proc, SPIE, 1549, 134.
4. Zhang, W., Giles, A.B., Jahoda, K., Soong, Y., Swank, J.H., and Morgan, E.H., 1993, in *EUVE, X-Ray and Gamma Ray Instrumentation for Astronomy IV*, Proc, SPIE, 2006, 324.
5. Bradt, H.V., Rothschild, R.E., and Swank, J.H., 1993, *A&A Suppl. Ser.*, 97, 355.
6. Stassinopoulos, E.G., 1977, *World Maps of Constant B, L, and Flux Contours*, Scientific and Technical Information Division, NASA, Washington, DC, NASA SP-3054.
7. Gruber, D.E., 1994, private communication.

The Solar and Heliospheric Observatory (SOHO) Mission : An Overview of Flight Dynamics Support of the Early Mission Phase

R. Short, J. Behuncik
National Aeronautics and Space Administration
Goddard Space Flight Center
Greenbelt, Maryland, USA 20771

Abstract

The SOHO spacecraft was successfully launched by an Atlas IIAS from the Eastern Range on December 2, 1995. After a short time in a nearly circular parking orbit, the spacecraft was placed by the Centaur upper stage on a transfer trajectory to the L₁ libration point where it was inserted into a class I Halo orbit. The nominal mission lifetime is two years which will be spent collecting data from the Sun using a complement of twelve instruments.

An overview of the early phases of FDF support of the mission will be given. Maneuvers required for the mission will be discussed and an evaluation of these maneuvers will be given with the attendant effects on the resultant orbit. Thruster performance will be presented as well as real time monitoring of thruster activity during maneuvers. Attitude areas that will be presented are star identification process and roll angle determination, momentum management, operating constraints on the star tracker, and guide star switching. A brief description of the two Heads Up Displays will be given.

I. Introduction

On December 2, 1995, the Solar and Heliospheric Observatory (SOHO) spacecraft was launched by an Atlas IIAS with a Centaur upper stage into a near-circular parking orbit. After a brief coasting period in a parking orbit, the Centaur upper stage ignited at the Transfer Trajectory Insertion (TTI) point, placing SOHO on a direct transfer trajectory to the Sun-(Earth-Moon Barycenter) libration point L₁ and its Halo Orbit Insertion (HOI) point. The halo orbit is centered around the L₁ point, approximately 1.5×10^6 km toward the Sun along the earth-Sun line. The mission duration is two years with an extension of up to six years if spacecraft health and consumables allow. SOHO is a component of the International Solar and Terrestrial Physics (ISTP) program, which is an international effort reflecting the cooperation of the European Space Agency (ESA), the Institute of Space and Astronomical Science (ISAS - Japan), and the National Aeronautics and Space Administration (NASA). The objective of the ISTP program is to study the Sun and its interaction with the Earth. The objective of the SOHO mission is to investigate the outer layer of the Sun, to study the solar wind streams and associated wave phenomena at the L₁ point, and to probe the interior structure of the Sun. The Flight Dynamics Facility (FDF) at NASA's Goddard Space Flight Center provided, in addition to pre-mission support, early mission support for SOHO in the areas of maneuver planning and observation, orbit determination, attitude determination, and Attitude and Orbit Control System (AOCS) checkout.

II. Mission Overview

a. Baseline Trajectory

The baseline trajectory for SOHO is a direct transfer to a large-amplitude halo orbit around L₁. Figure 1 displays the baseline trajectory, including planned maneuver locations, and Figure 2 displays the baseline timeline. Three main maneuvers were baselined for SOHO. The first mid-course correction (MCC1) maneuver to correct for launch vehicle errors was planned for Launch (L) +24 hours. The second mid-course correction (MCC2), at L+24 days, would be performed if needed to correct for errors from MCC1. The baseline location for HOI was at the Rotating Libration Point (RLP) x-z plane crossing on the earth-side. Stationkeeping maneuvers were optimally planned at eight week intervals around the halo orbit.

Maneuver optimization during the transfer orbit was possible, but not investigated pre-mission due to a strict baseline definition. Also, studies indicate cheaper locations for the HOI maneuver (Reference 1) such as a sun-side insertion, but these were considered for contingency only.

Since the actual maneuver scenarios and locations differed somewhat from the baseline, Figure 3 is included to indicate these actual locations and times.

b. Spacecraft Attitude

The spacecraft is three-axis stabilized, with the positive spacecraft x-body axis pointing to the Sun. The z-body axis is pointed toward the northern celestial sphere and the y-body axis completes the orthogonal right-handed-triad. The mission requirement is to maintain the attitude such that the solar spin axis is contained in the x-body -z-body plane as the spacecraft proceeds around the Sun. This results in the spacecraft rolling between approximately -7.25 and +7.25 degrees over the course of a year. Attitude is maintained through the use of three reaction wheels, with a fourth wheel being held in reserve. The wheels are unloaded through the use of thrusters at eight week intervals (a mission requirement), to be performed in conjunction with the station keeping maneuvers required to maintain the Halo Orbit (also a mission requirement).

III. Spacecraft Description and Operation

a. The Spacecraft

Figure 4 displays the spacecraft with its relevant subsystems labeled. The SOHO spacecraft mass at launch was 1863.7 kg wet mass, with a 251 kg fuel load. The spacecraft was manufactured through the European Space Agency by Matra Marconi Space, France. The propulsion system consists of 2 branches of eight hydrazine thrusters in pairs, providing around 4 Newton (1 pound) thrust each. These thrusters are labeled in Figure 4. All thrusters are used for orbit maneuvers, momentum management, and attitude control in certain modes.

b. Thrusting and Maneuvers

The SOHO maneuvers are divided into two components: along the earth-sun line, and perpendicular to the earth-sun line components. These are referred to as x-axis and z-axis maneuvers, corresponding to the location of the thrusters on the spacecraft body axes. Thruster pairs 1 and 2, and 3 and 4, aligned with the x-body axis, are used for the maneuver components along the sun-line. Thruster pairs 1 and 2 are for negative x-axis thrust, and are canted 30° out in order to minimize plume impingement on the payload module. Pairs 3 and 4, on the bottom of the spacecraft, are for positive x-axis thrust. Thruster pairs 5 and 6 and 7 and 8 are aligned with the spacecraft z-axis and are for the perpendicular maneuver components. Although the spacecraft may be rolled by some amount around the x-axis and may have thrust components along the Rotating Libration Point (RLP) y and z axes, these maneuvers are still perpendicular to the sun-line and are thus still referred to as z-axis components. Total maneuver magnitude is determined by the sum of the x and z components instead of the root-mean-square.

FDF has several tools available to monitor the actual thruster firing. Although FDF has the capability to monitor spacecraft telemetry, both from telemetry packets and graphical data sent over from the SOHO Payload Operations Control Center (POCC), FDF developed a Head's Up Display (HUD) which reads certain telemetry items, processes them, and displays the results graphically. Section V discusses the HUD in more detail.

In addition to all these forms of telemetry monitoring, FDF uses tracking data observation to assess accuracy and completion of each maneuver segment. Reference 2 discusses the tracking data observation in detail. The basic procedure is to compare a file with modeled thrust, created before the maneuver segment, and against observed Doppler values collected during the maneuver segment. Plotting these comparisons provides a clear indication of anomalous thrust, as an early or late thruster cutoff would show up as a change in the slope of the plot. The ability to verify thruster cutoff at maneuver completion arose from a

requirement for FDF to provide independent verification of thruster cutoff separate from telemetry indications.

In addition to anomalous thrusting, these plots also provided a preliminary estimate of thruster performance. The preliminary estimates of maneuver performance referred to in subsequent maneuver sections were determined using Doppler analysis.

c. Attitude Control

The Attitude and Orbit Control Subsystem (AOCS) has an attitude sensor complement of two Fine Pointing Sun Sensors (FPSS), three Rate-Integrating Gyros, all with the input axes on the spacecraft x-body axis, and two Charge Coupled Device (CCD) based Star Trackers comprising the Star Sensor Unit (SSU). The actuators are a set of four Reaction Wheels arranged symmetrically in a pyramidal orientation about the x-body axis and the redundant set of eight one pound thrusters.

IV. Post-Launch

a. Launch Window

The monthly launch window for SOHO was limited only by the position of the moon. Pre-mission analysis (Reference 3) determined that for certain days during each month the lunar perturbations had too great an affect on the trajectory. The November-December launch window extended from November 23 to December 15, inclusive. In addition to the monthly window, an optimum daily launch time was determined from the geometry of the transfer orbit, and the extent of the daily window was determined from a number of factors. For example, a requirement to have separation from the Centaur in view of a Deep Space Network (DSN) station limited the launch time due to the launch time's effect on the separation location. Daily launch window duration for the November-December block due to required DSN coverage of separation ranged from 55 to 91 minutes (Reference 4). The actual durations were slightly smaller due to additional launch vehicle constraints (including launch azimuth and range safety limitations).

b. Launch and Very Early Orbit

On December 2 the launch window opened at 07:34:00 GMT and closed at 08:25:00 GMT. The AC-121/SOHO combination experienced a hold during the final launch countdown due to a Centaur problem, determined to be non-launch critical during the hold. Also during this hold one Advanced Range Instrumentation Aircraft (ARIA) went red, meaning one of the two aircraft used to cover the second stage burn was not able to support launch. This loss shortened the window by fifteen minutes, to 08:10:00 GMT. Due to the launch hold, the actual launch occurred just prior to window close, at 08:08:00.859 GMT (Reference 5).

The Atlas carrying SOHO ascended for approximately 10 minutes until it reached the near-circular low-earth parking orbit. Reference 5 contains actual times for each event in the launch sequence, as well as the pre-flight nominal expected values. The Centaur/SOHO combination coasted in the parking orbit for 74 minutes. The Centaur upper stage then ignited (Main Engine Start (MES) 2 - MES2) at the specified Transfer Trajectory Insertion (TTI) point and shut down (Main Engine Cut Off (MECO) 2 - MECO2) after approximately 118 seconds, placing SOHO on its transfer orbit. Due to the DSN separation viewing requirement, the Centaur remained attached to SOHO until 35 minutes after TTI. The separation vector received by FDF from the launch vehicle contractor contained an epoch of 10:10:27 GMT. The Madrid tracking station acquired SOHO just prior to separation.

After separation, initial orbit and attitude determination were critical. FDF received a preliminary indication of the launch vehicle performance, both the Atlas and the Centaur, from several Orbital Parameters Messages (OPM's) provided by the launch vehicle contractor, which were both faxed and teletyped to FDF. Initial indications from both the post-MECO2 and the post-separation vector indicated the launch vehicle performance was a little less than 1 sigma (1σ) hot, which translated into an extra 0.7 m/s of velocity. Later orbit determination confirmed that the launch vehicle performance was slightly hot, predominantly in the

velocity direction with very small out-of-plane errors. The pre-mission analysis had indicated a 3σ velocity dispersion error of 2.15 m/s (Reference 3).

The spacecraft, after initiation of the AOCS, acquired the Sun and began a slow roll that continued until a star of magnitude 8, or brighter, was acquired. The roll rate was nulled, a mapping of the tracker field of view was performed and the data were sent to the ground for processing to identify the stars and determine the roll angle. Section VI provides more detail about the attitude determination.

c. Early Mission and First Mid-course correction

Using the initial vector information, impulsive maneuver planning for SOHO indicated an MCC1 maneuver of 4.66 m/s using thrusters 1 and 2 for the x-axis components, and 0.34 m/s using thrusters 7 and 8 for the z-axis components. This maneuver sequence was planned for start time at TTI plus 24 hours. The x-axis burn was split into two segments separated by 90 minutes in order to provide an initial assessment of the thruster performance. Pre-mission analysis had determined the worst case MCC1 to be 30 m/s total performed at TTI + 24 hours (Reference 3). This magnitude increases the farther out from TTI the maneuver is performed. Delays in the maneuver start times subsequently increased the maneuver magnitudes.

Due to a desire by FDF to receive additional tracking data, MCC1 was re-scheduled for 16:00:00 GMT on December 3, approximately TTI+30 hours. Before this could occur, the spacecraft experienced a thermal anomaly. Since the spacecraft had to go through thermal reconfiguration, as well as accommodating a science instrument checkout request, the maneuver was rescheduled again to start at 23:30:00 GMT on December 3.

Finite maneuver planning determined that the two new x-segment maneuvers would be 3.04 m/s and 1.577 m/s, still using thrusters 1 and 2. One lone z-segment, determined to be 29 cm/s, was eliminated, since it was small and eliminating the maneuver did not significantly affect the HOI costs. The final maneuver replan changed the second x-segment slightly, to 1.578 m/s.

The actual maneuver start time was delayed by 51 minutes due to delays acquiring SOHO from the Canberra DSN tracking station. The first segment was executed successfully, and Doppler data provided a preliminary indication of a 2% cold maneuver. The second segment was replanned for 03:00:00 GMT, December 4, with a new predicted magnitude of 1.6354 m/s. Before this maneuver could be executed, the spacecraft experienced an Emergency Sun Reacquisition (ESR) at 02:05:00 GMT. {Discussed in section ?} The recovery from this ESR pushed the start time of the second segment to 18:00:00 GMT, with an expected magnitude of 1.878 m/s. The second segment was completed on time and preliminary indications were also for a 2% cold maneuver. Later maneuver calibration based on orbit determination indicated that MCC1 maneuver performance was 2.46% cold. (Reference 6)

d. Second Mid-Course Correction

Preliminary analysis for MCC2 produced several options. The first option was to continue the maneuvers as baselined, with MCC2 sometime around 24 days after launch and HOI at the earth-side RLP x-z plane crossing. The second option involved not performing MCC2 and instead waiting until HOI. The third option, which turned out to be the best, was to optimize the MCC2 and HOI to find the best sum of the two. Initial analysis and the optimization of these two maneuvers is discussed in Reference 7.

For option 1, planning the maneuver for January 4 in order to avoid the holidays produced a total maneuver size of around 1 m/s. The corresponding HOI maneuvers, still planned as baselined for the x-z plane crossing, then totaled around 44 m/s. Option 2, canceling MCC2 due to its small size, produced HOI numbers of approximately 54 m/s total.

Option 3 proved to be the most viable. By changing MCC2 to an orbit shaping maneuver instead of a simple error correction maneuver and increasing its magnitude, the sum total of the two maneuvers was reduced. Preliminary planning indicated MCC2 could be performed in three segments, one x-segment of 6

m/s using thrusters 1 and 2, and two z-segments, one 15.7 m/s and one 10.0 m/s, again with thrusters 7 and 8. (The z-axis maneuver was split up since it was the first use of z-axis thrusters for an orbit maneuver) This reduced the HOI maneuver to one x-axis segment of approximately 14 m/s. The biggest advantage to Option 3 was a reduction in the number of maneuver segments required, from 6 (two segments at MCC2 and 4 at HOI) to 4 (three at MCC2 and 1 at HOI). Another advantage was elimination of a roll maneuver from the HOI scenario. This greatly simplified maneuver operations and reduced total maneuver operations duration.

After some debate option 3 was chosen, with the z-axis maneuvers performed first and then the single x-maneuver. Once again, the initial segment was delayed due to tracking station handover problems; so the second segment was slightly re-planned to account for the delay. The first z-segment occurred at 00:45 GMT on January 5. Doppler evaluation during the maneuver indicated it was 1.5% hot. The second z-segment was performed at 04:15 GMT, and the x-segment at 05:55 GMT. Preliminary indications were also for slightly hot maneuvers. Later maneuver calibration from orbit determination indicated the overall performance was 1.3 % hot.

e. Halo Orbit Insertion

A preliminary HOI study produced a wide range of possible dates leading up to the baseline date. Reference 8 discusses HOI maneuver planning in detail. These maneuvers were all single x-axis segments again using 1 and 2, and ranged from February 16 (3.1 m/s) to March 15 (12.7 m/s). The baseline HOI location was at the earth-side RLP x-z plane crossing on March 14. This range of dates provided flexibility for scheduling of the DSN as well as spacecraft events. As analysis indicated, the earlier the maneuver was performed the lower the cost. Additional analysis provided several more dates on either side of the initial block. The actual maneuver date selected was February 14. In conjunction with HOI a trim maneuver was planned anywhere from 3 to 8 weeks past HOI in order to fine tune the halo orbit. This maneuver was executed on March 20.

During the maneuver on February 14, approximately 8 minutes into the maneuver, the primary tracking antenna went down, later determined to be a hardware problem. The backup antenna continued to track SOHO, however the switch in antennas corresponded to 7 minute loss of tracking data. For that reason the preliminary estimate of maneuver efficiency from Doppler data could not be performed accurately, but was estimated at 2% cold. A final resolution performed after collection of post-maneuver data indicated a 2.1% cold maneuver.

As stated above, an HOI trim maneuver was performed on March 20, with a magnitude of 89 cm/s using thrusters 1 and 2.

V. Head's Up Display

SOHO was the first mission to use Heads-Up-Displays based on HP workstations. Two were developed, one for attitude and the other for maneuver support. Figure 5 and Figure 6 present representative samples of each. For attitude, displays of all sensors and actuators are presented, as well as on board computed attitude in both tabular and graphical form. Information on the current High Gain Antenna gimbal angles is also available, as well as the current telemetry type and AOCs control mode. The display is heavily used for attitude support to monitor sensor behavior, guide star status in the star tracker field of view, wheel speed progress, and telemetry type and control mode switching.

The maneuver display is an integral part of the support of all maneuvers. Thruster on time, for all thrusters separately as well as total on-time is displayed by sliding bars as well as numerically. The same is true for tank temperature and pressure. These thruster on-times are monitored closely, as is the polar plot displaying the progress of each burn. This plot is a representation of the projection of the current velocity vector, both instantaneous and cumulative, onto a plane normal to the desired velocity vector at the center of the plot. Consequently, a path is projected that is expected to show a convergence to the center of the plot. If the thrust vector deviates significantly from the center, then an anomaly is known to have occurred and immediate corrective actions can be initiated. There is also a graphical representation of each of the active thrusters and whether the "A" or "B" side set of thrusters is in current use.

Both displays were very useful to the support of the SOHO mission. A detailed description of both HUDs is to be found in Reference 9.

VI. Attitude

a. Star Identification and Roll Angle Determination

After acquisition of the Sun and transition to the Fine Pointing Sun Sensor the spacecraft began a slow roll about the x-body axis with the star tracker active. When the star tracker acquired a star of visual magnitude of 8.0, or brighter, this star was used as a guide star by the control system to null out the roll rate. A mapping of the field of view was initiated and all stars obtained were transmitted to the ground for processing. The stars were processed using a multi-star-identification algorithm described in Reference 10. The results are presented in Figure 7. The outer rectangle shows the total field of view and the inner rectangle shows the reduced field of view that is used for routine operations. The spacecraft roll-labeled axis is the spacecraft x-body, and science instrument, axis. The “+” symbols represent the stars from the catalog; the “o” symbols represent the observed stars. Eight stars were identified. The orientation of the spacecraft z-body axis was determined and the identified stars were used with the Sun sensor data to determine the spacecraft attitude. The goodness of fit is represented by the root-sum-square of the angular separation between the observed and the catalog stars which is seen to be 0.04 degrees. The attitude was determined to be a roll of 96.33, a pitch of 0.1 and a yaw of 0.0 degrees.

As stated above, before the second segment of the MCC1 maneuver could be executed, an ESR was triggered at 02:05:00 GMT on December 4, and transition to the “B” side of the AOCS was performed. A dump of the flight software was taken for detailed analysis on the ground by the supporting staff of Matra Marconi Space, and technical staff of ESA, to determine the specific chain of events that led to the ESR. After analysis of the data, it was found that there was an improper response to a ground command to reset the AOCS. A large roll rate developed, causing the Failure Detection Electronics to trigger an ESR. The process of recovering from this mode of operation took approximately eight hours. At the end of this interval with the spacecraft in the Roll Maneuver with Wheels (RMW) mode another star mapping was done. The resulting data was again processed and eight stars were identified. The results are presented in Figure 8. The goodness of fit is 0.09 degrees. The attitude was subsequently found to be a roll angle of 141.4 degrees. Shortly thereafter the Flight Operations Team (FOT) switched to the “A” side of the AOCS, and another star mapping performed. Figure 9 shows that nine stars were identified with a goodness of fit of 0.05 degrees. The attitude was found to be 141.0 degrees. It was determined that the performance of star tracker B was not as good as that of star tracker A. This can be seen by comparison of Figure 8 with Figure 9. The goodness of fit of tracker B is almost twice as large as that of tracker A, reflecting the larger random scatter between the observed and the catalog stars. This observation led FDF to recommend that tracker “A” be used for the continued normal operation of the spacecraft.

Whenever the spacecraft was reoriented to a new roll orientation, either to the normal mission orientation or to a different one to support a station-keeping maneuver, the performance of the star identification algorithm produced results similar to those shown in Figure 9.

b. Star Tracker Operational Constraints

The star trackers were required to produce star data in the visual magnitude range of from 2.0 to 8.0. Therefore, pre-mission analysis to determine star availability indicated that there should be no difficulty in having an adequate number of stars to be tracked during the mission lifetime. FDF had indicated that it would be beneficial to track three stars, the current guide star and two others. It was also recommended that the magnitude threshold of the star tracker be set at the limit for the dimmest stars, viz., 8.0, to allow the largest number of stars to be available when mappings would occur. Both recommendations were accepted. However, early into the mission the star tracker began to send Single Event Upsets (SEUs) to the AOCS. An SEU is determined to occur in the tracker if the location of the star shifts by one pixel, or the magnitude shifts across a gain threshold gap. There are four gain values depending on the magnitude of the star and each applies to a range of magnitudes, ranging from 2.0 to 8.0 for gains 1 to 4. The magnitude ranges are not contiguous, but rather have gaps of 0.05 between these ranges. Furthermore, there is a tolerance on the

limits of less than 0.025. There can arise, therefore, many situations where due to the electronic noise in the tracker, especially for dimmer stars where the noise is the largest, and for stars with magnitudes near a range boundary, the magnitude may vary from measurement to measurement across a gain boundary and back. If more than a preset number of SEUs occur within a prescribed time interval, then an SEU is sent to the AOCS. This was found to be happening early in the mission after the ESR had occurred. Because of this the Matra-ESA engineers modified the mode of operation of the star trackers. The magnitude threshold was to be set at 7.0 for future star mappings and the guide star designated by the FDF had to be 6.0, or brighter.

c. Guide Star Switching

Because of the limitation on the magnitude of the star selected to be used as the guide star certain operational constraints ensued. The star tracker, when performing a mapping, starts from the center of the field of view and spirals outward in a stepwise fashion until the entire field of view has been covered. When a roll maneuver has occurred and a mapping automatically is obtained, the first star encountered could be brighter than 7.0 in magnitude but not necessarily brighter than 6.0. It therefore became necessary to switch stars. There were two possible ways in which this could be done; one more conservative, and consequently more time-consuming, and the other more direct and quicker to accomplish. The former required the continuous tracking of the original star while the FOT was directed to command the tracker to an empty area of the field of view and then to command the tracker to the area containing the new guide star. This was a more tedious approach for FDF as both areas were required to contain a minimal number of pixels and FDF personnel had to scrutinize the whole field of view and do this quickly as the timeliness of the information was important. The latter required only the search area of the new star to be obtained. It was also more daring inasmuch as the original guide star was dropped at the start of the switch before the new guide star was established. After the first few guide star switches it was decided by the FOT in consultation with FDF and SOHO Project personnel to use only the more direct method. However, because of the problems associated with the star trackers and the resultant constraints arising therefrom, more previously unscheduled support was required from the FDF and more commanding of the spacecraft by the FOT was necessary.

d. Momentum Management

At the L_1 point, on mission orbit, effectively the only external environmental torque that acts upon the spacecraft is that due to the solar radiation. As the resultant torque on the spacecraft is compensated for by commanding the reaction wheels, over time the wheels need to be "unloaded". The mission requires that momentum management be performed no sooner than eight (8) weeks, in conjunction with the station keeping maneuvers required to maintain the halo orbit. This, coupled with the requirement that the solar spin axis be contained within the x-body-z-body plane, ensures a relatively long period of continuous observation of the sun's surface as it rotates across the scientific instruments fields of view.

Momentum management consists of monitoring the wheel speeds, predicting their future secular variation and, therefore, when the next wheel dumping need be performed, and determining the new speeds for each wheel. Actual wheel speeds are also compared with the predicted speeds to detect any unanticipated activities that might have happened on the spacecraft. Wheel speeds are also selected to perform roll maneuvers to achieve the orientation to support station keeping maneuvers. Description of the algorithm is contained in Reference 11.

Figure 11 presents the predicted wheel speeds for the reorientation of the spacecraft from its roll of 141 degrees, which it attained after recovery from ESR, to the normal mission roll of -7 degrees. This is typical of the wheel variations resulting from any such roll maneuvers. The actual wheel speed variations, if presented on the same plot, would not be discernible. This was found to be the true in almost all cases.

Figure 12 presents a sample of actual versus predicted wheel speeds for a period of several days starting on the third day. There is good agreement between the two and it was determined that the solar torques acting on the spacecraft over this span were of the order of 10^{-5} Newton-meters, two orders of magnitude larger than pre-mission expectations.

As an example of unanticipated activities affecting the spacecraft, Figure 13 presents the actual versus predicted wheel speeds for the period of twenty days following the span of time from the previous figure, viz., from December 15, 1995 into January 1996. It is clear from the figure that on about December 21, 1995 something occurred that caused a change in the resultant torque acting on the spacecraft. Consultation with the FOT and SOHO project personnel provided no explanation as far as any known spacecraft activity. This was found to occur again during the transfer trajectory. The departure between the actual and predicted wheel speeds was just as pronounced but less dramatic. The graphical representation of the second case is not given herein.

Figure 13 presents the same information as the previous two figures for a span of approximately 12 days starting on February 16, 1996, two days after Halo Orbit Insertion. The agreement between the actual and predicted wheel speeds is even better than before and the solar radiation torques were found to be of the order of 10^{-7} Newton-meters, as expected from pre-mission analysis.

VII. Summary

As the SOHO mission proceeded, scheduled activities were postponed, the sequence of events was changed, and it became necessary to respond quickly to previously unexpected requests for analysis support to help explain spacecraft responses to command sequences. For example, the initial star mapping and the subsequent analysis to determine the spacecraft attitude was delayed several hours because of a spacecraft thermal problem. The spacecraft was triggered into a safehold mode with unexpected behavior of the star tracker as a contributing factor, causing the second segment of MCC1 to be postponed and to be completely replanned several different times. The use of the star tracker was changed, causing additional support activity to be provided by the FDF. However, despite these and other problems that occurred, FDF support personnel continually provided the highest level of support in an apparently routine manner. Generally, the flight support systems, both the institutional and those systems and utilities developed specifically for this mission, performed quite well. The system support staff, with insightful observations and suggestions from operational personnel, responded quickly to correct the few resident quirks as they were discovered. The support provided by the FDF for the SOHO mission was highly successful.

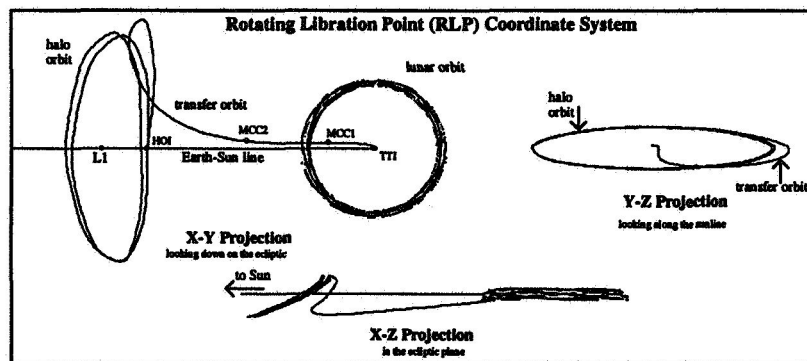


Figure 1. Baseline SOHO Trajectory

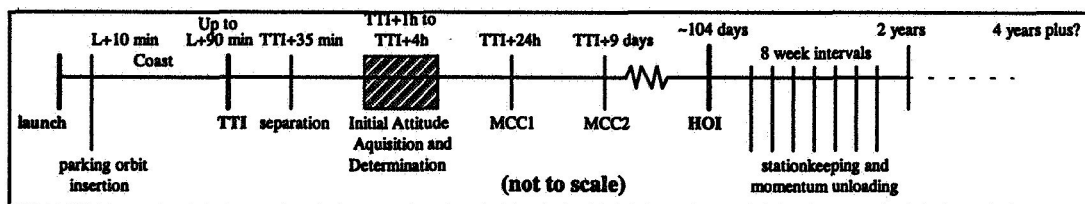


Figure 2. Mission Timeline

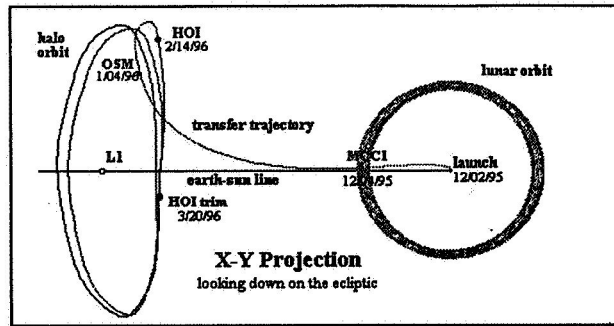


Figure 3. Actual SOHO Trajectory with Maneuver Locations

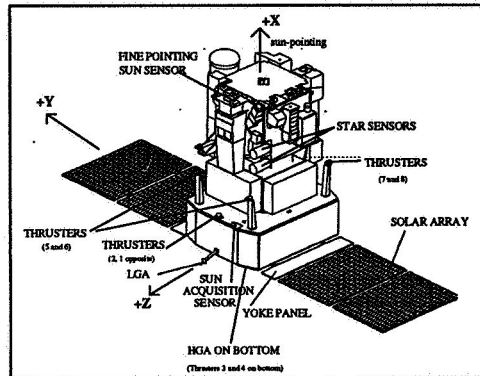


Figure 4. The SOHO Spacecraft

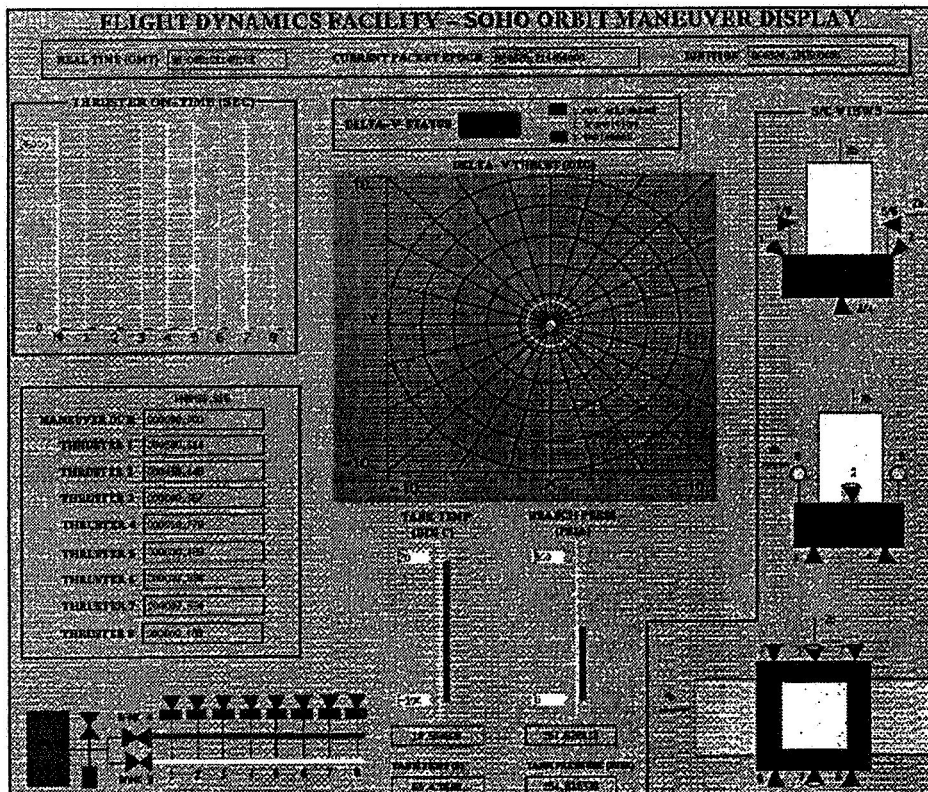


Figure 5. Maneuver HUD Display

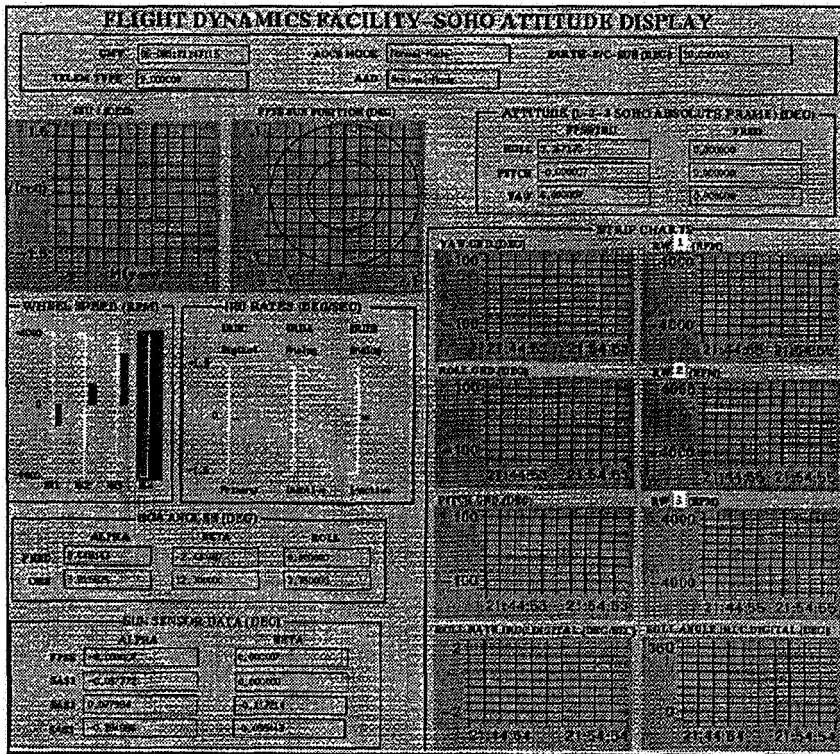


Figure 6. Attitude HUD Display

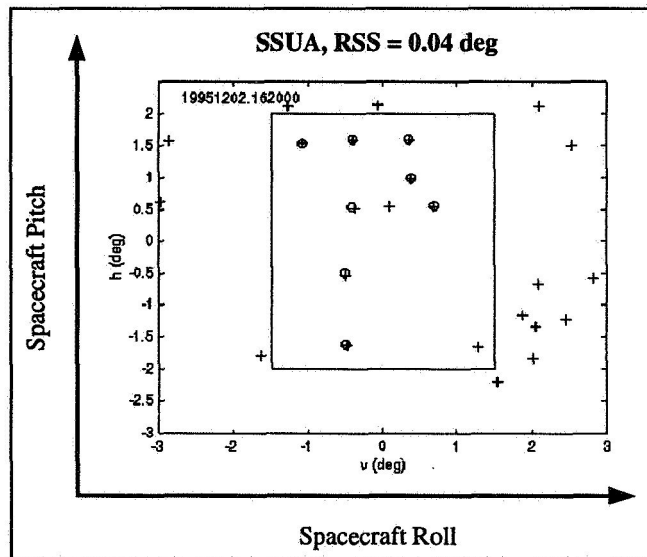


Figure 7. Initial Star Mapping and Identification Results

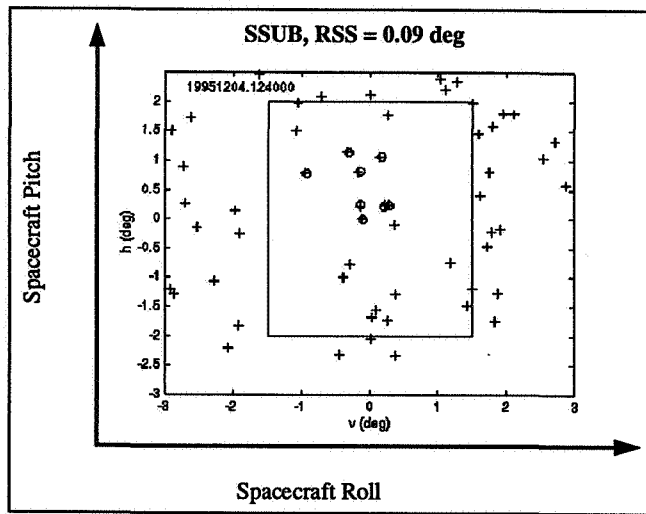


Figure 8. Star Mapping and Identification During Recovery ESR - Star Tracker B

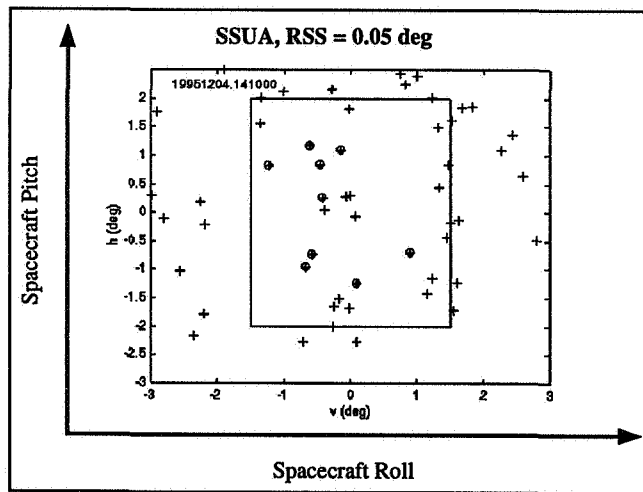


Figure 9. Star Mapping and Identification After Recovery From ESR - Star Tracker A

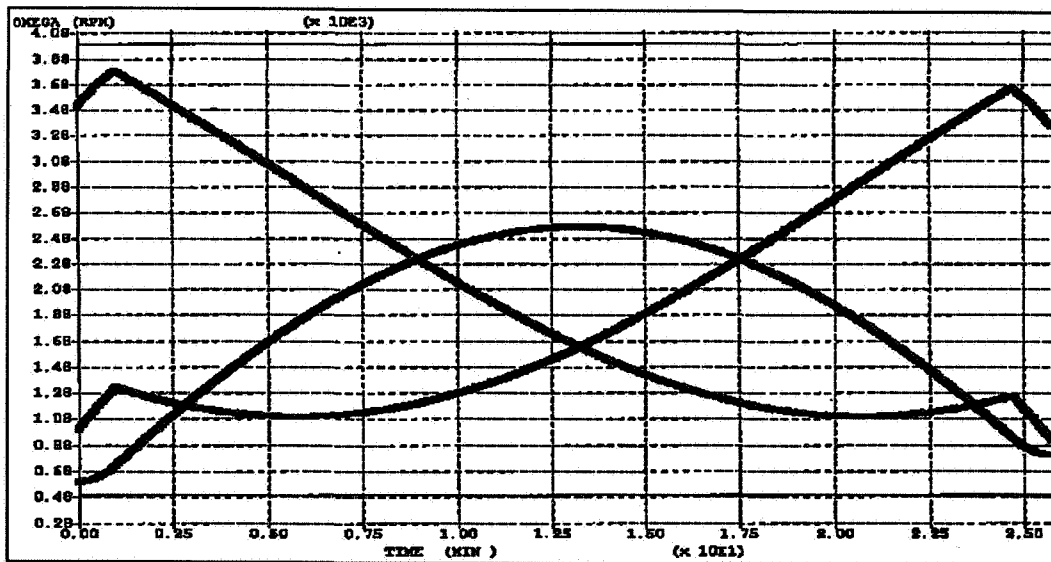


Figure 10. Predicted Wheel Speeds for First Wheel Unloading

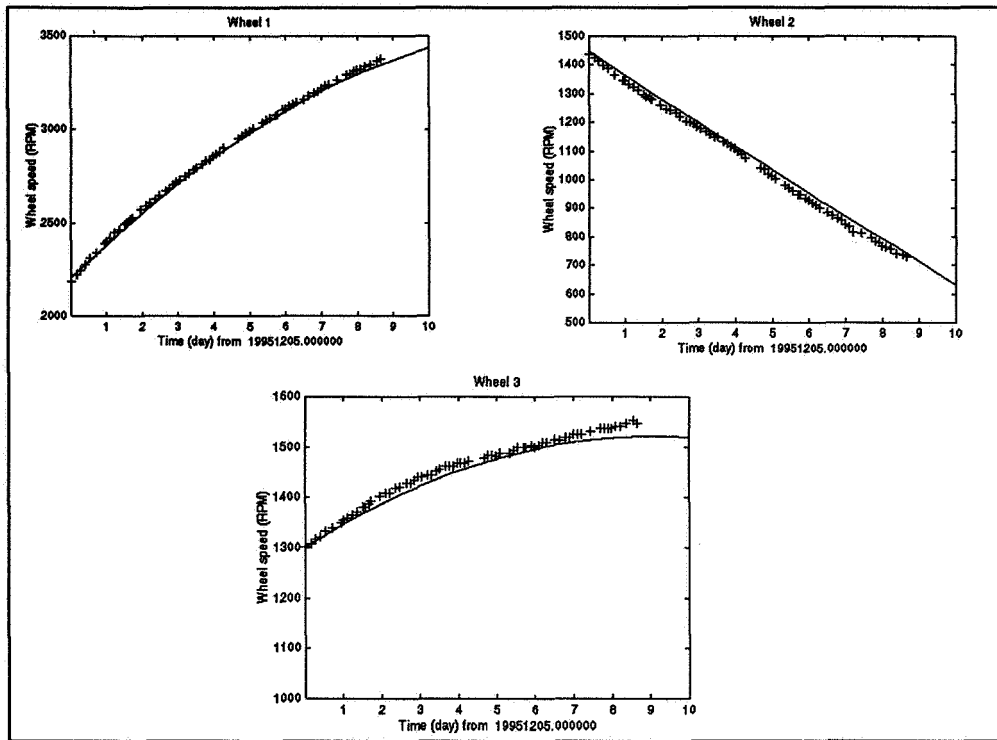


Figure 11. Early Mission Predicted/Observed Wheel Speed Comparison

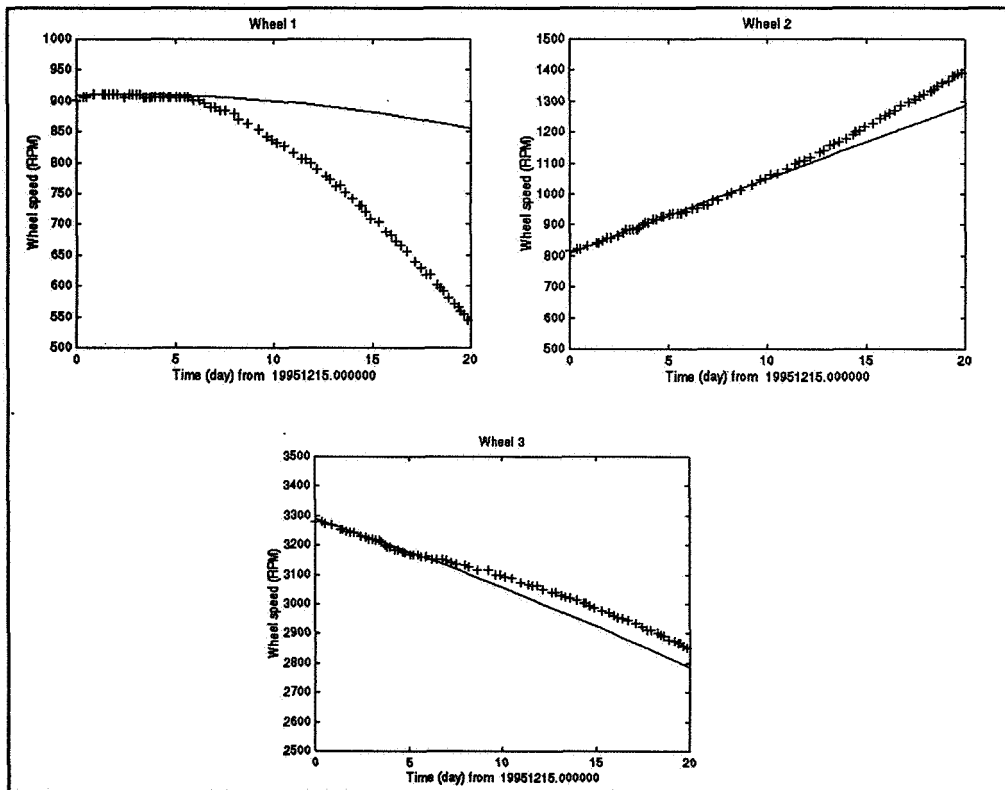


Figure 12. Predicted/Observed Wheel Speed Comparison Showing Sudden Change in Torque

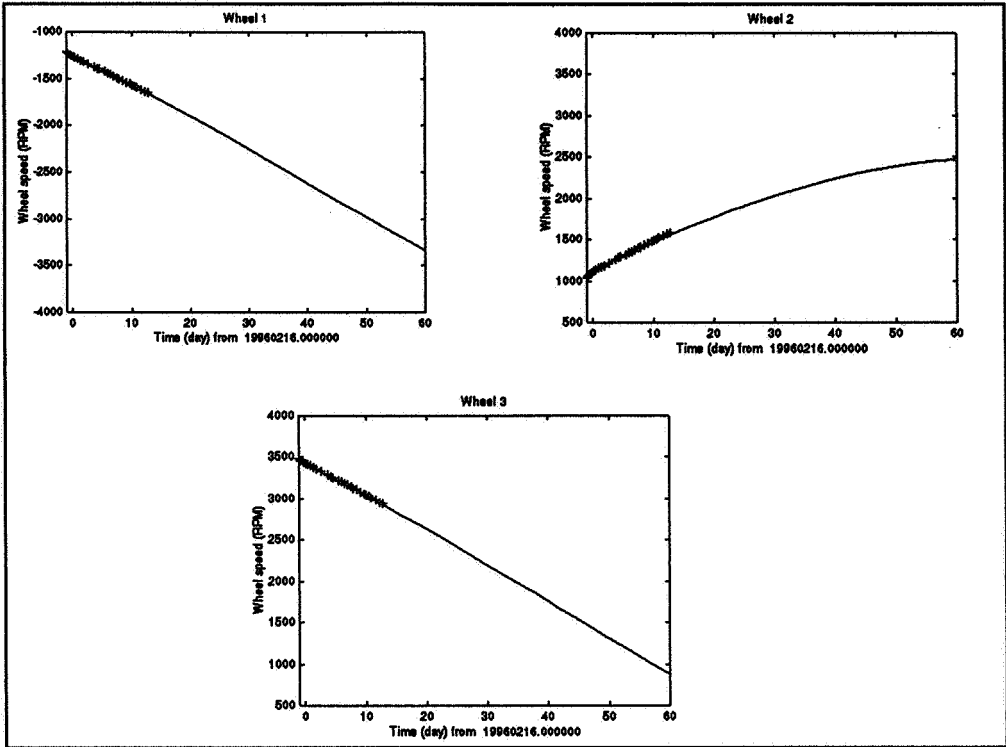


Figure 13. Predicted/Observed Wheel Speed Comparison During Normal Operations

Acknowledgments:

The authors of this paper would like to thank the SOHO FDF mission support team for all their hard work on the mission and contributions to this paper. Specifically, they would like to acknowledge Mr. T. Becher and Mr. J. Rowe for providing information for this paper.

Direct References:

1. S. Stalos, D. Folta, B. Short, J. Jen and A. Seacord, AAS 93-553, *Optimum Transfer to a Large-Amplitude Halo Orbit for the Solar and Heliospheric Observatory (SOHO) Spacecraft*, 1993
2. C. Knapp, FDF Report #56712-07, *Postmission Report on SOHO Trajectory Determination Support*, March 28, 1996
3. Computer Sciences Corporation, 554-FDD-91/026R0UD0, CSC/TM-91/6030R0UD0, *Solar and Heliospheric Observatory (SOHO) Mission Description and Flight Dynamics Analysis Reports, Revision 2*, September 1993
4. R. Short, FDF internal memo, *DSN Constrained Daily Launch Window Close Times*, October 30, 1995
5. Lockheed Martin Astronautics Space Systems, Report # ATS-96-008, *AC-121 Postflight Data Report*, February 1996
6. M. Hametz, FDF Report #56712-09, *Summary of SOHO Maneuver Activities from Launch through HOI*, March 27, 1996
7. M. Hametz, FDF Report #56712-03, *SOHO MCC-2 Maneuver Design*, March 28, 1996
8. M. Hametz, FDF Report #56712-02, *SOHO HOI Maneuver Design*, March 28, 1996
9. Computer Sciences Corporation, 552-FDD-94/045R0UD0, CSC/SD-94/6112R0UD0, *International Solar Terrestrial Physics (ISTP)/Collaborative Solar Terrestrial Research (COSTR) Initiative Solar and Heliospheric Observatory (SOHO) Head's Up Display (HUD) User's Guide and System Description*, June 1995
10. R. van Bezooijen, *Automated Star Pattern Recognition*, PhD thesis, Stanford University, 1989
11. National Aeronautics and Space Administration, 553-FDD-92/095R0UD0, *Solar Heliospheric Observatory Mission, Flight Dynamics Support System - Functional Specifications, Revision 1*, December 1994

Additional References:

P. Jordan, draft, *SOHO Maneuver Team Operational Procedures*, November 1995

Mission Operations and Data Systems Directorate, Flight Dynamics Division, Goddard Space Flight Center, *SOHO Attitude Analysis Compendium*, September 1993

Flight Dynamics Mission Support and Quality Assurance Process*

InHwan Oh
Computer Sciences Corporation
Lanham-Seabrook, Maryland 20706 USA

Abstract

This paper summarizes the method of the Computer Sciences Corporation Flight Dynamics Operation (FDO) quality assurance approach to support the National Aeronautics and Space Administration Goddard Space Flight Center Flight Dynamics Support Branch (Code 553). Historically, a strong need has existed for developing systematic quality assurance using methods that account for the unique nature and environment of satellite Flight Dynamics mission support. Over the past few years, FDO has developed and implemented proactive quality assurance processes applied to each of six phases of the Flight Dynamics mission support life cycle: system and operations concept, system requirements and specifications, software development support, operations planning and training, launch support, and on-orbit mission operations. Rather than performing quality assurance as a final step after work is completed, quality assurance has been built in as work progresses in the form of process assurance. Process assurance activities occur throughout the Flight Dynamics mission support life cycle. The FDO Product Assurance Office developed process checklists for prephase process reviews, mission team orientations, in-progress process reviews, and end-of-phase audits. This paper will outline the evolving history of FDO quality assurance approaches, discuss the tailoring of CSC's process assurance cycle procedures, describe some of the quality assurance approaches that have been or are being developed, and present some of the successful results.

1.0 Background

Since 1988, the Computer Sciences Corporation (CSC) Flight Dynamics Operation (FDO) has supported the National Aeronautics and Space Administration (NASA) Goddard Space Flight Center (GSFC) Flight Dynamics Support Branch (Code 553) as part of the CSC System, Engineering and Analysis Support (SEAS) contract. In January 1991, the FDO Product Assurance Office (PAO) performed its first formal audit with the Solar, Anomalous, and Magnetospheric Particle Explorer (SAMPEX) mission team members at the end of their system installation and acceptance phase. The audit was based on the SEAS System Development Methodology (SSDM) Standards and Procedures (S&Ps). As a result of this session, the PAO and SAMPEX team members realized that better audit results could have been achieved if the audit had been preceded by a coaching session. Since that first audit session, the goal and method of FDO audits have been redirected to assist mission team members in performing their mission support as the work progresses by identifying quality checkpoints and quality criteria and by reviewing the process rather than checking the end results. Consequently, the PAO entered into process reengineering with the FDO technical and management personnel in order to build quality into the work processes. (The terms *product assurance* and *process assurance* are used interchangeably throughout this paper.) Later in the stage of the FDO's audit coaching or proactive quality assurance (QA) process development, the CSC SEAS process assurance cycle (PAC) procedures became available and were tailored to enhance the FDO process. The SEAS PAC comprises a series of reviews and audits before, during, and after each phase of the life cycle. In fact, the FDO has contributed to the SEAS PAC procedure development by providing FDO experiences and review comments for the draft SEAS PAC procedures. In FDO, the technical staff prefer the in-progress process review (IPPR) over the in-progress process audit (IPPA) by the PAO because it fosters a spirit of cooperative problem solving via process reviews, rather than giving the technical staff the impression that the PAO is checking on them.

* This work was supported by the National Aeronautics and Space Administration (NASA)/Goddard Space Flight Center (GSFC), Greenbelt, Maryland, under Contract NAS 5-31500.

2.0 Introduction

The process assurance activities continue throughout the Flight Dynamics mission support life cycle, which comprises six phases:

- System and Operations Concept
- System Requirements and Specifications
- Software Development Support
- Operations Planning and Training
- Launch Support
- On-Orbit Mission Operations

For convenience, the term life cycle *phase* is used here; however, in reality, a specific process such as requirements and specifications may go well beyond the requirements and specifications phase, which is normally considered complete at system requirements review (SRR). Likewise, all other adjacent phases often overlap, particularly during a rapid prototyping process for which a traditional waterfall model is not suitable. Further studies are required to model PAC procedures for such a prototyping process and also for the anticipated changes to a workstation support environment.

Note that those phases that follow the requirements and specifications phase differ from the traditional system development life cycle phases. This difference shows the unique nature of the FDO mission support life cycle. For example, during the software development support phase, the FDO analysts support software development via walkthroughs and respond to developer questions after the system requirements and specifications documents are delivered. The CSC Software Engineering Operation (SEO) performs development in support of GSFC Code 552, Software Engineering Branch.

Prior to the publication of this paper, no known published works have thoroughly described the QA processes for the entire life cycle of the GSFC Flight Dynamics mission. A great deal of effort has been expended within FDO to develop a set of systematic and proactive QA approaches tailored to the unique nature and environment of Flight Dynamics mission support. First, CSC FDO consolidated the existing QA activities and developed a process where those activities occur before the start of and/or during each mission phase in a proactive manner. The proactive QA activities are skills training, weekly internal mission reviews, document QA plans, dry runs, prephase preparation, mission team meeting (combined with just-in-time training for the upcoming phase), IPPRs, and prelaunch readiness reviews. Next, FDO PAO consulted with experienced staff to develop QA checklists for the six FDO mission support life cycle phases. Checklists are used to guide discussion at the IPPRs and LCPAs. The FDO just-in-time (JIT) training materials for the various FDO mission support life cycle phases and FDO document QA checklists were used for the phase IPPR and end of LCPA checklists.

FDO's strategy for producing quality products and services consists of the previously mentioned consolidated QA activities, techniques of coaching/training, lessons learned and feedback for process improvement, defect causal analysis, identification of quality checkpoints and associated quality criteria, identification of S&Ps and development of appropriate guidelines or S&Ps, and innovation. Each mission team within the FDO is responsible for developing and documenting improvements and continuing good practices based on the lessons learned during day-to-day activities or during the generation of products and services. The vehicle used to deploy this approach is the FDO PAC procedure described in the following sections. The FDO PAC procedure is supplemented by maintaining a project lessons learned database, FDO lessons learned database, DCA database, reports, and electronic files or bulletin boards. Communication is promoted among FDO projects on tools and methodologies that may contribute to improved quality and productivity. Methodology effectiveness is monitored and evaluated for improvement.

3.0 FDO PAC Procedure

The FDO quality goals and PAC procedure are described in this section.

3.1 FDO Quality Goals

The goal of the FDO's quality assurance effort is to maximize the quality of FDO products and services. This occurs by maximizing the quality and consistency of the technical processes used and detecting any problems in processes or quality early in the FDO mission support life cycle phases. Corrective actions are taken as early as possible to ensure that all deliverable FDO products and services are of high quality. Documents and reports produced are quality assured using the FDO Product QA Plan with the baseline quality criteria.

3.2 FDO PAC Procedure

The purpose of the FDO PAC procedure is to ensure that task teams have a consistent understanding of FDO mission support processes, products, and S&Ps before the start of each project and mission support life cycle phase. The PAC also shifts the emphasis of product assurance personnel from the traditional role of product inspector to that of process advisor (i.e., the technical personnel are responsible for ensuring the quality of a product or service.) In addition, use of the PAC helps the technical staff and the PAO identify and improve process-related weaknesses as early as possible in the life cycle. Early identification of items that should be changed is a most effective cost reduction/avoidance method. Finally, the PAC provides a standard, efficient, and repeatable mechanism for encouraging process improvement. The SEAS PAC applied to FDO comprises the following five activities:

- Documentation of approach
- Prephase Process Review (PPR)
- Phase Orientation Meeting (POM)
- In-Progress Process Review (IPPR)
- Life cycle phase audit (LCPA)

Figure 1 depicts the flow of the PAC process in each phase.

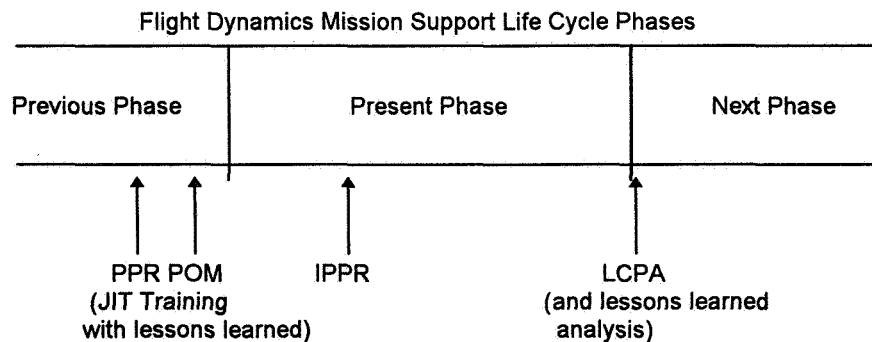


Figure 1. FDO Process Assurance Cycle (PAC) Flow Before/During/After a Phase

The FDO documentation of approach consists of project or task implementation plan, work package plan, and mission support life cycle phase activity plan. The PPR is an informal meeting of the project leader or mission manager with the PAO to review and update the approach (the project- or mission-specific checklist) for the upcoming life cycle phase. The PPR is intended to ensure that the activities, products, and events that are expected to occur during the upcoming life cycle phase are all identified and have corresponding S&Ps. The PPR should take place a few weeks before the start of the life cycle phase. POM is to ensure that all mission or project team

members have a consistent understanding of the S&Ps to be used, the processes that are to be followed, and the products and services to be delivered during the current life cycle phase. The POM is an opportunity for providing JIT training and lessons learned from previous missions for task or mission team members. Depending on the duration of the phases for a given mission or project, it may be appropriate to conduct a POM covering multiple phases. The IPPRs ensure that reviews are performed for task implementation plan, work package plan, and mission support phase activities. The IPPR provides an assessment of the mission or project team members' understanding and conformance to the S&Ps and provides processes that have been designated for use on the task through the mission- or project-specific checklist. The IPPRs occur approximately 15 to 25 percent into the calendar schedule of the task or mission support life cycle phase. This is early enough to correct any weaknesses detected in the process. The IPPR can occur more than once during the phase depending on the results of the first IPPR. At the conclusion of each phase, an LCPA is conducted to ensure that all the requisite activities have occurred and that it is appropriate to proceed to the next life cycle phase. Lessons learned data are collected and analyzed for training and process improvement during this audit.

The FDO adaptation of the PAC procedure uses process checklists for each of the mission support life cycle phases. The FDO Mission Support Process Group and the FDO PAO developed these checklists because the SSDM S&Ps do not address the FDO's mission support phases (Reference 1). The checklist for a given phase provides a list of the SSDM and FDO S&P applicable to the products and services that are developed and/or delivered during that phase. The process checklists may be tailored to meet the particular needs of a project.

4.0 Flight Dynamics Mission Support Life Cycle Phases and Key Processes

Figure 2 depicts the FDO mission support life cycle phases, reviews, and process overlaps. For convenience, numbers are assigned for the life cycle phases in Figure 2a. The activities supported by CSC SEO are identified in the right side of the figure. The reviews (Figure 2b) include system and operations concept review (SOCR), system requirements review (SRR), preliminary design review (PDR), critical design review (CDR), operations readiness review (ORR), and division operations readiness review (DORR). The processes of adjacent life cycle phases actually overlap as shown in Figure 2c. This figure also shows the relative effort of a mission team over time, but process assurance effort is about the same level throughout the life cycle.

Key activities dominate all others for a given life cycle phase. The associated numbers help map activities between the GSFC Flight Dynamics mission life cycle phases and the CSC FDO life cycle phases. The key processes characterizing each phase are summarized as follows:

- ***System and Operations Concept Process (1)***
 - Investigate existing systems to fulfill anticipated mission support requirements using trade-off studies. If no existing system satisfies the requirements, a new system must be developed.
- ***Requirements and Specifications Process (2)***
 - Review and expand the high-level requirements in the detailed mission requirements (DMR) documents; identify items related to orbit and attitude. This process will result in additional refinements and further detailing of the Flight Dynamics support requirements.
 - Create a detailed Flight Dynamics support requirements table and clearly establish traceability of requirements. Continue to maintain the table as a quick reference to critical Flight Dynamics mission support requirements.
- ***Software Development Support Process (3,4,5)***
 - Respond to questions from the software development team. Specifications modifications may be needed as a consequence of the questions.

GSFC FLIGHT DYNAMICS MISSION SUPPORT LIFE CYCLE

CSC FDO LIFE CYCLE PHASES (SHADED)

- System & Operations Concepts Phase (1)
 - Requirements and Specifications Phase (2)
 - Software Development Support Phase (3, 4, 5)
 - Operations Planning & Training Phase (6)
 - Launch Support Phase (7)
 - On-Orbit Operations Phase (8)
- Design (3)
 - Development (4)
 - Testing (5)
 - Maintenance (9)

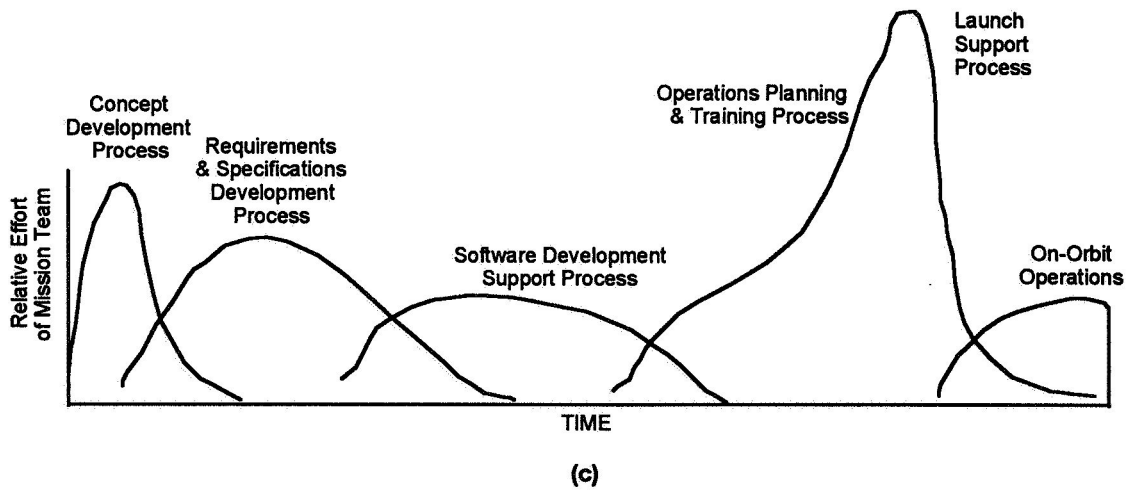
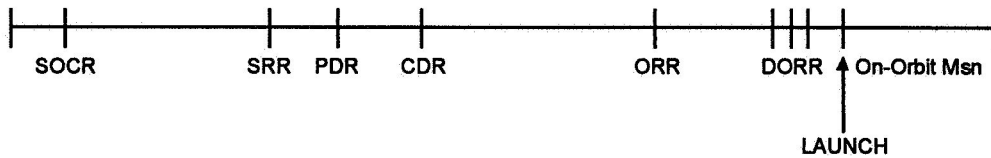
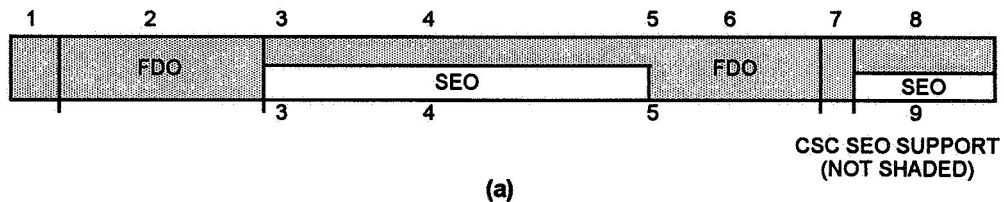


Figure 2. GSFC Flight Dynamics support life cycle consisting of CSC FDO- (and SEO-) supported life cycle phases (a), reviews after each phase (b), and process overlaps (c)

- ***Operations Planning and Training Process (6)***
 - Develop mission support procedures. These procedures are standardized sets of ordered activities that may include software execution and other functions such as requesting, transmitting and archiving data, and logging.
 - Develop mission support timeline and operational scenarios (for example, scenarios for orbit acquisition, attitude acquisition, sun sensor calibration, and spacecraft ascent maneuvers). Each scenario consists of a collection of standardized procedures designed to satisfy mission requirements at the defined milestones in the timeline.
 - Participate in project simulations where the emphasis is on the interdivisional interfaces.
- ***Launch Support Process (7)***
 - Support early mission activities by monitoring spacecraft orbit and attitude, and data related to its health and safety. Plan and execute spacecraft orbit ascent maneuvers and attitude maneuvers. Validate onboard computer (OBC) attitude and orbit compared to the ground attitude and orbit.
 - Support calibration activities by planning and executing attitude sensor calibration maneuvers, if needed. Process calibration telemetry data and estimate sensor biases and misalignments. Send the results to the flight operations team for uplink to the spacecraft.
 - Generate orbit and acquisition data products.
- ***On-Orbit Mission Operations Process (8)***
 - Perform routine on-orbit operations, special requests, and analysis as needed. Produce status reports as required.

5.0 Building Proactive QA Into the Flight Dynamics Mission Support Process

This section discusses FDO's approach, the in-progress process reviews, and the payoff involved in building a proactive quality assurance process for GSFC Flight Dynamics mission support.

5.1 Proactive QA Approach in the Form of Process Assurance

The emphasis of the FDO's QA approach is on proactive prevention of problems by the following activities:

- Build quality checkpoints into FDO project plans, work package plans, mission support phase activity plans, and product QA plans. These checkpoints with appropriate quality criteria ensure that all pertinent activities are quality assured during the process before moving into the next phase of work.
- Provide and/or assist in PPRs to project leader and POMs with just-in-time training to the technical staff before the start of a project or mission support phase and ensure awareness of quality checkpoints by technical staff.
- Monitor the work and/or mission support phase processes and detect any deviations from the established processes and quality standards so that corrective action can be taken as early as possible in a mission or project life cycle. Regular internal mission reviews, IPPRs, preliminary reviews, dry runs before formal reviews, walkthroughs, and peer reviews are in this category.
- Ensure compliance with all policies, standards, and procedures for all processes, products, and services.
- Collect quality-related data, analyze, and feedback for process improvement. Coordinate with the FDO's Defect Causal Analysis (DCA) and Lessons Learned programs.

A comprehensive QA approach is implemented at the FDO mission support project and task levels. An FDO mission support project is a task or a set of tasks involved in a given Flight Dynamics mission. An FDO mission support plan, prepared by a mission manager or project leader, defines all the major Flight Dynamics activities and

events that occur during the development and initial deployment of a mission. One example of this proactive approach is the conducting of IPPRs as described in Section 5.2.

5.2 IPPRs for the FDO Mission Support Life Cycle

The IPPRs are performed for all six phases of the FDO mission support life cycle. The IPPR assesses project team members' understanding of and conformance to the S&Ps and provides an LCPA checklist for the mission-or project life cycle phase. The review occurs approximately 15 to 25 percent into the calendar schedule of the mission support life cycle phase. The PAO uses the mission phase-specific checklist to evaluate the phase activity progress. An assessment guideline for each phase has been set to an 80 percent or higher satisfaction level to determine whether the phase activities are on track. This guideline has proven to be achievable.

Quality/process checklists were developed for the IPPR using the FDO mission support JIT training materials. The FDO Mission Support process coordinator and associates offer this JIT training to the mission teams before the beginning of each phase of the FDO mission support life cycle. PAO participates in training coordination. The training normally occurs 2 to 3 weeks before the start of each phase. These mission phase IPPR checklists are updated and enhanced periodically using the feedback comments from the project leaders, mission managers, team members, and lessons learned. Two sample IPPR checklists for the operations planning and training, and launch support phases are as shown in Tables 1 and 2, respectively. The questions labeled as P1, P2, and P3 were added to collect additional comments or suggestions for the process and overall assessment.

5.3 Proactive QA and Payoff

The quality approaches too often have been reactive rather than proactive in industry as a whole. Therefore, the cost has been high and the reactive QA also caused delays in the delivery schedule. The proactive quality approach, on the other hand, builds quality assurance into the work processes as the mission support life cycle progresses. While the reactive approach deals with the end products, the proactive approach deals with the processes, which prevents errors or rework. In this way, errors and inefficiencies can be detected earlier and corrected quickly, preventing excessive rework after a product is produced. Results of high-quality work from one phase will provide a sound foundation for the subsequent phase. The proactive quality assurance costs are small and repay well in quality products and services and timely delivery. Currently a little more than one PAO staff member has been supporting 150 FDO staff members effectively. The impact of process assurance activities on the quality of the final products and services could be considered minor; while the prime responsibilities are performed by the mission team. However, the cost savings via the process assurance could be significant to the multimillion-dollar space missions.

6.0 Actual Implementation and Findings

Over the past few years, CSC's FDO has implemented a comprehensive proactive QA process applied to each of six phases of the Flight Dynamics mission support life cycle and the documents produced during each phase. As advocated, the quality approach has been proactive rather than reactive. In this way, errors, inefficiencies, and, therefore, rework have been prevented, and quality products and services were delivered on time. This subsection presents the status of how often and to what missions those proactive QA processes were applied (i.e., PPRs, POM, coordination of JIT training, internal mission reviews, dry runs or preliminary reviews before formal reviews, walkthroughs, audit coaching, IPPRs, and LCPA). It is difficult, if not impossible, to measure numerically the results or effectiveness of the processes. However, the proactive QA process has been well received by the line management and technical staff. It has served as a useful reminder on aspects of the process that can be forgotten in day-to-day work. The impression of the perceived improvement has been good as expressed by the mission managers. The FDO missions supported recently by this process were SAMPEX, Deep Space Program Science Experiment (DSPSE), Geostationary Operational Environmental Satellite (GOES) -I and -J, WIND, POLAR, X-ray Timing Explorer (XTE), and Solar and Heliospheric Observatory (SOHO) that were launched successfully, and Submillimeter Wave Astronomy Satellite (SWAS), Fast Auroral Snapshot Telescope (FAST), Total Ozone Mapping Spectrometer (TOMS), Tropical Rainfall Measurement Mission (TRMM), Advanced Composition Explorer (ACE), Wide-Field Infrared Explorer (WIRE), and Earth Observing System (EOS) that are to be launched in the near future.

Table 1. IPPR Checklist for the FDO Operations Planning and Training Phase

Question Number	Question
1	Have you established a training coordinator, a training plan, and discussed the training plan with your ATR(s)?
2	Has the team begun drafting procedures and is there a central repository for these procedures?
3	Has a mechanism been established to track action items?
4	Has a readiness matrix been prepared? (Coordinate with the Flight Dynamics Institution of Simulation and Training (FIST) group.)
5	Have you contacted the mission coordinator concerning the development of the Mission Support Plan (MSP)?
6	Were any lessons learned recorded for this phase?
7	Have any software problems that were detected (during use for training and simulations) been documented and provided to the development/maintenance personnel? What is the resolution status?
8	What will be the products produced and Standards & Procedures (S&Ps) applied?
P1	Was the JIT training adequate to start the phase?
P2	Any other problems encountered in this phase or suggestions?
P3	Overall Assessment: P.1 Is the phase support on track? P.2 If not, what is the resolution?

Table 2. IPPR Checklist for the Launch Support Phase

Question Number	Question
1	Who is the central contact point during the launch support?
2	What is the chain of reporting in the Flight Dynamics Facility (FDF) for emergency (within CSC and with the GSFC chain)?
3	What are the launch support components, group leaders and members, and communications required between the component groups?
4	What shift groups are there, who are the members and leaders, and are phone numbers available?
5	What are the unique nature and requirements of this launch support?
6	What are recent procedure changes and terms are not familiar to everybody on the team?
7	What are the interfaces external to FDF, communications/data transfers required, and different terms used?
8	What are the potential problems or mishaps and resolution (or mitigation) strategy? Do all the team members know how to respond to those emergencies or contingencies?
9	Have you obtained any lessons learned from the previous missions and team members for this mission support?
10	Are there any problems or pending items that make the team uneasy at this point?
P1	Was the JIT training adequate to start the phase?
P2	Any other problems encountered in this phase or suggestions?
P3	Overall Assessment: P.1 Is the phase support on track? P.2 If not, what is the resolution?

The examples in Table 3 show various types of in-progress reviews conducted at different stages of the life cycle phases for the XTE mission. An IPPR was not conducted for every phase of the entire mission life cycle. The reviews supported were performed only when PAO had available time; therefore, the lists are not as complete as they could be.

In addition to the reviews listed in Table 3, FDO internal mission reviews are performed regularly (for example, once or twice a month with the FDO management until launches). The PAO attends these review meetings. After IPPRs, DORRs, LCPAs, and other reviews, PAO writes review reports and distributes copies to the project or mission team leader. Lessons learned data are used for process improvement and are disseminated to the next mission teams. The project or mission managers are interviewed before and after the launch to evaluate the impacts of PAO's reviews. They have made the following observations:

- The FDO PAC procedure provides a comprehensive reminder list for the phase activities while the team members are otherwise occupied.
- The PAO review motivates FDO mission manager and team members to move on to the next phase. Occasionally, the team experience some difficulty starting up a new activity following the completion of a phase.
- The review educates new mission managers who have not managed the entire mission support life cycle.
- JIT training before the phase was useful to mission managers and team members.
- Coordination or providing lessons learned for the mission manager and team was helpful.
- Knowing ahead of time about the lessons learned from the previous missions was helpful for the mission manager and team when planning future resolutions.
- The prelaunch readiness review meeting improved the morale of the team and helped team building.

The following were lessons learned:

- JIT training needs to be done at the right time (but it is difficult to define that time), and JIT needs to be repeated or spread throughout the phase with different emphasis; overview, details, and refresher.
- Deployment of the process was suggested to all members of the organization rather than limited to mission managers or project leaders.

The survey continues and feedback comments are collected in FDO for both the process itself and associated checklists. The same in-progress process assurance principle as used in the mission support phase IPPR has been applied to FDO document quality via the Product QA Plan. In the Product QA Plan, quality checkpoints are identified and appropriate quality criteria are provided ahead of time for QA reviewers.

7.0 Document Reviews and FDO Product QA Plan

Another aspect of FDO process assurance is to ensure that documents produced are quality assured and to provide the QA reviewers some guidance on how to perform the QA. One of the primary approaches to achieving technical quality in products is the FDO Product QA plan. Products include documents, memoranda, technical papers, and presentation materials. The Product QA Plan form for each FDO deliverable product includes key steps that verify

Table 3. FDO In-Progress Reviews for the XTE Missions

Review	Date
Requirements and Specifications Phase IPPR	04/08/93
Software Development Support Phase IPPR	09/01/93
Project IPPR	04/21/95
DORR (L-60)	06/29/95
DORR (L-30)	07/27/95
Launch Phase PPR	07/28/95
Launch Phase POM	07/31/95, 12/05/95
Operations Planning and Training Phase IPPR	11/21/95
XTE Launch	12/30/95
Lessons-Learned Workshop	03/29/96

whether an appropriate QA reviewer has been selected, S&Ps have been identified, QA checkpoints have been identified with appropriate QA checklists (both generic and document-specific) attached, coordination with FDD Configuration Management Office (CMO) and Technical Publications has been scheduled, and QA data collection has been planned for analysis.

The QA reviewer may be anyone in the FDO who is technically qualified to perform the review and who does not report administratively to the line manager responsible for the product. The intent of this review is to ensure the technical quality of products, but their appearance and adherence to schedule may also be reviewed.

In the FDO Product QA Plans, key quality review steps or checkpoints are identified and the corresponding quality criteria are attached for document reviews such as for system and operations concepts, requirements specifications, functional specifications, mathematical specifications, presentation slides for SOCR, SRR, and DORR, mission support plan, analysis reports, professional paper, etc. The QA reviewers then use the quality criteria to review the documents. The Product QA Plan form and associated QA checklists have been updated and enhanced periodically using the feedback comments from the QA reviewers and authors, and lessons learned. Historically, lists of document quality criteria were developed in FDO earlier than the IPPR checklists for the Flight Dynamics mission support life cycle phases. Some of the document quality criteria were used to generate phase IPPR checklists as mentioned earlier in the paper.

An example of specific quality criteria for a requirements specifications document (used with an FDO Product QA Plan) is shown in Table 4. In the document review process, general QA categories are also incorporated such as for technical accuracy, internal consistency, conciseness, freedom from redundancy, clarity, and adherence to the established standards and format.

Table 4. Quality Criteria for the Requirements Specifications Document

Criteria Number	Criteria
1	Are the DMR and related studies referenced when necessary?
2	Are all requirements defined for all mission phases?
3	Are the assumptions reasonable and precisely stated?
4	Does the requirements summary correctly trace requirements to a high level source document?
5	Does the requirements summary include all requirements critical to the definition of the system and operations concepts?
6	Are items such as major external interfaces summarized?
7	Is there consistency between the high-level and low-level requirements?
8	Does the document provide complete information to facilitate the following: <ul style="list-style-type: none"> • The analysts in preparing functional specifications? • The analytical and acceptance test teams in preparing test plans?
9	Other (Specify)

8.0 Process Improvement Through Lessons Learned

Each mission team within the FDO is responsible for developing and documenting improvements and continuing good practices based on the lessons learned during day-to-day activities or during the generation of products and services. The vehicles used to deploy lessons learned are the project lessons learned database, the FDO lessons learned database, reports, electronic files or bulletin boards, training, and DCA reports. These lessons learned are fed back into the process for continuous improvement. The PAO identifies and evaluates S&Ps that are appropriate for FDO products and services. It also establishes and/or assists in developing S&Ps for FDO products and services when appropriate S&Ps do not already exist. The PAO promotes communication among FDO projects and/or missions on tools and methodologies that may contribute to improved quality and productivity. A continual effort is made to improve process assurance and quality assurance methodologies for the FDO-unique mission analysis and support activities. Process and QA methodology changes include those due to changes in mission requirements,

institutional changes, and lessons learned. Methodology effectiveness is closely monitored and evaluated for improvement.

A few examples of the lessons learned that contributed to the FDO process improvement are as follows. The IPPR checklist for the launch support phase (Table 2) was improved after it was learned that other NASA centers, ground stations, and the European Space Agency (ESA) often use different terms from those used at GSFC. A prelaunch readiness review or phase orientation meeting with the PAO-generated review item check list was very positive in team building and morale boosting for the DSPSE mission. Since then, the GOES-I, GOES-J, WIND, SOHO, XTE, and POLAR mission teams used this process. Concerning FDO document reviews, it was observed (in general) that the review results vary depending on the QA reviewers even after a review checklist was given ahead of time. Document review skills training is being considered in FDO.

9.0 Summary and Recommendations

The FDO PAC procedure incorporates process/quality checklists for each of the six FDO mission support life cycle phases. The findings from the actual implementation of the phase IPPRs showed that perceived quality improvement and feedback comments have been very positive. The intermediate results have been good. For further improvement to the FDO process assurance, it is recommended to (1) implement all in-progress process reviews over the entire life cycle from concepts to on-orbit mission operation phase, (2) devise a scheme to measure the cost of this process compared with the total mission cost, and (3) adapt the FDO PAC model to the needs of evolving technology—commercial off-the-shelf software, personal computers and/or workstations, and joint application development (JAD) or rapid application development (RAD) approaches. In the areas of FDO product QA, more training must be provided for authors as well as QA reviewers concerning the QA checkpoints, quality criteria and review skills. The proven processes and lessons learned need to be promulgated throughout FDO.

Acknowledgments

The author wishes to thank the following people for their helpful discussions and reviews of this paper: Kenneth Hall, Ronald Nieman, and Leonard Schreiber of CSC; and James Cooley of GSFC. Thanks are also given to Avinash Beri of CSC and John Lynch of GSFC for their support of this effort.

References

1. Computer Sciences Corporation, *Flight Dynamics Operations Product Assurance Plan (Revision 1)*, I. Oh, May 1994
2. ---, *FDO Mission Support Process Handbook*, G. Nair, September 1993
3. ---, *FDO Mission Support Process Standards and Procedures*, and QA-related materials
4. ---, *SEAS System Development Methodology (SSDM) Standards and Procedures*, Updates, G. Page, et al., August 1994

Experiences in Interagency and International Interfaces for Mission Support *

G. T. Dell, W. J. Mitchell, T. W. Thompson, and J. O. Cappellari, Jr.
Computer Sciences Corporation
Lanham-Seabrook, Maryland, USA 20706

F. Flores-Amaya
National Aeronautics and Space Administration
Goddard Space Flight Center
Greenbelt, Maryland, USA 20771

Abstract

The Flight Dynamics Division (FDD) of the National Aeronautics and Space Administration (NASA) Goddard Space Flight Center (GSFC) provides extensive support and products for Space Shuttle missions, expendable launch vehicle launches, and routine on-orbit operations for a variety of spacecraft. A major challenge in providing support for these missions is defining and generating the products required for mission support and developing the method by which these products are exchanged between supporting agencies. As interagency and international cooperation has increased in the space community, the FDD customer base has grown and with it the number and variety of external interfaces and product definitions. Currently, the FDD has working interfaces with the NASA Space and Ground Networks, the Johnson Space Center, the White Sands Complex, the Jet Propulsion Laboratory (including the Deep Space Network), the United States Air Force, the Centre National d'Etudes Spatiales, the German Spaceflight Operations Center, the European Space Agency, and the National Space Development Agency of Japan).

With the increasing spectrum of possible data product definitions and delivery methods, the FDD is using its extensive interagency experience to improve its support of established customers and to provide leadership in adapting/developing new interfaces. This paper describes the evolution of the interfaces between the FDD and its customers, discusses many of the joint activities with these customers, and summarizes key lessons learned that can be applied to current and future support.

1.0 Introduction

In the early days of the space program, the interfaces between supporting elements were much simpler than they are today. As the feasibility of international space exploration and satellite communication was demonstrated, more countries and agencies joined the space community. Also, as missions progressed, other agencies were spun off from NASA, such as the Deep Space Network (DSN) and the Eastern Range (ER), and elements within NASA developed independent identities, such as the Flight Dynamics Facility (FDF) of the Goddard Space Flight Center (GSFC) Flight Dynamics Division (FDD). In the remainder of this paper, the term FDF is used to refer generically to the support functions of the GSFC FDD as performed in the FDF.

The FDF currently provides both analytical and operational support for an average of seven Space Shuttle missions and ten expendable launch vehicle (ELV) launches each year. It also provides routine on-orbit support and products for a variety of operational spacecraft. A major challenge in providing support for these missions is defining and generating the products required for mission support and developing the method by which these products are exchanged between supporting agencies.

Since its inception, the FDF has developed a large number of products for support of an increasing number of interfaces with customers both inside and outside the GSFC community. The types of products and services that

* This work was supported by the National Aeronautics and Space Administration (NASA)/Goddard Space Flight Center (GSFC), Greenbelt, Maryland, under Contract NAS 5-31500.

the FDF provides for spacecraft launches and Shuttle mission support are discussed in this paper. In addition, the paper chronicles the FDF experience with interagency and international interfaces and joint activities for mission support as they have evolved through the years. The paper also discusses a number of the lessons learned during this evolution. For more detailed information on FDF support services to its customers, see Reference 1, which can be accessed on the Internet at "http://fdd.gsfc.nasa.gov/FDD_EOY95.html".

Section 2 of this paper discusses the FDF products and services, and Section 3 provides details of the major FDF interfaces and activities with key centers and agencies. Section 4 gives a summary of the key lessons learned during the evolutionary process.

2.0 FDF Products and Services

On April 12, 1996, NASA celebrated the 15th anniversary of the launch of the first Space Shuttle mission, Space Transportation System-1 (STS-1). In the early days of the Shuttle program, every day seemed to bring a new customer with a new requirement. FDF customers were no longer limited to the GSFC community. To meet the commitments required to support the Shuttle program, the FDF established new relationships with other NASA centers and agencies within the Department of Defense (DOD). On many occasions, new products and methods of delivery were identified, developed, tested, and implemented before the official paperwork was received. However, those early days provided a solid foundation for the changes, in both product and customer, that were to take place over the next 15 years. Table 1 shows the chronology and extent of the growth in FDF customer support that has taken place since 1978. More specifically, the significant growth in Shuttle product and customer support between 1981 and 1996 is illustrated in Figure 1.

3.0 Interfaces and Activities

In addition to exchanging products with other centers and agencies, the FDF has engaged in a large number of joint activities with these organizations in the area of flight dynamics. This section describes the *major* interfaces that the FDF has with external organizations and discusses some of the joint activities the FDF has performed with these organizations. Figure 2 illustrates these major interfaces. In this figure, the home agency and the section number of this paper that describes the FDF interface with the organization is indicated in each box.

3.1 Johnson Space Center (JSC)

The FDF has participated in a number of joint activities with several different government and contractor support groups within the Flight Dynamics Design Division (FDDD) at the Johnson Space Center (JSC) in support of the Shuttle program, including Ground Navigation, the Flight Dynamics Officers, the Instrumentation and Communications Officers (INCOs), Houston Track (which handles flight-dynamics-related communications with external elements) and the Ascent/Descent group. In the remainder of this section, the term JSC will refer generically to the JSC FDDD.

The FDF/JSC joint activities have included the following:

- Verification of the consistency of the orbit determination and orbit propagation software and astrodynamics constants used at JSC and at the FDF
- Navigation certification efforts to certify the validity of Shuttle orbit determination based on Tracking and Data Relay Satellite (TDRS) System (TDRSS) tracking data
- Ongoing verification of FDF-generated Shuttle orbit determination solutions for Emergency Mission Control Center (EMCC) support
- Efforts to maintain consistency in implementation of the mean equator and equinox of J2000.0 coordinate system
- Ongoing efforts to maintain a consistent set of tracking station geodetics
- Ongoing verification of new tracking data capabilities, such as the Doppler-compensation-enabled capability at the White Sands Complex (WSC)

Table 1. Growth in FDF Customers Outside the GSFC Community

Customer/Milestone	Starting Date	New Customer	New Product(s)
Space Shuttle support requirements	1978	Y	Y
Ariane support requirement [Centre National d'Etudes Spatiales (CNES), the French Space Agency]—Provide launch support for all launches	1981	Y	N
University of Arizona requirement for Space Transportation System (STS)	1982	Y	N
Ames Research Center—STS	1983	Y	N
Langley Research Center (LaRC) for STS	1982	Y	Y
Tracking and Data Relay Satellite (TDRS) System (TDRSS) support requirements	1983	Y	Y
Naval Research Laboratory (NRL) for STS	1984	Y	N
North American Aerospace Defense Command (NORAD) support requirements	1985	Y	N
Centaur G' support requirements—Lewis Research Center (LeRC)	1985	Y	Y
Network Consolidation Plan—Canberra, Goldstone, and Madrid transferred to Jet Propulsion Laboratory (JPL)	1985	Y	N
CNES Systeme Probatoire d'Observation de la Terre-1 (SPOT-1) spacecraft support (first of many)	1986	Y	N
Privatization of the Delta launch vehicle	1988	Y	Y
Ariane support requirement change (CNES)—Provide launch support for only northerly launches	1989	N	N
Launch procedures for Shuttle rendezvous missions	1990	N	N
Marshall Space Flight Center (MSFC)—STS payload	1990	Y	Y
Pegasus support requirement—Provide launch support for NASA missions	1991	Y	N
Ocean Topography Experiment (TOPEX) spacecraft support	1992	Y	Y
Long Duration Balloon Program	1993	Y	N
National Oceanic and Atmospheric Administration (NOAA)—New tracking data interface	1994	N	N
United States Space Command (USSPACECOM) tracking data in NORAD B3 format	1994	Y	Y
White Sands Complex (WSC) stationary vectors with velocity	1995	Y	Y
Express spacecraft support—German Space Operations Center (GSOC)	1995	Y	N
Titan support requirement (USAF)—TDRSS supporting launch	1995	Y	N
National Space Development Agency of Japan (NASDA)—Engineering Test Satellite VI (ETS-VI)/Upper Atmospheric Research Satellite (UARS) experiment (1995)	1995	Y	N
Atlas/Centaur support requirement returns—TDRSS supporting Atlas Centaur	1996	Y	N
NASDA—Tropical Rainfall Measuring Mission (TRMM)/ Communication and Broadcasting Engineering Test Satellite (COMETS)	1998	N	Y

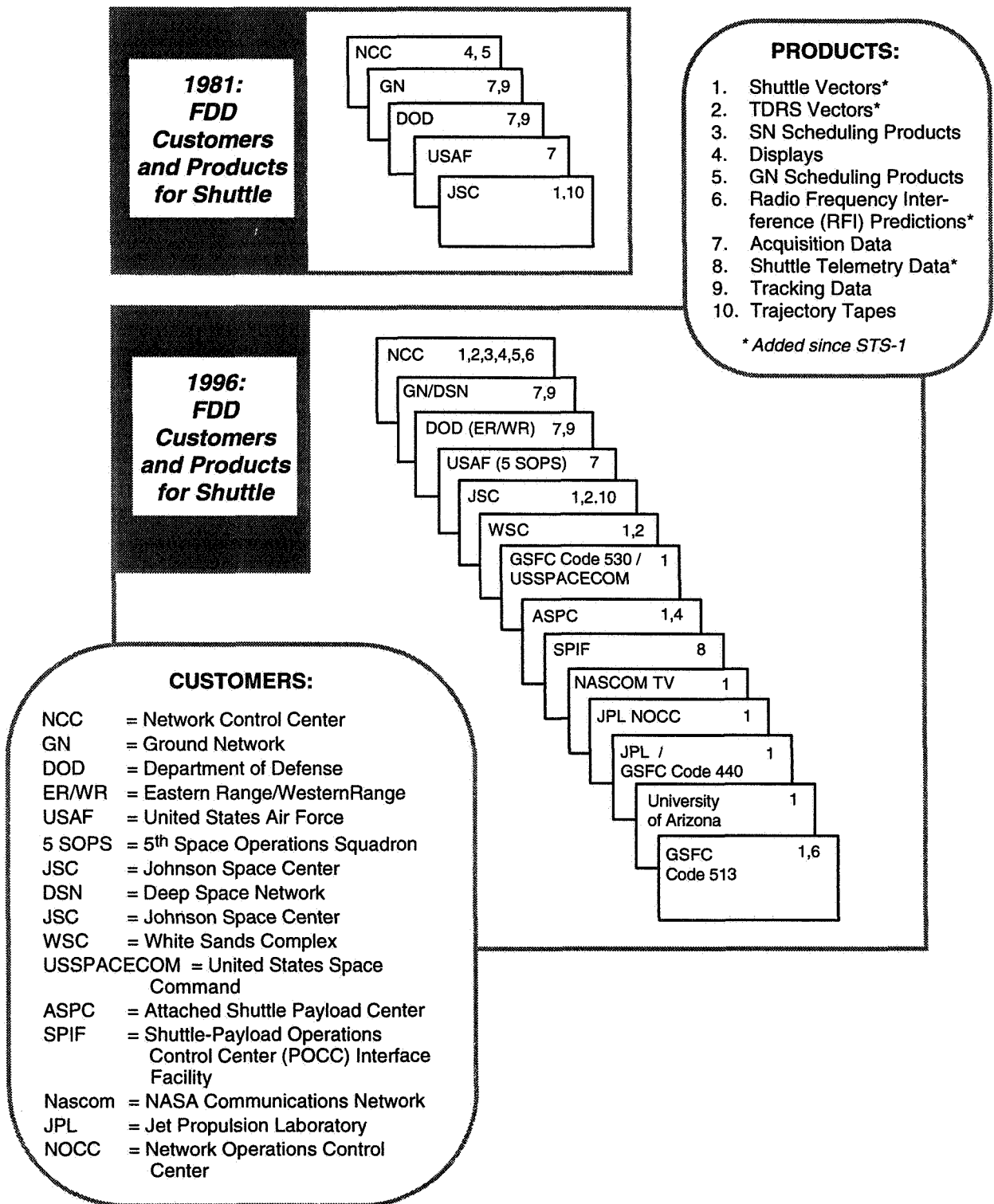


Figure 1. FDF Shuttle Product and Customer Growth Comparison: 1981 and 1996

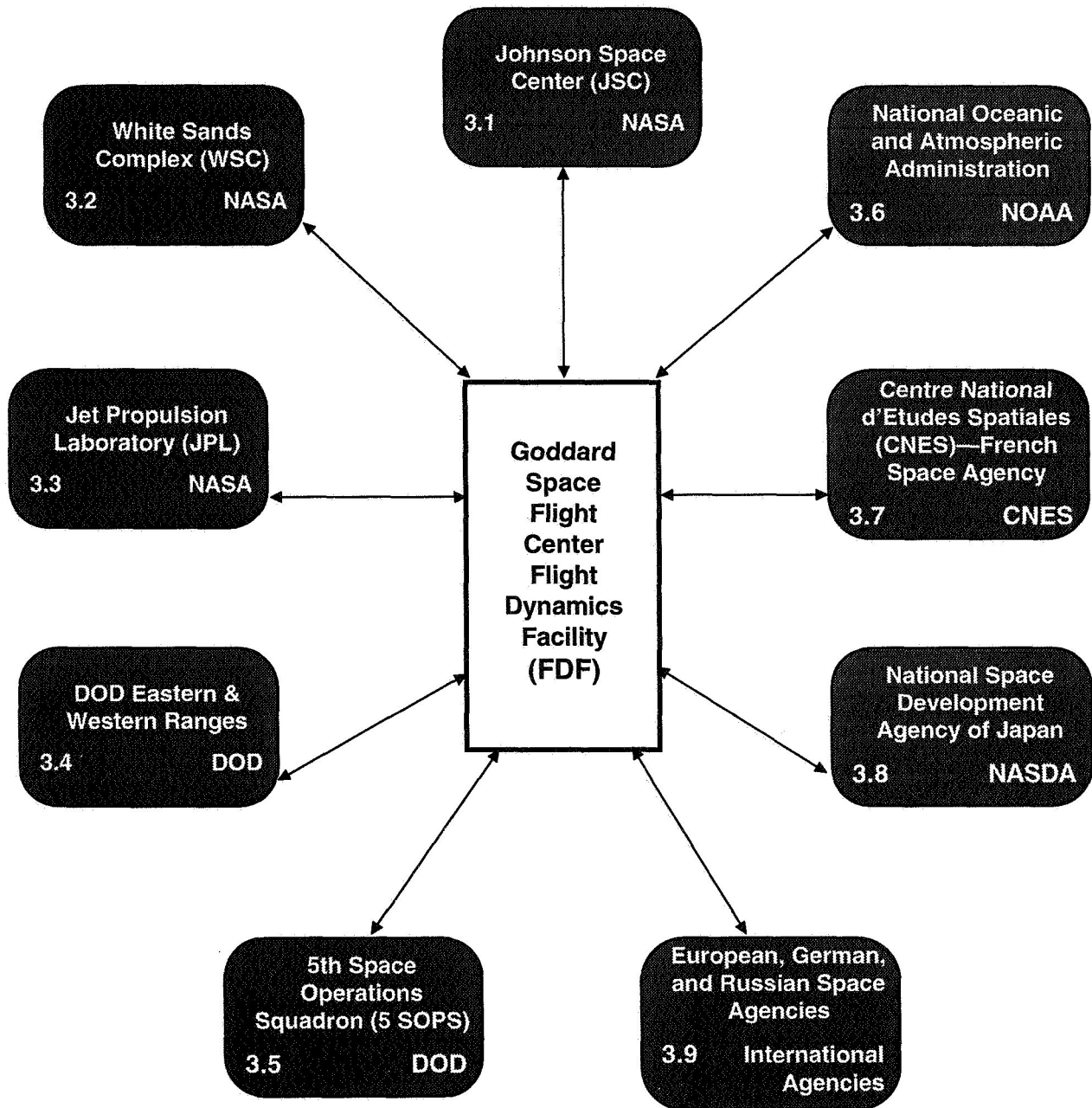


Figure 2. Major FDF Interfaces With External Organizations for Launch and Shuttle Support

Most of these joint activities have been performed under the umbrella of the TDRSS Orbit Determination and Navigation Working Group (TODNWG). The TODNWG is an intercenter working group that was established to address operational and technical problems associated with TDRSS navigation and to provide a forum for technical interchange between JSC and GSFC. This working group is composed of technical personnel from the JSC Navigation Integration Office and from the GSFC FDD and their respective contractors—Computer Sciences Corporation (CSC/GSFC), AlliedSignal (ATSC/GSFC and JSC), and Rockwell Space Operations Company (RSOC/JSC). This group began meeting in 1982 to develop a STS/TDRSS Navigation Certification Plan (Reference 2) and to carry out preliminary software testing and verification between the two centers.

The major early TODNWG goal was the certification of TDRSS for Shuttle navigation support. The first step in this process was verifying the consistency of the orbit determination and orbit propagation software and astrodynamics constants used at JSC and at the FDF. JSC and the FDF performed parallel orbit determination and orbit propagation runs and then compared the results. From August 1983 (the beginning of TDRSS tracking services) to October 1984 (the end of the STS-41G mission), the TODNWG members discussed and analyzed the results of Shuttle tracking tests during the STS-41C and STS-41G missions and successfully completed the augmented single-TDRS (TDRS-East plus ground stations outside the TDRS-East coverage) certification effort (Reference 3). Following the launch and on-orbit checkout of the second TDRS, the next step in the certification process was a successful joint JSC/GSFC two-TDRS certification effort to certify the TDRS East/TDRS-West configuration (without ground station augmentation) for nominal on-orbit navigation support of Shuttle flights (Reference 4). The two-TDRS certification missions were STS-29 and STS-30 (nonrendezvous missions) and STS-32 (a rendezvous mission).

A consistent set of tracking station geodetics has been maintained at JSC and the FDF through joint TODNWG efforts. The World Geodetic System 1984 (WGS 84) geodetic reference system (Reference 5) is the current baseline system for the catalog of tracking station geodetic locations maintained by the FDF and documented in Reference 6. However, both JSC and the FDF currently use the Spaceflight Tracking and Data Network 1973 (STDN 73) geodetic reference system in their orbit determination and orbit propagation software. Consequently, the FDF WGS 84 geodetic database must be transformed to the STDN 73 system before use. The converted FDF locations are periodically compared with the JSC values to ensure consistency.

Another TODNWG activity was coordinating the implementation of the mean equator and equinox of J2000.0 coordinate system at JSC and at the FDF, including the algorithms for converting to and from the previous standard coordinate system, which was the mean equator and equinox of B1950.0 system. The algorithms used for these conversions at JSC and at the FDF were exchanged and discussed, and it was agreed that they were consistent to within acceptable tolerances. The final step in this process was an electronic interface test in which J2000.0 state vectors in the form of improved interrange vectors (IIRVs) were successively generated and transmitted from the JSC mission operations computer (MOC) to the FDF and from the FDF to the JSC MOC.

During each Shuttle mission, routine Shuttle orbit determination is performed by the JSC Ground Navigation group. Houston Track transmits hourly Shuttle state vectors based on these solutions and, when appropriate, on-orbit maneuver sequences to the FDF. These vectors are then processed by the FDF to generate Space and Ground Network acquisition data. Houston Track also keeps the FDF informed of any important developments in Shuttle support. The FDF, in turn, provides Houston Track with daily TDRS state vectors for use by JSC Ground Navigation in performing Shuttle orbit determination with TDRSS tracking data.

In the event that an EMCC situation occurs during a Shuttle flight, the JSC Mission Control Center (MCC) function will be transferred to the Kennedy Space Center (KSC). A JSC flight control team and their support computer will fly from JSC to KSC and continue Orbiter support from there until the JSC MCC is in operation again or until the Shuttle lands. Because the EMCC computer does not have an orbit determination capability, the Shuttle orbit determination function will be assumed by the FDF, and the FDF will provide acquisition data directly to the Space and Ground Networks, as well as to the flight control team at KSC. To verify the FDF capability to provide orbit determination support for a Shuttle EMCC, joint JSC/GSFC EMCC exercises are performed at approximately 6-month intervals during actual Shuttle flights. The FDF performs Shuttle orbit determination using the software and modeling that would be used during an actual EMCC support, and the resulting solutions are transmitted electronically and via facsimile from the FDF to the JSC Ground Navigation

group. (In an actual EMCC situation, the solutions would be transmitted via facsimile to the JSC flight support team at KSC for manual entry into the EMCC support computer.) These solutions are then compared with the corresponding solutions obtained by the JSC Ground Navigation group to ensure that the FDF solutions are within allowable tolerances, especially for deorbit burn support. EMCC exercises were performed during the STS-47, STS-64, STS-67, and STS-74 missions.

The most recent joint activity has been to verify the new White Sands Complex (WSC) Doppler-compensation-enabled capability to generate valid Doppler tracking data during periods when forward-link Doppler compensation is enabled. This new capability makes it possible to maintain solid TDRSS acquisition of a spacecraft and to obtain valid Doppler tracking data at the same time. Tests of the new capability have been performed with TDRSS user spacecraft (Reference 7) and during the STS-74, STS-75, and STS-76 missions. The STS-76 mission was the formal verification mission for the new Doppler-compensation-enabled capability.

The interactions with the JSC INCOs have been primarily concerned with maintaining communications with the Orbiter during any type of spacecraft contingency, such as a return to launch site (RTL), transoceanic abort landing (TAL), or abort-once-around (AOA). The FDF Space Network (SN) acquisition data for contingency support is usually based on trajectory tapes and/or hardcopy data provided by the JSC ascent/descent group. For most contingency cases, the acquisition data are sufficiently accurate to maintain good communications with the Orbiter. However, in the event of a ditch contingency or an EMCC end-of-mission landing, only minimal trajectory information will be available from JSC, and this has been a matter of great concern in the past. However, with the advent of the new Second TDRSS Ground Terminal (STGT), FDF personnel recognized that a modification to the STGT vector processing algorithms would greatly enhance the accuracy of the acquisition data for these particular contingencies. The modification recommended by the FDF has been implemented at WSC, which now makes it possible to provide good TDRS acquisition data for both ditch cases and EMCC landings.

The JSC Ascent/Descent group is responsible for providing users with premission Shuttle trajectory data covering the nominal launch and all possible launch contingencies. In the past, this has meant the transfer of several trajectory data tapes, called D-tapes, for each Shuttle mission (Reference 8). For some time, JSC and FDF personnel have been investigating better ways of transferring the trajectory data and methods for reducing the number of tapes required for each mission. In support of this effort, the FDF acquisition data group has built up a large library of D-tapes, which are now available for use as generic D-tapes where appropriate. The first step in the direction of using generic D-tapes for mission support was the designation of D-tapes for RTL, TAL, and AOA landings as generic, i.e., it is no longer necessary for JSC to provide mission-specific D-tapes for these contingency cases. A joint analysis of the D-tape requirements for nominal launches is nearing completion; the results are expected to support extensive use of generic, rather than mission-specific, D-tapes for nominal launch support. This is particularly important for rendezvous missions, which typically require up to five D-tapes to cover the ascent variations across the launch window (Reference 9).

3.2 White Sands Complex (WSC)

The FDF has maintained a strong interface with the White Sands Complex, beginning with the original White Sands Ground Terminal (WSGT) and continuing with the new STGT and the White Sands Ground Terminal Upgrade (WSGTU). The early WSGT interface was through the White Sands/NASA Interface Working Group (WNIWG). The early focus of the joint activities between the FDF and WSC was in the areas of TDRS orbit determination, TDRSS tracking data quality, and user state vector processing, especially for Shuttle support.

Initially, WSGT performed their own TDRS orbit determination, based on single-station tracking data from the Tracking, Telemetry, and Command (TT&C) System, for TDRSS user and stationkeeping support. The FDF, on the other hand, required more accurate TDRS orbit determination for processing TDRSS tracking data for user orbit determination. The FDF TDRS solutions were based on multistation (bilateration) tracking using the Bilateration Ranging Tracking System (BRTS) (Reference 10). Typically, tracking data from a White Sands BRTS transponder were combined with tracking data from an Ascension Island, American Samoa, or Alice Springs, Australia, BRTS transponder. In 1986, a joint WSGT/FDF TDRS Orbit Determination Working Group (TOWG) was formed to consider the feasibility of using the more accurate FDF BRTS-based TDRS orbit solutions for TDRSS user support at WSGT. As a result of this effort, the FDF TDRS solutions based on BRTS tracking have

been used at WSGT/WSC since April 1987. The FDF also provides quick-turnaround (4-hour) TDRS orbit solutions based on intensive BRTS tracking to WSC following each TDRS stationkeeping maneuver. These 4-hour solutions are also provided to JSC whenever a Shuttle mission is in progress at the time of the TDRS stationkeeping maneuver because high-accuracy TDRS solutions are required for Shuttle orbit determination.

A continuing joint activity between the FDF and WSC has been the coordination and verification of solar/lunar/planetary ephemeris (SLP) files, geopotential files, and astrophysical constants used in the FDF and WSC software. A major joint effort was carried out in 1984 to verify that the Goddard Earth Model-9 (GEM-9) geopotential was properly implemented at WSGT. In 1990, the FDF provided the STGT Project with an SLP file in VAX format for use at STGT, and a series of orbit propagation tests was performed to verify the STGT modeling and propagation software. These tests gave excellent results, with propagation differences in the submeter range (Reference 11). To maintain consistency in TDRS maneuver planning and execution, the FDF uses the same SLP file that was provided to STGT when processing STGT-generated TDRS state vectors. This avoids the necessity of continually updating the UT1-UTC* values used at WSC to maintain consistency with the FDF values. Since the time of this original calibration, the FDF has updated its geopotential field twice, first to the GEM-T3 model and then to the Joint Gravity Model-2 (JGM-2) model. In addition, the FDF recently provided STGT with an updated SLP file and performed propagation tests to verify the STGT installation of this SLP file and implementation of the JGM-2 geopotential.

A very important joint activity is in the area of testing and improving the state vector processing algorithms at WSC, particularly with regard to the processing of launch, on-orbit, and landing maneuver sequences, which allow the TDRS antennas to accurately follow powered flight and reentry trajectories. The specific algorithms for processing so-called "stationary" vectors is also important, because these vectors are used extensively by the FDF to support Shuttle and Expendable Launch Vehicle (ELV) launches and to generate backup support for Shuttle contingency trajectories in case there is a problem with the transmission or processing of maneuver sequences. The FDF, the GSFC Network Control Center (NCC), and WSC conduct exhaustive vector processing tests for new vector processing capabilities, and a mission-specific vector verification test is performed before each Shuttle mission to verify the readiness of WSC to support all acquisition data support requirements for the flight. As discussed in Section 3.1, these tests often lead to recommended improvements in the vector processing capabilities at WSC.

3.3 Jet Propulsion Laboratory (JPL)

The FDF interface with the Jet Propulsion Laboratory (JPL) became more extensive when the Deep Space Network (DSN) was implemented under JPL. The DSN includes antenna sites at Canberra, Australia; Madrid, Spain; and Goldstone, California. These sites are frequently scheduled for Shuttle and ELV launch support. The FDF provides acquisition data and tracking data evaluation for the DSN sites. The interface for acquisition data is to transmit the data via high-speed lines to JPL. JPL then forwards the data to the individual sites. The FDF also maintains a low-speed interface directly with the sites. The high-speed transmission format is currently limited to vector transmissions such as IIRVs and Extended-Precision Vectors (EPVs) (Reference 12). For launch support, single vectors are insufficient for support, and antenna pointing angles are provided directly to the sites via low-speed lines from the FDF.

3.4 Department of Defense (DOD) Eastern Range/Western Range (ER/WR)

For most Shuttle and ELV launches, the FDF provides acquisition data to the DOD for stations at either the Eastern or Western Range. The DOD also has the capability of transmitting data to these sites. In this unique situation, the FDF and DOD have the capability of providing backup support to each other. In other situations, the FDF and the DOD have had to develop procedures to ensure that they do not override each other's data.

For Shuttle missions, the FDF is the prime provider of data for the Orbiter, and the DOD is the prime provider for any deployed payloads. If the FDF were unable to satisfy the acquisition data requirement, the DOD would be

* UTC = coordinated universal time; UT1 = universal time corrected for polar motion

called up to provide that function. If the DOD were unable to provide acquisition data for a deployed satellite, then the FDF would be requested to provide the support.

With the increasing number of satellite launches, the FDF and DOD have had to work closely to coordinate overlapping activities, such as an ELV launch during a Shuttle mission.

3.5 5th Space Operations Squadron (5 SOPS)*

The FDF provides acquisition data support to the Air Force Satellite Control Network (AFSCN) Remote Tracking Stations (RTSs) for Shuttle and ELV missions. The acquisition data are provided to the RTSs through 5 SOPS at the Onizuka Air Station (OAS) in Sunnyvale, California.

For Shuttle missions, the FDF provides premission acquisition data to 5 SOPS for the RTS sites approximately 7 days before the scheduled launch day. After launch, the FDF provides 5 SOPS with regular updates for the RTSs as defined in STS requirements. Because of the FDF's indirect interface with the RTS, a 15- to 30-minute delay can be expected between the FDF and the sites. Additional procedures have been developed in the cases where real-time updates may not be possible in time.

ELV support is mission dependent, but it usually includes providing 5 SOPS with premission marked event vectors (i.e., cut-off and injection vectors) for RTS acquisition. Updated information is provided to 5 SOPS for RTSs in near real time. The deliveries for ELV support are usually done via facsimile.

Within the past year, the FDF has had the opportunity to support Titan/Centaur missions using the SN. For Titan support, the FDF has been working with 5 SOPS to develop a high-speed transmission interface for the FDF to receive updated launch information from 5 SOPS. The high-speed interface and the SN support of launches has been successfully implemented and demonstrated during the last several Titan missions. Because of the success of this interface, a similar high-speed interface with the ER will be used for SN support of Atlas/Centaur launches.

3.6 National Oceanic and Atmospheric Administration (NOAA)

The FDF has supported the National Oceanic and Atmospheric Administration (NOAA) for both the Geostationary Operational Environmental Satellite (GOES) and NOAA satellite series. For both of these series, the FDF provides acquisition data to the Ground Network after spacecraft injection. However, for the GOES satellites, the FDF support is more extensive and includes providing attitude and orbit determination support to the GOES Satellite Operations Control Center (SOCC) during the early mission phase. For the NOAA satellites, the FDF's primary requirement has been to provide accurate acquisition data to the Ground Network.

For all NOAA satellites, the FDF has a requirement to provide acquisition data support for the first 3 weeks of the mission. This requirement was developed based on the experience that 3 weeks was the appropriate amount of time to define a stable orbit for the satellite and to transition to the standard NOAA satellite tracking schedule. During the launch support phase, the FDF receives a number of data sources for initial orbit determination, such as (1) an injection vector from the NOAA Automated Ground Equipment (NAGE) and the General Electric Real-Time System (GERTS), (2) data from the Launch Trajectory Acquisition System (LTAS), and (3) North American Aerospace Defense Command (NORAD) elements provided by the United States Space Command (USSPACECOM). Of the data sources, the NORAD elements were identified as the most accurate. The FDF was able to use the NORAD elements in orbit determination solutions to determine short predictions (approximately 48 hours) of the satellite orbit. The FDF requires up to 2 weeks of NORAD elements before the orbit determination predictions are accurate for longer periods (up to 1 week).

For the NOAA-J mission, the FDF performed premission analysis and determined that the FDF would be able to provide orbit determination that converged to a stable orbit in a much shorter period of time if C-band tracking data were made available to the FDF. The FDF did receive the C-band tracking data and was able to define a stable orbit within 10 hours after launch. As a result, NOAA had a better initial orbit definition, and the FDF required less frequent acquisition data updates.

* Previously the 750th Space Group (750 SGP) and before that the Consolidated Space Test Center (CSTC).

3.7 Centre National d'Etudes Spatiales (CNES)

As discussed in Section 2, the FDF has provided varying levels of support to Centre National d'Etudes Spatiales (CNES) through the years. The involvement with CNES was initiated with the NASA support of Ariane launches in 1981. The FDF participated in a series of working group meetings with CNES personnel to define the interface. For the Ariane launches in the 1980s, the FDF provided acquisition data support to the NASA Ground Network stations and provided early orbit estimation to CNES. The acquisition data and estimation were based on LTAS data from both NASA and CNES Ground Network sites.

The support increased to include early orbit support for the SPOT missions. The SPOT missions required an understanding of the changing launch trajectory through the launch window and close coordination with CNES for the appropriate trajectory selection during launch. The FDF early launch support was critical to ensuring first pass acquisition at the Fairbanks, Alaska, station. The support for the SPOT mission set a precedent for cooperation for subsequent missions such as TOPEX and Helios.

Recently, the FDF has been working with CNES in utilizing CNES Ground Network resources for NASA launches. The latest cooperation was for Kerguelen Station tracking of the Delta/Polar launch on February 24, 1996. The Kerguelen station was instrumental in providing verification of the spacecraft orbit injection.

3.8 National Space Development Agency of Japan (NASDA)

Recently, the FDF has been sharing its expertise in SN orbit determination and spacecraft acquisition with the National Space Development Agency of Japan (NASDA). NASDA is currently developing a tracking and data relay satellite system, and it has worked with the FDF to develop interfaces to facilitate system validation and future interoperability. Specifically, NASDA plans to accomplish the following:

- Validate forward-link commanding from NASDA's tracking and relay satellite to a user spacecraft
- Validate receipt of return-link telemetry from the user spacecraft at the spacecraft's operations control center
- Validate the orbit solutions obtained from tracking the user spacecraft from NASDA's tracking and relay satellite

The first two objectives were successfully demonstrated during tests conducted between NASDA's Engineering Test Satellite (ETS)-VI and NASA's Upper Atmospheric Research Satellite (UARS) in June and July of 1995. Tests to accomplish the latter objective are planned to occur in 1998 between NASDA's Communication and Broadcasting Engineering Test Satellite (COMETS) and the Tropical Rainfall Measuring Mission (TRMM) satellite, a joint project between NASA and NASDA.

To achieve these objectives, agreement was needed on the following interfaces:

- Format and media for state vector exchange
- Format and media for tracking data exchange
- Source and update times of environmental data and values of physical constants

In addition, the propagation models needed to be examined and understood to ensure meaningful results when comparing orbit determination solutions.

Negotiating the new interfaces revealed two minor problems. First, NASDA's tracking data format was incompatible with any existing NASA format, and other priorities precluded modifying the FDF's tracking data processing software to accept the NASDA format. Consequently, NASA will not be able to use NASDA tracking data in the near future. Secondly, the FDF preferred to exchange vectors in a rotating Earth-fixed coordinate system, whereas NASDA wished to use the geocentric true of date (GTOD) coordinate frame. Use of the GTOD frame introduces the potential for increased error resulting from inconsistencies in UT1-UTC information in environmental data files. Coordinating file updates with external centers is not practical because the FDF frequently must freeze its configuration due to mission support requirements. As a result, in the future both

agencies need to be aware of updates to the UT1–UTC data and its impact on state vector exchange and propagation.

A valuable lesson learned from these experiences was that a thorough understanding of the processes behind interfaces, together with good communications between the groups involved, can help achieve early recognition of potential interface problems. This makes it possible to develop a problem resolution or workaround or can minimize problems further down the line that will be more costly to resolve.

3.9 Other International Agencies

The FDF has also developed mission support interfaces with other international agencies:

- **European Space Operations Center (ESOC).** For the Earth Resources Satellite (ERS) mission launched onboard an Ariane, the FDF coordinated support with ESOC for early orbit support.
- **German Space Operations Center (GSOC).** The FDF has also developed a support interface with GSOC. For the Experiment Reentry Space System (EXPRESS) mission, the FDF worked with GSOC to develop an electronic high-speed interface for vector exchange. The interface developed for Express mission support was also used for the recent Radarsat launch support.
- **Russian Space Agency.** FDF involvement with the Russian Space Agency started with support of the Apollo/Soyuz Mission in 1975. More recently, the FDF interfaced with the Russian Space Agency in the preparations for and the launch of the Total Ozone Mapping Spectrometer (TOMS) instrument onboard the Soviet Meteor-3 satellite in August 1991. For this mission, the FDF received vectors from the Soviet Central Aerological Observatory (CAO) and was able to coordinate with Soviet flight dynamics specialists to compare and coordinate vector propagation modeling techniques (Reference 13). Now in the age of the international space station, the FDF is supporting communication with the Russian space station Mir by providing acquisition data to the Wallops and Dryden stations.

4.0 Summary

As the FDF interfaces with external elements evolved over the years, a number of lessons were learned that will be useful in developing new interfaces in the future. These lessons include the following:

- It is important to establish common, well-defined interfaces and processes from the beginning.
- The number of common parameters that must be maintained between elements should be held to a minimum consistent with meeting all support requirements.
- Error-prone elements and processes should be eliminated wherever possible. For example, use of a rotating, Earth-fixed coordinate system (instead of an inertial system) when exchanging state vectors between centers eliminates the potential for errors resulting from inconsistencies in the values of UT1–UTC used at the two centers.
- It is important to thoroughly understand the processes underlying each interface. For example, an in-depth understanding of the vector processing algorithms used at STGT enabled FDF personnel to recommend an enhancement to these algorithms that significantly improved the accuracy of SN acquisition data for certain Shuttle contingency cases.
- Flexibility and adaptability must be maintained in all interfaces. The requirements and customers for any given interface are constantly evolving.
- Interoperability—the cooperative cross-support between agencies involving the use of the data relay satellites of one agency to support users of the data relay services of the other agency—should be encouraged.
- Open communication between individuals in different organizations is very helpful in resolving any interface problems that may arise.

- Those responsible for developing and maintaining interfaces must be kept informed of all activities and agreements related to the interfaces.
- Feedback from the interface process is vital in the design and building of new hardware and software systems.

Application of these lessons has resulted in external interfaces that are manageable and robust, allowing the FDF to support an increasing numbers of customers.

The FDF's interfaces continue to evolve. The FDF and its customers are moving into new technologies that permit more flexible interfaces. As established interfaces are adapted to these new technologies and new interfaces are developed, it becomes increasingly important to apply the lessons learned from the earlier development efforts.

References

1. Goddard Space Flight Center (GSFC), Flight Dynamics Division, *Flight Dynamics Division End of Fiscal Year 1995 Report*, Flight Dynamics Division (FDD)/Code 550, October 1995
2. TDRSS Orbit Determination and Navigation Working Group, *STS/TDRSS Navigation Certification Plan*, J. Teles (GSFC) and R. Osburn (JSC), January 1983
3. Lyndon B. Johnson Space Center and Goddard Space Flight Center, JSC-22971, *The Joint JSC/GSFC STS/TDRSS Navigation Certification Interim Report: Single-TDRS Results*, J. B. Joyce (GSFC) and J. K. Weaver (JSC), April 1988
4. Lyndon B. Johnson Space Center and Goddard Space Flight Center, JSC-24795, *Joint JSC/GSFC Two/TDRSS Navigation Certification Final Report*, J. B. Joyce (GSFC) and F B. Lowes (JSC), December 1990
5. The Defense Mapping Agency, DMA TR 8350.2, *Department of Defense World Geodetic System 1984, Its Definition and Relationships With Local Geodetic Systems*, R. W. Smith, September 30, 1987
6. Goddard Space Flight Center, Flight Dynamics Division, *NASA Directory of Station Locations, Fourth Edition*, T. Gunther (CSC), February 1978
7. Goddard Space Flight Center, Flight Dynamics Division, Memorandum 56759-01, *Orbit Determination Results From Doppler Compensation Testing*, W. Forcey and J. Cappellari, February 12, 1996
8. Lyndon B. Johnson Space Center, JSC-22689 Rev A, *Trajectory D-Tape Interface Control Document, Revision A, March 1991*
9. P. Powers (CSC), J. Cappellari (CSC), L. March (CSC), J. Lynch (GSFC), and G. Marr (GSFC), *Goddard Space Flight Center Flight Dynamics Division Ascent Acquisition Support of Space Shuttle Rendezvous Missions*, Paper No. AAS 95-441, presented at the AAS/AIAA Astrodynamics Specialist Conference, Halifax, Nova Scotia, August 14–17, 1995
10. Computer Sciences Corporation, CSC/TM-86/6703, *Analysis of Bilateral Ranging Transponder System (BRTS) Tracking Requirements for Tracking and Data Relay Satellite System (TDRSS) User Support*, J. O. Cappellari, Jr., E. G. Mack, and A. M. Nicholson, January 1986
11. Goddard Space Flight Center, Flight Dynamics Division, Memorandum to O. Cuevas, J. Lynch, and G. Marr, (GSFC Code 553), *STGT TDRS Orbit Propagation Validation Report*, prepared by J. O'Malley, J. O. Cappellari, Jr., and W. Burton (CSC), October 5, 1992
12. Goddard Space Flight Center (GSFC), STDN 724, *Tracking and Acquisition Handbook for the Spaceflight Tracking and Data Network, Revision 5*, March 1990
13. Goddard Space Flight Center (GSFC), Flight Dynamics Division, 553-FDD-92/010R0UD0, *Meteor-3/Total Ozone Mapping Spectrometer (TOMS) Project Permission and Early Mission Orbit Analysis Results*, J. O. Cappellari, Jr., et al. (CSC), prepared by Computer Sciences Corporation February 1992

PULSED PLASMA THRUSTERS FOR SMALL SPACECRAFT ATTITUDE CONTROL

Melissa L. McGuire
Analex Corporation
NASA Lewis Research Center
Cleveland, Ohio 44135

Roger M. Myers
NYMA Inc.
NASA Lewis Research Center
Cleveland, Ohio 44135

ABSTRACT

Pulsed Plasma Thrusters (PPTs) are a new option for attitude control of a small spacecraft and may result in reduced attitude control system (ACS) mass and cost. The primary purpose of an ACS is to orient the spacecraft configuration to the desired accuracy in inertial space. The ACS functions for which the PPT system will be analyzed include disturbance torque compensation, and slewing maneuvers such as sun acquisition for which the small impulse bit and high specific impulse of the PPT offers unique advantages. The NASA Lewis Research Center (LeRC) currently has a contracted flight PPT system development program in place with Olin Aerospace with a delivery date of October 1997. The PPT systems in this study are based upon the work being done under the NASA LeRC program. Analysis of the use of PPTs for ACS showed that the replacement of the standard momentum wheels and torque rods systems with a PPT system to perform the attitude control maneuvers on a small low Earth orbiting spacecraft reduced the ACS mass by 50 to 75% with no increase in required power level over comparable wheel-based systems.

1. INTRODUCTION

In this age of shrinking spacecraft size and smaller launch vehicle capacity, there is a greater need to fit more payload for more science return on a given spacecraft. For a given launch vehicle, increasing the payload mass requires a reduction of the mass and volume of the other spacecraft subsystems. Mass, volume, system complexity, reliability, and cost are critical areas in the design of a small spacecraft. Any additional subsystem increases spacecraft complexity and mass. In order to decrease spacecraft bus size or to increase the payload for a given bus, the core systems need to be made smaller and lighter. This paper presents a new option for ACS which may achieve these goals.

This study is a feasibility analysis of a Pulsed Plasma Thruster (PPT) system to perform disturbance torque compensation and deadband control for a small spacecraft in low earth orbit (LEO) orbital altitude. Pulsed plasma thrusters accelerate small quantities of ablated fluorocarbon propellant to generate very small

impulse bits (~100 μ Ns) at high specific impulse (1000 s). These characteristics make PPTs an attractive option for ACS functions. State-of-the-art attitude control systems consist of hardware such as momentum wheels, magnetic torque rods, and/or thrusters, typically hydrazine (N_2H_4), used to stabilize the spacecraft against disturbance torques resulting from either environment or spacecraft operation. The capabilities of PPTs will be examined to perform the total ACS functions in this study. Since momentum wheels are well known and trusted, replacement of the magnetic torque rods or thrusters in dumping the momentum wheels, or replacement of two of the three momentum wheels used in 3-axis stabilization are also viable options for the use of PPTs and will be left as topics of further studies.

Section two of this paper will present a background of attitude control functions as well as a baseline of current ACS. Section three offers a description of PPTs with information about present and future ground test demonstrations and brief history of the PPT program. With this material, the analysis in section four presents the results of using PPTs to perform both the momentum compensation in place of wheels and

slewing maneuvers. Finally, section five summarizes the conclusions of this preliminary feasibility analysis.

2. ATTITUDE CONTROL SYSTEMS

The attitude control system of a spacecraft stabilizes and orients it in the desired direction and to the desired fidelity as dictated by the mission. Disturbances which threaten to corrupt this attitude arise from the environment around the spacecraft (gravity-gradient, solar pressure, magnetic field interactions, and atmospheric drag) as well as from the spacecraft itself (propellant sloshing, thruster misalignment, and offsets between the center of gravity and center of pressure).¹ The wheels counter the angular momentum induced by these torques through spinning, while thrusters are fired to balance the external torques.²

A typical ACS in use today consists of four wheels (three primary and one backup to cover three axes), an electronics unit, and a wheel desaturation system. The latter can be either magnetic torque rods which use an electric current to produce a magnetic field which interacts with the earth's magnetic field to produce a torque, or hydrazine thrusters which produce a force that acts on a moment arm on the spacecraft also to produce a torque. Four wheel, three-axis systems for attitude control can be massive and high volume, and have suffered from reliability problems. As one example, the ESA (European Space Agency) spacecraft SOHO (Solar and Heliospheric Observatory) experienced difficulties with its momentum wheels which threatened the impending launch date. The wheels had to be replaced completely.² Estimate of a four wheel ACS range from \$700k to \$1 million for a given spacecraft.³

Two examples of current small spacecraft and their ACS hardware are the TOMS-EP (Total Ozone Mapping Spectrometer - Earth Probe), and the WIRE (Wide Field Infrared Explorer). The TOMS-EP spacecraft is part of the Mission to Planet Earth and will measure the ozone and sulfur dioxide content of the atmosphere for a minimum of two years. WIRE is a part of the SMEX (Small Explorer) project and its four month mission is to study galaxy evolution through the use of cryogenically cooled telescopes and infrared detectors.⁴ A breakdown of the components and masses of the TOMS-EP and WIRE spacecraft are presented in Table 2-1.⁵ The attitude control systems represent a large fraction of the dry mass of the two spacecraft. For the TOMS-EP system with 72.6 kg of hydrazine onboard, the ACS is 20% of the total spacecraft dry mass. For the WIRE spacecraft, with its short lifespan, the ACS represents 10% of the dry mass. These examples show

that the ACS can be a significant percentage of the total spacecraft mass depending upon the specific mission.

3. PULSED PLASMA THRUSTERS

Pulsed plasma thrusters are currently under development for a wide range of functions including attitude control. PPTs rely on the Lorentz force generated by the interaction of an arc passing from anode to cathode with the self-induced magnetic fields to accelerate a small quantity of ablated chlorofluorocarbon propellant. As shown in Figure 3-1, the thruster system consists of the accelerating electrodes, energy storage unit, power conditioner, ignition circuit, propellant feed system, and telemetry. During operation, the energy storage capacitor is first charged to between 1 and 2 kV. The ignition supply is then activated to generate a low density plasma which permits the energy storage capacitor to discharge across the face of the fluorocarbon propellant bar. This arc ablates, heats, and accelerates the propellant to generate thrust. Peak arc current levels are typically between 5 and 15 kA, and the arc duration is between 5 and 20 μ s. The pulse cycle is repeated at a rate compatible with the available spacecraft power, which for ACS applications would likely be well below 10 W. The ability to use the same thruster over a wide range of spacecraft power levels without sacrificing performance or having a complex throttling algorithm is one of the advantages of PPTs. The propellant feed system consists solely of a negator spring which pushes the solid fluorocarbon bar against a stop on the anode electrode, eliminating safety and reliability concerns with valves or pressurized systems. There are no other moving parts on the PPT, resulting in a propulsion system which is extremely inexpensive to integrate onto spacecraft and can be stored indefinitely with little concern for storage environment. The latter was recently demonstrated when PPTs stored for over 20 years were successfully fired at both the NASA Lewis Research Center (LeRC) and the Olin Aerospace Company (OAC). The largest mass components of the PPT are the energy storage unit (a capacitor or pulse-forming network) and the system electronics, including the power conditioning unit, discharge initiation, and logic and telemetry circuits. Recent developments in these technologies provide several options which can result in a system mass reduction by a factor of two.

PPTs were extensively developed in the late 1960's and early 1970's. Figure 3-2 shows the range of impulse bits demonstrated on flight or flight-qualified systems. The PPT system developed during that period with the most flight experience was used on the Navy's

TIP/NOVA navigation satellites and operated at a peak power level of 30 W during firing. The NOVA PPT had a specific impulse (I_{sp}) of 543 s, an impulse bit of 400 μ N-s, a total impulse capability of 2450 N-s, and a fueled system mass of 6.8 kg.⁶ The baseline technology for the ongoing NASA program is the flight-qualified LES 8/9 PPT system, which was selected because of its higher I_{sp} of 1000 s and demonstrated total impulse capability of 10,500 N-s and over 10^7 pulses.⁷ The LES 8/9 operated at power levels of 25 or 50 W, produced an impulse bit of 300 μ N-s, and had a fueled system mass of 6.7 kg.⁷

The immediate NASA program objectives are to develop a flight PPT system by October 1997 with a fueled system mass of 3.5 kg capable of providing a total impulse of 20,000 N-s. The flight system is being built by Olin Aerospace. The factor of two mass reduction and total impulse improvement over the LES 8/9 baseline will be accomplished via use of recently developed capacitors, integrated circuit technology for both telemetry and power electronics, new structural materials, and an increase in PPT performance. The projected flight system component masses are 0.85 kg for capacitor, 0.89 kg for electronics and cabling, 0.53 kg for structure and electrode assembly, and 1.23 kg for fluorocarbon fuel. The system is to be qualified for 2×10^7 pulses. Following completion of the initial program, an effort is planned to continue miniaturizing the PPT if there is sufficient interest in the small spacecraft community.

For the ACS function, a single electronics unit could be used to charge capacitor/thruster units placed in appropriate locations (selected to provide required torques) about the spacecraft. While this option would reduce system mass significantly, for this study a complete PPT system was assumed to be located with each thruster set, with a maximum of three thrusters per capacitor/electronics unit. The three thrusters would be oriented to thrust perpendicular to one another, providing control on all three axes. In this study, three levels of PPT technology were included: the LES 8/9 baseline, the lightweight, higher performance PPTs currently under development, and a higher I_{sp} system which could be built under a future program and is well within the demonstrated capabilities of laboratory thrusters.

The dry mass of the LES 8/9 PPTs in a three thrusters about a shared capacitor configuration is assumed to be 5.2 kg (Table 3.1). For the near term advanced technology thrusters having I_{sp} 1000 to 1500 sec, the

dry mass for the same configuration is assumed to be 2.7 kg. The next generation advanced PPT with a higher I_{sp} of 2000 sec is assumed to have a dry mass of 5.2 kg for the same configuration. Therefore, in the 6 and 12 thrusters arrangements, the dry masses for the LES 8/9 through the advanced PPTs are as shown in Table 3-1.

4. ANALYSIS

This section develops a system level comparison of a PPT system and current small spacecraft ACS hardware for providing attitude control for a generic 50 to 300 kg, 30 to 150 W (total power from the solar arrays) spacecraft in a 400 km circular low earth orbit (LEO) at 0° inclination. Due to the top-level nature of this study, the worst case disturbance torques are used to model the environment of a small spacecraft in a 400 km circular orbit. The PPT propellant mass, thrust time, and average power are determined through a momentum balancing, rather than a torque balancing, perspective.

4.1 ORBITAL ASSUMPTIONS & ENVIRONMENT

The first step in the analysis is to evaluate the average disturbance torques over one orbit. Table 4-1 lists the magnitudes of environmental contributions from aerodynamic pressure torque, magnetic field interactions, solar pressure torques and gravity-gradient effects used in this analysis. From the assumed mission life of five years, the total disturbance (T_D) to the spacecraft is calculated. While the orbit is assumed to be circular 0° inclination for this analysis, for polar orbits the only change would be a decrease in magnetic torque by a factor of one-half. While important for detailed estimates, this is within the margin in the analysis presented here. Both the momentum wheel system and PPT ACS will use these torques in sizing calculations. Following the estimation of the state-of-art ACS, two operational scenarios will be presented. The operational scenario presented for the PPTs will be two-fold. First, section 4.3 will present the results of using PPTs to replace momentum wheels in the ACS function of control against disturbance torques. Second, in section 4.4, the capabilities of the PPTs to perform slewing maneuvers will be examined.

4.2 CURRENT ATTITUDE CONTROL SYSTEM

In order to compare the PPT ACS with a typical ACS, a generic momentum wheel system with associated

dumping thrusters is developed to establish its characteristics as a function of spacecraft mass and cross-sectional area. The assumptions for sizing the momentum wheel system used for comparison to the PPT system are based on storing angular momentum imparted to the spacecraft from the circular torques. The time between the dumping cycles of the wheels is established by the magnitude of the secular angular momentum. From this cyclic torque, the total angular momentum accumulated to the spacecraft over its five year lifetime is calculated. The momentum wheel system used in this study is sized to store one order of magnitude greater than this momentum over three orbits before dumping. Wheel mass and radius directly contribute to the amount of momentum the wheel is capable of storing. The larger the diameter of the wheel, the less massive it has to be to absorb the same amount of momentum. Additionally, thrusters or magnetic torque rods are needed to desaturate the wheels once they have reached their maximum speed. The mass of the baseline wheel system includes six hydrazine thrusters and propellant for desaturation, structure at 10% of the total system mass, and drive electronics at 0.9 kg per wheel. Table 4-2 shows a breakdown of the assumptions and masses of the calculated four wheel system.

To establish state-of-the-art ACS characteristics independent of specific mission requirements, off-the-shelf component specifications are used in this trade study. An example wheel, capable of running in both momentum wheel bias mode and reaction wheel mode, has a mass of 3.2 kg, height of 183.5 mm, diameter of 204.0 mm and steady state power levels of 3 to 5 W.⁸ Therefore, four of these wheels would have a mass 12.8 kg. To size the wheel desaturation system, magnetic torque rods which provide enough torque to desaturate the wheels are assumed. Typical torque rods weigh 1.8 kg, have dimensions 64 cm length by 2.7 cm in diameter, and consume 5 W power. In order to cover all three axes, three torque rods are assumed on the spacecraft with a total mass of 5.4 kg. A typical attitude control electronics package off-the-shelf has mass of 2.7 kg, dimensions of 195 x 170 x 110 mm, and power input of 3 W.⁹ This results in a system with mass of 21 kg, volume of 0.104 m³, and peak power level of 30 W without cabling mass, hydrazine heater or valve power, or margin. Note that this system is intermediate to the TOMS-EP and WIRE systems described in section two. Some missions require the higher momentum dumping capabilities of thrusters, which would be included in the overall mass, volume, and cost of the ACS.

4.3 PPT ACS SYSTEM

The total disturbance impulse (angular momentum) from the environment evaluated in section 4.1 is used in sizing the mass of propellant the PPT system will burn to provide the restoring impulse against the disturbances. While momentum wheels only absorb cyclical torques, the PPTs are used to cancel out all disturbances, both the cyclical (magnetic, atmospheric, gravity-gradient) and secular torques (solar pressure). All torques are factored into the T_D estimation.¹⁰ Twelve thrusters are typically used for full 6 degree of freedom (DOF) control of three-axis spacecraft using an all propulsive ACS. For example, both Magellan and Galileo used twelve thrusters for attitude control.¹¹ In cases where full redundancy is not necessary, fewer thrusters can be used, resulting in the mass of the PPT system being reduced even further. For a single string failure system, it is possible to control roll, pitch and yaw through either six dedicated or four canted thrusters. In these cases, one thruster failure will result in loss of propulsive ACS. Both Landsat 7 and TRMM use eight thrusters for redundant attitude control.¹² Twelve thrusters for full 6 DOF control and redundancy are included in this analysis. Assuming the torque is evenly distributed over time and space, the 12 thrusters located two on each face of the spacecraft see an equal amount of firing.

The thrust level required by the mission dictates the impulse bit and pulse rate of the PPT ACS system. The impulse bit and number of pulses dictate the momentum deliverable by the PPT system. The momentum imparted to the spacecraft by the PPT system should be greater than the disturbance angular momentum (H_D). H_D is the angular momentum accumulated between pulses from the PPT system. The total angular momentum (H_T) during the lifetime of the mission is calculated by multiplying H_D by the total number of orbits. In the following equations T_D is the sum of both the cyclic and secular disturbance torques.¹ The total number of pulses can also impact on lifetime issues of the PPTs.

For this analysis, the total momentum is assumed to be evenly distributed across all three axes allowing each thruster to see an equal amount of firing. Thus, for the pulsed thruster, the number of required pulses per thruster for the entire mission is:

$$\left(\frac{\text{pulses}}{\text{thruster}} \right)_T = \frac{H_T}{n \cdot I_b \cdot L}$$

Here I_b is the impulse bit of the thruster (in N-s), L is the moment arm (in m), n is the number of thrusters. The propellant mass per thrusters is given by:

$$m_p = \frac{I_b}{I_{sp} \cdot g} \left(\frac{\text{pulses}}{\text{thruster}} \right)_T$$

Here I_{sp} is the specific impulse and g is the standard acceleration due to gravity. The total mass of propellant is independent of the number of thrusters placed on the spacecraft. With more thrusters, the time of operation per thruster decreases, but the total torque to balance the disturbance does not change. Thrust time of the PPT system is:

$$\Delta t = n \cdot \frac{H_T}{L \cdot n \cdot I_b \cdot \text{pps}}$$

The total thrust time of the PPT system is also independent of the number of thrusters. More thrusters result in the duty cycle of each thruster being shortened. The energy necessary to balance the disturbance impulse is constant for a given mission. The total energy of the maneuver is independent of the number of thrusters, I_{bit} , or pulse frequency. However, the latter two variables drive the peak operating power of the PPT system. In addition, the PPT pulse rate (pps) and impulse bit directly affect the thrust time to complete a maneuver. The pulse rate of the thruster firing directly impacts the amount of time spent in thrust during the lifetime of the mission. Lower pulse rates will result in more time of the mission spent thrusting at a lower power level. Likewise, higher pulse firing rates will lessen the time spent thrusting at a higher power level.

The above equations were used to size the PPT ACS for spacecraft with varying mass and cross sectional area. The spacecraft power level influenced cross-sectional area of the arrays and, consequently, the disturbance torques from the atmosphere and solar pressure.

Spacecraft mass does not influence the levels of the environmental disturbance torques as much as a change in spacecraft cross-sectional area for the baseline configuration. Increase in power requires an increase in solar array area, which in turn results in higher solar pressure and atmospheric drag contributions. Other factors such as a change in spacecraft geometry from the addition of antennae, booms, etc., can also contribute to an increase in cross-sectional area. For the purpose of this study, the spacecraft bus was simplified and only

the arrays significantly change the cross-sectional area. The solar array aspect ratio and area are based on the Solar Electric Propulsion Stage (SEPS) array technology (66 W/kg).¹³ Figures 4-1 and 4-2 show the ACS system masses (both wheel and PPT) for disturbance impulse balancing as a function of spacecraft mass and cross-sectional area respectively. As shown in figure 4-2, the mass of the ACS system which absorbs the increase in momentum caused by the increase in cross-sectional area must increase. The momentum wheel system mass increases as the physical size of the spinning mass increases to absorb the increased disturbance momentum. In the PPT system, an increase in momentum translates to an increase in propellant and thrust time.

The first comparison between the baseline wheel system and the PPT system for momentum compensation is mass. It can be seen in Figures 4-1 and 4-2 that the PPT attitude control system (12 kg) for disturbance torque compensation is 50% to 25% of the mass of the momentum wheel system (20-40 kg) for varying spacecraft mass. In the case of varying spacecraft cross-sectional area, the PPT ACS mass is 50% to 12% of the mass of the momentum wheel system (20-80 kg).

The energy of the PPT operation in the maneuver determines the power requirements to this subsystem. The energy per pulse (E_p) multiplied by the number of pulses per second defines the average power of the PPT system. Peak power levels while the PPTs are firing are directly related to impulse bit and pulse rate at which they are operating. A maneuver requiring more thrust will also require a higher power level.

In order to determine whether this is a reasonable system from the standpoint of operation and lifetime of the PPTs, the number of pulses and power levels of the PPTs to perform the momentum balancing is calculated. The number of pulses per thruster increases as the amount of disturbance angular momentum increases. At the low end (spacecraft mass 100 kg, cross-sectional area 1.7 m²), there are 1.5x10⁶ pulses required per thruster, and at the high end (spacecraft mass 300 kg, and cross-sectional area 3.2 m²) the number of pulses required per thruster is 3.18x10⁶. Both are well under the expected life of 10⁷ pulses. The average power consumed by the PPT system for angular momentum compensation throughout the five year life of the spacecraft is constant for a given spacecraft configuration (mass and cross-sectional area). An impulse bit of 580 μ Ns is used in both the PPT with I_{sp} 1000 s and I_{sp} 1500 s. For the low end

mentioned previously, the average power is 0.08 W for the PPTs with I_{sp} of 1000 s, and 0.13 W for PPTs with I_{sp} of 1500 s, and 0.37 W. At the high end configuration, the average power is 0.18 W for the system with I_{sp} of 1000 s and 0.28 W for the 1500 s system. These average power numbers result in 9.42×10^{-3} and 2.01×10^{-2} pulses per thruster per second respectively over the lifetime of the spacecraft. This amounts to a pulse roughly every one to two minutes. The deadband angular spacecraft drift between pulses for these two power levels is 0.03° and 0.014° respectively. Higher frequencies will result in smaller deadband angles. The average power during operation is driven by the pulse frequency at which the PPTs are fired. Higher pulse frequencies result in higher average power levels. For example, in the low end spacecraft case, a pulse frequency of 0.05 Hz results in average power during firing of 0.9 W, where a frequency of 3 Hz results in a average power of 54.8 W. Therefore, the power consumption of the PPT system is a function of the demands of the mission.

4.4 SLEWING MANEUVERS

A second function the PPTs are analyzed to perform is a slew maneuver of 360° . Assuming that the spacecraft is in an unknown orientation, and it must rotate about one axis, the maneuver is split into two maneuvers in opposite directions. One half maneuver is to start the rotation, and one to stop. For slewing maneuvers in which a large angular rotation to the vehicle is required, the required PPT power levels increase as the required maneuver time decreases. Average power is independent of pulse rate or impulse bit for these calculations, and is solely a function of time required for the maneuver. In the case of the complete rotation, as the time constraint is reduced, a larger torque is needed and therefore either a higher impulse bit or higher pulse rate. Each of these increases results in a higher average power for the PPT system. The result is illustrated in figure 4-3 which shows the average power levels of different I_{sp} PPTs versus the time required for a complete 360° spacecraft rotation. The moment arm is assumed to be 0.5 m. For maneuver time requirements of less than 10 minutes, average power levels are 0.1 W and greater. If more than 50 minutes is allowed to the maneuver, the average power levels are 0.001 W and lower. From figure 4-3, average power versus time to perform the slew maneuver, it can be seen that the lower the time, the higher the power requirement from the PPT system becomes. For maneuvers that must be performed in less than a minute, the power requirements from the PPTs asymptotically approach infinity. However, if

the times are relaxed, the PPT system become more feasible for this application. An alternate point of view of the PPT system for slew maneuvers is presented in Figure 4-4. Time of maneuver is also a function of pulse rate for varying impulse bits. Pulse rate in turn drives the average power required from the PPT system. This analysis serves to corroborate the relationship between time of maneuver and average power requirements of the PPT system.

5. CONCLUSION

This study demonstrated the feasibility of using pulsed plasma thrusters to provide the momentum levels needed to balance the angular momentum from disturbance torques imparted to a small (100 - 300 kg) spacecraft in LEO. Because of their high I_{sp} (1000 to 2000 sec), PPTs use a small amount of propellant to perform the equivalent maneuver of a hydrazine thruster system. The 12 thruster redundant PPT ACS configurations in this study were consistently half the mass or less of an equivalent baseline momentum wheel system. Average power levels for the attitude control functions range from 0.08 W to 0.28 W in worst case scenarios. PPT ACS systems are less massive and require lower average power than the counterpart wheel/thruster systems. Therefore, it is feasible to use PPTs to perform the momentum countering functions of momentum wheels systems.

For slewing maneuvers, the PPT system performs well for maneuvers that are given longer time to complete. Average power levels for slewing maneuvers range from 0.01 W or less for times of greater than 50 minutes. Maneuvers of less than 10 minutes would require larger power levels, or a different type of actuator, such as thrusters or a momentum wheel. Therefore, from this initial analysis, PPTs seem capable of performing slower slew maneuvers in small spacecraft.

Further work remains in the areas of controls and torque matching in order to better model the use of PPTs for attitude control. Additionally, the area of deadband control through the use of pulsed plasma thrusters is a next logical step in the study of the application of PPTs to small satellite attitude control.

6. REFERENCE

- ¹ Larson, Wiley J., and James R. Wertz (ed.), Space Mission Analysis and Design, Microcosm Inc, and Kluwer Academic Publishers, Torrance, 1992.

² Selding, Peter B., "Reaction Wheel Concern Clouds Nov. 23 SOHO Launch," *Space News*, November 6-12, 1995.

³ Joseph Cassady, Olin Aerospace, personal communication, November 1995.

⁴ SMEX homepage, <http://sunland.gsfc.nasa.gov/smex/smexhomepage.html>, 3-27-96.

⁵ Todd Mendenhall, TRW, personal communication, 8/21/1995.

⁶ Brill, Y., A. Eisner, and L. Osborn, "The Flight Application of a Pulsed Plasma Microthruster; the NOVA Satellite," paper no. AIAA-82-1956, AIAA/JSASS/DGLR 16th International Electric Propulsion Conference, 1982.

⁷ Ebert, W.L., S.J. Kowal, and R.F. Sloan, "Operational Nova Spacecraft Teflon Pulsed Plasma Thruster System," paper no. AIAA-89-2497, AIAA/ASME/SAE/ASEE 25th Joint Propulsion Conference, Monterey, CA, July 10-12, 1989.

⁸ Ithaco, Inc., online catalog located at <http://www.newspace.com/industry/ithaco>, 3-5-96.

⁹ Satellites International Limited, online catalog at <http://www.sil.com/space/9sacemds.html>, 3-4-96.

¹⁰ Fortescue, Peter and John Stark, Spacecraft Systems Engineering, Wiley Publishers, Chichester, 1991.

¹¹ Carl Englebrecht, Jet Propulsion Laboratory, Personal communication, April 1, 1996.

¹² Steve Andrews, Goddard Space Flight Center, personal communication April 2, 1996.

¹³ SEPS technology developed by Lockheed Missiles and Space.

TOMS-EP			WIRE		
Wet mass	288.6	kg	Wet mass	270	kg
Dry Mass	216	kg	Dry Mass	250	kg
3 reaction wheels	27.6	kg	4 reaction wheels	14.4	kg
electronics	5.85	kg	3 torque rods	7.24	kg
3 magnetic torque rods	8.58	kg			
total ACS mass	42.03	kg	total ACS mass	21.6	kg
Mass fraction of ACS	20	%	Mass fraction of ACS	9	%

Table 2-1: Example Spacecraft Attitude Control Systems

Specifications	Current			Next Generation
	LES 8/9			
unit dry mass (kg)	5.2	2.7	2.7	5.2
6 thruster dry mass (kg)	10.4	5.4	5.4	10.4
12 thruster dry mass (kg)	20.8	10.8	10.8	20.8
total impulse (N-s)	10000	20000	20000	20000
efficiency (%)	8	16	16	16
Isp (sec)	1000	1000	1500	2000

Table 3-1: Pulsed Plasma Thruster Characteristics

Solar Pressure	Ts	1.9E-06
Aerodynamic	Ta	8.7E-05
Gravity gradient	Tg	3.9E-07
Magnetic Field	Tm	2.6E-05
Total torque:	Td	1.1E-04

Table 4-1: Magnitudes of Disturbance Torques at 400 km Altitude

Component	Value	
wheel speed	3000	rpm
disk radius	0.08	m
individual spinning mass	3.60	kg
drive electronics	0.91	kg
total structure (4 wheels)	2.00	kg
dumping thruster mass	0.4	kg
total thruster mass (6)	2.4	kg
200s Isp propellant mass	5.23	kg
280s Isp propellant mass	3.73	kg
<i>Totals: 4 wheels & 6 thrusters</i>		
Four wheel system mass	20.04	kg
six thruster 200 Isp mass	7.63	kg
six thruster 280 Isp mass	6.13	kg

Table 4-2: Four wheel system baseline assumptions

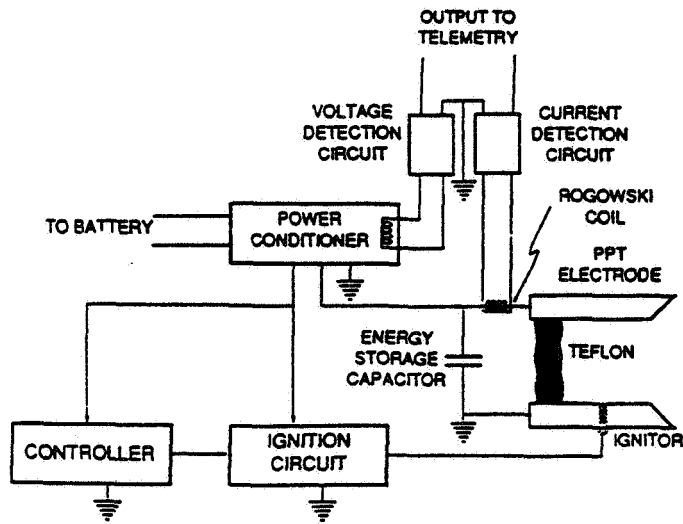


Figure 3-1: PPT flight system schematic. Telemetry signals depend on application.

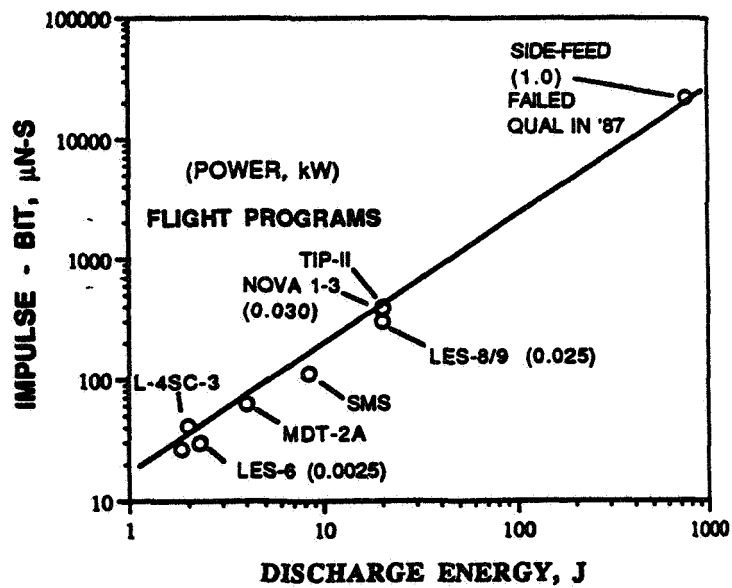


Figure 3-2: Impulse bit vs. stored energy for a range of flight and flight-qualified PPT systems.

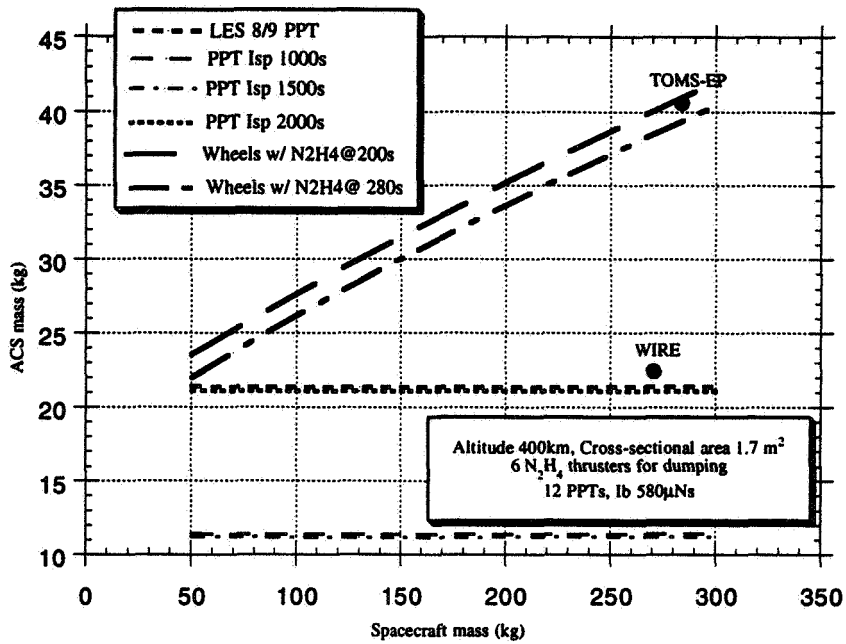


Figure 4-1: Attitude Control System Mass for Varying Spacecraft Mass

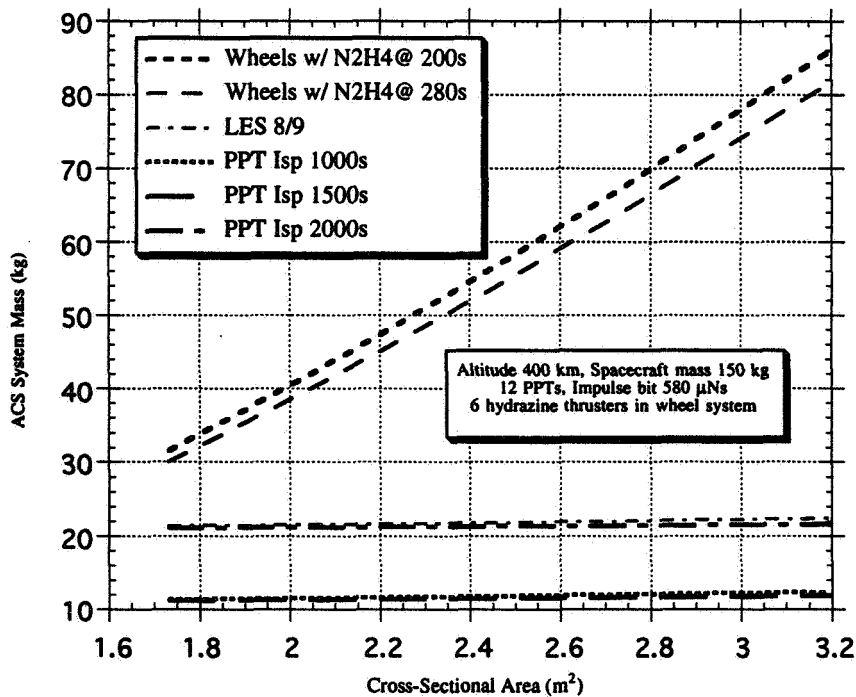


Figure 4-2: Attitude Control System Mass for Varying Spacecraft Cross-Sectional Area

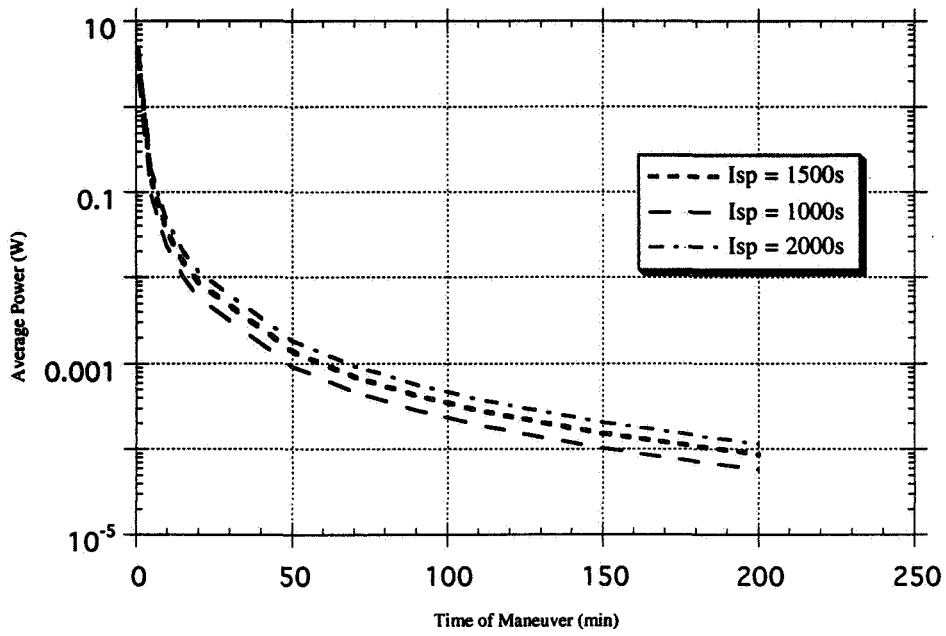


Figure 4-3: Power Levels for PPT System Slewing Maneuvers Times

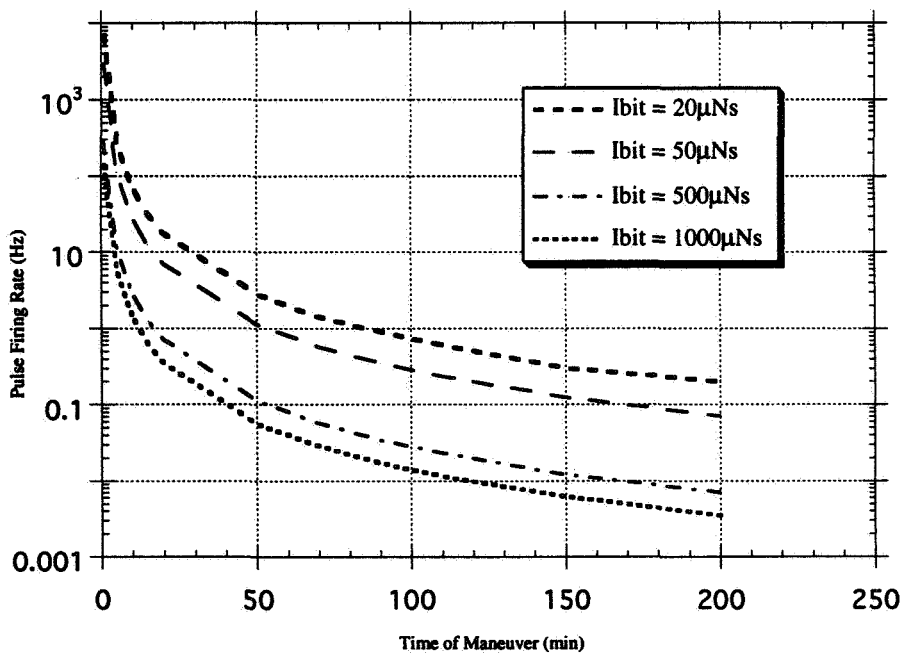


Figure 4-4: Maneuver Times for Pulse Firing Rates of Differing Impulse Bits

HOMOTOPY SOLUTIONS OF KEPLER'S EQUATIONS

Norman Fitz-Coy† and Jiann-Woei Jang★
AeMES Department
University of Florida
Gainesville, FL

Abstract Kepler's Equation is solved using an integrative algorithm developed using homotopy theory. The solution approach is applicable to both elliptic and hyperbolic forms of Kepler's Equation. The results from the proposed algorithm compare quite favorable with those from existing iterative schemes.

I Introduction

The problem of relating orbital position and time in the two-body problem requires the solution of Kepler's Equation, i.e.,

$$M = E - e \sin E \quad (1)$$

where E is the eccentric anomaly, and M is the mean anomaly for the elliptic orbits. The applications of Kepler's Equation can be classified into two categories [1],

- (1) given a probe's position in the orbit, determine the time when the probe is at that position

or

- (2) given the time since last periapsis passage, determine a probe's position in the orbit at that time.

The first case is rather trivial. By substituting the current eccentric anomaly E into Eq. (1), one can immediately determine the mean anomaly M , and hence t . The second case, however, is more complex than the first one, since Kepler's Equation has no closed-form solution for the eccentric anomaly E . In the literature, most solution approaches for E use iterative methods [1-5]. Recently, a non-iterative method was proposed in Ref. [6]

In this paper, an alternate solution approach based on homotopy theory is presented. In section II, a preliminary introduction to homotopy theory is given. The homotopy algorithm for the elliptic form of Kepler's Equation is developed in sections III and the algorithm for the hyperbolic form is discussed in section IV. A summary and conclusion is presented in section V. It is not our intent to claim that our approach is superior (or inferior) to the existing iterative approaches, but rather to demonstrate that alternative approaches do exist. However, in order to demonstrate that our approach is indeed viable, we do make comparisons with some existing iterative methods [1-5]. These comparison results are included in sections III and IV.

II Homotopy Theory

Mathematical Model

The homotopy theory introduced in this paper is based primarily on the research work of Zangwill and Garcia [7]. Given a system of nonlinear equations to be solved, the homotopy algorithm starts with a simple solution (a solution to a similar but easily solved system of linear/non-linear equations) and through a series of integrations, reaches the exact solution of the original system of nonlinear equations.

Let \mathcal{R}^n be an Euclidean n space. Given $f(x) : \mathcal{R}^n \rightarrow \mathcal{R}^n$; i.e., $x \in \mathcal{R}^n$, we want to find the solution, $x^* = [x_1^*, \dots, x_n^*]^T$, of

† Assistant Professor, Member: AAS, AIAA

★ Post Doc., Student Member: AIAA

$$f(x) = 0 \quad (2)$$

The homotopy procedure for solving Eq. (2) can be stated as follows:

- (1) Identify an easily solved system of equations, say

$$g(x) = 0 \quad (3)$$

where $g(x): \mathbb{R}^n \rightarrow \mathbb{R}^n$. Determine the solution x^0 of Eq. (3).

- (2) Define a homotopy function $H(x, \lambda)$, such that

$$H(x, 0) = g(x) \quad (4)$$

$$H(x, 1) = f(x) \quad (5)$$

- (3) Generate a path (from $\lambda = 0$ to $\lambda = 1$) which leads the solution from x^0 to x^* .

Homotopy Functions

Although there exist numerous forms of the homotopy function, the following three are the most commonly used forms:

- (1) Newton homotopy

$$H(x, t) = f(x) - (1 - \lambda)f(x^0) \quad (6)$$

- (2) Fix-point homotopy

$$H(x, t) = (1 - \lambda)(x - x^0) + tf(x) \quad (7)$$

- (3) Linear homotopy

$$\begin{aligned} H(x, t) &= \lambda f(x) + (1 - \lambda)g(x) \\ &= g(x) + \lambda(f(x) - g(x)) = 0 \end{aligned} \quad (8)$$

The homotopy paths start from an arbitrary point, x^0 , for either the Newton homotopy function or the fix-point homotopy function; hence, they are the most popular forms of the homotopy function currently in use. However, if an easily solved system of equations can be identified, and it is very "close" to the original system of equations, the linear homotopy function might be a better mathematical model to use. However, the above homotopy forms can be converted to each other; for example, $f(x) - f(x^0)$ in Eq. (6) and $x - x^0$ in Eq. (7) are equivalent to $g(x)$ in Eq. (8).

Path Following Algorithm and the Homotopy Differential Equation

The differentiation of any homotopy function with respect to the homotopy variable, λ , is 0, since a homotopy function is defined to be zero in (x, λ) ; i.e.,

$$\frac{dH}{d\lambda} = \frac{\partial H}{\partial \lambda} + \frac{\partial H}{\partial x} \frac{dx}{d\lambda} = 0 \quad (9)$$

Equation (9) is referred to as the Davidenko differential equation in the literature [8]. Manipulation of Eq. (9) yields

$$\frac{dx}{d\lambda} = - \left(\frac{\partial H}{\partial x} \right)^{-1} \frac{\partial H}{\partial \lambda} \quad (10)$$

which, along with the condition $x(0) = x^0$, defines an initial value problem for the path from x^0 to x^* . Thus, integrating Eq. (10) over λ from 0 to 1 yields the desired solution of Eq. (2). Let $x \in D \subset \mathbb{R}^n$, and $T = \{ \lambda \mid 0 \leq \lambda \leq 1 \}$. In order to guarantee the path existence, the regularity of H or the inversion of the Jacobian matrix, $\frac{\partial H}{\partial x}$, in Eq. (10) should always hold for all (x, λ) in H^{-1} , where H^{-1} is defined as the set of all the solutions of $H(x, \lambda)$; i.e.,

$$H^{-1} = \{(x, \lambda) \in D \times A \mid H(x, \lambda) = 0\} \quad (11)$$

Path existence for homotopy methods are guaranteed by Sard's Theorem for almost all cases. The path existence fails only for points which are in a set of Lebesgue measure zero.

Theorem 1 Sard's Theorem (Zangwill [7], Ch. 22)

Let $H: \mathcal{K} \subset \mathbb{R}^q \rightarrow \mathbb{R}^n$, where \mathcal{K} is the closure of an open set and H be \mathcal{C}^k . If $k \geq 1 + \max\{0, q - n\}$, then H is regular for almost all ε , except for ε on a set of Lebesgue measure zero, where

$$H(\cdot) = \varepsilon \quad \square$$

Corollary 1 Extended Sard's Theorem (Zangwill [7], Ch. 22)

Let $D \subset \mathbb{R}^n$ be the closure of an open set, $H : D \times A \rightarrow \mathbb{R}^n$ be \mathcal{C}^2 , and $F : D \rightarrow \mathbb{R}^n$ be \mathcal{C}^1 , then the following three statements are equivalent,

- (1) H will be regular for almost all ε .
- (2) H will be regular at $\bar{\lambda}$ for almost all ε .
- (3) F will be regular for almost all ε . □

For a homotopy method, $q = n + 1$, hence if k is greater than or equal to 2, then $H(x, t)$ is regular for almost all ε . In other words, as long as $H(x, t) \in \mathcal{C}^2$, Sard's theorem states that for an arbitrary ε , $H(x, t)$ is almost assuredly regular. It can be shown that the second derivative of Kepler's Equation is continuous. This implies that even if the integration path bifurcates during the solution of Kepler's Equation via the homotopy method, a slight perturbation of the starting point of the homotopy equation guarantees that a new integration path exists.

III Kepler's Equation in Elliptic Orbits

Homotopy Function for Kepler's Equation: Elliptic Orbits

Homotopy methods has been used to solve a system of nonlinear equations [7][8]. To apply the homotopy method, first rewrite Kepler's Equation (Eq. (1)) as

$$f(E) = E - e \sin E - M = 0 \tag{12}$$

An easily solved equation is chosen as

$$g(E) = E - M_0 = 0 \tag{13}$$

where

$$M_0 = M + \frac{e \sin M}{1 - \sin(M + e) + \sin M}$$

The linear homotopy function is

$$\begin{aligned} H(E, \lambda) &= g(E) + \lambda(f(E) - g(E)) \\ &= E - M_0 + \lambda(M_0 - M - e \sin(E)) = 0 \end{aligned} \tag{14}$$

Differentiating the above equation with respect to the homotopy variable, λ yields

$$(1 - \lambda e \cos E) \frac{dE}{d\lambda} = e \sin E \tag{15}$$

or

$$\frac{dE}{d\lambda} = \frac{e \sin E}{1 - \lambda e \cos E} \tag{16}$$

Notice that the denominator in Eq. (16) is nonzero since $\lambda e \cos E < 1$ for all E . Hence the the homotopy integration path can never bifurcate.

An algorithm for the solution of Kepler's Equation using homotopy methods is as follows:

- Step 1. Identify an appropriate function $g(E)$ (e.g., Eq. (13)) and develop the homotopy function $H(E, \lambda)$ (e.g., Eq. (14)).
- Step 2. Form the initial value problem; i.e., differentiate Eq. (14) to obtain Eq. (16) and solve Eq. (13) for the initial condition.
- Step 3. Numerically integrate the initial value problem from $\lambda = 0$ to $\lambda = 1$.
- Step 4. Stop.

Numerical Results

In order to demonstrate the viability of the homotopy approach, Kepler's Equation was solved over a range of M and e values using the proposed approach and also using the Newton-Raphson method presented in Ref. [1]. The mean anomaly, M , was varied from 0 to 2π in increments of $\pi/250$ and the eccentricity, e , was varied from 0 to 1 in increments of 0.02. The numerical integration was accomplished using MATLAB's ode45 function with $tol = 5 \times 10^{-7}$, $h = hmax = 1$ and $hmin = 1/20000$. The terminal condition for the Newton-Raphson scheme was $|f| < 10^{-12}$, where $f(E) = E - e \sin E - M$.

The contour plot in Fig. 1 shows the number of integration steps required to solve Kepler's Equation as a function of mean anomaly M and eccentricity e using the homotopy approach. There are two "4+" regions in Fig. 1; the maximum number of integration steps for the left "4+" region is 11 and the maximum number of integration steps for the right "4+" region is 29. The maximum number of integration steps in the right "4+" occurs when $e = 1$; excluding the case of $e = 1$, the maximum number is 27. The contour plot in Fig 2 shows the number of iterative loops required to solve Kepler's Equation as a function of mean anomaly M and eccentricity e using the Newton-Raphson algorithm. In Fig. 2, there also exist two "4+" regions; the maximum number of iterations in the left "4+" region is 10, and the maximum number of iterations in the right "4+" region is 48,818. In the right "4+" region, the maximum occurs when $e = 1$ (note: if $e = 1$ is excluded, then the maximum number of iterations is 957).

It is important to observe that, for the Newton-Raphson approach, each iteration involves two function evaluations, whereas, for the homotopy approach, each integration involves six function evaluations (using ode45.m). Improvements in the performance of the homotopy approach can be achieved by an appropriate selection of the function $g(E)$. Our preliminary results indicate that the number of integration steps can be reduced significantly (i.e., the contour in the Me -plane is predominantly a 1 integration step region). Our experiments here were rather ad hoc and we suspect that a more systematic approach may indeed yield an "optimal" choice for $g(E)$.

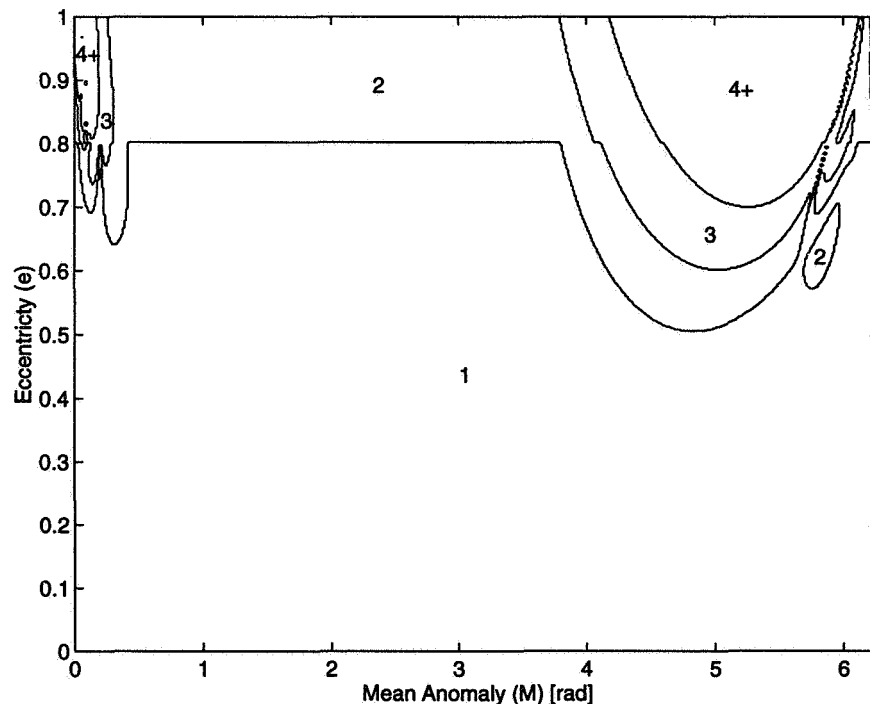


Figure 1 Elliptic Case using a Homotopy Algorithm

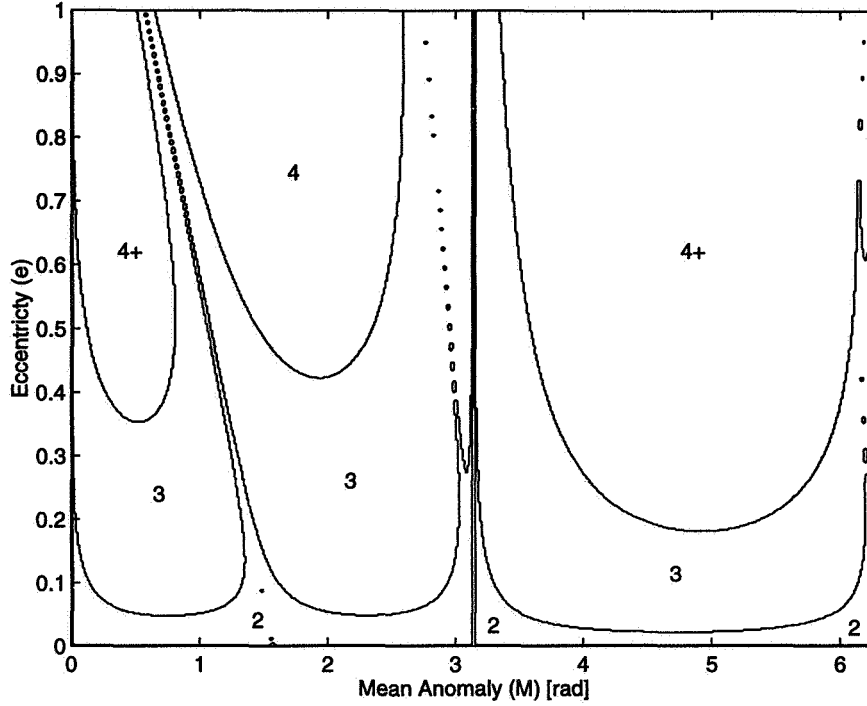


Figure 2 Elliptic Case using a Newton-Raphson Algorithm

IV Kepler's Equation in Hyperbolic Orbits

Homotopy Function for Kepler's Equation in Hyperbolic Orbits

For hyperbolic orbits, Kepler's Equation is

$$M = e \sinh F - F \quad (17)$$

where F is the hyperbolic anomaly, and as before, M is the mean anomaly. To apply the homotopy method, Eq. (17) is rewritten as

$$f(F) = e \sinh F - F - M = 0 \quad (18)$$

and an easily solved equation is chosen as

$$g(F) = e \sinh F - M = 0 \quad (19)$$

Following the algorithm developed in section III, the linear homotopy function is

$$\begin{aligned} H(F, \lambda) &= g(F) + \lambda(f(F) - g(F)) \\ &= e \sinh F - M + \lambda(-F) = 0 \end{aligned} \quad (20)$$

which yields the following Davidenko's differential equation.

$$(e \cosh F - \lambda) \frac{dF}{d\lambda} = F \quad (21)$$

Thus, the homotopy differential equation for the hyperbolic case is

$$\frac{dF}{d\lambda} = \frac{F}{e \cosh F - \lambda} \quad (22)$$

Once again, observe that the denominator of Eq. (22) is nonzero since $e \cosh F > \lambda$ for all F . Hence the the homotopy integration path can never bifurcate.

Numerical Results

For this case, the homotopy algorithm was evaluated against two Newton-Raphson algorithms; the first algorithm was the “conventional” quadratic convergence algorithm and the second was a quartic convergence algorithm [3]. The mean anomaly M was varied from 0 to 3π in increments of $\pi/150$ and the eccentricity e was varied from 1 to 6 in increments of 0.01. The numerical integrations associated with the homotopy algorithm were again accomplished using MATLAB’s ode45 function with $tol = 5 \times 10^{-7}$, $h = hmax = 1$ and $hmin = 1/20000$ and the termination condition for both Newton-Raphson algorithms was $|f| < 10^{-12}$, where $f(F) = e \sinh F - F - M$. The results are shown in Figs. 3-5.

The contour plot in Fig. 3 shows the number of integration steps required to solve Kepler’s Equation as a function of mean anomaly M and eccentricity e using the homotopy algorithm. The maximum number of integration steps for the “5+” region is 9. If instead of Eq. (19), the “known-solution” function was chosen as

$$g(F) = e \sinh F - (M + 0.01) = 0, \quad (23)$$

the maximum number of integration steps for the “5+” region is reduced to 7.

The results shown in Figs. 4 and 5 are based on an initial guess determined from

$$F_0 = \ln\left(\frac{2M}{e} + 1.8\right)$$

Figure 4 shows the results for the Newton-Raphson algorithm with quadratic convergence. The maximum number of iterations in the “6+” region is 21. Figure 5 shows the results for the quartic convergence Newton-Raphson algorithm. In Fig. 5, there are two “4+” regions; the maximum number of iterations in the left “4+” region is 11 and the maximum iteration number in the right “4+” region is 5.

Again, it is important to observe that the quartic convergence Newton-Raphson algorithm requires two function evaluations for each iteration, whereas the homotopy algorithm requires six function evaluations for each integration. Also, the Newton-Raphson algorithm with local quartic convergence [3] requires five function evaluations for each

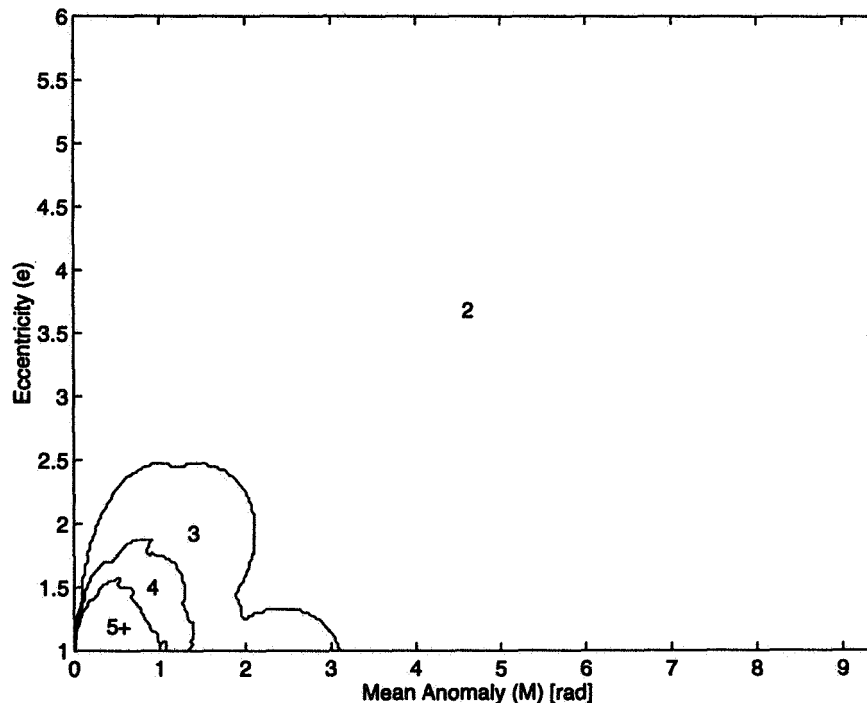


Figure 3 Hyperbolic Case using a Homotopy Algorithm

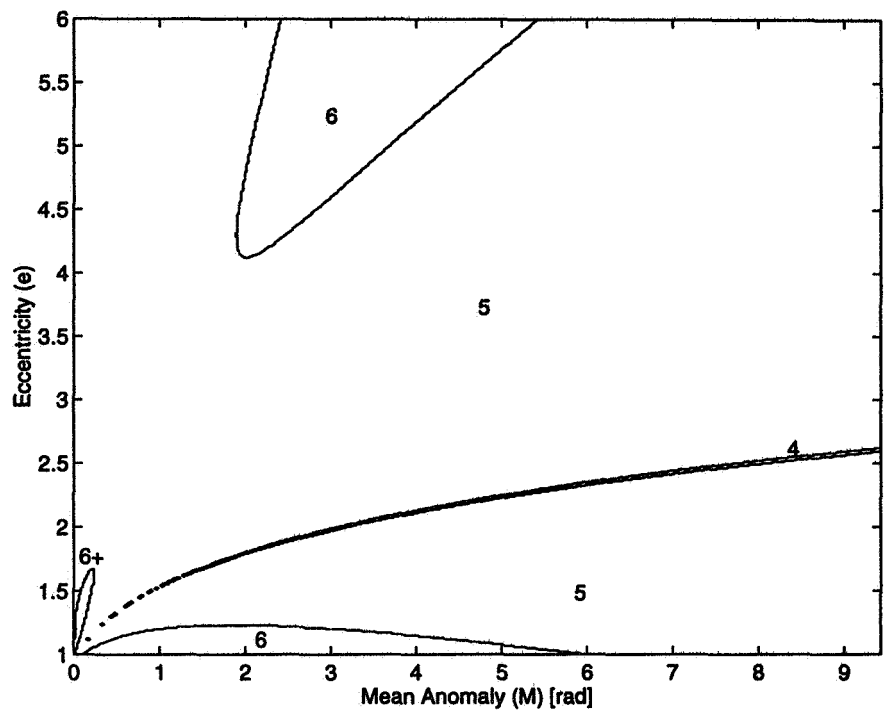


Figure 4 Hyperbolic Case using a Newton-Raphson Algorithm

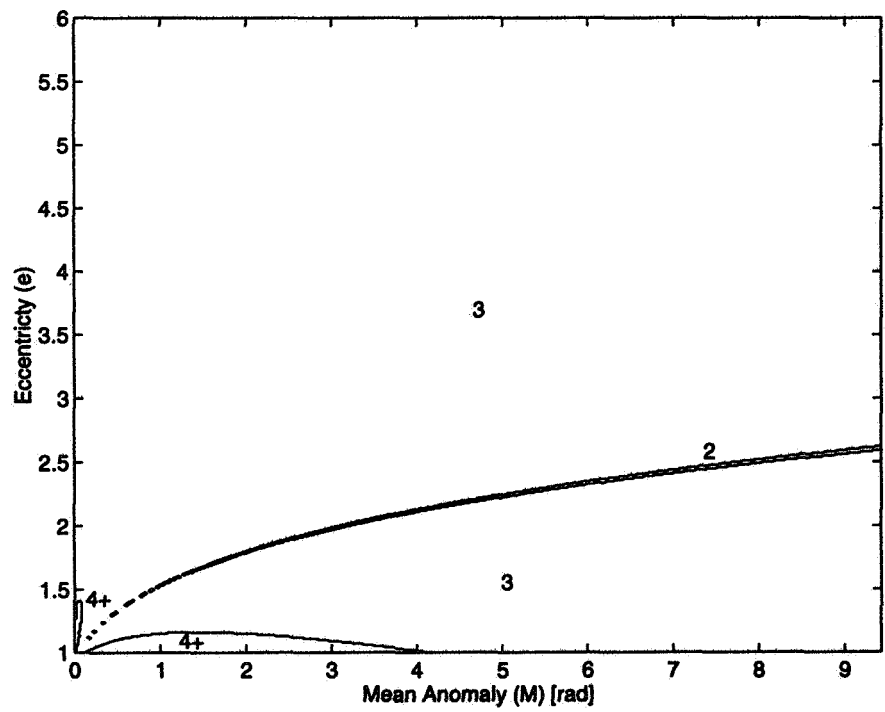


Figure 5 Hyperbolic Case using a Newton-Raphson Algorithm with Quartic Convergence

iteration step. Thus, for the Me -plane analyzed in this paper, the homotopy approach appears to have a computational advantage over the quartic convergence iterative approach. Again, additional improvements in the performance of the homotopy approach can be achieved by proper selection of $g(F)$.

VI Summary

In this paper, we present a new algorithm to solve Kepler's Equation based on homotopy theory. The procedure transforms the root finding problem into an initial value problem which can be integrated to yield the desired solution. Although no attempts were made to optimize the developed algorithm, it compared quite favorably with some existing iterative algorithms. Improvements in the algorithm can be obtained by investigating appropriate "known functions" ($g(E)$ or $g(F)$) and by investigation other numerical integration schemes.

References

- [1]. Prussing, J. E., and Conway, B. A., Orbital Mechanics, Oxford University Press, New York, 1993.
- [2]. Danby, J. M. A., and Burkardt, T. M., "The Solution of Kepler's Equation I," Celestial Mechanics, Vol. 31, 1983, pp. 95-107.
- [3]. Burkardt, T. M., and Danby, J. M. A., "The Solution of Kepler's Equation II," Celestial Mechanics, Vol. 31, 1983, pp. 317-328.
- [4]. Conway, B. A., "An Improved Algorithm Due to Laguerre for the Solution of Kepler's Equation," Celestial Mechanics, Vol. 39, 1986, pp. 199-211.
- [5]. Odell, A., and Gooding, R. H., "Procedures for Solving Kepler's Equation," Celestial Mechanics, Vol. 38, 1986, pp. 307-334.
- [6]. Markley, F. L., "Kepler's Equation Solver," Proceedings of the 1995 Flight Mechanics/Estimation Theory Symposium, NASA CP-3299, pp. 47-57.
- [7]. Zangwill, W. I., and Garcia. C. B., Pathways to Solutions. Fixed Points, and Equilibria, Prentice-Hall, Englewood Cliffs, N.J., 1981.
- [8]. Collins, Jr., E., Davis, L. and Richter, S., "Homotopy Algorithm for Maximum Entropy Design," Journal of Guidance, Control and Dynamics, Vol. 17, No. 2, March-April, 1994, pp. 311-321.

FLIGHT MECHANICS/ESTIMATION THEORY SYMPOSIUM

MAY 14-16, 1996

SESSION 5

Conversion of Osculating Orbital Elements to Mean Orbital Elements

Gim J. Der and Roy Danchick

TRW

Abstract

Orbit determination and ephemeris generation or prediction over relatively long elapsed times can be accomplished with mean elements. The most simple and efficient method for orbit determination, which is also known as epoch point conversion, performs the conversion of osculating elements to mean elements by iterative procedures. Previous epoch point conversion methods are restricted to shorter elapsed times with linear convergence. The new method presented in this paper calculates an analytic initial guess of the unknown mean elements from a first order theory of secular perturbations and computes a transition matrix with accurate numerical partials. It thereby eliminates the problem of an inaccurate initial guess and an identity transition matrix employed by previous methods. With a good initial guess of the unknown mean elements and an accurate transition matrix, converting osculating elements to mean elements can be accomplished over long elapsed times with quadratic convergence.

Basic Concepts

This paper presents new methods to solve the following problems:

- A user's propagator requires a mean orbital element set (e.g., NORAD--North American Aerospace Defense Command two-card element set or any other mean element set) as input but the element set is not available.
- For ground based radar acquisition and space sensor surveillance, a single osculating state vector of an object at the current time is available, but the mean elements corresponding to an epoch a few days, weeks or months earlier are not. If the set of mean elements at an epoch can be computed, then the object can be identified with respect to a known catalog (e.g. NORAD element set for Resident Space Objects). The mean elements at an epoch are needed to efficiently provide radar or sensor pointing commands.

The osculating orbital elements represent, in a general sense, the true position and velocity vectors of a satellite, but are poorly behaved over time as a basis for prediction. The mean orbital elements do not represent the true position and velocity vectors of a satellite, but are well behaved over time. An orbit described by a set of mean orbital elements is said to be perturbed or non-Keplerian.

By way of notation all vectors are in bold unless specified. For the sake of simplicity, the osculating elements and the mean elements are respectively denoted as:

$$\mathbf{y}(t) = [\mathbf{a} \ \mathbf{e} \ \mathbf{i} \ \mathbf{\Omega} \ \mathbf{\omega} \ \mathbf{M}]^T \quad \text{and} \quad \bar{\mathbf{y}}(t) = [\bar{\mathbf{a}} \ \bar{\mathbf{e}} \ \bar{\mathbf{i}} \ \bar{\mathbf{\Omega}} \ \bar{\mathbf{\omega}} \ \bar{\mathbf{M}}]^T$$

where \mathbf{a} is the semimajor axis, \mathbf{e} is the eccentricity, \mathbf{i} is the inclination, $\mathbf{\Omega}$ is the longitude of the ascending node, $\mathbf{\omega}$ is the argument of perigee and \mathbf{M} is the mean anomaly. The six elements of $\mathbf{y}(t)$ or $\bar{\mathbf{y}}(t)$ can be chosen in a variety of ways and the classical orbital elements are chosen to enhance theoretical understanding. The singularities of small eccentricity, small inclination or critical inclination do not exist in the conversion of osculating elements to mean elements, but the reverse is not true. The transformations between classical orbital elements, $\mathbf{y}(t)$, and predicted or true position and velocity vectors, $\mathbf{r}(t)$ and $\mathbf{v}(t)$, are simple. The transformation of the mean elements, $\bar{\mathbf{y}}(t)$, to the mean position and velocity vectors, $\bar{\mathbf{r}}(t)$ and $\bar{\mathbf{v}}(t)$, is straightforward, but the reverse is difficult. By way of definition, a *transformation* between vectors is an instantaneous conversion. A *conversion* between vectors involves an elapsed time greater than or equal to zero.

The ballistic coefficient of a satellite is defined as $B = \frac{C_{d0}A}{2m}$, where C_{d0} is the zero drag coefficient, A is the reference area of the satellite and m is the mass of the satellite. The problem of converting osculating orbital elements at a final time, t , to mean orbital elements at an initial time, t_0 , can be stated as

Given: B, t_0, t and $y(t)$

Find: $\bar{y}(t_0)$

Depending on the perigee altitude of the satellite, previous methods presented by References 1 and 2 that use iterative procedures, are restricted to a short elapsed time, $(t - t_0)$. Reference 3, which uses a combination of Kozai's and Izsak's theories, calculates the difference between the osculating elements and mean elements with zero elapsed time. The difference, $y(t_0) - \bar{y}(t_0)$, is the very small variation of orbital elements due to short-periodic perturbations. The method presented in this paper allows the elapsed time to be extended over much longer intervals. Only the case of non-negative elapsed time, $(t - t_0) \geq 0$, is formulated, however, the method also holds for negative elapsed time as well.

To understand our approach to solve the above problem, a background on some basic concepts is required. The state prediction problem for a satellite orbiting about a central body such as the Earth is to find the position and velocity vectors, $r(t)$ and $v(t)$, at time t that satisfy the vector equation of motion

$$\frac{d^2 \mathbf{r}}{dt^2} = -\frac{\mu}{r^3} \mathbf{r} + \mathbf{a}_d \quad (1)$$

subject to the given initial conditions $\mathbf{r} = \mathbf{r}_0$ and $\mathbf{v} = \mathbf{v}_0$ at time $t = t_0$. In Equation (1), μ is the gravitational constant and \mathbf{a}_d is the total disturbed acceleration vector due to disturbed gravity, atmospheric drag, lunisolar gravitational attractions, solar radiation pressure, tidal friction, n-body gravitational attractions and thrust. The first term on the right-hand-side of Equation (1) is the acceleration vector due to central gravity.

If \mathbf{a}_d is zero, then Equation (1) can be solved analytically by one of Kepler's methods and the osculating elements (a, e, i, Ω, ω) describing the size, shape and orientation of the satellite orbit remain constant in time. The osculating mean anomaly, M , defines the angular position of the satellite in its orbit with respect to time. For a typical non-thrusting, near-Earth satellite between the theoretical atmospheric altitude of 91 km (300,000 ft) and a 12-hour orbit altitude of approximately 20,000 km, the disturbed acceleration vector, \mathbf{a}_d^* , is due mainly to the Earth zonal gravitational harmonics, J_2, J_3 and J_4 , and atmospheric drag. Lunisolar gravitational attractions and solar radiation pressure, whose effects may be formulated similar to atmospheric drag, are neglected in this study. The orbital elements affected by the disturbed acceleration vector, \mathbf{a}_d^* , are defined as the *osculating elements*, $y(t)$. [Strictly speaking the *osculating elements* are affected by \mathbf{a}_d .] The disturbed accelerations of \mathbf{a}_d^* cause secular, short-periodic and long-periodic variations in the classical orbital elements ($a, e, i, \Omega, \omega, M$). Short periods are on the order of time of one satellite passage around the Earth. Long periods are on the order of time of one complete perigee passage around the Earth. If the periodic effects are removed, then the new orbital elements are defined as *mean elements*, $\bar{y}(t)$. That is, the mean elements are affected only by secular perturbations.

Periodic variations occur in all osculating elements and are induced by all zonal gravitational harmonics. However, the variations in osculating elements induced by periodic perturbations are much smaller than those induced by secular perturbations as the elapsed time increases. The variations in osculating elements induced by secular perturbations are constant or non-periodic, and only even zonal gravitational harmonics and atmospheric drag give rise to secular effects. Atmospheric drag can be a significant part of the secular perturbations if the perigee altitude of a typical satellite orbit is less than 500 km. In summary:

- Secular perturbations >> Periodic perturbations (for long elapsed time)
- Secular perturbations = Disturbed acceleration due to gravity (J_2 and J_4) and Drag (perigee altitude < 500 km)

Figures 1 to 6 show the variations of the osculating elements due to the disturbed acceleration vector, \mathbf{a}_d^* , for a non-thrusting Low Earth Orbit satellite with a perigee altitude of approximately 200 km. Osculating elements are computed by four methods: numerical integration, two NORAD propagators (SGP and SGP4) and a first order theory of secular perturbations. The osculating elements predicted by the first order theory of secular perturbations are depicted by the thick solid line. As shown in Figures 1 to 3, the first order secular effects on the osculating elements a , e and i are almost negligible and are induced only by drag, and therefore the averaged time derivatives $\left. \frac{da}{dt} \right|_{av}$, $\left. \frac{de}{dt} \right|_{av}$ and $\left. \frac{di}{dt} \right|_{av}$ are almost zero (the thick solid lines are almost horizontal). The mean elements, $\bar{y}(t_0)$, are the initial values of osculating elements at time $t_0 = 0$ on the thick solid line. The solutions computed by numerical integration, SGP and SGP4, are depicted respectively by the thin solid line, the triangle and the square.

As shown in Figures 4 to 6, the secular effects on the osculating elements Ω , ω and M are significant and are induced by both gravity and drag. The averaged time derivatives $\left. \frac{d\Omega}{dt} \right|_{av}$, $\left. \frac{d\omega}{dt} \right|_{av}$ and $\left. \frac{dM}{dt} \right|_{av}$ are almost constant to first order even if the time dependent contributions due to drag are included. At 200 km altitude, the disturbed acceleration due to J_2 is at least one or two orders of magnitude greater than that due to J_4 . It is well known in general perturbations theory that the osculating elements (a , e , i , Ω , ω) are “slow” variables and that M is a “fast” variable. This implies that $\left. \frac{dM}{dt} \right|_{av}$ is much greater than $\left. \frac{d\Omega}{dt} \right|_{av}$ and $\left. \frac{d\omega}{dt} \right|_{av}$. If the elapsed time, $(t - t_0)$, is long, then the averaged time derivative due to drag, $\left. \frac{dM}{dt} \right|_{drag}$, must be included for a typical Low Earth Orbit satellite with a perigee altitude of 200 km even though References 4 to 6 and many excellent textbooks have recommended otherwise.

Since the satellite orbit of this example is almost circular, the first order estimates of the osculating eccentricity and argument of perigee are not equal to their averaged values during the two periods of the satellite orbit as shown in Figures 2 and 5. However, the first order estimates of the other osculating elements are very close to the averaged values of the osculating elements as predicted by the NORAD propagator SGP.

If a NORAD propagator is used, then the mean mean motion, \bar{n} , which replaces \bar{a} of $\bar{y}(t)$, must be carefully computed. The osculating mean motion, n , is determined from the equation: $\mu = n^2 a^3$. If the elapsed time is short (less than a day), the errors arising from interchanging the osculating mean motion and mean mean motion are negligible. If the elapsed time is long (on the order of days), the mean mean motion, \bar{n} , must be used in evaluating the averaged time derivatives (except for initialization). It should be clear that $\mu \neq \bar{n}^2 \bar{a}^3$.

From general perturbations theory, the osculating elements and the mean elements have a first order secular relationship given by

$$\mathbf{y}(t) = \bar{\mathbf{y}}(t_0) + \left. \frac{d\mathbf{y}}{dt} \right|_{av} (t - t_0) \quad (2)$$

where the averaged time derivatives valid between t_0 and t , are defined as

$$\left. \frac{d\mathbf{y}}{dt} \right|_{av} = \frac{1}{2\pi} \int_0^{2\pi} \frac{d\mathbf{y}}{dt} dM = \frac{1}{2\pi} \int_0^{2\pi} (1 - e \cos E) \frac{d\mathbf{y}}{dt} dE \quad (3)$$

and E is the eccentric anomaly. The instantaneous time derivative, $\frac{d\mathbf{y}}{dt}$, can be obtained from Lagrange's planetary equations for secular perturbations. Analytic solutions of $\left. \frac{d\mathbf{y}}{dt} \right|_{av}$, which are not difficult to obtain, are relatively accurate except for Low Earth Orbit satellites. If the elapsed time is long and the disturbed

acceleration due to drag is significant (e.g. for a Low Earth Orbit satellite), then the analytic averaged time derivatives of the semimajor axis and eccentricity can be an order of magnitude in error with respect to their numerically integrated values. This can happen even if the elapsed time is less than one period for some satellite orbits.

From Reference 7, the averaged time derivatives due to the disturbed gravity (J_2 and J_4) for secular perturbations are given by

$$\left. \frac{da}{dt} \right|_{\text{gravity}} = 0 \quad (4)$$

$$\left. \frac{de}{dt} \right|_{\text{gravity}} = 0 \quad (5)$$

$$\left. \frac{di}{dt} \right|_{\text{gravity}} = 0 \quad (6)$$

$$\left. \frac{d\Omega}{dt} \right|_{\text{gravity}} = -\frac{3\bar{n}\cos\bar{i}r_e^2}{2\bar{p}^2} \left\{ \begin{array}{l} J_2 - \frac{J_2^2 r_e^2}{16\bar{p}^2} \left[(12 - 80\sin^2\bar{i}) - \bar{e}^2(4 + 15\sin^2\bar{i}) \right] \\ - \frac{5J_4 r_e^2}{16\bar{p}^2} \left[(4 - 7\sin^2\bar{i})(2 + 3\bar{e}^2) \right] \end{array} \right\} \quad (7)$$

$$\begin{aligned} \left. \frac{d\omega}{dt} \right|_{\text{gravity}} &= \frac{3\bar{n}J_2 r_e^2}{4\bar{p}^2} [4 - 5\sin^2\bar{i}] \\ &+ \frac{9\bar{n}J_2^2 r_e^4}{384\bar{p}^4} \left[10\sin^2\bar{i}(76 - 89\sin^2\bar{i}) + \bar{e}^2(56 - 36\sin^2\bar{i} - 45\sin^4\bar{i}) \right] \\ &- \frac{15\bar{n}J_4 r_e^4}{32\bar{p}^4} \left[(16 - 62\sin^2\bar{i} + 49\sin^4\bar{i}) + \bar{e}^2 \left(18 - 63\sin^2\bar{i} + \frac{189}{4}\sin^4\bar{i} \right) \right] \end{aligned} \quad (8)$$

$$\begin{aligned} \left. \frac{dM}{dt} \right|_{\text{gravity}} &= \bar{n} + \frac{3n_0 J_2 r_e^2 (1 - \bar{e}^2)^{1/2}}{4\bar{p}^2} [2 - 3\sin^2\bar{i}] \\ &+ \frac{9\bar{n}J_2^2 r_e^4 (1 - \bar{e}^2)^{1/2}}{96\bar{p}^4} \left[\sin^2\bar{i}_o (100 - 131\sin^2\bar{i}) + \bar{e}^2 (20 - 98\sin^2\bar{i} + 67\sin^4\bar{i}) \right] \\ &- \frac{45\bar{n}J_4 r_e^4 (1 - \bar{e}^2)^{1/2}}{128\bar{p}^4} \left[\bar{e}^2 (8 - 40\sin^2\bar{i} + 35\sin^4\bar{i}) \right] \end{aligned} \quad (9)$$

where $\bar{p} = \bar{a}(1 - \bar{e}^2)$. In satellite state prediction, an accurate solution must always be computed numerically. Therefore, the averaged time derivatives due to drag should be integrated numerically for the semimajor axis and eccentricity. From References 8, the averaged time derivatives due to drag for secular perturbations are given by

$$\left. \frac{da}{dt} \right|_{\text{drag}} = -2B\bar{n}\bar{a}^2 \left[\frac{1}{\pi} \int_0^\pi \rho Q_1^2 (1 + \bar{e} \cos E) \sqrt{\frac{(1 + \bar{e} \cos E)}{(1 - \bar{e} \cos E)}} dE \right] \quad (10)$$

$$\left. \frac{de}{dt} \right|_{\text{drag}} = -2B\bar{n}\bar{p} \left[\frac{1}{\pi} \int_0^\pi \rho Q_1 Q_2 \sqrt{\frac{(1 + \bar{e} \cos E)}{(1 - \bar{e} \cos E)}} dE \right] \quad (11)$$

$$\left. \frac{di}{dt} \right|_{\text{drag}} = 0 \quad (12)$$

$$\left. \frac{d\Omega}{dt} \right|_{\text{drag}} = 0 \quad (13)$$

$$\left. \frac{d\omega}{dt} \right|_{\text{drag}} = 0 \quad (14)$$

$$\left. \frac{dM}{dt} \right|_{\text{drag}} = \frac{\dot{n}}{2} (t - t_0) = -\frac{3\bar{n}}{4\bar{a}} \left. \frac{da}{dt} \right|_{\text{drag}} (t - t_0) \quad (15)$$

where the rotating Earth factors are:

$$Q_0 = \frac{\omega_e \cos \bar{i} \sqrt{1 - \bar{e}^2}}{\bar{n}}$$

$$Q_1 = 1 - Q_0 \frac{(1 - \bar{e} \cos E)}{(1 + \bar{e} \cos E)}$$

$$Q_2 = \cos E - \frac{Q_0}{2(1 - \bar{e}^2)} (1 - \bar{e} \cos E) (2 \cos E - \bar{e} - \bar{e} \cos^2 E)$$

and ω_e is the constant scalar Earth rotational rate and ρ is the instantaneous density at a reference altitude with respect to the mean anomaly E .

The drag-induced averaged time derivatives of inclination, longitude of the ascending node and argument of perigee are normally much smaller than those of their gravity counterparts, and therefore are neglected. The averaged second time derivatives of the semimajor axis and eccentricity are at least three orders of magnitudes less than the averaged time derivatives and therefore are also neglected.

Since the disturbed accelerations are additive, the averaged time derivatives of the osculating elements $y(t)$ due to secular perturbations are the sum of the gravity and drag components. Substituting the averaged time derivatives of Equations (4) through (15) into Equation (2) and rearranging, a good initial guess of the unknown mean elements $\bar{y}(t_0)$ at time t_0 is given by

$$\begin{bmatrix} \bar{a}(t_0) \\ \bar{e}(t_0) \\ \bar{i}(t_0) \\ \bar{\Omega}(t_0) \\ \bar{\omega}(t_0) \\ \bar{M}(t_0) \end{bmatrix} = \begin{bmatrix} a(t) \\ e(t) \\ i(t) \\ \Omega(t) \\ \omega(t) \\ M(t) \end{bmatrix} - \begin{bmatrix} \left. \frac{da}{dt} \right|_{\text{drag}} (t - t_0) \\ \left. \frac{de}{dt} \right|_{\text{drag}} (t - t_0) \\ 0 \\ \left(\left. \frac{d\Omega}{dt} \right|_{\text{gravity}} \right) (t - t_0) \\ \left(\left. \frac{d\omega}{dt} \right|_{\text{gravity}} \right) (t - t_0) \\ \left(\left. \frac{dM}{dt} \right|_{\text{gravity}} + \left. \frac{dM}{dt} \right|_{\text{drag}} \right) (t - t_0) \end{bmatrix} \quad (16)$$

The mean elements \bar{a} , \bar{e} , \bar{i} and \bar{n} in the averaged time derivatives of Equations (4) through (15) are initially replaced by the respective osculating elements to start the initial guess process of Equation (16). Fortunately, the variations of these mean elements are normally slow. Now, given B , t_0 , t and $y(t)$, the right-hand-side of Equation (16) can be computed to give a good initial guess of the unknown mean elements $\bar{y}(t_0)$ at time t_0 .

Methods for Converting Mean Elements to Osculating Elements

A method of general perturbations for satellite theory seeks the solution of Equation (1) by series expansion and term-by-term analytic integration of the disturbed acceleration. General perturbations methods circumvent numerical integration but must initiate with mean elements. The NORAD element set propagators, which are general perturbations methods, start with a given mean vector, $\bar{y}(t_0) = (n_0, e_0, i_0, \Omega_0, \omega_0, M_0)$ at a given epoch time, t_0 . The given mean mean motion, n_0 , can be converted to the mean semimajor axis, a_0 , as described in Reference 9. Reference 10 documented five NORAD models for propagating Resident Space Objects (RSO) and satellites around the Earth. The Simplified General Perturbations (SGP) model, which contains most of the first order gravitational terms as described in References 11 and 12, computes the drag terms as linear functions of time. The SGP4 model, which uses the gravitational model of References 13 and 14, calculates the drag terms by a power density function of the atmosphere. The SGP4 model is customarily used for near-Earth satellites. A space object is classified by NORAD as near-Earth if its period is less than 225 minutes; it is classified as deep-space otherwise. The SDP4 model, which includes the gravitational terms due to third-body effects of the Sun and Moon and the Earth sectorial and tesseral harmonics, is an extension of SGP4 for deep-space objects. The SGP8 model is an extension of SGP4 with the same gravitational and drag models, but predicts state vectors more accurately especially when the satellite altitude is under 200 km. The SDP8 model is an extension of SGP8 and SDP4 for deep-space objects. The two higher order propagators, SGP8 and SDP8 were briefly considered as replacements for the SGP4 and SDP4, but the increased computational time and only slight improvement in state prediction accuracy have discouraged the changeover until the present time.

New and improved versions of SGP4 and SDP4 may be obtained directly from NORAD. However, using a UNIX workstation which is linked to Internet, a version of the five NORAD propagators (SGP, SGP4, SDP4, SGP8 and SDP8) can be downloaded from a computer at the Air Force Institute of Technology. The comprehensive instructions of Reference 10 and all the necessary algorithms downloaded from Internet do not guarantee that the reader can use the NORAD propagators immediately. Reference 9 discusses the problems and solutions.

The NORAD propagators were developed from the satellite theories of Kozai and Brouwer to propagate mean elements to osculating elements. Other mean element to osculating element propagators such as those described in References 16 and 17 will not be considered since their improvements in computational speed, memory storage and state vector accuracy are insignificant for our purpose. A method of converting osculating elements to mean elements requires a "forward" propagator which converts mean elements to osculating elements. Figures 1 to 6 show that the predicted osculating elements propagated by SGP are closer to those predicted by the first order theory of secular perturbations (the thick solid line) for most satellite orbits. If the

forward propagator is SGP, then $\frac{\dot{n}}{2} = -\frac{3\bar{n}}{4\bar{a}} \frac{da}{dt}\Big|_{\text{drag}}$ and $\frac{\ddot{n}}{6} = -\frac{5\dot{n}}{12\bar{a}} \frac{da}{dt}\Big|_{\text{drag}}$ are required and can be

computed from Equation (10). If an accurate $\frac{\ddot{n}}{6}$ is required, then $\frac{d^2a}{dt^2}\Big|_{\text{drag}}$ needs to be computed. If the

forward propagator is SGP4 or SDP4, then $B_{\text{sgp4}}^* = 6378137.0 K \rho_0 B$, where $2 \geq K \geq 1$ is a constant related to the density model used to calculate ρ_0 at the altitude of 120 km. The units of ρ_0 and B are respectively kg/m^3 and m^2/kg . As a concrete example, a SGP or NORAD propagator has been chosen as the forward propagator in this paper even though the choice is arbitrary.

The NORAD element set propagators all start with a given mean vector, $\bar{y}(t_0)$, and their output is the predicted position and velocity vectors, $r(t)$ and $v(t)$, which can then be transformed to the osculating elements, $y(t)$. Osculating elements are the ones that are usually available and the reconstruction of mean elements must begin with osculating elements.

Previous Methods for Converting Osculating Elements to Mean Elements (Ref. 1 to 3)

A method for converting osculating elements to mean elements which uses a transition matrix

$$T = \left[\frac{\partial y(t)}{\partial \bar{y}(t_0)} \right] \quad (17)$$

for the equation

$$\delta y(t) = T \delta \bar{y}(t_0) \quad (18)$$

is known as a method of differential corrections or a transition matrix algorithm in applied optimal control theory. A transition matrix algorithm usually begins with a guessed nominal $\bar{y}(t_0)$ at time t_0 , and then propagates forward to a nominal $y(t)$ at time t , which in turn gives $\delta y(t)$. Therefore the differential corrections at time t_0 is

$$\delta \bar{y}(t_0) = T^{-1} \delta y(t) \quad (19)$$

using Equation (18). In practice, accurate transition matrices are computed numerically. Chapter 7 of Reference 18 provides the algorithm to numerically compute a transition matrix such as that of Equation (17). Reference 19 describes the technique of accurate numerical partials.

Reference 1 suggests an iterative procedure by using the given osculating elements $y(t)$ as the initial guess of the mean elements $\bar{y}(t_0)$ and assuming an identity transition matrix. That is, the averaged time derivatives of Equation (16) are zero for any elapsed time and Equation (19) is reduced to

$$\delta \bar{y}(t_0) = \delta y(t) \quad (20)$$

since $T = I$. If the elapsed time is less than one day, this iterative procedure may convert $y(t)$ to $\bar{y}(t_0)$ for some Low Earth Orbits. This method converges linearly at best. If the elapsed time is greater than a day, this method fails for most Low Earth Orbits. The cause of failure is a combination of:

- The neglected drag terms for semimajor axis, eccentricity and mean anomaly are not small.
- The identity matrix is a poor approximation to the transition matrix and Equation (20) is not valid.

Recalling that the problem is to find $\bar{y}(t_0)$ given B , t_0 , t and $y(t)$. The iterative procedures of Reference 1 may be summarized as follows:

1. Let the initial guess of the mean elements at the given time t_0 be the same as the given osculating elements, $y(t)$. That is

$$\bar{y}_k(t_0) = y(t)$$

where k is the iteration number ($k = 0$ at this point).

2. Propagate forward (using a SGP propagator) from $\bar{y}_k(t_0)$ to $x_k(t)$ and then transform $x_k(t)$ to $y_k(t)$. The difference in osculating elements at time t is

$$\delta y(t) = y(t) - y_k(t) = \delta \bar{y}(t_0)$$

using Equation (20).

3. Compute the new guess of the mean elements at time t_0 as

$$\bar{y}_{k+1}(t_0) = \bar{y}_k(t_0) + \delta \bar{y}(t_0)$$

For $\delta y = |y(t) - y_k(t)| > 10^{-10}$, then procedure 2 is repeated with the new guess

$\bar{y}_{k+1}(t_0)$; otherwise the desired mean elements at time t_0 is

$$\bar{y}(t_0) = \bar{y}_{k+1}(t_0)$$

References 2 and 3 are transformations between osculating and mean elements with $t = t_0$. Reference 2 is an iterative method that uses the Frazer elements (position and velocity vectors and their variations), includes the short- and long-periodic perturbations. Reference 3, which uses a combination of Kozai's and Izsak's theories, calculates the difference between the osculating elements and mean elements only due to short-periodic perturbations. The methods of these two references are only instantaneous conversions or transformations, and therefore are not described in this paper.

A New Method for Converting Osculating Elements to Mean Elements

This method uses a good initial guess derived from a first order theory of secular perturbations and a transition matrix computed by accurate numerical partials. As shown in Figures 1 to 6, the osculating elements computed from a first order theory of secular perturbations (the thick solid straight line) behave linearly with respect to time and are close to the average values of the SGP solutions. This implies that the initial guess of the mean elements computed from Equation (16) will be close to the desired mean elements, $\bar{y}(t_0)$, at time t_0 . A traditional transition matrix algorithm requires 7 forward propagations (1 nominal and 6 neighboring trajectories). The stepsize h_i is usually set to 10^{-6} of the i^{th} mean element; this may be too small for eccentricity but too large for the semimajor axis. The transition matrix algorithm based on accurate numerical partials requires 25 forward propagations (1 nominal and 24 neighboring trajectories). The iterative procedures of this method may be summarized as follows:

1. Compute the averaged time derivatives of Equation (4) to (15). Let the given osculating elements, $y(t)$, be Y , then the initial estimate of the mean semimajor axis, mean eccentricity, mean inclination and mean mean motion are given by:

$$\begin{aligned}\bar{a} &= a(t) - \lambda \left. \frac{da}{dt} \right|_{\text{drag}} (t - t_0) \\ \bar{e} &= e(t) - \lambda \left. \frac{de}{dt} \right|_{\text{drag}} (t - t_0) \\ \bar{i} &= i(t) \\ \bar{n} &= n(t)\end{aligned}$$

where the empirical constant λ is 0.5 for Low Earth Orbits and zero otherwise.

2. Initialize $\frac{\dot{n}}{2}$ and $\frac{\ddot{n}}{6}$ for the forward propagator SGP and the initial guess of the mean mean anomaly, \bar{M} , by numerically integrating $\left. \frac{da}{dt} \right|_{\text{drag}}$ of Equation (10), then

$$\bar{M}, \quad \text{by numerically integrating } \left. \frac{da}{dt} \right|_{\text{drag}} \text{ of Equation (10), then}$$

$$\frac{\dot{n}}{2} = -\frac{3\bar{n}}{4\bar{a}} \left. \frac{da}{dt} \right|_{\text{drag}} \quad \text{and} \quad \frac{\ddot{n}}{6} = -\frac{5\dot{n}}{12\bar{a}} \left. \frac{da}{dt} \right|_{\text{drag}}. \quad \text{If the forward propagator is SGP4 or SDP4, then } B_{\text{sgp4}}^*$$

is required.

3. Compute the nominal mean elements $\bar{y}^*(t_0)$ guess from Equation (16) and then propagate forward to t giving the nominal osculating elements $y^*(t)$
4. Compute the nominal differential correction of osculating elements at t as

$$\delta y(t) = Y - y^*(t)$$

5. Compute the transition matrix, $T = \left[\frac{\partial y(t)}{\partial \bar{y}(t_0)} \right]$ by accurate numerical partials.

Propagate forward by a SGP propagator 6 times in the neighborhood of the nominal trajectory (step 3) using

$$\bar{y}(t_0) = \bar{y}^*(t_0) + \delta \bar{y}(t_0)$$

For the i^{th} neighboring trajectory ($i = 1, 2, \dots, 6$), four "neighboring" neighboring trajectories are computed from 4 stepsizes of $\frac{h_i}{2}$, $-\frac{h_i}{2}$, $\frac{\rho h_i}{2}$ and $-\frac{\rho h_i}{2}$. The corresponding 4 osculating elements computed by a SGP propagator at time t are y_1, y_2, y_3 and y_4 . The partial derivatives of the i^{th} column of T is given by

$$\frac{\partial y(t)}{\partial \bar{y}_i(t_0)} = \frac{(y_3 - y_4) - \rho^3(y_1 - y_2)}{\rho h_i (1 - \rho^2)}$$

The 6 x 6 transition matrix can be approximated as

$$T = \begin{bmatrix} \frac{\partial y(t)}{\partial \bar{y}(t_0)} \end{bmatrix} = \begin{bmatrix} \frac{\partial y(t)}{\partial \bar{y}_1(t_0)} & \frac{\partial y(t)}{\partial \bar{y}_2(t_0)} & \dots & \frac{\partial y(t)}{\partial \bar{y}_n(t_0)} \end{bmatrix}$$

In computing T, 24 propagation by the forward propagator SGP are required. A good choice of ρ is 1/2 and that of the stepsize h_i is 10^{-4} of each mean element.

6. Update the nominal $\bar{y}^*(t_0)$ at t_0 as

$$\bar{y}^*(t_0) \Big|_{\text{new}} = \bar{y}^*(t_0) \Big|_{\text{old}} + T^{-1} \delta y(t)$$

Step 3 to 6 are repeated until the magnitude of $\delta y(t)$ is reduced to an acceptably small value (10^{-12}).

Examples

Two examples are given to illustrate the performance of the new method for satellites at a Low Earth Orbit and a High Earth Orbit. Using a first order theory of secular perturbations, the initial guess of the slow variables, $(\bar{a}, \bar{e}, \bar{i}, \bar{\Omega}, \bar{\omega})$, can be estimated in the vicinity of their unknown values at time t_0 . If the initial guess of the fast variable, \bar{M} , can be predicted to within approximately 30 degrees of its unknown value, then convergence is fast. This is not a problem for almost any satellite orbit if the elapsed time is less than one day.

The variations of the osculating mean anomaly, M, at time t for the example Low Earth Orbit satellite are shown in Figures 6. The initial guess of \bar{M} at time t_0 is related to M at time t by Equation (16). For short elapsed times, the 30 degree requirement can be satisfied easily. The primary reason is that the unknown mean semimajor axis, \bar{a} , has changed only slightly in a short elapsed time, and as a consequence the effects on the terms due to $\left. \frac{dM}{dt} \right|_{\text{gravity}}$ and $\left. \frac{dM}{dt} \right|_{\text{drag}}$ are small. The right-hand-side of Equation (16) can then be computed quite accurately giving a good initial guess of \bar{M} .

In the following examples, first we assumed to know the mean elements, $\bar{y}(t_0)$, at time t_0 , and then we used a forward propagator (SGP4 for *Example 1* and SDP4 for *Example 2*) to get the osculating elements, $y(t)$, at time t. In what follows, we discard the mean elements, $\bar{y}(t_0)$, and no knowledge of the mean elements at time t_0 will be used. The problem is:

Given B, t_0 , t and $y(t)$; retrieve $\bar{y}(t_0)$.

Example 1

The mean elements, $\bar{y}(t_0)$, at time t_0 are taken out of the SGP4 example of Reference 10 with minor adjustments for double precision computation. Also the ballistic coefficient, B, is replaced by that of the LANDSAT-D. The osculating elements, $y(t)$, at time t are computed by using SGP4 with B_{sgp4}^* computed from Equation (18).

Given: $C_{d0} = 2.0$, $A = 12.2778 \text{ meter}^2$, $m = 1710.0 \text{ kg}$, $B = \frac{C_{d0}A}{2m} = 0.00718 \frac{\text{meter}^2}{\text{kg}}$

$t_0 = 0.0$, $t = 0, 1, 5 \text{ days}$

$$y(0 \text{ day}) = \begin{bmatrix} 6641.774062 \\ .0096661858 \\ 72.85385095 \\ 115.9622955 \\ 59.40458042 \\ 103.8371428 \end{bmatrix}, \quad y(1 \text{ day}) = \begin{bmatrix} 6633.640850 \\ .0083375605 \\ 72.85513567 \\ 113.4116703 \\ 56.77943987 \\ 130.9131346 \end{bmatrix}, \quad y(5 \text{ days}) = \begin{bmatrix} 6589.666059 \\ .0053578232 \\ 72.84433117 \\ 103.0554340 \\ 54.07490762 \\ 349.1054119 \end{bmatrix}$$

Following the procedures 1 to 3 of the new method, the initial guesses of the nominal mean elements, $\bar{y}^*(t_0)$, at time t_0 for the cases of $t = 0, 1, 5$ days are computed as:

$$\bar{y}^*(t_0)|_{0 \text{ day}} = \begin{bmatrix} 6641.7740 \\ .00966618 \\ 72.853850 \\ 115.96229 \\ 59.404580 \\ 103.83714 \end{bmatrix}, \quad \bar{y}^*(t_0)|_{1 \text{ day}} = \begin{bmatrix} 6638.4631 \\ .00869400 \\ 72.855135 \\ 115.97053 \\ 59.232901 \\ 105.09619 \end{bmatrix}, \quad \bar{y}^*(t_0)|_{5 \text{ days}} = \begin{bmatrix} 6641.9257 \\ .00834486 \\ 72.844331 \\ 115.93401 \\ 66.308201 \\ 138.72967 \end{bmatrix}$$

Comparison of results:

Days from t_0	Method of Reference 1 (Walter)		New Method (Der&Danchick)	
	# of iterations required: N_1	# of SGP4 calls N_1	# of iterations required: N_2	# of SGP4 calls N_2
0	12	84	3	75
1	40	280	3	75
5	not converged	---	4	100

Found: The mean elements, $\bar{y}(t_0)$, at time t_0 for the cases of $t = 0, 1, 5$ days:

$$\bar{y}(t_0) = \begin{bmatrix} 6637.68397 \\ .0086731 \\ 72.84350 \\ 115.9689 \\ 52.69880 \\ 110.5714 \end{bmatrix}$$

One reason to change the ballistic coefficient from that of Reference 10 is to investigate how close the new method works during the satellite orbital decay. Using the lifetime equation of Reference 4, this satellite has a lifetime of approximately 9000 minutes or a little over six days from time t_0 . Numerical integration shows that the lifetime is approximately 10 days from time t_0 . After 5 days, the perigee altitude of the satellite is close to 150 km and the state vectors predicted by the SGP4 propagator become inaccurate. Nevertheless, the new method converges very close to $\bar{y}(t_0)$ in the last few days before satellite re-entry.

Example 2

The mean elements, $\bar{y}(t_0)$, at time t_0 are constructed from a Molniya orbit with perigee altitude of 500 km and apogee altitude of 40000 km. Critical inclination (63.4 degrees) is chosen for this HEO to demonstrate that there is no singularity at any inclination for the conversion from osculating elements to mean elements. The ballistic coefficient, B , which is not important for this HEO, is chosen to be the same as that of example 1. The osculating elements, $y(t)$, at time t are computed by using the SDP4 propagator. The effect of drag is negligible on this HEO satellite.

Given: $C_{d0} = 2.0$, $A = 12.2778 \text{ meter}^2$, $m = 1710.0 \text{ kg}$, $B = \frac{C_{d0}A}{2m} = 0.00718 \frac{\text{meter}^2}{\text{kg}}$,

$t_0 = 0.0$, $t = 10, 100, 200 \text{ days}$

$$y(10 \text{ days}) = \begin{bmatrix} 26626.70165 \\ .7415398328 \\ 63.45549845 \\ 118.5145116 \\ .0695130482 \\ 137.6237041 \end{bmatrix}, \quad y(100 \text{ days}) = \begin{bmatrix} 26630.49652 \\ .7364330943 \\ 63.36886054 \\ 105.0926980 \\ .4435084366 \\ 77.71324416 \end{bmatrix}, \quad y(200 \text{ days}) = \begin{bmatrix} 26626.65222 \\ .7323070455 \\ 63.72013696 \\ 90.19640476 \\ .7794822322 \\ 26.78924405 \end{bmatrix}$$

Following the procedures 1 to 3 of the new method, the initial guesses of the nominal mean elements, $\bar{y}^*(t_0)$, at time t_0 for the cases of $t = 10, 100, 200 \text{ days}$ are computed as:

$$\bar{y}^*(t_0) \Big|_{10 \text{ days}} = \begin{bmatrix} 26626.798 \\ .74154077 \\ 63.455498 \\ 119.93263 \\ .07822485 \\ 144.12848 \end{bmatrix}, \quad \bar{y}^*(t_0) \Big|_{100 \text{ days}} = \begin{bmatrix} 26630.570 \\ .73643493 \\ 63.368860 \\ 119.43259 \\ .43299544 \\ 158.12109 \end{bmatrix}, \quad \bar{y}^*(t_0) \Big|_{200 \text{ days}} = \begin{bmatrix} 26626.686 \\ .73230790 \\ 63.720136 \\ 117.80345 \\ 1.5247843 \\ 156.05599 \end{bmatrix}$$

Comparison of results:

Days from t_0 (days)	Method of Reference 1 (Walter)		New Method (Der&Danchick)	
	# of iterations required: N_1	# of SDP4 calls N_1	# of iterations required: N_2	# of SDP4 calls N_2
10	13	91	3	75
100	20	140	4	100
200	not converged	---	7	175

Found: The mean elements, $\bar{y}(t_0)$, at time t_0 for the cases of $t = 10, 100, 200 \text{ days}$:

$$\bar{y}(t_0) = \begin{bmatrix} 26626.96632 \\ .7416966 \\ 63.33610 \\ 120.0032 \\ .0077000 \\ 143.8417 \end{bmatrix}$$

Conclusions

- If the constants given in the data block of the five NORAD propagators are defined in double precision, then the osculating state vectors can be predicted much more accurately especially for satellite orbits without the influence of atmospheric drag. With this simple modification, the five NORAD propagators can be used as forward propagators for the conversion of osculating elements to mean elements.
- The method presented by this paper achieves quadratic convergence due to accurate numerical partials. It has uniformly good performance over the three test cases, succeeds where the Reference 1 method failed, and is generally more computationally efficient.

- For Low Earth Orbits (the example described by Figures 1 to 6), the initial guess of the fast changing mean mean anomaly, \bar{M} , at time t_0 must include the term computed from the averaged time derivative due to drag. In this case, the conversion of osculating elements to mean elements can be extended from an elapsed time of one day to the last few days before satellite re-entry
- For High Earth Orbits, the initial guess of the fast changing mean mean anomaly, \bar{M} , at time t_0 can be predicted accurately even for long elapsed times. In this case, the elapsed time for the conversion of osculating elements to mean elements can be extended to months.
- For Geosynchronous Earth Orbits (results not included in this paper), the initial guess of the fast changing mean mean anomaly, \bar{M} , at time t_0 can also be predicted accurately even for long elapsed times. In this case, the elapsed time for the conversion of osculating elements to mean elements can be extended to years.
- The determination of mean orbital elements can be radically streamlined with the new method and made applicable for mean elements orbit determination with observations made by heterogeneous sensor types over long spans of elapsed time.

References

1. Walter, H.G., "Conversion of Osculating Orbital Elements into Mean Elements", The Astronomical Journal, Volume 72, Number 8, October, 1967.
2. O'Connor, J.J., "Methods of Trajectory Mechanics", RCA International Service Corporation, Eastern Space and Missile Center, Patrick Air Force Base, Florida, ESMC-TR-80-45, May, 1981.
3. Uphoff, C., "Conversion Between Mean and Osculating Elements", JPL IOM 312/85.2-927, January 23, 1985.
4. King-Hele, D.G., "Theory of Satellite Orbits in an Atmosphere", Butterworths, London, 1964.
5. Danby, J.M.A., "Fundamentals of Celestial Mechanics", Second Edition, Willmann-Bell, Inc, Richmond, Virginia, 1988.
6. Roy, A.E., "Orbital Motion", Third Edition, Adam Hilger, Bristol and Philadelphia, 1988.
7. Blitzer, L., "Handbook of Orbital Perturbations", unpublished internal TRW report, September 1, 1970.
8. Sterne, T.E., "Effect of the Rotation of a Planetary Atmosphere Upon the Orbit of a Closed Satellite", ARS Journal, October, 1959.
9. Der, G.J., Danchick, R., "Conversion of Osculating Orbital Elements to Mean Orbital Elements", Unpublished paper, April, 1995.
10. Hoots, F.R., Roehrich, R.L., "Spacetrack Report No. 3, Models for Propagation of NORAD Element Sets", Office of Astrodynamic Applications, Fourteenth Aerospace Force, Ent AFB, December, 1980.
11. Hilton, C.G., Kuhlman, J.R., "Mathematical Models for the Space Defense Center", Philco-Ford Publication No. U-3871, 17-28, November, 1966.
12. Kozai, Y., "The Motion of a Closed Earth Satellite", Astronomical Journal Vol 64, Page 367-377, November 1959.
13. Brouwer, D., "Solution of the Problem of a Artificial Satellite Theory without Drag", Astronomical Journal Vol. 64, Page 378-397, November 1959.
14. Lane, M.H., Cranford, K.H., "An Improved Analytical Drag Theory for the Artificial Satellite Problem", AIAA/AAS Astrodynamics Conference, August, 1969.
15. Kaplan, G.H., "Naval Observatory Vector Astrometry Subroutines", United States Naval Observatory, 15 March, 1990.
16. Williams, K.E., "POCP: A System for Long-Term Satellite Ephemeris Predictions", AAS 93-115, 1993.
17. Hoots, F.R., "A short Efficient Analytical Satellite Theory ", J. of Guidance and Control, AIAA, Vol. 5, No. 2, March-April, 1982.
18. Bryson, A.E., Ho, Y.C., "Applied Optimal Control", Hemisphere Publishing, New York, 1975.
19. Danchick, R., "Accurate Numerical Partial with Applications to Maximum Likelihood Methods ", Internal Rand Report, 1975.

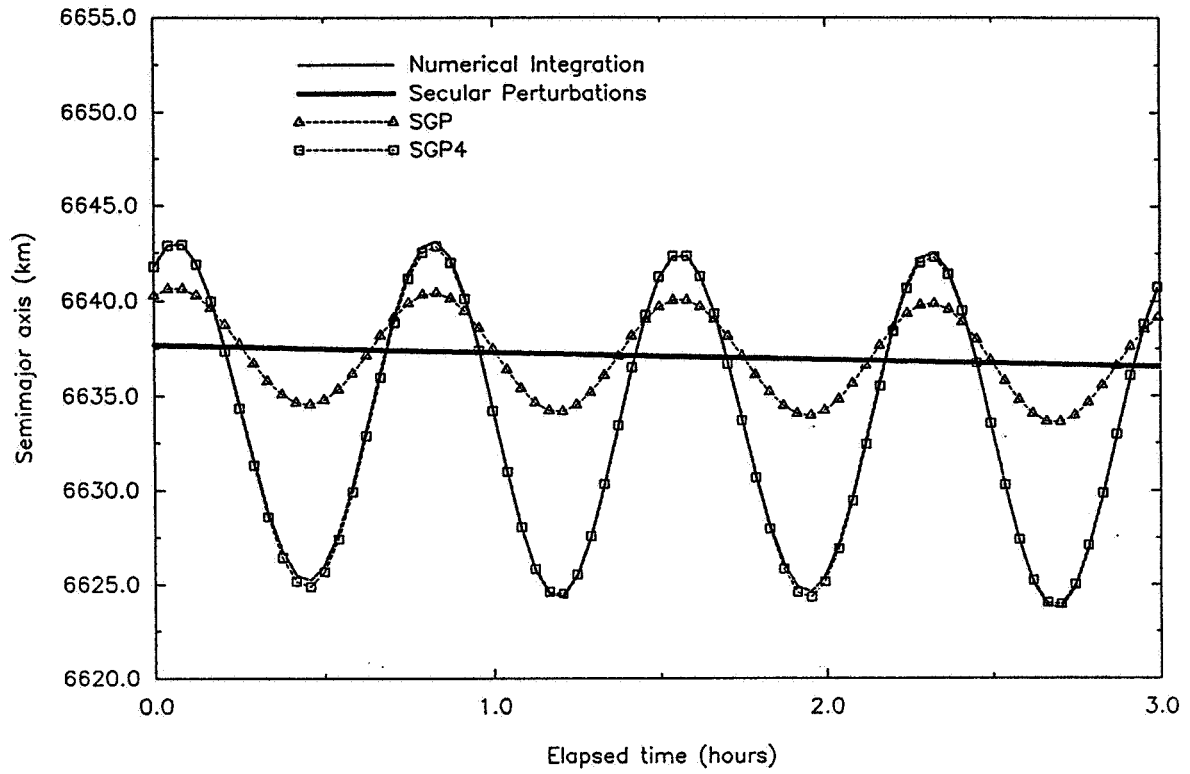


Figure 1. Effects of gravity and drag on semimajor axis for 2 Low Earth orbits

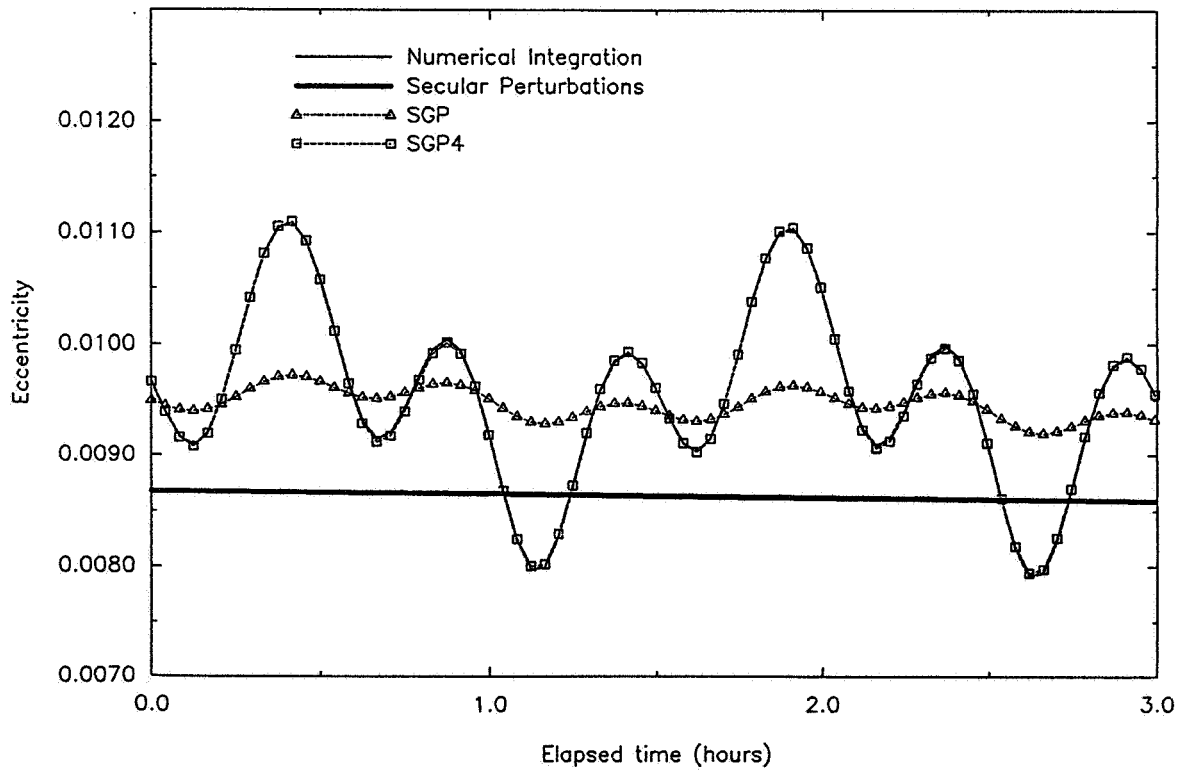


Figure 2. Effects of gravity and drag on eccentricity for 2 Low Earth Orbits

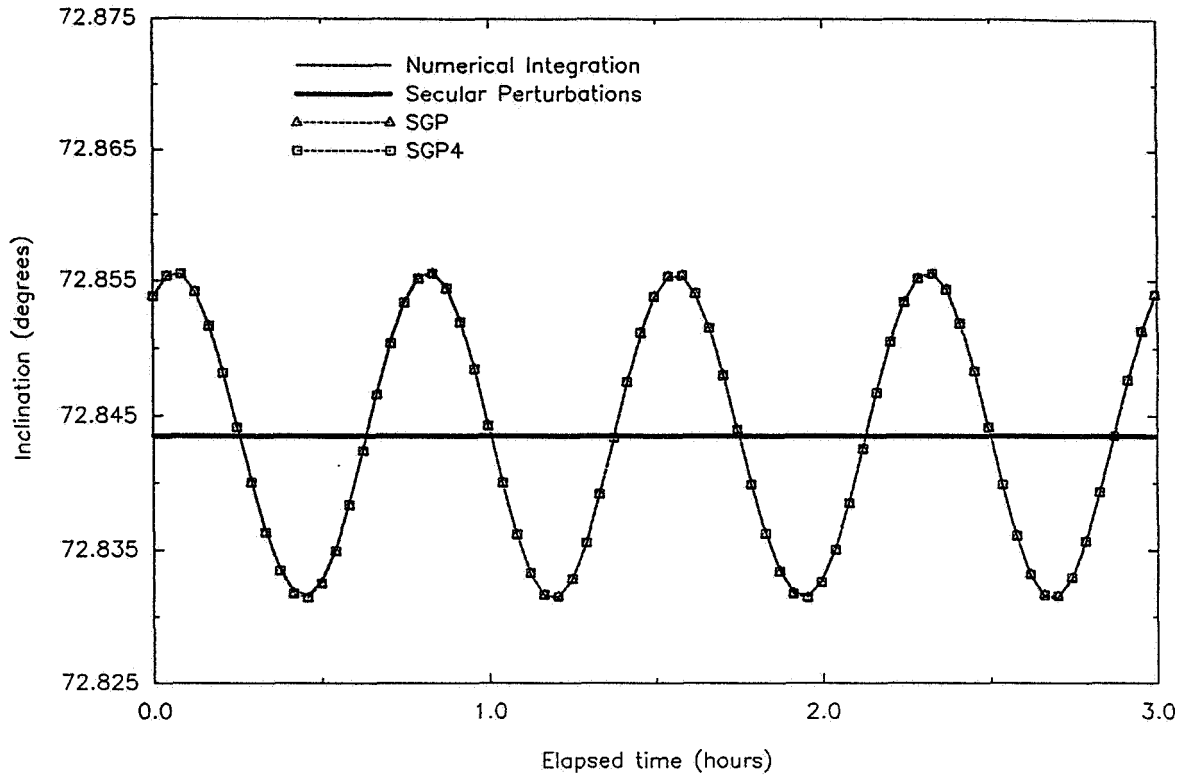


Figure 3. Effects of gravity and drag on inclination for 2 Low Earth Orbits

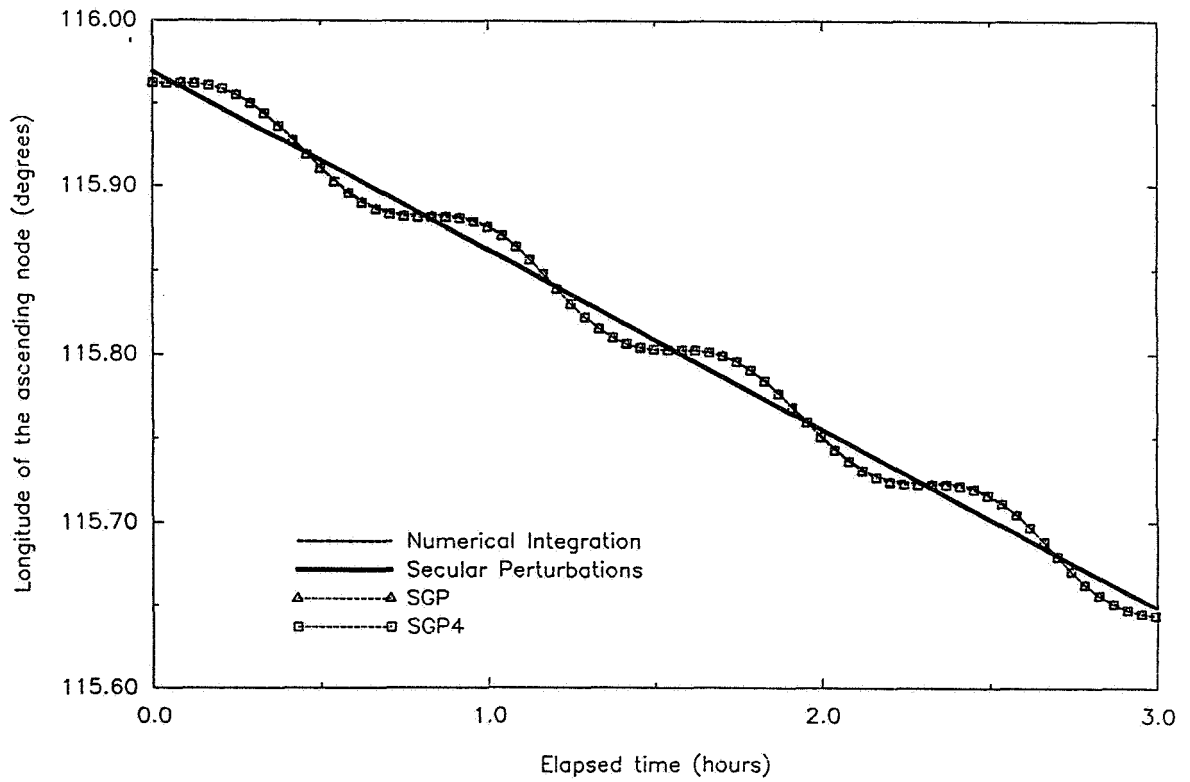


Figure 4. Effects of gravity and drag on longitude of the ascending node for 2 Low Earth Orbits

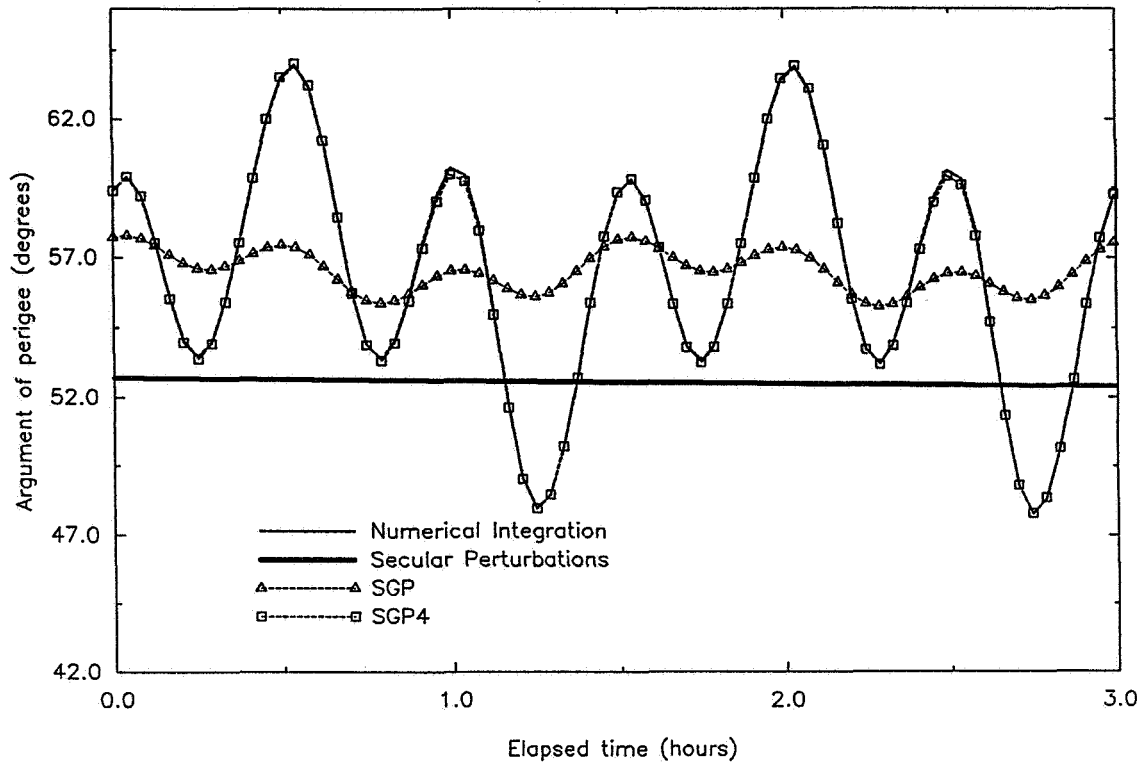


Figure 5. Effects of gravity and drag on argument of perigee for 2 Low Earth Orbits

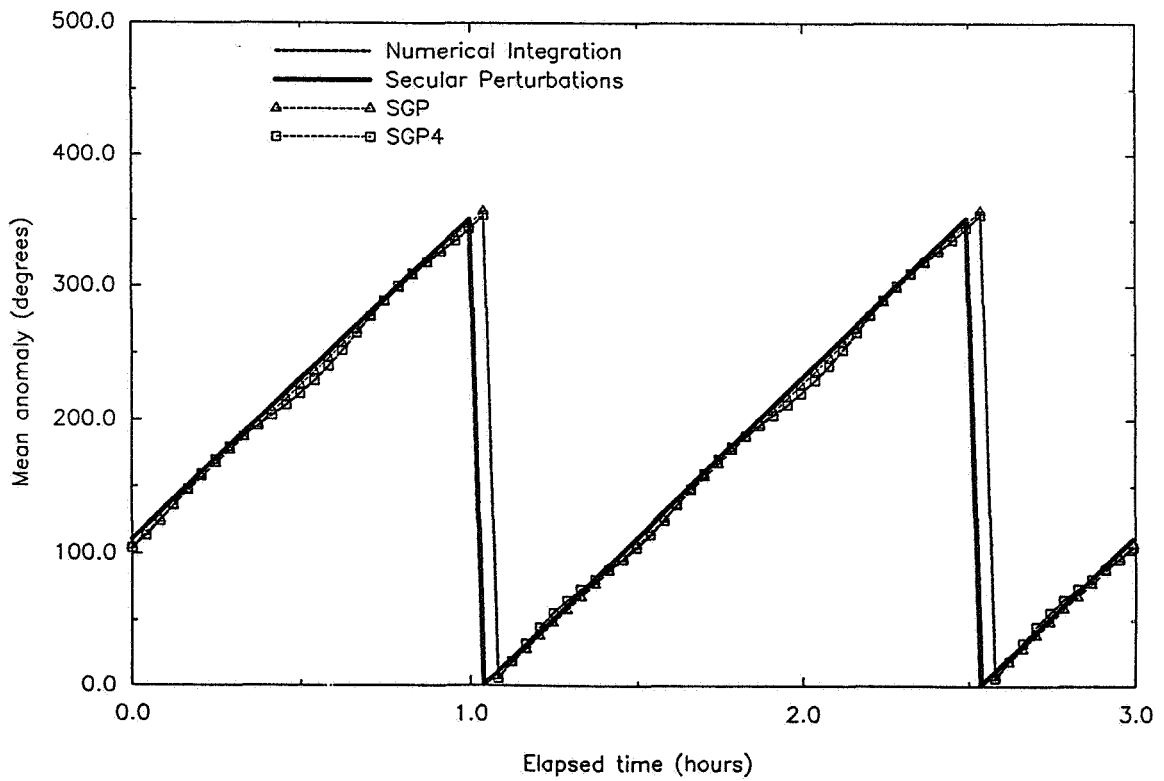


Figure 6. Effects of gravity and drag on mean anomaly for 2 Low Earth Orbits

Downlink Probability Density Functions for EOS-McMurdo Sound

P. Christopher
Stanford Telecom
Reston, VA

A. H. Jackson
Goddard Space Flight Center (GSFC)
Greenbelt, MD

Abstract

The visibility times and communication link dynamics for the EOS-McMurdo Sound direct downlinks have been studied recently. The 16-day EOS periodicity may be shown with the Goddard Trajectory Determination System (GTDS), and the entire 16-day period should be simulated for representative link statistics. We desire many attributes of the downlink, however, and a faster orbital determination method is desirable. We use the method of osculating elements for speed and accuracy in simulating the EOS orbit. The accuracy of the method of osculating elements is demonstrated by closely reproducing the observed 16-day Landsat periodicity. An autocorrelation function method is used to show the correlation spike at 16 days.

The entire 16-day record of passes over McMurdo Sound is then used to generate statistics for innage time, outage time, elevation angle, antenna angle rates, and propagation loss. The elevation angle probability density function is compared with a 1967 analytic approximation which has been used for medium to high altitude satellites. One practical result of this comparison is seen to be the rare occurrence of zenith passes. The new result is functionally different than the earlier result, with a heavy emphasis on low elevation angles. EOS is one of a large class of sun synchronous satellites which may be downlinked to McMurdo Sound. We examine delay statistics for an entire group of sun synchronous satellites ranging from 400 km to 1000 km altitude. Outage probability density function results are presented three dimensionally.

1. Introduction

A new series of environmental spacecraft, such as the Earth Observation Satellite (EOS), may use the Tracking and Data Relay Satellite System (TDRSS) in some unique ways. Polar orbiting environmental spacecraft spend an appreciable portion of their orbit over the poles. The polar orbit of EOS or of Landsat may be represented as in Figure 1-1. The individual views are taken as a series of snapshots at 8.2 minute intervals. It is seen to be slightly retrograde, with a 98-degree inclination. EOS and other environmental spacecraft may find it more convenient to downlink their data directly to a ground station in Antarctica rather than relaying it over a distance of six earth radii to a geosynchronous relay. We examine these downlinks in some detail.

A ground station at McMurdo Sound, Antarctica has been constructed by NASA to answer these needs. A polar satellite such as an Earth Observation Satellite (EOS) would be able to link to McMurdo Sound in a visibility region as shown in Figure 1-2. McMurdo would then uplink to TDRS West, to complete the link to the White Sands Complex (WSC).

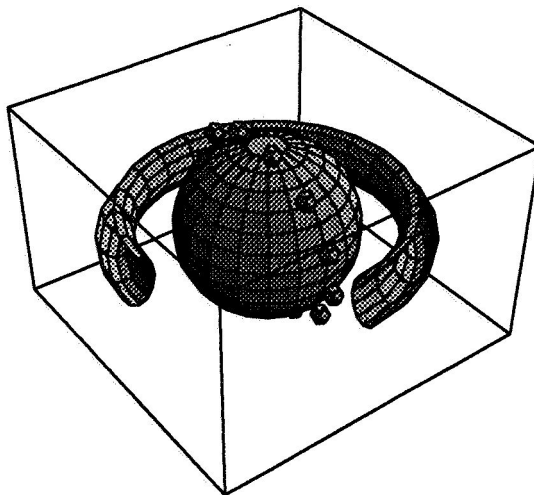
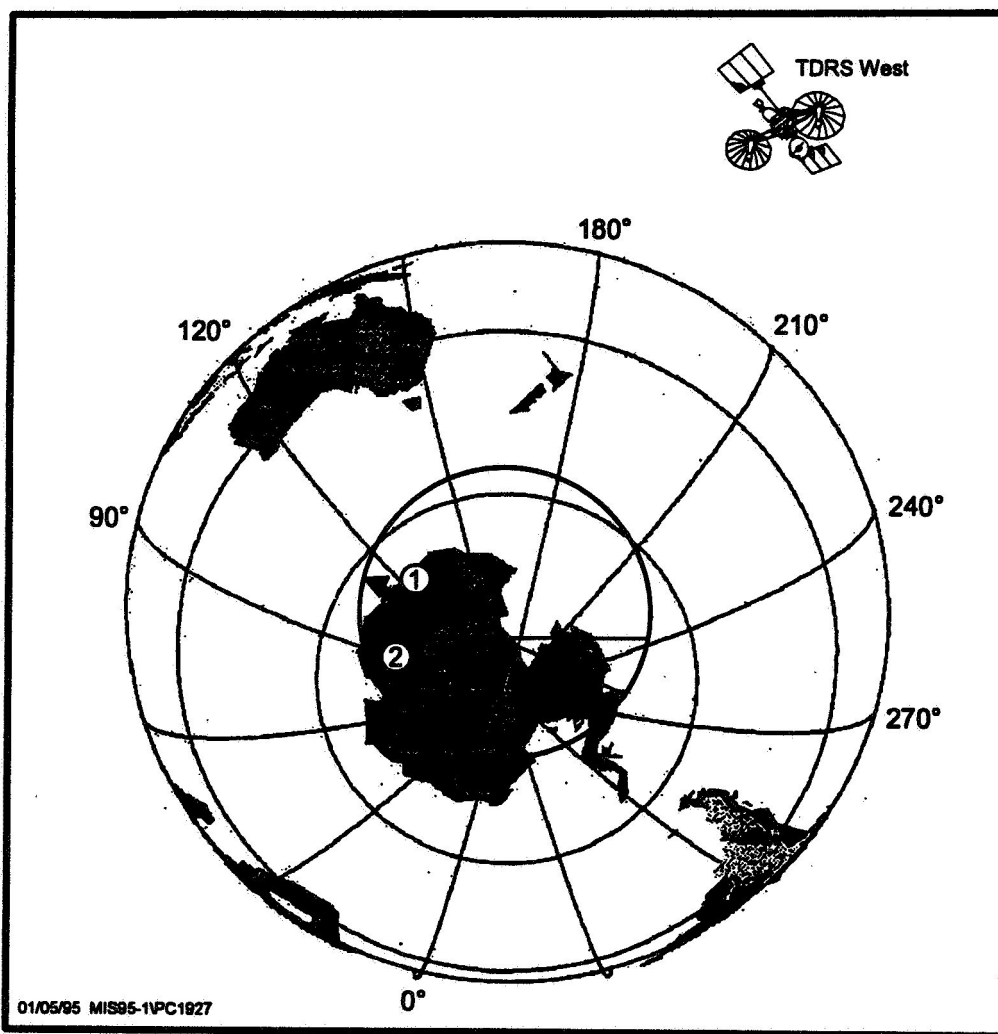


Figure 1-1: Inclined Landsat (EOS) Orbit Inside VanAllen Belt



Note the first EOS pass, labelled (1).

Figure 1-2: McMurdo Sound-EOS Visibility Region Radius 25.6°

We address some of the communication link dynamics for the user satellite pass over McMurdo Sound. Sun synchronous satellites will be of widespread interest, and we closely examine arrival times, departure times, and atmospheric signal loss as a function of time during the pass over the ground station. These data may be further examined to generate interarrival time statistics, link duration statistics, and signal loss statistics as an aid to the system designer. EOS, as a clearly important member of the class of sun synchronous satellites, gets special attention.

Many long computer simulations are necessary for this report. The method of osculating orbits (1) is used here for speed and accuracy. The oblate earth perturbation terms are vital to descriptions of the 16-day EOS periodicity. Indeed, the 16-day periodicity can be used as a simulation check against existing Landsat4 data. Most of our EOS runs include the entire 16-day periodic interval as a key check. However, only small portions of the output tables are included here because of space limits. The report begins with a brief description of oblate earth perturbation terms which are necessary for the method of osculating elements.

Atmospheric attenuation on the McMurdo-satellite link is closely related to the orbital computations because the attenuation depends strongly on the ground station elevation angle. We use two new attenuation results as an integral part of the orbital program. The first new propagation result is due to Liebe (2). The new propagation results are used but not included because of space limitations. A short portion of a long EOS simulation follows. The long-term EOS statistics are included as a way to keep the results brief. General sun synchronous results conclude the report. Sun synchronous altitudes between 400-1000 km will be seen to offer short interarrival times at McMurdo Sound, but altitudes below 500 km will occasionally skip an orbit before visibility repeats.

Appendix A condenses the long 16 day simulation into short graphical output.

2.0 Analysis

The anticipated long 16-day periodicity of EOS leads us to consider methods to reproduce the entire 16-day period with suitable accuracy. Anything less would cause serious doubts about the ground elevation statistics and the propagation loss studies which follow. The method of osculating elements, with analytic approximations for the perturbed motion, is useful for fast and relatively accurate orbit prediction for missions of long duration. Moulton (3) gives the basis of the method as the partial derivatives of the instantaneous orbital elements as a function of a perturbing potential. Brouwer (4), Kozai (5), and Blitzer (6) have used the method to achieve exhaustive insights into the motion of low earth orbiting satellites. Their results for satellite perturbations may be subdivided into secular components, long cycle components, and short cycle components. We desire only the secular components here, and omit the long and short cycle terms because they tend to cancel out their effects over the long term. Omission of the short cycle component has implied a maximum instantaneous orbital error of a few kilometers for the 1958 Vanguard orbit. We accept that error, along with the error due to lunar perturbations (although lunar perturbations can be included with the method of osculating elements with the aid of results by Ash (1)).

The key secular terms are:

$$\dot{W} = \frac{1}{a} \sqrt{\frac{u}{a}} \left\{ -\frac{3}{2} J_2 \left(\frac{R}{P} \right)^2 \cos(i) + \frac{3}{32} J_2^2 \left(\frac{R}{P} \right)^4 \right. \\ \left. \bullet \left[(4 + 12\sqrt{1-e^2} - 9e^2) \cos(i) + (-40 - 36\sqrt{1-e^2} + 5e^2) \cos^3(i) \right] \right. \\ \left. - \frac{15}{32} J_4 \left(\frac{R}{P} \right)^4 (2 + 3e^2) (3 - 7 \cos^2(i)) \cos(i) \right\} \quad \text{Rad/Sec} \quad 2-1$$

$$\begin{aligned} \dot{W}_r = \frac{1}{a} \sqrt{\frac{u}{a}} \left\{ \frac{3}{4} J_2 \left(\frac{R}{P} \right)^2 (-1 + 5 \cos^2(i)) + \frac{3}{128} J_2^2 \left(\frac{R}{P} \right)^4 \right. \\ \bullet \left[-10 + 24\sqrt{1-e^2} - 25e^2 + (-36 - 192\sqrt{1-e^2} + 126e^2) \cos^2(i) \right. \\ \left. + (430 + 360\sqrt{1-e^2} - 45e^2) \cos^4(i) \right] \\ \left. - \frac{45}{128} J_4 \left(\frac{R}{P} \right)^4 \left[12 + 9e^2 + (-144 - 126e^2) \cos^2(i) \right. \right. \\ \left. \left. + (196 + 189e^2) \cos^4(i) \right] \right\} \quad \text{Rad/Sec} \end{aligned} \quad 2-2$$

$$\begin{aligned} \dot{M} = \frac{1}{a} \sqrt{\frac{u}{a}} \left\{ 1 + \frac{3}{4} J_2 \left(\frac{R}{P} \right)^2 \sqrt{1-e^2} (-1 + 3 \cos^2(i)) + \frac{3}{128} J_2^2 \left(\frac{R}{P} \right)^4 \sqrt{1-e^2} \right. \\ \bullet \left[10 + 16\sqrt{1-e^2} - 25e^2 + (-60 - 96\sqrt{1-e^2} + 90e^2) \cos^2(i) \right. \\ \left. + (130 + 144\sqrt{1-e^2} - 25e^2) \cos^4(i) \right] - \frac{45}{128} J_4 \left(\frac{R}{P} \right)^4 \sqrt{1-e^2} \\ \bullet (3 - 30 \cos^2(i) + 35 \cos^4(i)) \left. \right\} \quad \text{Rad/Sec} \end{aligned} \quad 2-3$$

with the key variables defined below

The method of osculating orbital elements allows the Keplerian orbital elements to be continuously updated without concern for the time interval between updates. It also offers a concise orbital description, which allows other important satellite communication features such as link propagation to be included in the same computer code.

The secular perturbations may be abbreviated further, while usually retaining over 99% of the accuracy of the secular terms. The oblateness effects have been found to give a regression of nodes

$$\dot{W} = -\frac{3}{2a} \sqrt{\frac{u}{a}} J_2 \left(\frac{R}{P_L} \right)^2 \cos(i) \text{ rad/sec} \quad 2-4$$

The argument of perigee changes as

$$\dot{W}_r = \frac{3}{4a} \sqrt{\frac{u}{a}} J_2 \left(\frac{R}{P_L} \right)^2 (-1 + 5 \cos^2(i)) \text{ rad/sec} \quad 2-5$$

and the mean anomaly changes as

$$\dot{M} = \frac{3}{4a} \sqrt{\frac{u}{a}} J_2 \left(\frac{R}{P} \right)^2 \sqrt{1-e^2} (-1 + 3 \cos^2(i)) \text{ rad/sec} \quad 2-6$$

W = right ascension, rad

W_p = argument of perigee, rad

R = earth radius, km

Where

- μ = earth gravitational constant
= $0.39860064 * 10^6 \text{ km}^3/\text{sec}^2$
- P = $a(1-e^2)$ = semilatus rectum
- J_2 = $1.082635 * 10^{-3}$
- e = eccentricity
- i = inclination, rad.

3.0 EOS Simulation Results

Table 3-1 indicates a first pass (labeled 1) of EOS over the McMurdo Sound ground station. It uses 1992 Landsat4 orbital elements. Table 3-1 lists the first and second passes in an abbreviated simulation output. Elevation angle, attenuation, and subsatellite point are listed as a function of time for the EOS passes. The first attenuation column is for a single link, and the second represents a dual switched link. Attenuation is chosen at the 0.997 precipitation probability level for a 1.0 km altitude precipitation layer (7,9). The subsatellite point is recognized as North Latitude and East Longitude. Time is in hours from start of the Epoch (note 1 minute increments). Range is in megameters.

Table 3-1: EOS Downlinked to Antarctica

EOS DOWNLINKED TO ANTARCTICA							TAVG(K)= 201	
EOS LINK ; X BAND GND SITE-78.11 166.2272 GFHZ= 8.2875E+09								
RP PREC. RATE(MM/HR) = 1.498039 AVAIL= .997 PRECIP. HT.= 1								
A,E,I= 7077.79 .0014055 98.39766								
MASK ANGLE= 1 DEG								
I	ELEV	(SINGLE,	DUAL,	CLEAR A)	NLAT	ELON	TIME	RANG, MM
1.000	1.079	3.592	2.756	2.219	-69.334	263.313	1.150	2.989
2.000	5.205	0.897	0.702	0.612	-72.583	258.031	1.167	2.582
3.000	10.174	0.440	0.350	0.315	-75.652	250.604	1.183	2.179
4.000	16.527	0.265	0.213	0.195	-78.396	239.637	1.200	1.785
5.000	25.313	0.172	0.140	0.130	-80.528	223.122	1.217	1.408
6.000	38.572	0.115	0.095	0.089	-81.569	200.274	1.233	1.071
7.000	58.628	0.081	0.068	0.065	-81.124	175.823	1.250	0.825
8.000	68.386	0.073	0.062	0.060	-79.380	156.536	1.267	0.765
9.000	47.904	0.095	0.079	0.075	-76.841	143.511	1.283	0.929
10.000	31.266	0.140	0.114	0.107	-73.880	134.820	1.300	1.230
11.000	20.539	0.212	0.172	0.158	-70.688	128.769	1.317	1.591
12.000	13.127	0.337	0.269	0.245	-67.364	124.337	1.333	1.978
13.000	7.543	0.604	0.476	0.423	-63.957	120.938	1.350	2.378
14.000	3.036	1.598	1.238	1.049	-60.496	118.227	1.367	2.783
15.000	2.627	1.868	1.443	1.212	-66.368	242.138	2.783	2.835
16.000	6.994	0.654	0.515	0.456	-69.714	238.066	2.800	2.432
17.000	12.329	0.360	0.287	0.260	-72.947	232.587	2.817	2.036
18.000	19.251	0.226	0.183	0.169	-75.988	224.838	2.833	1.653
19.000	28.865	0.151	0.123	0.115	-78.680	213.341	2.850	1.298
20.000	42.619	0.105	0.087	0.082	-80.714	196.072	2.867	1.004
21.000	57.172	0.082	0.069	0.066	-81.596	172.672	2.883	0.837
22.000	52.827	0.088	0.073	0.070	-80.981	148.547	2.900	0.875
23.000	37.117	0.119	0.098	0.092	-79.119	130.029	2.917	1.097
24.000	24.921	0.174	0.142	0.132	-76.517	117.610	2.933	1.419
25.000	16.414	0.267	0.215	0.197	-73.522	109.294	2.950	1.786
26.000	10.144	0.441	0.351	0.315	-70.311	103.472	2.967	2.175
27.000	5.200	0.898	0.702	0.613	-66.975	99.182	2.983	2.574
28.000	1.081	3.592	2.756	2.219	-63.561	95.876	3.000	2.979

Elevation Angles at McMurdo

The time variation of elevation of EOS or Landsat over McMurdo Sound may be seen with some elevation and attenuation plots. The first satellite pass over McMurdo may be seen in the lower left corner of Figure 3-1. Elevation is shown with data points, and the corresponding atmospheric attenuation of a hypothetical 27 GHz link is shown with a solid line. The data points are chosen at one minute intervals, and most passes are seen to be limited to less than 10 minutes. The long period between passes is taken out of the figure so that almost two days of satellite passes may be fitted onto the figure. The passes are seen to group as several high passes followed by a group of very low passes barely above the assumed 5 degree mask. The simulated elevation after 16 days is shown in the following figure (Figure 3-2). The figure is strikingly similar to that for the initial passes, but other methods should be used to confirm a true 16-day periodicity.

Figure 3-3 shows the result of an autocorrelation of the entire 21.75-day elevation simulation with itself. The autocorrelation peaks at 1.0 when the series is cross correlated with itself for zero phase delay. It is seen to have a cyclic correlation with later passes. As the lag times get longer, the cross correlation is rarely over 0.4 until the lag time is set at 16 days (Figure 3-4) when the autocorrelation peaks at over 0.7. Longer phase differences also match the initial autocorrelation function (labeled Rx) well, but not perfectly.

Elevation Probability Density Functions

Elevation angle probability density functions (pdfs) have been interesting and important since the early '60s. Lutz and Dorosheski (9) recognized that satellite ground station economics depended on the ground station elevation angles. They looked at the entire ensemble of ground stations seen by a geosynchronous satellite, and treated the ensemble of elevation angles as a pdf. Sugai and Christopher (10) derived a simpler pdf which was useful for medium altitude to geosynchronous orbits. The simpler pdf was of the form:

$$p(E) = \frac{\left(\frac{\pi}{180}\right) \cos\left(\frac{\pi}{180}E\right) \left(1 - 2s \sin\left(\frac{\pi}{180}E\right)\right)}{\left(1 - s \cos^2\left(\frac{\pi}{36}\right) - \sin\left(\frac{\pi}{36}\right)\right)} \quad 3-1$$

Where

- E = elevation, deg.
- E_{\min} = minimum elevation, deg. = 5°
- s = earth radius/semimajor axis = 1/6.6227 for geo satellite

Figure 3-5 shows the emphasis on low elevation angle for the pdf generated by equation 3-1 for Geo altitudes. However, the 16-day simulation of Landsat4 passes over McMurdo Sound and shows an entirely different emphasis on low elevation angles, as seen in Figure 3-6. A fit for the McMurdo elevation pdf may be found as:

$$p(E) = 0.00064269 \csc^2\left(\frac{\pi}{180}E\right) + \frac{0.003228 \pi \cos\left(\frac{\pi}{180}E\right) \left(1 - 1.087 \sin\left(\frac{\pi}{180}E\right)\right)}{\left(1 - 0.5435 \cos^2\left(\frac{\pi}{36}\right) - \sin\left(\frac{\pi}{36}\right)\right)} \quad 3-2$$

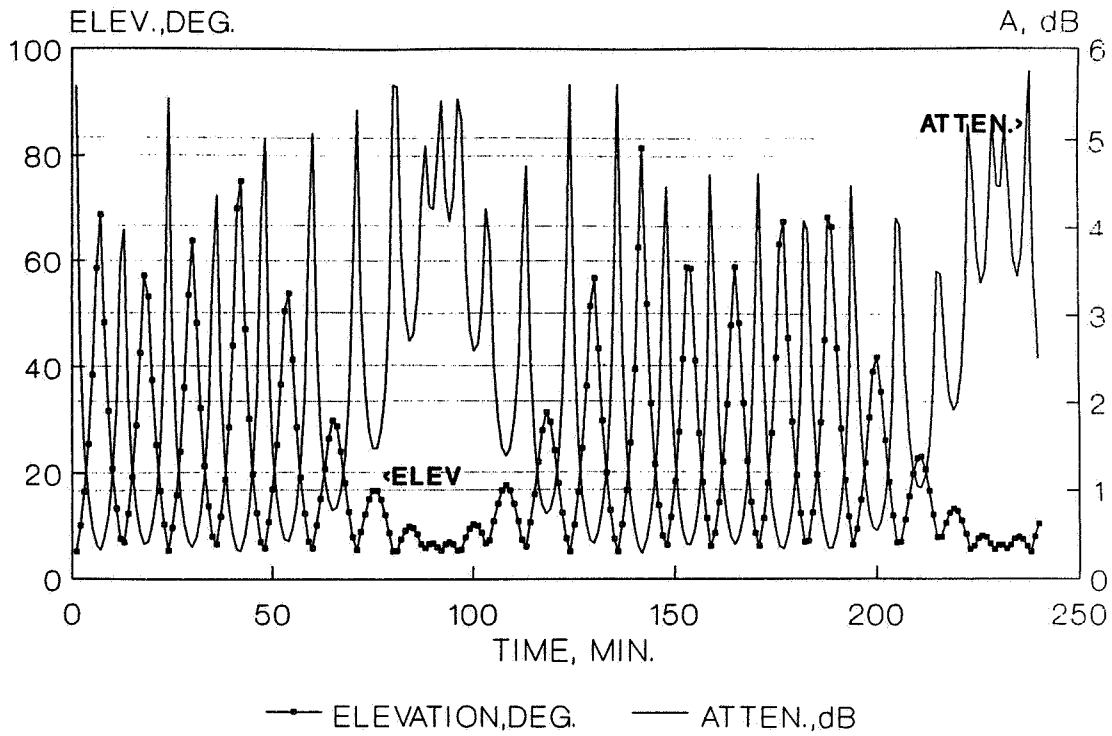


Figure 3-1: Elevation for McMurdo-EOS for Successive Passes

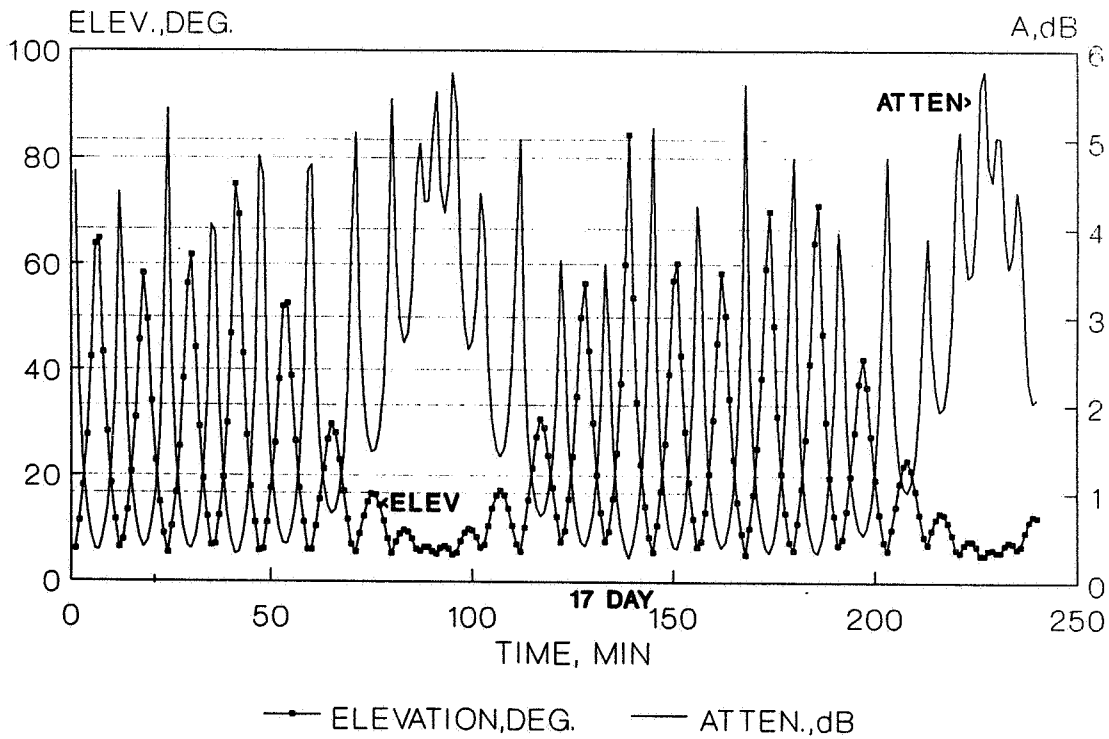


Figure 3-2: Elevation at 16 Days for McMurdo-EOS

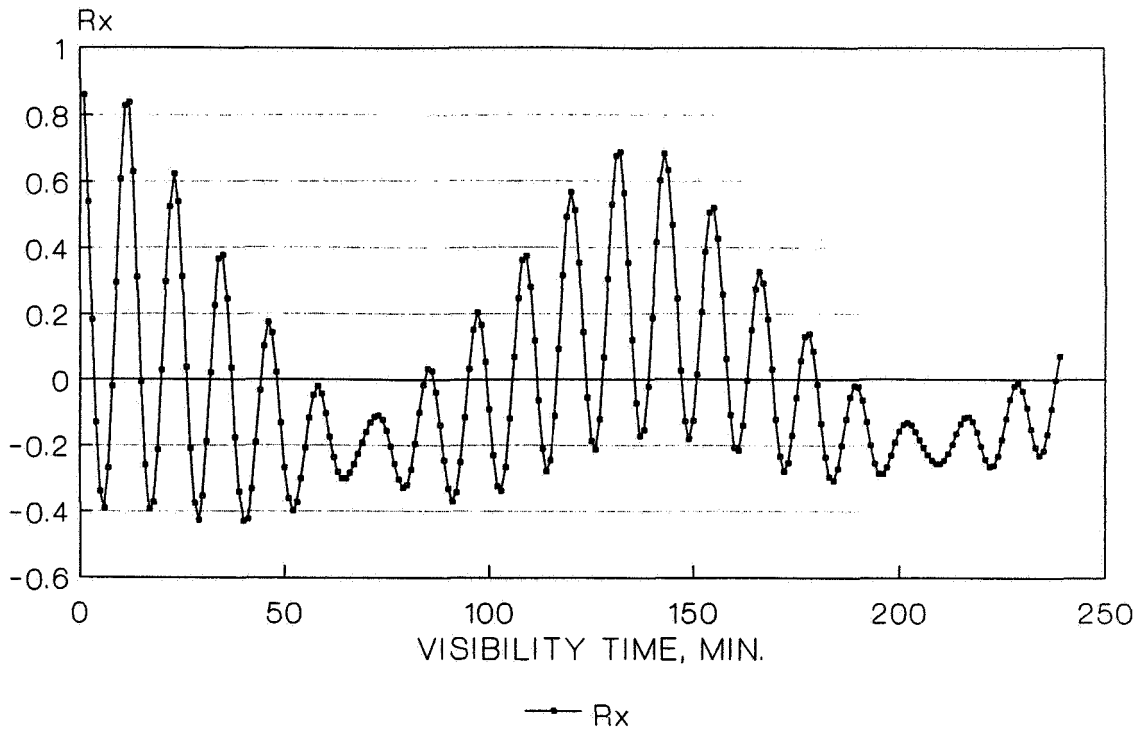


Figure 3-3: Elevation Autocorrelation vs. Lag Time, Min.

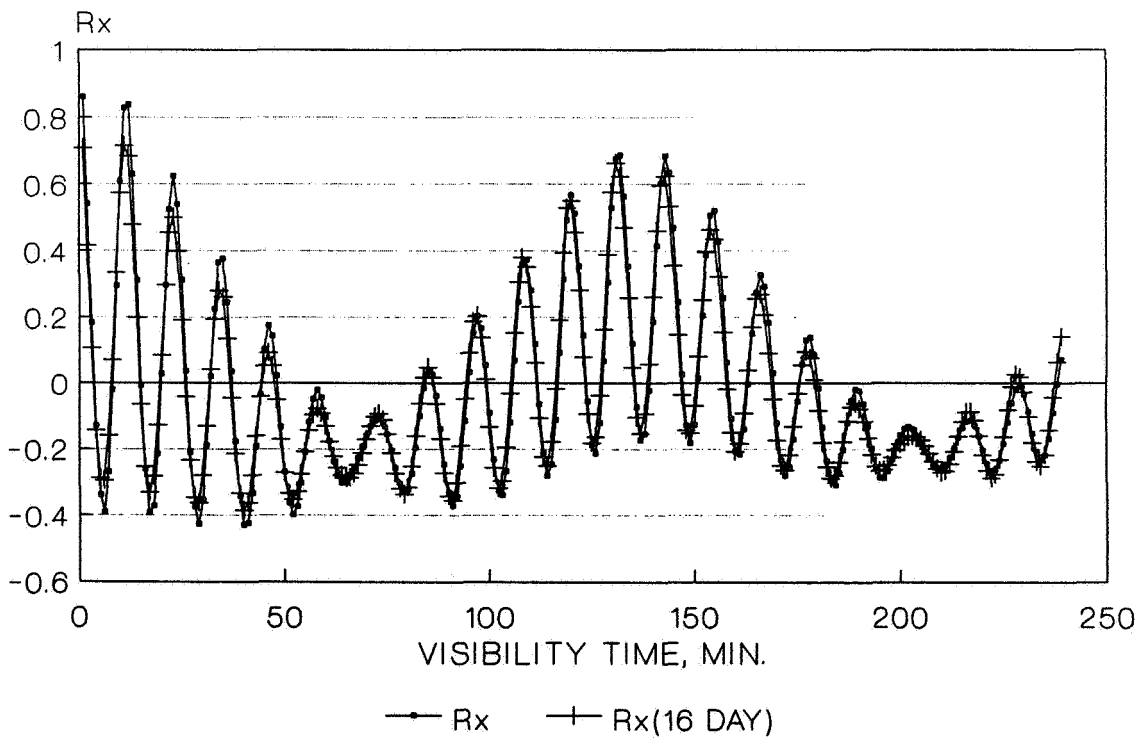


Figure 3-4: Elevation Autocorrelation Compared to 16-Day Autocorrelation

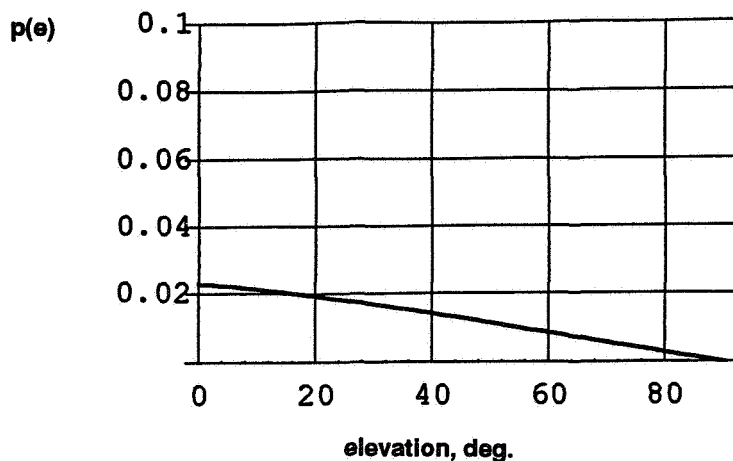


Figure 3-5: Ground Elevation Probability Density Function to Geosynchronous Satellite

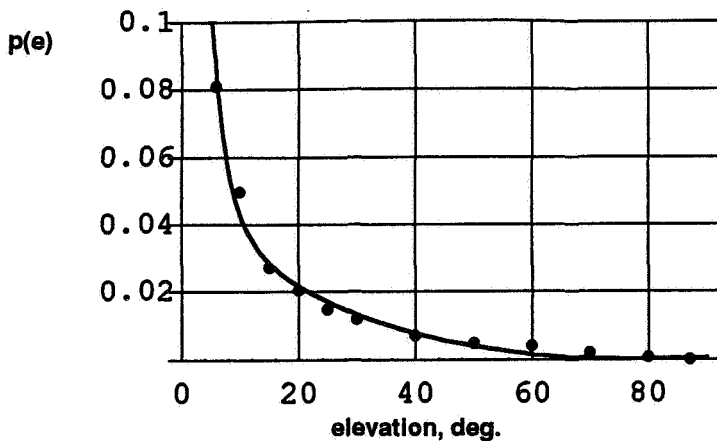


Figure 3-6: Elevation PDF for McMurdo Sound-EOS

Equation 3-2 is compared with the McMurdo data in Figure 3-7. It is useful, because it emphasizes the importance of the ground site's ability to acquire Landsat or EOS quickly at the horizon. The overall communication time available increases sharply if the minimum elevation at the ground site can be 3 deg., for example, rather than 5 deg.

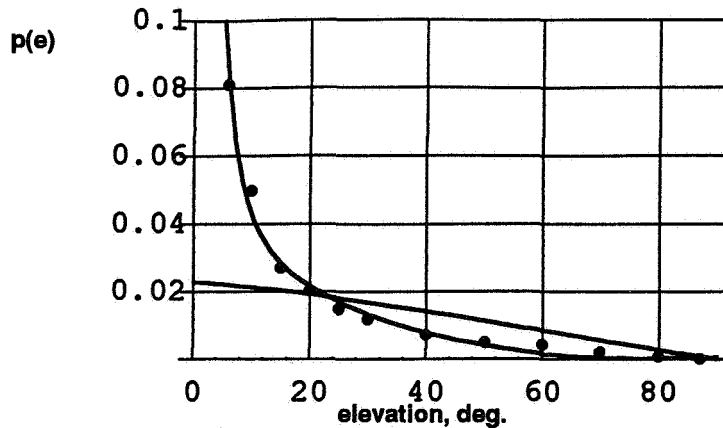


Figure 3-7: McMurdo Elevation PDF Compared to Geosynchronous PDF

Appendix A shows the full 16-day periodicity of actual Landsat 4 elements (assumed to be identical to EOS elements here). The interarrival interval statistics and other link statistics may be summarized as in Table 3-2.

Table 3-2: EOS Downlink Statistics to McMurdo Sound

F = 8.28 GHz Precipitation Height = 1.0 km 0.997 Availability

	Mean	Standard Deviation	Maximum
in view, hr (min)	0.1848 (11.08)	0.032 (1.92)	0.2167 (13.0)
out of view	1.4609 (87.6)	0.0526 (3.15)	1.550 (93.0)
attenuation, dB	0.70	0.80	3.59
elevation (deg)	17.653	16.868	90
Rate (deg/sec)			
elevation	0	0.1353	0.586
azimuth	-0.057	0.3495	18.82

With maximum antenna rates from a separate run with 5 sec. increments

4.0 Outages For General Sun Synchronous Satellites

A large range of altitudes of sun synchronous satellites may be considered for use with a McMurdo Sound ground site. Low-altitude, low-cost satellites such as reported for a November 1994 Pegasus launch may be considered a prime opportunity for the McMurdo site. This section shows the variation in outage statistics as a function of altitude.

The inclination of sun synchronous satellites is actually function of altitude (Figure 4-1). This feature, along with the increased viewing region associated with high altitudes, has noticeable effects on outage times and viewing times. Long simulation can be done at each altitude and outage statistics extracted. Figure 4-2 shows the mean outage times ranging from 1.45 hours at 550 km altitude to 1.5 hours at altitudes slightly greater than 1000 km. Altitudes much less than 500 km, however, may actually skip an orbit before seeing McMurdo again. This appears as long outage time in Figures 4-2 and 4-3.

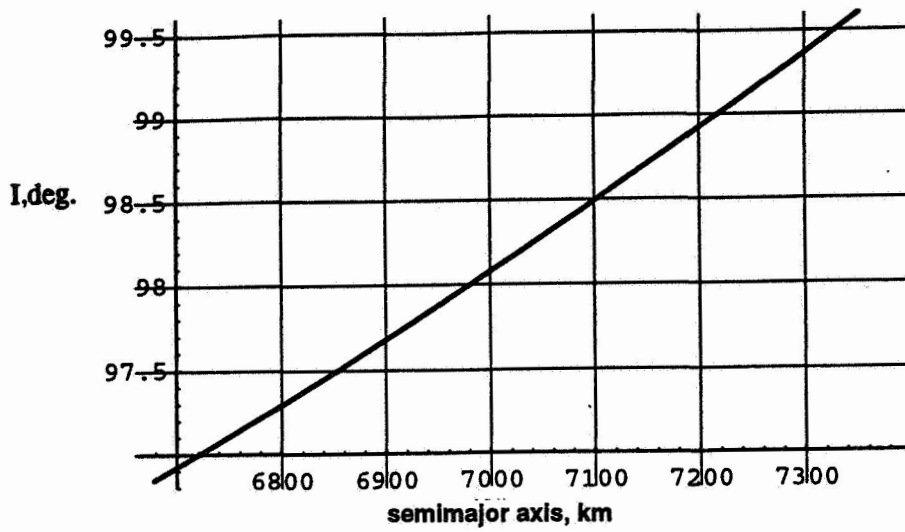


Figure 4-1: Required Inclination for Sun Synchronous Satellites

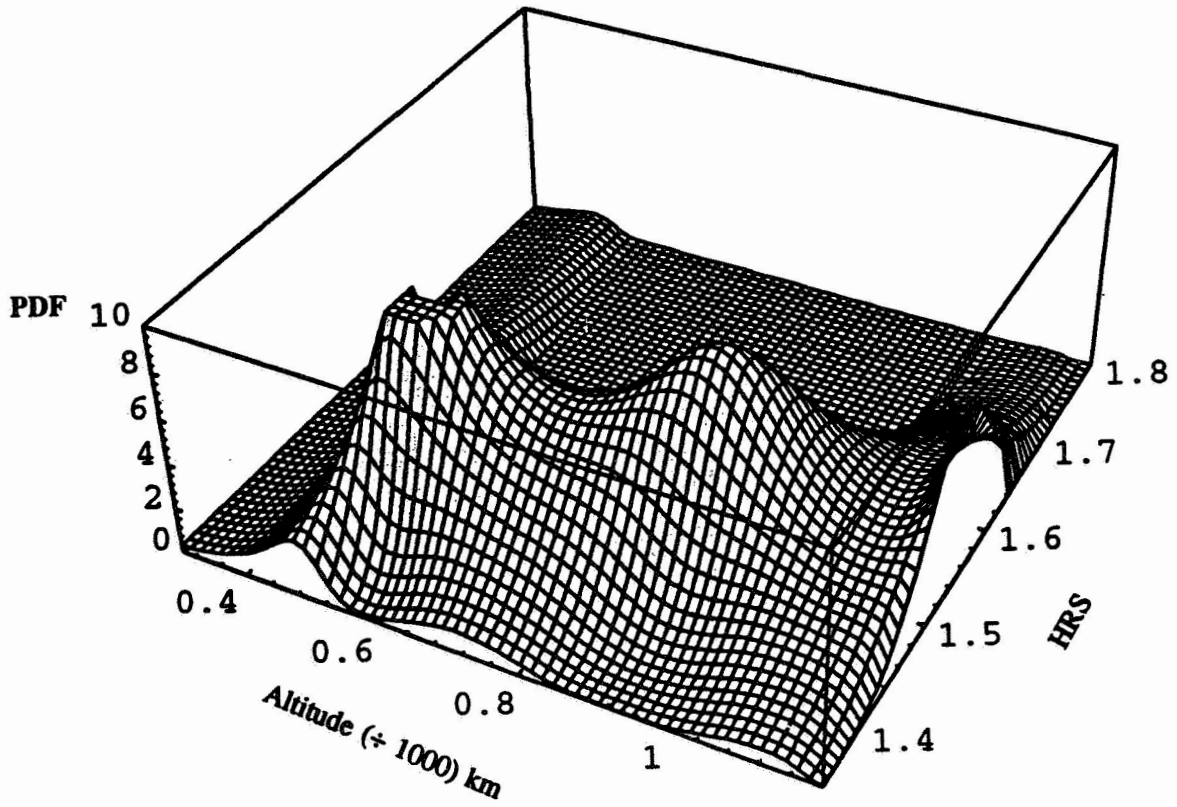


Figure 4-2: Outage PDF vs. Altitude1000

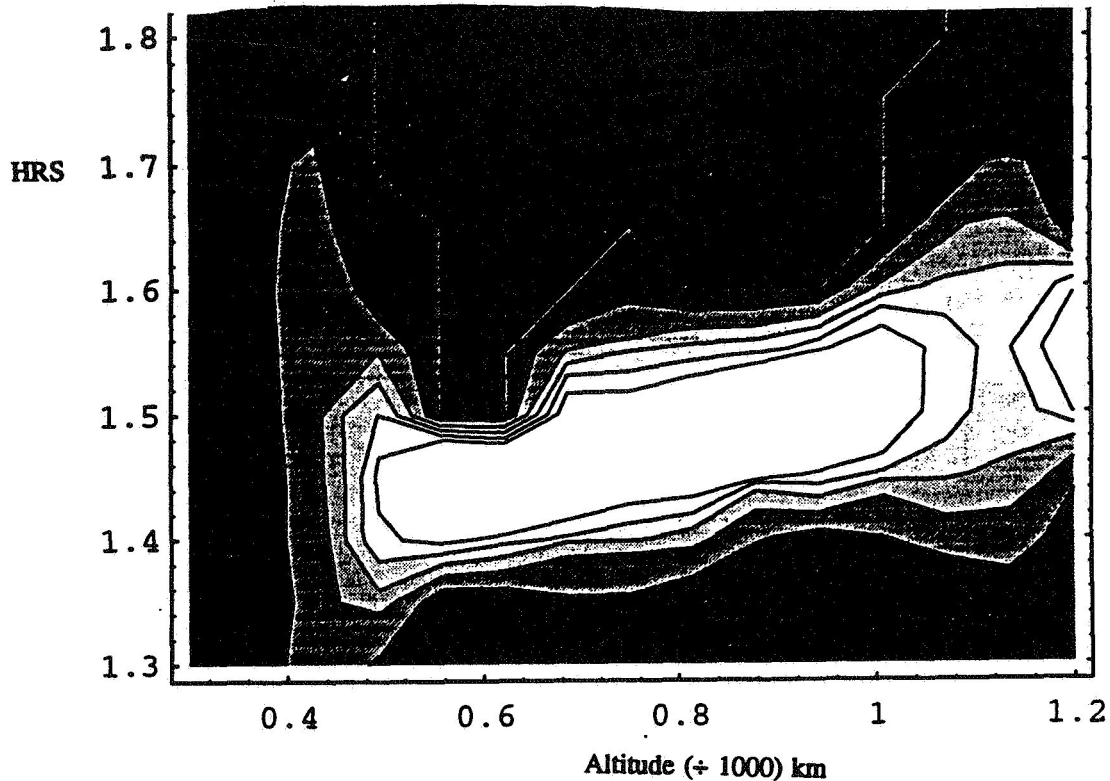


Figure 4-3: Contour Plot of Probability Density Function

Conclusions

We have discussed outage intervals, innage intervals, and dynamic propagation losses for a sun synchronous-McMurdo Sound ground site. Antenna rates have also been extracted from the link dynamics. McMurdo Sound has been shown to be an attractive ground site for a wide range of sun synchronous satellites from 500-1000 km altitude. EOS and Landsat were examined in detail. The observed 16-day Landsat periodicity was closely reproduced in the simulation. A unique elevation probability density function for McMurdo Sound was shown.

Acknowledgments

D. Thring of Stanford Telecom introduced legibility to the equations. J. Murphy pointed out, at the February 1996 AIAA Conference, that Analytic Graphics Inc. has also enjoyed a successful combination of speed and accuracy with the method of osculating elements.

Abbreviated References

- [1] A. H. Jackson, P. Christopher, "Optimum Satellite Relay Positions," Proc. of Flight Mechanics and Estimation Symposium, NASA GSFC, May 1994.
- [2] H. J. Liebe, P. W. Rosenkranz, and G. A. Hufford, "Atmospheric 60 GHz Oxygen Spectrum: New Laboratory Measurements and Line Parameters," J. Quantum Spectroscopy and Radiative Transfer, Vol. 48, No. 5/6, pp. 629-643, 1992.
- [3] F. Moulton, "Celestial Mechanics," Macmillan, 1914.
- [4] D. Brouwer, "Solution of the Problem of Artificial Satellite Theory Without Drag," Astron J., Vol. 64, No. 9, 1959, pp. 378-396.

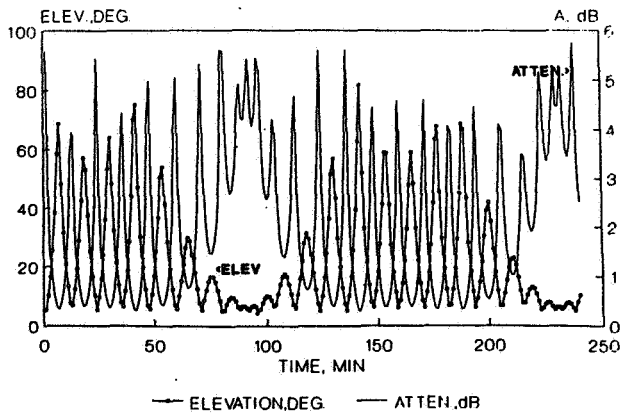
- [5] Y. Kozai, "The Motion of a Close Earth Satellite.," *Astron J.* Vol. 64, No. 9, 1959, pp. 367-377
- [6] L. Blitzer, M. Weisfield, and D. Wheelon, "Perturbation of a Satellite Orbit Due to the Earth's Oblateness," *J. Appl. Physics* 27, No. 10, Oct. 1956, pp. 1141-1149.
- [7] L. J. Ippolito, R. D. Kaul, and R. G. Wallace, "Propagation Effects Handbook for Satellite Systems Design," NASA Reference Publication 1082 (second edition), Dec. 1981.
- [8] R. K. Crane, "Prediction of Attenuation by Rain," *IEEE Transactions on Communications*, Vol. Com 28, No. 9, September 1980.
- [9] S.G. Lutz and G. Dorusheski, "Earth Antenna Beam Elevation Angles of Multiple-Access Satellite Communication Systems," Hughes Research Lab., Malibu, CA, Dept. 7, Contract NASW-495, August 1963.
- [10] I. Sugai and P. Christopher, "Note on Distribution of Antenna Elevation Angles in Comsat System," *IEEE Trans. on Aerospace and Electronic Systems (Corres.)*, Nov. 1967, pp. 981-982.
- [11] A. K. Kamal, P. Christopher, "Communication at Millimeter Wavelengths," *Proc. of International Communications Conference*, Denver, June 1981.
- [12] S. Wolfram, *MATHEMATICA a System for Doing Mathematics by Computer*, Second Edition, Adios Wesley Publishing Co., 1991.

APPENDIX A: CONDENSED ELEVATION ANGLE RECORD AT MCMURDO SOUND

A tabular output for ground antenna angles, times, and propagation loss is indispensable, and can be obtained from an April 1995 STel report. The figures below extract all the outage time to allow almost 1.7 days of EOS passes to be presented on each figure. They also allow a hypothetical 27 GHz downlink to be examined for atmospheric losses (11). Figure A-1 shows elevation angle vs time for the first 1.7 days. A quasi-cyclic period can be seen every day when very low elevation angles are seen at McMurdo. The elevation angles (data points) are read off the left scale. Atmospheric attenuation is read off the right scale.

Figures A-2 to A-10 extend the elevation angle record consecutively to 17.28 days.

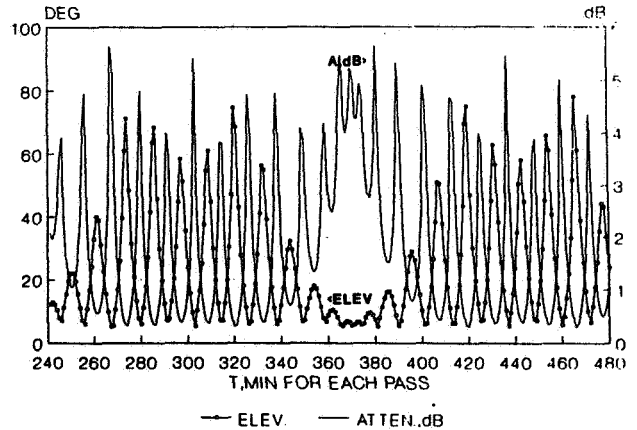
ELEVATION FOR MCMURDO-EOS FOR SUCCESSIVE PASSES



EXAMINE 27 GHz LINK LOSS AT P=0.997

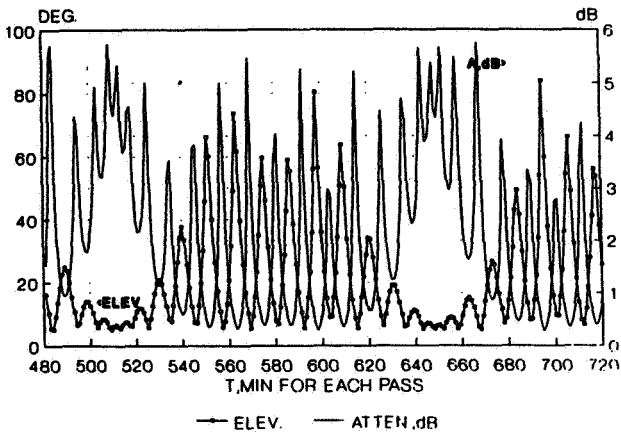
A-1

MCMURDO PASSES; DAYS 1.7- 3.3



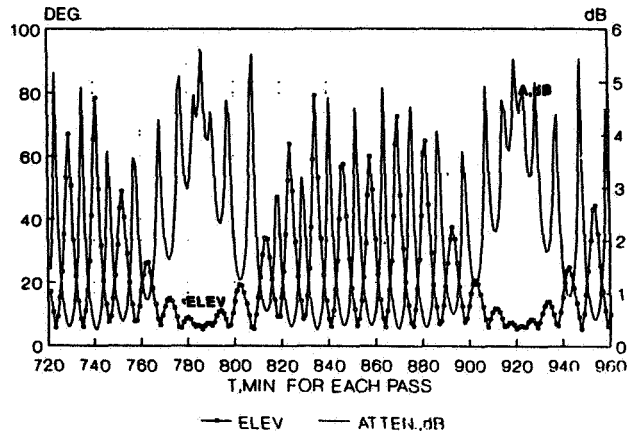
A-2

MCMURDO PASSES; DAYS 3.3-5.1



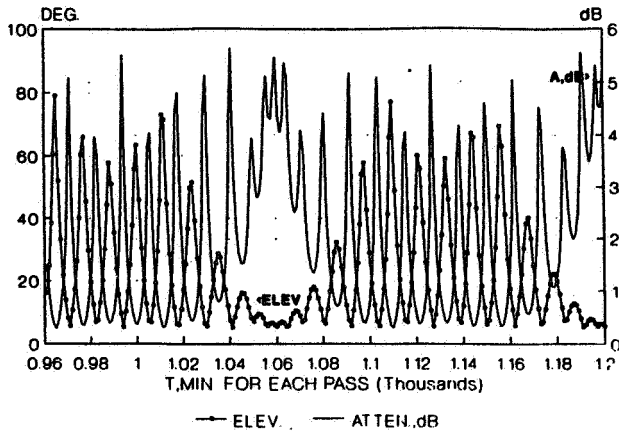
A-3

MCMURDO PASSES; DAYS 5.1-6.98



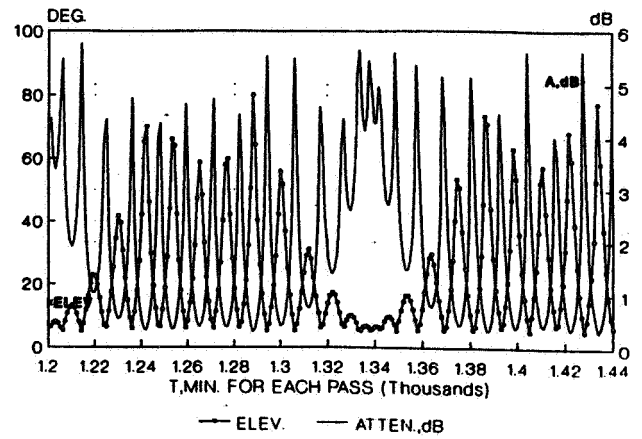
A-4

McMURDO PASSES; DAYS 6.98-8.63



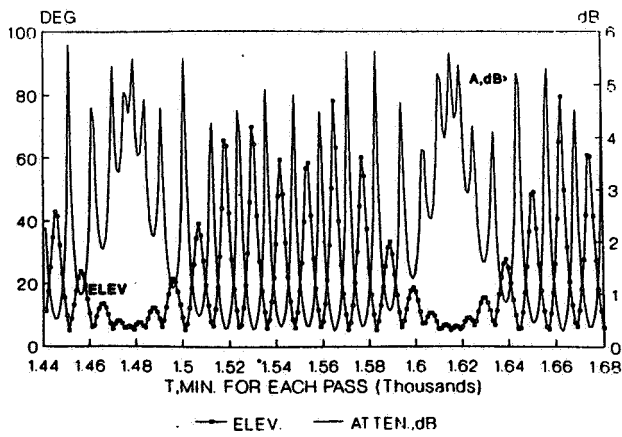
A-5

McMURDO PASSES; DAYS 8.63-10.34



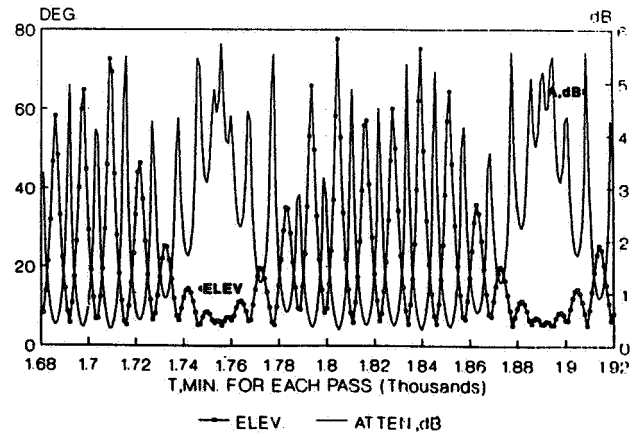
A-6

McMURDO PASSES; DAYS 10.34-12.07



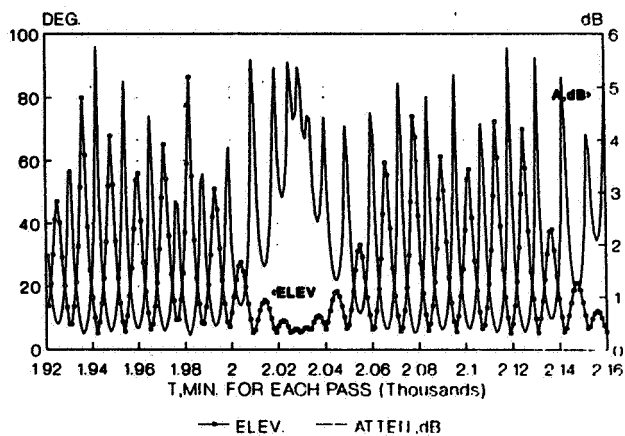
A-7

McMURDO PASSES; DAYS 12.1-13.9 DAYS



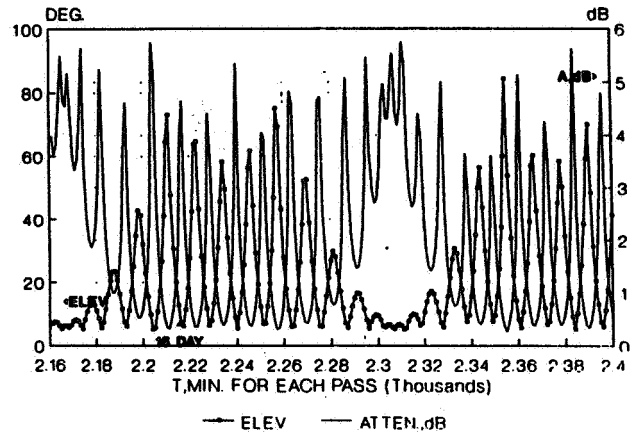
A-8

McMURDO PASSES; DAYS 13.9-15.56 DAYS



A-9

McMURDO PASSES; DAYS 15.56-17.28



A-10

Heuristic Modeling for TRMM Lifetime Predictions*

P. S. Jordan and P. J. Sharer
Computer Sciences Corporation
Lanham-Seabrook, Maryland, USA 20706

R. L. DeFazio
National Aeronautics and Space Administration
Goddard Space Flight Center
Greenbelt, Maryland, USA 20771

Abstract

Analysis time for computing the expected mission lifetimes of proposed frequently maneuvering, tightly altitude-constrained, Earth-orbiting spacecraft has been significantly reduced by means of a heuristic modeling method implemented in a commercial-off-the-shelf spreadsheet product (QuattroPro) running on a personal computer (PC). The method uses a look-up table to estimate the maneuver frequency per month as a function of the spacecraft ballistic coefficient and the solar flux index, then computes the associated fuel use by a simple engine model. Maneuver frequency data points are produced by means of a single 1-month run of traditional mission analysis software for each of the 12 to 25 data points required for the table. As the data point computations are required only at mission design start-up and on the occasion of significant mission redesigns, the dependence on time-consuming traditional modeling methods is dramatically reduced. Results to date have agreed with traditional methods to within 1 to 1.5 percent.

The spreadsheet approach is applicable to a wide variety of Earth-orbiting spacecraft with tight altitude constraints. It will be particularly useful to such missions as the Tropical Rainfall Measurement Mission (TRMM), scheduled for launch in 1997, whose mission lifetime calculations are heavily dependent on frequently revised solar flux predictions.

1.0 Introduction

In the past, TRMM lifetime predictions have been performed using the Goddard Mission Analysis System (GMAS) average variation-of-parameters (VOP) propagator—including detailed modeling of atmospheric drag, solar radiation pressure, and the effects of the nonspherical Earth—followed by an elaborate data processing effort involving several PC and mainframe routines and a spreadsheet. In addition, because TRMM's tight altitude constraints require frequent maneuvering (Reference 1), the calculated lifetime is heavily dependent on solar flux predictions (produced by Dr. Kenneth Schatten, References 2 and 3) and must be recomputed following each of the approximately quarterly updates of those predictions. The spreadsheet-based lifetime estimation tool, using a heuristic modeling method that is based on 25 years of mission design experience, has been developed to provide lifetime analysis of the scope required for such projects at acceptable cost. Results to date have agreed with traditional analysis methods to within 1 to 1.5 percent, with a time reduction of as much as 95 percent for a full study incorporating six of Dr. Schatten's nine predicted flux-level cases.

2.0 The Spreadsheet Concept

The underlying assumption of the spreadsheet approach to mission lifetime estimation is that, within a given set of mission altitude constraints, maneuver frequency is ultimately dependent on two parameters: the prevailing solar flux level and the ballistic coefficient of the spacecraft. To implement this assumption, time-independent maneuver-frequency data points, indexed by ballistic coefficient and predicted solar flux level, are computed as described in Section 3 and provided in a look-up table that the spreadsheet draws on for its computations. Using as indices the ballistic coefficient and solar flux level predicted for a given month, the spreadsheet interpolates

* This work was supported by the National Aeronautics and Space Administration (NASA)/Goddard Space Flight Center (GSFC), Greenbelt, Maryland, under Contract NAS 5-31500.

between the data points in the table to predict the number of maneuvers for that month, then uses a simple engine model to compute the fuel use associated with that maneuver activity for the current propulsion system state. The available fuel is then decremented, the propulsion system state is updated, and computation continues for the succeeding month, iterating until all available fuel has been used. At the conclusion of the computation, all input and computed values are available in the spreadsheet for continuing analysis and/or convenient graphical output.

Traditional propagation methods, based on the spacecraft design and altitude constraints for the given mission, are used to design any maneuvers needed to achieve the initial target orbit and to compute the time-independent maneuver frequency data points for the look-up table. These computations are required only at mission design start-up and on the occasion of significant mission redesigns. It is further recommended that a single traditional lifetime study be performed at mission design start-up for purposes of spreadsheet verification and estimation of the Semi-Annual Effect (Section 3.3). Detailed descriptions of key concepts, models, and algorithms implemented in the spreadsheet, and a discussion of supporting functions, are provided in Sections 3 and 4. Full user-oriented documentation is provided in the spreadsheet.

3.0 The Heuristic Model Rule Base—Producing the Look-Up Table

The methods and assumptions involved in producing the time-independent maneuver-frequency data points for the look-up table are described below.

3.1 Determining the Solar Flux and Ballistic Coefficient Index Values

Maximum and minimum solar flux and ballistic coefficient index values for the maneuver frequency table are selected to provide comfortable margins above and below the ranges of those values expected during the mission lifetime. Intermediate index values are computed by the spreadsheet based on the desired matrix dimensions. The ballistic coefficient computation is given below.

3.2 Computing the Data Points

The maneuver frequency look-up table comprises as many as 25 data points (depending on mission needs—TRMM uses 12) in units of maneuvers per month. Each of the data points is computed in an “average” 1-month propagation run using the GMAS VOP propagator or another appropriate propagation tool with full modeling capabilities. Inputs for the run include the ballistic coefficient and Schatten flux values defined as the indices (see above) for the data point being computed, the maximum and minimum altitudes defined as the mission stationkeeping constraints, and parameters reflecting the modeling assumptions listed below. The resulting data points can be used for all subsequent lifetime predictions for the mission in question, unless the altitude requirements are redefined or the spacecraft itself is redesigned so dramatically that the original range of ballistic coefficients is no longer sufficient. In such cases, the data points must be recomputed and/or additional points must be provided.

3.2.1 Atmospheric Drag Assumptions

For computation of the data points, the TRMM mission uses the Jacchia-Roberts (J-R) atmospheric drag model, with a specially prepared “flat” (or constant-flux) J-R data file reflecting the Schatten flux value defined as the index for the data point being computed. (Preparation of the special J-R data files is described in the spreadsheet documentation page.)

Because a single ballistic coefficient value, defined as

$$\text{Ballistic Coefficient} = \text{Spacecraft Mass} / (\text{Spacecraft Cross-Section} * \text{Drag Coefficient})$$

cannot be input directly into the GMAS propagation software, the value specified as the ballistic coefficient index for the data point being computed is obtained by judicious selection of the component factors, which are input separately. The components are chosen as follows: the spacecraft cross-sectional area and the drag coefficient are held constant at the mission-specified values. The spacecraft mass is computed from these values and the desired ballistic coefficient value by the following reformulation of the ballistic coefficient equation:

$$\text{Spacecraft Mass} = \text{Ballistic Coefficient} * \text{Spacecraft Cross-Section} * \text{Drag Coefficient}$$

Design changes in either the spacecraft mass or spacecraft cross-section will not require additional data-point computation unless the range of ballistic coefficients resulting from the redesign exceeds that provided for in the look-up table index.

3.2.2 The Average Month

The propagations used to compute the data points for the look-up table are run for one average month, which (for missions using the Jacchia-Roberts atmospheric drag model, see Section 3.3) is defined to be September of a convenient mid-mission year. The duration of the average month is chosen as described below.

As Section 3.2.1. explains, the maneuver frequencies computed for the average month are based on a drag model that uses a flat solar flux data file, which is necessary to preserve the time-independent nature of the look-up table. It results, however, in a maneuver frequency data point that is based on a series of maneuvers performed at fixed intervals across the month. In a “natural” month, by contrast, solar flux index values will either increase or decrease as time advances. In periods approaching solar maximum, the solar flux levels increase across the month, producing increasing drag and a proportional shortening of the intervals between maneuvers. In periods approaching solar minimum, decreasing solar flux leads to decreasing drag and a proportional lengthening of the intervals between maneuvers. A natural month could, therefore, require more or fewer maneuvers than the estimate provided by the average month, depending on the phase of the solar cycle.

It was observed that the maneuver frequency estimate could be improved, without jeopardizing the time-independent nature of the look-up table, by choosing the average month to be longer (by 1 day) for missions prior to solar maximum and shorter (by 1 day) for missions prior to solar minimum. Thus, a maneuver in the *last day* of the average month will be *omitted* from the maneuver frequency data point when maneuver intervals are increasing (after solar maximum). Conversely, a maneuver in the *first day after* the average month will be *included* in the maneuver frequency data point when maneuver intervals are decreasing (prior to solar maximum).

The rule of thumb for the duration of the average month is as follows:

- 31 days for a mission primarily on the increasing leg of the solar cycle
- 29 days for a mission primarily on the decreasing leg of the solar cycle
- 30 days for a mission that evenly bridges either the maximum or the minimum

3.2.3 Computing the Data Point Value

The data point resulting from each 1-month propagation is the number of whole and fractional maneuver intervals ($N.nn$) occurring in the average month for the ballistic coefficient and flux level being modeled. Fractional maneuver intervals are used instead of integer maneuvers to ensure that the decay time remaining after the final maneuver in each 1-month computation is fully accounted for in the lifetime estimation. The $N.nn$ value is determined as follows:

$$N = \text{the number of impulsive maneuvers actually modeled within the average month, and}$$

$$.nn = (B - A) / (C - A)$$

where

- A = the date of the final maneuver in the average month
- B = the date of the end of the average month (see above)
- C = the date of the first maneuver following the end of the average month

3.3 Dealing With the Semi-Annual Effect

The semi-annual effect (SAE) is an empirically determined seasonal variation in maneuver frequency that is applied in the Jacchia-Roberts drag model as a variation in atmospheric density both by season and by altitude (Reference 4). Because the TRMM mission design uses the Jacchia-Roberts model, the SAE is clearly an issue for

this mission. However, some other drag models (such as the Harris-Priester model) do not apply this variation, so its use may not be appropriate to all missions. For this reason, an approximation of the SAE, as described below, is provided as a user option in the spreadsheet. Maneuver frequency studies for the TRMM spacecraft using the same Schatten solar flux prediction set, but with the SAE turned on in one and off in the other, are shown in Figures 1 and 2, respectively.

The SAE has raised two important questions in development of the spreadsheet. First, given that the maneuver frequency look-up table must provide a clean, time- and season-independent representation of maneuver frequency as a function of ballistic coefficient and flux level *alone*, and given that data points for the table are computed using the Jacchia-Roberts drag model, how can the SAE be removed from the table? Second, once the SAE is removed to provide time-independent data points for the table, how can it be reapplied to the resulting time-dependent maneuver-frequency profile once the mission lifetime computation is complete?

The answer to the first question is illustrated in Figure 3. As shown there, the maneuver frequency curve from a recent traditional TRMM lifetime study was smoothed using a standard curve-fitting routine, then plotted against the original unsmoothed curve. The seasonal variation that characterizes the SAE is clearly evident in the original curve, in which the first month of each season has been marked. The smoothed curve is completely free of seasonal effects. (It is interesting to note that its linear profile suggests that of the Schatten index curve for the period, only flatter, as if modified by the influence of the ballistic coefficient curve from the same lifetime study.) Note that the September frequency point from the original curve lies on or near the September frequency point from the smoothed curve in all mission years. For this reason, the month of September is assumed to be the month in which the pure maneuver frequency (computed from ballistic coefficient and solar flux level alone) is least affected by the SAE as applied by the Jacchia-Roberts atmospheric model. September was, therefore, selected as the average month for computation of the data points for the maneuver frequency look-up table.

Question two, regarding the SAE adjustment to be applied at user option to the maneuver frequencies computed from the look-up table, is addressed by analysis of the differences between the original curve from Figure 3 (“GMAS: + JR SAE” in Figure 4) and the maneuver frequency profile for the same period as computed in the spreadsheet (“Sheet: no SAE” in Figure 4). The data points from these two curves were differenced for each of the 44 months of the traditional mission lifetime study and an adjustment factor was produced in each case by the following formula:

$$\text{Adjustment factor} = (\text{GMAS mnvr freq} - \text{spreadsheet mnvr freq}) / \text{spreadsheet mnvr freq}$$

A monthly SAE adjustment factor was computed for each calendar month as the average of the individual adjustment factors produced for the three or four occurrences of that calendar month in the lifetime study. (For example, the adjustment factor to be applied each January from 1998 through 2001 was computed as the average of the individual adjustment factors produced for January 1998, January 1999, January 2000, and January 2001). The adjustment factors produced in this manner for each of the 12 calendar months were input into the spreadsheet together with the corresponding Schatten solar flux predictions (the January adjustment factor with each January flux level, and so on) and the spreadsheet lifetime study was repeated. The resulting maneuver frequency curve is shown as “Sheet: + SAE Adj” in Figure 4. Figures 1 and 2 further illustrate the effect of this adjustment. For new missions, the SAE adjustment factors can be prepared in the same way, using the traditional lifetime study performed to verify the spreadsheet results. (See the spreadsheet documentation page for details.) A flag, provided on the spreadsheet’s data input page, allows the adjustment to be selected or deselected with ease.

4.0 Performing Lifetime Analysis

This section discusses the set up, computation sequence, and key mathematical models involved in lifetime computation via the spreadsheet. The complete spreadsheet functional outline is given in Reference 5.

4.1 Setting Up the Spreadsheet for Mission Design

In addition to computation of data points for the look-up table, spreadsheet initialization for mission design includes the operations and data inputs outlined below.

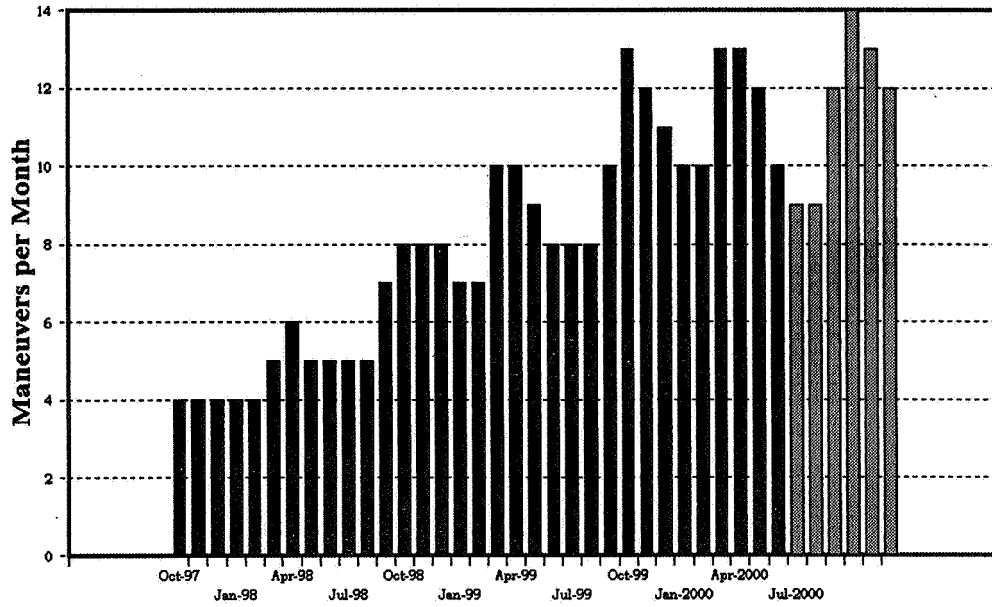


Figure 1. Representative TRMM Lifetime With Semi-Annual Effect

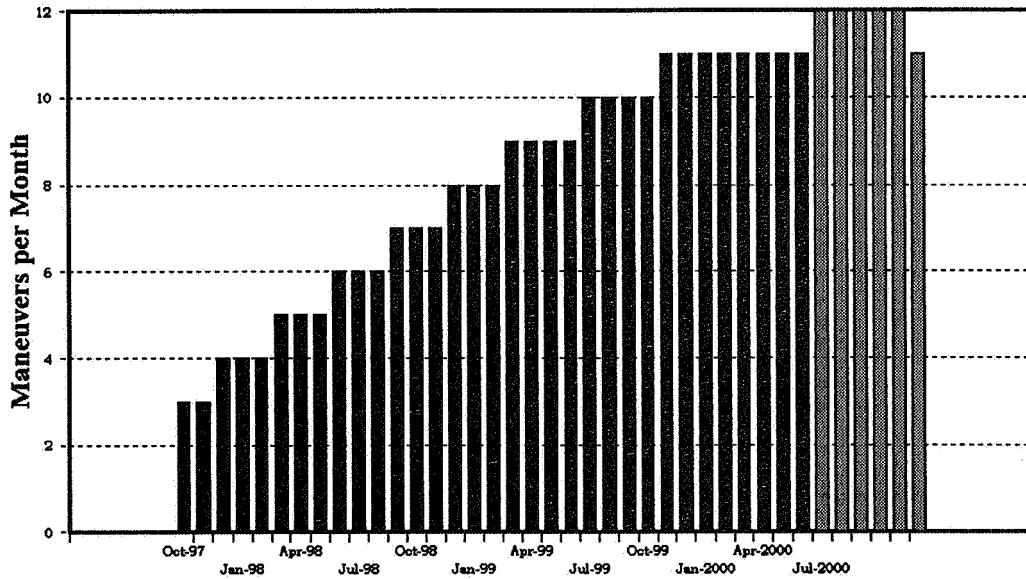


Figure 2. Representative TRMM Lifetime Without Semi-Annual Effect

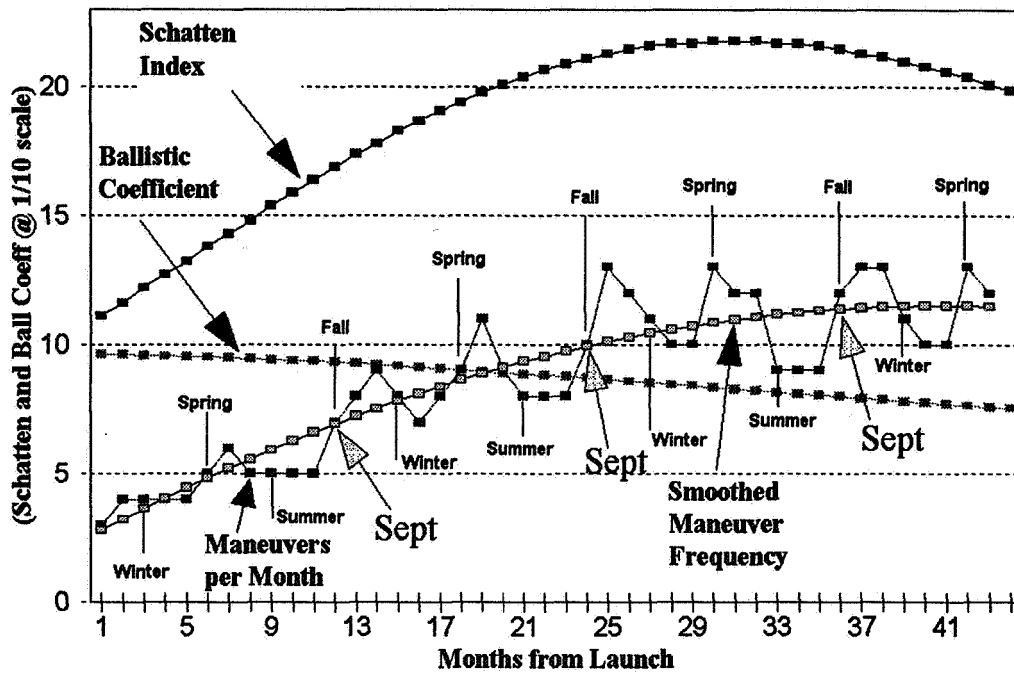


Figure 3. Removing the Semi-Annual Effect From Tabular Data

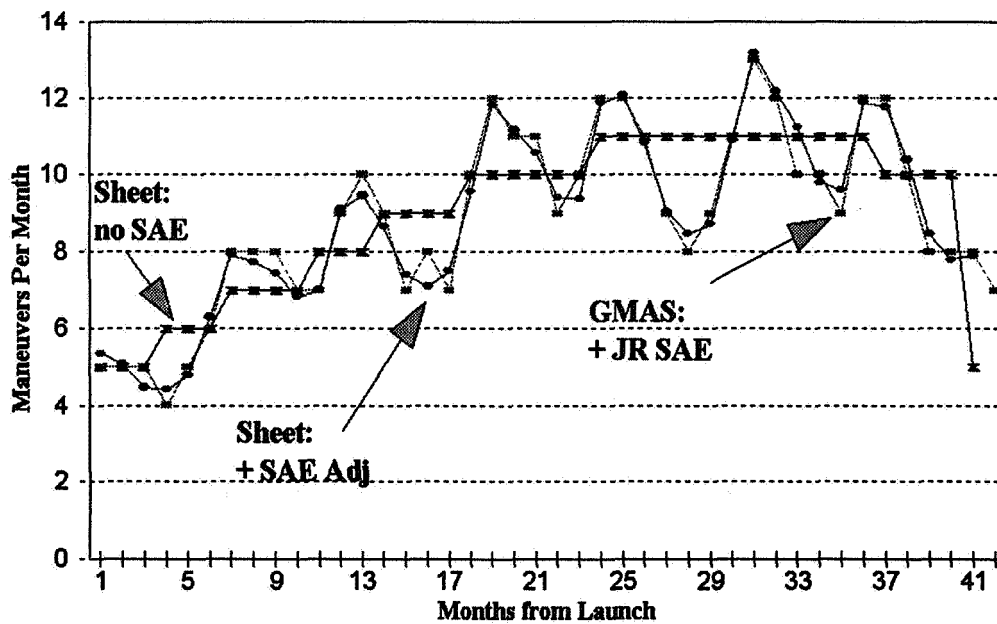


Figure 4. Adjusting for the Semi-Annual Effect in the Spreadsheet

4.1.1 The Early Mission Profile

Determination of the early mission profile requires GMAS or another propagation method to plan an initial ascent or descent to bring the spacecraft from its post-launch altitude to the nominal top-of-the-box altitude on the date when the operational mission and stationkeeping activities are scheduled to begin. The ignition and burnout semimajor axis values computed by this method are used in the spreadsheet to estimate the fuel-use for the initial maneuver and deduct it from the loaded fuel mass prior to normal stationkeeping computations. This option allows evaluation of the changing costs of these early-mission maneuvers as launch dates change, so the semimajor axis values need not be recomputed unless the launch date, the altitude constraints, or the spacecraft design changes significantly. The early mission step can be avoided by inputting a post-launch altitude identical to the nominal top-of-the-box altitude and reducing the loaded fuel mass value by the amount required for the ascent or descent.

4.1.2 Standard and Mission-Specific Parametric Values

The spreadsheet accepts user inputs for such values as gravitational constants, spacecraft dry and fuel masses, the spacecraft cross-sectional area and drag coefficient, mission altitude constraints, propulsion system parameters, and a variety of similar data types.

4.1.3 Schatten Solar Flux Data and SAE Adjustment Factors

Schatten solar flux predictions are input into the spreadsheet in columns, in the form of sequential solar flux levels time-tagged by month and year. The timespan is selected to begin with the first month of the nominal mission lifetime and to continue well beyond its anticipated end. A third column is provided for the corresponding SAE adjustment factors, which are described in Section 3.3.

4.2 The Computation Sequence

As described in Section 2, the spreadsheet uses the ballistic coefficient and predicted solar flux level for a given month as indices to estimate the corresponding maneuver frequency from a look-up table. The ballistic coefficient index is shown in the third column from the left and the flux index in the second row from the bottom of the look-up table, as illustrated in Table 1. The spreadsheet then computes the fuel-use associated with the maneuver frequency taken from the table, decrements the available fuel, and updates the propulsion system state for the subsequent month's computations, iterating these operations until all available fuel is used. The interpolation method, engine model, and propulsion system model used for these computations are described below.

Table 1. Maneuver Intervals per Month as a Function of Ballistic Coefficient and Schatten Flux Index

S/C Mass (kg)	row	Ballistic Coefficient	S/C Cross-Section: 17 m ²				
			Drag Coefficient: 2.2				
5510	(0)	150					
486	(1)	130					
372	(2)	110	0.86	2.8	5.5	9.3	
246	(3)	90	1.04	3.4	7.25	11.5	
231	(4)	70	1.35	4.5	9.3	15	
		Flux Index:	50	112.5	175	237.5	300
		col:	(0)	(1)	(2)	(3)	(4)

Notes:

- The Ballistic Coefficient column (3rd from left) and Flux Index row (2nd from bottom) show the index values used in computing the maneuvers-per-month data points given in the table.
- The 'row' (2nd column from left) and 'col' (bottom row) numbers are those used in QuattroPro's internal tabulation function.
- The S/C Mass column (farthest left) reports the spacecraft mass required to achieve the associated Ballistic Coefficient index value for the spacecraft cross-sectional area and drag values specified.

4.2.1 The Interpolation Method

The maneuver frequency prediction for a specific month is computed from the tabulated (i.e., from the look-up table) and current index values by a bilinear interpolation scheme that was obtained from Reference 6 and is implemented in the spreadsheet.

For a 4-point grid square identified by Points 1, 2, 3, and 4 as shown in Figure 5, the Point $y(x_1, x_2)$ is obtained by the following:

$$y(x_1, x_2) = (1 - t)(1 - u)y_1 + t(1 - u)y_2 + ty_3 + (1 - t)uy_4$$

where

$$t \equiv (x_1 - x_1[j]) / (x_1[j+1] - x_1[j])$$

$$u \equiv (x_2 - x_2[k]) / (x_2[k+1] - x_2[k])$$

where

$$x_1 \equiv \text{current solar flux}$$

$$x_2 \equiv \text{current ballistic coefficient}$$

$$x_1[j] \leq x_1 \leq x_1[j+1] \quad \{x_1 \text{ with bounding flux indices}$$

$$x_2[k] \leq x_2 \leq x_2[k+1] \quad \{x_2 \text{ with bounding bal. coeff. indices}$$

and

$$y_1 \equiv y[j][k] \quad \{\text{pt.1 in Figure 5}$$

$$y_2 \equiv y[j+1][k] \quad \{\text{pt.2 in Figure 5}$$

$$y_3 \equiv y[j+1][k+1] \quad \{\text{pt.3 in Figure 5}$$

$$y_4 \equiv y[j][k+1] \quad \{\text{pt.4 in Figure 5}$$

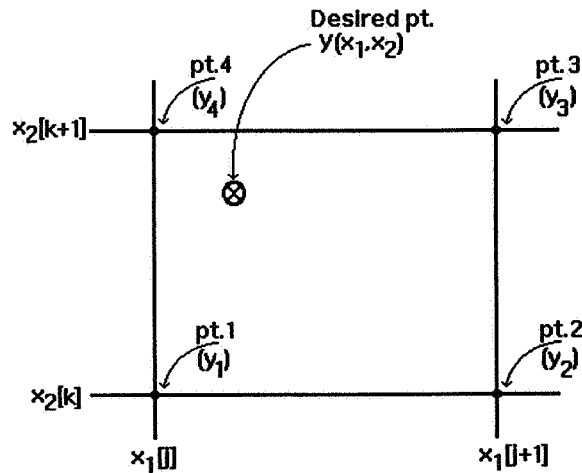


Figure 5. The Bilinear Interpolation Scheme

4.2.2 The Engine Model

Both the post-launch adjustment and operational orbit maintenance maneuvers are modeled impulsively as Hohmann transfers for computation of delta-V. Fuel use and other propulsion system parameters are computed from the impulsive delta-V using the rocket equation in the formulation given below:

$$W_f = W_i / e^{(dV/(G * I_{sp}))}$$

where

- W_f ≡ final (end of the month) spacecraft weight
- W_i ≡ initial (beginning of the month) spacecraft weight
- dV ≡ computed delta-V for the month
- G ≡ the gravitational coefficient
- I_{sp} ≡ current specific impulse

4.2.3 The Propulsion System Model

The propulsion system model includes a user-specified number of tanks (all of the same user-specified volume) and input options allowing specification of a pressure-regulated mode, a blowdown mode, or a combination of the two with transition from one to the other based on a fuel-remaining threshold. The tank pressure and the specific impulse (I_{sp}) for both modes are computed by the equations given below. The spreadsheet accepts user inputs for coefficients and scale factors for both modes.

$$P = P_i / ((1 + F) / (P_i * V_p))$$

where

- P = current pressure
- P_i = initial pressure
- F = fuel used to date
- V_p = pressurant volume

$$I_{sp} = (C1 + C2 * P + C3 * P^2 + C4 * P^3) * SF$$

where

- I_{sp} = specific impulse
- C_n = coefficient n
- P = pressure
- SF = scale factor

4.3 Dealing With the Final Month

Because of the units (maneuvers-per-month) used for the points in the look-up table, the mission lifetime is initially computed to the end of the month in which the fuel was exhausted. To obtain the final mission day and to account for the fuel mass required for deorbiting maneuvers, the spreadsheet reduces the number of maneuvers computed for the final month by a percentage derived from the fuel use computed for the month versus the amount of fuel actually available for use. The final month's delta-V and fuel use are then reduced by the same percentage, and the mission lifetime is determined to end on the final maneuver date plus the number of days required to decay to the minimum mission altitude. These adjustments are fully reflected in the output summary and final tabulated results.

5.0 Spreadsheet Evaluation: Agreement With Traditional Methods

While all mission lifetime computation methods provide, at best, an approximation of a mission's life expectancy, the GMAS method—which uses the average variation of parameters propagator and models stationkeeping maneuvers impulsively—has come to be used most consistently for FDF mission design, including previous TRMM lifetime computations. As such, it was the logical choice for a yardstick against which the reasonableness

of the spreadsheet results could be evaluated. The same approach should be taken for verification purposes (Section 2.0) when the spreadsheet is being set up for a new or significantly redesigned mission. The verification run can also provide data for the SAE adjustment factors (Section 3.3) as well as the early-mission semimajor axis values required for the post-launch maneuver fuel-use computation (Section 4.1.1).

5.1 The Comparison

As Table 2 shows, spreadsheet and GMAS results were compared for five TRMM cases, comprising various permutations of two spacecraft load masses, two launch dates (October 1997 and April 1998), two sets of I_{SP} scale factors, and two Schatten prediction sets (December 1994 and May 1995 predictions for the +2 sigma, nominal timing case). For each of the five cases, the table compares the GMAS and spreadsheet results in total maneuvers performed and total days in the mission lifetime, both with and without the Semi-Annual Effect. In each comparison, the percentage of disagreement between GMAS results and spreadsheet results was by:

$$[(GMAS\ value - spreadsheet\ value) / GMAS\ value] * 100\%$$

5.2 The Results

As Table 2 shows, the greatest differences between GMAS and spreadsheet results *without* the Semi-Annual Effect were 1.6 percent (Cases 3 and 5) for the total number of maneuvers and 2.4 percent (Case 4) for total duration. When the Semi-Annual Effect was turned on, the greatest differences were 1.4 percent (Case 3) for the total number of maneuvers and 1.5 percent (Case 2) for total duration. This is reasonable, considering that the spreadsheet results were being compared with GMAS results, which always use the SAE. The higher-than-usual 2.4 percent disagreement between GMAS and the spreadsheet (without the SAE) in Case 4 occurred for two reasons. First, the mission duration in that case was not evenly divisible into 6-month intervals, so the effect of the semi-annual variation in the GMAS run did not average out over the mission lifetime as well as in other cases. Second, the mission ended in the August-to-September timeframe, following the three lowest maneuver months of the SAE scheme. That meant that the GMAS run, benefiting from significantly fewer maneuvers than the spreadsheet run (without the SAE) in the final months, had the fuel available to continue almost a month longer than the spreadsheet computation.

Table 2. Comparison of Lifetime Results From GMAS and the Spreadsheet With and Without the Semi-Annual Effect

Test Cases Examined					% Difference Between GMAS and the Spreadsheet*			
Case	Schatten Prediction	Launch Date	Fuel Mass**	Isp Scale Factor (%)	Without SAE		With SAE ***	
					Mnvrs	Dur	Mnvrs	Dur
1	Dec-94	Oct-97	890 kg	4.5	0.5	0.4	0.3	0.3
2	May-95	Oct-97	890 kg	4.5	0.8	1.3	1.1	1.5
3	May-95	Oct-97	890 kg	5.5 / 7.5	1.6	1.0	1.4	0.9
4	May-95	Apr-98	890 kg	5.5 / 7.5	1.1	2.4	1.1	0.8
5	May-95	Apr-98	790 kg	5.5 / 7.5	1.6	1.2	1.0	0.4

Notes:

* The spreadsheet agrees with GMAS to within the percentage of disagreement shown.

** Total spacecraft mass is 3620 kg in all cases.

*** The method of approximating the Semi-Annual Effect is described in the text.

Shaded blocks indicate the smallest difference between GMAS and the spreadsheet in each case.

Dual scale factors are applied as follows: 5.5% inefficiency for the pressure regulated mode and 7.5% inefficiency for the blowdown mode.

6.0 Spreadsheet Maintenance

As mentioned above, updates of spreadsheet parameters computed by the traditional propagation method may need to be performed if the mission is significantly redesigned. Other changes, such as the arrival of new Schatten predictions, will require less time-consuming updates. The information in Table 3 is provided to clarify when updates are necessary, which specific inputs need to be changed, and how.

Table 3. Spreadsheet Maintenance Requirements

Condition	Flux data: Update	Flux data: Adj Timespan	Data pts: Rerun	Data pts: Add Points	Early Mission: Rerun	SAE Factors: Recompute
New Schatten Predictions	√					
Launch Date Change (mos)		√				
Launch Date Change (yrs)		√			√	√
New Altitude Constraints			√		√	√
Ballistic Coef Exceeds Range				√		
Schatten Index Exceeds Range				√		

7.0 Summary and Applications

The spreadsheet approach allows lifetime analysis using all nine Schatten flux-level cases to be performed in a matter of minutes. It is designed for flexibility in terms of spacecraft and mission design and is well-documented internally for the convenience of users. Its results agree well enough with traditional lifetime computation methods (to within 1 to 1.5 percent) to be useful for normal lifetime recomputations such as those following solar flux level updates or moderate spacecraft reconfigurations. This makes it useful to a wide variety of altitude-constrained Earth-orbiting spacecraft whose mission lifetimes depend heavily on frequently updated solar flux predictions.

8.0 References

1. Goddard Space Flight Center, Flight Dynamics Division, 554-FDD-92/039R0UD0, *Tropical Rainfall Measurement Mission (TRMM) Updated Mission Profile*, T. Maddy (CSC), prepared by Computer Sciences Corporation, May 1992
2. Schatten, K. H., et al., "Using Dynamo Theory to Predict the Sunspot Number During Solar Cycle 21," *Geophysical Research Letters*, 1978.
3. Schatten, K. H., and Sofia, S., "Forecast of an Exceptionally Large-Numbered Solar Cycle," *Geophysical Research Letters* 14(6), 623–635, 1987
4. Jacchia, L. G., *Thermospheric Temperature, Density, and Composition: New Models*, Smithsonian Institution Astrophysical Observatory SPECIAL REPORT 375, March 15, 1977, pages 47–50
5. Computer Sciences Corporation, CSC#56716-04, "TRMM Flight Dynamics Support, LIFESPAN Spreadsheet Lifetime Prediction Method," P. Jordan (CSC), February, 1996
6. Press, W. H., Teukolsky, S. A., Vetterling, W. T., and Flannery, B. P., *Numerical Recipes in C: The Art of Scientific Computing*, 2nd ed., Cambridge University Press, 1992, pages 123–125

Autonomous Navigation With Ground Station One-Way Forward-Link Doppler Data*

G. M. Horstkamp and D. J. Niklewski
Computer Sciences Corporation
Lanham-Seabrook, Maryland, USA 20706

C. J. Gramling
National Aeronautics and Space Administration
Goddard Space Flight Center
Greenbelt, Maryland, USA 20771

Abstract

The National Aeronautics and Space Administration (NASA) Goddard Space Flight Center (GSFC) has spent several years developing operational Onboard Navigation Systems (ONSs) to provide realtime autonomous, high-accuracy navigation products for spacecraft using NASA's space and ground communication systems. The highly successful Tracking and Data Relay Satellite System (TDRSS) ONS (TONS) experiment on the Explorer Platform/Extreme Ultraviolet Explorer (EP/EUVE) spacecraft, launched June 7, 1992, flight demonstrated the ONS for high-accuracy navigation using TDRSS forward-link communications services. In late 1994, a similar ONS experiment was performed using EP/EUVE flight hardware (the ultrastable oscillator (USO) and Doppler extractor (DE) card in one of the TDRSS transponders) and ground system software to demonstrate the feasibility of using an ONS with ground station forward-link communication services. This paper provides a detailed evaluation of ground-station-based ONS performance over the 20-day period of data collected.

The Ground-station ONS (GONS) experiment results are used to project the expected performance of an operational system. The GONS processes Doppler data derived from scheduled ground station forward-link services using a sequential estimation algorithm enhanced by a sophisticated process noise model to provide onboard orbit and frequency determination. Analysis of the GONS experiment performance indicates that realtime onboard position accuracies of better than 125 meters (1σ) are achievable with two or more 5-minute contacts per day for the EP/EUVE 525-kilometer altitude, 28.5-degree inclination orbit. GONS accuracy is shown to be a function of the fidelity of the onboard propagation model, the frequency/geometry of the tracking contacts, and the quality of the tracking measurements. GONS provides a viable option for using autonomous navigation to reduce operational costs for upcoming spacecraft missions with moderate position accuracy requirements.

1.0 Introduction

Due to recent advances in space-qualified components such as high-capacity solid state recorders and the trend toward smaller spacecraft that cannot support Tracking and Data Relay Satellite System (TDRSS) services, either from cost or power perspectives, many future spacecraft missions are returning to ground stations (GSs) for their communication support. Traditionally, GSs provide command, telemetry, and tracking services for user spacecraft, which can be costly and operationally intensive. New ground terminals are being designed that provide increased autonomy to reduce operations costs. However, these new ground terminals will provide only command and telemetry services, requiring users to acquire spacecraft navigation data from alternate sources, such as an autonomous navigation system.

Autonomous navigation using an onboard system has distinct advantages. Autonomous navigation products can be included directly in the science telemetry and forwarded to the scientific investigators located worldwide, with remote communication links to the mission operations centers. Autonomous navigation solutions can be used onboard as input to other subsystems, such as attitude control, ground track generation, maneuver definition and

* This work was supported by the National Aeronautics and Space Administration (NASA)/Goddard Space Flight Center (GSFC), Greenbelt, Maryland, under Contract NAS 5-31500.

control, and communication signal acquisition. Autonomous navigation systems also can provide a time maintenance or determination function for the spacecraft, increasing spacecraft self-sufficiency and reducing ground operations.

The Goddard Space Flight Center (GSFC) Flight Dynamics Division (FDD) has spent several years developing high-accuracy onboard navigation systems for spacecraft using National Aeronautics and Space Administration (NASA) space and ground communications systems. The highly successful TDRSS Onboard Navigation System (TONS) experiment on the Explorer Platform/Extreme Ultraviolet Explorer (EP/EUVE) spacecraft flight qualified high-accuracy algorithms for autonomous navigation using TDRSS carrier signals (Reference 1). As a result, the Earth Observing System-AM1 (EOS-AM1) is implementing TONS as its prime operational navigation system.

To address increases in the planned use of ground stations as the sole communication medium for future low-Earth orbiting spacecraft, the FDD performed an experiment to investigate the potential of onboard navigation using Doppler measurements of the S-band communication signals transmitted from ground stations. After this Ground-station Onboard Navigation System (GONS) experiment, several parametric studies were performed to investigate the sensitivity of GONS navigation accuracy. These studies included decreasing the accuracy of the initialization/a priori state, reducing the gravity model size used for state propagation, and increasing the measurement sampling interval used in state estimation. Reference 2 contains details of the GONS experiment not presented in this paper; Reference 3 discusses GSFC FDD's initiative to integrate the GONS capability with a spacecraft communications receiver to provide an "off-the-shelf" navigation package.

Section 2.0 of this paper discusses the GONS flight qualification experiment, and Section 3.0 describes the flight hardware performance. GONS navigation performance and GONS parametric studies are described in Sections 4.0 and 5.0, respectively. Section 6.0 gives the conclusions of the study, followed by acknowledgments and a list of the references cited in the paper.

2.0 GONS Flight Qualification Experiment

The EP/EUVE spacecraft houses hardware previously used for TONS to accurately measure the Doppler shift of a one-way forward signal from TDRSS to a user spacecraft. This hardware consists of a second generation TDRSS user transponder with the optional Doppler Extractor (DE) card and an Ultrastable Oscillator (USO). Using this same equipment, the GONS experiment was conducted for 20 days, beginning in September 1994. The objectives of the GONS experiment were to demonstrate the transponder's capability to extract accurate Doppler measurements of a GS carrier signal when referenced to an USO, to determine the achievable navigation accuracy from this data, and to analyze the potential of a single-station orbit determination solution.

For the TONS experiment, the DE card was added to transponder-B on EP/EUVE, and the USO provided the external frequency reference to this DE. In April 1994, a failure occurred in transponder-B's transmitter, without causing harm to the receiver. At that time, the omni-directional antenna was switched to transponder-B's receiver. For the GONS experiment, acquisition of a GS carrier could still occur through the transponder-B receiver. However, due to the failure of the associated transmitter, the return-link data could not be telemetered to the ground in realtime.

Given the circumstances onboard EP/EUVE, each contact was handled via a blind acquisition of the spacecraft. The blind acquisition used a single frequency sweep at a rate of 20 kilohertz per second over a range of 200 kilohertz around the receive center frequency, 2106.406300 megahertz, anticipating that the second generation transponder receiver would acquire the forward-link signal during the sweep. The Doppler measurements were then telemetered to the ground during a subsequent TDRSS contact to dump playback data and retrieved from processed telemetry tapes. The GONS experiment configuration is illustrated in Figure 1.

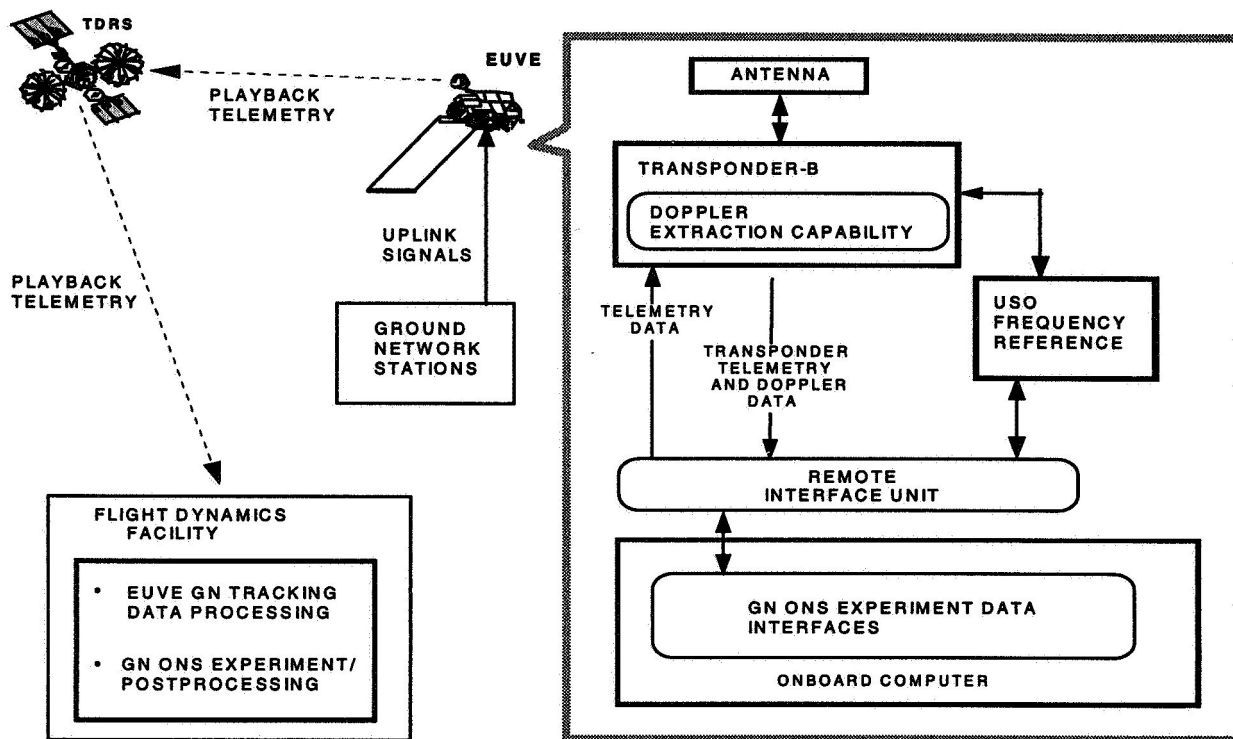


Figure 1. GONS Experiment Configuration

To support the GONS experiment, contacts were scheduled on a noninterference basis from Deep Space Network (DSN) GSs in Goldstone, California (GDS), Madrid, Spain (MAD), and Canberra, Australia (CAN), resulting in zero to five contacts per day, with lengths varying from 3 to 10 minutes. The experiment tracking data distribution, shown at the top of Figure 2, provided four significant analysis periods: two data gaps of 74 hours (days 4–7) and 47 hours (days 18–20), respectively, and two 4-day periods (days 0–4 and 11–15) with more than two contacts per day.

3.0 Flight Hardware Performance

The EP/EUVE flight transponder performs differently when configured in the GS service mode. The Doppler shift is measured in the DE by accumulating the difference between the received carrier frequency and the receiver's numerically controlled oscillator (NCO), which is referenced to the USO. The difference is rectified by a 24-bit internal frequency control word (FCW) sent simultaneously to the NCO and to an accumulator. In the TDRSS mode, the NCO updates every 500 microseconds (μs), thereby accumulating 20480 updates over the 10.24-second Doppler count interval in the DE. To track the higher dynamics between the user and the ground in the GS mode, the second-generation transponder NCO updates every 250 μs . Therefore, accumulation of 20480 updates occurs in 5.12 seconds in the GS mode, providing Doppler data at twice the TDRSS-mode rate.

To measure the performance of the hardware that provided the GONS Doppler measurement function, namely the DE and the USO, measurement residual statistics were computed and analyzed. To determine the USO frequency bias and drift, the measurement residuals (shown in Figure 2) were computed with respect to a TDRSS-only EUVE reference solution. The GONS experiment initial USO bias of 117 hertz and drift rate of -0.1 hertz per day are consistent with earlier TONS experiment results. Prefit residuals from the GONS navigation solution were analyzed to determine GONS measurement noise characteristics, as shown in Figure 3. Analysis of the prefit residuals from the entire 20-day period indicates a low systematic error of less than 0.006 hertz, with a standard deviation of 0.023 hertz.

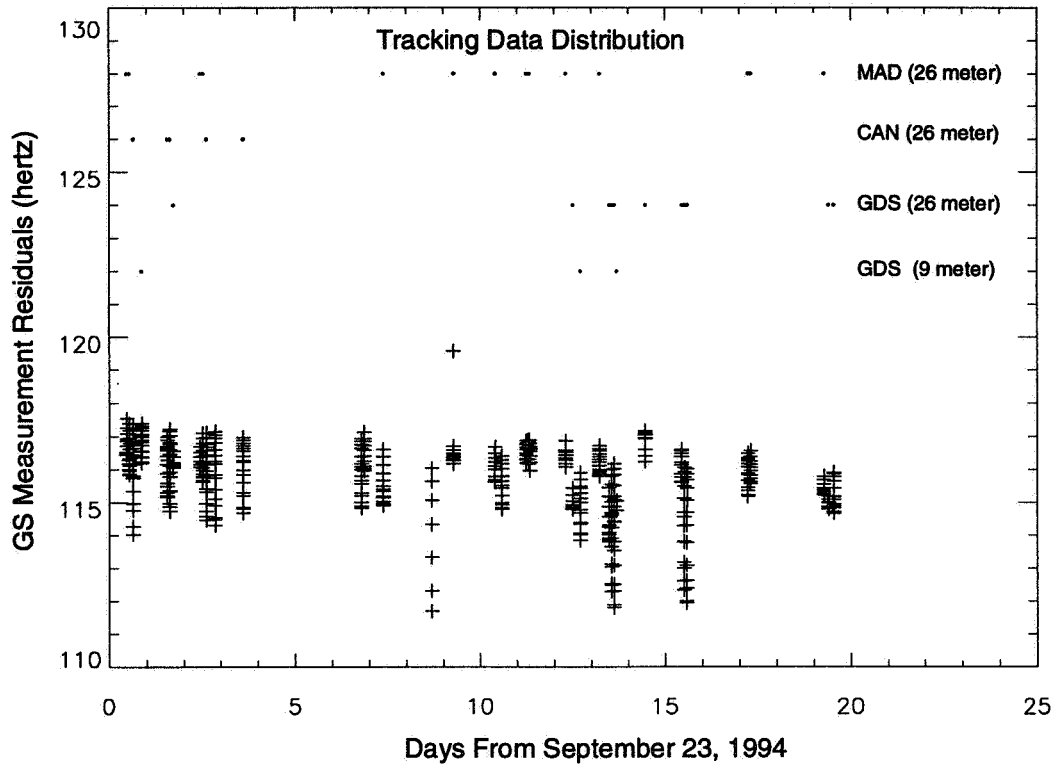


Figure 2. EUVE Ground Tracking Data Distribution and Measurement Residuals

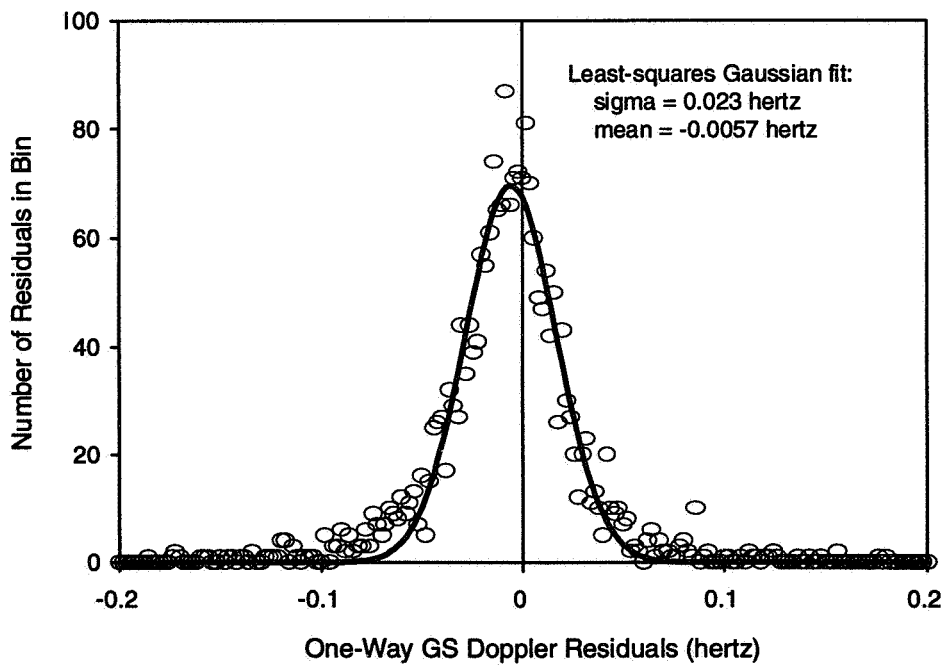


Figure 3. Histogram of Prefit Measurement Residuals

4.0 GONS Navigation Performance

To assess the accuracy of the navigation solution obtained using GONS experiment measurements, a reference solution was computed using an extended Kalman filter to process TDRSS range and two-way Doppler measurements for EUVE and Bilateral Ranging Transponder System (BRTS) range data for the TDRSS spacecraft. The filtered TDRSS reference solution state consisted of the EUVE position, velocity, and atmospheric drag coefficient; the position, velocity, and solar radiation pressure coefficient for each of the two TDRS spacecraft; and the measurement biases. The filtered TDRSS reference solution used a full 70×70 Joint Gravity Model-2 (JGM-2) gravity model and accurate atmospheric data to provide a very-high-accuracy state propagation model.

To simulate an onboard computing environment, the GONS experiment one-way forward Doppler measurements were also processed using an extended Kalman filter. The solution state consisted of the EUVE position, velocity, atmospheric drag coefficient, and USO frequency bias. This GONS solution used the JGM-2 gravity model truncated to 30×30 and averaged atmospheric density tables to simulate the limitations imposed by an onboard environment. Although hosted on a ground processor, these navigation algorithms used in the GONS experiment meet the strict throughput and memory budgets associated with onboard environments. A summary of the GONS algorithms is provided in Table 1.

The EUVE position estimation, atmospheric drag coefficient estimation, and USO frequency bias estimation are described in the following subsections, followed by a discussion of the GONS navigation performance with northern hemisphere GS tracking.

Table 1. Summary of GONS Experiment Algorithms

Algorithm Type	Algorithm
Primary Coordinate System	Mean equator and equinox of J2000.0 with analytic coordinate transformations, UT1 offset from coordinated universal time (UTC) updated daily
Primary Time system	UTC
Filter Spacecraft Acceleration Model	<ul style="list-style-type: none"> • 30×30 Joint Gravity Model-2 (JGM)-2 nonspherical geopotential • Earth, solar, and lunar point masses with analytic ephemeris • CIRA72 atmosphere density model with average atmospheric density tables
Spacecraft State Transition Matrix	Semianalytic formulation including J_2 and Earth point-mass acceleration partial derivatives
Frequency Reference Bias Propagation	Linear model with frequency drift input by user
Estimator	Extended Kalman filter with physically connected process noise models
Estimation State	<ul style="list-style-type: none"> • User position and velocity vectors • Atmospheric drag coefficient • Spacecraft frequency reference bias
State Process Noise Model	<ul style="list-style-type: none"> • Radial/in-track/cross-track (RIC) formulation of Earth gravity model errors • Gauss-Markov model for atmospheric drag coefficient and frequency reference bias
Measurement Model	<ul style="list-style-type: none"> • GS one-way forward-link Doppler with iterated light-time solution • Tropospheric measurement corrections • Relativistic corrections
Measurement Editing	<ul style="list-style-type: none"> • Doppler data validity checks • Measurement residual n-sigma test

4.1 EUVE Position Estimation

Figure 4 shows the root-sum-square (RSS) spacecraft position differences between the GONS and filtered TDRSS reference solutions for the entire experiment period. The GONS solution converges to below the 100-meter level after the first three contacts, which occur on consecutive orbits, and maintains a smooth, well-behaved signature except during large data gaps. During the first data gap of 74 hours (ending on day 6), the GONS solution propagates well, with a peak RSS position difference of 550 meters when compared with the filtered TDRSS reference solution, which includes TDRSS tracking during that interval. The predicted position standard deviation increases to 1 kilometer by the end of the 74-hour data gap, indicating a very realistic covariance propagation. The GONS solution recovers immediately following the start of the next tracking contact to the 100-meter level.

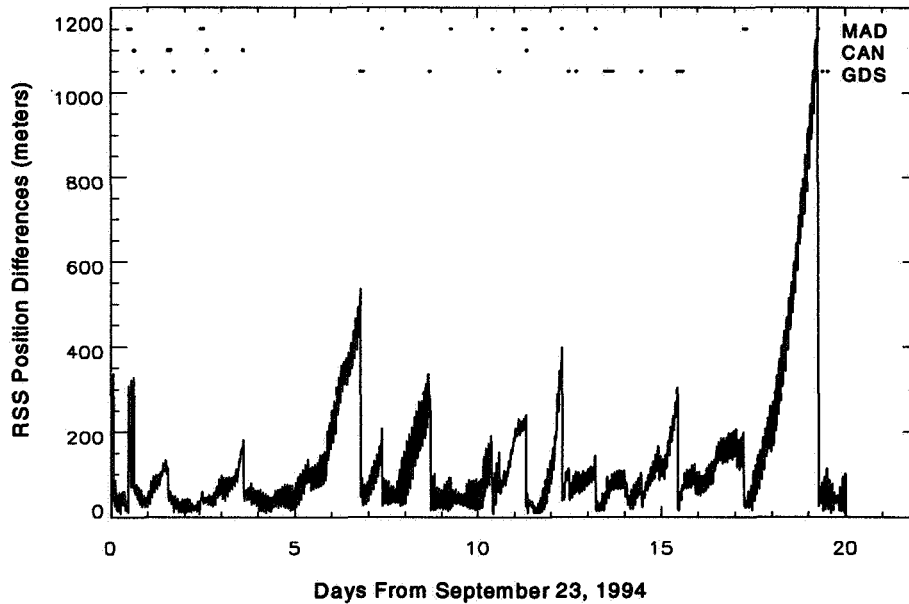


Figure 4. EUVE Total Position Differences Between the GONS and Filtered TDRSS Reference Solutions

During the second data gap interval of 47 hours (ending on day 19), the RSS position differences increase to 1.2 kilometers. The larger RSS differences seen during the second propagation period can be attributed to less accurate atmospheric density modeling during the propagation, as well as to a TDRSS spacecraft maneuver during the propagation period that adversely affected the TDRSS filter reference solution. The GONS solution differences show an immediate recovery to the 100-meter level upon processing data from the next contact, an important attribute for an autonomous navigation system.

During the two 4-day periods when there were three to four GS contacts per day, data from the filtered TDRSS reference solution was processed in a Rauch-Tung-Striebel smoother to provide a more accurate reference solution. As shown in Figure 5, the RSS position differences between the GONS solution and the smoothed TDRSS reference solution for the first 4-day period of interest are below 100 meters following processing of the first three GS contacts, except during an 18-hour propagation. The large differences seen in the first day of processing are during the first 3 contacts and are due to initializing GONS with a large initial covariance. Figure 6 shows similar results during the second 4-day period. The root mean square (RMS) of the position differences over the two 4-day periods are 81 meters and 124 meters, respectively. These results indicate that a highly stable autonomous navigation solution of better than 125 meters (1σ) can be achieved with a moderate GS tracking schedule, with highly reliable propagation during data gaps and immediate recovery during processing of the next contact.

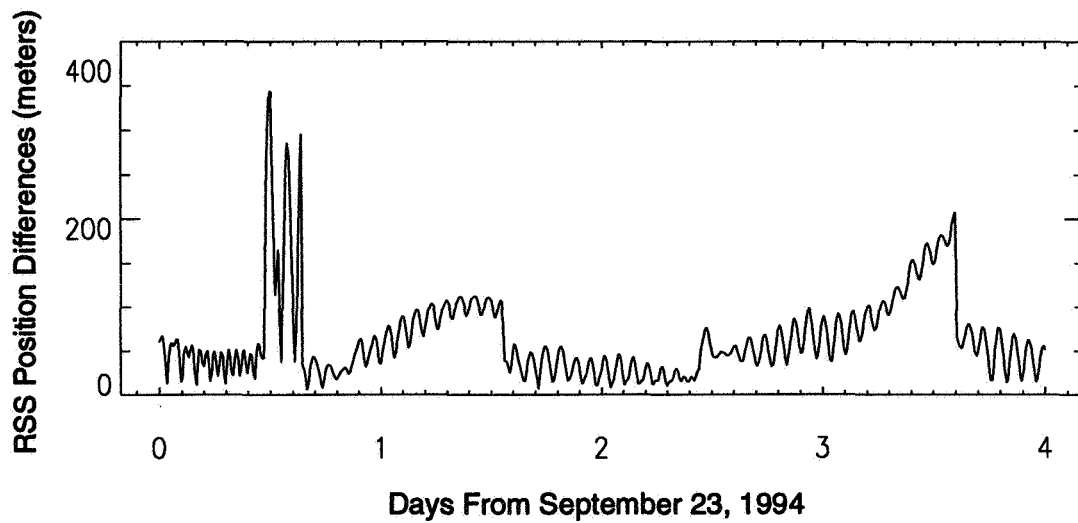


Figure 5. EUVE Total Position Differences Between GONS and First Smoothed TDRSS Reference Solutions

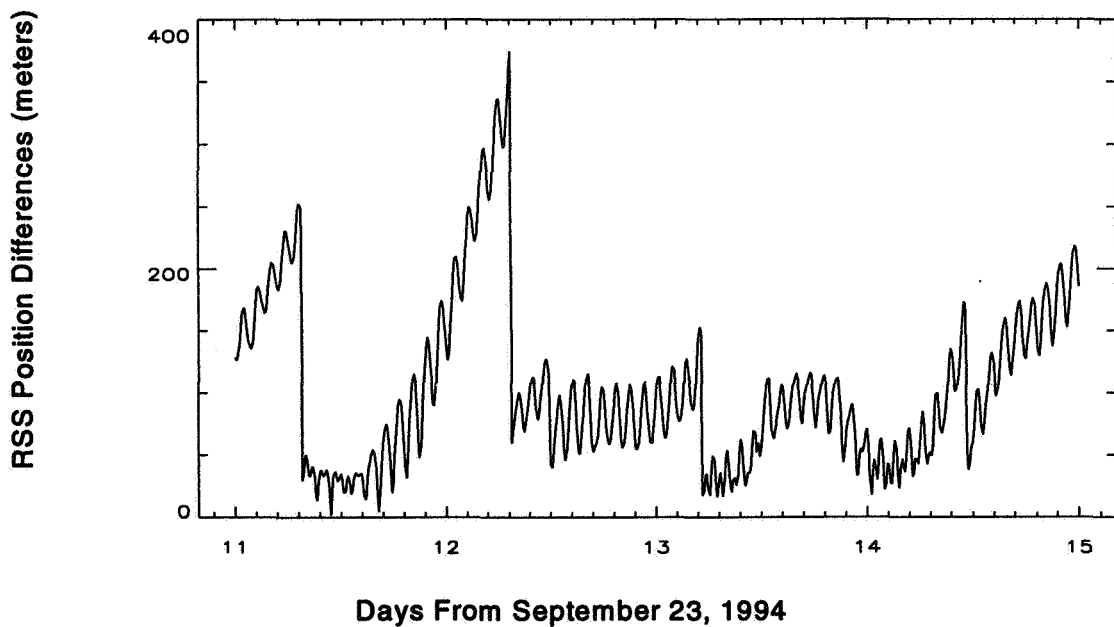


Figure 6. EUVE Total Position Differences Between GONS and Second Smoothed TDRSS Reference Solutions

4.2 EUVE Atmospheric Drag Coefficient Estimation

The GONS solution used different values for the Gauss-Markov coefficient of drag (C_D) sigma and C_D half-life than the TDRSS solution because of the tracking data frequency and larger uncertainty in atmospheric density. The filtered TDRSS reference solution used a nominal a priori drag coefficient value of 2.0, with a C_D sigma of 0.4 and a C_D half-life of 20 days. The GONS solution used a C_D sigma of 1.0 and a C_D half-life of 10 days. These values were chosen to allow the drag model to accommodate larger periods of propagation, because GS tracking was only available, on average, two to three times per day. The propagation of the drag coefficient is such that the correction will decay to zero exponentially, leaving an a priori drag coefficient of 2.0. Figure 7 compares the drag coefficient estimation for the two solutions. Early in the GONS solution, the drag estimate corrects to roughly 1.25. At the same time, the filtered TDRSS reference solution drag estimate is between 1.0 and 1.5. The subsequent corrections to the drag estimate in the GONS solution leave the drag coefficient oscillating around 1.0, until day 11; after day 11, the drag estimate is adjusted to between 2.0 and 2.5 for the rest of the solution. It is interesting to note that the filtered TDRSS reference solution drag estimate remains near 1.0 until day 15 and that the RSS position differences between the two solutions are not adversely affected

The definitive atmosphere model used in the TDRSS solutions shows nominal solar activity during the filter time period. The 3-hourly A_p geomagnetic index values increase more than 50 points near the middle of the 20-day solution. The $F_{10.7}$ solar flux is near $80 (\times 10^{-22}$ watts per meter² per hertz) (nominal to low value) with a slight upward trend. The change in A_p , which is not modeled in the GONS solution, may drive the adjustments in the drag coefficient estimate around day 10 of the GONS solution.

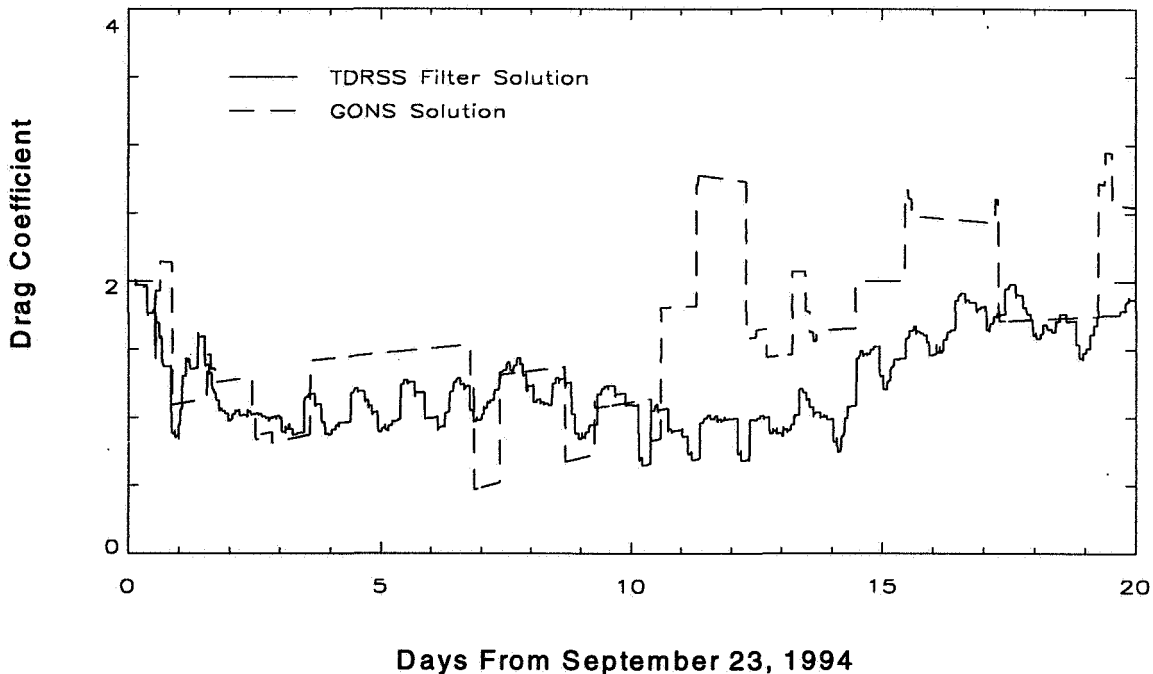


Figure 7. EUVE Drag Coefficient Estimation for GONS and Filtered TDRSS Reference Solutions

4.3 USO Frequency Bias Estimation

USO frequency bias estimation is required for accurate processing of the one-way forward GS tracking data in this solution. The a priori USO frequency bias was set to 118 hertz and the drift constant was set to 0.1 hertz per day. The bias was modeled as a Gauss-Markov parameter with a sigma of 10 hertz and a half-life of 100 days. The long half-life of the bias correction causes it to propagate at almost a constant value.

Figure 8 shows the total USO frequency estimation (frequency bias plus integrated drift) for the GONS solution. From the initial values, the frequency bias initially reduces to 117.5 hertz and the total USO frequency estimation drifts to approximately 115.8 hertz. This estimate is very close to that shown by the residuals in Figure 2. The frequency bias estimate is on track during the entire 20 day period

4.4 GONS Navigation Performance With Northern Hemisphere GS Tracking

The GONS experiment data were analyzed to simulate autonomous navigation solutions using a single GS by deleting the Southern Hemisphere station from the GONS solution. Both Northern Hemisphere stations were used, because too many data gaps exist to establish realistic results using a strictly single-station solution. Figure 9 shows that initial convergence of the GONS Northern Hemisphere solution (30×30) to the 200-meter level occurs after the first contact, with convergence to the 100-meter level occurring after two additional contacts. During the first data gap, now lasting 94 hours, the RSS position differences of the GONS Northern Hemisphere solution versus the TDRSS reference solution increase to 1.9 kilometers, with an immediate recovery to the 100-meter level upon processing of the data from the next contact. After this period, the RSS position differences of the GONS Northern Hemisphere solution versus the TDRSS reference solution are virtually identical to those from the GONS solution using data from all stations. Therefore, after filter convergence, a single-station autonomous navigation solution with a moderate tracking scenario (i.e., one to two contacts per day) can provide onboard real-time position accuracies of better than 125 meters.

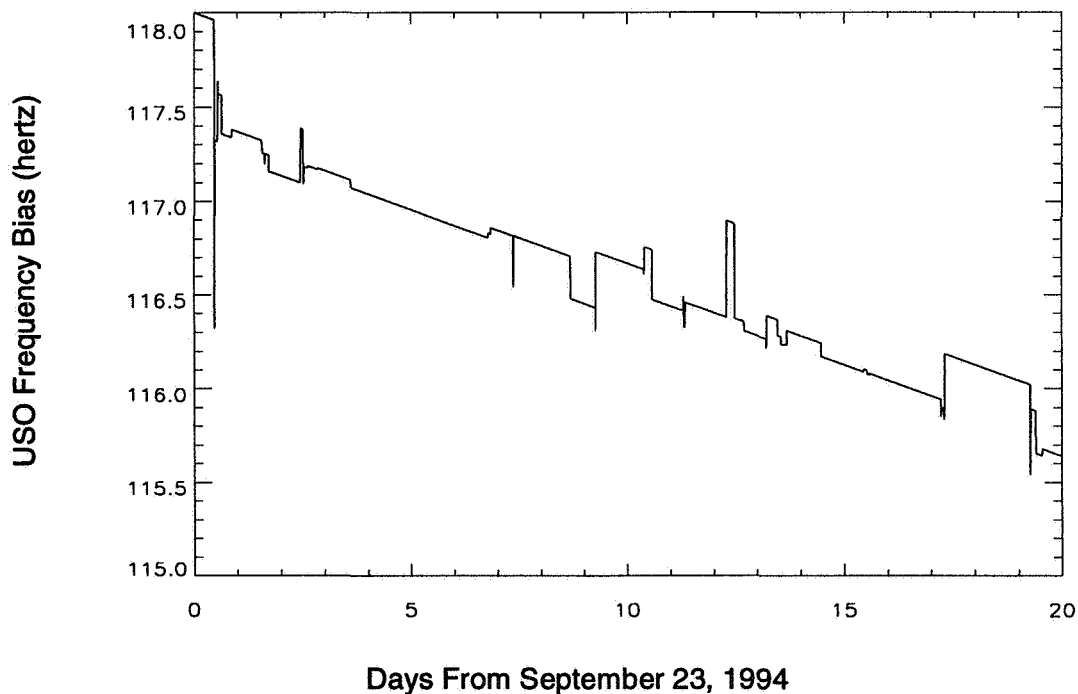


Figure 8. Total EUVE USO Frequency Bias Estimation From GONS Solutions

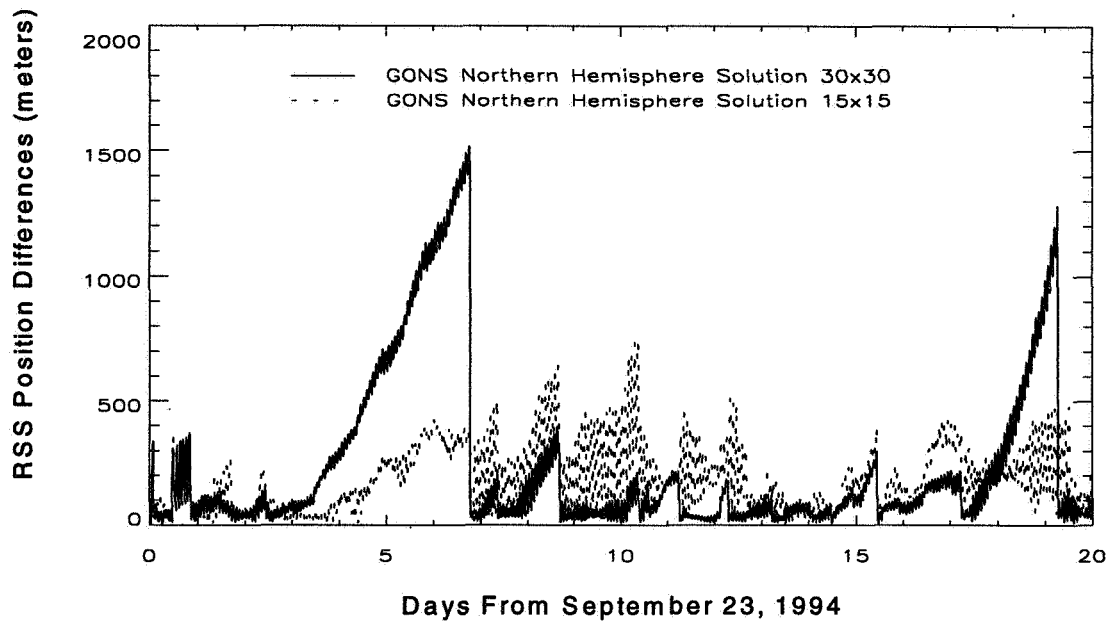


Figure 9. GONS Northern Hemisphere Solution Versus Filtered TDRSS Solution Differences

5.0 GONS Parametric Studies

The FDD's interest in navigation system requirements for spacecraft missions with moderate orbit determination accuracy led to the following studies of GONS performance. These studies included reducing the gravity model size used for ephemeris propagation, decreasing the accuracy of the initialization/a priori state, and increasing the measurement sampling interval used in state estimation. The intent of these analyses is to understand more about how GONS can be implemented to reduce spacecraft operations costs and still meet navigation requirements.

GONS performance with reduced gravity modeling, with offset initial state, and with increased sampling intervals are described in Sections 5.1, 5.2, and 5.3, respectively.

5.1 GONS Performance With Reduced Gravity Modeling

The 30×30 geopotential model used in the GONS experiment is the major contributor to the amount of onboard central processing unit (CPU) required for the navigation system. For this reason, a parametric study of the size of the geopotential model versus the system's navigation accuracy was performed. The GONS solution and the GONS Northern Hemisphere solution were run with the JGM-2 geopotential model reduced to 15×15 and 5×5 . Table 2 shows the peak RSS differences from the filtered TDRSS reference solution for the first 17 days and the RMS of the RSS position differences from the second smoothed TDRSS solution (days 11–15) for the geopotential model sizes of 30×30 , 15×15 , and 5×5 . Table 2 includes the difference in RMS values for days 11–15 that the new solutions have from the GONS solution. Figure 9 shows the RSS position differences between the GONS Northern Hemisphere solution with 15×15 geopotential model and the filtered TDRSS reference solution for the entire 20-day experiment period.

These and other GONS solutions indicate that the most significant change in performance with respect to gravity model size occurs when the order of the geopotential model is smaller than the orbital revolutions per day. For the EP/EUVE orbit, this resonance occurs below the 15×15 geopotential model. The 15×15 gravity model solutions in Table 2 show that a 75-percent reduction in CPU results in only a moderate accuracy penalty of roughly 100 meters RMS after the GONS solution has converged and two or more GS contacts per day are available.

Table 2. Reduced Geopotential Size Results

Gravity Model Sizes	RSS Position Differences From TDRSS Solutions (meters)		Degradation From GONS Solution (meters)
	Peak During Day 0-17	RMS for Day 11-15	RMS for Day 11-15
<i>GONS Solution</i>			
30 × 30	525 (day 6)	124	N/A
15 × 15	730 (day 10)	191	67
5 × 5	3800 (day 6)	687	563
<i>Northern Hemisphere GONS Solution</i>			
30 × 30	1900 (day 6)	90	-34
15 × 15	740 (day 10)	192	68
5 × 5	4500 (day 6)	802	678

5.2 GONS Performance With Offset Initial State

All of the solutions presented thus far have started from a definitive user state (position and velocity) accurate to approximately 100 meters. Operationally, GONS would have to be initialized with a predicted state. To see how this would affect GONS performance, the GONS Northern Hemisphere 15 × 15 solution was run with initial in-track offsets of 1 kilometer and 10 kilometers. Figure 10 illustrates the additional convergence time these offset solutions require. The RSS differences between the GONS and TDRSS solutions have been orbit-averaged to take out the orbital variation that would make these solution differences difficult to compare. The 1-kilometer offset solution settles after 1 full day and three GS contacts, and the 10-kilometer run takes a full 7 days and eight GS contacts. The 4-day tracking data gap after day 4 adversely affects the convergence time of the 10-kilometer offset solution. For each offset solution, the position and velocity components of the initial state covariance matrix were adequately enlarged to accommodate the initial state errors.

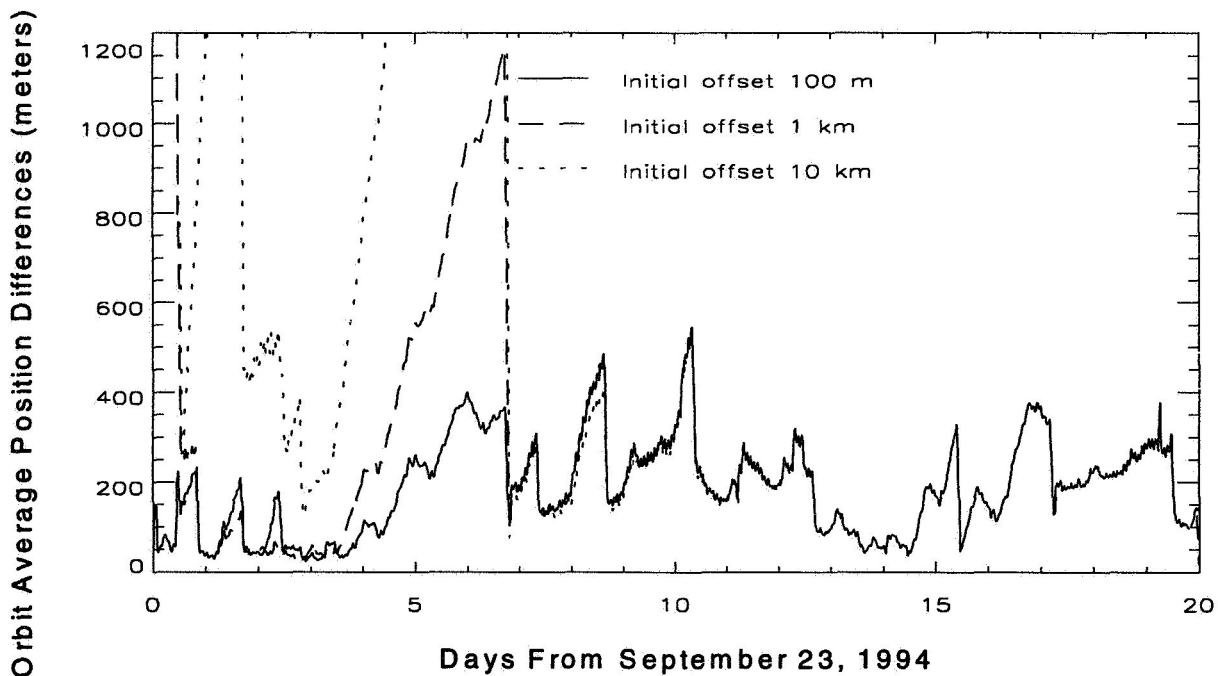


Figure 10. GONS Northern Hemisphere 15 × 15 Solution With Varying Initial State

5.3 GONS Performance With Increased Sampling Intervals

Another factor that influences the amount of onboard CPU required for GONS is the measurement sampling interval. In the GONS solutions so far, each have processed all available tracking data from all or the Northern Hemisphere stations. To see how the sampling interval affects GONS, new GONS Northern Hemisphere solutions were made at data rates of every other (10.24-second) and every sixth (30.72-second) tracking measurement. Table 3 shows the peak RSS differences from the filtered TDRSS reference solution for the first 17 days and the RMS of the RSS position differences from the second smoothed TDRSS solution for each tracking measurement data rate. Table 3 includes the difference in RMS values for days 11–15 that the new solutions have from the GONS solution. The values in this table show moderate accuracy improvements for an increased tracking measurement rate. This result is consistent and may be due to measurement standard deviation used during estimation. This analysis shows that measurement sampling, which produces significant CPU savings in measurement processing, has little effect on overall navigation performance.

Table 3. GONS Northern Hemisphere 15 × 15 Solution

Measurement Rate (seconds)	RSS Position Differences From TDRSS Solution (meters)		Degradation From GONS Solution (meters)
	Peak During Day 0–17	RMS for Day 11–15	RMS for Day 11–15
5.12	740 (day 10)	192	68
10.24	700 (day 10)	180	56
30.72	600 (day 10)	156	32

6.0 Conclusions

The GONS experiment using the EUVE spacecraft was successful, despite the use of blind signal acquisitions, a sparse tracking schedule, and extensive data processing requirements. The three objectives of the experiment were all met: to demonstrate the transponder's capability to obtain accurate Doppler observations of the GS carrier signal when referenced to a USO, to determine the achievable navigation accuracy from the data, and to analyze the potential of a single station orbit determination solution. The navigation accuracy of the GONS solution was found to be better than 250 meters (1σ) with tracking data gaps of up to 3 days. When the tracking frequency is greater than two contacts per day, a navigation solution on the order of 125 meters (1σ) is possible onboard the user spacecraft. The GONS solution RSS position differences demonstrated an immediate recovery from the 1900-meter level to the 100-meter level following a 3-day data gap. The selective use of tracking data from the Northern Hemisphere GSs created a solution with accuracies comparable to the GONS solution (using all one-way forward GS tracking data) after the filter had fully converged. However, tracking from Southern Hemisphere stations reduces the length of time required for the filter to converge.

The parametric studies of the GONS performance indicate that gravity model size and measurement sampling interval can be adjusted to suit individual CPU and navigation requirements. A GONS solution using a 15 × 15 gravity model and with measurement data processing once every 30 seconds can still meet many future spacecraft processing requirements. Comparable accuracy can also be achieved using an uplinked initial state with errors of up to 10 kilometers after filter convergence is achieved.

This experiment demonstrates the GONS navigation concept. GONS passively uses the user spacecraft communication system and has no extra power/weight/volume requirements. The accuracies found in this experiment support most of the existing navigation requirements of future NASA spacecraft. The system uses high-fidelity models, including a propagator that could provide backup navigation data. The Northern Hemisphere solution analysis indicates that GONS support of a user spacecraft with a single ground tracking station is feasible. Future directions for GONS analysis and development include investigating GONS performance with Doppler

measurements referenced to a temperature-compensated crystal oscillator (TCXO) and design/ implementation of GONS in a spacecraft transponder (Reference 3).

Acknowledgment

The authors wish to acknowledge Anne Long of Computer Sciences Corporation for her technical guidance during the GONS experiment.

References

1. C. J. Gramling et al., "TDRSS Onboard Navigation System (TONS) Flight Qualification Experiment," *Proceedings of the Flight Mechanics/Estimation Theory Symposium 1994*, NASA Conference Publication 3265, May 17–19, 1995, p. 253
2. Goddard Space Flight Center, Flight Dynamics Division, 553-FDD-95/016R0UD0, *Analysis of Ground One-Way Forward Doppler Tracking Data Using the Prototype Filter Smoother (PFS)*, G. Horstkamp and D. Niklewski (CSC), prepared by Computer Sciences Corporation, September 1995
3. C. J. Gramling, A. C. Long, and G. M. Horstkamp., *Autonomous Navigation Integrated With Spacecraft Communication Systems*, Paper No. AAS 96-003, presented at the 19th Annual AAS Guidance and Control Conference, Breckenridge, Colorado, February 7–11, 1996

Reducing On-Board Computer Propagation Errors Due to Omitted Geopotential Terms By Judicious Selection of Uploaded State Vector

Mark Beckman
Goddard Space Flight Center

Several future, and some current missions, use an on-board computer (OBC) force model that is very limited. The OBC geopotential force model typically includes only the J_2 , J_3 , J_4 , $C_{2,2}$ and $S_{2,2}$ terms to model non-spherical Earth gravitational effects. The Tropical Rainfall Measuring Mission (TRMM), Wide-Field Infrared Explorer (WIRE), Transition Region and Coronal Explorer (TRACE), Submillimeter Wave Astronomy Satellite (SWAS), and X-ray Timing Explorer (XTE) all plan to use this geopotential force model on-board. The Solar, Anomalous, and Magnetospheric Particle Explorer (SAMPEX) is already flying this geopotential force model. Past analysis has shown that one of the leading sources of error in the OBC propagated ephemerides is the omission of the higher order geopotential terms. However, these same analyses have shown a wide range of accuracies for the OBC ephemerides.

Analysis was performed, using EUVE state vectors, that showed that the EUVE four day OBC propagated ephemerides varied in accuracy from 200 m. to 45 km. depending on the initial vector used to start the propagation. The vectors used in the study were from a single EUVE orbit at one minute intervals in the ephemeris. Since each vector propagated practically the same path as the others, the differences seen had to be due to differences in the initial state vector only.

An algorithm was developed that will optimize the epoch of the uploaded state vector. Proper selection can reduce the previous errors of anywhere from 200 m. to 45 km. to generally less than one km. over four days of propagation. This would enable flight projects to minimize state vector uploads to the spacecraft. Additionally, this method is superior to other methods, in that no additional orbit estimations need to be done. The definitive ephemeris generated on the ground can be used, as long as the proper epoch is chosen. This algorithm can easily be coded in software that would pick the epoch, within a specified time range, that would minimize the OBC propagation error.

This technique should greatly improve the accuracy of the OBC propagations on-board future spacecraft such as TRMM, WIRE, TRACE, SWAS, and XTE without increasing complexity in the ground processing.

INTRODUCTION

Several future, and some current missions, use an on-board computer (OBC) propagator known as the *Landis propagator*. These missions include TRMM, WIRE, TRACE, SWAS, XTE, and SAMPEX. This propagator is a simple two-body propagator with additional force models added for atmospheric drag and nonspherical Earth harmonics. The geopotential model uses only the zonal harmonics J_2 , J_3 , and J_4 and sectorial harmonics $C_{2,2}$ and $S_{2,2}$. The modeling in the propagator is limited by OBC memory and CPU constraints. Ideally, each mission using this propagator would want the generated ephemeris to closely match the ground determined ephemeris which uses more advanced modeling. The error in the ground generated ephemeris is dominated by uncertainties in the daily f10.7 solar flux level. This error would be found in any ground generated or on-board ephemeris, regardless of other modeling, unless solar flux prediction techniques improve. The leading error in the difference between the ground generated ephemeris and the OBC ephemeris is the geopotential model. It is this error that is examined in this paper.

All accuracy numbers quoted in this paper are three sigma.

FORCE MODELING

The *Landis Propagator* was developed by Peter Hui of Advanced Technology Research Corporation and modified slightly by Dr. Landis Markley of the Goddard Space Flight Center¹. The propagator was developed to provide simple on-board ephemeris propagation.

A gravitational potential model for a nonspherical body is commonly represented by a finite series of associated legendre polynomials (ALPs). The size of such a model is determined by the maximum degree and order of the ALPs included in the expansion series. The gravitational potential of the Earth can be expressed by the following spherical harmonic representation²:

$$V(r, \phi, \lambda) = \frac{\mu}{r} + \frac{\mu}{r} \sum_{n=2}^{\infty} C_n^0 \left(\frac{R_E}{r} \right)^n P_n^0(\sin \phi) + \frac{\mu}{r} \sum_{n=2}^{\infty} \sum_{m=1}^n \left(\frac{R_E}{r} \right)^n P_n^m(\sin \phi) (S_n^m \sin m\lambda + C_n^m \cos m\lambda)$$

where

V = gravitational potential

μ = Earth's GM

R_E = equatorial radius of the Earth

P_n^m = ALP of degree n and order m

S_n^m, C_n^m = harmonic coefficients

r = magnitude of radius vector

ϕ = geocentric latitude

λ = geocentric longitude

The current geopotential model used by the Flight Dynamics Facility (FDF) is the Joint Gravity Model (JGM)-2. This geopotential model has degree and order 50 and is considered the most accurate geopotential model available. An ephemeris propagated with this full geopotential model would be

considered the most accurate available. The on-board ephemeris accuracies quoted later in this paper are compared to a truth ephemeris propagated with the following force modeling:

- JGM-2 degree and order 50
- atmospheric drag with the Jacchia-Roberts model
- solar radiation
- Earth tides
- Sun and Moon point masses

The *Landis Propagator* has the following force modeling:

- Earth nonspherical gravitational effects: zonal harmonics J_2 , J_3 , and J_4
sectorial harmonics $C_{2,2}$ and $S_{2,2}$
- Earth atmosphere: modified Jacchia-Roberts '71 model
- solar radiation pressure: not modeled
- Earth tides: not modeled
- noncentral point masses: not modeled

Covariance analysis of the OBC propagator error was performed using the error model shown in Table 1.

TABLE 1: OBC Error Model

<u>Parameter</u>	<u>Uncertainty</u>
Earth nonspherical gravitation effects	100% of the harmonic coefficients excluded in the OBC model
Earth atmosphere	none
solar radiation	100% of C_r
Earth tides	100% of second Love number
noncentral point masses	100% of GM of Sun and Moon

The Earth atmosphere error contribution was not included because the atmospheric models used on the ground and on the OBC are very similar and any inherent error in the modeling would appear in both propagations.

The covariance analysis was performed using state vectors from the Extreme UltraViolet Explorer (EUVE). The results of the covariance analysis indicate that, for the EUVE mission orbit, the above error model contributed approximately the errors shown in Table 2 to the OBC ephemeris after four days:

TABLE 2: Covariance Analysis Results

<u>Parameter</u>	<u>Position Error (m.)</u>
Earth nonspherical gravitation effects	200 to 44600
solar radiation	40
Earth tides	55
Moon point mass	350
Sun point mass	50

The omission of the additional geopotential terms is clearly the dominate source of error in the OBC propagation compared with the ground ephemeris. The range of the geopotential errors is explained later in this paper.

PAST RESULTS

The initial purpose of this analysis was to investigate the true errors introduced by using a severely truncated geopotential model for onboard propagation and to explain the differences seen in past results.

Pre-mission analyses were performed for both TRMM and XTE. Ref. [3] stated that the XTE OBC propagation would degrade to 60 km. in accuracy in 5.4 to 9.3 days. However, this analysis incorporated f10.7 solar flux uncertainties in the prediction accuracy. Since the predicted uncertainties are dominated by uncertainties in both the f10.7 solar flux and the geopotential, the errors quoted in this report could not be attributed solely to the geopotential. Ref. [4] stated TDRS OBC accuracies for prediction onboard XTE. The seven day predicted accuracy was three km. This result was not relevant because of the small geopotential effect on geosynchronous orbits. Ref. [5] stated TRMM OBC accuracies at both beginning of life (BOL) and end of life (EOL). The 32 hour prediction accuracy was 22 km. for BOL and 32 km. for EOL. These results however were based upon orbits with different semi-major axes and also included f10.7 solar flux uncertainties. Ref. [6], by A. Schanzle, stated XTE OBC accuracies for five different arcs based upon five different epochs. The five epochs were each one day apart. F10.7 solar flux uncertainties were not considered. The four day prediction accuracy ranged from 1.2 to 43.0 km. The leading error contribution to the prediction error was the geopotential which confirmed the covariance analysis mentioned in the last section. It was this report that gave the first documented results of large variations in the OBC predicted ephemeris accuracy.

Schanzle had speculated that "... the large variation in the magnitude of the propagation differences noted in the [software] results is a consequence of the epoch semi-major axis relative to its average value. If this is the case, then errors in an OBC-generated trajectory may be minimized by uplinking a state vector to the OBC that occurs at a time when the semi-major axis is close to its average value." The correlation between OBC propagation accuracy and the difference between the osculating semi-major axis and the mean semi-major axis is shown in Figure 1. The correlation coefficient between the two was 0.75 but the sample was very small. Schanzle made two additional simulations later that are also shown in Figure 1. These two additional points did not confirm his theory and, in fact, brought the correlation coefficient down to 0.35.

ANALYSIS

The first step was to perform covariance analysis using different epochs but at a much closer interval than the one day interval for the samples in Ref. [6]. The goal was to determine some sort of pattern from the seemingly random OBC propagation errors. Two different spacecraft orbits were chosen: SAMPEX and EUVE. In each case, an operational mission vector was propagated for four hours using full force modeling. Then, covariance analysis was performed on a four day OBC propagation using an initial vector every 20 minutes from the four hour ephemeris. The results are shown in Figures 2 and 3.

The SAMPEX OBC errors after four days ranged from 1.1 to 49.3 km. The EUVE OBC errors after four days ranged from 2.5 to 40.0 km. Neither graph shows a smooth pattern of how the OBC propagation error changes with the epoch. It is clear, however, that the OBC error predictions vary even with epochs from the same orbit. This, despite the fact, that the epochs were just minutes apart and that they covered almost the identical trajectory in their propagations over the four days. This indicated that there was some characteristic of the initial starting vector that contributed greatly to the OBC propagation error, even over several days. The unknown OBC errors between each of the points on these graphs needed to be

determined to investigate how the OBC errors change.

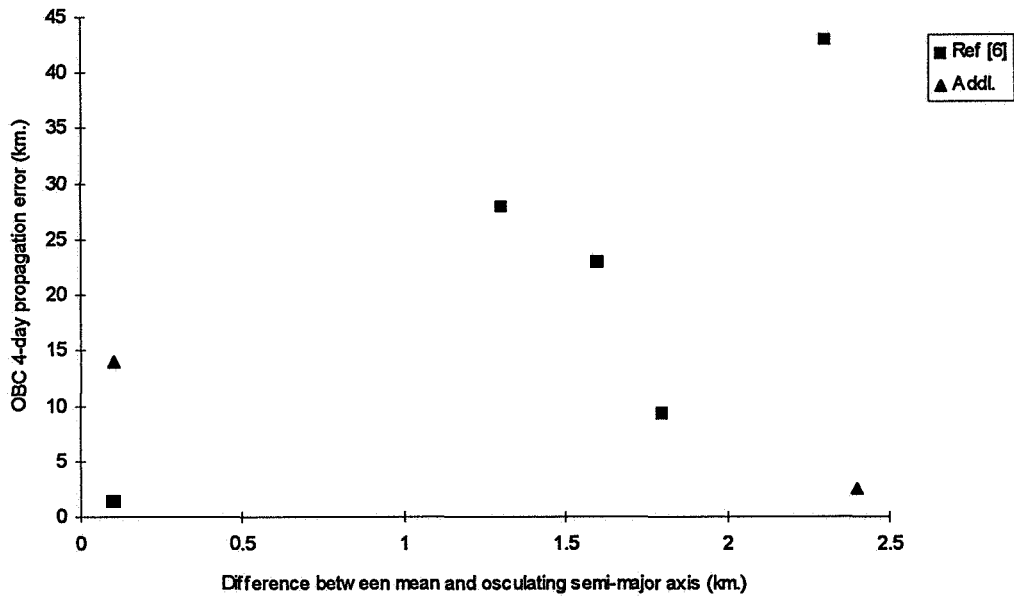


FIGURE 1: Schanzle's OBC Propagation Error vs. Semi-major Axis

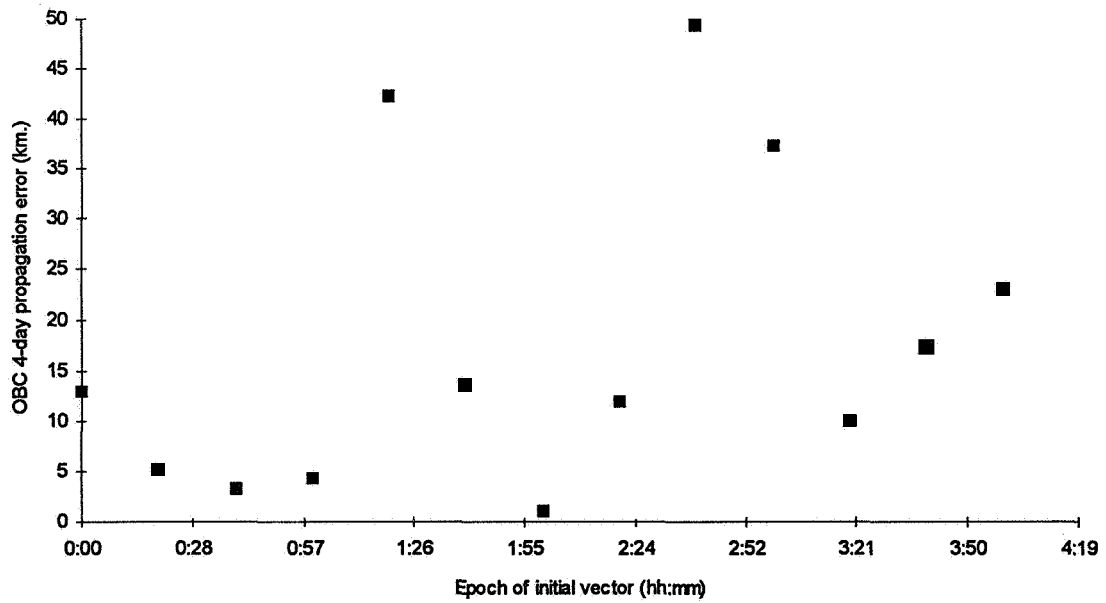


FIGURE 2: SAMPEX 4-day OBC Propagation Errors

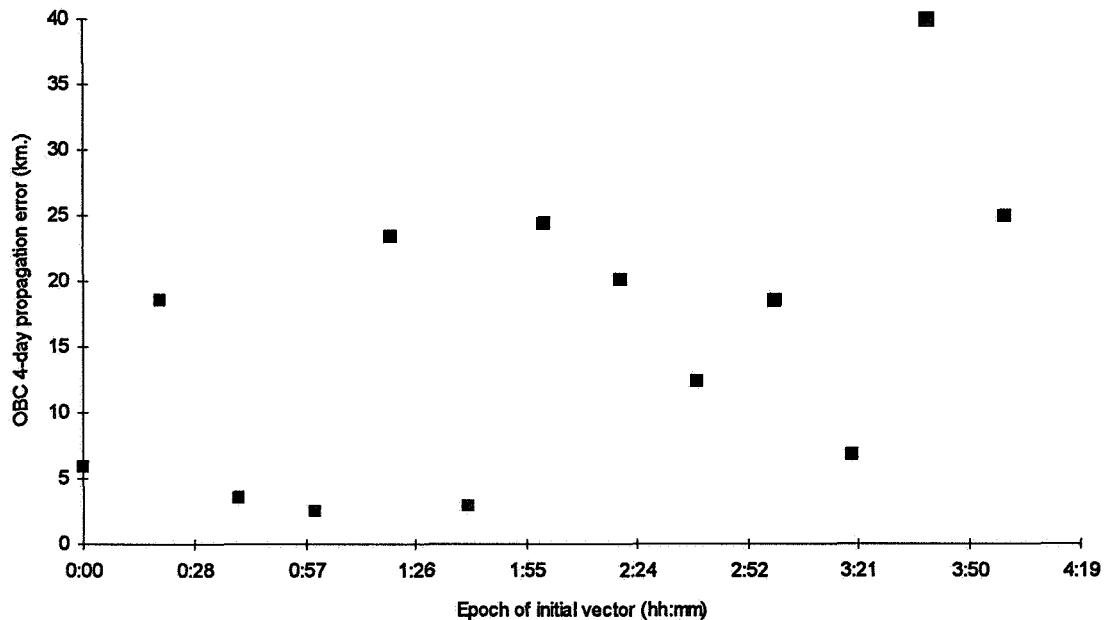


FIGURE 3: EUVE 4-day OBC Propagation Errors

The EUVE mission orbit was chosen and covariance analysis of a four day OBC propagation was done using EUVE vectors every one minute for an entire EUVE orbit of 95 minutes. The results are shown in Figure 4.

The pattern is finally clearly seen, and seems to exhibit a smoothly changing error that reverses itself abruptly at zero, which may indicate that the error has changed sign. The OBC propagation errors ranged from 0.2 to 44.6 km. The problem was now reduced to finding some characteristic of the initial vector that exhibited some correlation with this OBC propagation error pattern.

To further investigate Schanzle's theory, the EUVE OBC propagation error was compared to the difference between the mean and the osculating semi-major axis, shown in Figure 5. The correlation coefficient between the two was only -0.12.

The OBC propagation error was far too complex to be correlated to the altitude of the spacecraft around the orbit (correlation coefficient of 0.16 with altitude). The OBC propagation error also did not correlate with the eccentricity (correlation coefficient of 0.11) or the argument of latitude (0.30).

The analysis was then concentrated on the gravitational potential at the epoch. The two ephemerides being compared, the ground generated ephemeris and the OBC generated ephemeris, had two different gravitational potentials at the epoch. Therefore, they also had different gravitational forces and energy at epoch. The OBC propagation errors were compared to various potentials, gravities, and energies in various directions as shown in Table 3. The symbols g_{50} , G_{50} , V_{50} , and E_{50} represent the gravitation acceleration magnitude, acceleration vector, potential, and total energy, respectively, of the full geopotential model up to degree and order 50, as is used in the ground generated ephemeris. The symbols g_{OBC} , G_{OBC} , V_{OBC} , and E_{OBC} represent the gravitational acceleration magnitude, acceleration vector, potential, and total energy, respectively, of the OBC truncated geopotential model. The arguments: x , y , z , r , i , c , e , and n , represent directions: inertial Cartesian x , y , and z , radial, intrack, crosstrack, east, and north.

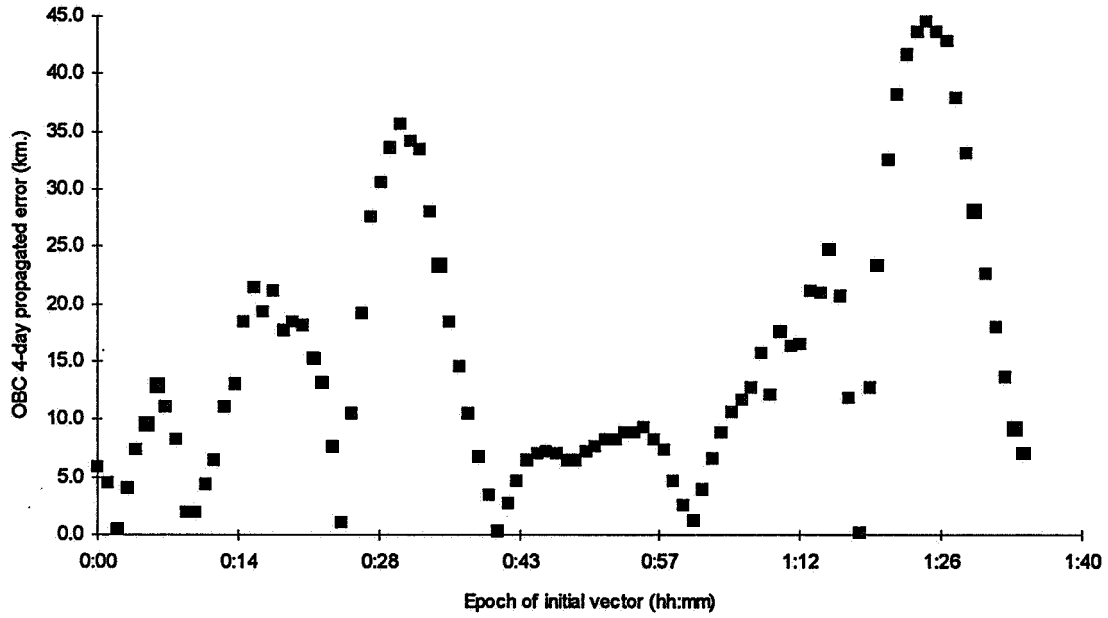


FIGURE 4: EUVE 4-day OBC Propagation Errors At One Minute Intervals

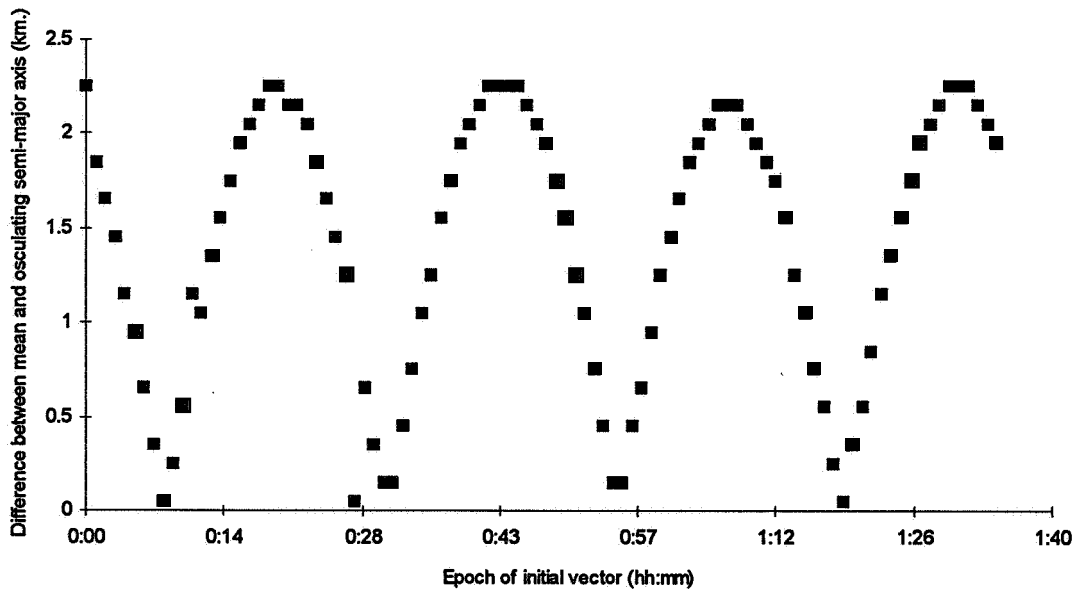


FIGURE 5: EUVE Osculating Semi-major Axis

TABLE 1: Correlation Coefficients

Characteristic	Correlation Coefficient	Characteristic	Correlation Coefficient
g50	-0.19	$\Delta(gOBC(r)-g50(r))$	0.01
gOBC	-0.18	$gOBC(i)-g50(i)$	0.00
$ g50-gOBC $	0.79	$ gOBC(i)-g50(i) $	-0.01
$\Delta g50-gOBC $	0.08	$\Delta(gOBC(i)-g50(i))$	0.00
$ G50-GOBC $	0.52	$gOBC(c)-g50(c)$	0.17
$\Delta G50-GOBC $	-0.03	$ gOBC(c)-g50(c) $	-0.31
$gOBC(x)-g50(x)$	-0.57	$\Delta(gOBC(c)-g50(c))$	0.06
$ gOBC(x)-g50(x) $	0.49	$gOBC(e)-g50(e)$	0.00
$\Delta(gOBC(x)-g50(x))$	0.15	$ gOBC(e)-g50(e) $	-0.09
$gOBC(y)-g50(y)$	-0.20	$\Delta(gOBC(e)-g50(e))$	0.07
$ gOBC(y)-g50(y) $	0.11	$gOBC(n)-g50(n)$	0.16
$\Delta(gOBC(y)-g50(y))$	-0.32	$ gOBC(n)-g50(n) $	-0.09
$gOBC(z)-g50(z)$	0.26	$\Delta(gOBC(n)-g50(n))$	0.16
$ gOBC(z)-g50(z) $	0.25	VOBC-V50	0.23
$\Delta(gOBC(z)-g50(z))$	-0.27	$ VOBC-V50 $	0.96
$gOBC(r)-g50(r)$	-0.15	EOBC-E50	-0.20
$ gOBC(r)-g50(r) $	0.79		

Three characteristics of the epoch show marked correlation with the OBC propagated errors:

- the differences in the magnitude of the gravitational acceleration vectors between the full 50 by 50 model and the OBC model
- the differences in the radial acceleration vector between the full 50 by 50 model and the OBC model
- the differences in the gravitational potential between the full 50 by 50 model and the OBC model

The potential differences are extremely well correlated with a correlation coefficient of 0.96! The three characteristics are shown together in Figure 6 over the full 95 minutes of the EUVE orbit.

It can be seen from this graph that the differences in the magnitude of the acceleration vectors is due mostly to the differences in the radial direction.

Since the potential differences showed the highest correlation, they are shown together with the OBC propagation errors in Figure 7.

The differences in the gravitational potential between the full and the OBC fields is a clear indicator of the OBC propagation accuracy.

ALTERNATIVE TECHNIQUES

Alternative techniques have been suggested to improve OBC propagation accuracy. Roger Hart, Flight Dynamics Division, Goddard Space Flight Center, has developed and demonstrated a technique that also eliminates the OBC propagation error due to the truncated geopotential field. The technique is as follows:

1. Generate a predicted ephemeris based upon an orbit estimation using full force modeling.

2. Convert the state vectors in the predicted ephemeris into tracking measurements.
3. Use the simulated tracking measurements in an orbit estimation using the OBC truncated geopotential model.
4. Generate a definitive ephemeris from the orbit estimation state.
5. Generate the Extended Precision Vector (EPV) from the definitive ephemeris.

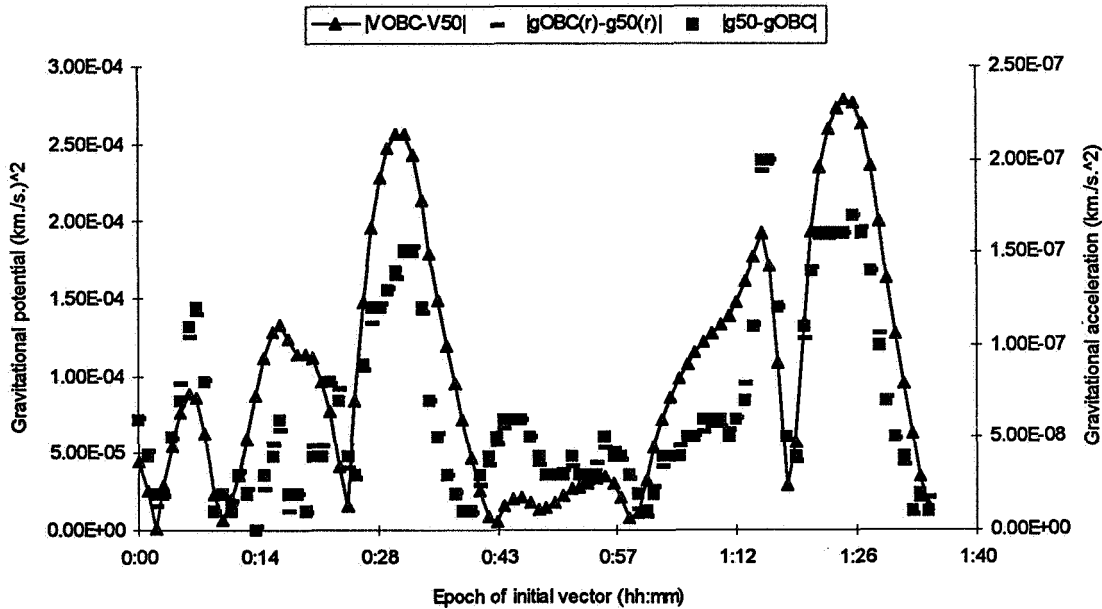


FIGURE 6: Potential & Acceleration Differences Between Full & OBC Geopotential Models

The algorithm uses an EPV generated using the same force modeling that is on-board the OBC. Thus, the EPV will propagate the same as the definitive ephemeris generated on the ground. This definitive ephemeris is forced to fit the ground generated predicted ephemeris using full force modeling. So the OBC propagation will be generally similar to the ground generated predicted ephemeris for the span of the ephemeris.

The drawback to this method is the complexity of the procedure. Three additional steps are added to the current procedure: simulating the tracking measurements, performing a batch orbit estimation, and generating the definitive ephemeris. None of the above steps is trivial. Experiments using this technique have been generally favorable though.

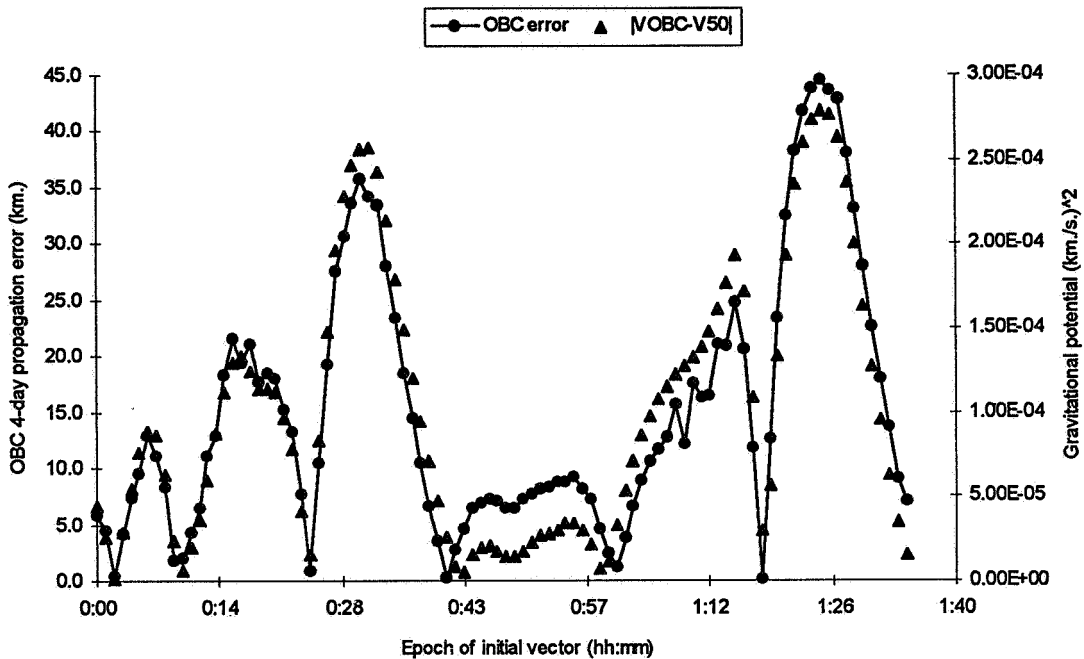


FIGURE 7: Comparison Between Gravitational Potential and OBC Propagation Errors

IMPACT

The impact of this finding is that each of the missions using this OBC geopotential force model can greatly improve the accuracy of the OBC propagation by a simple selection of the epoch of the uploaded state vector.

EPVs are uploaded to the spacecraft for SAMPEX, which is the only current mission using the *Landis propagator*. An additional piece of EPV optimization software, approximately 150 lines of code, would be needed to select the optimum epoch between user defined boundaries. The flowchart for a prototype of this software is shown in Figure 8. The minimum potential difference is found between user defined boundaries and the epoch of this minimum is output. The software checks each state vector in the definitive ephemeris, so if the definitive ephemeris is at 60 second intervals, then the optimized epoch will be chosen to the minute.

Currently for SAMPEX, EPVs at 00:00 Greenwich Mean Time (GMT) on the day of the orbit determination are uploaded to the spacecraft. To take advantage of the improvements detailed in this paper, EPVs with epochs from approximately 23:15 GMT to 00:45 GMT would have to be uploaded. This would give an entire orbit of varying potential differences and should ensure propagation accuracies of less than one km. after four days.

Current FDF ground operations, including orbit determination, predicted ephemeris propagation, coordinate transformation, and EPV generation, are highly automated. The use of this EPV optimization software would not impact that automation. The data flow for FDF ground operations is shown in Figure 9.

The EPV optimization would have to be individually tailored to meet the specific needs of each mission.

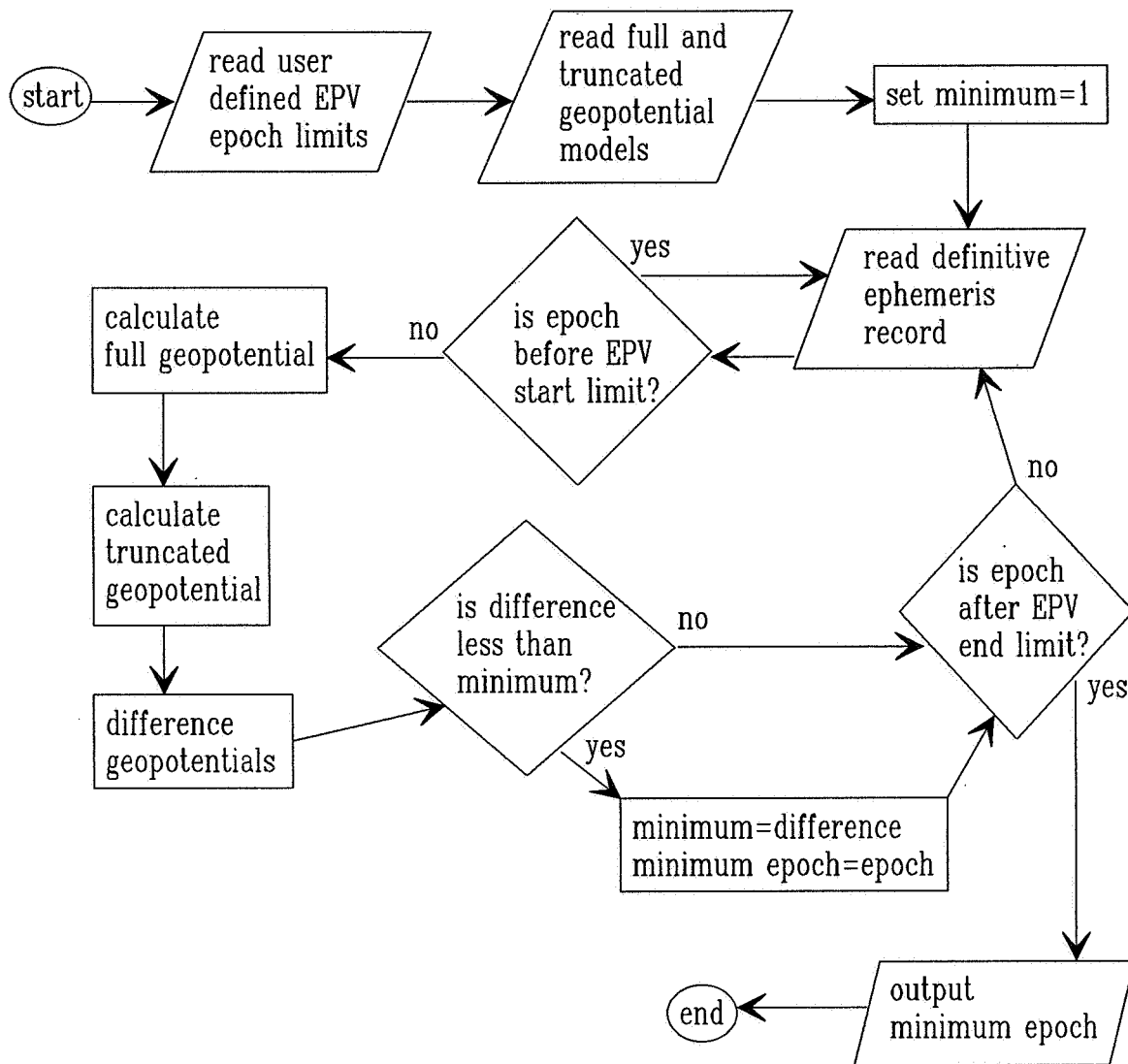


FIGURE 8: EPV Optimization Software Flowchart

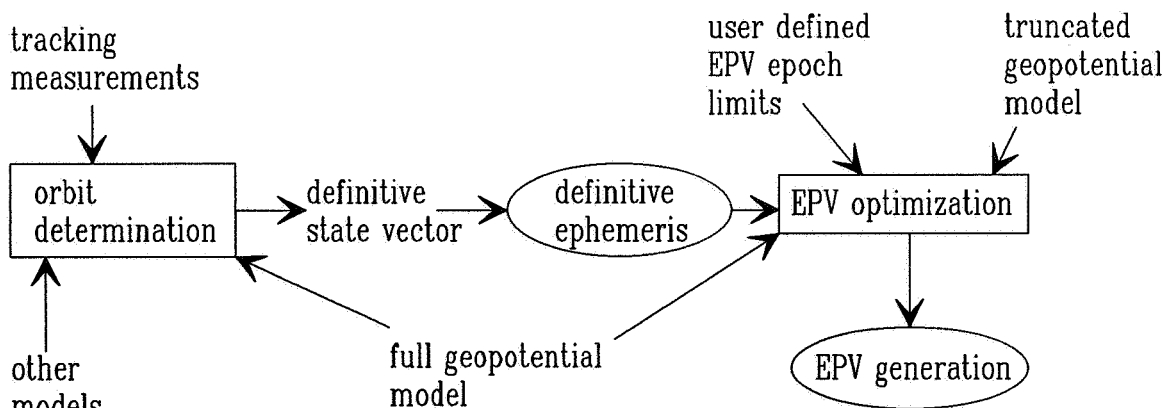


FIGURE 9: Data Flow for FDF Ground Operations

CONCLUSIONS

OBC propagation errors due to gravitational potential effects can be greatly reduced by simple judicious selection of the epoch of the uploaded state vector. The OBC propagation accuracy is highly correlated to the difference in gravitational potential at epoch between the full geopotential model and the truncated OBC model. Simple software can be added to the automated generation of the uploaded EPVs that will select the optimum epoch to use. Use of this procedure can increase OBC propagation accuracy by up to 1000% when compared to the ground generated ephemeris. Generally, a four day OBC propagation can be optimized to less than one km. in accuracy.

ACKNOWLEDGMENTS

The author wishes to acknowledge Mr. Roger Hart for his help in the analysis performed in this investigation.

REFERENCES

1. Markley, Dr. Landis. Private communication, February 1996.
2. Goddard Space Flight Center, Flight Dynamics Division, *Orbit Determination Error Analysis System (ODEAS) Mathematical Specifications, Revision 2*, 554-FDD-90/029R2UD0, T. Lee and C. Yee (Computer Sciences Corporation), September 1993.
3. Goddard Space Flight Center, Flight Dynamics Division, *Report on the XTE Onboard Computer Prediction Capabilities* (memorandum), A. Schanzle (Computer Sciences Corporation), February 3, 1993.
4. Goddard Space Flight Center, Flight Dynamics Division, *Report on Propagated Errors in the Position of a TDRS Using the XTE OBC* (memorandum), A. Schanzle (Computer Sciences Corporation), May 21, 1993.
5. Goddard Space Flight Center, Flight Dynamics Division, *Report on Error Analysis of Tropical Rainfall Measuring Mission (TRMM) Maneuver Recovery and Onboard Computer (OBC) Prediction Capabilities* (memorandum), D. Kelbel and A. Schanzle (Computer Sciences Corporation), March 23, 1994.
6. Goddard Space Flight Center, Flight Dynamics Division, *Geopotential Error Model Calibration for the OBC* (memorandum), A. Schanzle and M. Hoppe (Computer Sciences Corporation), September 22, 1995.

Application of Tracking and Data Relay Satellite (TDRS) Differenced One-Way Doppler (DOWD) Tracking Data for Orbit Determination and Station Acquisition Support of User Spacecraft Without TDRS Compatible Transponders*

A. D. Olszewski, Jr., and T. P. Wilcox
Computer Sciences Corporation (CSC)
Lanham-Seabrook, Maryland, USA 20706

M. Beckman
National Aeronautics And Space Administration
Goddard Space Flight Center (GSFC)
Greenbelt, Maryland, USA 20771

Abstract

Many spacecraft are launched today with only an omni-directional (omni) antenna and do not have an onboard Tracking and Data Relay Satellite (TDRS) transponder that is capable of coherently returning a carrier signal through TDRS. Therefore, other means of tracking need to be explored and used to adequately acquire the spacecraft. Differenced One-Way Doppler (DOWD) tracking data are very useful in eliminating the problems associated with the instability of the onboard oscillators when using strictly one-way Doppler data.

This paper investigates the TDRS DOWD tracking data received by the Goddard Space Flight Center (GSFC) Flight Dynamics Facility (FDF) during the launch and early orbit phases for both the Interplanetary Physics Laboratory (WIND) and the National Oceanic and Atmospheric Administration (NOAA)-J missions. In particular, FDF personnel performed an investigation of the data residuals and made an assessment of the acquisition capabilities of the DOWD-based solutions. Comparisons of DOWD solutions with existing data types were performed and analyzed in this study. This evaluation also includes atmospheric editing of the DOWD data and a study of the feasibility of solving for Doppler biases in an attempt to minimize error. Furthermore, by comparing the results from WIND and NOAA-J, an attempt is made to show the limitations involved in using DOWD data for the two different mission profiles. The techniques discussed in this paper benefit the launches of spacecraft that do not have TDRS transponders on board, particularly those launched into low Earth orbit. The use of DOWD data is a valuable asset to missions which do not have a stable local oscillator to enable high-quality solutions from the one-way return-link Doppler tracking data.

Introduction

Differenced One-Way Doppler (DOWD) (Reference 1) is an open-loop type of tracking data used to minimize the effects of the user spacecraft transmit frequency offset. The user spacecraft return signal is received by two Tracking and Data Relay Satellites (TDRSs), frequency translated, and then relayed independently to the White Sands Complex for processing. (See Figure 1.) TDRS-4 (East) and TDRS-5 (West), supported through the White Sands Ground Terminal (WSGT), were the two relay spacecraft used for the DOWD tracking test for the Interplanetary Physics Laboratory (WIND) mission. TDRS-3 (Spare/West) and TDRS-4 (East), supported through WSGT and the Second TDRS System (TDRSS) Ground Terminal (STGT), respectively, were the two TDRSs used for the National Oceanic and Atmospheric Administration-J (NOAA-J) DOWD tracking test.

Individual one-way Doppler measurements are dominated by atmospheric refraction, user spacecraft antenna offset, transponder delays, and oscillator frequency bias. If a user spacecraft has a wide-beam antenna system, or if two omni antennas are available, the signal can be received by two or more TDRSs simultaneously. The signals received from the TDRSs will have essentially the same biases. Therefore, differencing the measurements will almost completely cancel out the biases, and the resulting DOWD tracking data are as accurate as two-way Doppler measurements (Reference 2).

This paper gives a description of the DOWD methodology and the results of its application to the WIND and NOAA-J missions, followed by a summary and conclusions.

* This work was supported by the National Aeronautics and Space Administration (NASA)/Goddard Space Flight Center (GSFC), Greenbelt, Maryland, under Contract NAS 5-31500.

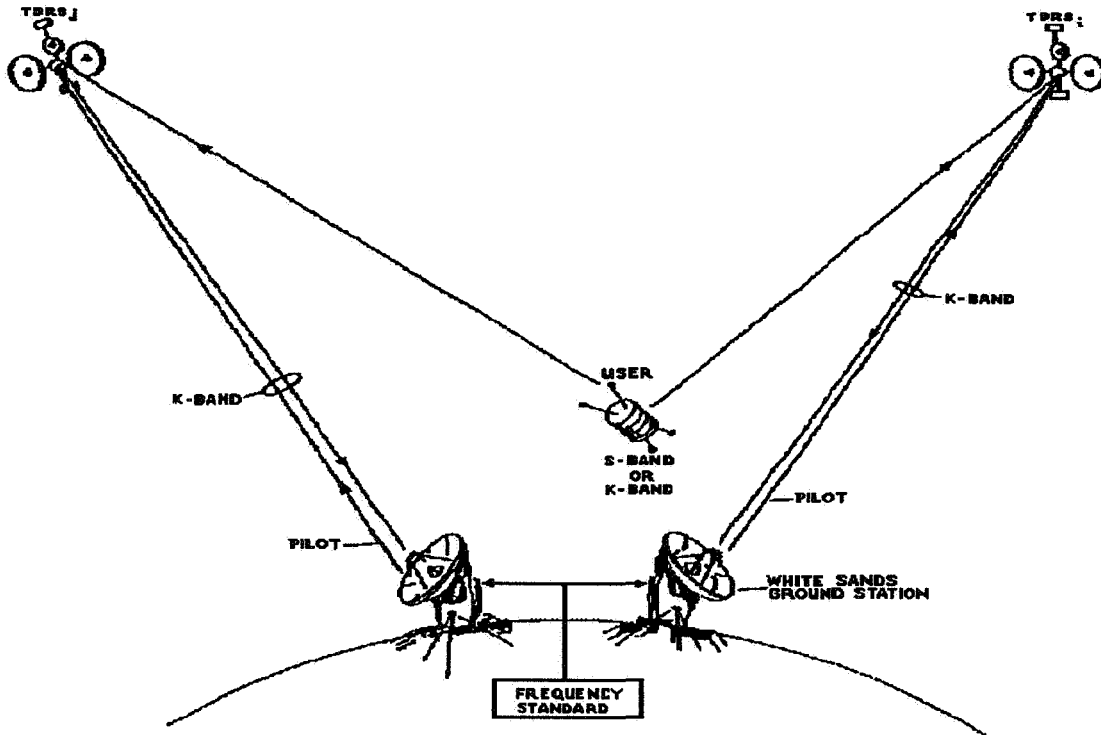


Figure 1. Differenced One-Way Doppler Tracking Configuration (Reference 3)

Methodology

The Goddard Trajectory Determination System (GTDS) was used to obtain differential correction (DC) orbit solutions. Because the DOWD tracking data were routed to the Goddard Space Flight Center (GSFC) Flight Dynamics Facility (FDF) in a format that is not directly usable by GTDS, special processing was required to convert the data and then difference the TDRS one-way Doppler measurements for each matching time. Previous DC orbit solutions determined the TDRS position states used in these calculations. Therefore, the TDRS states were considered known at any instant of time, allowing only the WIND or NOAA-J states to be estimated. The following equation was used to compute the difference of the already reduced one-way Doppler measurements. (See Reference 4.)

$$\Delta v_d(T) = [v_d(T)]_{compare} - [v_d(T)]_{reference} \quad (1)$$

where

- $\Delta v_d(T)$ = computed differenced one-way Doppler measurement at time T
- $[v_d(T)]_{compare}$ = comparison TDRS one-way Doppler measurement (TDRS_i)
- $[v_d(T)]_{reference}$ = reference TDRS one-way Doppler measurement (TDRS_j)

When solving for the bias of a DOWD solution, the effects due to atmospheric refraction and the user biases cancel out. This occurs because the intrinsic nature of DOWD tracking is such that the data are the difference of two Doppler measurements and the biases associated with those Doppler measurements. The algorithms used in GTDS assume that the atmosphere is spherically symmetric with respect to the center of the Earth, meaning that the index of refraction varies radially with the altitude. The atmospheric biases attributed to each TDRS are theoretically the same. Therefore, the solved-for bias is simply the difference between two TDRS biases, which is a very small number. This can be shown mathematically as

$$\beta_{total} \equiv (\beta_{user} + \beta_{atm} + \beta_{TDRS-i}) - (\beta_{user} + \beta_{atm} + \beta_{TDRS-j}) = \beta_{TDRS-i} - \beta_{TDRS-j} \quad (2)$$

where

- β_{total} = total biases
- β_{user} = user biases
- β_{atm} = atmospheric biases
- $\beta_{TDRS-i/j}$ = TDRS-i and TDRS-j biases

The application of this methodology to the WIND and NOAA-J missions is described below.

WIND Support

FDL personnel conducted tests using data from the launch of the WIND spacecraft on November 1, 1994, at 09:31:00.057 universal time coordinated (UTC). Several DC solutions were performed, four of which are described below. Of the four solutions presented, two solutions are DOWD-only runs with differing tracking data spans, one solution contains both DOWD and Deep Space Network (DSN) tracking data measurements, and the fourth solution is a DSN-only based solution.

The test was run in parallel with the actual operational launch support. An operational solution, generated by the launch support team during launch, will be used for comparison purposes. This solution will be referred to as the reference solution throughout this report. The observation span of the reference solution is slightly more than 4 hours and includes 26-meter range-rate data from the Goldstone, California, and Madrid, Spain, DSN tracking sites (referred to as DS16 and DS66, respectively, throughout this report). DSN 26-meter range data were also received from the DS16 site. Only 4 hours of data could be included in this solution because of a spacecraft maneuver. Table 1 lists the tracking data, excluding angles, that were available for orbit determination through 12:52:00 UTC, which was the end of the DS66 one-way and two-way data. The transition from the noncoherent mode to the coherent mode occurred at approximately 11:16:42 UTC. Table 2 lists the data types and the parameters used in generating the four solutions. Angle data were not used in this analysis so as to simulate support using 34-meter antennas, even though the support was done with 26-meter antennas. The 34-meter antennas do not have autotrack capability and therefore do not provide valid angle measurements. This simulates the worst-case scenario.

For the first solution, the nominal premission spacecraft separation vector from the WIND Mission Support Plan was used as the a priori state. Keplerian covariance constraints were applied to the a priori state to allow the estimation of the semimajor axis, eccentricity, and mean anomaly. This effectively allows estimation of the energy and perigee position, while restricting the a priori orbit plane, which was assumed to be generally accurate due to the geometry of the WIND trajectory during the transfer orbit phase.

Table 1. WIND Tracking Data

Time of Tracking Data Pass on November 1, 1994 HHMMSS-HHMMSS (UTC)	Type of Tracking Data	Supporting Station
105700-114200	DOWD (total span)	TDRS-4/TDRS-5
105700-111642	DOWD (valid span)	TDRS-4/TDRS-5
111910-113150	Range-Rate	DS16 (two-way)
113200-113800	Range-Rate	DS16 (one-way)
113200-113800	Range-Rate	DS66 (one-way)
113810-121900	Range-Rate	DS16 (two-way)
113810-121900	Range-Rate	DS66/DS16 (three-way)
121910-122200	Range-Rate	DS16 (one-way)
121940-125200	Range-Rate	DS66 (two-way)
122210-125200	Range-Rate	DS16/DS66 (three-way)
111919-121817	Range	DS16 (two-way)
122044-125140	Range	DS66 (two-way)

Table 2. WIND Solution Parameters

Solution	Data Type	A Priori State	Constrained Solution	Data Arc Selected (hh:mm:ss)	Usable Valid Span (mm:ss)
1	DOWD only	Nominal separation vector	Yes (Keplerian)	10:57:00–11:04:26	DOWD 04:14
2	DOWD only	Solution 1	No	10:57:00–11:42:00	DOWD 15:45
3	DOWD and DSN	Solution 1	No	11:00:04–11:28:40	DOWD 15:46 DS16 10:26
4	DSN only	Solution 1	No	11:00:10–11:38:40	DS16 20:00
Reference	DSN only	Operational intermediate solution	No	11:19:10–15:21:00 12:19:40–12:52:00	DS16 241:50 DS66 32:20

To simulate support using only DOWD data, the solution state from the first DC solution was used as the a priori state in the second DOWD-only solution. The a priori state for the DSN-only solution was also the same as the a priori states from the second and third solutions. Two attempts were also made at solutions using only 10 and 15 minutes of valid DSN data; however, these attempts were unsuccessful and the solutions did not converge.

NOAA-J Support

Task personnel conducted tests using data from the launch of the NOAA-J spacecraft that occurred on December 30, 1994, at 10:02 UTC. Several DC solutions were performed, nine of which are described below. Of the nine solutions presented, five solutions are DOWD-only with differing data spans, three solutions contain both DOWD and C-Band (skin tracking) data, and the ninth solution is based on C-band tracking data only. Table 3 lists the tracking data that were available for orbit determination.

Table 3. NOAA-J Tracking Data

Time of Tracking Data Pass on December 30, 1994 HHMMSS–HHMMSS (UTC)	Type of Tracking Data	Supporting Station
114343–115510	DOWD	TDRS-3/TDRS-4
114500–115200	C-Band	Pillar Point, California (PPTQ)
114800–120042	C-Band	Kaena Point, Hawaii (KPTQ)
121846–123000	DOWD	TDRS-3/TDRS-4
132648–133918	C-Band	Kaena Point, Hawaii (KPTQ)
133048–134624	C-Band	Kwajalein Island (KMRT)
142000–143736	C-Band	Ascension Island (ASCQ)
151018–152706	C-Band	Kwajalein Island (KMRT)
160154–161454	C-Band	Ascension Island (ASCQ)

An operational solution, generated by the launch support team, is used for comparison. This solution will be referred to as the reference solution throughout this report. The observation span of the reference solution is slightly more than 6 hours and includes all the C-band tracking data that were available on the day of launch. This reference solution, considered the best estimate of the orbit, was used to update acquisition data at launch plus 7 hours.

Table 4 lists the tracking data types and the parameters used in generating the NOAA-J solutions. The first solution was based on all the DOWD data that were available at 115510 UTC, which is when Earth occultation occurred for TDRS-4. Because of the geometry of NOAA-J and the TDRSs, atmospheric editing was performed for the DOWD data that were below 200 kilometers (km) in altitude to obtain a convergent solution for solutions 2, 4, 5, 7, and 8. Atmospheric editing was not applied to the shorter arc solutions because too much data were edited out and the solutions would not converge.

The modeling for solution 6 was identical to the modeling for solution 1, except that the position was tightly constrained (to 10 centimeters). In addition, the modeling for solution 8 was identical to that for solution 7, except that solution 8 solved for the TDRS biases. Solution 9 was generated during real-time support of NOAA-J based on all the C-band data available for orbit determination at launch plus 3 hours. This solution was considered to be the best estimate of the orbit at that time.

Table 4. NOAA-J Solution Parameters

Solution	Data Type	Atmospheric Editing / Bias Solve-For	Constrained Solution	Data Arc Selected (hh:mm:ss)	Usable Valid Data (mm:ss)
1	DOWD only	No / No	No	11:43:43–11:55:10	DOWD 11:27
2	DOWD only	Yes (below 200km) / No	No	11:43:43–12:30:00	DOWD 22:41
3	DOWD and C-Band	No / No	No	11:43:43–11:55:10	DOWD 11:27 PPTQ 01:42 KPTQ 04:18
4	DOWD and C-Band	Yes (below 200km) / No	No	11:43:43–12:30:00	DOWD 22:41 PPTQ 04:36 KPTQ 11:00
5	DOWD and C-Band	Yes (below 200km) / No	No	11:43:43–16:15:00	DOWD 22:41 PPTQ 04:24 KPTQ 20:24 KMRT 09:54 ASCQ 15:06
6	DOWD only	No / No	Yes (position constrained to 10 cm)	11:43:43–11:55:10	DOWD 11:27
7	DOWD only	Yes (below 200km) / No	Yes (position constrained to 10 cm)	11:43:43–12:30:00	DOWD 22:41
8	DOWD only	Yes (below 200km) / Yes	Yes (position constrained to 10 cm)	11:43:43–12:30:00	DOWD 22:41
9	C-Band only	No / No	No	11:45:00–12:00:42	PPTQ 04:30 KPTQ 10:54
Reference	C-Band only	No / No	No	11:45:00–16:14:54	PPTQ 04:42 KPTQ 20:30 KMRT 09:54 ASCQ 16:12

Results

The results from applying the DOWD methodology to the WIND and NOAA-J missions are given below.

WIND Mission

Table 5 lists the pertinent parameters for the four solutions. The target semimajor axis of this transfer orbit mission phase was 249475.5340 km. The reference solution was based on slightly more than 4 hours of data. This solution used tracking data from two DSN antennas (DS16 and DS66). Compared to the reference solution, the shorter arc solutions significantly underestimated the size of the orbit.

The DOWD data residuals for the entire span of the accepted data only are shown in Figure 2. These residuals range from ~ -9 to ~ +9 hertz.

Table 5. WIND Solution Parameters

Solution No.	Solution	Semimajor Axis (km)	Eccentricity	Inclination (degrees)	RAAN	Argument of Latitude	DOWD Mean Residual (hertz)	DOWD Standard Deviation (hertz)
1	DOWD-only (short span)	249475.5340	0.9737	28.7353	2.3860	30.4191	-0.0026	6.162
2	DOWD-only (full span)	248604.2948	0.9736	30.5321	0.9950	31.7291	0.711	6.121
3	DOWD and DSN	245342.8617	0.9732	28.7815	2.3470	30.5752	2.144E-06	6.119
4	DSN-only	246308.2120	0.9734	28.7828	3.0666	29.9468	N/A	N/A
5	Reference	248941.0706	0.9732	28.7541	2.4186	30.5168	N/A	N/A

NOTE: All elements are osculating true-of-date Keplerian, with an epoch of 941101 10:52:05.532 UTC, except for the reference solution, which has an epoch of 10:52:41.000 UTC. N/A = not applicable; RAAN = right ascension of the ascending node

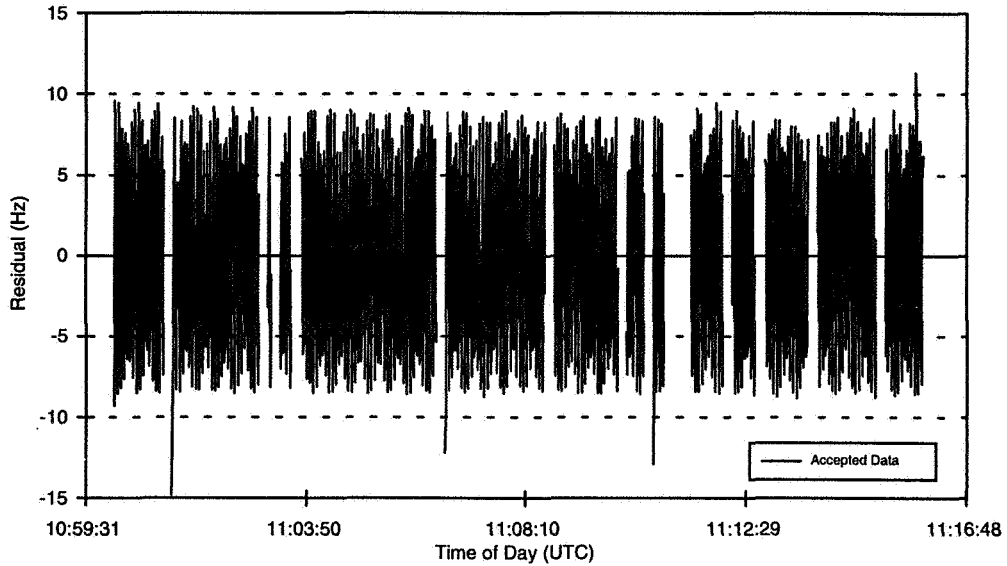


Figure 2. WIND Orbit Determination DOWD Residuals

To better characterize the nature of the residuals, a 1-minute span was evaluated. Figure 3 shows the DOWD residuals for a 1-minute span of the data arc. The standard deviation of the residuals shown in Figure 3 is 6.112 hertz. This is comparable to the 6.121 hertz value for the entire DOWD-only solution. The sinusoidal nature of the plot is due to the spin rate of the WIND spacecraft (~ 15.6 rpm). The modulation of the amplitude is a result of the sampling rate of the data (one per second). The high residuals are caused by the lack of modeling of the spin in the DC solution. The two omni antennas were not aligned along the spin axis. (A more detailed spin rate analysis is given in Reference 5).

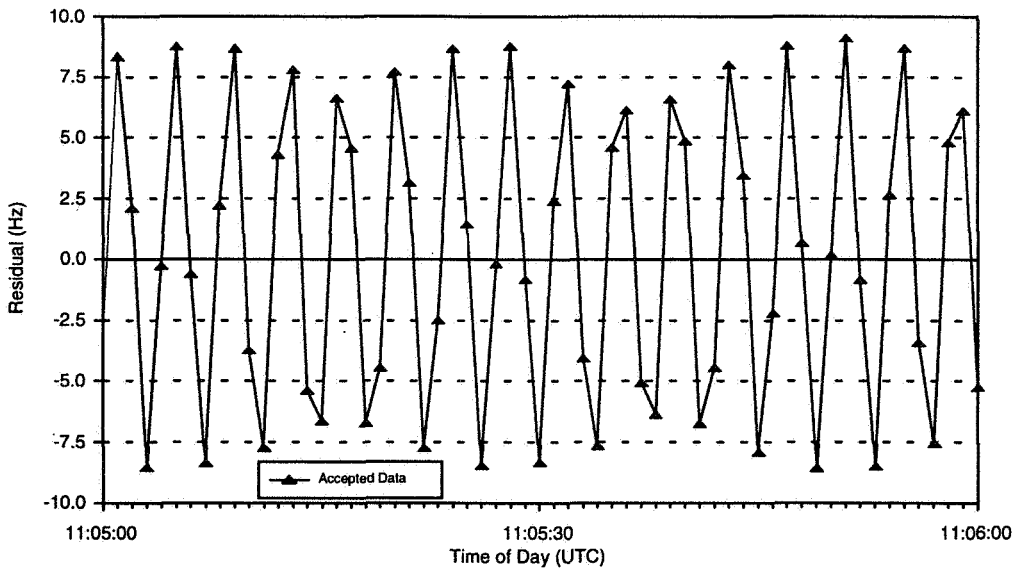


Figure 3. WIND Orbit Determination DOWD Residuals

The antenna-pointing acquisition tolerance for the WIND spacecraft was a half-cone angle of 0.13 degree during the early, postseparation phase for the 34-meter antennas. To determine if this tolerance was met, the azimuth and elevation angles for WIND acquisition from the DS16 and DS66 sites were generated for both the DOWD-only solution and the reference

solution. It is assumed that acquisition aid antenna capabilities do not exist, thus simulating the worst case scenario. The total angle differences were then determined with respect to each site, using the following equation:

$$\Delta\Theta = \cos^{-1}[\sin(El_1)\sin(El_2) + \cos(El_1)\cos(El_2)\cos(\Delta az)] \quad (3)$$

where

- $\Delta\Theta$ = total angle difference between trajectories
- Δaz = azimuth angle difference between trajectories
- $El_{1/2}$ = elevation angles for DOWD solution and reference solution, respectively

Figures 4 and 5 display that the full-span, DOWD-only solution was within the acquisition tolerance for approximately 40 minutes after the end of the definitive data arc. The total angle differences rapidly increase over the next 4 hours, up to nearly 0.6 degree, which is well above the acquisition tolerance. The data from acquisition of signal (AOS) through the end of the definitive data span were omitted from the figures because only the predictive acquisition capabilities were of interest.

Similar analyses were performed for the DOWD/DSN solution and the DSN-only solution. The DOWD/DSN solutions (Figures 6 and 7) show that the 0.13-degree tolerance is met for several hours after AOS at both DS16 and DS66. However, the DSN-only solution (Figures 8 and 9) did not meet the tolerance at any time for either site.

Figures 4 through 9 illustrate the importance of having a sufficient mix of tracking data types in the solution. As these figures show, the DSN-only solution was insufficient for acquisition capabilities, and the full-span, DOWD-only solution was only sufficient if the spacecraft could be acquired and lock maintained in the short time that the tolerance is not exceeded. However, the combined DSN and DOWD solutions were more than capable of acquiring the spacecraft throughout the entire tracking span. This shows that the solution state is much more stable over time for combined data type solutions than for single data type solutions.

Several other solutions were performed in addition to the test case solutions described above. Solutions using atmospheric editing of the DOWD data showed that the editing had no effect on the solution because the WIND-to-TDRS line of sight is outside the Earth's atmospheric effects throughout the DOWD tracking data span. Other solutions were generated using position constraints in an attempt to improve the estimate of the velocity. Permission error analysis showed that angle data should not be used for constrained solutions (Reference 6). A better estimate of the velocity allows a determination of whether a correction burn is necessary to achieve the nominal trajectory. However, when these constrained solutions are propagated over time, the ephemeris accuracy degrades rapidly. The DOWD-only constrained solution did not give an accurate estimate of the velocity, primarily due to the short span of the data arc. When the DOWD data are combined with 10 minutes and 26 seconds of DSN data (as in solution 3), the velocity estimate improves considerably.

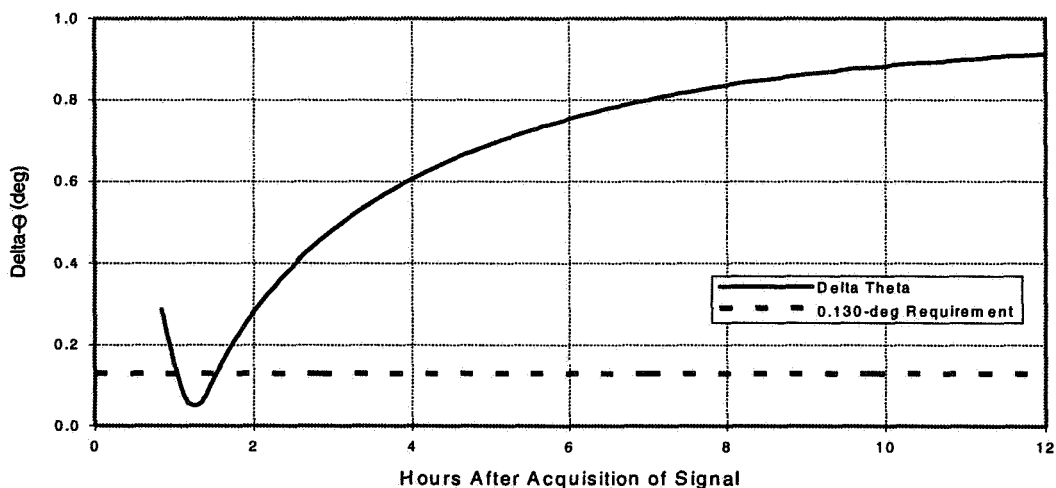


Figure 4. WIND Angle Difference for DS16 During Contact Times Only (DOWD Only)

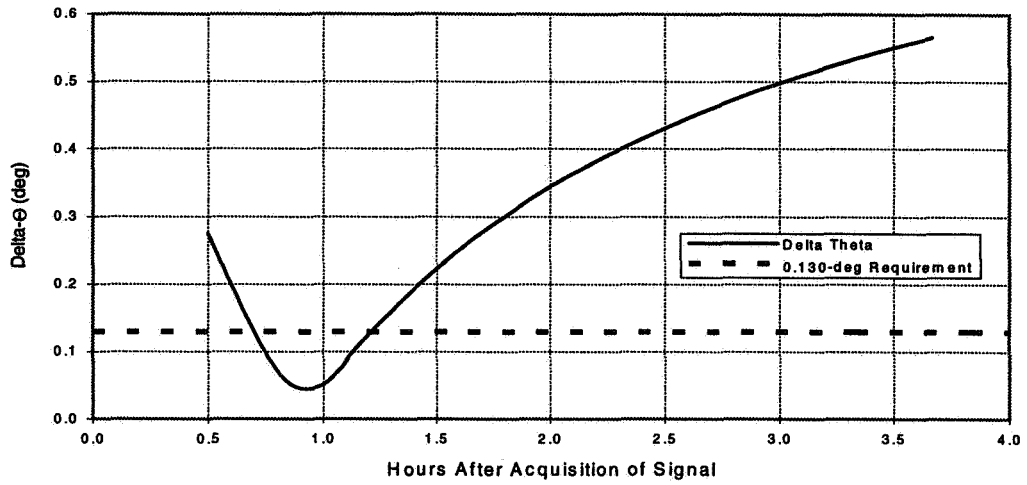


Figure 5. WIND Angle Difference for DS66 During Contact Times Only (DOWD Only)

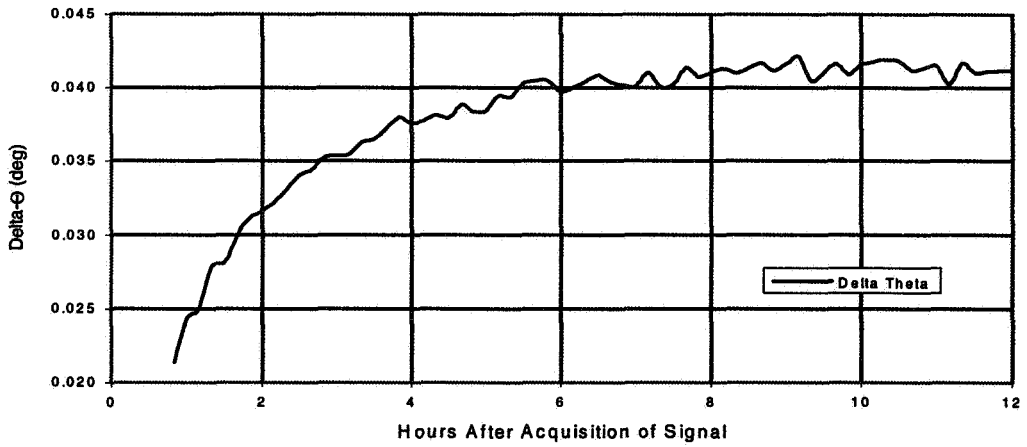


Figure 6. WIND Angle Difference for DS16 During Contact Times Only (DOWD/DSN)

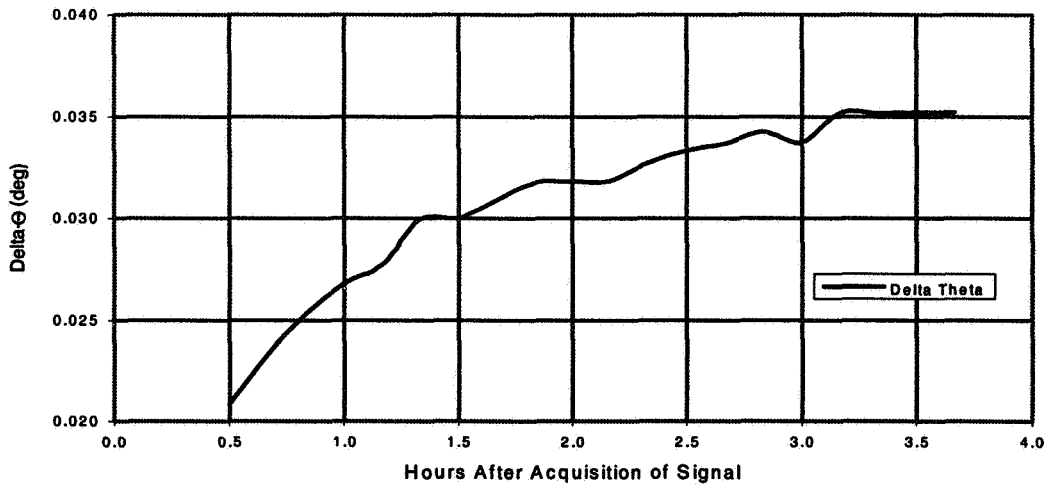


Figure 7. WIND Angle Difference for DS66 During Contact Times Only (DOWD/DSN)

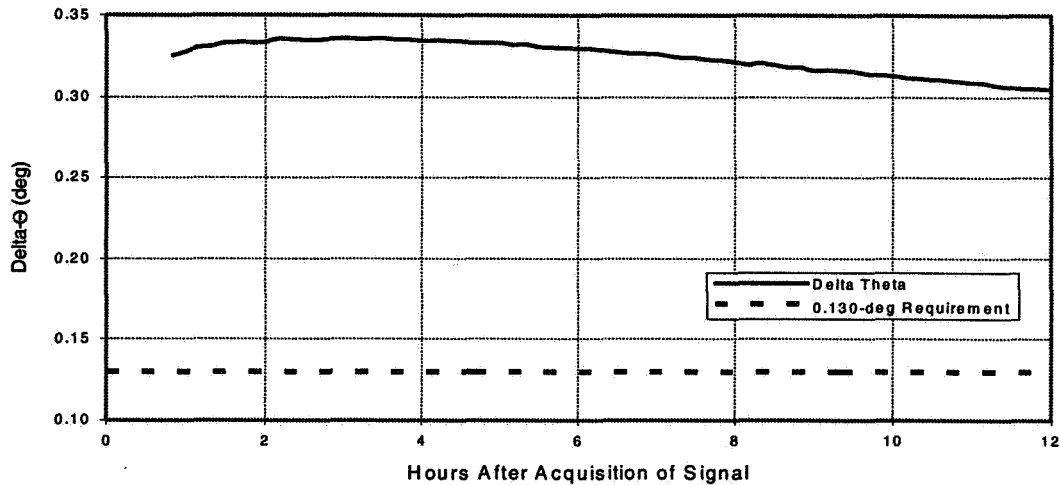


Figure 8. WIND Angle Difference for DS16 During Contact Times Only (DSN Only)

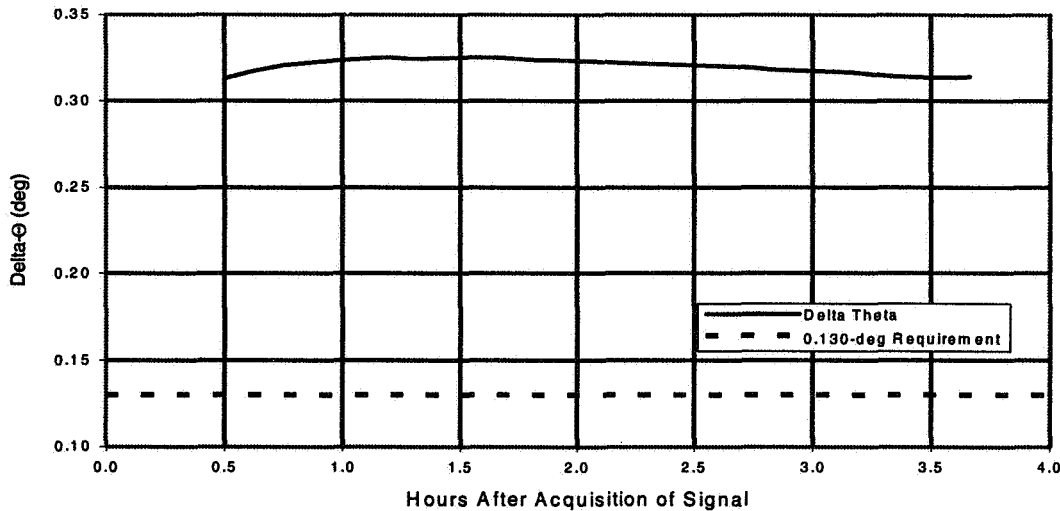


Figure 9. WIND Angle Difference for DS66 During Contact Times Only (DSN Only)

NOAA-J Mission

Table 6 lists the pertinent parameters for the test case solutions, and for other intermediate, operational support solutions and ephemerides.

Comparisons were made between the ephemeris for each solution and the reference solution ephemeris to determine how the small differences in the elements affect the solution state over time. This is of critical importance to acquisition capabilities because if the solution state diverges rapidly (from the truth) and is not updated, then acquisition of the spacecraft can be inhibited and possibly not occur. Figures 10 through 12 show how the ephemerides compare over time.

The DOWD data residuals for the entire span of the accepted data only are shown in Figure 13. These residuals range from ~ -0.12 to ~ +0.16 hertz.

Table 6. NOAA-J Solution Parameters

Hours From Injection	Solution Number	Solution	Semimajor Axis (km)	Eccentricity	Inclination (degrees)	RAAN	Argument of Latitude
0:00:00	–	Nominal injection	7237.3832	0.00024	98.8622	303.4543	181.3522
0:00:00	–	LTAS	7242.8635	0.00404	98.8542	303.4335	182.0072
0:50:38	–	NORAD two-liner	7239.7017	0.00049	98.8891	303.4503	181.5041
1:37:55	1	DOWD	7238.2915	0.00042	98.8879	303.4435	181.4571
1:37:55	6	DOWD (position constraints)	7238.1937	0.00042	98.8924	303.4449	181.4544
1:37:55	3	DOWD and C-Band	7238.6703	0.00045	98.8778	303.4420	181.4735
1:43:37	9	C-Band	7238.2479	0.00037	98.8803	303.4416	181.4548
2:12:55	2	DOWD	7238.2216	0.00045	98.8861	303.4446	181.4491
2:12:55	4	DOWD and C-Band	7238.4648	0.00043	98.8795	303.4414	181.4616
2:12:55	7	DOWD (position constraints)	7238.2306	0.00045	98.8867	303.4448	181.4503
2:12:55	8	DOWD (position constraints; bias solve-for)	7238.2306	0.00045	98.8867	303.4448	181.4503
3:30:19	–	C-Band	7238.4657	0.00041	98.8801	303.4412	181.4647
4:20:31	–	C-Band	7238.4606	0.00043	98.8791	303.4417	181.4614
5:10:01	–	C-Band	7238.4640	0.00043	98.8795	303.4415	181.4618
5:57:49	Reference	C-Band	7238.4637	0.00043	98.8794	303.4415	181.4618
5:57:49	5	C-Band and DOWD	7238.4616	0.00043	98.8795	303.4415	181.4614

NOTE: All elements are osculating true-of-date Keplerian, with an epoch of 941230 10:17:05 UTC, except for the nominal injection ephemeris, which has an epoch of 10:17:02.418 UTC.

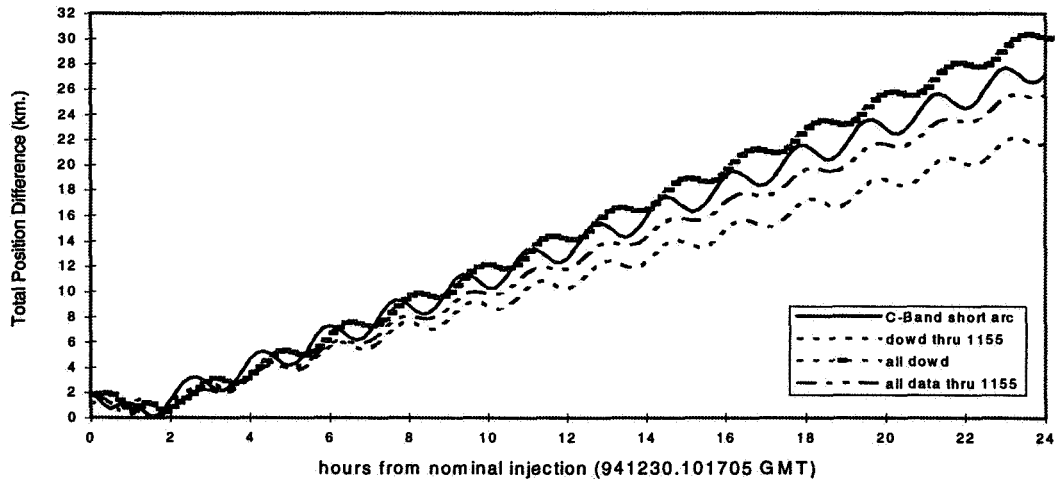


Figure 10. NOAA-J Comparisons of Solutions With Reference Solution

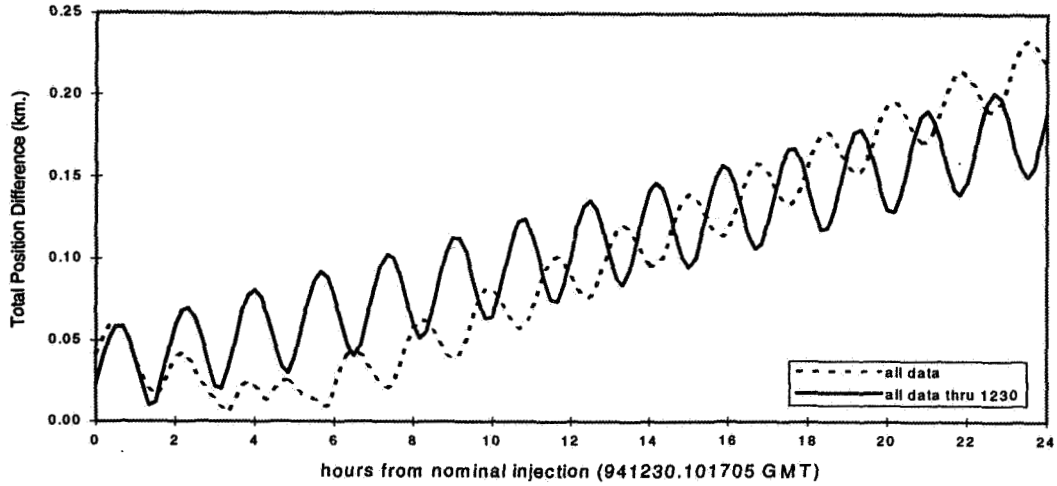
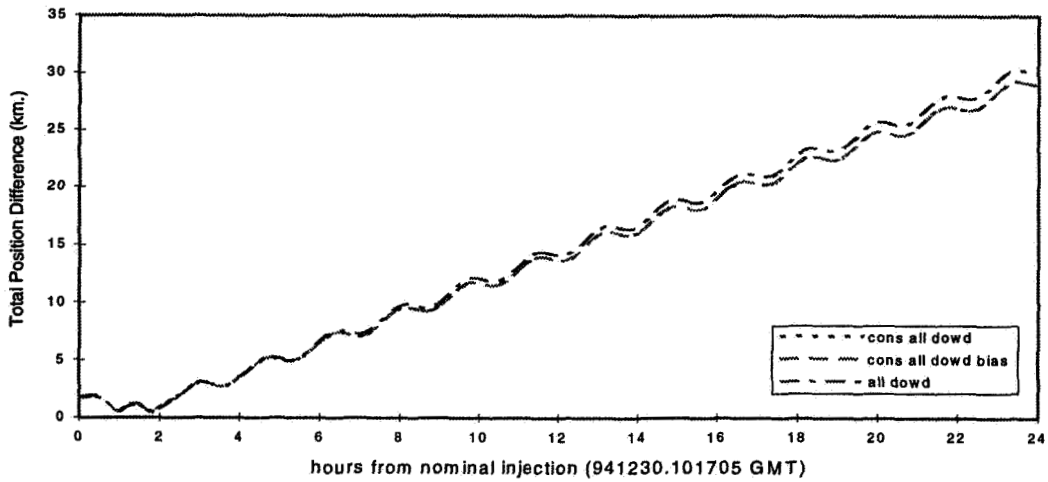


Figure 11. NOAA-J Comparisons of Solutions With Reference Solution



Figures 12. NOAA-J Comparisons of Solutions With Reference Solution

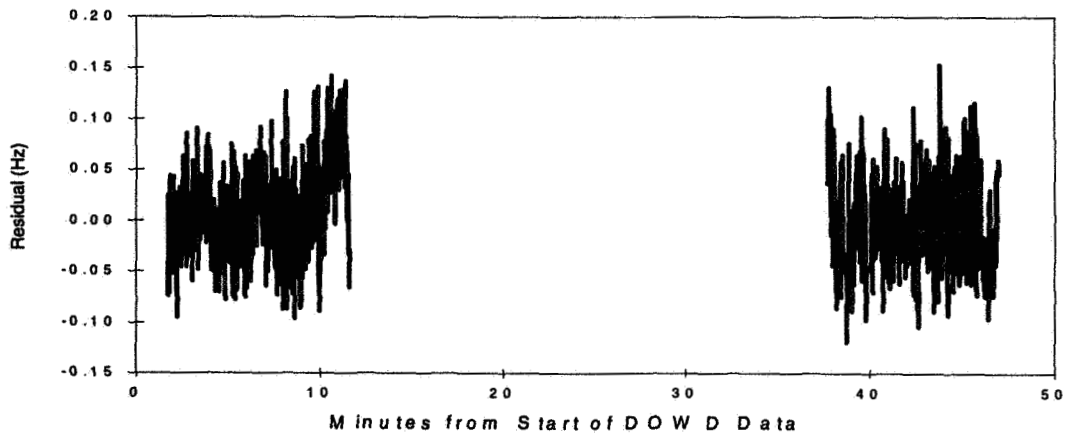


Figure 13. NOAA-J Differenced One-Way Doppler Residuals for Accepted Data

To better characterize the residuals, a 2-minute span was evaluated. The results of this evaluation are shown in Figure 14. It is apparent from Figure 14 that NOAA-J is not a spin-axis stabilized spacecraft. The two omni antennas were not aligned along the neutral axis of the spacecraft.

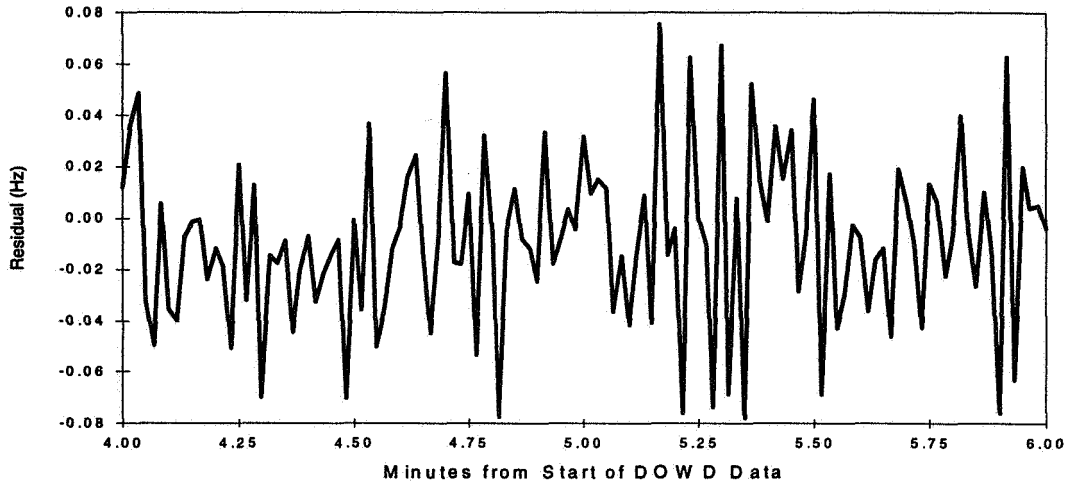


Figure 14. NOAA-J Differenced One-Way Doppler Residuals for Accepted Data

The antenna-pointing acquisition tolerance for the NOAA-J spacecraft was a half-cone angle of 0.215 degree and 0.220 degree for the Wallops and Ascension sites, respectively. As with WIND, the azimuth and elevation angles for NOAA-J acquisition from the Wallops and Ascension sites were generated for both the full-span, DOWD-only solution and the reference solution to determine if the acquisition tolerances were met. The total angle differences were also determined with respect to each site.

Figures 15 and 16 show that the DOWD-only solution (solution 1) was within the acquisition tolerance throughout most of the data arc. There are some spikes that exceed the tolerance in the angle differences; however, the spacecraft would probably still be acquired because there are approximately 20 minutes of data before these spikes that could be used for acquisition. These spikes represent the times at which NOAA-J is at the maximum elevation; hence, the corresponding velocity is also a maximum, which could inhibit the ability to acquire. It should be stressed that solution 1 was based on only 11 minutes and 27 seconds of useable DOWD data. Figures 17 and 18 show that the DOWD/C-band short-arc solution (solution 3) and the C-band-only short-arc solution (solution 9) are also within tolerance throughout most of the data arc.

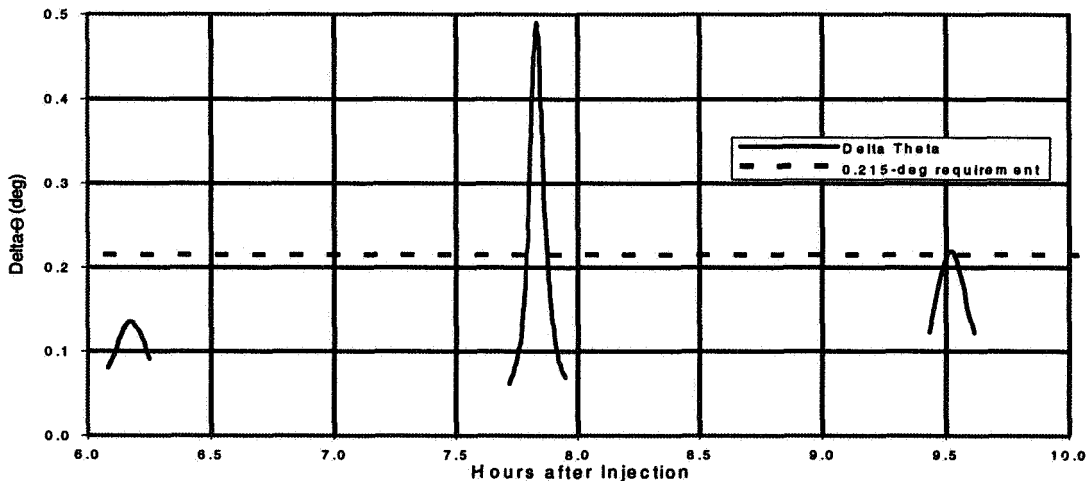


Figure 15. NOAA-J Angle Difference for Wallops During Contact Times Only (Solution 1)

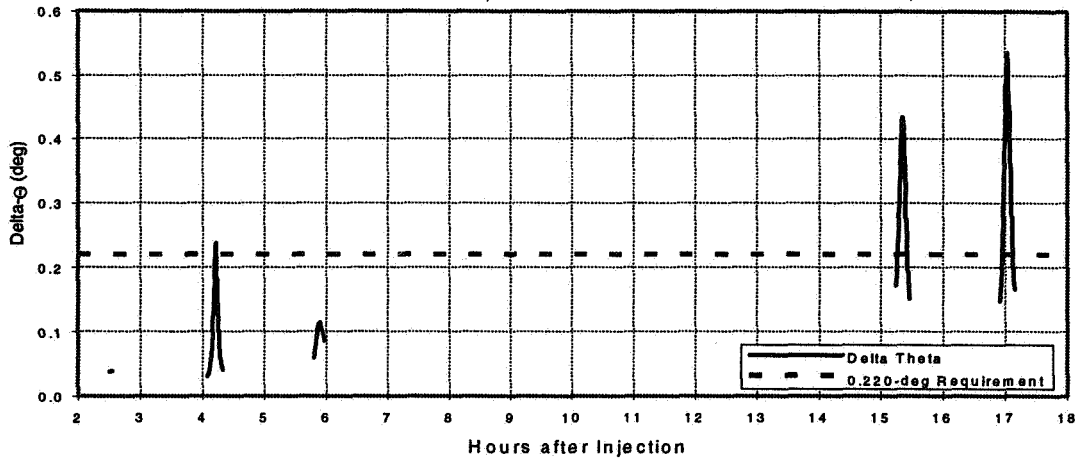


Figure 16. NOAA-J Angle Difference for Ascension During Contact Times Only (Solution 1)

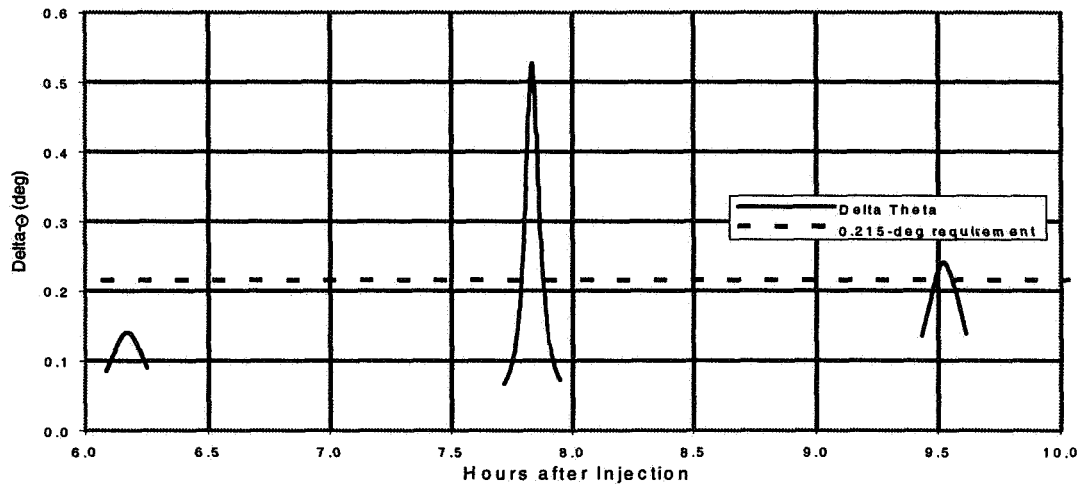


Figure 17. NOAA-J Angle Difference for Wallops During Contact Times Only (Solution 3)

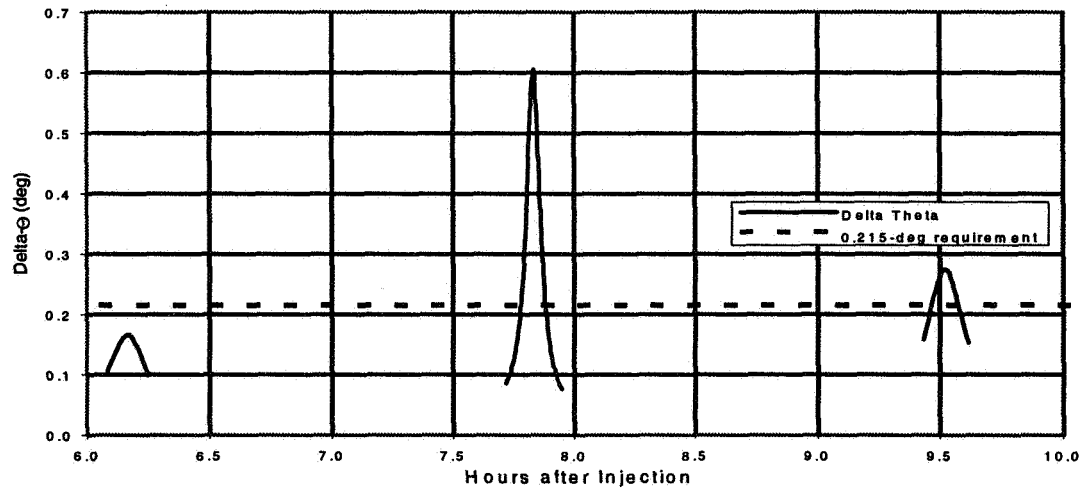


Figure 18. NOAA-J Angle Difference for Wallops During Contact Times Only (Solution 9)

In addition to the test case solutions described above, several other solutions were performed. In particular, several solutions were generated using all of the available DOWD data while changing the atmospheric editing criteria. The solutions did not converge when the editing criterion was set to edit the data below 100 km, 400 km, and 600 km. The solution also diverged when the atmospheric editing option was not implemented, i.e., all of the data were considered in the solution regardless of any possible atmospheric effects. When the criterion was set at 300 km, the solution did converge; however, the maximum position difference between the solution ephemeris and the reference ephemeris was 63.3 km. The final solution had the atmospheric editing criterion set at 200 km. This solution converged and compared better with the reference ephemeris than the solution with the atmospheric editing criteria set at 300 km.

Attempting to solve for the TDRS biases did not significantly improve the solution. TDRS biases are inherently small, and the combined solved-for bias, which is the difference of the two TDRS biases, was only -0.01170 hertz.

Summary and Conclusions

This investigation determines the viability of using TDRS DOWD tracking data during the critical launch and early orbit phases of both the WIND and the NOAA-J missions. Orbit determination solutions were generated using solely the DOWD tracking data, as well as DOWD data in conjunction with standard data types such as C-band, DSN range, and DSN range-rate. The quality assessment was based on determining whether the antenna beamwidth constraints were met using the acquisition data (azimuth and elevation angles) derived from the DOWD-based ephemerides.

The results showed that the DOWD-only solution for WIND was theoretically viable for a 30-minute period after separation. Note that in actual mission operations, the DOWD-only solution might not be timely enough for acquisition purposes. By the time the DOWD tracking data are processed and used in an orbit determination solution for an ephemeris propagation, and the acquisition data are generated and transmitted, the stations might not have enough time to use these acquisition data. (More than 30 minutes would probably have elapsed.) On the other hand, using the DOWD data in conjunction with only 10 minutes of DSN range-rate data yielded far better results in terms of meeting the antenna beamwidth constraints for extended periods of time (at least 12 hours). The DSN-only, single-station solution, based on 10 minutes of range-rate data, was not acceptable for acquisition purposes at any time. Therefore, the DOWD data were essential for generating a quality solution based on minimal amounts of tracking data. This would have been significant if a contingency had arisen during the WIND mission calling for more immediate acquisition data updates.

For the WIND spacecraft, deleting data through the use of atmospheric editing criteria had no effect on the solution because the WIND trajectory was outside the effects of the Earth's atmosphere throughout the span of DOWD data. Also, attempting to solve for a TDRS bias would not be prudent because the data arc is extremely short and because of the highly elliptical nature of the orbit. Errors are introduced into the solution when solving for a bias over such a short arc, because another variable must be solved for in addition to the orbital state variables.

The NOAA-J results showed that all the solutions were viable for acquisition throughout the entire early orbit support period of approximately 10 hours. These solutions included DOWD-only and C-band-only tracking data spans. When the DOWD and C-band tracking data were combined over shorter tracking data spans, the solutions were enhanced, thus improving acquisition capabilities. The optimal solutions were obtained when the atmospheric editing criterion was set at 200 km. However, this is dependent on the amount of tracking data available and the type of orbit. If the tracking data available are sparse, then no atmospheric editing should be done, so as to permit the maximum amount of data to be brought into the solution.

Solving for TDRS biases did not improve the solutions for NOAA-J because the solved-for biases were simply the difference of two TDRS biases and were therefore very small. This is due to the fact that the atmospheric effects and the user transponder biases are effectively cancelled out. Combining the DOWD data with the C-Band data drastically improved the solution state of NOAA-J. This was the case for the short-arc solution as well as for the longer arc solution. This is of great importance early in a mission when the tracking data can be scarce, or when the mission is nonnominal.

Both the WIND and the NOAA-J results show the possible benefits of TDRS DOWD tracking data for critical launch and early orbit support. The WIND short-span solutions were only viable when DOWD data were included in the solution. The NOAA-J DOWD-only solutions were viable without any other data types included in the orbit determination. This is significant for a contingency scenario, such as a ground station going down before an expected pass. Given the nature of some orbit profiles, specifically polar-orbiting spacecraft, the available ground station coverage might not be sufficient for a timely orbit determination solution unless DOWD data were available.

An additional benefit of the DOWD data was investigated with the WIND spacecraft. Because WIND is a spin-stabilized spacecraft where the omni antennas are not aligned along the spin axis, the tracking data residuals could be processed to give an estimate of the rotational rate of the spacecraft. This procedure could be used for other missions as an additional means of quantifying the rotational status during critical support periods.

In summary, the availability of TDRS DOWD tracking data reduces the reliance on ground stations by providing an alternative source of tracking data via the SN. DOWD data could prove beneficial for missions that have significant gaps in ground station coverage if the spacecraft can radiate to two TDRS's simultaneously. (See References 2 and 7.)

Acknowledgments

The authors would like to acknowledge M. Maher, S. Hendry, and S. Ambarkedar of Allied Signal Technical Services Corporation (ATSC), and J. Jackson, and G. Marr of NASA for their contributions to the DOWD analysis and implementation and to the spin-rate analysis. This paper utilizes the WIND and NOAA-J TDRSS tracking data received as a result of the premission analysis and coordination work done by M. Maher and G. Marr. They would also like to acknowledge J. Cappellari of CSC for his technical review of the paper.

References

1. Goddard Space Flight Center, Flight Dynamics Division, Memorandum 56749-01, *Results of Differenced One-Way Doppler Tracking Data Test For the Wind and NOAA-J Spacecraft*, A. Olszewski and T. Wilcox (CSC), December 14, 1995
2. J. Jackson (GSFC), G. Marr (GSFC), and M. Maher (ATSC), *Tracking and Data Relay Satellite System (TDRSS) Support of User Spacecraft Without TDRSS Transponders*, Paper No. AAS 95-443, presented at the AAS/AIAA Astroynamics Specialist Conference, Halifax, Nova Scotia, August 14–17, 1995
3. Goddard Space Flight Center, X-572-80-26, *Tracking and Data Relay Satellite System (TDRSS) Range and Doppler Tracking System Observation Measurement and Modeling*, P. B. Phung, V. S. Guedeney, and J. Teles, September 1980
4. Goddard Space Flight Center, Flight Dynamics Division, FDD/552-89/001, *Goddard Trajectory Determination System (GTDS) Mathematical Theory, Revision 1*, A. C. Long and J. O. Cappellari, Jr. (CSC) and C. E. Velez and A. J. Fuchs (GSFC) [editors], prepared by Computer Sciences Corporation, July 1989
5. S. D. Hendry (ATSC), *Telemetry Down-link Doppler as an Attitude Sensor for Spin Stabilized Spacecraft*, presented at the GSFC FDD Flight Mechanics/Estimation Theory Symposium, Greenbelt, Maryland, May 16–18, 1995
6. Goddard Space Flight Center, Flight Dynamics Division, Memorandum 55708-02, *Post-TTI Orbit Determination Accuracy Study*, C. Cox, D. Oza, and J. Dibble (CSC), prepared by Computer Sciences Corporation, October 28, 1995
7. Goddard Space Flight Center, Flight Dynamics Division, Memorandum, *NOAA-J Launch Summary for Tracking and Data Relay Satellite System (TDRSS) Support*, T. Harrington (GSFC Code 553) to METSAT Mission Operations Manager, March 7, 1995

REPORT DOCUMENTATION PAGE

Form Approved
OMB No. 0704-0188

Public reporting burden for this collection of information is estimated to average 1 hour per response, including the time for reviewing instructions, searching existing data sources, gathering and maintaining the data needed, and completing and reviewing the collection of information. Send comments regarding this burden estimate or any other aspect of this collection of information, including suggestions for reducing this burden, to Washington Headquarters Services, Directorate for Information Operations and Reports, 1215 Jefferson Davis Highway, Suite 1204, Arlington, VA 22202-4302, and to the Office of Management and Budget, Paperwork Reduction Project (0704-0188), Washington, DC 20503.

1. AGENCY USE ONLY (Leave blank)		2. REPORT DATE May 1996	3. REPORT TYPE AND DATES COVERED Conference Publication/May 14-16, 1996	
4. TITLE AND SUBTITLE Flight Mechanics/Estimation Theory Symposium 1996			5. FUNDING NUMBERS Code 550	
6. AUTHOR(S) Scott Greatorex, Editor				
7. PERFORMING ORGANIZATION NAME(S) AND ADDRESS (ES) Goddard Space Flight Center Greenbelt, Maryland			8. PERFORMING ORGANIZATION REPORT NUMBER 96B00071	
9. SPONSORING / MONITORING AGENCY NAME(S) AND ADDRESS (ES) National Aeronautics and Space Administration Washington, DC 20546-0001			10. SPONSORING / MONITORING AGENCY REPORT NUMBER NASA CP-3333	
11. SUPPLEMENTARY NOTES S. Greatorex is Head, Attitude Section, Flight Dynamics Support Branch, Goddard Space Flight Center, Greenbelt, Maryland				
12a. DISTRIBUTION / AVAILABILITY STATEMENT Unclassified - Unlimited Subject Category 13 Availability: NASA CASI (301) 621-0390.			12b. DISTRIBUTION CODE	
13. ABSTRACT (Maximum 200 words) This conference publication includes 34 papers and abstracts presented at the Flight Mechanics/ Estimation Theory Symposium on May 14-16, 1996. Sponsored by the Flight Dynamics Division of Goddard Space Flight Center, this symposium featured technical papers on a wide range of issues related to orbit-attitude prediction, determination, and control; attitude sensor calibration; attitude determination error analysis; attitude dynamics; and orbit decay and maneuver strategy. Government, industry, and the academic community participated in the preparation and presentation of these papers.				
14. SUBJECT TERMS Flight Mechanics, Estimation Theory, Attitude Determination, Mission Analysis, Spacecraft Dynamics, Orbit Determination			15. NUMBER OF PAGES 416	
			16. PRICE CODE	
17. SECURITY CLASSIFICATION OF REPORT Unclassified	18. SECURITY CLASSIFICATION OF THIS PAGE Unclassified	19. SECURITY CLASSIFICATION OF ABSTRACT Unclassified	20. LIMITATION OF ABSTRACT UL	

National Aeronautics and
Space Administration

Goddard Space Flight Center
Greenbelt, Maryland 20771

Official Business
Penalty for Private Use, \$300

SPECIAL FORTH-CLASS RATE
POSTAGE & FEES PAID
NASA
PERMIT No. G27



POSTMASTER: If Undeliverable (Section 15
Postal Manual) Do Not Return